KATHOLIEKE UNIVERSITEIT LEUVEN
Faculty of Engineering
Department of Mechanical Engineering
Production engineering, Machine design and Automation (PMA)
Celestijnenlaan 300B, bus 2420
B-3001 Heverlee (Leuven)

Manufacturing by Combining Selective Laser Melting and Selective Laser Erosion / Laser Re-Melting

Jury:
Prof. dr. ir. P. Van Houtte, Chairman (preliminary defense)
Prof. dr. ir. Y. Willems, Chairman (public defense)
Prof. dr. ir. J.-P. Kruth, supervisor
Prof. dr. ir. B. Lauwers
Prof. dr. ir. J. Van Humbeeck
Prof. dr. ir. J. Duflou
Prof. Richard Hague
(University of Loughborough)

Dissertation presented in partial fulfillment of the requirements for the degree of Doctor in engineering

by
Evren YASA

2011D01

January 2011

D/2011/7515/3

ISBN 978-94-6018-297-6

ACKNOWLEDGEMENTS

It would not have been possible to write this doctoral thesis without the help and support of the kind people around me, to only some of whom it is possible to give particular mention here.

First, I would like to express my sincerest gratitude to my supervisor, Prof. Jean-Pierre Kruth for his help and guidance during my research and study at Catholic University of Leuven. His perpetual energy and enthusiasm in research had motivated all his advisees, including me. In addition, he was always accessible and willing to help his students with their research. As a result, research life became smooth and rewarding for me. Prof. Lauwers and Prof. Van Humbeeck also deserve special thanks as my advisor committee members.

All my colleagues in the research group of additive manufacturing at PMA made it a convivial place to work. In particular, I would like to thank Tom Craeghs (for all the fruitful discussions and openly sharing thoughts), Simon Van Bael (always being there when I needed his help), Jan Deckers (for sharing the same side for more than 2 years and for the good collaboration in research), Mohsen Badrossamay (for bringing an international environment in the office), Stijn Clijsters (for always being so positive), Lore Thijs (for bringing a 'female' perspective in the AM discussions) and Karolien Kempen (for making the team stronger) for the fruitful discussions and mutual work. My colleagues taught me that working is more than pleasure if you have good friendships in the office and lab. Moreover, for their contributions in my research, I would like to thank our neighbours from Dimensional Metrology and Quality research group, Dr. Philip Bleys, Nick Van Gestel, Frank Valkenhuyzen, Kim Kiekens, Dr. Haibin Zhao and Bart Boeckmans. It was also a big pleasure to work with my ex-colleagues, Dr. Martin Van Elsen, Dr. Jonas Vaerenbergh, Dr. Peter Mercelis and Dr. Ben Vandenbroucke who left PMA some time ago to experience the industrial taste of manufacturing. Moreover, I should thank Dr. Marleen Rombouts and Dr. Jan Luyten from VITO for their contributions to my thesis regarding material aspects.

I am also very thankful to our lab technicians at PMA and MTM, especially Dirk Bastiaensen and Eddy Smets. Without their support and willingness to help, this study would not come to reality.

From the financial point of view, I should acknowledge TUBTAK, (The Scientific and Technological Research Council of Turkey) for its financial support given in the beginning of my doctoral study under the program of "Ph.D. support program for students in foreign countries".

My deepest gratitude goes to my husband and my family. Starting a doctoral study together along with moving to a foreign country may not always be a very easy task but Tolga, being from the 'support team', was always there encouraging me and making life easier for me. Despite the distance, I felt the support of my lovely parents, my sister and brother-in-law all the time. I especially thank to my mother who always believed in me more than I deserved and stood behind all my decisions in my life. I cannot finish my thank word without mentioning the little lady who joined our family during my doctoral study. My niece, Pelin, makes me notice that time is passing by fast.

ABSTRACT

Selective Laser Melting (SLM) is a layer-wise material addition process that allows generating complex and functional three-dimensional parts by selectively melting successive layers of metal powder on top of each other, using the thermal energy of a focused and computer controlled laser beam. It provides various advantages compared to convectional subtractive production techniques. First of all, there is no need for a tool eliminating the burdensome pre-processing steps like tool path generation and other issues like tool wear compensation. The SLM process is also very suitable for mass customization and individualization of products. This makes the dental and medical parts suitable to be manufactured by SLM due to their complex geometry that has to fit to the amorphous anatomical shape and their strong individualization since every patient is different. On the other hand, it has some limitations preventing the process to be widely used in different industrial fields regarding various aspects. Most of these limitations are either inherent to layer manufacturing, e.g. stair-effect or related to high thermal gradients due to full melting and rapid solidification, e.g. residual stresses, insufficient micro machining capability. Furthermore, 1-2% porosity may be present in the SLM parts despite the full melting leading to detrimental influences on mechanical properties. Additive Manufacturing Group at K.U.Leuven mainly aims at improving the SLM process to a level enabling production of functional parts and tools with good part and material properties, even when very complex geometries are involved, in a competitive way. This thesis mainly targets to improve the SLM process regarding various aspects such as surface roughness, density, mechanical properties and precision and micro machining capability by employing secondary processes such as Selective Laser Erosion (SLE) and laser re-melting. In order to accomplish manufacturing by combining SLM with SLE or laser re-melting, the secondary processes were first studied in detail to understand the different mechanisms in those processes other than SLM. SLE and laser re-melting experiments were conducted on a Concept Laser M3 Linear machine with stainless steel.

SLE can be considered as the reverse operation of SLM due to its subtractive nature. In SLE, the energy of a high intensity laser beam, operated in the pulsed mode, is used to remove material by different mechanisms. SLE is a complex process since it involves different mechanisms like melting, evaporation, melt pool expulsion, plasma formation and recoil pressure. Therefore, the SLE process has been systematically studied in three steps: one-dimensional erosion (laser marking), two-dimensional erosion (laser milling) and three-dimensional erosion (laser engraving). The effects of most influential factors on the process outputs are explored and the dominant mechanisms behind these relations are investigated. The next step is to combine Selective Laser Melting and Selective Laser Erosion, exploring the advantages and limitations while processing AISI 316L stainless steel. Depending on the ultimate goal, combining these two processes can be done in several ways, i.e. applying SLE after every SLM layer either only on contours or on the whole layer area, or applying SLE after the SLM process is completed on the top surfaces to achieve a better in-layer accuracy and surface quality or to make small features. On the other hand, applying SLE during SLM brings some problems like ‘bark’ formation and longer production times.

Combining SLM and laser re-melting also provides a significant enhancement in the surface roughness, even more than what SLE provides. 90% improvement in the surface roughness is accomplished by applying laser re-melting on the top surfaces. Surface roughness of slanted surfaces are also improved by applying laser re-melting on those surfaces after the process is completed and the surrounding powder is blown away. Surface quality enhancement by laser re-melting also leads to a fully dense shell around the part. Since surface porosity is known to affect both the stress distribution and deformation of subsurface layers leading to subsurface crack formation and propagation, fully dense shell is especially important for applications requiring high wear resistance. Not only wear but also other surface properties such as thermal and electrical conductivity are highly dependent on the surface porosity. Applying laser re-melting after every layer improves the part density which is already very high even with only SLM (98-99%). Yet, laser re-melting assures that there is no aligned or irregular porosity formation and reduced the porosity in the parts. However, the process parameters in laser re-melting affect the results significantly and therefore should be selected properly. For an effective improvement in density, too high energy inputs to the substrate should be avoided by not selecting very low scan spacing or scan speed values. In this manner, the additional production time is kept to a minimum. The main disadvantage of laser re-melting is found to be the formation of elevated edges of the solidified material which deteriorates the dimensional accuracy and causes collisions with the hard scrapers of the coater. This phenomenon is not only seen in laser re-melted parts but also in all processes involving melt pools like SLM, EBM and LENS. The possible reasons causing this undesired effect are investigated and possible solutions are searched in the scope of this work, like post-fill scan strategy, applying different parameters for scanning contours, etc.

In the scope of this doctoral study, some other aspects of SLM are also studied without applying any secondary process. Firstly, optimization of a commonly used material in tooling applications, maraging steel 300 (18-Ni 300), is performed taking density, surface quality and productivity into account. This work showed how the optimum process parameters (in terms of productivity and density) may deviate from the ones recommended by SLM equipment vendors. For a more productive process, the scan speed, the layer thickness and the scan spacing are considered as the most important parameters if the maximum laser power is set as constant. Among these three factors, the layer thickness plays the most critical role since it determines the total time for laying powder together with total scanning time. The effect of different process parameters, namely the scan speed and layer thickness, is studied on the obtained density and surface roughness on two machines (a Concept Laser M3 Linear and an EOSINT M270) employing different laser sources. Moreover, the hardness of this material after SLM is tested in micro and macro scales. The effect of aging, which is standard for maraging steel 300, is tested by applying different aging times and temperatures to find out the best combination giving highest hardness improvement taking the post-processing time into account. 5 hours at 480°C is found out to give high hardness within a relatively short time. With aging tests, it is seen that keeping the specimens at a prolonged times in the heat treatment may deteriorate the material properties since it causes the precipitates to coarsen and austenite reversion. In the scope of this study, the constants in the expression derived from Avrami equation are determined for maraging steel 300 as a result of aging treatments done at different temperatures. Secondly, the results regarding Charpy impact toughness testing of this material together with other commonly used materials in SLM (AISI 316L stainless steel and Ti6Al4V) are reported. The experiments are carried out to test the influence of various factors on the toughness, such as roughness of SLM parts, building direction, heat treatments, etc. It is concluded that SLM may lower the impact toughness when compared to conventionally manufactured parts. It may be due to the nature of the process, e.g. un-molten powder particles, 1-2% porosity or undesired brittle phases due to high cooling rates for some materials like Ti6Al4V. However, this does not imply that all materials processed by SLM exhibit a lower toughness: for example, stainless steel processed on the EOSINT M270 exhibits a toughness as high as the one obtained by conventional techniques. In addition to the nature of SLM, process defects like a dirty laser window or improper selection of process parameters, can reduce the toughness dramatically. For repeatable mechanical properties, the material composition of the powder should also be well controlled and kept in a limited range; the process defects should be avoided and proper heat treatments to form desired ductile phases should be employed. Thirdly, island scanning is taken under investigation to test if this strategy can solve some limitations of SLM. The scan spacing factors between successive scan tracks and neighbouring sectors are studied to test how they influence the surface quality and the obtained part density. The scan spacing between successive scan tracks (a_1) is found to be optimal at 62% of the spot size at constant process parameters (a scan speed of 300 mm/s, a laser power of about 105 W and a spot size of 180 µm). Very low scan spacing factors, in other words very high overlaps, resulted in excessive energy intensity into the powder material resulting in irregular and big pores, whereas very high scan spacing factors resulted in unmelted regions between tracks resulting in aligned and excessive porosity. The effect of island offset (a_2) on density and surface quality is also studied revealing that the island scanning may result in poor connections between sectors which will deteriorate the mechanical properties significantly unless a suitable overlap is set. Finally, the island scanning is shown to reduce the residual stresses compared to common scan strategies, especially when the orientation of the scan tracks is set to 45°. The sector size does not play any significant role on the residual stresses.

NOMENCLATURE

Cr_e	Chromium equivalent [%]
Ni_e	Nickel equivalent [%]
$d(v, 0.1)$	Volume diameter where 10% of the distribution is below this value [µm]
$d(v, 0.9)$	Volume diameter where 90% of the distribution is below this value [µm]
$d(v, 0.5)$	Volume median diameter where 50% of the distribution is below this value [µm]
$d\gamma/dT$	Surface tension gradient [N/(m°C)]
w_g	Groove width [µm]
d_g	Groove depth [µm]
w_r	Rim width [µm]
d_r	Rim depth [µm]
d_t	Total depth of laser mark [µm]
w_{rr}	Rim distance [µm]
U_p	Overlap between laser pulses [%]
v	Scan speed [mm/s]
f	Pulse frequency [kHz]
d	Spot diameter of the laser beam [µm]
n_s	Number of erosion scan tracks
w_s	Width of simulation area in 2D erosion [mm]
l_s	Length of simulation area in 2D erosion [mm]
μ	Mean height in 3D roughness measurements
M	Number of points along x direction in 3D roughness measurements
N	Number of points along y direction in 3D roughness measurements
$z(x,y)$	Height measured at position (x,y) in 3D roughness measurements
t_{scan}	Needed time to scan one scan track [s]
t_{total}	Needed total time to scan the whole area [s]
MRR	Material removal rate [mm^3/s]
$d_{erosion}$	Depth of erosion per layer [µm]
D_0	Waist diameter of a Gaussian beam [µm]
R_0	Waist radius of a Gaussian beam [µm]
λ	Wavelength of the laser beam [µm]
M^2	Beam quality factor for the focusability
a_1	Scan spacing factor [%]
R_a, S_a	Average roughness without any cut-off filter[1] [µm]
R_q, S_q	RMS roughness without any cut-off filter[1] [µm]
R_t, R_y, S_y	Total roughness without any cut-off filter[1] [µm]
R_z, S_z	Averaged total roughness of 10 peaks without any cut-off filter[1] [µm]
S_{sk}	Skewness without any cut-off filter
S_{ds}	Density of summits without any cut-off filter [$peak/mm^2$]

[1] S_a and R_a are interchangeably used throughout the text and no cut-off filter was used unless otherwise is stated.

ℓ	Layer thickness [µm]
s	Step size to define the stair-effect [µm]
α_{inc}	Slope of a slanted surface [°]
h_e	Edge height [µm]
h_{p1}	Height of the first peak of the part [µm]
l_0	Mean value of the average profile of the top surface [µm]
e	Edge elevation [µm]
e_R	Relative edge elevation [%]
S_{max}	Maximum peak height on the average profile of the measured surface [µm]
$\mathbf{a_2}$	Island overlap factor [%]
$\mathbf{a_3}$	Island offset for elongation of scan tracks in the scanning direction [%]
ΔH	Increase in hardness [HV]
t	Aging time [h]
K	Temperature dependent rate constant in Avrami equation
n	Time exponent in Avrami equation
β	Orientation of the islands with respect to powder coating direction [°]
ℓ_i	Island length (and width) [µm]
α	Curling angle, an indicator for residual stresses in SLM parts [°]
α_{ref}	Curling angle for the reference part [°]

GLOSSARY

1D	One-dimensional
2D	Two-dimensional
3D	Three-dimensional
AM	Additive Manufacturing
AISI	American Iron and Steel Institute
ASTM	American Society for Testing and Materials
CAD	Computer Aided Design
CC	Chemi-capillary effect
CNC	Computer Numerically Controlled
CW	Continuous
DIN	Deutsches Institut für Normung (German Institute for Standardization)
DMLS	Direct Metal Laser Sintering
EBM	Electron Beam Melting
EDM	Electro Discharge Machining
EDX	Energy Dispersive X-Ray (Spectroscopy)
GIS	Geographic Information System
HIP	Hot Isostatic Pressing/Pressurized
HRC	Rockwell C Hardness
HV	Vickers Hardness
ILT	Institut für Lasertechnik (Institute for Laser Technique)
LSR	Laser Surface Re-melting
LENS™	Laser-engineered Net Shaping
MEMS	Micro Electro-Mechanical Systems
Nd:YAG	Neodymium Yttrium Aluminum Garnet
OM	Optical Microscopy
SEM	Scanning electron microscopy
SLE	Selective Laser Erosion
SLM	Selective Laser Melting
SLS	Selective Laser Sintering
SPIP™	Scanning Probe Image Processor
TC	Thermo-capillary effect
XRD	X-ray Diffraction

TABLE OF CONTENTS

LIST OF FIGURES

Chapter 3

Chapter 5

LIST OF TABLES

1 Introduction

This thesis mainly aims at helping to develop the Selective Laser Melting (SLM) process to a level enabling manufacturing of complex, customized and functional metallic parts in a competitive way. Although this is a very broad ambition, it can be fulfilled partially by overcoming some of the limitations of the process. In the scope of this thesis, the limitations were addressed among others by employing secondary laser processes during SLM such as laser re-melting and Selective Laser Erosion (SLE), or utilizing different solutions in the frame of SLM such as different scan strategies or process parameters. In this chapter, SLM is first introduced by explaining the technology and main limitations encountered in the process (§1.1). Secondly, the scientific objectives of the thesis are defined based on these limitations (§1.2). In the same section, the experimental equipment used for SLM and SLE is presented (§1.2.1) as well as the metallic materials applied in the scope of this thesis (§1.2.2).

1.1 Selective Laser Melting

Selective Laser Melting (SLM) is one of the layer additive manufacturing (AM) processes which refer to a group of technologies used for building physical models, prototypes, tooling components and functional parts, all from 3D computer-aided design (CAD) data or 3D scanning systems data, medical scanners, or other geometry representations. Besides SLM, AM also includes processes such as stereolithography, selective laser sintering, 3D printing, fused deposition modeling and electron beam melting. Different terms are used as synonyms of additive manufacturing, i.e. rapid manufacturing, freeform fabrication, layer manufacturing, direct digital manufacturing, etc. The technology in AM depends on building three-dimensional parts layer upon layer by adding liquid, powder, or sheet materials on top of each other to form objects. In principle, AM can reduce or eliminate many stages of the traditional supply chain, reducing lead times, inventory and supply chain transactions and logistics costs. Due to this fact, there has been a significant increase in the number of companies using AM for a broad range of application areas [1]. According to Wohlers Report 2009 [2], consumer products/ electronics is the leading industrial sector, followed by motor vehicles and medical/dental applications [3] (See Figure 1.1a). The “other” category includes a wide range of industries such as commercial marine products and non-consumer sporting goods. In addition, the following list shows for what purposes the industries use AM (see Figure 1.1b):

- Visual aids (for engineers, designers, architects, medical professionals, etc.)
- Presentation models (including architectural and GIS models)
- Functional models
- Fit and assembly
- Patterns for prototype tooling
- Patterns for metal castings
- Tooling components (created directly on an AM system)
- Direct part production (custom, short run, series production)
- Other

The basic principle of all additive manufacturing processes is the same although they employ different types of materials and binding mechanisms. After the creation of a three-dimensional computer model, it is sent to a computer program which slices the model into very thin layers and generates the necessary scanning paths for each layer. This information is then sent to the AM machine which builds the part layer by layer to completion (see Figure 1.2). Various additive

manufacturing processes uses the same working principle. Table 1.1 presents the aggregation state in which the material is processed (liquid/solid/powder/gas), how the layers are created and the phase change induced during the build of a three-dimensional part [4]. In the scope of this thesis, only one AM process is studied, i.e. Selective Laser Melting. SLM is also referred to as Direct Metal Laser Sintering and Laser Cusing by commercial machine manufacturers, i.e. by EOS and Concept Laser, respectively.

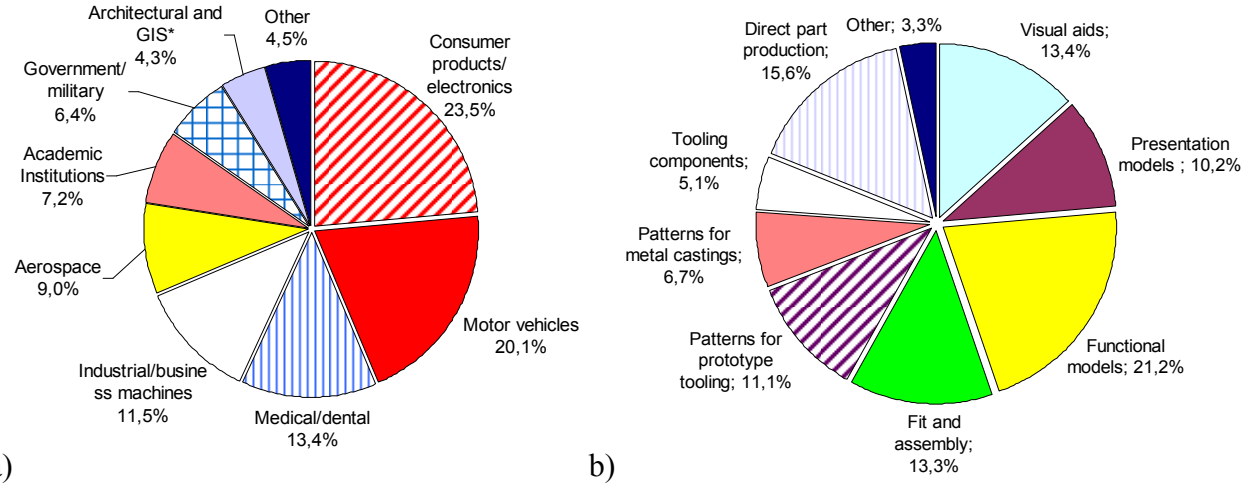

*GIS: Geographic Information System

Figure 1.1: The results of a survey made with 29 AM system manufacturers; and 65 service providers answering the question a) what industries they serve and b) how their customers use AM parts [2]

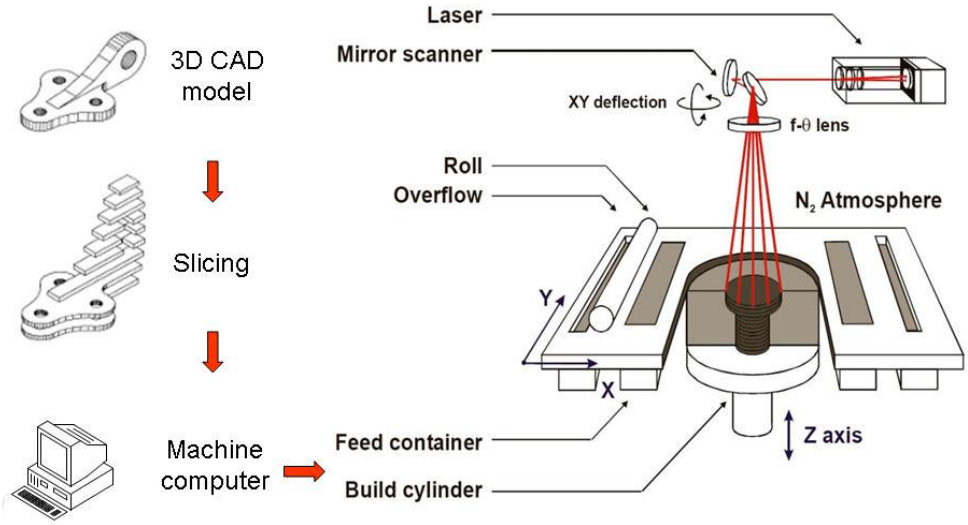

Figure 1.2: Overview of Selective Laser Melting from CAD file to the process

Selective Laser Melting and Selective Laser Sintering (SLS) processes are very similar. They both use the energy of a laser beam to bind powder particles to each other in a layer-wise manner. However, the laser energy density applied in SLM is higher than the one in SLS providing full melting. Moreover, no binder material or post-process like infiltration should be applied unlike some SLS variants. SLM/SLS can fabricate ceramic, metal and polymer parts. A typical configuration of an SLS or SLM machine is depicted in Figure 1.2. Most SLM machines are equipped with a Nd:YAG, fiber or disc laser for processing metals [5]. For selective laser melting, all commercial machines use a continuous laser beam which has a power output with little or no fluctuation in time [6]. However, at research level, some investigations are performed with pulsed laser sources [6-10]. The laser beam is deflected by a scanning system (galvano mirrors) which

controls the movement of the laser beam over the powder bed. The scan speed of the laser beam depends on the provided laser power and the material, typically ranging from 100 to 1000 mm/s. When the laser is absorbed by the powder particles, they heat up and bind to each other and to the previously melted layer underneath. In selective laser melting, the powder particles fully melt and parts with almost full density are fabricated whereas common SLS processes only induce partial melting [11]. After scanning a layer, the building platform moves one layer down and a coater (roller) puts a fresh layer of powder with a uniform thickness typically ranging from 20-80 μm for SLM. Then the laser beam scans the powder bed according to the current layer data. Since the process is accompanied by high thermal gradients, the parts are built on top of a thick base plate in order to prevent any significant part deformation. To lower the thermal stresses, different scanning strategies such as island scanning [12] can be applied as well as post-processing heat treatments [13]. Pre-heating the base plate may also help to solve the problem partially [14]. The process needs to be carried out under a protective atmosphere (nitrogen or argon depending on the material) to avoid oxidation of the material.

Table 1.1: Overview of principal additive manufacturing processes [4]

Supply	**Process**	**Lay-out**	**Layer creation technique**	**Phase change**	**Materials**
LIQUID	Stereolithography	Liquid resin in a vat	Liquid layer deposition	Photo-polymerization	Acrylates, epoxies, filled resins
	Fused Deposition Modeling	Material melted in a nozzle	Continuous extrusion and deposition	Solidification by cooling	Polymer (ABS, PA), wax, filled polymers, metals
	Ink-jet Printing	Droplets of melted material	Drop on demand deposition	Solidification by cooling	Polymers, wax
POWDER	Three-dimensional printing	Binder and powder in bed	Layer of powder and drop on demand deposition	No phase change of powder, solidification of binder by cooling/evaporation	Ceramics/metals/ polymers with binder
	Selective Laser Sintering / Melting	Powder in bed	Layer of powder	Sintering and melting by laser and re-solidification by cooling	Filled polymers, metals with binder, (pure) metals, ceramics (with metals)
	Laser Cladding	Powder delivery through nozzle	Continuous injection of powder	Laser melting and solidification by cooling	Metals
SOLID	Laminated Object Manufacturing (LOM)	Feeding, cutting and binding of sheets	Deposition of sheet material	No phase change of sheet, binding by phase change of solder, glue or otherwise.	Paper, polymer (foam), composites, metals, ceramics
GAS	Selective Laser Chemical Vapour Deposition	Gas flow in laser	Condensation of gas	Forming solid material from gas by chemical reaction	Metals, ceramics

Successful manufacturing of functional components with high density and good mechanical properties depends on the correct setting of process and material parameters. Regarding the process,

scan speed, laser type, laser power, scan spacing, scan strategy, spot size and remaining oxygen level in the chamber are very important parameters whereas laser absorptivity, conductivity, melting temperature, solidification range, specific heat, surface tension, wetting properties, viscosity can be listed as the most influential parameters regarding the material properties. Moreover, the powder characteristics such as apparent density, particle morphology, oxidation state at surface and particle size distribution affect the processability to a great extent in SLM [6]. Some problems encountered in the SLM process may be simply solved by changing some of these parameters which can be directly controlled.

The major problems encountered in SLM are mostly inherent to layer manufacturing such as stair-effect or related to high thermal gradients due to full melting and solidification to room temperature in a very short time. An important issue is the accuracy and surface quality of SLM parts which is lagging behind at competing technologies like CNC milling [5]. Density tests with SLM prove that the technology is able to produce near full dense objects with some remaining porosity. The reasons for gas bubble formation in SLM parts may be various: evaporation of elements with a high vapor pressure, trapped gas, chemical reaction, reduction in the solubility of the dissolved elements in the melt pool during cooling and solidification [6]. Generally the requirements for maximum density and high productivity contradict due to their implications on scan speed, scan spacing and layer thickness [14]. Although the achieved density is very high (98-99%) in SLM, reaching 100% density is still very difficult by merely changing process parameters or scanning strategies [5]. The mechanical properties of SLM parts highly depend on the density and microstructure of the parts. The microstructures obtained in SLM are a result of high cooling rates and layer-wise production. Generally, the mechanical properties are comparable to those of conventionally produced parts [14]. As previously mentioned, the thermal stresses may cause significant part deformations after SLM. During the process, the temperature difference between the material being melted and the remainder of the part together with the base plate and environmental temperature is very large. Therefore special measures need to be taken to avoid problems related to residual thermal stresses. An important limitation in SLM is the manufacturing of overhanging surfaces which are defined as a down-facing or bottom surface of an object that is supported by underlying loose powder material instead of any solidified material. Since the heat conductivity of the underlying powder bed is very small compared to bulk material, the conductive heat transport away from the melt pool is very little leading to overheating of the melt pool. The volume of the melt pool increases resulting in a melt track that is too wide and too deep [15, 16]. Then, the melt pool sinks in the loose powder by gravitation and capillary forces, leading to a very bad surface quality and geometrical deviations (see Figure 1.3a). Moreover, if the overhang angle is too small (<40º) and the overhang surface is large, warping may occur preventing any further layer deposition. To avoid this geometrical limitation, support structures can be designed and manufactured together with the part. The support structures can be easily removed after the SLM process by taking some simple measures such as thin connection points to the part and applying low energy inputs to generate weak support structures.

The stair stepping effect, which is inherent to all layered manufacturing processes, contributes to the surface roughness of the part and depends on the layer thickness as well as the inclination angle (Figure 1.3b). The minimum layer thickness is mainly limited by the particle size of the powder, while powder deposition, safety concerns and costs prevent to use very small powder size ranges (for common SLM processes the limit lies around 20-30 μm) [5]. The use of thin layers is not only beneficial for improving the stair stepping effect but also tends to result in better approximation of the desired geometry due to higher resolution. The process also suffers from lack of micro machining capability. The minimum feature size depends on the size of the melt pool which is greater than the spot size of the laser beam. The powder particles surrounding the melt pool are dragged and enlarge the melt pool which is also known as bobble effect [17]. In fact, this is also the reason of the elevated edges formed around the SLM parts, deteriorating the flatness and geometry

of the top surfaces (Figure 1.3c). One of the other main problems encountered in SLM is the long processing times reducing the productivity even though the group of additive manufacturing is sometimes referred to as 'Rapid Manufacturing'. The productivity in SLM is directly connected to the scan speed, layer thickness and speed of layer deposition. Current feasible scan speeds in SLS are much higher (10 m/s) than the ones in SLM due to lower energy requirement [14]. While there are a number of works regarding productivity issue in SLS in terms of either process improvement or even developing alternative faster processes [18-20], only a few published studies deal with SLM productivity enhancement. At ILT Aachen, an improvement from 1.2 mm^3/s to 6.5 mm^3/s building rate is reported by using a wider laser beam diameter along increasing laser power from 250 to 600 W [21]. Despite of such significant improvement in the productivity, process resolution is likely to be sacrificed because of expanded laser beam.

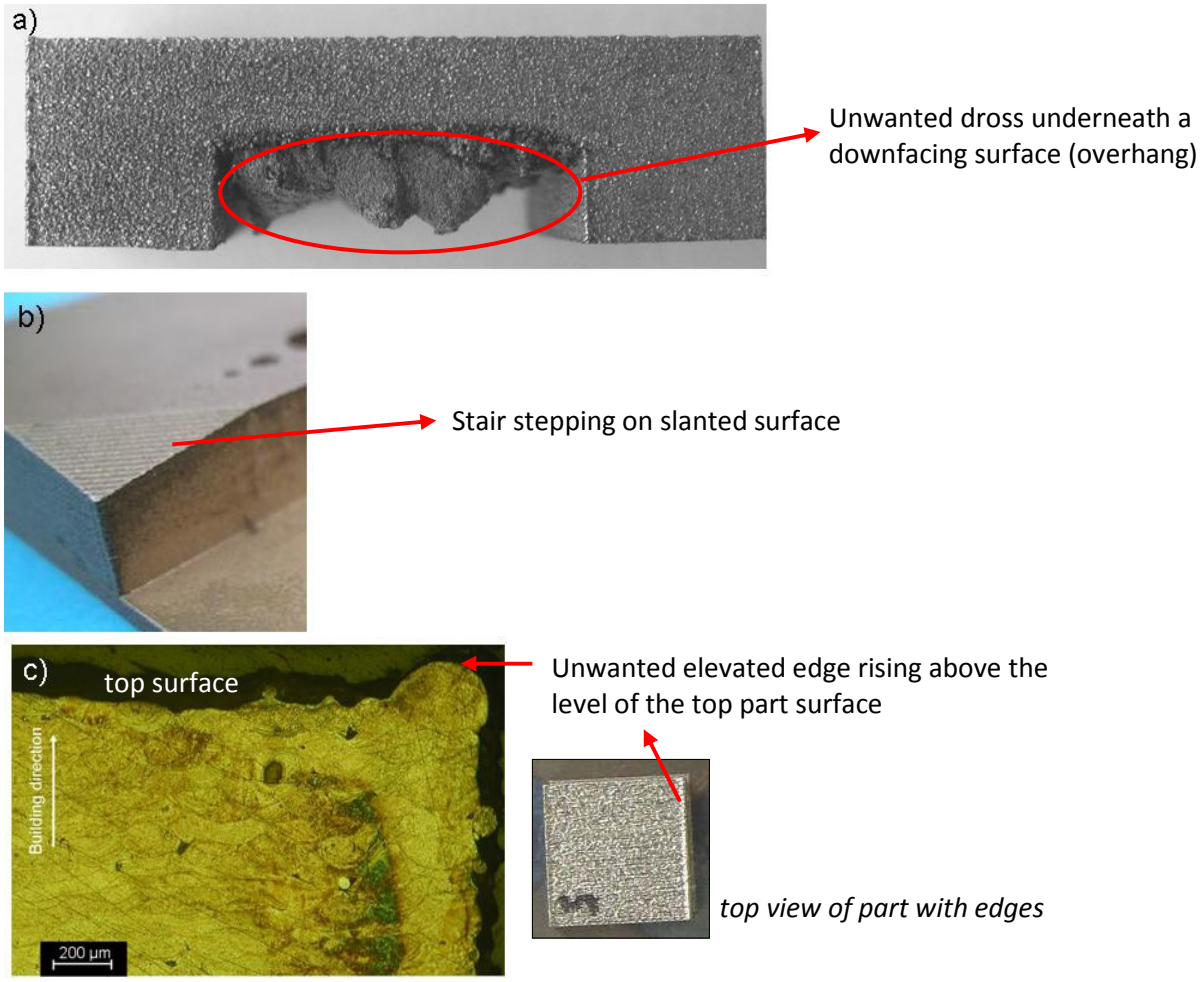

Figure 1.3: a) Excessive dross formation due to local overheating in an overhang structure b) stair stepping effect c) elevated edges formed during SLM

To sum up, Selective Laser Melting is an advantageous manufacturing process providing almost unlimited geometrical complexity, mass customization, possibility to process very hard materials, shortened design to cycle time and no need for a tool or die. However, this manufacturing technology is comparatively new, unlike well established conventional techniques like milling. Therefore, there is significant need for research to overcome the major problems explained above.

1.2 Scientific objectives and contents of this doctoral thesis

As mentioned before, this thesis mainly aims at improving the Selective Laser Melting (SLM) process to a level enabling manufacturing of complex, customized and functional metallic parts by employing secondary laser processes, such as Selective Laser Erosion and laser re-melting. The main targets aimed by this work are

- An improved micro machining capability to be able to make complex and customized parts with small features
- A better surface quality comparable to those of conventional techniques for improved surface properties
- A higher density to achieve better mechanical properties such as toughness and strength and a good understanding between mechanical properties and microstructural features
- A better building resolution to avoid undesired problems like stair stepping effect

In order to apply SLE in combination with SLM, the fundamentals of the erosion process are first studied regarding laser marking (one-dimensional laser erosion), laser milling (two-dimensional laser erosion) and laser engraving (three-dimensional laser erosion) and presented in the following chapter (Chapter 2). The third chapter reports about an experimental study of manufacturing by combining SLE and SLM. Chapter 4 deals with laser re-melting as employed during SLM to improve the surface quality and density removing 1-2% remaining porosity. Chapter 5 on Selective Laser Melting presents the work where SLM is taken as the initial process, mostly without using any complimentary process, although laser re-melting has been used in some investigation to further improve the properties of SLM parts in terms of density, toughness, hardness, etc. This chapter summarizes the work done to improve or investigate the part and material properties of metallic SLM parts.

1.2.1 SLM/SLE Equipment

Most of the SLM/SLE experiments in the scope of this thesis were conducted on a Concept Laser M3 Linear machine. However, some experiments with Ti6Al4V were conducted on an LM1 machine which is an in-house developed machine of K.U.Leuven.

a. Concept Laser M3 Linear

For most of the SLM and SLE experiments carried out in the scope of this thesis, a Concept Laser M3 Linear Machine was used. It is a SLM machine employing a ~100 W diode pumped Nd:YAG laser from Rofin Sinar with a wavelength of 1.064 μm. There are two available aperture settings yielding a spot size ($\emptyset_{1/e^2}$) of 70 μm (small aperture) and 130 μm (big aperture) on the work plane.

The beam characterization of the laser for small and big apertures has been analyzed with a Primes FocusMonitor system (see Figure 1.4a) which is capable of measuring the beam radius, beam position in the focal region, the caustic and the beam propagation ratio (M^2). As shown in Figure 1.4b, the measurement of the power density is done by a rotating pinhole scanning through the beam cross-section at different height. The pinhole diverts a small part of the radiation towards two mirrors that lead the signal to a detector. The pinhole can be moved automatically in the vertical direction to scan along the focal region and to record the beam profile in 3D. On the Concept Laser M3 machine, measurements were conducted inside the process chamber that the laser beam passed through many optical components. Figure 1.5 and Figure 1.6 depict the beam profile measurement results for the big and small apertures respectively. The radius of the beam (x-axis) at different locations along the building axis (y-axis) is depicted. A summary of the information obtained from these measurements is given in Table 1.2.

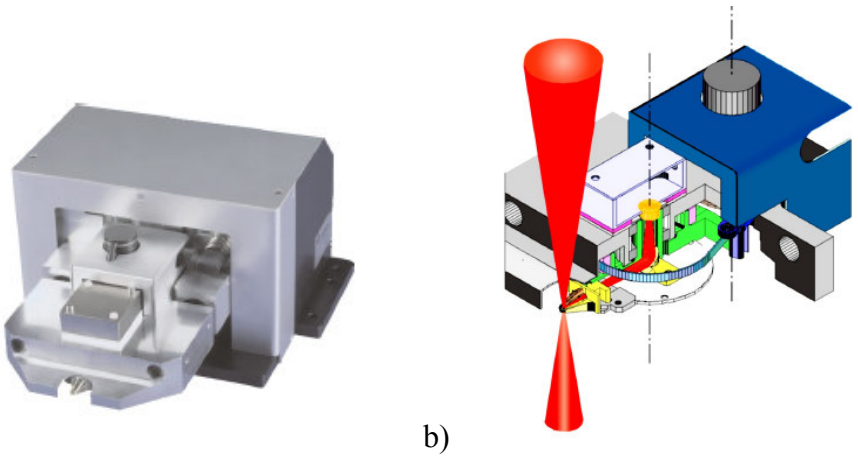

a) b)

Figure 1.4: a) FocusMonitor system from Primes b) working principle of the system

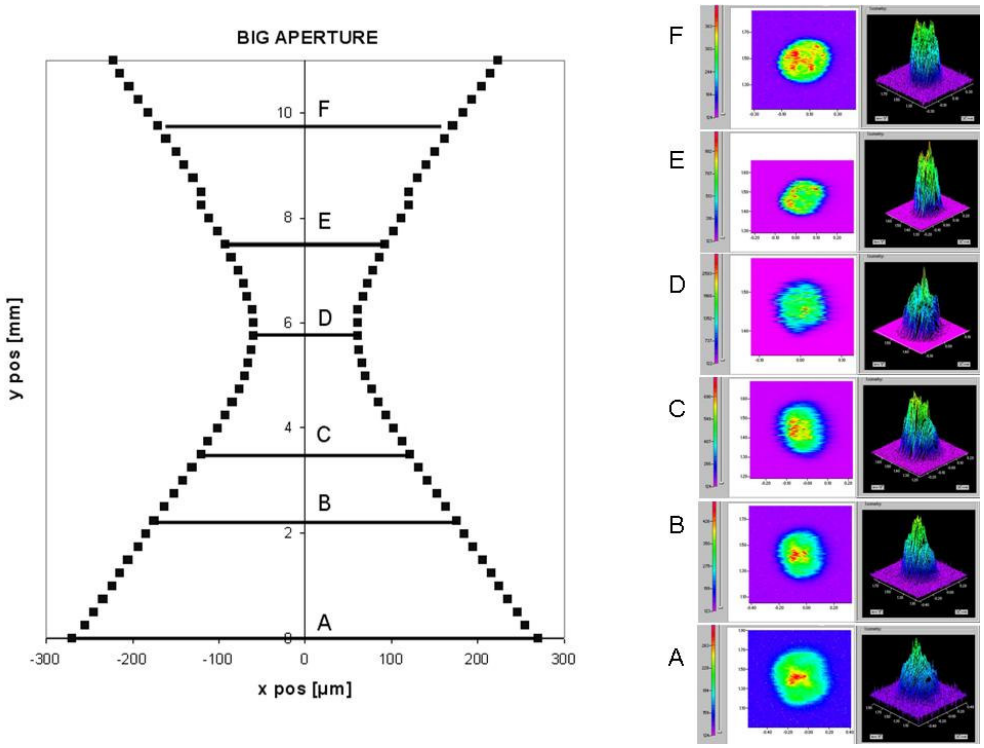

Figure 1.5: Beam profile measurements at different positions along the building axis, beam diameter $\emptyset_{1/e^2}$ values are indicated along y-axis for the big aperture on a Concept Laser M3 Linear machine with a diode pumped Nd:YAG laser

The aperture selection does not only affect the spot size but also varies the average power brought to the substrate. The average power is adjusted by changing the pump current. The relationship can be assumed to be linear (See Figure 2.34). However the power that corresponds to a pump current depends on the lifetime of a laser. As the laser ages (due to break down of diodes in time), more current is needed to provide the same laser power. The laser can also operate in Q-switching pulsed mode. This mode is used for laser erosion and for combining SLM and SLE in the scope of this thesis. Q-switching is a technique that is used to produce laser outputs of higher power (of the order of megawatts) and shorter duration (of the order of nanoseconds). To explain the principle behind Q-switching, a laser cavity in which a shutter (mechanical, electro-optic, acousto-optic or passive [22]) is placed in front of one of the mirrors should be considered. When the shutter is closed, the light energy cannot reach the second mirror and is reflected back into the cavity. As pumping of the laser continues, the population inversion keeps building up (see Figure 1.7). When a significantly high value of population inversion is achieved, the shutter is suddenly opened. The

high energy accumulated as a result of the large difference between the instantaneous and threshold population inversion is then released as an intense beam of short duration.

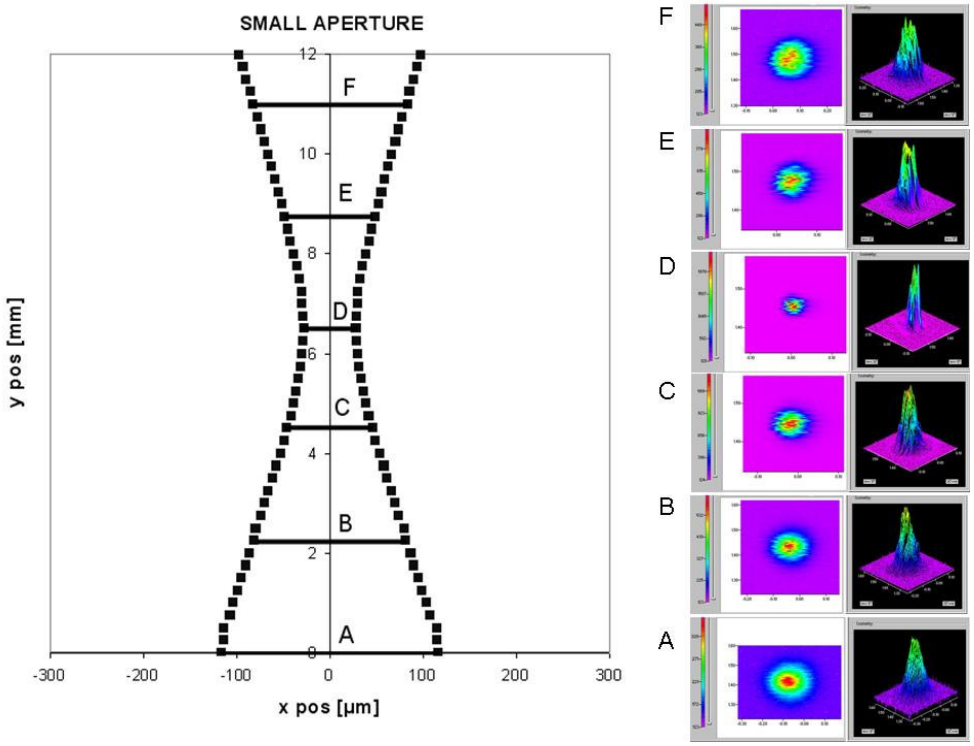

Figure 1.6: Beam profile measurements at different positions along the building axis, beam diameter $Ø_{1/e^2}$ values are indicated along y-axis for the small aperture on a Concept Laser M3 Linear machine with a diode pumped Nd:YAG laser

Table 1.2: Measured characteristics of the Nd:YAG laser equipping the Concept Laser M3

		small	***big***
Beam radius ($Ø_{1/e^2}$)	µm	35	65
Beam quality factor *K*		0.57	0.11
Beam quality M^2		1.75	9.09
Rayleigh length	mm	1.918	1.273
Beam parameter product *BPP*	mm.mrad	0.595	3.035
Divergence angle	mrad	35.2	97.6

The scanner system, one of the important machine components, deflects the laser beam in a controlled manner in two dimensions via a pair of rotating galvano mirrors (see Figure 1.2). Laser scan speeds on this machine can vary up to 5000 mm/s. A general view of the Concept Laser M3 Linear machine is depicted in Figure 1.8a. One of the important components of the machine is the 'cusing module' which can exchangeably be used with the erosion module (Figure 1.8b and c). The term 'cusing' comes from the fact that Concept Laser uses the term LaserCUSING for the same process which other companies refer to as 'Selective Laser Melting' or 'Direct Metal Laser Sintering'. Cusing is a word made by combining concept and fusing of the powder particles. The cusing module can be moved out of the machine before and after the build for handling the powder and the produced parts. The build platform is 250 mm x 250 mm square. In this study, the parts were produced on a smaller steel base plate (100 mm x 100 mm). The build platform and the powder deposition system are integrated in the cusing module. The powder deposition system has a translating coater unit with two scrapers (or blades), one on each side, making it possible to deposit

powder from left to right or from right to left. However, it is also possible to specify that the powder deposition should always occur from the same side. The excessive powder staying between coater blades falls in the overflow reservoir after the deposition. A powerful motor drives the coater to make sure that the coater is not stuck when one of the scrapers collide with an irregularity on the laser melted surface. To avoid severe collisions with the coater, the parts are located on the base plate in a rotated position so that no large edges are perpendicular to the scraper's moving direction. The 'erosion module', shown in Figure 1.8c, can be interchanged with the cusing module for applications requiring only laser erosion (i.e. only subtractive manufacturing with no additive laser melting). The erosion module has a bigger process platform compared to the cusing module since there is no place required for powder storage. The erosion module can move in the vertical direction to provide that the laser beam stays in focus during multi-layer SLE.

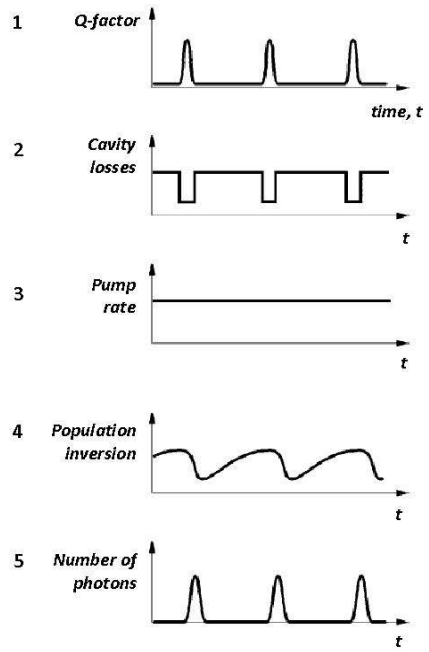

Figure 1.7: Time evolution of the Q-switching process for continuous pulsing [22]

a) 

b) 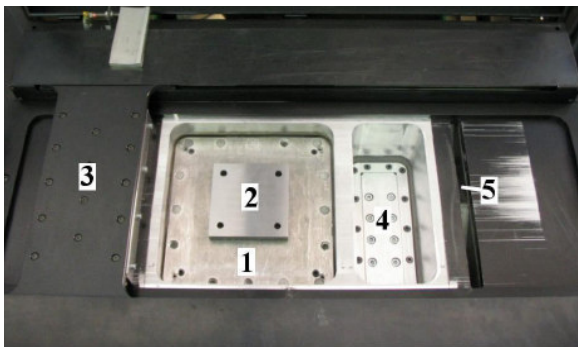

c) 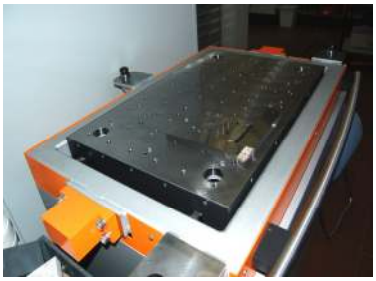

Figure 1.8: a) Concept Laser M3 Linear machine b) cusing module used for SLM (1) powder platform (2) base plate (3) coater (4) powder platform (5) entrance to overflow bottles; c) erosion module used for subtractive laser machining

Selective Laser Melting experiments are conducted under a protective atmosphere, either in argon or nitrogen depending on the material processed. The SLM/SLE experiments in this thesis are done only with steel on the Concept Laser M3 Linear machine. Therefore, only nitrogen gas is used during the SLM experiments. Most of the SLE experiments were conducted with the erosion module which makes it impossible to flush nitrogen/argon in the chamber due to software limitations. Therefore most of the SLE tests were done under ambient air. For SLM tests, after the base plate and powder are prepared, the module is placed in the machine and the protective gas (N_2 or Ar) is flushed into the chamber with a high flow rate (pre-flushing) so that very little amount of oxygen remains (<1% for steels and <0.1% for titanium alloys). During the SLM build, a lower flow of gas is sufficient to keep the oxygen level at low values to avoid oxidation. The pressure inside the process chamber is, during pre-flushing and processing, slightly above atmospheric pressure.

b. K.U.Leuven Laser Melting (LM1) Machine

This machine, shown in Figure 1.9, was developed at the Mechanical Engineering Department of K.U.Leuven [16, 23,]. This machine has some particular features that commercial machines lack. First of all, the build platform is positioned into a vacuum chamber which can be evacuated until a pressure of 2 mbar. Before the process starts, the process chamber is evacuated and flushed with the protective gas three times. During the process, the pressure in the chamber is about 600 mbar and there is no continuous gas flow. The LM1 machine therefore consumes very little protective gas compared to commercial machines. Moreover, this machine is equipped with a monitoring and feedback control system applying a photodiode and a high-speed CMOS camera for observing the melt pool during the process and for control system.

a) 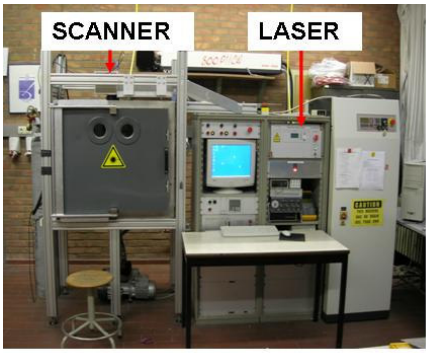

b) 

Figure 1.9: a) A general overview of K.U.Leuven LM1 machine; b) building platform and powder deposition system

The LM1 machine employs a Yb:YAG fibre laser with a wavelength of 1070 nm. This laser can only be operated in continuous mode. The maximum laser output power in continuous mode is 300 W and the standard beam diameter $Ø_{1/e^2}$ is about 50 µm.

1.2.2 Powder Materials

The powder materials that were used in this work for SLM experiments are mainly AISI 316L stainless steel, maraging steel 300 (18Ni-300) and Ti6Al4V. The following sub-sections give some explanation about these materials and about the tested powder characteristics.

a. AISI 316L Stainless Steel

Stainless steels are iron-base alloys with at least 10.5% Cr which gives their stainless characteristic through the formation of an invisible and adherent chromium-rich oxide surface film [24]. Stainless steels are commonly divided into five groups one of which is the austenitic stainless steels with a face-centered cubic (fcc) structure. These steels are non-magnetic in the annealed condition and can

be hardened by cold working. The *3xx* types contain larger amounts of nickel and up to 2% Mn. AISI 316L belongs to this group with a material composition: 16-18.5% Cr, 10-14% Ni, 2-3% Mo, <2% Mn, <1% Si, <0.045% P, a very low carbon content (<0.03% C) and the balances being iron. The austenitic structure gives this material extremely good toughness results even at cryogenic temperatures [25]. Typical applications for this material include food preparation equipment, pharmaceuticals, marine applications, fasteners and some medical tools.

Two different powders with different particle size distributions, but from the same supplier (Concept Laser GmbH), have been used. The SEM images from coarse and fine powders are presented in Figure 1.10. The particle size distributions are also given in Figure 1.11a and b for coarse and fine powders, respectively. As evident from two figures, the fine powder has very small particles ranging from 2 to 50 μm, whereas the coarse powder covers a higher particle size range (12-400 μm although the volume percentage for the range higher than 120 μm is small). The average diameter is 17 and 42 μm for the fine and coarse powders, respectively. The comparison between fine and coarse powder particles regarding the achieved density and surface quality of produced SLM parts can be found in [14] which is also presented in Appendix 1.

a) 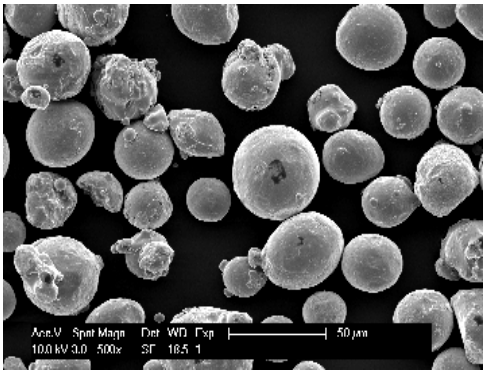 b) 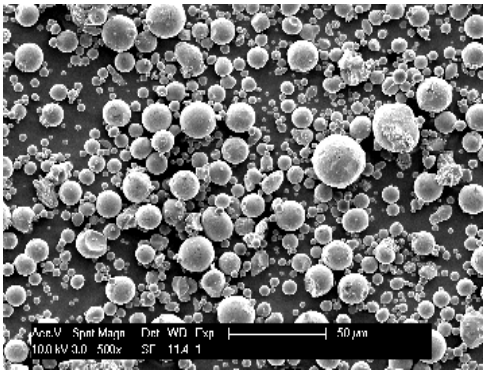

Figure 1.10: SEM images of AISI 316L powders from Concept Laser (CL20ES) a) coarse powder b) fine powder

One significant difference between wrought and cast stainless steels is the microstructure of cast austenitic stainless steels. There is almost always a small amount of δ-ferrite (high temperature ferrite) present in austenitic stainless steel castings, in contrast to the single-phase austenitic structure of the wrought alloys [24]. Depending on the nickel, chromium and carbon contents, cast austenitic alloys have 5-20% δ-ferrite distributed in discontinuous pools throughout the matrix due to high cooling rates. Selective Laser Melting, like casting process, involves high temperatures and high cooling rates resulting in a similar microstructure, with high temperature delta ferrite in the austenitic matrix. Therefore, the composition of the powder used in SLM is very important in determining the final microstructure. The main reason for nickel addition to stainless steels is to promote austenite structure and generally increases ductility and toughness, whereas chromium promotes ferrite formation increasing the corrosion resistance and resistance to oxidation at high temperatures. Therefore the ratio of austenite and ferrite promoting alloying elements is important. The relationship between the ferrite in volume percentage and the equivalent Cr_e / Ni_e ratio (see Eq. 1.1) is shown in Figure 1.12. Although the composition of the powder stays in the standard composition of AISI 316L, it is possible that a high amount of δ-ferrite is formed during the SLM process leading to a weakly magnetic part with different mechanical properties. Delta ferrite has especially a detrimental effect on impact toughness. The influence of ferrite becomes more severe for applications requiring high temperature performance.

$$\begin{aligned} Cr_e &= \%Cr + 1.5(\%Si) + 1.4(\%Mo) + \%Nb - 4.99 \\ Ni_e &= \%Ni + 30(\%C) + 0.5(\%Mn) + 26(\%N - 0.02) + 2.77 \end{aligned} \tag{1.1}$$

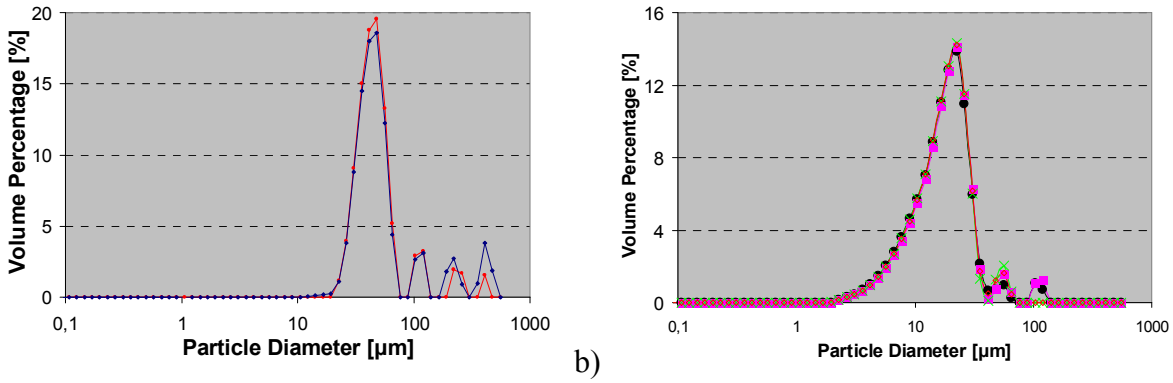

Figure 1.11: Particle size distributions of AISI 316L powders from Concept Laser (CL20ES) a) coarse powder b) fine powder

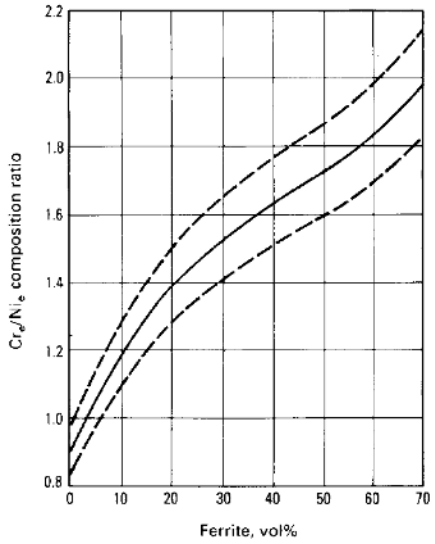

Figure 1.12: Schoefer diagram for estimating the ferrite content of steel castings where dashed lines denote scatter bands caused by uncertainty of the chemical analysis of individual elements [24]

Normally, AISI 316L is a material that is commonly used in SLM without any heat treatment. However, as explained above, slight changes in the composition of this material might lead to the formation of ferrite due to the nature of the SLM process as in casting. Therefore, the mechanical test specimens from AISI 316L are recommended to be heat treated (full annealing -2 hours at 1095°C) to provide that delta ferrite is mostly transferred to austenite when the mechanical properties are tested to see the effect of different scan strategies, machines or powder suppliers. This is also a standard procedure for cast equivalent of AISI 316L. Throughout the text, if there is any, the type and conditions of the heat treatments are given for all materials, including AISI 316L. Some mechanical properties of wrought AISI 316L is given in Table 1.3.

Table 1.3: Mechanical properties of wrought AISI 316L [24]

Condition	**Product form**	**Tensile strength [MPa]**	**0,2% Yield strength [MPa]**	**Elongation [%]**	**Reduction in area [%]**
Annealed	wire	480	170	35	50
Hot finished and annealed	bar	480	170	40	50
Cold finished and annealed	bar	480	170	30	40

b. Maraging Steel 300

Maraging steels are a special class of high-strength steels that differ from conventional steels in that they are hardened by a metallurgical reaction that does not involve carbon [24]. Maraging steels are hardened by the precipitation of intermetallic compounds at temperatures about 480 ºC. The term 'maraging' denotes the age hardening of a low carbon, iron-nickel lath martensite matrix. One of the important advantages of this material is the dimensional stability during age hardening. Therefore, it is a perfect material to be easily machined in the soft condition and then hardened with a minimum distortion. Moreover, the maraging steels are good in terms of weldability and fracture toughness compared to other high-strength steels. Mainly maraging steels are used for two application areas: aircraft and aerospace in which superior mechanical properties and weldability of maraging steels are the most important features, and secondly in tooling applications which require superior machinability [24].

Maraging steel 300, which is also known as 18Ni(300), has the following material composition: 18% Ni, 5% Mo, 9% Co, 0.7% Ti, 0.1% Al and Fe (balance). Table 1.4 shows the mechanical properties of this material produced by conventional techniques in the heat treated condition (solution treatment 1 hour at 820 °C followed by aging 3 hours at 480 °C) [24].

Table 1.4: Mechanical properties of 18Ni(300) [24]

	18Ni(300)
Yield Strength (0.2% offset)	2000 Mpa
Ultimate Tensile Strength	2050 Mpa
Elongation	7%
Reduction of Area	40%

Some of the experiments in this thesis were conducted with 18Ni(300) material. There were mainly three suppliers: Concept Laser GmbH selling this material as CL50WS hot work tool steel, LPW which is a UK company offering powder for various applications [27] and EOS selling the material with a commercial name of MS1. All those powders are produced by gas-atomization and have almost the same composition but the particle size distribution changes. A SEM image and particle size distribution of the powder from Concept Laser (CL50WS) are given in Figure 1.13 whereas Figure 1.14 depicts the same properties of the powder from EOS (MS1). Both powders bear spherical or near-spherical morphology.

a) 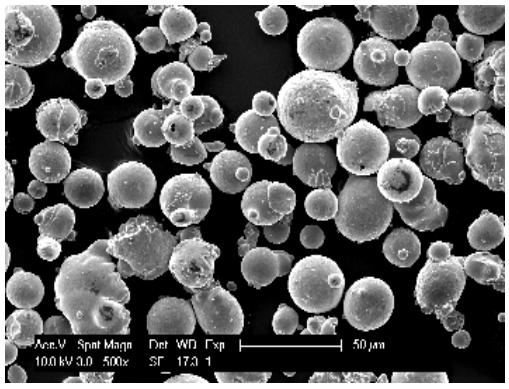

b) 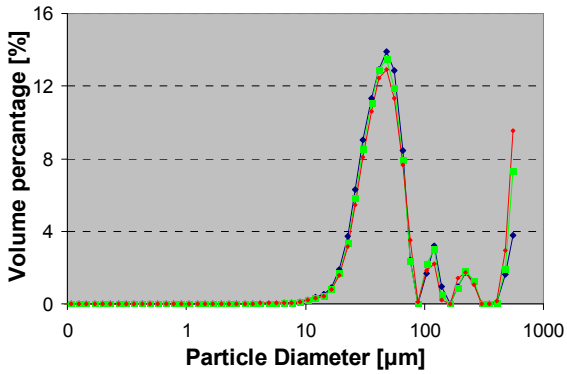

Figure 1.13: a) SEM image of 18Ni (300) powder from Concept Laser GmbH b) particle size distribution of the same powder

The average diameter for MS1 is 35 µm, whereas it is equal to 43 µm for CL50WS. Moreover, the particle size distribution for MS1 exhibits a sharper peak and less number of particles in the high particle diameter range (>50 µm). The powder from LPW has also been investigated under SEM. Some SEM images are given in Figure 1.15 in unpolished and polished conditions. The LPW powder bears the same morphology with the other two powders (MS1 and CL50WS) with a particle

size ranging in between 15 and 45 µm. Figure 1.15b shows almost no porosity inside the particles, eliminating one of the important factors which cause porosity in SLM. Table 1.5 shows the comparison of MS1 and CL50WS in terms of particle size distribution. Due to some reasons, different powders were used for different experiments. For example, the powder from EOS was only used at Layerwise on an EOSINT M270 machine for the production of Charpy specimens from maraging steel 300 (see §5.2.3c). Throughout the thesis, the powder supplier of this material is mentioned wherever needed.

a) 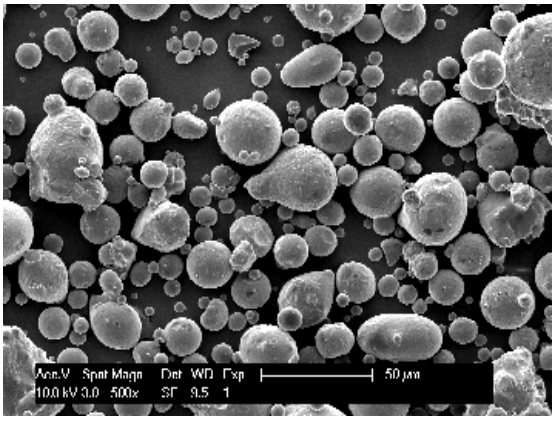

b) 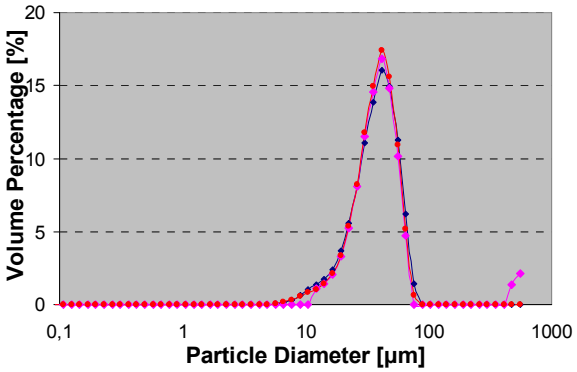

Figure 1.14: a) SEM image of 18Ni (300) powder from EOS b) particle size distribution of the same powder

a) 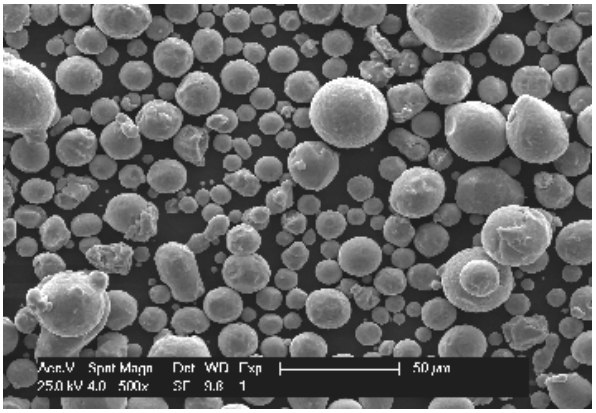

b) 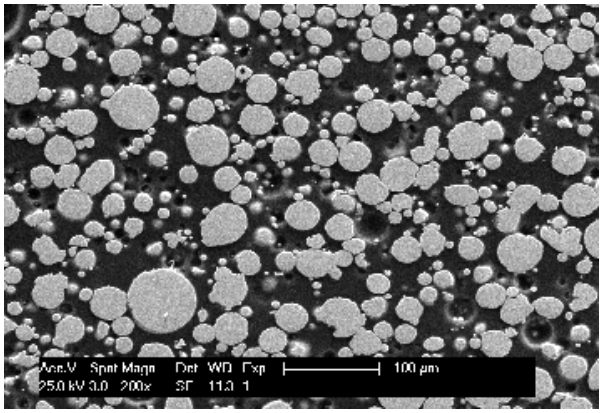

Figure 1.15: SEM images of LPW powder a) without polishing b) with polishing

Table 1.5: Particle size comparison of MS1 and CL50WS

	d(v,0.1)	***d(v,0.5)***	***d(v,0.9)***	
MS1 (EOS)	19	35	53	µm
CL50WS (Concept Laser)	24.4	43.7	275	µm

c. Ti6Al4V

Titanium and its alloys are used for many applications because of their high strength to weight ratio, outstanding corrosion resistance and biocompatibility making it a perfect candidate for medical, automotive, chemistry and aerospace industries. Regarding SLM, the disadvantages of titanium are its high reactivity with oxygen at elevated temperatures and high melting temperature. Ti6Al4V is the mostly used titanium alloy [26]. It features good machinability and mechanical properties and offers a good solution for weight reduction applications. The chemical composition and mechanical properties for this material is given in Table 1.6 and Table 1.7 respectively, for the cast and wrought cases.

The Ti6Al4V powder was characterized at the Department of Metallurgy and Materials Engineering of K.U.Leuven. Figure 1.16a depicts a SEM image of the powder which bears spherical morphology. The particle size distribution gives the relative number of particles (in volume percentage) for different particle size intervals as shown in Figure 1.16b. As a result of 6 measurements, the average particle size, d(v,0.5), is 34 µm whereas d(v,0.1) and d(v,0.9) are 16 and 49 µm, respectively. Smaller particles are beneficial since they fill voids between larger particles leading to higher packing density.

Table 1.6: Chemical composition of Ti6Al4V for cast and wrought material [26]

	Ti6Al4V (cast, ASTM F1108)	**Ti6Al4V (wrought, ASTM F1472)**
Aluminum, Al	5.5-6.75%	5.5-6.75%
Vanadium, V	4%	4%
Carbon, C	0.03%	<0.08%
Iron, Fe	0.10%	<0.3%
Oxygen, O	0.15%	<0.2%
Nitrogen, N	0.01%	<0.05%
Hydrogen, H	0.003%	<0.015%
Titanium, Ti	Balance	Balance

Table 1.7: Mechanical properties of Ti6Al4V for cast and wrought material [26]

	Ti6Al4V (cast, ASTM F1108)	**Ti6Al4V (wrought, ASTM F1472)**
Yield Strength (Rp, 0.2)	758 MPa	860 MPa
Ultimate Tensile Strength (0.2% offset)	860 MPa	930 MPa
Elongation	14%	>10%
Reduction of Area	40%	>25%

a) 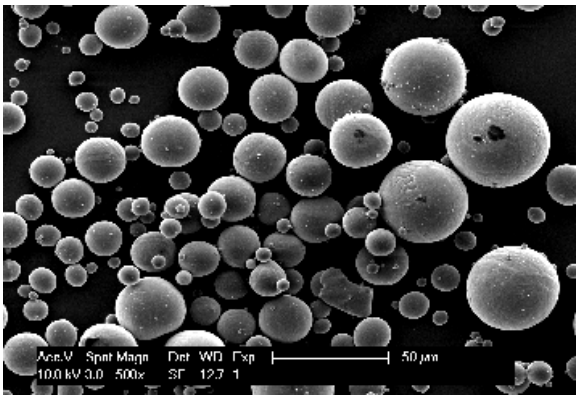

b) 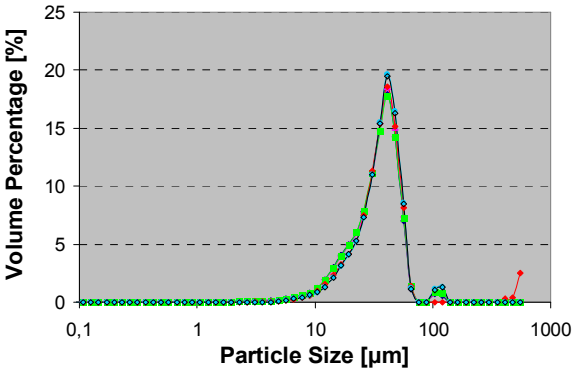

Figure 1.16: a) SEM image of Ti6Al4V powder used in this study b) the powder particle size distribution measured by Coulter analysis

2 Selective Laser Erosion

Unlike Selective Laser Melting (SLM), Selective Laser Erosion (SLE) is a subtractive layer manufacturing technique. In the scope of this thesis, it is used as a complementary process to improve an additive layer manufacturing process, i.e. SLM, in terms of various aspects. In order to combine SLM and SLE, there is a need of fundamental understanding of the relations between the process inputs and outputs for SLE. Therefore, a systematic investigation of these relations is conducted for one dimensional erosion (laser marking), two-dimensional erosion (laser milling) and three-dimensional erosion (laser engraving). Although the number of parameters that may influence the SLE process is quite high, only the most significant parameters which can be directly or easily changed by the machine operator are taken under investigation in the scope of this work. The relations between the process inputs and outputs help to understand the dominant physical phenomena occurring in SLE leading to proper selection of process inputs when combining SLE and SLM.

The first section in this chapter is about one-dimensional erosion, in other words laser marking (§2.1). It reports about the evolution of mark profiles obtained with different process parameters and discussed the factors behind it such as surface tension, recoil pressure, oxidation and porosity formation. The second section tells about laser milling (two-dimensional erosion) and presents the relations between several input parameters and outputs (mainly depth of erosion and surface quality) in addition to combining parameters for topography modelling (§2.2). Moreover, it presents the process window study to find out optimal process parameters (scan speed and laser power) for a good erosion regime. The last section summarizes the work done in the field of three-dimensional erosion to demonstrate the capability (§2.3).

2.1 One-Dimensional Erosion (Laser Marking)

2.1.1 Introduction and Literature Review

Laser marking is used here as a first step to study laser erosion and its applicability in combination to Selective Laser Melting (SLM). Several studies have been devoted to laser marking. This is because laser marking is gaining importance as product liability and environmental concerns call for product recognition and identification. As a result, the marking of products is rapidly gaining importance while quality, flexibility, speed and production costs are considered as necessary factors for the selection of a suitable marking method [28]. Laser marking is a relatively new method as compared to other marking technologies such as ink-marking, mechanical engraving and electro-chemical methods [29]. Yet, it has many advantages compared to other marking techniques: free choice of geometry to be marked, non-contact, fast, and clean processing [30]. More advantages lie in the range of materials that can be marked (metals, polymers, ceramics, glass, organic materials such as wood, paper, etc.), the ease of changing marked geometries through changes in the software, the quality of the mark and the low environmental impact. The process involves no additional handling in the moulding shop, no use of inks and no pre-treatment of the parts. Thus, laser marking is a suitable solution when there is a need for an indelible high-quality mark. Around 90% of industrial laser marking is carried out for product identification in industries including micro electronics, automotive and aerospace [31] (See Figure 2.1).

The laser marking process is mostly applied to satisfy the needs of traceability and product identification. It is promising for marking parts produced by laser Rapid Manufacturing (RM), since the same laser may be used for the main manufacturing process as well as the subsequent marking of the product. For instance; once dental implants become widely accepted to be produced in serial production by Selective Laser Melting (SLM), the identification of each individual part will be very

important to distinguish the implant of one customer from others. It may be necessary to put the name of the patient, the doctor or the clinic's name, operation date, etc. on the product. In a reverse way, marking might soon become a major requirement in AM to ensure high reliability: in case of a break down of a part, it is necessary to know on which machine and under which conditions and when the part was produced. A quick and easy method to satisfy this need in AM is the laser marking of the necessary information on the part as a final step even before it is removed from the machine.

Figure 2.1: Marked samples for different applications a) school logo on an egg shell [32] b) individualization of jewels [33] c) a metallic component [34]

The competing methods of marking are ink jet printing, metal stamping, pre-printed labels, chemical etching and other processes with high consumable costs or less clean operations. Laser marking is a clean process since no paints, inks or acids or involved. There is thus no need to dispose of toxic solvents and no risk of product contamination. The initial cost of a laser marker system is high, but the running costs are less compared to other marking methods. Pre-printed labels and metal stamping are not flexible processes. Permanence and legibility of the mark depends on the nature and topography of the substrate in the ink jet printing. Chemical etching provides marks of high permanence, but is relatively slow and brings environmental impact of chemicals. On the other hand, ink jet printing is superior to laser marking when organic products that cannot be marked by heat are involved. Laser marking competes when high volumes are to be marked on substrate in different geometry and properties [31].

Marking cannot be categorized as a process that only depends on heating, melting or vaporization since various thermal mechanisms, i.e. foaming and micro cracks, discolouration, bleaching, engraving and ablation are involved. Each mechanism is associated with a particular group of materials and the wavelength of the laser beam; in other words it depends on the material-laser interaction (See Figure 2.2). Foaming, which is a common marking method for polymers, involves the formation of gas bubbles in surface regions at low temperatures. The bubbles are surrounded with melted material, providing adequate mark contrast. In this case, no thermal degradation or ablation occurs due to low laser intensity. For marking glass, micro cracking resulting from shallow surface melting (~20 μm) provides the light to scatter and contrast with the substrate. Discoloration is a thermal degradation which can be referred to charring in polymers and woods. When the surface needs to be flat, this method is used, especially for pigmented plastics and high alloy steel or brass. A photochemical reaction can be used for marking of special polymers using the colored pigments causing a color change and a permanent mark. This procedure is known as bleaching. Laser engraving and ablation are the most appropriate method for marking metals. Laser engraving involves localized melting or vaporization of the surface, typically to a depth of 100 μm and is especially desired when an abrasion-resistant mark is necessary. Ablation mechanism involves the highest temperature rise which is necessary for reaching the material vaporization temperature. It thus depends on material removal by sublimation, often with little disruption to the surrounding surface. The mechanisms involved in laser marking are shown in Figure 2.2 where x-axis denotes the normalized scan speed versus y-axis denoting the normalized laser power [31].

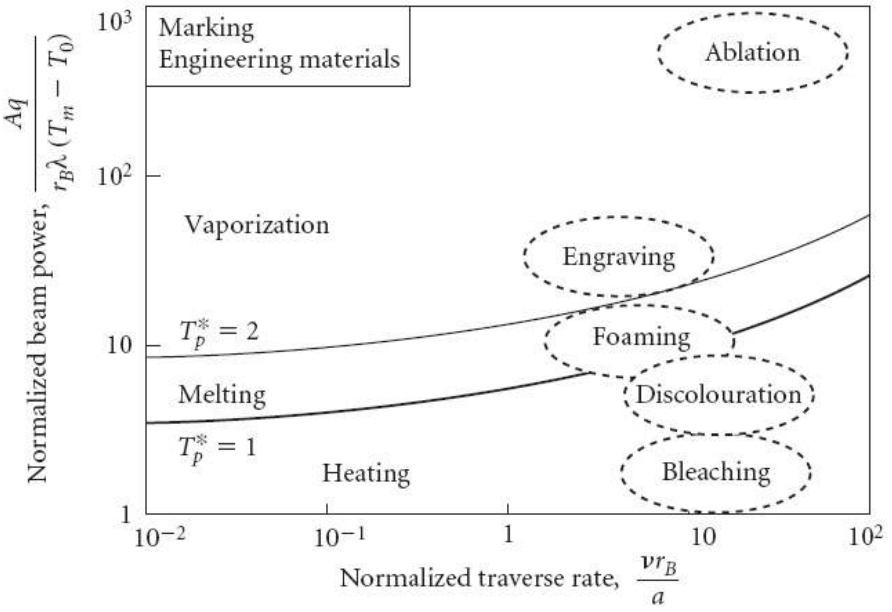

Figure 2.2: Normalized model-based diagram showing contours for the onset of surface melting and vaporization constructed from a surface heat flow model (solid lines); experimental data for various mechanisms of marking cluster into regions bounded by broken lines [31]

Although not mentioned along other marking mechanisms in [31], some studies [35, 36] refer to different mechanisms of ablation depending on the process parameters observed in laser marking, e.g. reactive ablation and melt ablation. High pulse energy and power result in direct sublimation of the material whereas reducing the pulse power leads in metal treatment to melting. This process is known as melt ablation where the melted material is blown away with a high pressure assist gas. The reactive laser ablation can take place under the following conditions: oxygen environment, low scan speeds and short laser pulses (nanosecond-to-microsecond durations). In this case, the metal is first transformed to the liquid state and then oxidized. The oxide is not blown away from the surface. Instead, it peels off the surface by the action of thermally induced stresses. To obtain a stable process, the processing parameters (mainly the processing speed and spot size) must be adapted into a certain process window which is quite limited. In the work of Schubart [35], it is stated that at a certain working speed, the temperature gradient will exceed the critical value for bending at lower intensities, whereas it does not at higher intensities, resulting in the chip remaining in the groove. The ablation mechanism involves four steps (See Figure 2.3) as explained in [35]:

I. The material surface is heated by the focused laser beam in the oxygen environment and as a consequence the surface is oxidized. The laser light absorption rises due to growing oxygen layer. Thus, heating becomes more effective.
II. When the surface temperature reaches the ignition temperature, combustion of the workpiece material starts. The surface temperature increases further due to the exothermal reaction and further laser heating resulting in melting of the oxide. The phase transition leads to a significant volume increase and generation of gas flaws in the oxide.
III. Once the laser beam moves out of the interaction zone, the liquid oxide cools down and solidifies which causes thermal stresses in the solidified oxide and leads to separation of the oxide layer from the metal.
IV. The oxide bends owing to the remaining thermal gradients (vertical to the workpiece surface) in the oxide layer.

Figure 2.4 shows the chip formation due to reactive ablation at low scan speeds and short pulse durations. As evident, the gas flaws cause spherical porosities in the chip.

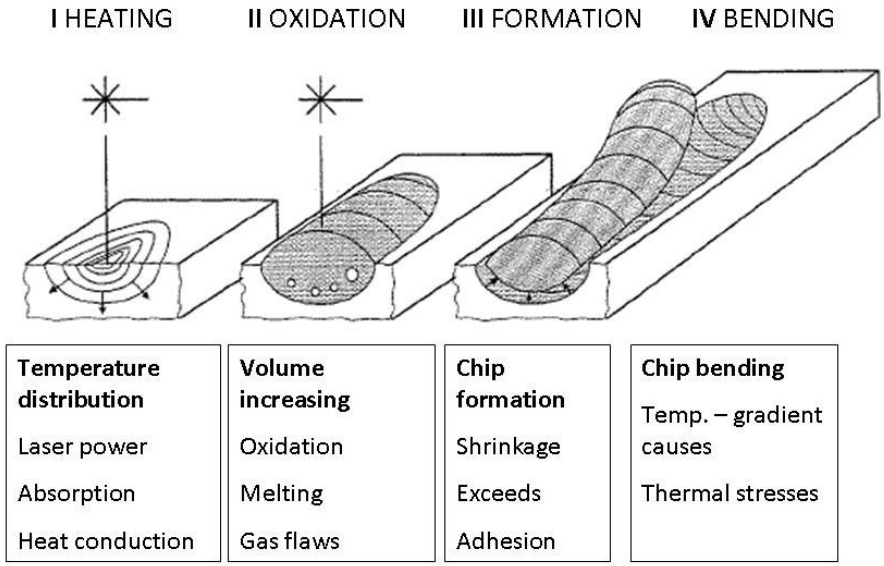

Figure 2.3: Four steps in the ablation process model [35]

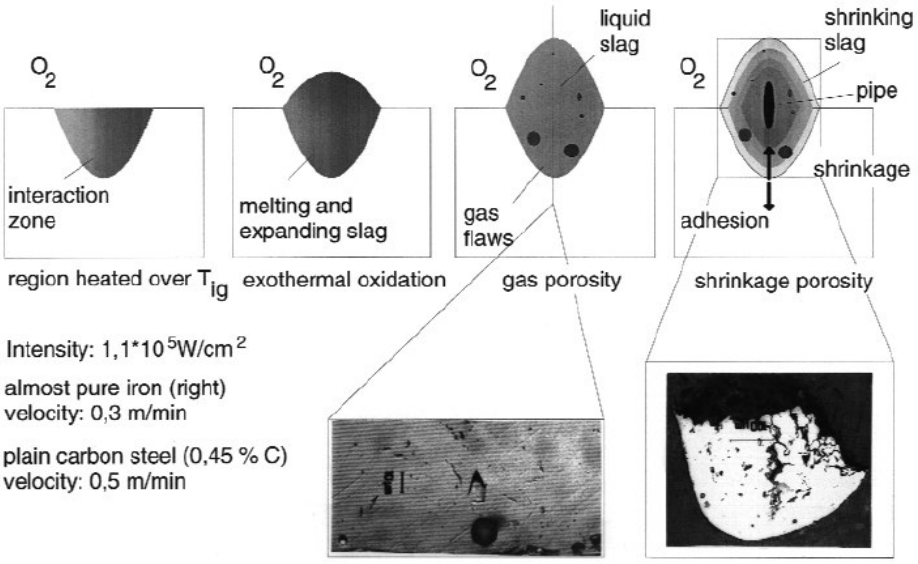

Figure 2.4: Formation of chip due to ablation at low scan speeds and short pulse durations in oxygen environment [35]

In laser marking, the marks can be made by illuminating a mask, or by a guided laser beam using computer controlled mirrors or by producing small dots in given patterns to generate the characters required. Mask marking is rapid compared to beam scanning if the mask does not need to be changed. The principle of mask marking is shown in Figure 2.5a. Alternatively, the laser beam can be used to scan over a marking area through galvanometer mirrors as shown in Figure 2.5b. In this way, the flexibility is higher at the cost of higher initial investment. The last laser marking method is utilizing dot matrices. Dot matrix marking systems, particularly suitable for alphanumeric codes, produce characters by producing small dots in a pre-specified pattern to generate the characters. The beam is scanned over the matrix and pulsed when a dot is required [31, 32, 37]. Dot matrix marking can be carried out in various manners. Several small scale lasers at the same time can be used to emit pulsed beams through mirrors and an f-theta lens focusing the beams on the surface of materials. This leads to uniformly melted micro holes on the surface so that patterns and characters are composed of these micro holes [32]. Alternatively one laser beam, operated in the pulsed mode, can be used to make all the pixels in the 2D data matrix. Each pixel can be generated either by one

or multiple laser pulses. Dot matrix marking can also be applied by using a mask to mark the complete matrix with one or several laser pulses without moving the sample [37]. Two examples for dot matrix marking are given in Figure 2.6.

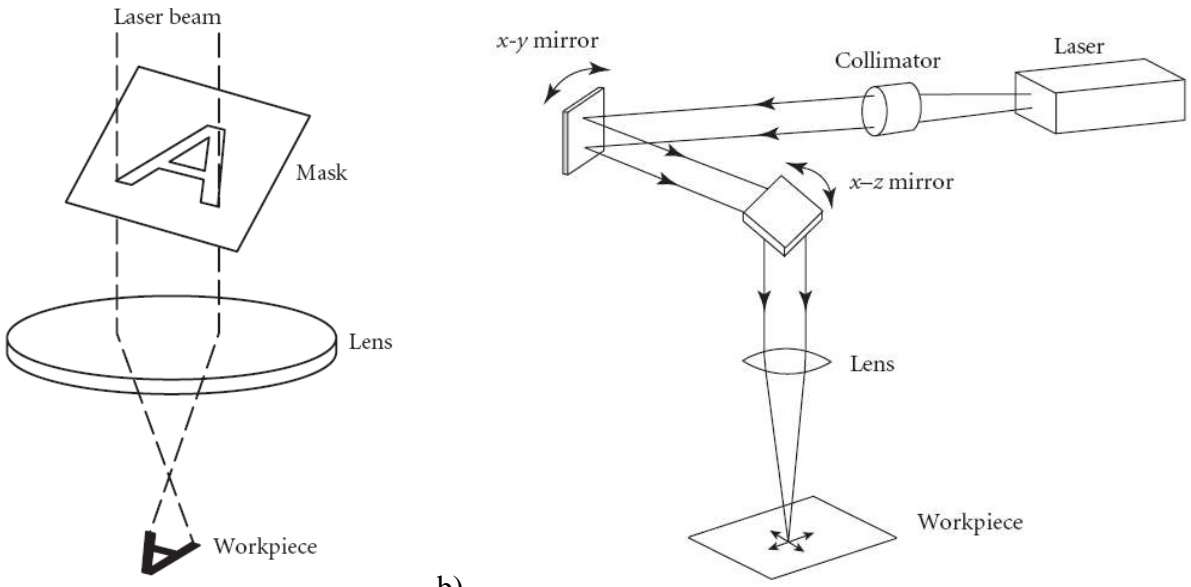

a) b)

Figure 2.5: a) Marking using a mask or b) rastering mirrors [31]

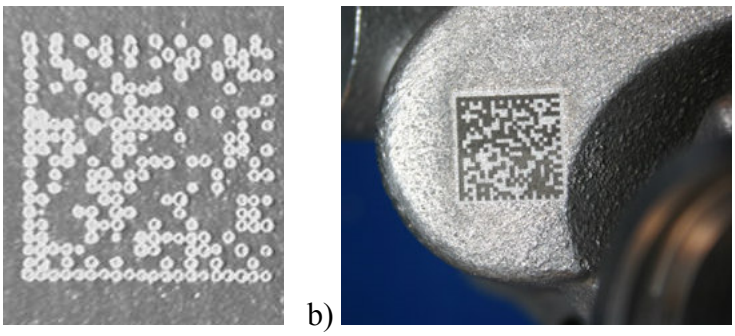

a) b)

Figure 2.6: a) A 2 mm square data matrix code containing 26 alphanumeric characters directly marked onto a printed circuit board [31] b) 2D data matrix mark [38]

Laser marking studies conducted with different lasers have recently been reported by many research groups. The effect of pulse frequency on mark quality was investigated by Qi et al. [30] concluding that the mark depth, width and contrast depend on the interaction process of the laser beam and the material, which is highly affected by the pulse frequency. Tam, et al. [39] and Tezuka and Yoshikawa [40] studied the laser marking of integrated circuit packages with pulsed Nd:YAG and Q-switched YAG lasers, respectively. Extensive research was conducted for the laser marking of polymers by Hoffmann et al. [41] and by Bosman [42]. Dynamical models relating the laser power and traverse speed and melt track width during laser marking of clay are developed by Peligrad et al. [43] and reasonable agreements between the measured data and the model outputs was achieved. Valette et al. [44] investigated the enhancement of corrosion resistance of laser marked surfaces in surgical applications using a laser source with femto-second pulses, which causes a small heat-affected area compared to longer pulse durations. Tam et al. [45] studied the sombrero bump formation on Ni-P discs and the effect of different laser parameters and substrate surface conditions. Despite the excessive number of studies in the field of laser marking, there is no single study focusing on the investigation of several process parameters on the laser mark profile for metallic surfaces. The present study aims to explore how the laser mark profile is changed due

to process parameters and to understand the mechanisms behind in order to use this information for optimization of process parameters in 2D and 3D erosion processes.

There are mainly three operating parameters used in laser marking, namely the pulse frequency, pump current (or laser power) and scan speed. In the present study, the effects of these parameters are explored using a Q-switched Nd:YAG laser equipping a Selective Laser Melting machine. Two different apertures can be inserted in the laser resonator: a big one (yielding a spot size of $Ø_{99\%}$ 180 μm) or a small one (yielding a spot size of $Ø_{99\%}$ 80 μm). Single factor experimental strategy is utilized to derive the initial understanding of their influences on the mark properties such as mark depth, width and rim formation. Later the methodology of design of experiments is employed to study the cross interactions if there exit any. Moreover, the profiles derived with different sets of process parameters are investigated in order to understand the mechanisms such as Marangoni effect and recoil pressure behind the laser marking process. Different parameter selections may result in obviously different laser mark contrast and readability. Marked samples with different parameters are shown in Figure 2.7.

Figure 2.7: Marked samples with different parameters

Two laser mark profiles obtained in the present study are shown in Figure 2.8 for two different scan speeds (3 and 50 mm/s) while the laser current is set to 39 A giving a laser power of approximately 100 W measured in the continuous (CW) mode (with the big aperture). The pulse frequency is 10 kHz and a big aperture yielding a spot size of approximately 180 μm is used. The average profiles of several cross-sections are plotted in Figure 2.8. As evident, increasing the scan speed from 3 mm/s to 50 mm/s changes the profile completely. At low scan speed (3 mm/s), a large bump formation is present in the central region with a significant volume increase, whereas the central region is suppressed and a crater is formed in the centre with shoulders at the sides of the crater at a higher scan speed (50 mm/s). As stated in [46], the transient evolution of temperature and fluid flow fields in melt pool, and then the pool shapes are influenced by the simultaneous occurrence of several physical phenomena taking place on the heating surface. When a laser beam is directed onto a solid target material which absorbs a fraction of the incident light energy, melting and then evaporation occurs which creates a back pressure on the liquid free surface (see Figure 2.9). This pressure pushes the melt away in the radial direction. Thus the material is removed by a combination of vaporization and liquid expulsion as stated in [47]. For melt expulsion, the pressure gradients acting on the surface due to vaporization should be sufficiently high to overcome the surface tension forces and expel the melted material from the hole. The relation between the peak temperature and recoil force is shown in Figure 2.10 for three different materials [48]. Thus, the possibly main driving forces of observed profiles are laser plume recoil pressure due to evaporation and surface tension gradients in the melt pool due to temperature gradients and change of the amount of surface active components. The oxidation also plays an important role in the final mark profile due to its contribution in the surface tension gradients and in the increased volume due to the ablation mechanism explained below from [36, 49].

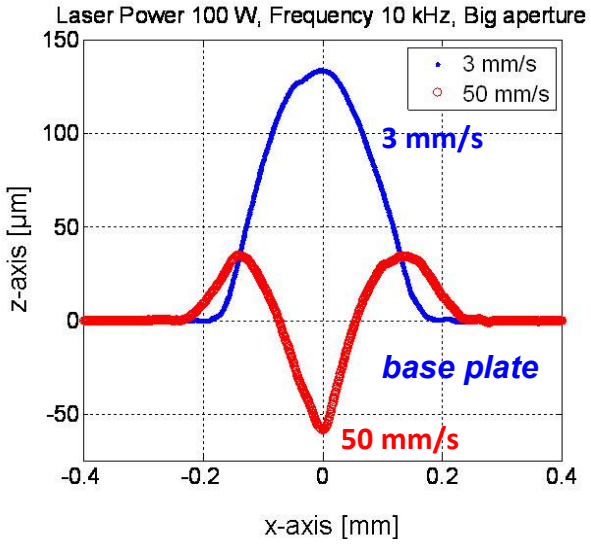

Figure 2.8: Different mark profiles for two conditions

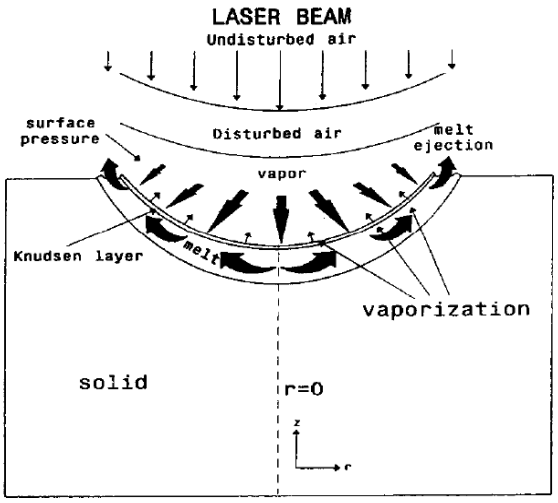

Figure 2.9: Schematic drawing of vaporization and melt expulsion [47]

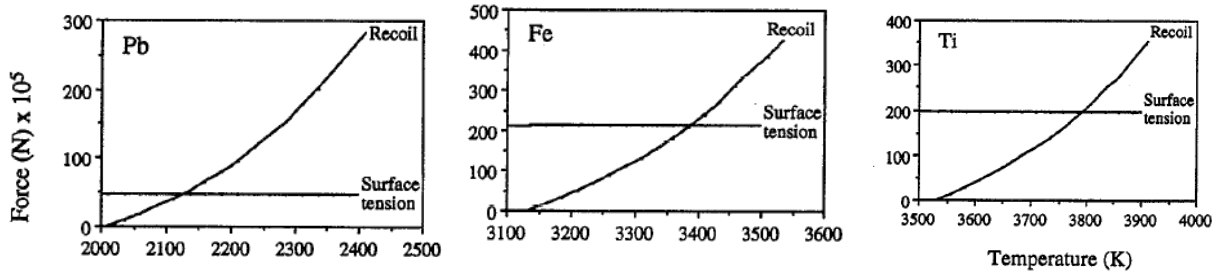

Figure 2.10: Recoil force as a function of peak surface temperature and the surface tension at the melting point for three different materials [48]

Surface tension, a thermodynamic property, is function of both melt temperature and concentration of surface active elements and it is a measure of the strength of the bond between two atoms at the free surface [45]. In general, the bond between two atoms gets weaker as the temperature is increased and this results in decreased surface tension. Thus, the surface tension gradients $d\gamma_{LV}/dT$ (liquid surface tension gradient) of pure metals and many alloys are negative. However, positive $d\gamma_{LV}/dT$ is reported for alloys containing sufficiently high content of surface-active elements such as iron-based liquids containing sulphur, oxygen or tellurium [46]. Of

particular practical significance is the reversal of the circulation direction in the melt pool which occurs in steels in the presence of very small amounts of surface active elements. Figure 2.11a illustrates the change of surface tension of pure liquid iron with increasing temperature. As the temperature increases, the surface tension decreases [50]. The slope of this relationship of pure metals can be estimated from material related factors such as melting temperature, molar volume, atomic number and heat of vaporization [51]. In the case of an iron-oxygen system as depicted in Figure 2.11b, the gradient is nihil at about 0.0017% of oxygen, while at higher concentrations, the gradient is positive, and becomes steeper with increasing concentrations of solute [51]. In this case, with an increasing temperature, the surface tension increases. This change of the slope of surface tension dependence on temperature from negative to positive is described as the chemicapillary (CC) effect.

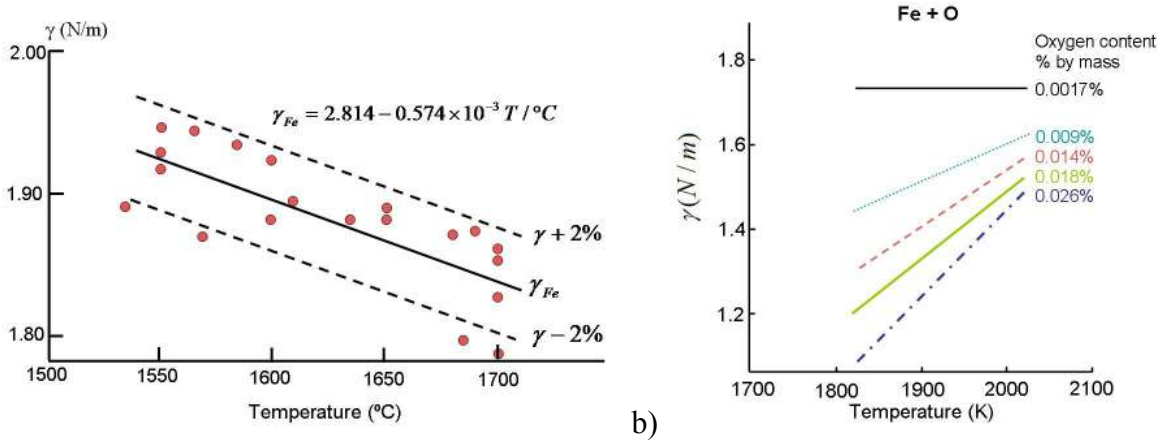

a) b)

Figure 2.11: Variation of surface tension with temperature (a) for pure iron, (b) for various concentrations of oxygen in liquid iron [50, 55]

The chemicapillary effect, caused by surface active elements such as sulphur and oxygen [45], tends to create a bump due to the movement of the melt pool from low surface tension to higher surface tension regions (Figure 2.12a). On the other hand, the thermocapillary (TC) effect, caused by only thermal gradients in the melt pool when there is no surface active elements, wants to produce a rim-only shape (Figure 2.12b). Schematic diagrams illustrating the melt flow with a positive and a negative surface tension gradient are shown in Figure 2.12. Thus, a high oxygen content in the melt pool plays an important role in the final mark profile [52]. Computer simulations showed that the final bump shape is extremely sensitive to the magnitude and timing of the thermocapillary and chemicapillary contributions to the surface tension gradient depending on the selection of laser pulse, pulse width and duration [45].

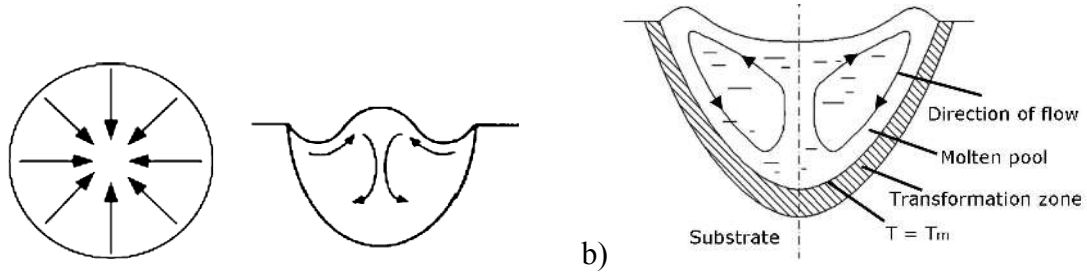

a) b)

Figure 2.12: a) Apparent fluid pattern on the melt pool surface and subsurface flow pattern in case of a positive dγ/dT gradient (CC effect) [52, 56] b) Circular flow in the melt pool in case of a negative $d\gamma/dT$ gradient (TC effect) [54]

Han et al. also studied the formation and development of the melt pool with different laser beam modes [53]. According to their results for TEM_{00} mode which satisfies the Gaussian distribution, the melted surface fluid at the melt pool centre is driven outwards due to the presence of high

temperature gradient causing strong Marangoni shear stress. This is the case where only the thermocapillary effect dominates the melt flow because the surface composition gradients are not taken into account in the mathematical model. The outward flowing fluid with a high temperature helps the heat to dissipate in the radial direction and partially extends the melt pool diameter. When the surface liquid is pulled away from the centre of the melt pool, the surface is depressed in the central region forming a crater. The displaced fluid builds up around the shoulder of the melt pool and causes the surface to bulge upward. Because of the gravity force, wall adhesion and surface tension, it is then dragged down to the solid surface of the substrate along the radial direction [53]. This is also studied by Zhang et al. to investigate the influence of laser processing parameters on the surface morphology of scanned tracks on 3Cr2W8V steel. They also concluded that the circular flow is induced under a driving force that is a composite force derived from the surface tension and gravity [54].

The competing force with the surface tension determining the final shape of the mark profile is the recoil pressure. When the laser intensity becomes sufficiently high (10^5-10^8 W/cm^2), surface vaporization is initiated and yields a vapor plume above the laser spot. This vaporization is so large that pressure is induced which results in a shock wave [57]. The shock wave is responsible for the recoil forces acting in the opposite direction. When the energy intensity is high, as is the case with a small beam diameter or with high laser power, the recoil pressure is greater. This vaporization recoil pressure generated in the process expels the liquid material from the crater centre to its sides and enlarges the height difference more. The effect of recoil pressure on the melt pool is examined by Han et al. [53] by conducting simulations with and without recoil vapor pressure. According to their results, the strong vapor pressure plays two apparent roles: firstly the surface fluid in high temperature is pushed to the outside and increases the melt pool diameter and secondly deeper surface depression facilitates the heat to dissipate in the depth direction and increases the melt pool penetration [53]. In hole drilling, the recoil pressure results in an undesirable ‘crown’ around the hole [58] as illustrated in Figure 2.13. On the other hand, there are some useful applications of the recoil pressure such as keyhole welding [59], Selective Laser Melting (SLM) [7] and laser surface modification of porous substrates [60]. In keyhole welding, recoil pressure expels the melted material away and creates a capillary filled with hot metal gas or plasma. Due to this generated keyhole, the energy is absorbed throughout the whole depth of the workpiece allowing high welding speeds and a high depth to width ratio with a small heat affected zone (HAZ). In SLM, recoil pressures facilitate the flattening of the melt pool abolishing the balling effect and resulting in a better surface quality and density, but this is only provided with low recoil pressures [7]. In laser surface modification, the recoil pressure generated due to the rapid evaporation at melt surface helps to drive the flow of the melted material into the porous substrate thus contributing to the overall observed depth of melting [60]. The recoil pressure encountered during laser marking is thus also very important to determine the final profile of the laser mark.

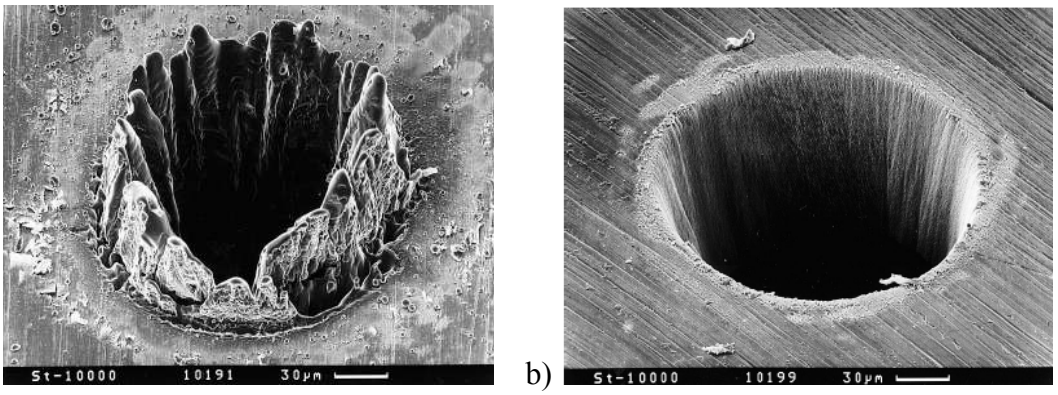

Figure 2.13: a) Crown generation in hole drilling in a 100 µm thick steel foil with 3.3 ns b) drilling with femtosecond pulse duration [58]

2.1.2 Experimental Procedure

Almost all laser marking experiments are carried out on a Concept Laser M3 Linear machine under oxygen atmosphere [61]. The machine employs an Nd:YAG laser with a wavelength of 1064 nm and a maximum laser output power in continuous mode of 105 W. It is operated in continuous wave (CW) mode for SLM but is used in Q-switched mode with nano-second pulse duration for all laser marking experiments. It is possible to adjust the spot size on the Concept Laser M3 Linear machine in two beam diameters $Ø_{1/e^2}$: 70 µm (small aperture) and 130 µm (big aperture). Experiments are carried out both for small and big apertures. Grinded workpieces of steel (AISI 1085) are marked according to a rectangular geometry under different marking parameter combinations (See Figure 2.14). The height of the part is measured and given as input to the Concept Laser software to move the building/erosion platform for keeping the laser in focus when it reaches the material.

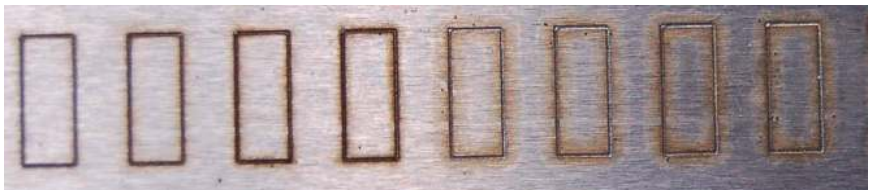

Figure 2.14 : Marked samples in M3 Linear machine

The surface profiles were then measured by means of a three dimensional surface profilometer, Form Talysurf 120L from Taylor Hobson, Ltd. [62], without applying any filter to the results. The instrument operates with a moving stylus that allows a horizontal travel of 120 mm with a position resolution of 0.5 µm (Figure 2.15). The velocity of the stylus can be selected as up to 10 mm/s. A hinge and a needle are attached to the end of the arm. A diamond cone, which is connected to the needle, has a tip with a radius of 1.5 µm (Figure 2.15c). A He/Ne laser interferometer measures the vertical movement of the needle with a resolution of 1 nm.

a) 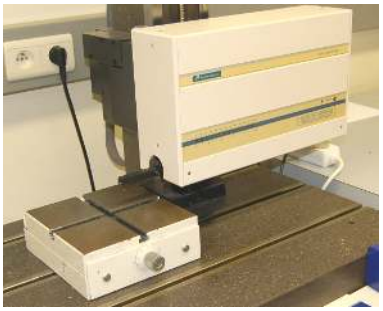 b) 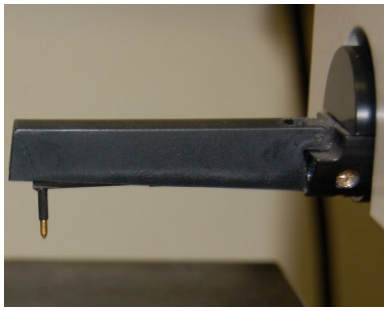 c) 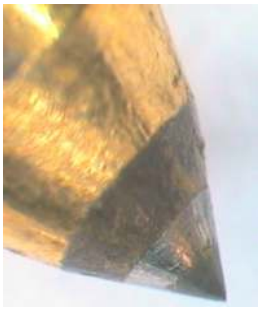

Figure 2.15 : a) Form Talysurf 120 L profilometer, b) moving stylus of the apparatus), c) diamond cone connected to the needle (right)

The device is equipped with a cross slide that allow 3D roughness/profile measurements. To have a general opinion of how the marks globally look like, the mark profiles are captured with 3D measurements which are built by conducting several 2D measurements along y-axis as shown in Figure 2.16. In order to make comparisons between different laser marks, all two-dimensional (in xz-plane) linear measurements for each mark, conducted at equally distanced locations along y axis (aligned with scanning direction of the laser beam), are averaged. The marking depth, width and other geometrical dimensions regarding the rim formation are derived using SPIP™ (Scanning Probe Image Processor) which is a micro scale image processing software. The view of a mark as displayed by the SPIP™ program is depicted in Figure 2.16. A three dimensional view of a laser mark is shown at top left whereas the average profile in the xz-plane (or along y-axis) is illustrated at the top right. For each parameter combination, at least a length of 1 mm in y-direction was measured with an interval (Δy) of 3 µm resulting in more than 300 lines for each mark (along y-axis) with a data length of 500 µm along x-axis. In order to observe what happens beneath the marked surfaces, optical microscopes are utilized to investigate the xz-planes. It is important to

notice that all tests except a few were conducted under oxygen atmosphere, as oxidation greatly influences the type of the mark profile that is obtained, especially at low scan speed and high laser power values.

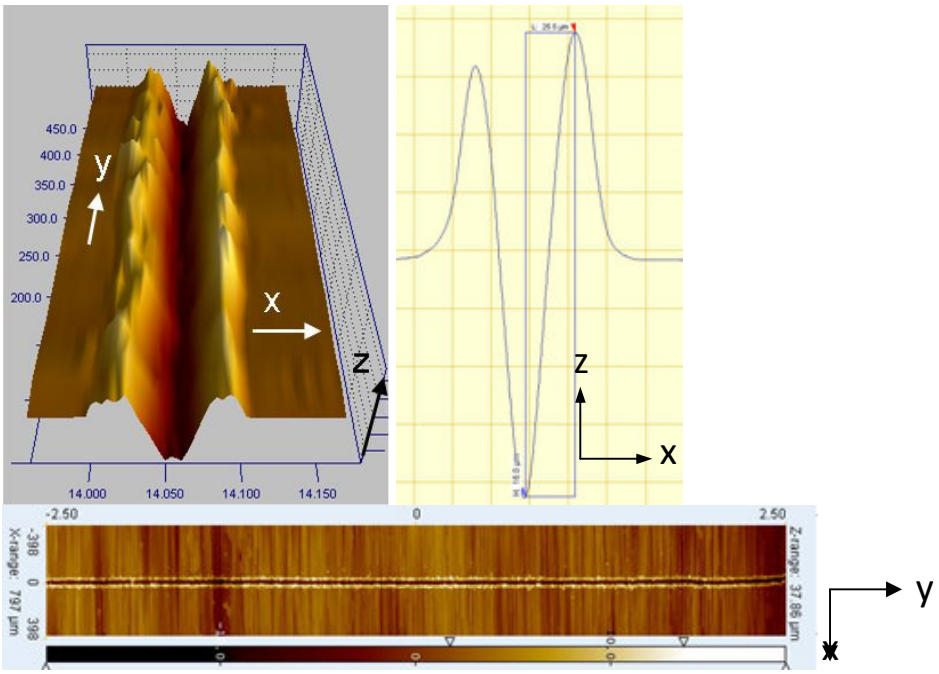

Figure 2.16 : Three-dimensional view of a laser mark with its average profile in xz-plane (above), height map of the laser mark (below)

2.1.3 Experimental Results

The results of the investigation on the laser mark profiles are presented in two main sub-sections. In the first sub-section, the input parameters are changed in a wide range to investigate which kinds of mark geometries are possible in laser marking and the discussion regarding the results is included. In the following sub-section, the change of the profile dimensions, such as mark depth and width, is studied in the high scan speed region by means of single-factor experiments as well as experimental design.

a. Laser Mark Profiles

The laser mark profiles made with different parameter settings are investigated in two manners: 1) They are measured with a Talysurf 120L surface profilometer to obtain the geometry and related dimensions or 2) the marked workpieces were cut by EDM and grinded to observe a zx cross-section to understand what happens beneath the surface. In this section, the measured profiles made with different parameter settings are first presented followed by optical micrographs explaining some phenomena encountered in the profiles.

Laser Mark Profiles Measured by Surface Profilometer

Figure 2.17 shows the change of the laser marks which were made with different combinations of scan speed and pump current (which directly changes the laser power, see Figure 2.33) using a small aperture at a fixed pulse frequency (45 kHz) relatively at a low peak energy and peak power. Each graph in the figure shows the average profile in xz-plane whereas the laser scanning was done in the y-direction during marking (See Figure 2.16). The plots show that a different profile is obtained for various selections of operating parameters. As explained in the introduction, the main driving force for the mark profiles is the dynamics between the recoil pressure and the surface tension, both depending significantly on the peak temperature.

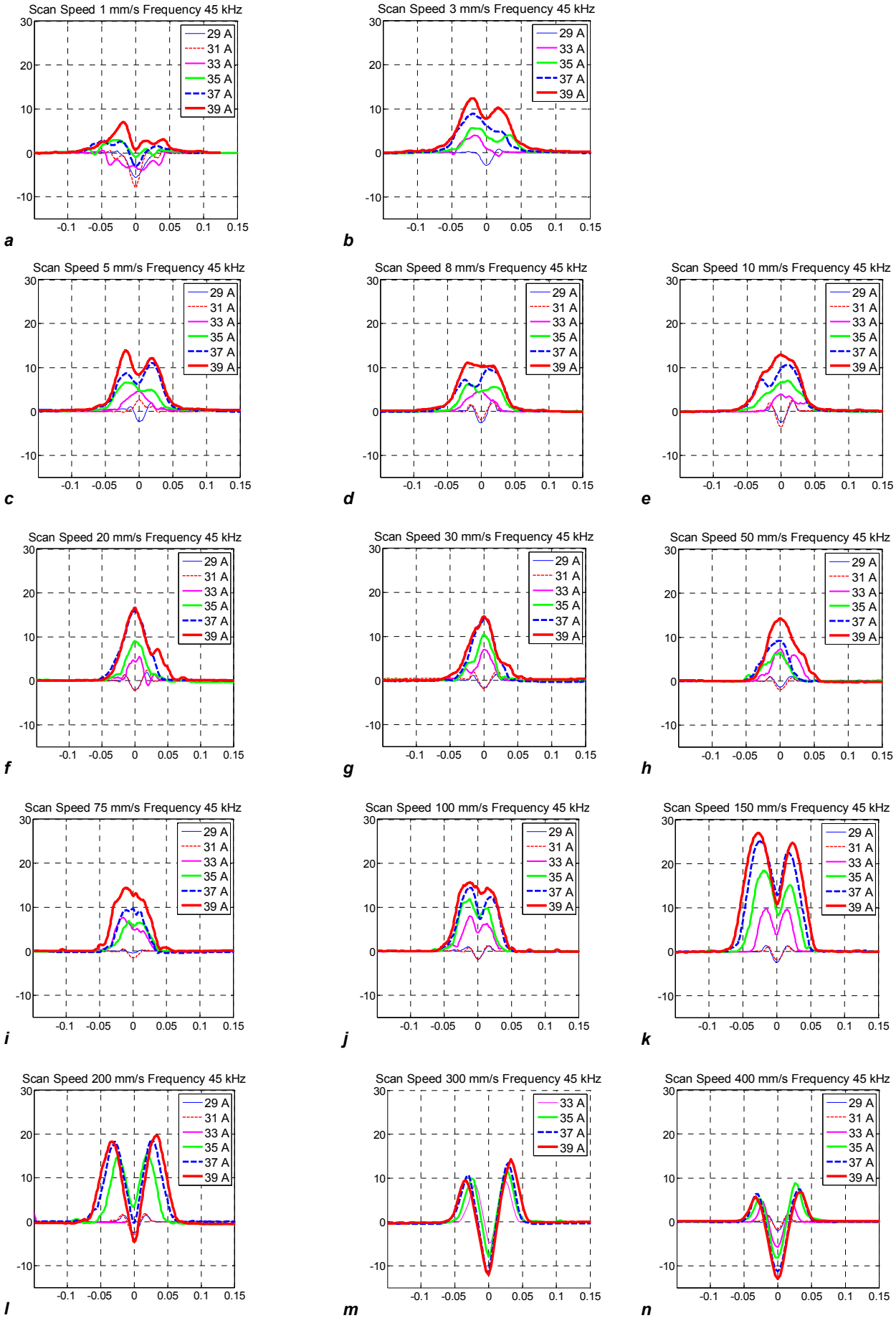

Figure 2.17: xz-profiles with different scan speeds and laser power (fixed pulse frequency; small aperture, x axis given in mm and y axis given in µm

At all scan speeds, low laser power values (29 and 31 A) result in a small crater with rim formations on the sides. During laser marking, melting first occurs when the surface is heated followed by evaporation if there is enough energy input. At low laser power values, it is seen that both melting and evaporation took place. The melted material in the groove is removed by the melt expulsion due to the recoil pressure.

When the laser power is increased, the obtained profiles evolve from a peak to a crater with shoulders as the scan speed is increased. At low scan speeds (Figure 2.17a-e), a sharp peak formation is observed. Due to high overlap between successive laser pulses, there is too much energy input into the substrate in this scan speed region. The same location on the substrate is exposed to laser radiation several times leading to higher heat conduction into the workpiece. Moreover, the high energy input per unit area causes high temperatures in the melt pool leading to significant oxidation taking place in the melt pool. The volume increase encountered with high laser power is related to the oxidation and formation of gas flaws resulting in porosity (as mentioned in the reactive laser ablation mechanism in the introduction). During the process, the laser partly couples into the oxide and melts the region which can be described by the isothermal curve of the melting temperature. This region is simultaneously melting and oxidizing and therefore expanding as seen in Figure 2.4 [35]. The expansion occurs due to several reasons: the oxide has a lower density and the liquid phase has a higher expansion than the thermal expansion of the bulk material. The liquid slag is getting under pressure and evades to the top. The expansion is additionally supported by the out-gassing of impurities which forms the gas flaws. The optical micrographs of two cases carried out at low scan speed region (less than 10 mm/s) with high laser power (39 A) are depicted in Figure 2.18a showing that the depth of affected material is quite high, being about 1.5 and 0.5 mm for these two cases, respectively. Thus, a large amount of the material melts throughout the workpiece and oxidation takes place leading to significant porosity throughout the mark profile. In some sources, the marking of a metallic surface by laser irradiation and oxidation is named as ‘metal oxidation’ which is an alternative marking method to ‘metal ablation’ [42]. The recoil pressure generated due to surface vaporization is not sufficiently high to countervail the expansion for the removal of melted material from the deep groove by melt expulsion. At high laser power values in low scan speed region (Figure 2.17a-e), it is seen that the central region of the bump is sometimes suppressed to a small extent causing a small crater in the middle (e.g. 39 A in Figure 2.17b). This may be attributed to higher recoil pressures encountered with higher laser energy density. At a scan speed of 1 mm/s, the profiles are not so clear for high laser power values and this may be a result of plasma generation due to the high energy input per unit length and thus the laser power cannot completely reach the substrate. Due to short and sufficiently high intensity laser beam pulses, plasma is formed from vaporised target material [63]. However, at low laser power values (29 or 31 A) with a scan speed of 1 mm/s, where plasma formation is not possible, the energy intensity is sufficient for evaporation making erosion of the workpiece possible. At medium scan speeds (20 to 150 mm/s), a sharper peak is observed in the central region of the profile (Figure 2.17f-k) which means the total depth of melted material is still high preventing the melted material to be totally removed by melt expulsion and oxidation dominates the profile. As the scan speed increases, the energy input into the substrate is reduced decreasing the peak temperatures reached in the melt pool. Thus, the recoil pressure is also lessened allowing the formation of a sharp peak in the middle [64].

At high scan speeds (>150 mm/s), the depth of melted material becomes smaller due to less overlap between pulses resulting in better material ejection from the groove and thus less heat conduction. The melt expulsion starts to dominate the process where the depth and width of the groove depend necessarily on the selection of process parameters. Please refer to §2.1.3b to read about the change of the process outputs with respect to the process inputs such as scan speed, laser power and pulse frequency at high scan speed.

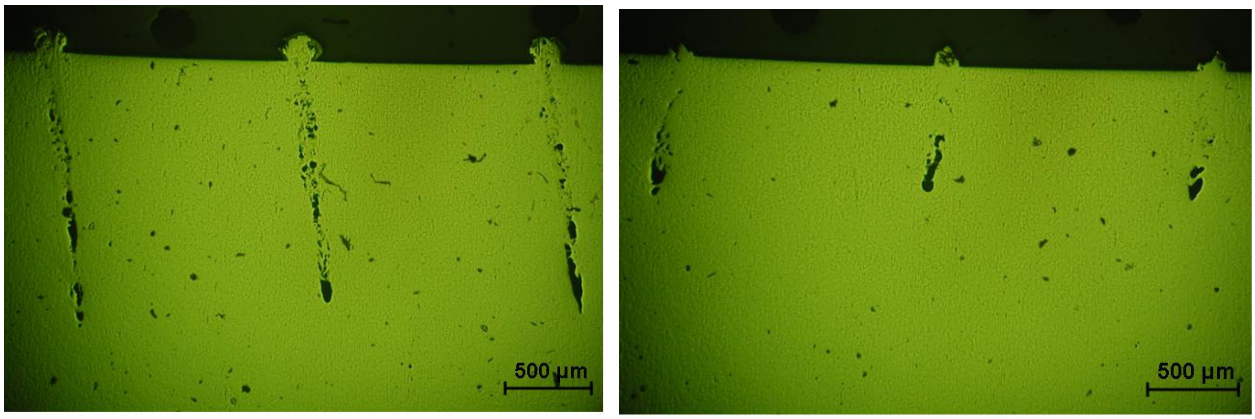

Figure 2.18: Laser marks made with a) 1 mm/s, 39 A, 5 kHz and big aperture b) 7 mm/s, 39 A, 10 kHz and big aperture

Figure 2.19 and Figure 2.20 show different laser mark profiles that were made with a fixed laser power (maximum pump current of 39 A) with the selection of the big and small apertures, respectively to investigate the effects of pulse frequency and scan speed together. With the big aperture (see Figure 2.19), only three frequency values are studied (10, 30 and 60 kHz). As the frequency is increased, the peak power that is reached within one pulse is reduced causing a significant reduction in the energy input per pulse to the marked sample. This is also evident from Figure 2.21 [64] and Figure 2.22 which depict the trend for the change of peak power with respect to pulse frequency. Figure 2.21 demonstrates this relationship at different average power values obtained with different pump current values. As the pump current, in other words the average power, is increased, the peak power reached in one pulse rises. Figure 2.22 depicts the relationship between the pulse frequency and peak power as well as pulse energy for the laser equipping the Concept Laser M3 Linear machine on which the experiments were carried out. The data used in Figure 2.22 is obtained from [65] since the measurement of peak powers in nanosecond durations was not possible due to technical limitations. Direct measurement of peak powers in the range of several hundreds of kilowatts is difficult by using power measurement devices. However, for longer durations, different measurement techniques can be applied such as reading the voltage output of the laser by an oscilloscope where the corresponding peak power is known for every volt [66]. With 60 kHz, it is evident that the material that is affected is much smaller than the cases with 10 and 30 kHz for different scan speed values. With the lowest frequency value (10 kHz) which provides the highest pulse energy, the low scan speed values result again in volume increase with a bump formation. As the scan speed is increased, the peak is suppressed in the middle. For medium frequency value (30 kHz), the situation is close to the case in Figure 2.17. Since the energy input is very low at 60 kHz, almost for all scan speed values, the melt expulsion determines the profile.

Figure 2.20 shows the change of the mark profiles when the small aperture is used with several combinations of pulse frequency and laser powers. The frequency is changed from 0 (corresponding to continuous mode) to 60 kHz as depicted in Figure 2.20a-f, covering the full frequency range that is possible for the machine. At low frequency values (5-10 kHz), the affected material which changed the surface profile of the workpiece by melting and re-solidification, is extremely large compared to medium and high frequency values. When the frequency is increased, the affected material is significantly decreased. The amount of affected material is smaller in the continuous mode. The continuous mode markings are only done at a scan speed varying between 3-75 mm/s. Above 75 mm/s, there was almost no melting on the marked surface. At low scan speeds (<50 mm/s), removal of material due to evaporation is present in the continuous mode.

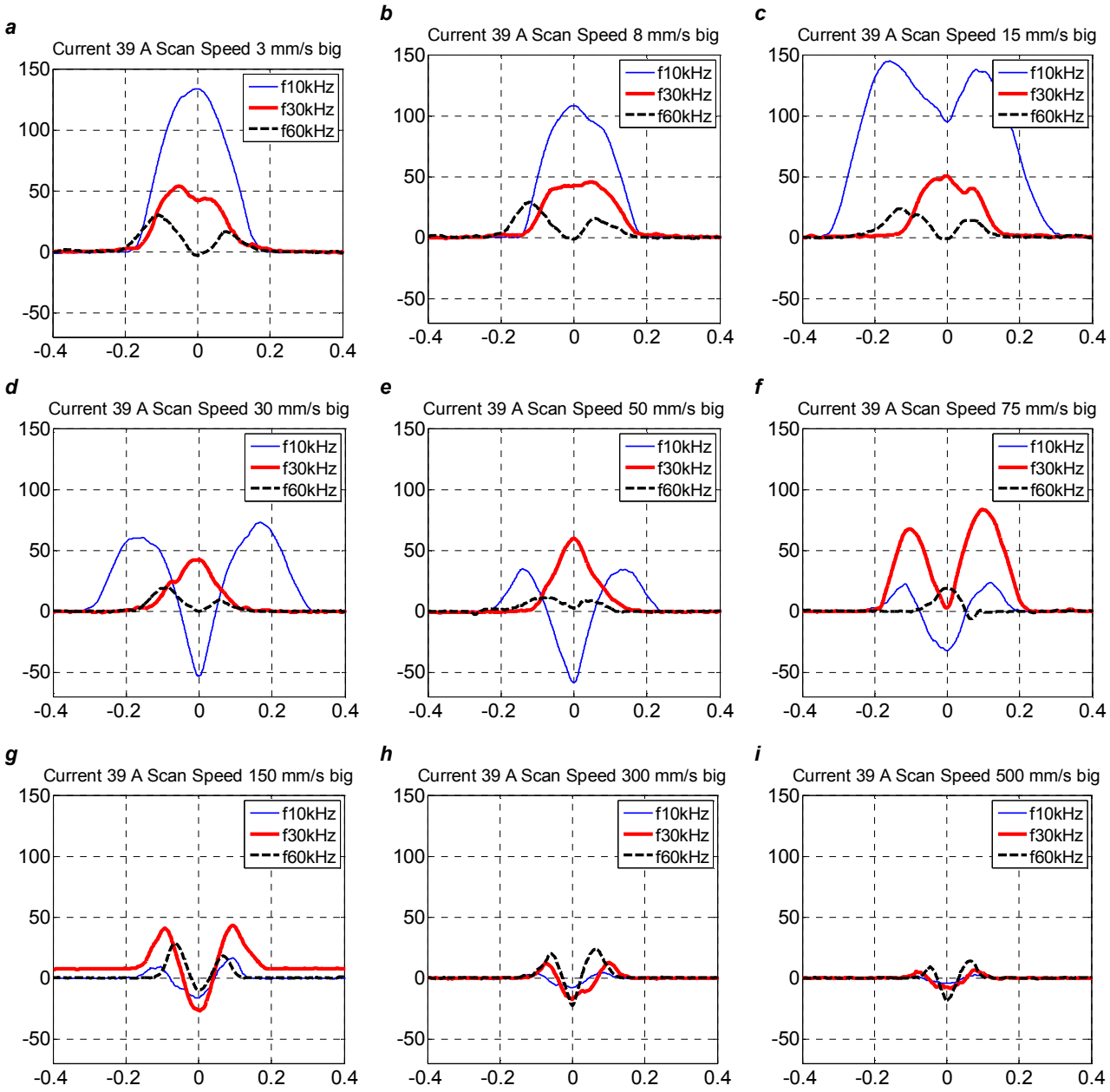

Figure 2.19: xz-profiles with different scan speeds and pulse frequency (fixed laser power; big aperture) x axis given in mm and y axis given in µm

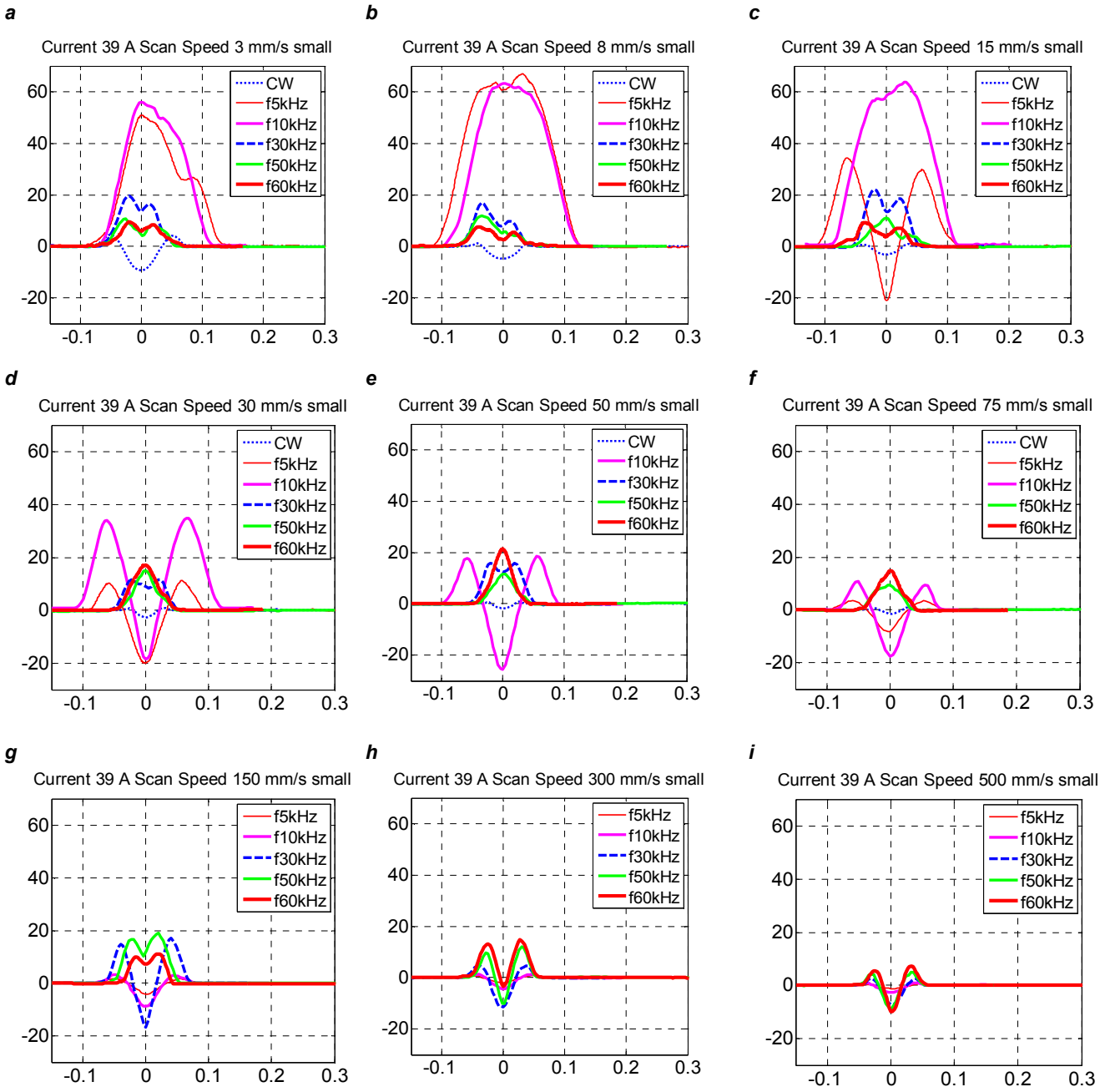

Figure 2.20: xz-profiles with different scan speeds and pulse frequency (fixed laser power; small aperture) x axis given in mm and y axis given in µm

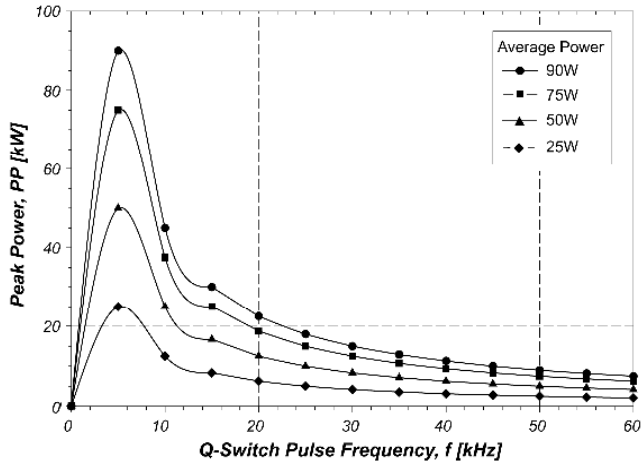

Figure 2.21: Peak power characteristics of a 9 W, Q-switched pulsed Nd:YAG laser marker [64]

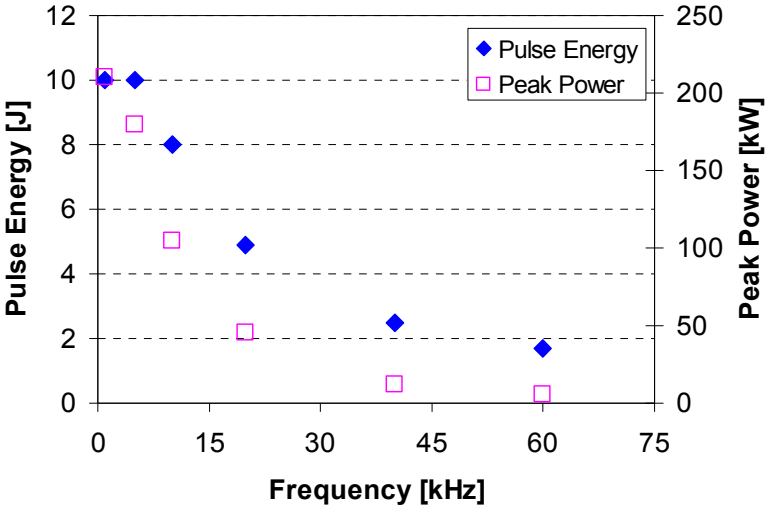

Figure 2.22: Pulse power and energy characteristics of a 100 W, Q-switched Nd:YAG laser equipping a Concept Laser M3 Linear machine at a fixed pump current (36 A) [65]

A comparison of the laser mark profiles obtained with small and big apertures is presented in Figure 2.23a-d. The marks were made at the maximum laser power (100 W and 25 W respectively for big and small apertures) and a fixed pulse frequency of 10 kHz. The figures show that the affected amount of material is much larger with the big aperture but the geometry of the profiles derived is more or less the same. As the scan speed is increased, the difference in the mark profiles becomes less for different spot sizes. Since the laser intensity (laser power divided by the spot area) derived with two apertures is approximately the same, it can be concluded that the mechanisms that define the final geometry of the mark highly depend on the laser intensity when the pulse frequency is kept constant. However, in the figure, it is evident that applying the same laser intensity with different spot sizes does not give the same results in terms of the amount of affected material. The reason for this is given in Figure 2.24.

Figure 2.24 shows the change of the pulse overlap with the spot size used. The pulse overlap values are derived with a scan speed of 300 mm/s and a pulse frequency of 45 kHz. As evident, with a bigger spot size, the overlap between successive pulses is higher since the overlapping is a function of the spot size. This means that the laser with a big spot size hits the same region more times than the one with a small spot size. Also, since the spot size is bigger, the covered area by the laser is larger. So the higher the spot size, the larger energy input per unit area. This results in a bigger affected area as seen in Figure 2.23.

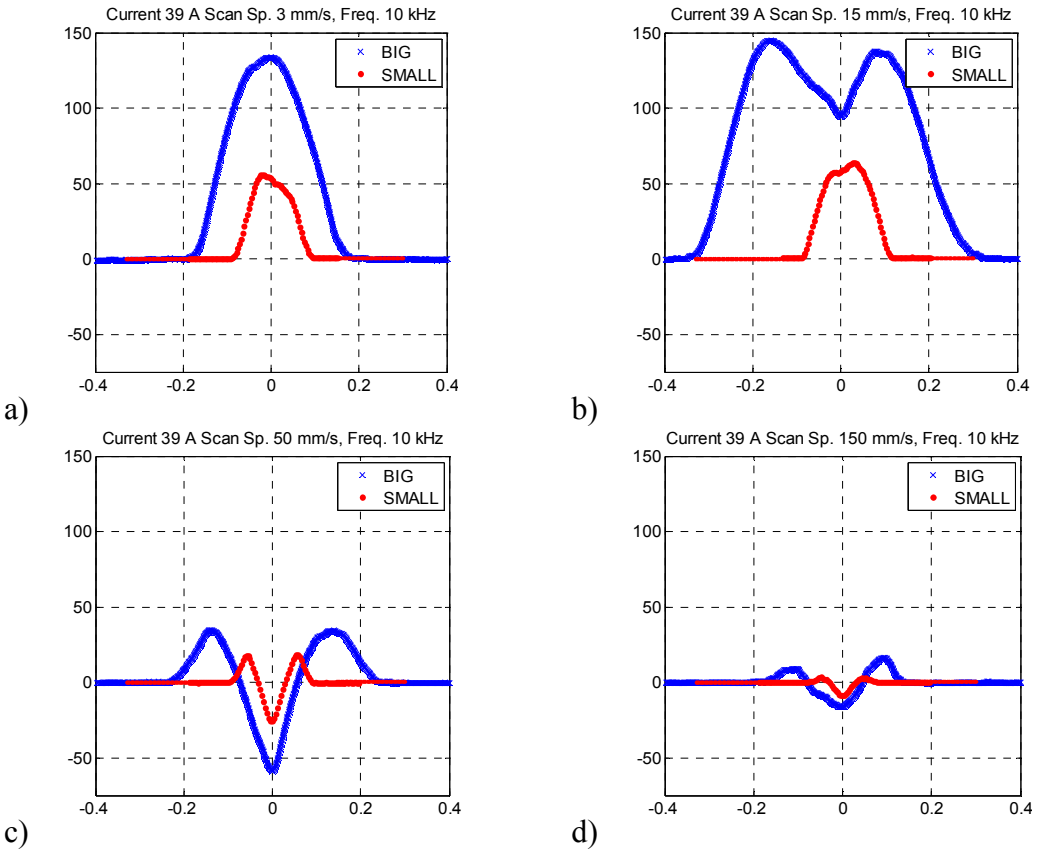

Figure 2.23: xz-profiles with different scan speeds and spot sizes (fixed pulse frequency and laser power) x axis given in mm and y axis given in µm

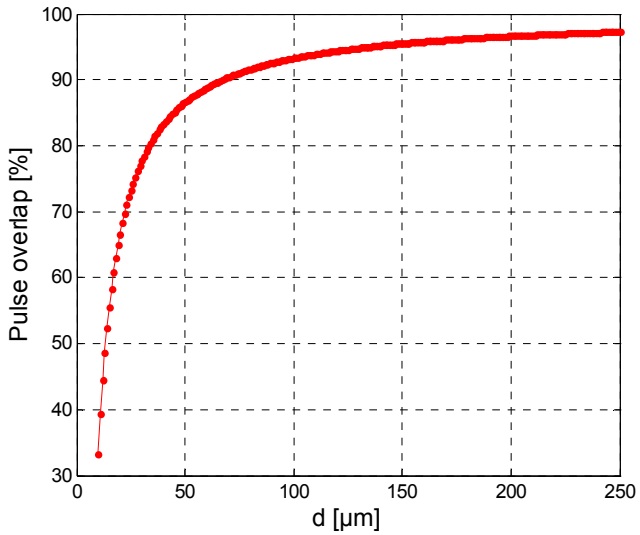

Figure 2.24: The change of the overlap factor vs. the spot size

In addition to other parameters, the effect of the environment is also tested. In Concept Laser M3 Linear machine, it is possible to fill the work volume with nitrogen gas to avoid oxidation. Steel samples were marked with the chamber filled with nitrogen with a remaining oxygen content of less than 1% and the results were compared to those of the experiments which were conducted in ambient air. The results are depicted in Figure 2.25. Conducting the tests in a nitrogen filled chamber with some remaining oxygen did not significantly alter the results obtained in ambient air atmosphere. There is a slight change in the mark depth or the height of the bump/crater in the middle, but the geometry stay the same for the two cases since the profile is more related to the

depth of the melted material and the recoil pressure which does not necessarily depend on the atmosphere. Therefore, doing the tests in an inert atmosphere with even very small amount of surfactants (1% of oxygen in our case) does not change the profiles from neither geometrical nor the dimensional aspects derived in laser marking. The fact that the melted material goes very deep due to the applied laser power and scan speed and gas flaws are entrapped causing porosity causes the volume increase and does not depend on the process gas.

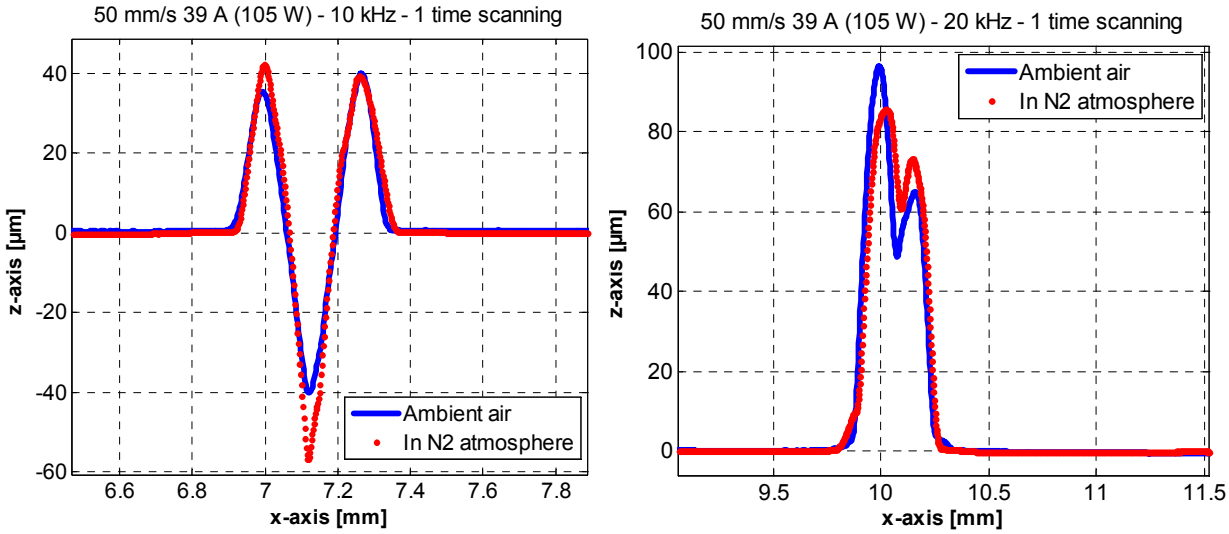

Figure 2.25: Laser marks made under ambient air or nitrogen atmosphere at different parameter settings

Investigation of Laser Mark Profiles with Optical Microscopy

When the substrate is exposed to laser irradiation in the pulsed mode, at the beginning it was expected that the material would be heated up and evaporated by the excessive energy of the laser beam compared to a laser energy operated in continuous mode. However, as depicted in Figure 2.23a, low scan speeds generally resulted in bump formation with a high peak in the middle of the laser mark. Hence, marked samples were cut and the cross-sections were investigated by an optical microscopy in order to understand how this material addition happens instead of material evaporation as observed with some laser mark profiles.

Figure 2.18a shows an example of bump formation which is made at a scan speed of 1 mm/s, a pump current of 39 A, a pulse frequency of 5000 Hz and with the selection of the big aperture. When the mark profile is measured from the level of the marked workpiece (0-level) by a Talysurf 120L surface profilometer, it seems that there is material addition on top of the surface. However, the optical micrographs show that the mark groove is not fully dense of melted and solidified material beneath the 0-level. As evident from three marks, there is a significant porosity formed along the depth of the melted groove which is approximately 1 mm. This kind of material addition forms only when very low scan speed settings are employed and is similar to reactive laser ablation as explained in §2.1. Due to the oxidation that takes place at elevated temperatures in the melt pool, a significant volume expansion and gas flaws in the oxide are formed. The parameter settings are probably not appropriate for the chip formation. Therefore, the oxidized material stays in the groove. A second example, which is made at a scan speed of 7 mm/s, a pump current of 39 A, a pulse frequency of 10 kHz and with the selection of the big aperture, is depicted in Figure 2.18b where the depth is of the melted pool about the half of the one given in Figure 2.18a.

An important observation about this kind of bump formation is related to the depth of the laser marks. If the scan speed is too low and the depth of the melted material is too high, it is not possible to evacuate this melted material totally from the formed crater or groove totally as it is possible with cases shown in Figure 2.27-2.30. Figure 2.26 shows a case where the depth is less than 500 µm. The

groove is almost open but some material still blocks the top of the groove which looks like material addition when looked from top view.

Another type of mark formation is illustrated in Figure 2.27 where the groove is completely visible from the top view. As seen, the crater has shoulders on both sides which result from the melt expulsion. At even higher scan speeds (see Figure 2.28 and Figure 2.29), the shoulders become less visible and the crater is much smaller.

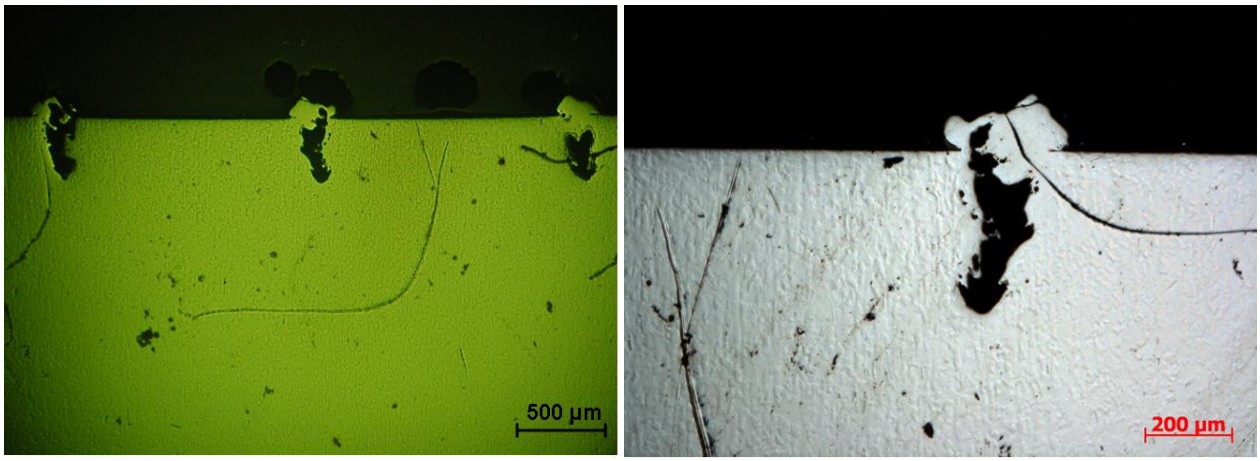

Figure 2.26: Laser marks made with 15 mm/s, 39 A, 10 kHz and big aperture at different magnifications

Figure 2.27: Laser marks made with 10 mm/s, 39 A, 5 kHz and big aperture

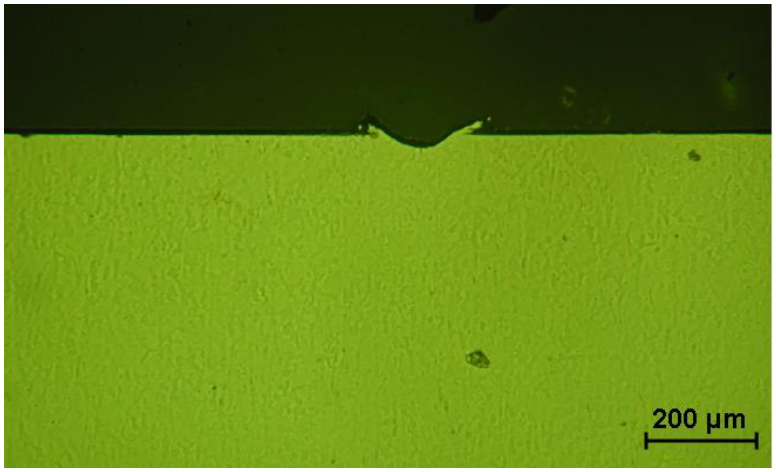

Figure 2.28: Laser marks made with 50 mm/s, 39 A, 5 kHz and big aperture

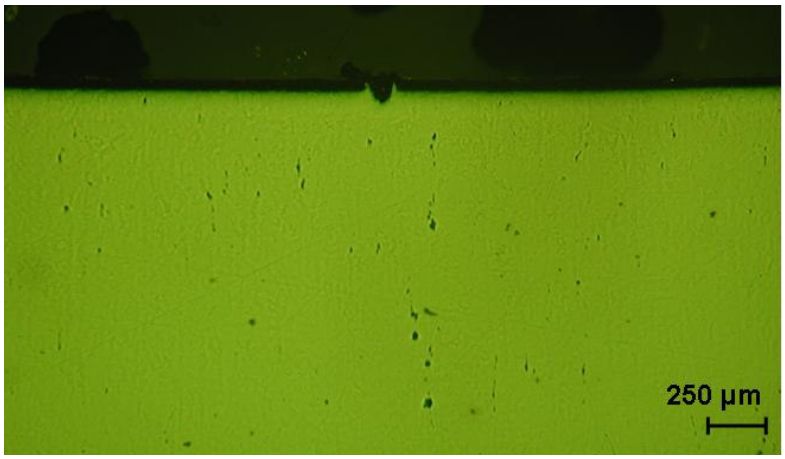

Figure 2.29: Laser marks made with 150 mm/s, 39 A, 45 kHz and small aperture

b. Investigation of Laser Mark Profiles at High Scan Speed

For high productivity, high scan speeds should be selected in laser marking. However, the dimensions of the laser mark depend on the process parameters. In this sub-section, it is aimed to investigate how these dimensions change with different sets of parameters with single-factor experiments. The sketch of a general cross-section of a marked line by a laser beam with nano-second pulse duration is shown in Figure 2.30. The groove depth (d_g) and width (w_g) play an important role for the readability of the mark whereas the output parameters such as rim distance (w_{rr}), rim width (w_r) and rim depth (d_r) are measured regarding the rim formation. These dimensions do not only depend on the parameters investigated here. One of the important parameters that play an important role on the rim formation is the pulse length. When material is irradiated with short pulses (pico- or femto-second durations), the penetration depth and, therefore, the interaction volume is generally smaller, slowing the material removal process. Since there are less secondary thermal effects, the pico- and femto-second machining process results in better quality without any rim formation around the mark and cleaner surfaces at the expense of high processing times [67, 68]: see also Figure 2.13.

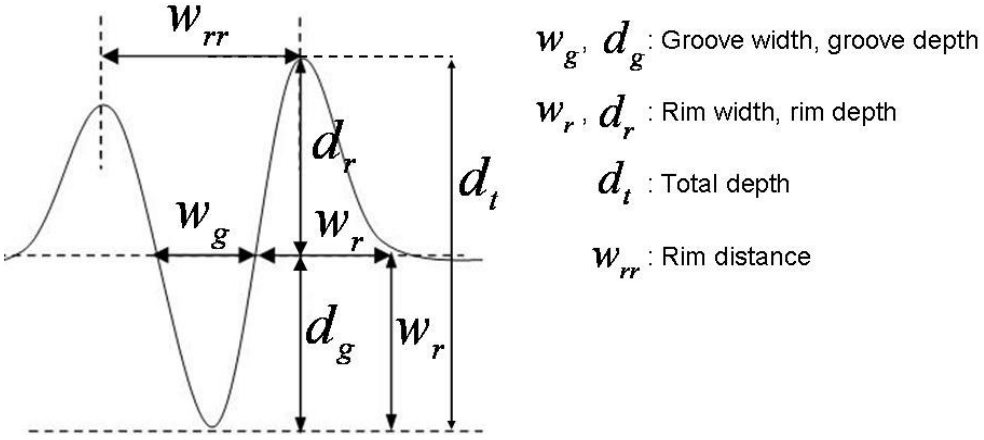

Figure 2.30: General cross-section of a laser marked line

In order to derive the general relationships between the input (scan speed, pulse frequency and pump current) and output parameters of the process, single factor experiments are first utilized. One of the parameters is changed gradually while keeping all others constant at pre-specified values. Thus, only the relation between the changed parameter and the output can be derived. The tested parameters are the scan speed, pump current (laser power) and pulse frequency.

Scan Speed

The results for varying scan speed are depicted in Figure 2.31 and Figure 2.32 for the depth and width values. The other parameters during these tests were fixed at the following values: a laser power of 20 W (with a pump current of 35 A), a pulse frequency of 30 kHz with selection of the small aperture. As observed from the figures, the effect of scan speed is more crucial for the depth values rather than for the width. As the scan speed increases, the groove depth (d_g) decreases and the same trend is followed by the total depth (d_t). This is caused by the reduced energy intensity on the marked surface due to less overlapping of consecutive pulses. The equation (Eq. 2.1) for the overlap factor between laser pulses clearly indicates this relationship [69]:

$$U_p = \left[1 - \frac{v}{f \cdot d}\right] \times 100 \qquad (2.1)$$

where v is the scan speed, f is the frequency, d is the spot diameter and U_p is the overlapping percentage of the laser pulses.

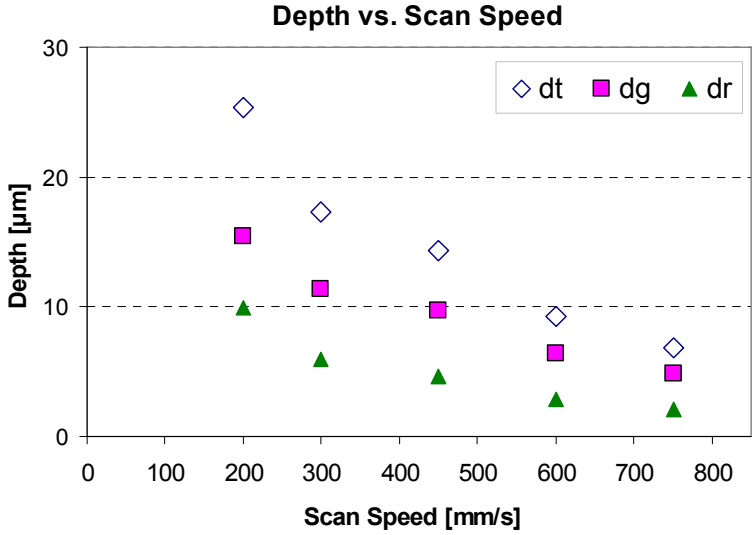

Figure 2.31: The influence of scan speed on marking depths

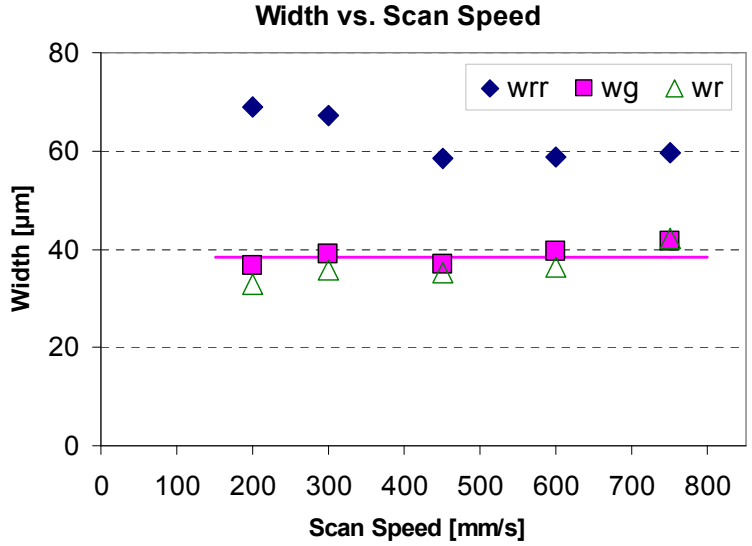

Figure 2.32: The influence of scan speed on marking widths

On the other hand, the marking widths can be considered as independent of the scan speed as shown in Figure 2.32. The width of the affected or melted area does not depend on the selected scan speed in the tested range.

Laser Pump Current (Laser power)

The laser pump current has a potent influence on the removal rate due to its direct effect on the laser power (Figure 2.33). A low limit for the laser power ensures the melting of material necessary for laser marking.

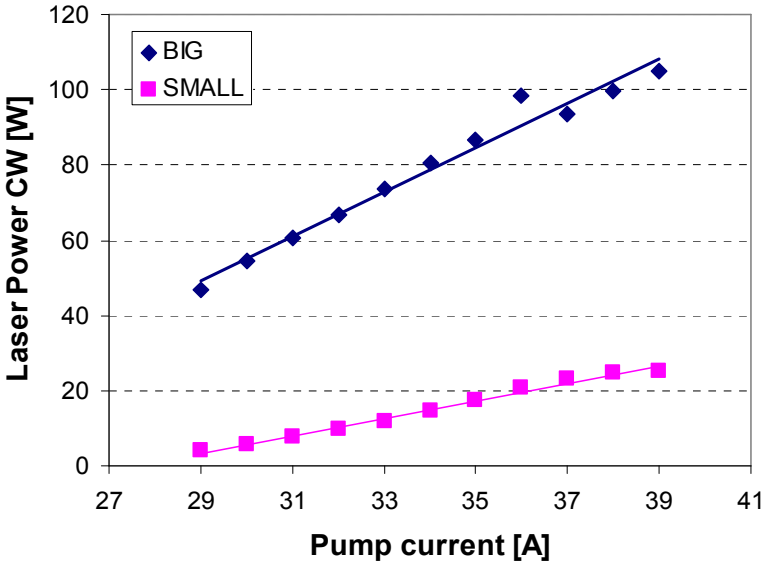

Figure 2.33: Laser power measured in cw mode vs. the pump current for big and small apertures

While investigating the effect of the pump current (or laser power), the other parameters were kept constant at the following values: a scan speed of 450 mm/s, a pulse frequency of 30 kHz and with the selection of the small aperture. The graphical representations of all results are depicted in Figure 2.34 and Figure 2.35. As the laser power is increased by raising the pump current, the groove and total depths (d_g and d_t) linearly increase following almost the same trend with similar slopes. Thus, the difference between these two depths or in other words, the rim depth, (d_r) stays almost the same at all pump current values as shown in Figure 2.34 with a zero-slope line. Increased laser power result in a higher energy given to the substrate resulting in a higher temperature increase and higher volume of melted material. The increased temperature gradients in the melted pool cause higher Marangoni convection forces resulting in a deeper crater. This is evident from the equation showing that the strength of the thermocapillary flow can be estimated from the dimensionless Marangoni number M_a [70]:

$$M_a = \frac{d\gamma_{LV}}{dT}\frac{dT}{ds}\frac{L}{2\eta\delta} \tag{2.2}$$

where $\frac{d\gamma_{LV}}{dT}$ is the surface tension gradient, $\frac{dT}{ds}$ the thermal gradient, L the characteristic length of the melted pool, η the viscosity and δ the thermal diffusivity.

The groove width (w_g) also increases with an increasing laser power as well as the rim distance (w_{rr}) (Figure 2.35). However, the width of the rims (w_r), which are present along the laser mark on two sides, stays almost constant for different laser power values. Hence, high current values give better results in terms of visibility.

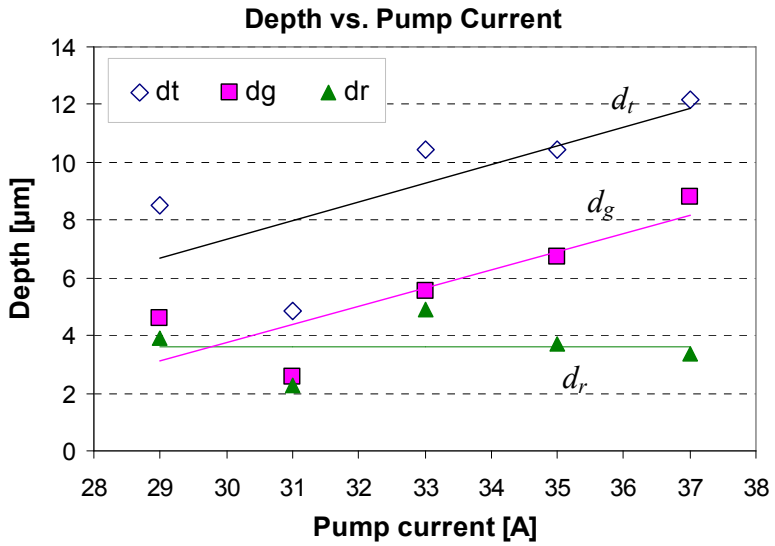

Figure 2.34: The effect of pump current on marking depths

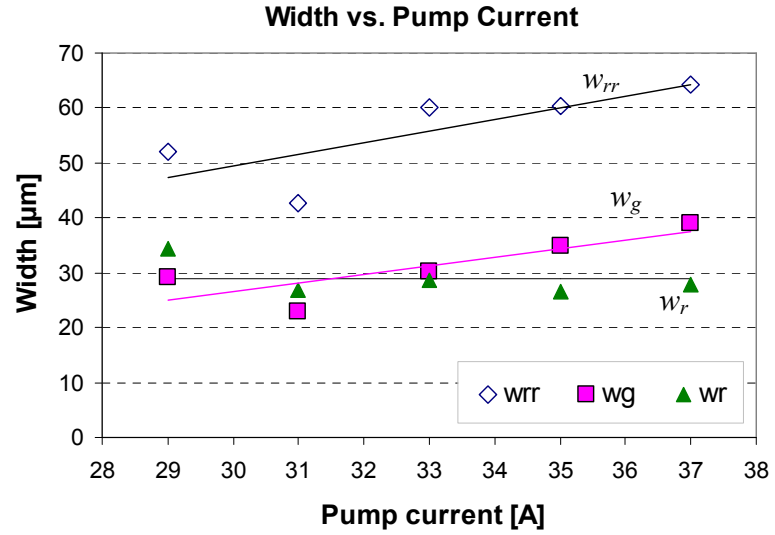

Figure 2.35: The effect of pump current on marking widths

Pulse Frequency

In single-factor experiments, the last processing parameter under investigation is the pulse frequency. Nd:YAG lasers are able to operate in both pulsed and continuous mode. In the pulsed-mode, the peak power of the laser beam is high enough to allow material removal by evaporation whereas in continuous mode, the energy for evaporation cannot be provided unless very low scan speeds are used (less than 50 mm/s for the maximum power of the Concept Laser M3 Linear machine).

The influence of the pulse frequency on the groove depth (d_g), groove width (w_g) and rim formation is presented in Figure 2.36 and Figure 2.37. As seen in Figure 2.36, the groove depth (d_g), reaches a maximum when the pulse frequency is approximately 40-45 kHz (medium frequency). This also holds true for the total depth (d_t). The relationship between the frequency and the depths can absolutely not be expressed linearly. A second-order fit is a better option as illustrated in the figures. The second-order relationship between the pulse frequency and the mark depths is explained by the change of peak and average output powers of the laser beam with changing pulse frequency [30]. The peak power decreases and the average output power increases with increase in the pulse frequency. At low frequency, the peak power is high enough to make materials evaporate

during laser marking. Then the volume of evaporated material is determined by the average output power. So at low frequencies, the driving power is the average power. In high frequencies, the peak power is not enough to evaporate material thoroughly and a part stays in melted state. Thus, the driving power becomes the peak power. This makes the relationship between frequency and depth values (d_t and d_g) rather complicated. Therefore, the maximum material removal is only possible at medium frequency values.

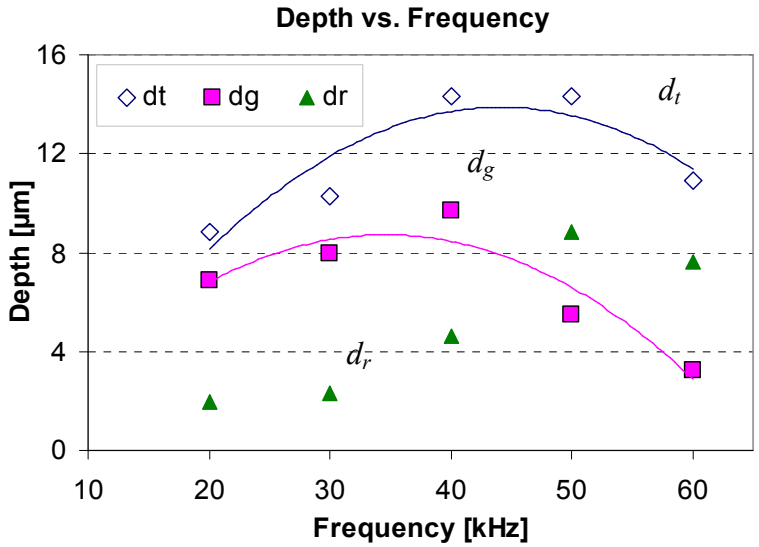

Figure 2.36: The effect of pulse frequency on marking depths

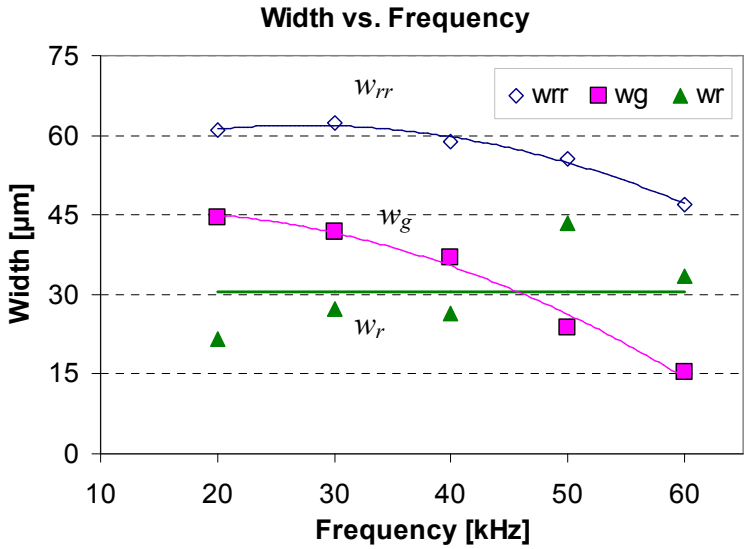

Figure 2.37: The effect of pulse frequency on marking widths

Regarding the widths, the rim distance (w_{rr}) shows a decreasing trend as the pulse frequency is increased. The groove width (w_g) also reduces as the frequency increases whereas the rim width (w_r) hardly depends on the pulse frequency. The relationships between the pulse frequency and the widths (w_{rr} and w_g) can be expressed either linearly or by a second-order fit. Looking at these results, one can consider that a more visible mark will be obtained at low frequency values. However, at low frequency values, it is evident that the heat affected zone around the mark groove is bigger causing the mark to be less sharp. The heat affected zone exhibits a noticeable colour change around the mark groove (see Figure 2.38) which is not observable in profile measurement results. This statement is valid for all rectangles marked with frequency values lower than 25 kHz in

the experiments. Therefore, higher frequency values should be preferred for better visual aspects at high scan speed region.

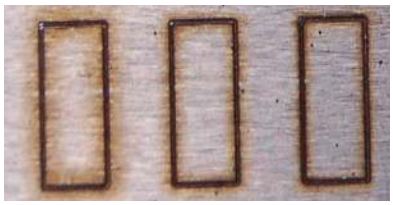

Figure 2.38: Marks made with a pulse frequency effect of 15, 30 and 45 kHz (from left to right)

2.1.4 Conclusions

Laser marking, which is an advantageous marking method for a wide range of materials, is experimentally investigated in this study to have a better understanding of the physical phenomena occurring during one dimensional laser beam scanning. The laser mark profiles made with different scan speed, laser power and pulse frequency values, are measured with a 3D surface profilometer and the cross-sectional views of the marks are obtained by an optical microscopy. The results showed that three process parameters play an important role on the obtained geometries of the laser marks. Depending on the dominant mechanisms determined by the used parameters, the laser mark had a different profile which changes the readability of the mark significantly. From visual aspect of view, the highest contrast is obtained by the marks having a sharp peak in the middle. However, the optical microscopy pictures revealed that these marks may have excessive porosity going 1.5 mm deep in the marked surface. Therefore, the laser marks with deep groove and short rims are more preferable without any porosity. It is also seen that most of the parameter combinations do not always result in the evaporation of material, but only melting and re-solidification. At very low scan speeds and high laser powers which lead to excessive laser intensity, the plasma generation limits the energy given to the substrate and resulting in no evaporation. Only low scan speeds in combination with low laser power values result in evaporation of material in one-dimensional erosion. Only enough overlapping of scan tracks at high scan speeds may give a possibility for two or three dimensional erosion.

The laser mark profiles are dimensionally investigated only at high scan speeds due to high productivity and the mark profile (groove with rim) to achieve better quality marks with high visibility and less rim formation. The investigation is carried out in two parts with different experimental strategies. The first part involves the investigation of the laser mark profiles in terms of depth and width by single factor experiments of which the results are reported in §2.1.3a. The second part involves the study of relations between process inputs and outputs by design of experiments and this part is presented in Appendix 2. The studied parameters namely scan speed, pulse frequency and laser pump current generally have significant influence on the process outputs. Single factor experiments are adequate to get a general understanding about the change of output factors (widths and depths) with respect to input parameters. However, they do not give any information about the interactions that may significantly affect the relationship between inputs and outputs. Thus, the important interactions are explored with factorial analysis using experimental design. The experimental data from the full factorial design are analysed by S/N ratio analysis and ANOVA. As a result of theses analyses, it is observed that all main factors play an important role on almost all outputs in their selected ranges. The pulse frequency is the major contributor to all the widths and the depths whereas the interaction between the frequency and the pump current is the most significant interaction excluding the rim width (w_r). For the depth values (d_t and d_g) and rim width (w_r), scan speed and pump current account for almost the same percentage. On the other hand, all significant main factors and interactions other than the pulse frequency account for a very small percentage for rim distance (w_{rr}) and groove width (w_g). For a clear mark, the depth (d_t and d_g) and groove width (w_g) are preferred to be high whereas the widths (w_{rr} and w_r) regarding the rim

effect are chosen to be minimum. Regarding the depth, the selection of a low scan speed, a high current (laser power) and a medium or high frequency give better results in the studied ranges for this type of material (AISI 1085). From the single-factor tests, it is apparent that the depth value decrease as one rises the frequency up to its limit around 60 kHz. Therefore, staying in the range of 30-45 kHz is recommended for the conditions mentioned above. Although the minimum for the rim distance (w_{rr}) is achieved at the highest frequency value (in the selected range in design of experiments), it is better to keep this parameter at a medium value. This is due to the fact that the groove depth (d_g) is also dependent on the frequency and its value at the highest value is very low for a readable and high-contrast mark. For the rim width (w_r), the frequency is not significantly of importance. According to the S/N ratio analysis, a low current and a high scan speed is necessary for low total width (w_{rr}); however, the effect of these two parameters is much more important for depth values. Therefore, a selection of a high pump current (37 A), a low scan speed (300 mm/s) with a selection of medium frequency (30-45 kHz) is the best set for optimum values of all marking dimensions.

2.2 Two-Dimensional Erosion

2.2.1 Introduction and Literature Review

In order to combine Selective Laser Melting and Selective Laser Erosion in a layer-wise manner, all relationships between process inputs and outputs must be well understood in two-dimensional erosion. In the laser marking study, there were mainly three significant process inputs, e.g. the scan speed, laser power and pulse frequency. Moreover, some other factors were studied, e.g. spot size, material and laser mode (CW or pulsed). However, in two-dimensional erosion, the number of process inputs becomes higher due to the interaction between scan tracks. The cause-effect diagram for two-dimensional erosion is depicted in Figure 2.39 regarding many aspects of the process such as the workpiece material, the laser source, the process variables and factors related to the spot size. Some of the parameters given in this figure also influence the process outputs in laser marking: e.g. pulse duration, intensity profile, pulse width etc. The effect of these parameters was not investigated in the scope of laser marking study due to diverse reasons. First of all, it was not possible to change the laser source due to technical limitations, neither the properties of the pulses due to software issues. The pulse frequency and laser power could be directly changed whereas the pulse energy was varied as a result of these settings. The overlap of the scan tracks or the scan strategy as well as the contour scanning are no process inputs since only single line scanning takes place in laser marking. However in two-dimensional erosion, these parameters become important process inputs. Therefore, in this chapter, the effects of scan strategy, scan spacing, scan speed, laser power, pulse frequency, atmosphere, spot size and selection of material on the process outputs, such as the depth of erosion per layer and surface quality left behind after erosion, are studied. Before the investigation of each parameter with single factor experiments, a process window study is conducted to find an optimum range of scan speed and laser power for a productive erosion process with a good surface quality. As a result of single factor experiments, it is concluded that the effect of one process parameter highly depends on the selection of other parameters. Therefore, an experimental design is utilized to explore the interactions between process parameters.

The two-dimensional use of Q-switched/pulsed lasers has some application areas in industry including laser alloying [71, 72], laser hardening [73-75], laser local softening [76, 77] to increase the formability of Al and laser surface texturing [78, 79] which is generally applied to change the surface properties of a product such as wettability, wear/friction performance, etc. to improve part efficiency and reliability and to improve safety [80, 81] or to add visual effects [82]. The most known and earliest application of surface texturing may be the one of cylinder liner honing [83]. Today surface texturing is used in many areas including the modern magnetic storage devices such

as blu-ray disc™ which is a trademark of Sony Corporation. Surface texturing is also used to overcome adhesion and stiction (static friction) in MEMS devices [84]. Competitive techniques of laser surface texturing are ion beam texturing, etching techniques and machining. Most surface texturing methods are motivated by the idea of making reservoirs to improve lubricant retention or micro traps to capture wear debris [85]. Due to several reasons, the laser surface texturing offers the most promising concept among all micro surface patterning methods. The reasons can be listed as: a fast and clean source of energy, short processing times, excellent control of shape and size of micro dimples and a good repeatability [85].

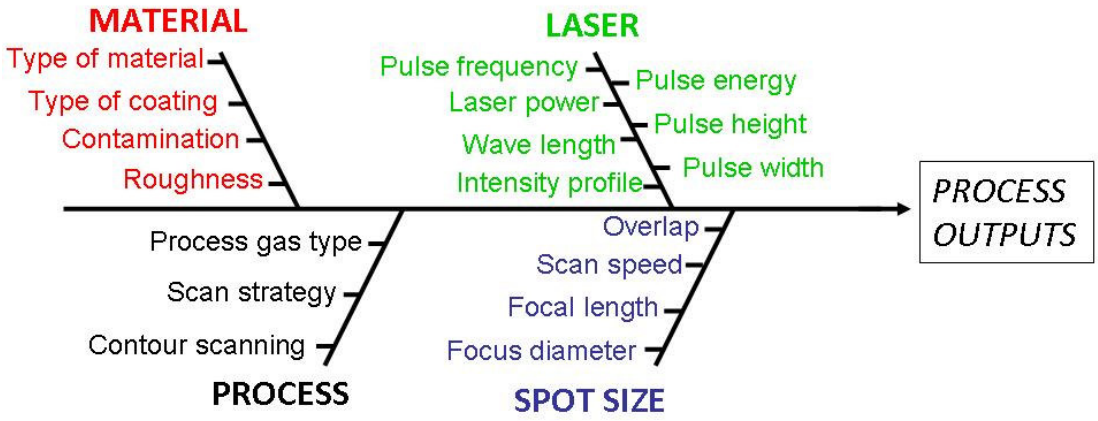

Figure 2.39: Cause-effect diagram for two-dimensional erosion

Laser surface texturing applications include the generation of nano/micro spikes via laser ablation of metals for the enhancement of some surface properties [86]. Surface modification by laser texturing is also employed in semiconductor industry [87]. Restructuring the surface of silicon or germanium, which are commonly used in electronics, may bring some advantages like improvement of effective surface area, entrapment of more light for fabrication of high efficiency optoelectronic devices, increase in catalytic reactions due to larger surface area and some benefits in biomedical applications [88]. Other than electronics, two-dimensional erosion is also employed in aeroplane industry for the paint removal [89-91] or for laser cleaning of contaminated surfaces in many areas including nuclear power industry [92, 93], in machinery for sheet roller texturing [56], for tooling applications [80, 94], for making tribological microstructures for hydraulic components [95] and for generation of liquid repellent on self-cleaning surfaces [78].

In the scope of this work, two-dimensional erosion is taken under investigation as a preliminary research for the combined process of SLM (i.e. additive manufacturing) and SLE (subtractive manufacturing). Therefore, the surface modifications by two-dimensional erosion are not studied to find optimum process parameters for the enhancement of some surface properties like wettability or wear. The main aim is to achieve efficient subtractive manufacturing and process outputs were the depth of erosion per layer which is directly linked to productivity of the process and the surface quality left behind after the erosion process. This chapter first explains the experimental set-up and measurement technique of process outputs and then presents the experimental results.

2.2.2 Experimental Procedure

The experiments were conducted on the same machine as for laser marking experiments, i.e. a Concept Laser M3 Linear machine. Grinded workpieces are eroded according to a square geometry with different parameters as shown in Figure 2.40. In the experiments except the ones conducted to study the effect of material, a type of carbon steel, AISI 1085 (with a composition of 0.8-0.93% C, 0.7-1% Mn, 0.04% (max) P, 0.05% (max) S, bal. Fe) is selected as the base plate material. After the tests are completed, the eroded squares were measured with a Talysurf 120L surface roughness and profilometer without any filters. Three-dimensional roughness measurements were conducted in

order to study the depth of erosion per layer and surface quality left behind as well as to get an overall insight about the surface profile.

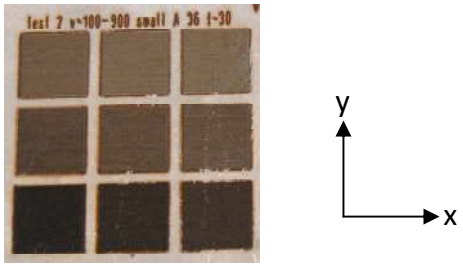

Figure 2.40: Test squares eroded with different parameters

After the three-dimensional measurements are conducted, the profiles are evaluated in a self-written Matlab code. First, the average z-value of several measurements is calculated for each x-position. An example of such an average profile for 5 eroded squares with different process parameters is shown in Figure 2.41. Then the inherent slope of this average profile is calculated based on the material in between eroded squares which is not exposed to laser radiation (See Figure 2.42). These non-processed regions are also used to calculate the depth of erosion per layer. The level of these regions is considered to be starting or zero level. The average profile is then plotted without the calculated slope. The mean level of eroded region is subtracted from the zero level (See Figure 2.43) and divided by the number of erosion layers giving the depth of erosion per layer. The surface quality is also evaluated depending on the three-dimensional measurements with the aid of SPIP software. 3D height maps and average profiles of eroded squares with different scan track overlapping factors are depicted in Figure 2.44 as an example (overlap expressed as percentage of $Ø_{99\%}$ laser spot size).

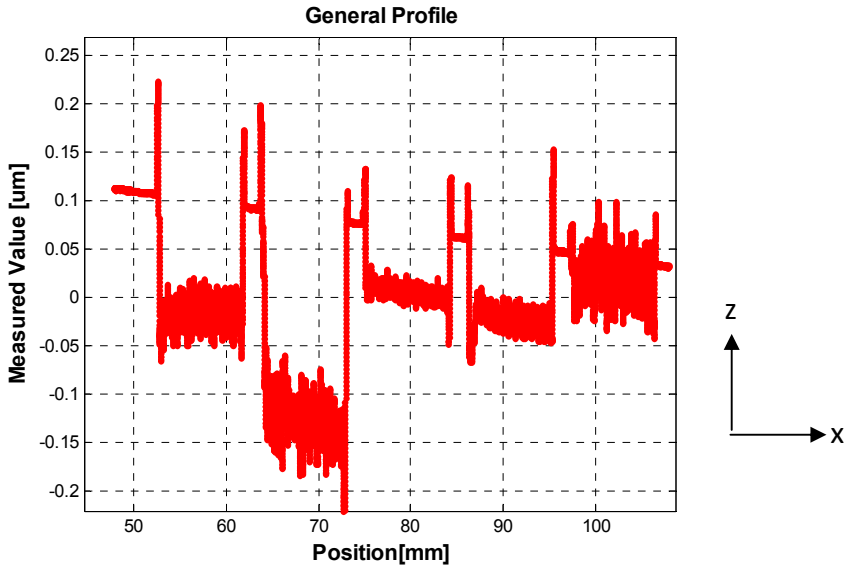

Figure 2.41: The raw data processed in Matlab

The roughness measurements presented in this chapter also depend on 3D measurement results and obtained from SPIP software. The average roughness (S_a) is calculated with the following equation

$$S_a = \frac{1}{MN}\sum_{k=0}^{M-1}\sum_{l=0}^{N-1}\left|z(x_k, y_l) - \mu\right| \tag{2.3}$$

$$\text{and } \mu = \frac{1}{MN}\sum_{k=0}^{M-1}\sum_{l=0}^{N-1} z(x_k, y_l) \tag{2.4}$$

where μ is the mean height, M number of points along x, N number of points along y, z is the height measured at position (x,y).

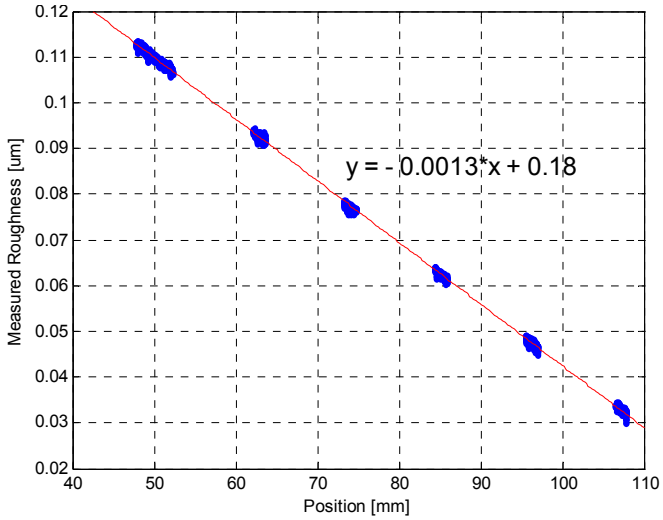

Figure 2.42: The removal of the slope from the raw data based on un-affected material

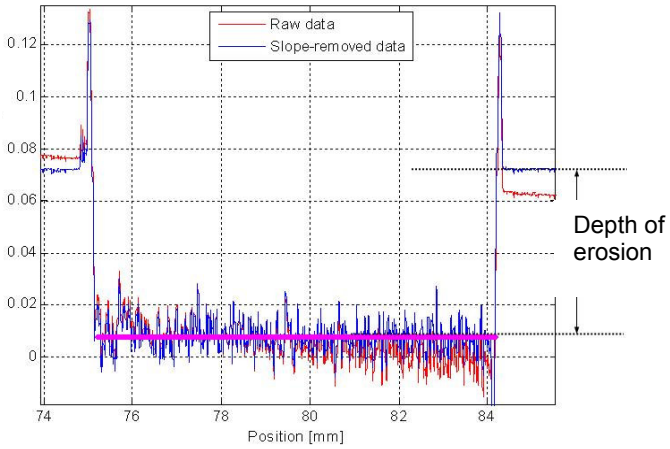

Figure 2.43: Final evaluation of the depth of erosion

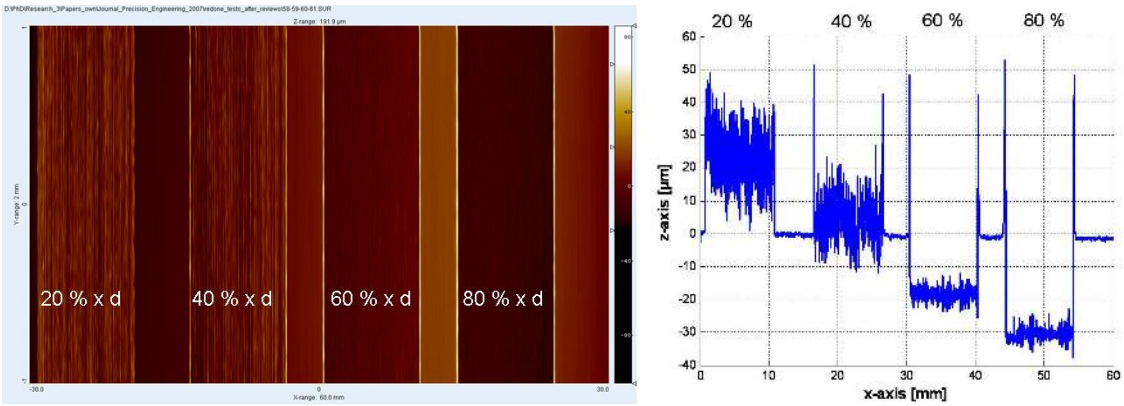

Figure 2.44: 3D height maps of eroded squares with different overlap factors from SPIP software and the average profiles

Therefore, the obtained roughness value is representative of the whole surface unlike with 2D measurements. In 2D roughness measurements, several linear measurements can be taken along different locations on the workpiece and then R_a values can be calculated for every measurement taken. An average of these measurements as well as confidence level can be calculated. With 3D

measurements, it is possible to calculate the standard deviation without repeating the measurements on different locations on the workpiece or on different parts. In this study, the measurements are only taken on one spot with several measurements along y-axis. Therefore, no confidence level is indicated in the figures. However, to give an insight of how big these variations would be, some analysis of 3D measurement results is done for one case, i.e. the tests conducted to investigate the effect of material selection on depth of erosion and roughness. 3D measurement results are analyzed as they were taken with 2D measurements. Each linear measurement is exported and roughness of each profile is calculated (See Figure 2.45a). For the case shown in Figure 2.45a, the average roughness (S_a) is calculated as 4.21 µm (using Eq.2.3) whereas the confidence interval with a 95% level is calculated to be 0.16 µm for 15 2D measurements. The confidence intervals obtained with this kind of analysis were less than 0.3 µm for all the results presented in §2.2.3. One example (change of surface roughness with respect to scan speed for maraging steel base plate) is shown in Figure 2.45b showing how small the error bars are.

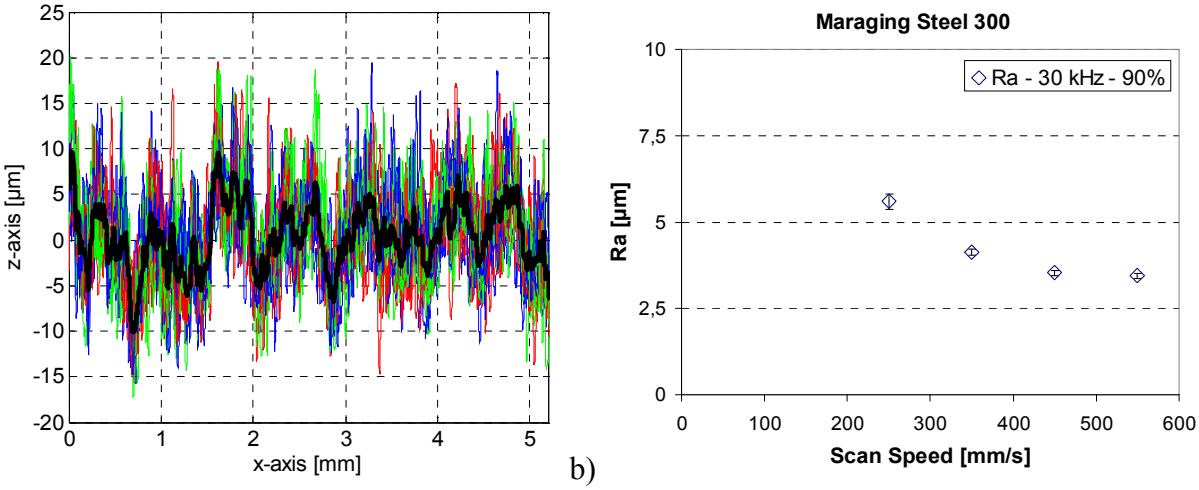

Figure 2.45: a) Analysis of a 3D measurement (maraging steel, 30 kHz, 90% overlap, 350 mm/s) as if they were taken in 2D, average profile shown with the thick line b) the roughness values shown in Figure 2.68 with error bars showing 95% confidence intervals

2.2.3 Experimental Results

a. Process Window for 2D Erosion

The process window of two-dimensional (2D) erosion involving the scan speed and laser power is obtained for two different settings for the rest of the process parameters. During the first process window study, the following process parameters are used: a scan spacing of 7 µm, a pulse frequency of 30 kHz, and selection of the small aperture giving a spot size ($Ø_{99\%}$) of approximately 80 µm. Many pairs of scan speed and laser power values (as shown with crosses in Figure 2.46) are tested to investigate at which points the given laser energy is enough to remove material with a good surface quality left behind. Some of the experiments gave very bad surfaces (black in color and very rough) whereas some were very difficult to recognize the change (very light color change with almost no depth).

As expected, high laser powers together with low scan speeds result in too much energy density and burned surfaces (See Figure 2.46). In this case, the color of the surface exposed to SLE is almost black. High scan speeds in combination with low laser powers, on the other hand, result in inadequate laser intensity and thus no erosion. In this case, the surface is only re-melted but no material can be removed. The region in between these two zones gives better results yielding a compromise in between good surface quality and high productivity (or a high depth of erosion).

In the second process window study, the big aperture was chosen giving a spot size ($Ø_{99\%}$) of approximately 180 µm. The pulse frequency was set to 45 kHz and a scan spacing value of 50 µm was utilized. As seen from Figure 2.47, the suitable working area is again in an almost triangular shape but has shifted upwards giving approximately the same average depth per layer, i.e. 3 µm. Although a higher laser power is obtained with the big aperture, the other process parameters, such as the higher scan spacing value and higher spot size lowered the energy input to the substrate per unit area.

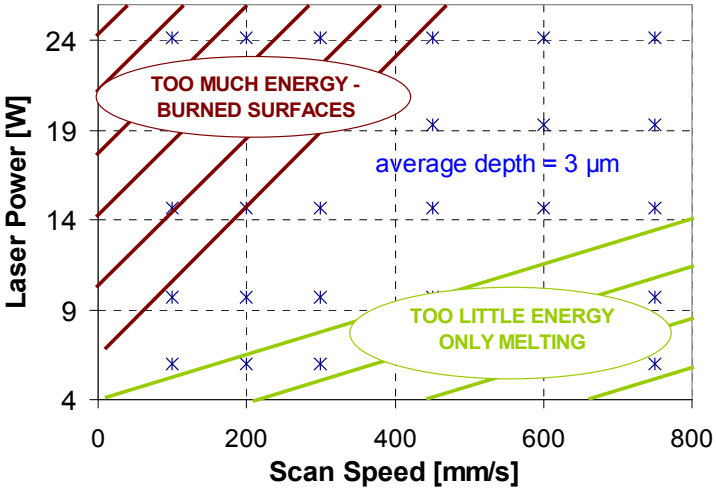

Figure 2.46 : The process window for SLE at a scan spacing of 7 µm and a pulse frequency of 30 kHz with the selection of small aperture on AISI 1085 grinded substrate

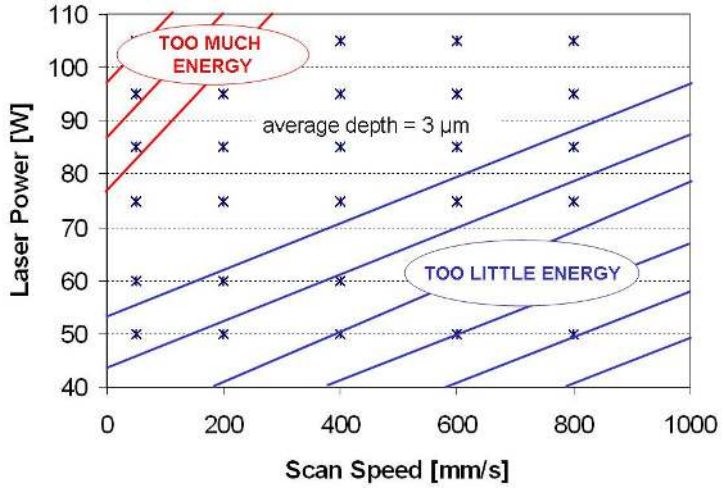

Figure 2.47 : The process window for SLE at a scan spacing of 50 µm and a pulse frequency of 45 kHz with the selection of big aperture on AISI 1085 grinded substrate

As a result of these two process window studies, it should be noted that the suitable processing conditions (laser power and scan speed in this case) highly depend on the other process parameters which are kept constant during the study. High energy densities result in higher depth of eroded material, and thus productivity but the eroded surfaces are quite rough whereas low energy densities result in only re-melting of the surface but no material removal.

b. Investigation of Process Parameters by Single Factor Experiments

In this section, the experimental results are given with an emphasis on each process parameter investigated. The process parameters that are taken under investigation are scanning strategy, scan speed, laser power, pulse frequency, scan spacing between laser tracks (or overlapping factor),

environment, material and spot size. All the experiments in this section are performed by changing one process parameter while all others are fixed.

Scanning Strategy

The scanning strategy is the manner in which the laser beam scans the surface of the workpiece. Scan strategies (or hatching) can differ in hatch angle, scan spacing, overlap factor and scanning direction (unidirectional or bidirectional). Different scanning strategies were tested and measured to investigate the effect of applying multiple scans with different hatch angles as shown in Figure 2.48. The first strategy is composed of a succession of two erosion scans or two eroded layers (repeated 6 times) which have scan lines perpendicular to each other (0° and 90°). In the second strategy, the hatch angles are selected as 45° and 135°, which is the same as the first strategy except that it is only rotated by 45°. The third scheme has only repetition of one scan (repeated 12 times, i.e. 12 layers with same scan pattern) which consists of 'vertical' scan lines (90°). The fourth one is a combination (repeated 6 times) of one scan (layer) of 'vertical' hatch lines followed by diagonal hatch lines (90° and 135°). The last one consists of four alternating scans or layers (repeated 3 times), each with a different hatch angle (0°-45°-90°-135°). During the tests, the other test parameters are selected as follows: a scan speed of 480 mm/s, a scan spacing of 7 µm, a pulse frequency of 30 kHz, a laser power of 25 W and the selection of the small aperture ($Ø_{99\%}$ spot size of 80 µm).

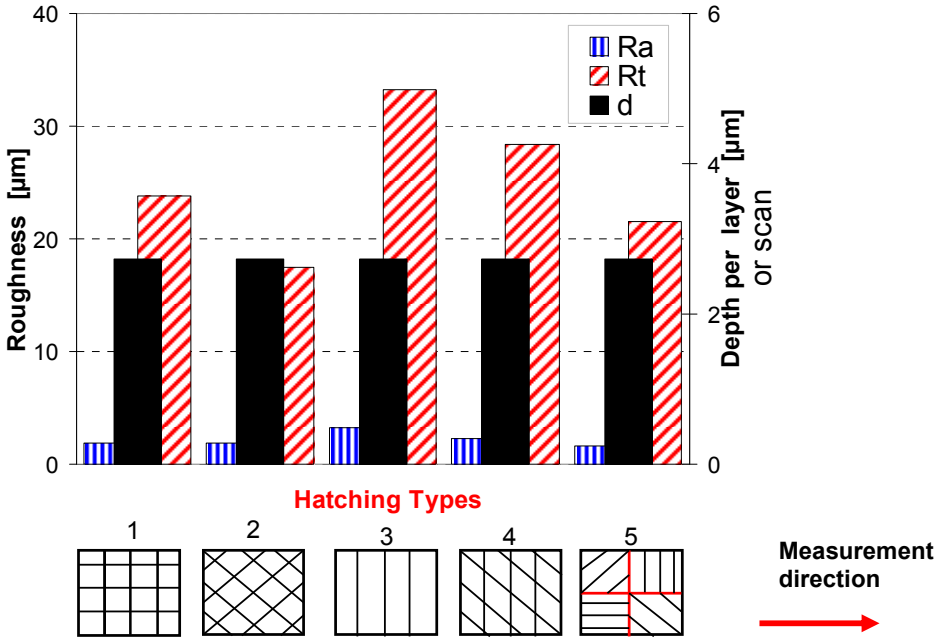

Figure 2.48: The effect of scanning strategy on the roughness (R_a and R_t) and depth of erosion per scan tested on AISI 1085 grinded substrate

The results and the direction of measurement are displayed in Figure 2.48. As observed, the depth of erosion per layer (d) is almost independent of the scanning strategy with a maximum variation in depth of about 4.5% which equals to 0.12 µm for the average depth value of 2.73 µm. This variation can be considered insignificant and due to experimental scatter (variations in oxygen content, temperature, etc.). However, the variations in roughness are pretty high and equal to 49% for average roughness R_a, and 33% for the total roughness R_t. As expected, the highest roughness values are exhibited by the third scanning strategy where all scan lines have the same orientation. This can be explained by the fact that when the same hatch pattern is applied successively, the created peaks and valleys by the laser scan lines on the surface get more severe. The fifth scanning strategy, which is made of four alternating hatch scans, achieves the best R_a, whereas the lowest R_t

is obtained by the second one. This conclusion is confirmed by [49], where substantial reduction of the surface roughness was achieved by changing the scanning direction (hatch angle) from scan to scan. As a result of these tests, it can be concluded that alternating scans improves the surface roughness significantly, by about 50% for both average and total roughness values whereas it has no significant effect on the rate of erosion.

In addition to comparisons of different scan strategies in terms of roughness and erosion depth, the average profiles of the surfaces along the measurement direction for a second set of tests are plotted in Figure 2.49a. The test parameters were as follows: a scan speed of 480 mm/s, a laser power of 25 W, a pulse frequency of 30 kHz and an overlap factor of 80% (a scan spacing of 16 µm), small aperture, 8 layers. The low surface quality of the scanning strategy consisting of only vertical scan lines (3) can also be observed from its average profile as given in Figure 2.49a. In Figure 2.49b, the 3D height maps of the same surfaces are also illustrated where the hatch angle of the scan tracks can easily be recognized. Due to closed source software of Concept Laser, it is not easy to adapt the scan strategy in any desired way like fractal scanning. Therefore, the tested strategies are limited to software possibilities.

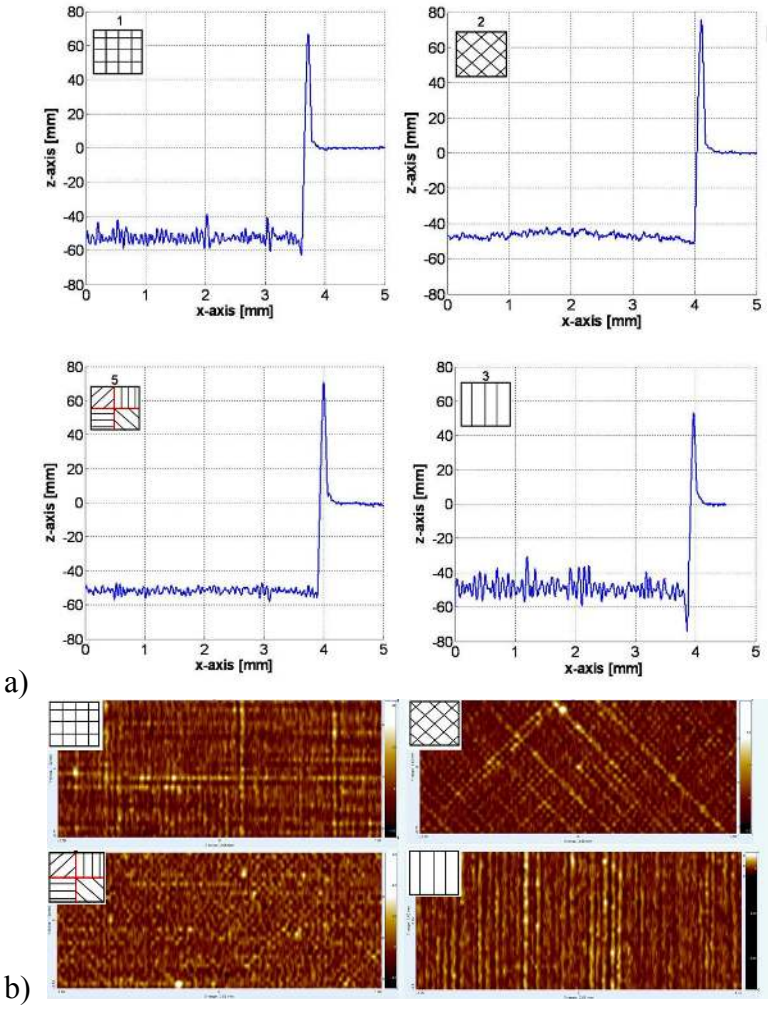

Figure 2.49: a) Profiles of the surfaces exposed to different scan strategies b) 3D height maps of the same surfaces

Scan Speed

The scan speed is a key parameter to the depth of erosion as well as roughness. As the scan speed increases, the energy entered into the substrate per unit area decreases, so does the depth of erosion per layer. On the contrary, the process time increases substantially when low scan speeds are

selected. The scan speed influences the overlap between subsequent laser pulses; the lower the speed, the greater the overlap and the larger the layer due to multi-pulse radiation. The results of the experiments conducted at different scan speeds are presented in Figure 2.50 and Figure 2.51 in terms of depth of erosion and roughness, respectively. The first case is a test performed with a scan spacing of 75 µm, a laser power of 100 W and a frequency of 30 kHz with a big aperture under nitrogen (N_2) environment with a remaining oxygen (O_2) content of less than 1%, whereas the second case is conducted at the same conditions except that it was carried out in regular air. The last case was also performed under regular air but with a scan spacing value of 25 µm instead of 75 µm. Figure 2.50 and Figure 2.51 show that depth of erosion and roughness are both inversely proportional to the scan speed. However, the slopes of LSQ fitted lines for different scan spacing values differ. This refers to the possible interactions between the test parameters, namely scan speed and scan spacing. The interaction between scan spacing and scan speed is found to be the most significant factor in the experiments where design of experiments is utilized for two-dimensional erosion. For more details on the results of design of experiments, [96] should be referred to. Since the scan speed and scan spacing together influence the overlapping factor between successive laser pulses and scan lines, this was an expected result. Another important observation is that the first and second cases give very close results for both average roughness and depth of erosion. Hence the influence of the environment (N_2 or regular air) on process outputs is insignificant for this material.

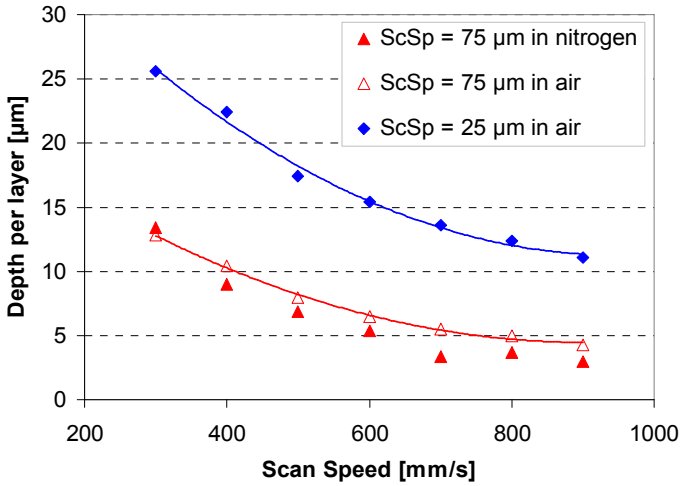

Figure 2.50: The effect of scan speed on the depth of erosion for different test conditions applied on AISI 1085 grinded substrate

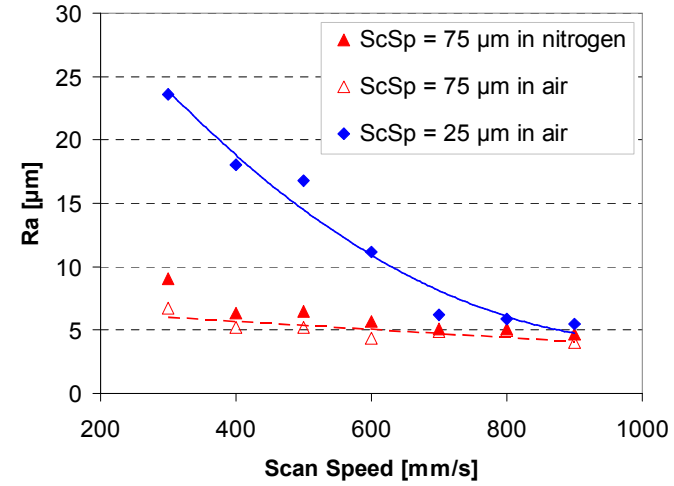

Figure 2.51: The effect of scan speed on the average roughness (R_a) for different test conditions applied on AISI 1085 grinded substrate

Scan Spacing

The scan spacing is the distance between two successive scan lines and is an important factor for the determination of overlapping between scan lines. For low values of scan spacing which correspond to high overlapping factor, the energy per unit area is high and results in higher amount of removed material. On the other hand, a scan spacing value which is greater than the effective laser spot diameter results in totally separate material removal tracks: some material in between tracks is not removed. This case is depicted in Figure 2.52. For a good connection between successive scan tracks and low roughness values, too high scan spacing values (almost no overlap values) should be avoided. The overlap factor is related to the scan spacing with the following equation in the Concept Laser machine software:

$$Scan\ Spacing = (1 - Overlap) \times Spot\ Size\ (\phi_{99\%}) \tag{2.5}$$

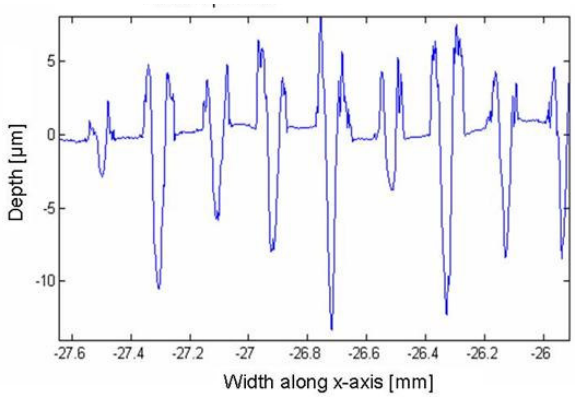

Figure 2.52: Totally separate tracks due to incorrect selection of scan spacing value

The depth of erosion measured with different overlap values between 10% and 95% are presented in Figure 2.53 for four different test conditions which are given in the table below the figure. The scanning was conducted in grid pattern (strategy number 1 in Figure 2.48) applied 4 times (8 layers) with the selection of small aperture ($Ø_{99\%}$ spot size of 80 µm). A lower scan spacing, i.e. higher overlap results in higher depth consistently with the expectations due to the increase of laser energy per unit area. At overlap values lower than 50%, there is no material removal (See Figure 2.54). The scanned surface is only melted and re-solidified leaving a very bad surface quality behind that even may be limited with a rising surface (induced porosity). Therefore, no value is specified in Figure 2.53 for these two overlap values (10-30%).

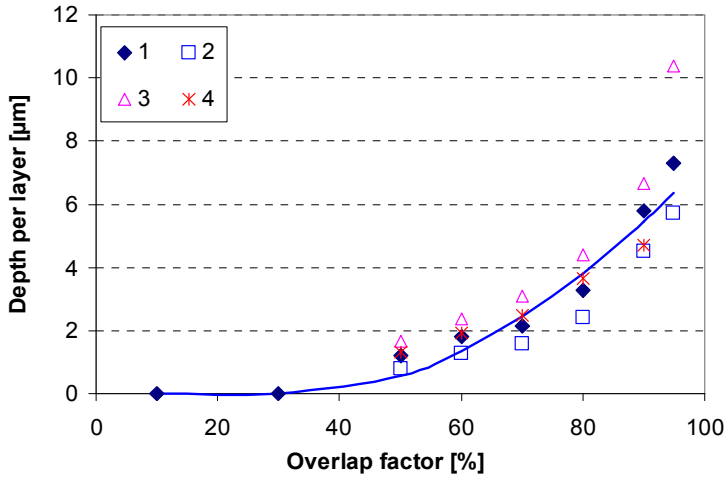

	v [mm/s]	P [W]	f [kHz]
1	600	18	45
2	800	18	45
3	600	23	45
4	600	18	30

Figure 2.53: The effect of scan spacing on the depth of erosion tested on AISI 1085 grinded substrate

In Figure 2.55, the variation of the average roughness is given with respect to overlap (scan spacing) for the same conditions given in Figure 2.53. An overlap factor of 10% or 30% results in very high average roughness. As the overlap factor is increased, the surface quality improves and reaches a minimum value. The relation between scan spacing and roughness changes after this critical overlap factor where the minimum R_a value for a specified set of conditions is achieved. As the overlap factor is further increased, the surface quality slightly deteriorates because of too high energy input. Generally, the critical overlap factor lies between 60-80%.

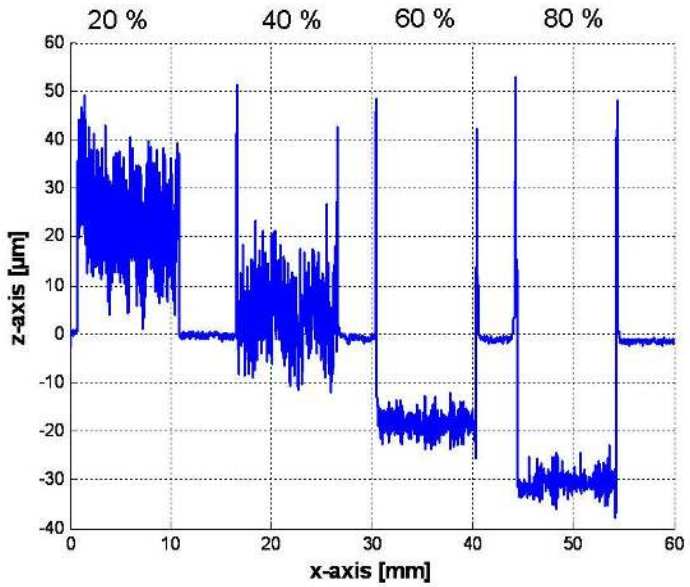

Figure 2.54: The derived profiles at different overlapping factors at 600 mm/s, 30 kHz, 20 W, small aperture, 8 layers of grid strategy tested on AISI 1085 grinded substrate

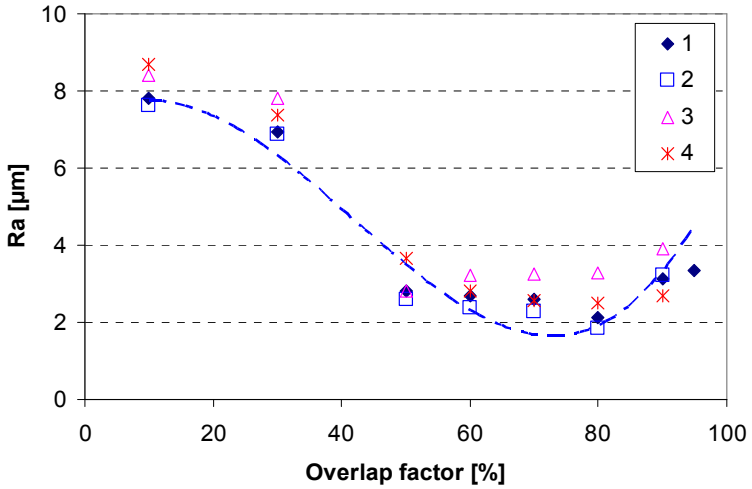

Figure 2.55: The effect of scan spacing on the average roughness (R_a) tested on AISI 1085 grinded substrate

The average profiles of the laser machined surfaces with different scan spacing values are illustrated in Figure 2.56 where the numbers above the graphs represent the overlap factors. The parameters were fixed at following values during this set of experiments: 600 mm/s, 20 W, 45 kHz, small aperture, 8 layers and with a selection of grid scanning strategy (strategy 1). The roughness improvement is clearly seen with an increasing overlap factor from very low factors to medium factors. The depth of erosion also increases substantially with decreasing scan spacing factor. The 3D height maps of the surfaces left behind are depicted in Figure 2.57 where it is seen that the low overlap factors below 50% result in a bad connection between successive tracks and there is no erosion for those overlap factors.

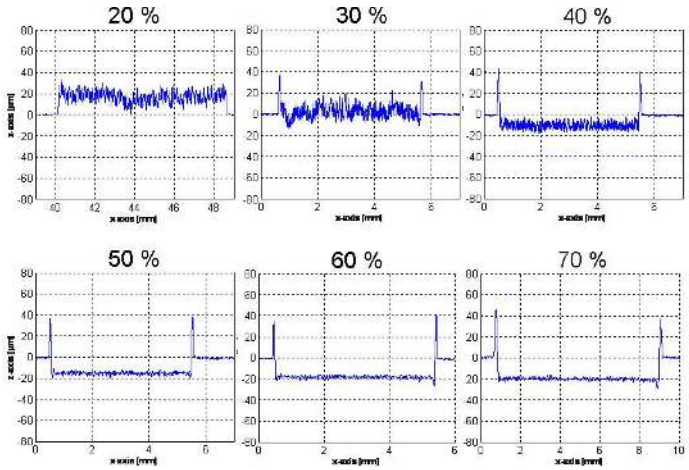

Figure 2.56: Average profiles of the scanned surfaces with different overlap factors

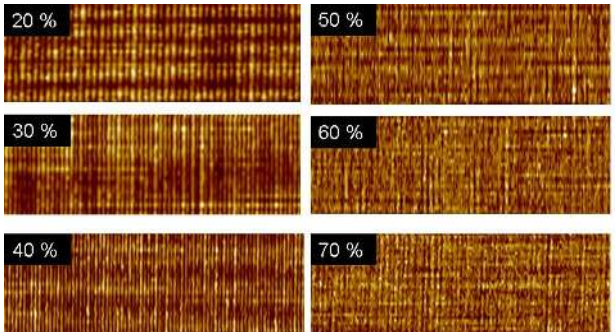

Figure 2.57: The 3D height maps of the surfaces in Figure 2.56

Laser Power

The pump current can be adjusted by the Concept Laser machine software to control the laser power and is one of the most important process parameters for SLE due to its direct effect on the removal rate. A lower limit for the laser power intensity ensures the evaporation of material necessary for SLE. If the laser power intensity is kept below a certain threshold, the workpiece material is only melted and not removed [96]. The relation between the pump current and laser power, which is measured in the continuous mode with the internal power measurement system installed in the machine, is a linear one as shown in Figure 2.33, however the laser power values that are obtained with a constant pump current may depend on some adjustment of optical components in the machine and may differ from time to time. Therefore, in this section, instead of pump current values, the average power measured in the continuous mode is used as the input value. It should be noted that the peak power obtained with the same current is much higher. The peak power also depends on the pulse frequency and pulse duration (Figure 2.22). Tests were carried out with a laser power (measured in CW mode) from 2 to 23 W to investigate the effect of the laser power on the outputs at different scan speeds whereas the pulse frequency was set to 30 kHz with a scan spacing of 7 µm and a selection of the small aperture. The laser power of the beam depends on the selected aperture (See Figure 2.33).

Figure 2.58 and Figure 2.59 depict the results of those tests. The depth of erosion is expected to be highly dependent on the pump current since the average power of the laser beam increases linearly as a function of the pump current: see Figure 2.58 where the effect of the scan speed is also illustrated. When the scan speed increases, the energy input per unit area to the workpiece becomes less and the depth per layer is thus reduced. The change of depth with varying laser power is therefore not an independent relation since the scan speed has a very significant influence.

Figure 2.59 shows the change of average roughness with different values of pump current and scan speed. The figure clearly indicates that as the current is increased, the surface quality

deteriorates. The influence of the scan speed is in the reverse way; increasing the scan speed lowers the average roughness values, which is also consistent with the results of the experiments conducted for the effect of scan speed and scan spacing.

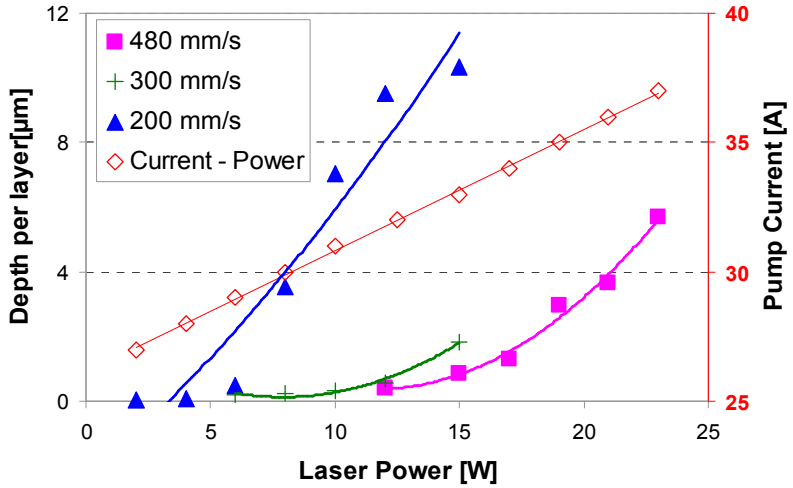

Figure 2.58: Effect of laser power on the depth per layer for different scan speeds (small aperture) tested on AISI 1085 grinded substrate

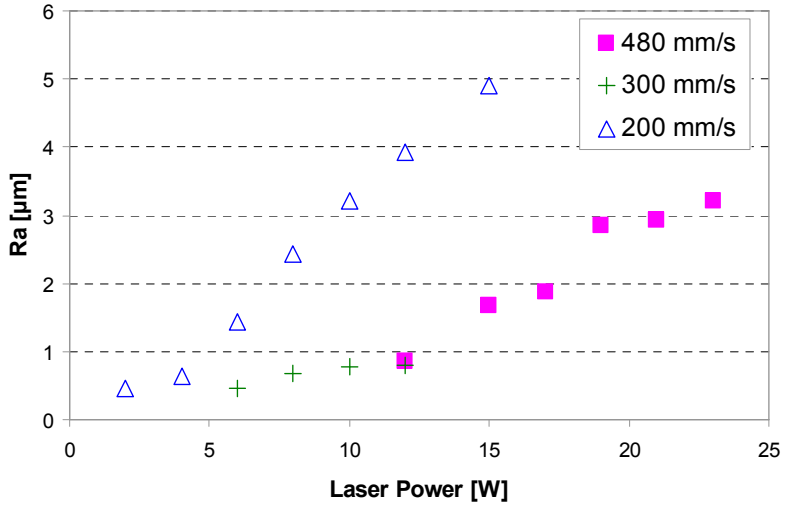

Figure 2.59: Effect of current on the average roughness (R_a) for different scan speeds (small aperture) tested on AISI 1085 grinded substrate

Pulse Frequency

The pulse frequency of a Q-switched Nd:YAG laser has a significant effect on the process. Experiments were done in a range of 20-50 kHz and the results are depicted in Figure 2.60 and Figure 2.61 for depth of erosion per layer and average roughness, respectively. The tests were conducted with a small aperture and a scan spacing of 7 µm. The tests are repeated for different laser powers and scan speeds. The relation between the frequency and the amount of material removed per layer is not the same for each selected set of testing conditions. For the first case (300 mm/s, 36 A corresponding to 21 W), the maximum depth of erosion is obtained at about 30-35 kHz and the relation can be best expressed with a quadratic polynomial. However, when the pump current, in other words the laser energy, is decreased, the relation of the pulse frequency with the depth of erosion approaches a linear trend. Furthermore, as the scan speed is raised from 300 mm/s to 480 mm/, the amount of material per layer decreases for the same level of laser power as expected.

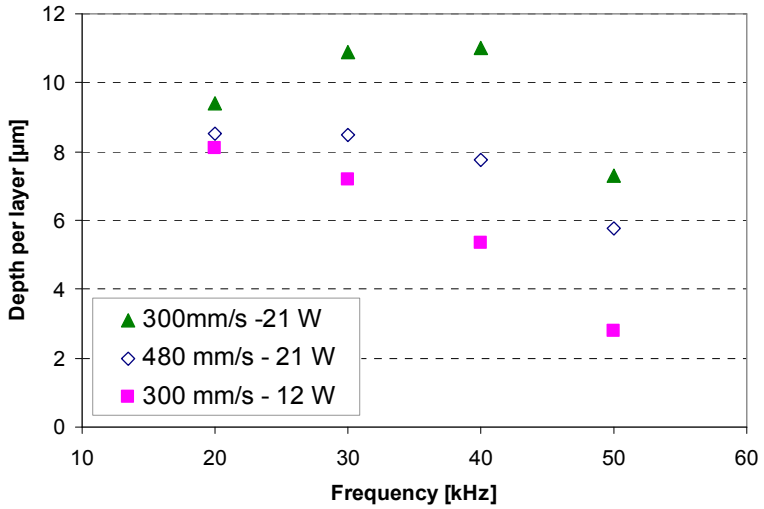

Figure 2.60: Change of depth of erosion versus pulse frequency under different test conditions (applied on AISI 1085 grinded substrate)

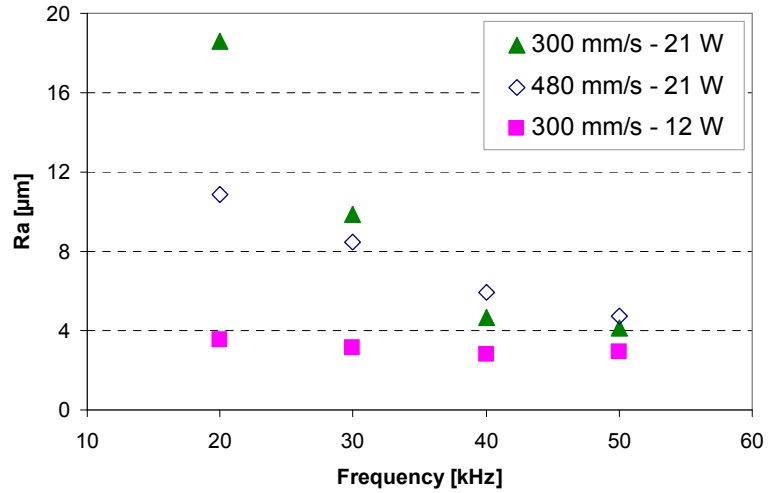

Figure 2.61: Change of average roughness (R_a) under different test conditions versus pulse frequency (applied on AISI 1085 grinded substrate)

It can be concluded that the relation between the frequency and depth of erosion highly depends on other testing conditions. This is due to the change in peak power and the average output power of the laser with change of the pulse frequency [30]. At low pulse frequency, the peak power is high enough to make materials evaporate during the process (See Figure 2.22). Thus, the amount of material removed increases with the average output power of the laser, which can be defined as the energy transferred into the materials per unit time. At high frequency values, the peak power decreases by increasing pulse frequency. The decreasing peak power is no longer high enough to evaporate the materials completely. Therefore, the peak power determines the amount of the material removed in high frequency values. The depth of erosion declines as the frequency increases.

Figure 2.61 illustrates the change of average roughness with respect to frequency. As frequency increases, the general trend for the roughness is a decreasing one. However, the amount of reduction is not independent of power and scan speed. For the low scan speed (300 mm/s) and high laser power (21 W), the lowest average roughness is achieved with the highest frequency value used in the experiments. This result is also valid at high scan speed (480 mm/s). For the low power (12 W)

and low scan speed (300 mm/s), the influence of frequency on the average roughness is rather limited and not very significant.

The 3D height maps of surfaces which were eroded with different pulse frequency values indicate one of the important application areas of two-dimensional erosion: laser surface texturing. If the parameters are set correctly, different patterns can be generated on the surface as depicted in Figure 2.62. During these tests, the frequency is changed from 5 to 60 kHz for 8 successive layers while keeping other parameters fixed at a scan speed of 300 mm/s, a laser power of 15 W, a scan spacing of 37.5 µm, a small aperture and grid scanning strategy. The obtained roughness results are also given below every 3D height map in the figure. In the scope of this study, no further investigation of optimum parameters for any specific purpose in the field of surface texturing was conducted.

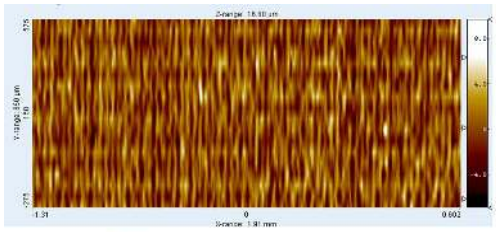

15 W, 300 mm/s, **5 kHz**, 8 layers (grid), small aperture, a scan spacing of 37.5 µm
Ra = 1.64 um Rt = 16.6 um

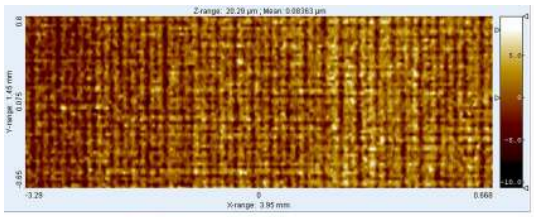

15 W, 300 mm/s, **10 kHz**, 8 layers (grid), small aperture, a scan spacing of 37.5 µm
Ra = 2.09 um Rt = 21.5 um

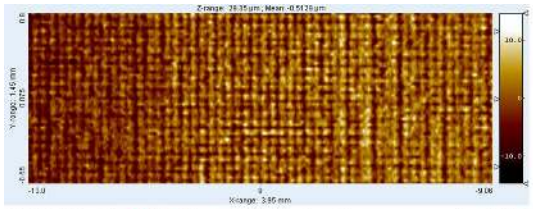

15 W, 300 mm/s, **20 kHz**, 8 layers (grid), small aperture, a scan spacing of 37.5 µm
Ra = 3.1 um Rt = 33 um

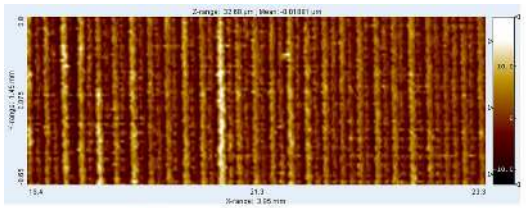

15 W, 300 mm/s, **40 kHz**, 8 layers (grid), small aperture, a scan spacing of 37.5 µm
Ra = 3.3 um Rt = 32.7 um

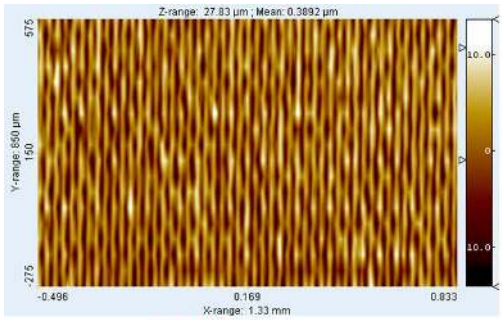

15 W, 300 mm/s, **60 kHz**, 8 layers (grid), small aperture, a scan spacing of 37.5 µm
Ra = 3.87 um Rt = 27.8 um

Figure 2.62: Laser surface texturing at different pulse frequency values

Spot Size

The power intensity of a laser is highly dependent on the spot size assuming a constant laser power. On the Concept Laser M3 Linear machine, there are only two available aperture settings yielding a spot size of $Ø_{1/e^2}$: 70 (small aperture) and 130 µm (big aperture). Four sets of experiments are carried out both for small and big apertures with different scan speeds and laser powers at fixed pulse frequency (30 kHz) and scan spacing (5 µm). The test conditions as well as the results are given in Figure 2.63 and Figure 2.64, regarding the depth of erosion and average roughness respectively. In the table given in Figure 2.63, the test conditions are shown. Please mind that the laser powers derived with big and small apertures are not the same at a given pump current. The experimental results show that the big aperture always results in higher values in both depth of

erosion and average roughness. The amount of the change from small to big spot size is not fixed and depends strongly on other parameters.

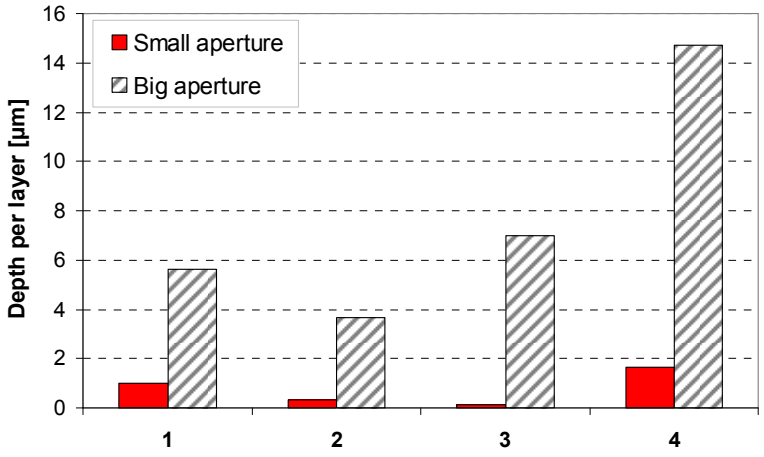

	I [A]	P [W]		v [mm/s]	f [kHz]	ScSp[µm]
		small	*big*			
1	30	9	25	1500	30	5
2	36	65	100	3000	30	5
3	36	65	100	1500	30	5
4	30	9	25	600	30	5

Figure 2.63: Variation of depth per layer for two different aperture openings (on AISI 1085 grinded substrate)

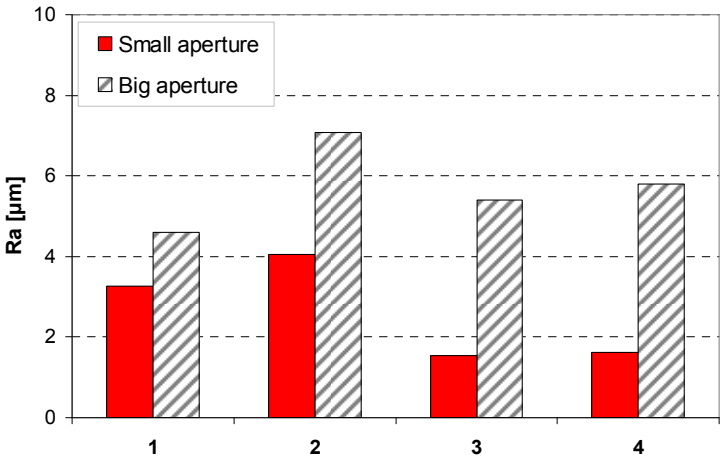

Figure 2.64: Change of average roughness (R_a) for two different spot sizes (on AISI 1085 grinded substrate)

In order to machine fine details and/or thin walls, the smaller spot size would be more suitable. However, when processing time is the most important parameter to be minimized, the big spot size is selected which shortens the processing time significantly.

In the experiments shown in Figure 2.63 and Figure 2.64 the scan spacing is chosen as 5 µm for both aperture openings. Thus, the overlapping between successive scan tracks for small and big apertures is different. If the scan spacing is taken as a fixed value, then the overlap factor, which is the ratio of the overlapping distance over the spot size, is higher for the big aperture, resulting in higher depth of erosion per layer.

In order to investigate the effect of small and big apertures on the surface quality and depth of erosion at a constant overlapping factor, more tests were conducted. The results are depicted in Figure 2.65 and Figure 2.66. The difference between the small and big aperture in terms of depth of

erosion is not severe especially at higher scan speed range which is due to the fact that the laser intensity is more or less the same with big and small apertures (due to different laser powers as well as spot sizes). However, the small aperture results in better surface quality within the tested scan speed range as shown in Figure 2.64.

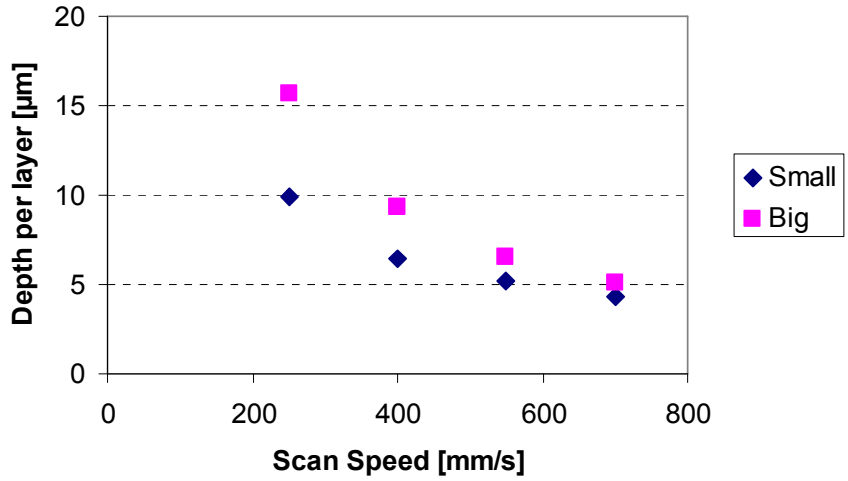

Figure 2.65: Variation of depth per layer for two different aperture openings at fixed overlapping tested on AISI 1085 grinded substrate

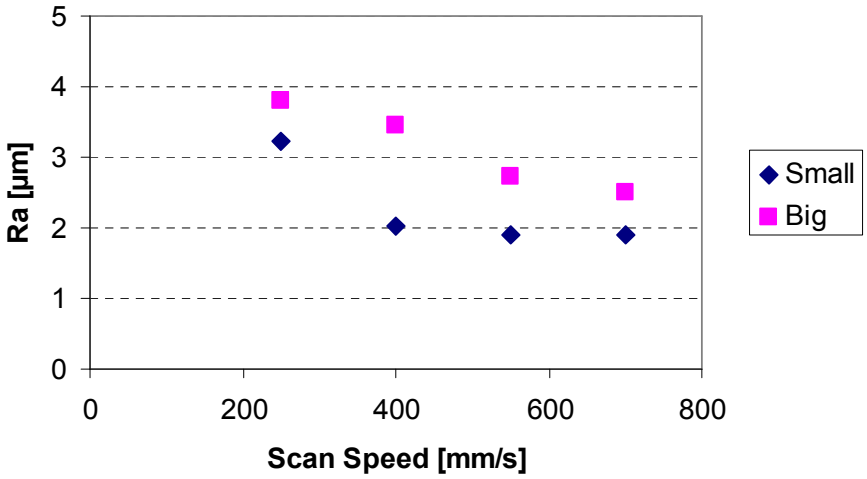

Figure 2.66: Variation of average roughness (R_a) for two different aperture openings at fixed overlapping tested on AISI 1085 grinded substrate

Material

The response of a material to laser radiation is influenced by a number of material characteristics such as laser absorptivity, thermal conductivity, evaporation and melting energy. The removal of the material by the laser light can only occur at wavelengths for which the particular material is strongly absorptive. A higher absorption generally results in a more effective laser process [49]. In order to increase the absorptivity, one shall create an appropriate surface finish prior to the erosion process.

Thermal conductivity affects the dissipation of the absorbed energy into the bulk of the material, the energy losses, the material removal efficiency and the dimensions for the heat-affected zone. Low thermal conductivity results in a more machinable material by laser radiation. The melting and evaporation energy are important because they are generally the determining factors in the phase

transitions that the material passes through during the process. For instance, ceramic materials compared to metals, are more difficult to melt, but are relatively easier to evaporate, which influences the laser ablation mechanism (regarding the melting and boiling temperatures).

In order to study the effect of material on the erosion results, 80×80×6 mm specimens were first built by SLM with optimized parameters for density on AISI 1085 base plates. While still on the base plate, they were grinded to eliminate the effect of roughness on the laser absorptivity. The effect of the scan speed on the depth per layer is tested at three different combinations of the scan spacing and the frequency while the laser power was set to 85 W with the selection of the big aperture. The scan tracks were taken perpendicular to the measurement direction and 5 layers of erosion are applied. The depth per layer of the tests conducted on maraging steel and AISI 316L stainless steel samples are depicted in Figure 2.67. For the maraging steel, there is a missing data for 30 kHz and 90% overlap at a scan speed of 150 mm/s due to very bad surface quality making the measurement with a contact probe impossible. At low scan speeds, the depth per layer is significantly higher with AISI 316L than the maraging steel 300. This may be due to higher thermal conductivity and melting temperature of maraging steel (see Table 2.1). For example, at a scan speed of 150 mm/s, the maraging steel is only eroded by 21 µm per layer while 29.5 µm of material is eroded with AISI 316L which is almost 40% more. As the scan speed is increased, AISI 316L still gives higher depth per layer but the differences in the results of two materials become less critical.

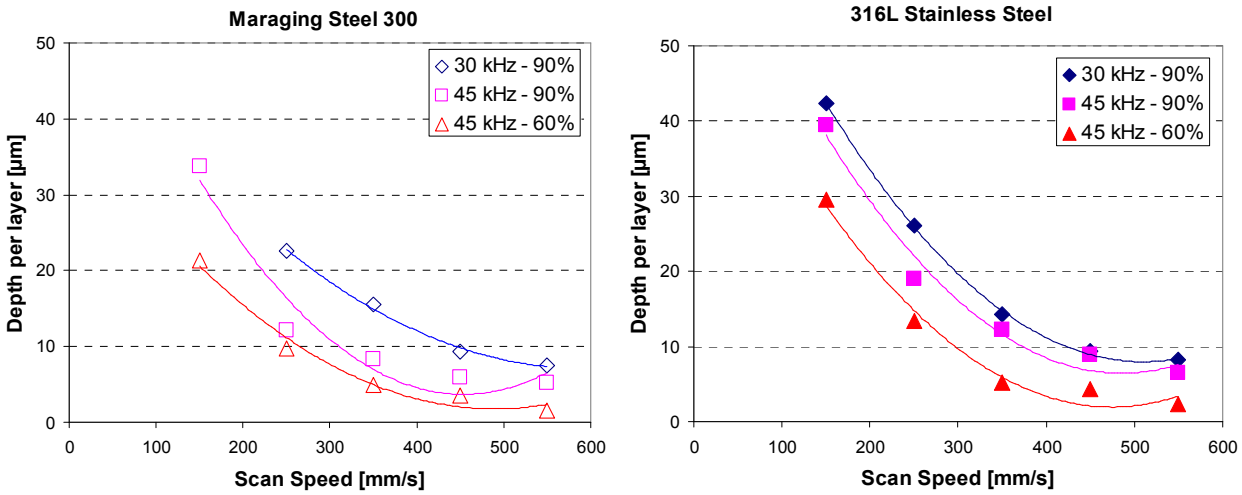

Figure 2.67: Variation of depth per layer for different sets of parameters tested on grinded maraging steel and 316L stainless steel substrates

Table 2.1: Material properties of 316L and maraging steel 300 (18-Ni 300)

Material	Melting Temperature (ºC)	Thermal Conductivity (W/m.K at 100 ºC)
316 L [97]	1375-1400	16.3
18-Ni 300 [98]	1400-1450	27

Figure 2.68 depicts the average roughness results for the maraging steel and stainless steel. The change in the frequency or the scan spacing does not significantly change the results, especially at high scan speeds. As the scan speed is reduced, the surface becomes rougher. This is actually more pronounced at the lowest scan speed, i.e. 150 mm/s. The average roughness R_a stays below or close to 5 µm if a scan speed greater than 300 mm/s is selected. Regarding the material, there is no significant difference especially at medium or low energy inputs. The measured total roughness (R_z) values follow the same trend as the average roughness (R_a).

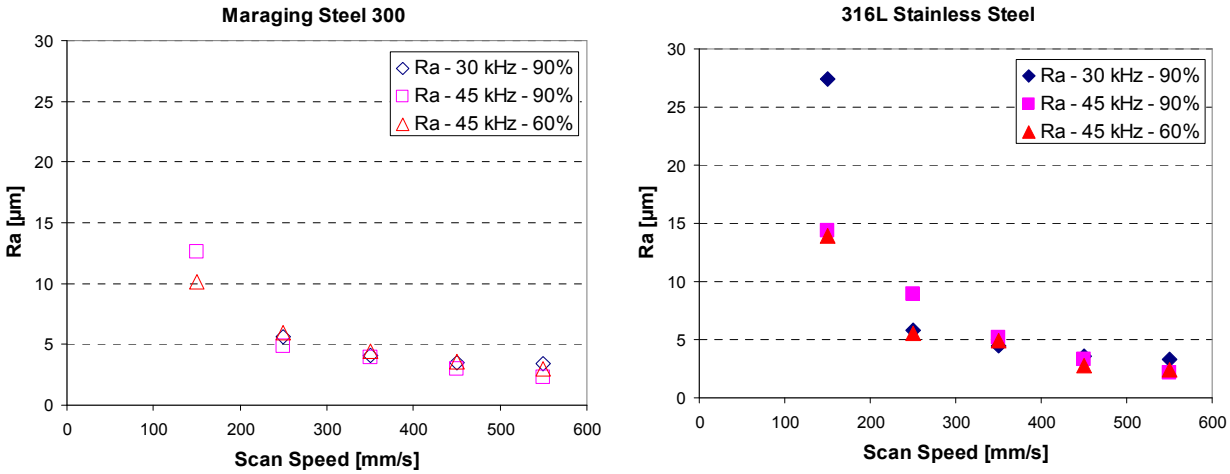

Figure 2.68: Variation of R_a for different sets of parameters tested on grinded maraging steel and 316L stainless steel substrates

The 3D height maps of two materials obtained with the same erosion parameters are depicted in Figure 2.69. The erosion tests for these two map heights are conducted at a scan speed of 150 mm/s, a frequency of 45 kHz, an overlap of 60% and a laser power of 85 W. As mentioned previously, the maraging steel sample gave a depth of 21 µm per layer whereas a 29.5 µm is eroded per layer for stainless steel. The average roughness values are 13.9 and 10.1 µm whereas the total roughness values are measured as 149 and 98.4 µm for stainless steel and maraging steel, respectively. When the three dimensional height maps are compared, it is seen that larger bumps are formed with the stainless steel deteriorating the surface quality.

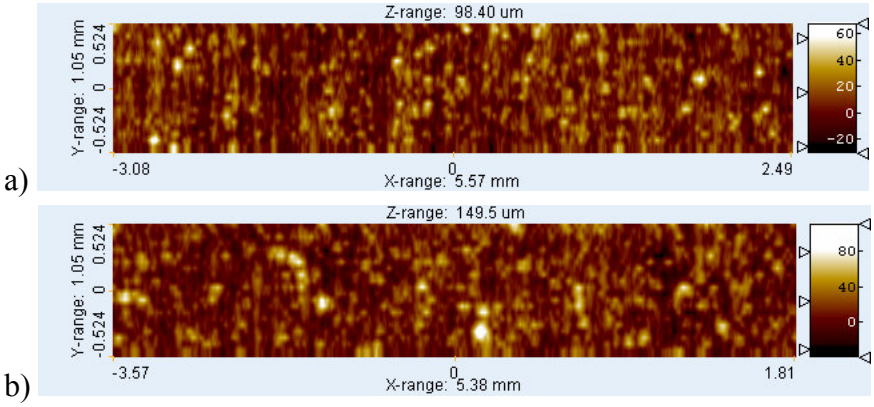

Figure 2.69: 3D height maps of (a) maraging steel and (b) stainless steel for erosion parameters of a scan speed of 150 mm/s, a pulse frequency of 45 kHz, 60% overlapping and a laser power of 85 W

As a conclusion, it is easier to erode the samples made from stainless steel rather than the maraging steel. However, the surface quality left behind will be worse with the stainless steel. The results are in good agreement with the conclusions of other tests stating that a higher roughness value is obtained when the surfaces are eroded more deeply.

Number of erosion layers/scans

In order to investigate if the number of applied erosion layers/scans makes any difference in terms of average depth of erosion per layer and the roughness values, some tests are conducted on AISI 316L base plate which is produced by SLM. Two sets of parameters are tested at five different numbers of SLE layers, i.e. 1, 3, 5, 10 and 15 layers. Too high number of SLE layers is not utilized in order to avoid the scanned surface to move out of focus. The common parameters in the two parameter settings were a laser power of 85 W (35 A), 90% overlap, the selection of the big aperture and vertical hatch lines. In the first set of parameters, a scan speed of 550 mm/s and a pulse

frequency of 30 kHz were utilized, while the second set of parameters involved a scan speed of 450 mm/s and a pulse frequency of 45 kHz.

The results are depicted in Figure 2.70 and Figure 2.71 for average depth of erosion per layer and average roughness (R_a), respectively. As depicted, the number of SLE layers does not significantly affect the depth of erosion per layer for the two cases. However, the surface quality significantly deteriorates as the number of SLE layers increases. The roughness values obtained with 15 layers are almost 1.5 times the values obtained with 1 layer. The reason of higher roughness values with higher number of SLE layers is due to the scanning strategy utilized in these experiments and was also explained in the sub-section entitled "Scan strategy". When the hatch angle (which is 90 degrees in these experiments) is kept constant from layer to layer, the surface quality is deteriorated significantly due to the accumulation effect. The scan tracks are always located at the same positions making the peaks and valleys formed in the process more pronounced, resulting in higher roughness values.

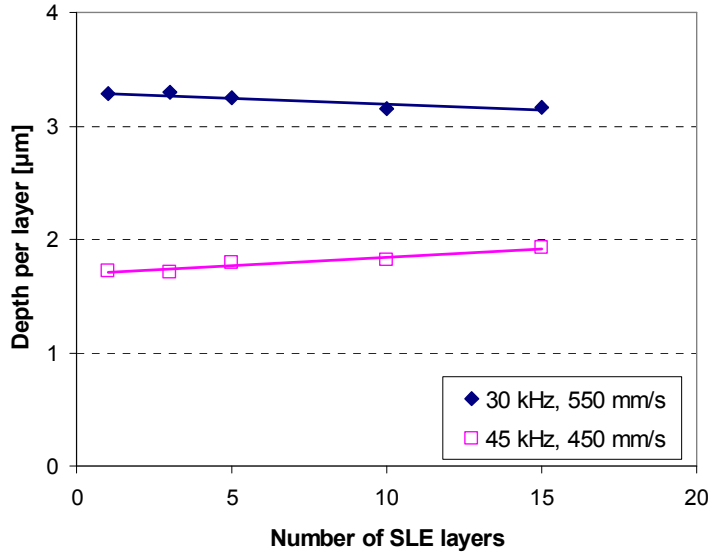

Figure 2.70: Variation of depth per layer for different number of SLE layers tested on AISI 1085 grinded substrate

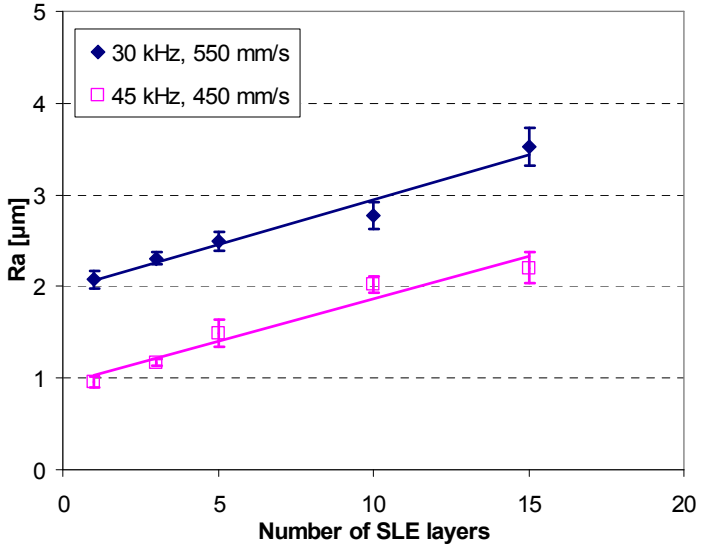

Figure 2.71: Variation of average roughness R_a for different number of SLE layers tested on AISI 1085 grinded substrate

c. Combining Parameters for Topography Modelling

The laser power intensity is highly dependent on the pulse overlap and the overlap between successive scan lines (See Figure 2.72). Thus, the material removal at a certain spot of the workpiece is proportional to the number of times laser beam hits that spot. The higher number of hits, the more energy is inserted on that spot and the more material is removed due to multi-pulsation. In order to have a complete physical model of the erosion process, the overlap factors between successive laser pulses and scan lines should be investigated to be able to calculate the number of laser beam hits on each spot. If the overlap factors were written as a function of other parameters, the number of laser and process parameters that need to be investigated for their effects on the process outputs could be reduced.

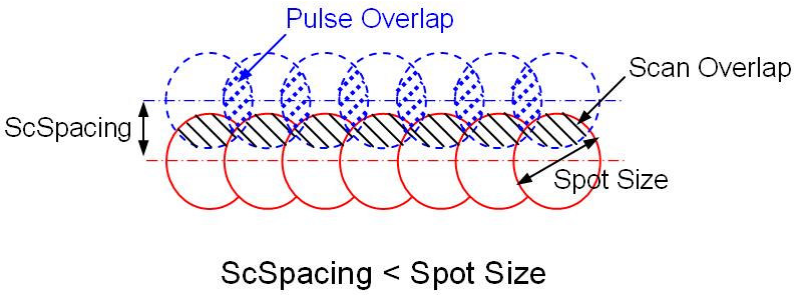

Figure 2.72: The overlapping between scan tracks (scan overlap) and between pulses (pulse overlap)

Figure 2.72 illustrates the relation between scan spacing, spot size and pulse overlap. The scan spacing together with the spot size defines the overlap between the successive scan lines whereas the pulse overlap is dependent on the selection of scan speed, frequency and spot size.

The percentage overlap between successive scan lines (scan overlap) is calculated by taking the scan spacing between scan tracks and the spot size into account (see Eq. 2.5) whereas the pulse overlap is a function of the scan speed, pulse frequency and spot size (see Eq. 2.1). An increasing scan speed, decreasing frequency and decreasing spot size reduce the pulse overlap whereas increasing scan spacing results in a lower scan overlap. Eq. 2.1 is illustrated in Figure 2.73 for a spot size of 80 µm.

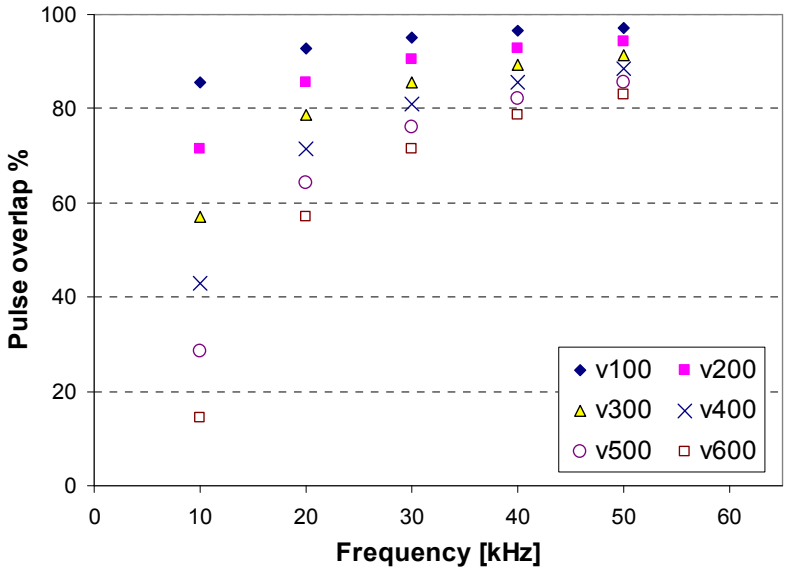

Figure 2.73: The relationship between frequency and pulse overlap at different scan speeds for d=80 µm

The mathematical formulation of overlapping factors gives an advantage for understanding the real physics behind the process. Using these equations, the number of pulses that target the same location on the workpiece can be calculated and the scanning of the surface can be simulated off-line before the process starts. A 3D measurement of a scanned track is given in Figure 2.74. The picture left gives a top view (2D) of a scan track. The two white lines are delimiting the area that is depicted in perspective view (3D) on the picture right. Obviously such picture could only be obtained (i.e. measured) after the process is completed. However, it would be very useful to get such picture before the process starts in order to be able to predict the resulting surface.

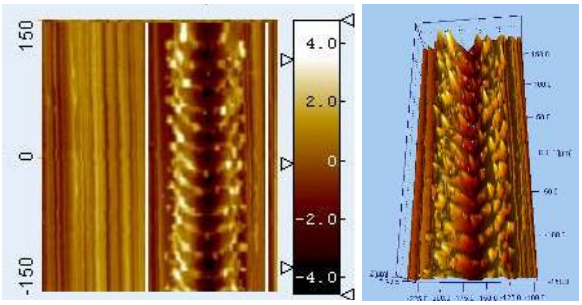

Figure 2.74: The 3D measurement results of one test case

A MATLAB code was written in order to simulate any given test conditions. Some examples are depicted in Figure 2.75 and Figure 2.76. In Figure 2.75, the effects of the scan speed and pulse frequency are shown. Figure 2.76 depicts the pulse and scan overlaps together in the same simulation. The sample given in Figure 2.75a with a pulse overlap of 70 µm is used with different scan overlaps. Figure 2.76a shows a case where the scan spacing is equal to a quarter of the spot size whereas the scan spacing is half of the spot size in Figure 2.76b. The last case depicts a case with a scan spacing value equal to the spot size ($Ø_{99\%}$), i.e. 80 µm for this case.

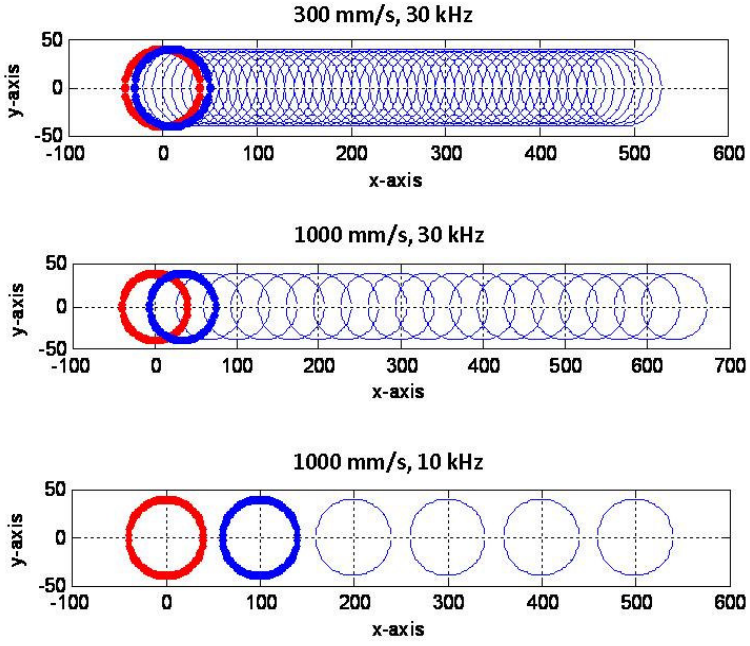

Figure 2.75: The effect of scan speed and pulse frequency on pulse overlap a) U_p = 70 µm b) U_p =47 µm c) $U_p < 0$

In the simulation, the number of hits at every grid point is calculated by representing a pre-specified sample area as a set of points located at very small distances from each other as shown in Figure 2.77. In the simulations, the grid distance is taken as 0.3 µm for a good resolution and accuracy. Then, the number of hits on each grid point in this area is calculated until the scanning process is completed by checking if the point lies in the moving laser beam spot. The result is a

contour plot showing the number of hits on each region in the pre-specified area. An example is given in Figure 2.78. The maximum number of hits occurs in the inner regions and in this example it is equal to 29 which means that those areas are hit 29 times in total.

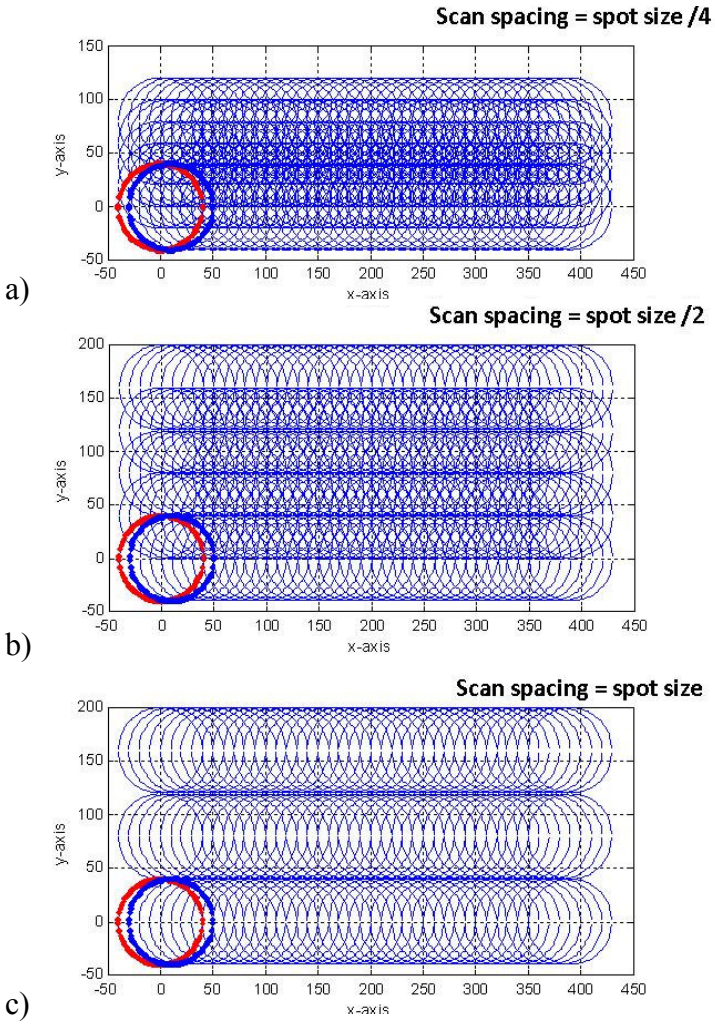

Figure 2.76: The effect of scan speed on the scan overlap a) U_p = 70 µm, Scan spacing = spot size/4, b) U_p = 70 µm, Scan spacing = spot size/2, c) U_p = 70 µm, Scan spacing = spot size

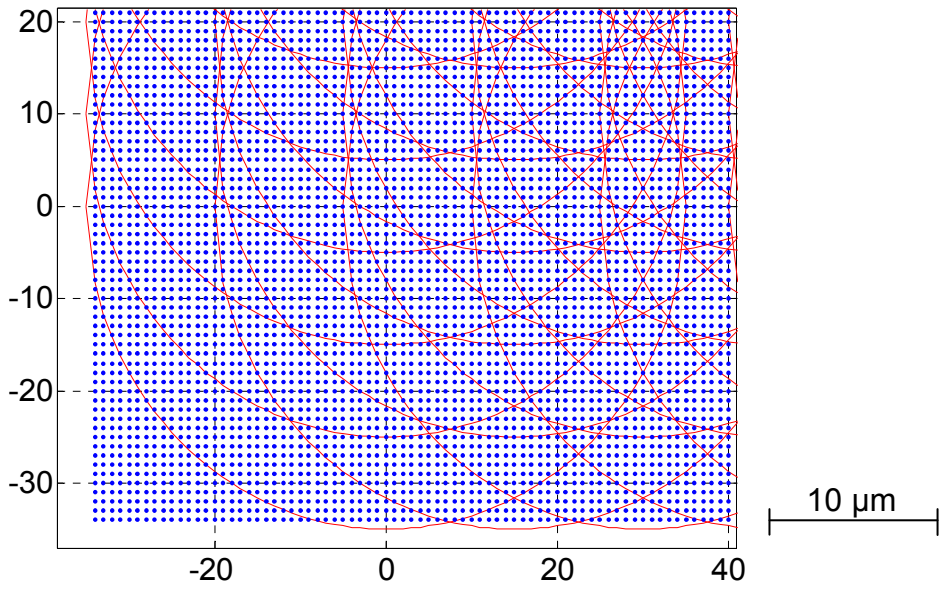

Figure 2.77: MATLAB code's working principle

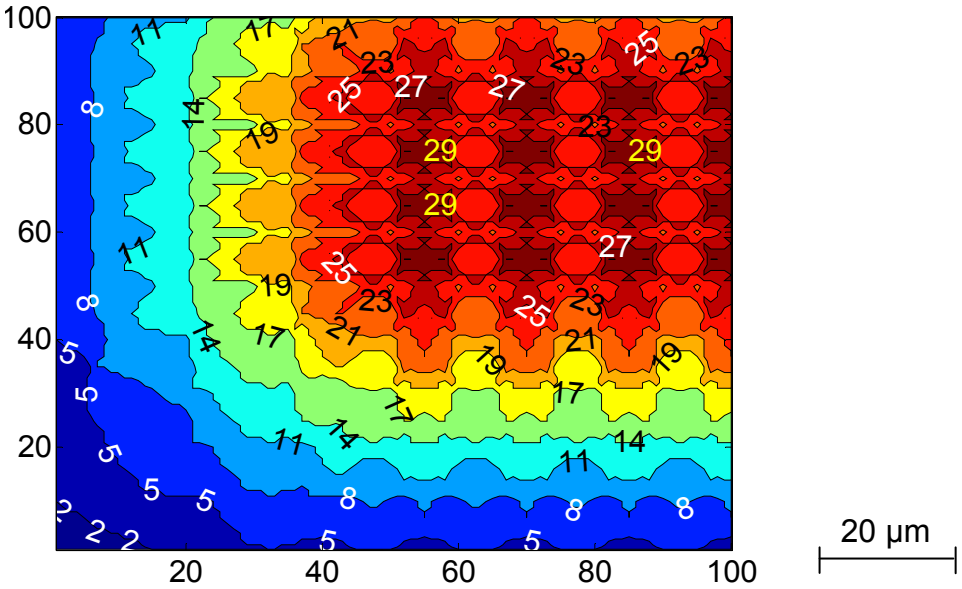

Figure 2.78: The contours showing the number of hits

Assuming a constant erosion depth per pulse, we can model the shape of the eroded surface in 3D. This gives us the opportunity to analyze the influence of various process parameters on outputs such as the surface roughness and depth of erosion per layer. As seen in Figure 2.78, the generated shape is rather complicated. The surface profile left behind is definitely a function of this topography which is further influenced by the interaction between the laser beam and material in terms of the laser power and material properties. On the other hand, the model only takes the number of hits on one point into account but not the Gaussian intensity profile of the laser beam or the melt flow. However, for low pulse overlap factors, the surfaces can be simulated.

The simulation for one scan line which is eroded by a scan speed of 600 mm/s, pulse frequency of 5 kHz, small aperture ($Ø_{99\%}$ 80 µm), laser power of 25 W, is shown in Figure 2.79. The first plot shows the MATLAB simulation result whereas the second one is 3D height map of the line that is derived by 3D measurements. The last plot illustrates the average profile along the scanning direction. A travel period of 1.5 mm is shown in the plots where 13 spots are visible both in simulation and experimental results. A second example for single line scanning is given in Figure 2.80. The good agreement between the experimental and simulation results is also present for this case which was also shown in Figure 2.74 as a sample test case.

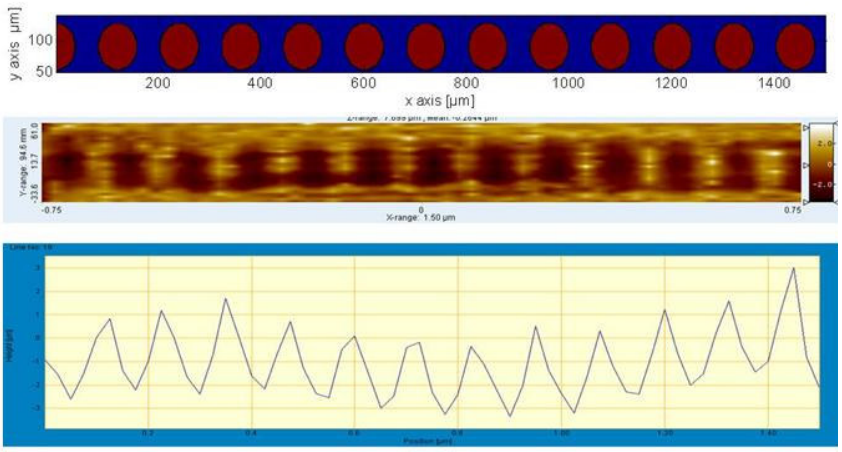

Figure 2.79: Comparison of simulation and experimental results for a single scanned line, case 1

Using the overlap factors, the need to study many process and laser parameters (spot size, scan speed, pulse frequency, scan spacing) is lessened since they are combined in one single parameter.

Therefore, the factors that affect the output parameters can be summarized as scan overlap, pulse overlap and laser power for one single layer. This absolutely helps to decrease the size of experiments, either in single-factor studies or in design of experiments.

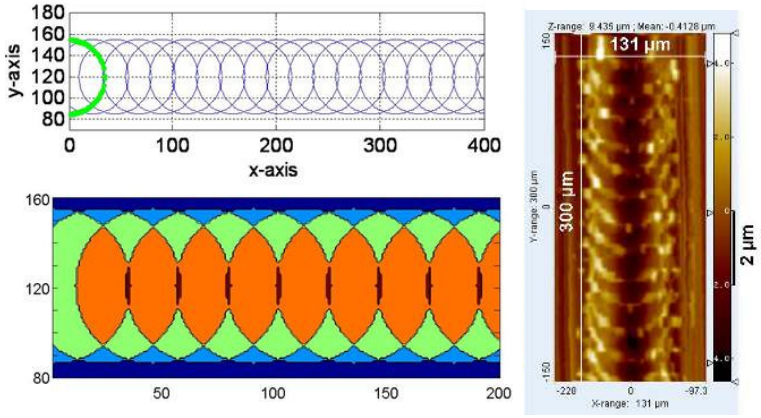

Theoretical U_p= 22.51 µm

Experimental U_p= 23.07 µm

Figure 2.80: Comparison of simulation and experimental results for a single scanned line, case 2

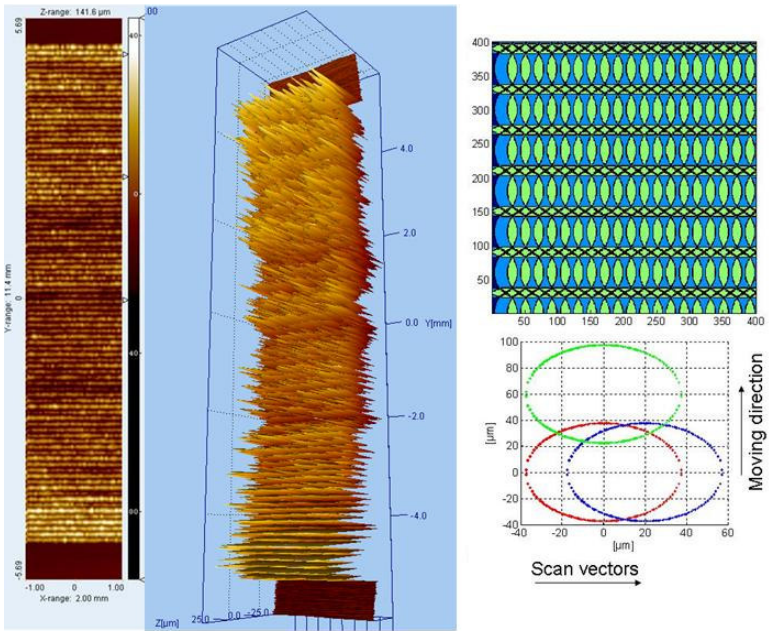

Figure 2.81: Comparison of simulation and experimental results for a scanned area

2.2.4 Conclusions

The process window studies to find out optimal combinations of laser power and scan speed conducted at two different settings for the rest of parameters showed that low scan speeds combined with high laser powers resulted in high erosion depths and very rough surfaces with a colour change, as expected. High scan speeds combined with low laser power lead to only melting or almost no change on the irradiated surfaces. The region in between these two zones gives better results yielding a compromise in between good surface quality and high productivity (or a high depth of erosion).

As a result of single-factor two-dimensional erosion tests applied on different materials, it is concluded that most of the investigated parameters in this study have very important influence on the depth of erosion, in other words erosion rate, and on surface quality. The optimal values of some parameters, e.g. scan spacing and pulse frequency, are the same when aiming for a high depth of erosion or a good surface quality. Depending on the application, parameters like scan speed and

laser power should be either adjusted for a good surface quality or for a high erosion rate or combinations of two regimes may be employed. Moreover, the interactions between some parameters, like scan speed and scan spacing, play an important role on the outputs.

2.3 THREE-DIMENSIONAL EROSION

Three-dimensional erosion can be defined as the removal of material in a layer-wise manner to make three-dimensional engravings/objects. For long ages, many methods have been used for engraving purposes such as chasing for shallow grooves in jewelry, hand engraving, milling and recently laser engraving. There is a wide range of materials that can be processed by laser engraving such as natural materials (wood, human tissues), plastics, metals, ceramics and glass. Being a non-contact method, there is no tool wear involved and inaccuracies due to this problem. This is considered to be an important advantage over alternative engraving technologies. Laser engraving is sometimes referred to as three-dimensional laser ablation or laser milling. Material removal happens by evaporation of material (such as in metals) or the material may fracture and flake off the surface as happens in stone and glass. Some examples of laser milling/engraving by commercial machines are depicted in Figure 2.82.

This chapter first explains the experimental set-up used in three-dimensional erosion tests. It then reports on the experimental results.

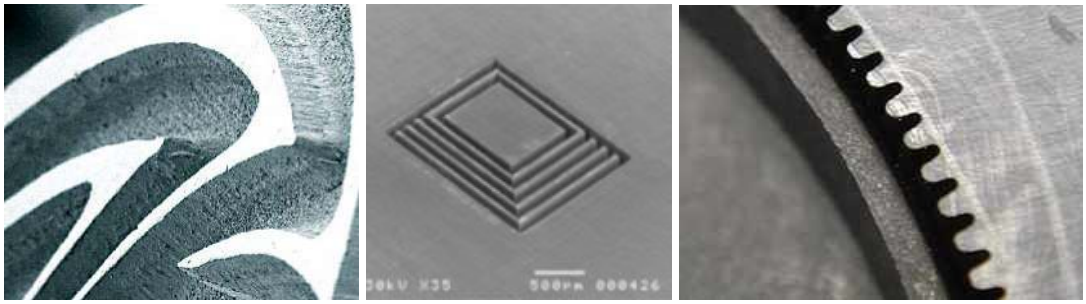

Figure 2.82: Laser erosion samples a) three dimensional laser ablation [99] b) micro milling [100] c) laser milling [101]

2.3.1 Experimental Procedure

In our experiments, a Concept Laser M3 Linear machine is used for three-dimensional erosion of metallic surfaces. As mentioned in the first chapter, the machine has two workpiece holding modules that can be interchanged: a cusing (selective laser melting) and an erosion module. The cusing module has a building platform, a feed cylinder and a deposition system which are required for SLM. However in the erosion module, there is only a single platform which can be moved in the vertical axis of the machine parallel to the laser beam. This movement provides that the workpiece stays in focus during the erosion process. Having the laser beam out of focus on the workpiece changes the available power density, and thus significantly affects the process output such as the depth of erosion or surface quality. Therefore, the laser beam should be in focus when it reaches the surface of the workpiece. In addition to the erosion module, the software used for erosion is different than the one used for SLM. In the erosion software, it is impossible to pump nitrogen into the chamber and conduct the experiments in an atmosphere with little oxygen. Thus, all 3D erosion experiments are carried out in ambient air. Moreover, the "teaching sensor", a secondary laser, helping the user to locate the workpiece on the erosion platform accurately, is an important tool in the erosion software. Since, in the scope of this research erosion is mainly used as a complementary process during SLM, 3D erosion is only conducted here to show the capability of the system, but not deeply investigated.

2.3.2 Erosion Regimes and Findings with 3D Erosion

In order to find the suitable parameters for three-dimensional erosion, the results from §2.2 on two-dimensional erosion are used. The knowledge coming from that section can be summarized as follows: From the results of two-dimensional erosion, it is evident that erosion with small aperture is much slower than the erosion with the big aperture. However, the surface quality and ability to produce small details and features is better with the small aperture due to the smaller focus diameter of the laser beam operated with the small aperture. Thus, only the small aperture is used for three-dimensional erosion. The effects of other parameters such as pulse frequency, scan speed and laser power as well as the scan spacing (or overlap) between successive scan tracks, are explored in the section about two-dimensional erosion. More tests are also conducted in this section to find out the right parameters both in terms of productivity and quality of engraved objects. In order to maximize the productivity, a pulse frequency of 30 kHz is used where the depth of erosion is at its maximum for the most of tested process parameter sets. The overlap between successive scan tracks should not be less than the half of the laser beam diameter for a complete evaporation. For a good surface quality, higher overlaps such as 90% (a_1=10%) of the laser beam diameter should be provided which conflicts with high production rates. For fast removal of material, 50% of the diameter is thus a limit value for the scan spacing factor (a_1). The maximum average power available from the laser source is 25 W for the small aperture but a better surface quality is obtained at lower laser power values. Thus, for fine erosion, it is better to keep the laser power at around 7 to 10 W. For rough erosion with high material removal rate and low surface quality, the laser power can be increased, e.g. 22 W. Thus, for three-dimensional erosion, three types of erosion regimes are defined as given in Table 2.2. All erosion parameters as well as the obtained surface quality in terms of average roughness R_a and depth of erosion per layer, together with material removal rate are reported in the same table.

Table 2.2: Three different regimes with appropriate parameter selections for 3D

Parameter	***Superfine Erosion***	***Fine Erosion***	***Rough Erosion***
Power [W]	7	10	22
Pump current [A]	31	33	39
Frequency [kHz]	30	30	30
Scan speed [mm/s]	200-400	200-600	200-400
Spot size $Ø_{99\%}$ [µm]	80	80	80
Aperture	small	small	small
Overlap	90 %	90 %	50 %
Depth of erosion per layer [µm]	0.2-0.3	0.4-0.7	2-2.5
Material removal rate [mm^3/h]	1.6-2.3	3.5-6	70-110
Surface roughness R_a [µm]	~0.65	~1	~4
Scan strategy	grid	grid	Grid

To calculate the material removal rate for a simple hatching strategy (vertical bi-directional scan lines), let's assume that a rectangular area with dimensions of w_s (width) and l_s (length) is to be scanned with scan tracks parallel to the length of the part. Then the number of scan tracks (n_s) and time to scan one track (t_{scan}) are calculated as follows:

$$n_s = \frac{w_s}{(1-overlap)\times d} \tag{2.6}$$

$$t_{scan} = \frac{l_s}{v} \tag{2.7}$$

where v is the scan speed and d is the spot size and overlap expressed as a fraction of spot size. The total time to scan the whole area (t_{total}) is calculated as given in the following equation:

$$t_{total} = n_s \times t_{scan} = \frac{w_s \times k_s}{(1 - overlap) \times d \times v} \tag{2.8}$$

As a result of Eq.s 2.6-2.8, the material removal rate (MRR) is found to be:

$$MRR = \frac{A_{scanned}}{t_{total}} \times d_{erosion} = v \times d \times (1 - overlap) \times d_{erosion} \tag{2.9}$$

where $d_{erosion}$ is the depth of erosion per layer.

The regime named as 'rough erosion' provides a significantly higher material removal rate (70-110 mm^3/hour) compared to 'fine' or 'superfine' regimes. On the other hand, the roughness is higher (R_a of 4 µm) than what is obtained with 'fine' or 'superfine' regimes which possess very similar results except that the superfine erosion results in slightly better surface quality and resolution as shown in the obtained average profiles after 10 layers of erosion in Figure 2.83. Thus superfine erosion is more suitable for small details which require good surface quality and small erosion volumes.

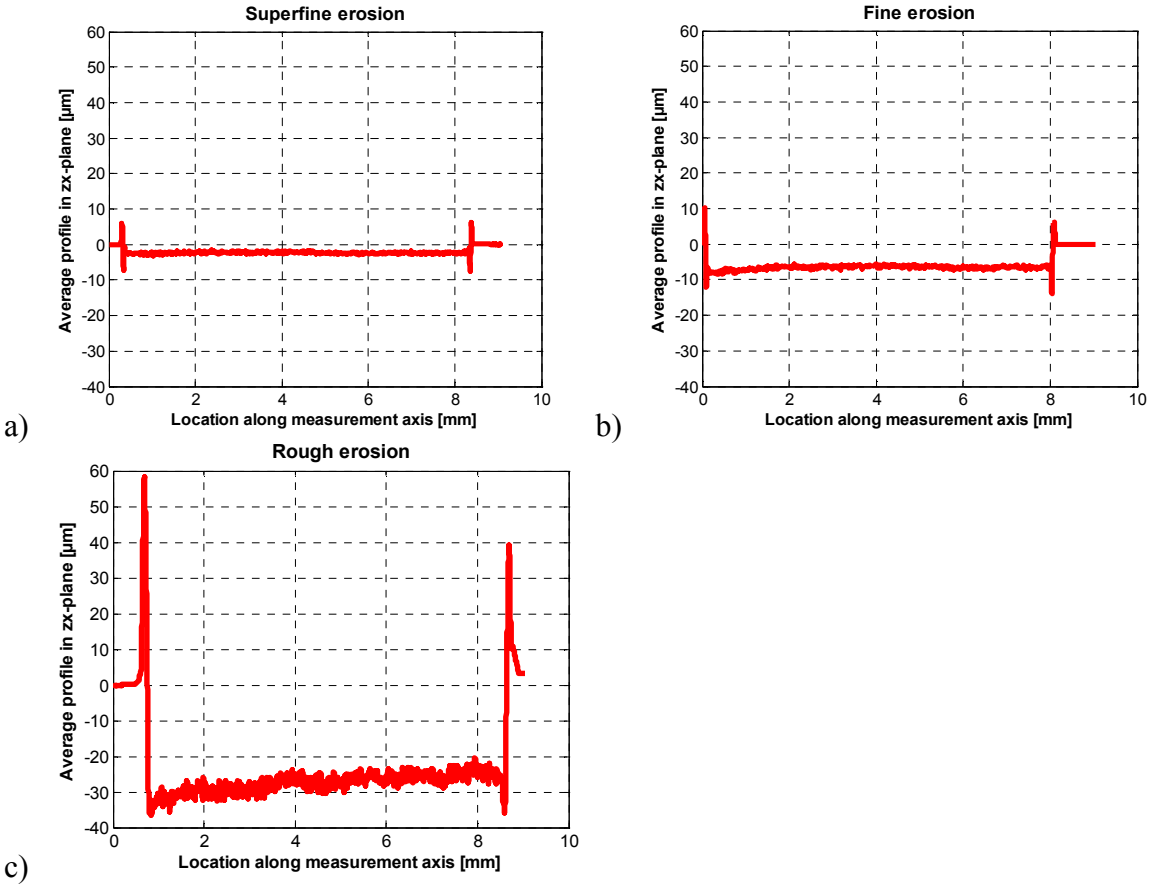

Figure 2.83: Obtained profiles at three different regimes after 10 layers of grid scanning a) Superfine erosion b) Fine erosion c) Rough erosion

One of the important features present in the average profiles depicted in Figure 2.83 is the deviations of the side wall angles from 90 degrees. This is illustrated in a close-up view of the average profile of an eroded cubic sample. This profile together with the actual designed profile

(shown with dashed lines) is illustrated in Figure 2.84. As evident, the vertical wall becomes an inclined surface with a deviation of about 15 degrees and a peak is formed at the side of the profile. Other researchers also revealed that laser ablation with a perpendicular incidence of light results in wall angles deviating from 90 degrees due to the Gaussian shape of the used laser beam [94, 102]. In order to avoid this problem, the workpiece can be tilted for post-processing only in the area of the walls after the cavity is made [102]. In the scope of this study, the deviation is not a real concern since high vertical walls will rather be produced by SLM, while SLE will only be applied in combination with SLM as a process to improve some part quality at an intermediate stage (i.e. after some layers are built) or at the end (i.e. after the last layer of a build) and no tilting is provided to the workpieces to correct this deviation. The peak formation at the edge of the eroded cavity is comparable to the edge formation in 1D erosion (Figure 2.13a and Figure 2.16) and 2D erosion (Figure 2.41 and Figure 2.44).

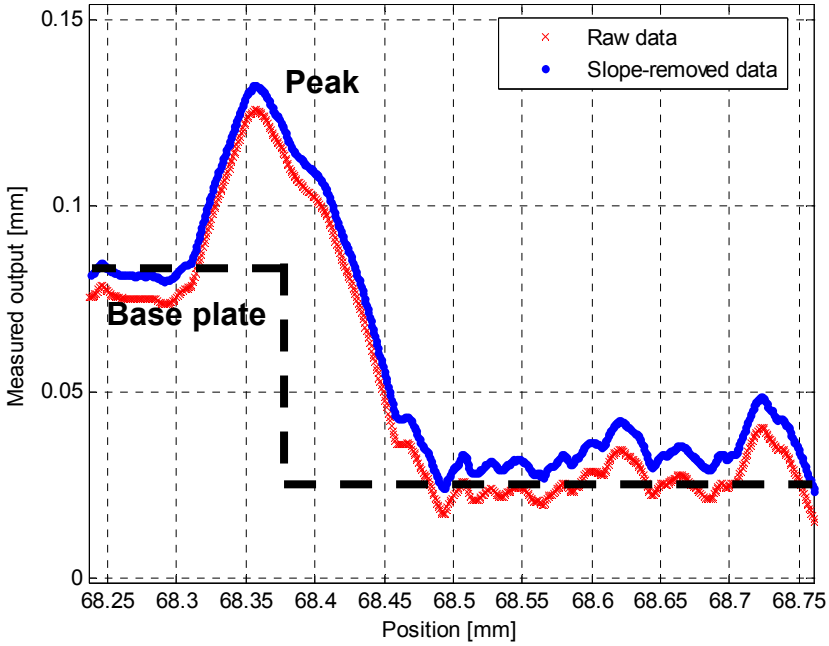

Figure 2.84: The wall angle deviation from 90 degrees

In order to demonstrate the ability of the machine of eroding three dimensional cavities or objects, a three-dimensional cavity with fine features is formed as shown in Figure 2.85. The box dimensions that envelope the object are 10x15x5 mm. The object is sliced with a layer thickness taken as 2.5 µm resulting in 2000 layers to be eroded. The result which did not satisfy the expectations is shown in Figure 2.86 whereby it is difficult to realize the fine details. The reason for such a result lies in the fact that the laser beam should always stay in focus when used for erosion of fine details, in order to provide a small spot size with a high energy density. Otherwise, the material will only melt and re-solidify. In order to be able to improve the three-dimensional erosion, it is important to understand the significance of the focus length in laser processing. Thus, the divergence of a laser beam together with the Rayleigh length is explained in the following paragraphs.

The Rayleigh length (or *Rayleigh range*) of a laser beam is the distance from the beam waist (in the propagation direction) where the beam radius (R_0) is increased by a factor of the square root of 2 as depicted in Figure 2.87. This means that the beam spot area is doubled at this point. The Rayleigh length depends on the wavelength and the minimum diameter waist of the beam [103].

For Gaussian beams, the Rayleigh length is determined by the waist radius R_0 and the wavelength λ as shown in Eq.2.10:

$$Z_R = \frac{\pi . R_0^{\,2}}{\lambda .} \tag{2.10}$$

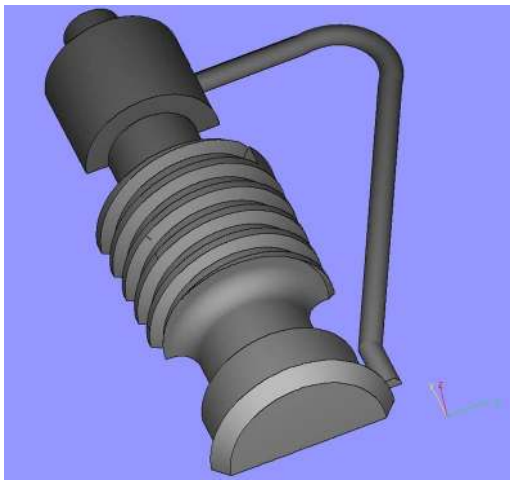

Figure 2.85: The design formed for the first erosion trial of a three-dimensional cavity

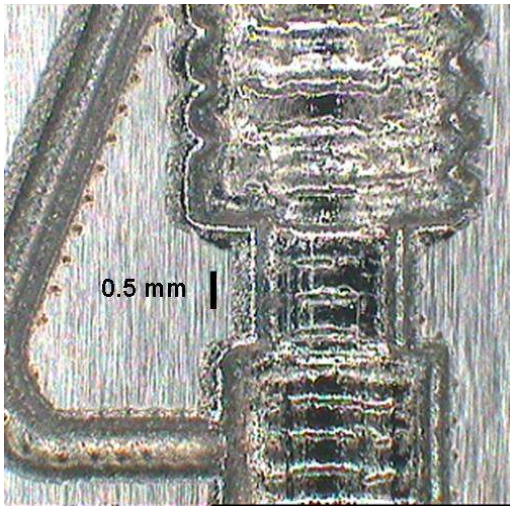

Figure 2.86: The result of the first erosion trial of a three dimensional cavity

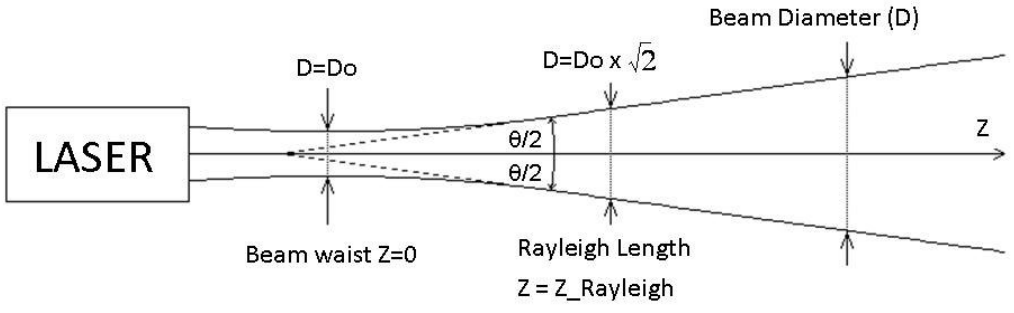

$$R_0 = D_0 / 2$$

Figure 2.87: Divergence, beam waist and Rayleigh length [103]

For beams with imperfect beam quality and a given waist radius, the Rayleigh length is effectively decreased by the so-called M^2 factor. It is a quality factor for the focusability of the laser beam and is also called as 'beam quality factor' or 'beam propagation factor' [103, 104]. The Rayleigh length is meaasured to be about 1.3 mm for the big aperture and 1.9 mm for the small aperture on the Concept Laser M3 Linear machine (§1.2.1a). Therefore, it is very important to stay in focus during erosion so that the energy density is not significantly reduced. In our case, the depth was 5 mm in total and the depth of erosion per layer was taken as 2.5 μm while it was less than that in reality resulting in a discrepancy between the actual and theoretical eroded surface as more layers

are eroded. This accumulation of error caused the laser beam to move out of focus and result in only melting. After this initial trial, the depth of erosion is measured more accurately and the layer thickness is set equal to the depth of erosion per layer. This resulted in a much better eroded cavity as shown in Figure 2.88.

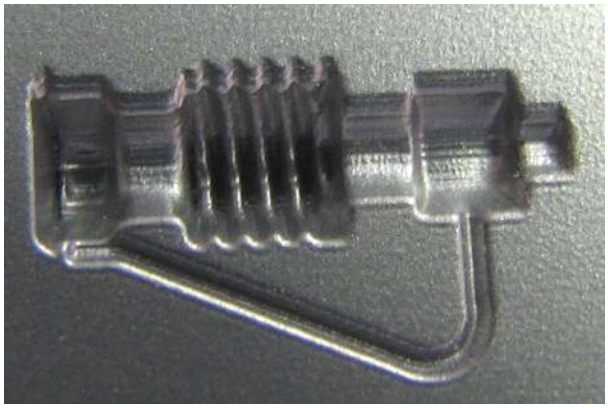

Figure 2.88: The best result obtained for this three-dimensional engraving

When used in combination with SLM, the roughness of the SLM process (R_a of 10-12 µm) will reduce the efficiency and quality of erosion as compared to the results obtained on grinded workpieces (R_a of 1 µm). Thus, in case of rough SLM surfaces, it might be appropriate to first apply laser re-melting of the surface in order to smoothen the surface (See Chapter 4) before applying laser erosion.

In terms of visual quality, the big aperture results in unsatisfying cavities and engravings. Therefore, the small aperture is standard for the three-dimensional erosion process since it provides a better tool for small details and a good surface quality at a cost of low erosion rates. The spot size ($Ø_{99\%}$) at focus with the small aperture is about 80 µm limiting the finest detail to have a diameter or width of 80 µm. Another reason for selecting the small aperture is the edge formation at the sides of the eroded layers as depicted in Figure 2.84. The edges that are inherent to laser processes with nano-second pulse durations cause a problem in 3D erosion. The height of this edge depends on the selected parameters and increase as the energy input increases, thus also with increasing depth of erosion per layer. In order to avoid this geometrical deviation, fine or superfine erosion regimes with the small aperture should be selected instead of rough erosion to be able to produce sharp corners or transitions. Two examples of stairs eroded with fine erosion with small aperture are depicted in Figure 2.89 where the measurement direction is also illustrated. The average profile is depicted in Figure 2.90. A short peak formation is visible in the transition from one step to another with an edge height less than 25 µm. The results are satisfying since the peaks do not significantly differ from the roughness peaks. However, when rough erosion parameters are employed (See Figure 2.83) or the big aperture is selected, the transitions exhibit higher peaks resulting in lower visual quality. With the big aperture, the peak height can exceed 200 µm.

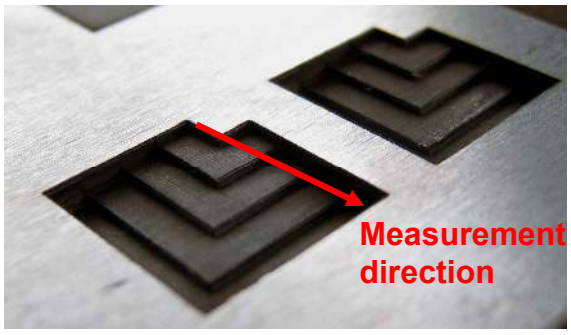

Figure 2.89: A sample of stairs eroded with fine erosion parameters resulting in sharp corners and transitions

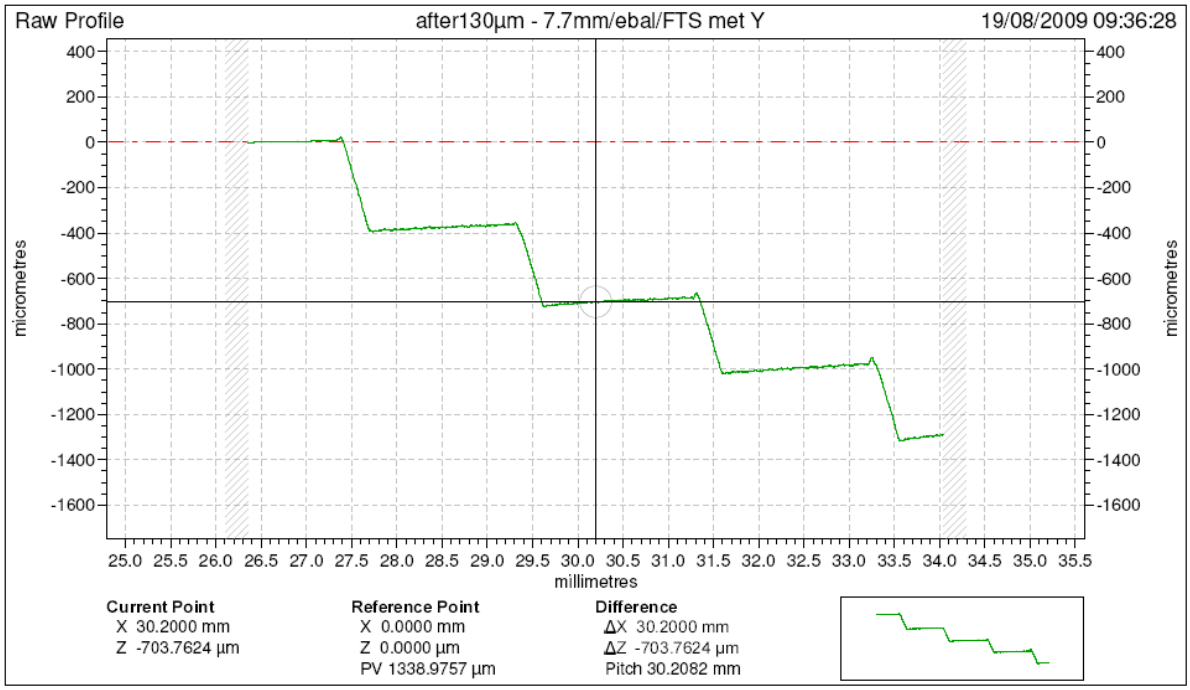

Figure 2.90: The average profile of the stairs measured with Talysurf 120L

During the preparation stage of slice data for 3D erosion, the layer thickness, entered to the slicing algorithm, should be equal to the actual depth of erosion per layer. Thus, it should be known before the process starts. Otherwise, the obtained cavity depth and geometry deviate from the actual ones. This is due to the accumulated error formed during focusing. Figure 2.91 shows how this deviation is formed. Assume that Figure 2.91a shows the nominal cavity to be formed with dashed lines and that d_{given} is the entered value for the layer thickness in data preparation while the actual depth d_{actual} is smaller than d_{given} as shown in Figure 2.91b. This wrong layer thickness results in a lower number of layers to be eroded. In this case, the final eroded shape will have a smaller depth than the one in the CAD model due to missing number of layers. This is illustrated in Figure 2.91c which clearly shows that the actual cavity has a lower depth than the nominal one. Therefore, the depth of erosion per layer should be accurately measured before the data preparation stage or there should be an online measurement system installed on the machine for monitoring the depth of erosion during the process.

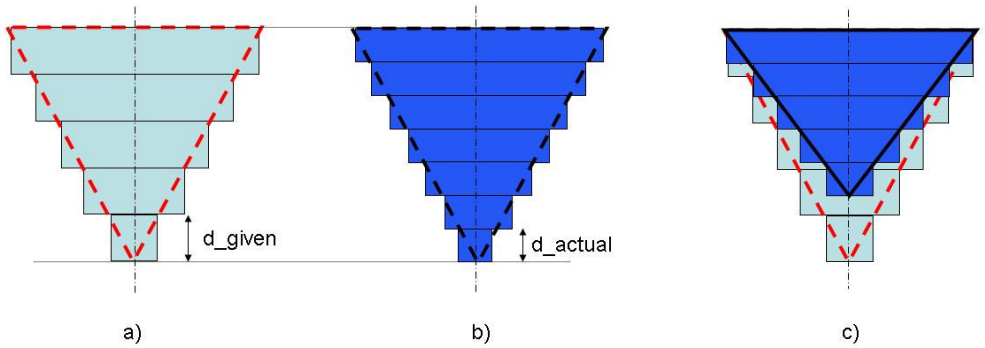

Figure 2.91: The deviation of the cavity geometry and erosion depth when the slice data is prepared with an inaccurate layer thickness

The focus length should be accurately adjusted as material is removed by evaporation in a layer-wise manner. If the workpiece that is targeted moves out of focus significantly, melting takes place instead of evaporation making removal of material impossible. The focus length can be adjusted after each layer or after a certain number of layers. A sample case is studied in order to determine the value for the number of layers after which the focus length should be adjusted. A square

pyramid with a base dimension of 5 mm and a height of 440 µm is eroded on the base plate. The rough erosion parameters are utilized. For one of the erosion tests, there was no adjustment of the focus length. For the other three tests, the adjustment of the focus length is performed either after each layer or after 10 layers or after 100 layers. The nominal (theoretical) geometry that was expected to be formed together with actual results is depicted in Figure 2.92. When there is no feed, meaning that there was no adjustment of the base plate's height to keep the target in focus, the resulting geometry has a lower depth than the nominal one. This is due to a greater spot resulting in a lower energy density and lower erosion rates. The other three test results depict more or less the same geometry which is a deeper than the nominal one with a difference of about 60 µm. This overcut might be due to the fact that the actual erosion depth is slightly higher than the one used for calculating the number of required erosion layers. From these tests, it can be concluded that the adjustment of the focus length should be performed but the number of layers after which it should be adjusted does not significantly alter the obtained geometry as long as the targeted workpiece surface stays in focus.

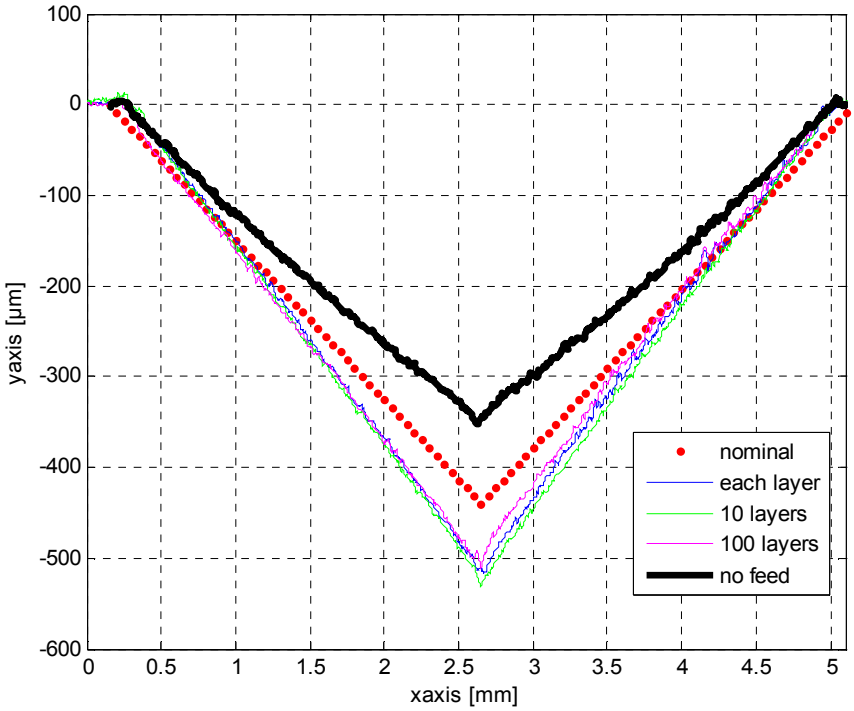

Figure 2.92: The nominal pyramid profile with profiles after erosion tests with no adjustment of the height of the workpiece, or adjusted height after a certain number of layers: 1, 10 or 100 layers

2.3.3 CONCLUSIONS

In this sub-section, three-dimensional erosion was taken under investigation. As a result of the tests carried out on a Concept Laser M3 Linear machine, it is concluded that the small aperture should be preferred in order to erode tiny structures or small details. The small aperture also gives better results in terms of visual quality due to lower edges formed during erosion compared to the big aperture. For satisfying results, the depth of erosion per layer should be precisely known before the process starts in order to be able to prepare the slicing data accurately. A better solution would be the measurement of the depth of erosion during the process. However, online monitoring of the depth of erosion is not currently possible on the Concept Laser M3 Linear machine. Like all electromagnetic beams, lasers are subject to divergence. Thus, the laser energy density varies as the targeted surface moves out of the focus with a distance more than the Rayleigh Length. This reduced the laser energy density due to increase in the spot size, which may result in only melting with no evaporation of the targeted material.

3 Manufacturing by combining Selective Laser Melting and Selective Laser Erosion

3.1 Introduction

This chapter presents the results of investigations to combine Selective Laser Melting (SLM) and Selective Laser Erosion (SLE) in order to improve the SLM process in terms of surface quality, precision and micro machining capability and building resolution. Selective Laser Erosion may be employed for different purposes during SLM. Firstly, it can be used to improve the surface quality after each layer to avoid recoating problems and as a remedy for elevated edges. In this case, a layer is first generated by SLM and then the surface area is partially (e.g. only contours) or completely exposed to laser erosion. Moreover, the same manner can be applied for improving the resolution and accuracy in the building direction by manufacturing with smaller effective layer thicknesses. Another approach may be to apply laser erosion after the SLM process is completed. In this case, the outer (or top) surfaces are targeted. In this case, SLE can be applied to improve surface roughness or to achieve surface engraving/texturing. Furthermore, SLE is used for machining small features (micro machining) and to improve the xy accuracy (i.e. in-layer accuracy). These issues will be introduced in the following paragraphs.

Because of the high roughness of built surfaces and formation of elevated edges during SLM, there are often collisions between the part and the blades of the coater, which puts a new homogenous powder layer on the workpiece. Tiny structures can easily break as a result of these collisions and this limits the utilization of SLM in micro machining applications. The formation of elevated edges of solidified material is a severe problem in laser processes since it deteriorates the surface topology and dimensional accuracy. In the scope of this doctoral research, the edge effect is also addressed to find optimum solutions yielding minimal edge height, when machining with SLM, without applying SLE (for more details, see §4.3.6). Optimization is done by changing the contour parameters or scan strategies, applying post-fill or random-fill strategies, etc. The physical phenomena behind the edge effect formation are discussed more in detail in Chapter 4 that deals with laser re-melting. As a conclusion of the study on the “edge effect”, it is found that it is not possible to completely eliminate the edge effect problem, especially after each layer. It is possible to apply post-fill strategy to improve the geometrical accuracy and visual outlook of the part after the last layer is built, but the edge formation after each layer still imposes a problem of collisions with the hard blades of the coater during powder deposition. One way to eliminate the problem after every layer is to apply SLE on the scanned area to remove the excessive material of the edges that yield collisions. The SLE is applied either with small or big aperture leading to different phenomena as explained in the following sub-sections in this chapter.

Combining SLE and SLM, may be a good solution for improving accuracy or machining small features in the xy-plane (i.e. micro machining applications such as making circular holes or thin slits/walls having dimensions less than 200-300 µm which are not possible to be made by SLM only). Especially the engraving of tiny structures on already made SLM parts is very easy by SLE, as was the case with three-dimensional erosion on grinded surfaces discussed in §2.3, and gives

better results in terms of resolution since it is does not involve any melt pool and powder particles. When applied after SLM is completed, SLE can improve the surface quality of SLM parts. In this work, the surface roughness improvement is done in a two-step approach and carried out only for top surfaces having a normal parallel to the building direction. First the area is exposed to SLE with parameters resulting in good surface quality and little material removal. Then the same area is scanned in the continuous mode for laser re-melting. In the latter case, smoothening of the surface is aimed other than any material removal. Since in SLM the enhancement of the surface quality by laser re-melting is much more significant than the one obtained by SLE, Chapter 4 will investigate laser re-melting in more detail and focus on other aspects. Among others, it will demonstrate that in addition to reducing the roughness values by more than 90%, the laser re-melting is very helpful for densifying part shells to 100% and improving the hardness in the re-melted zone. More details can be found in Chapter 4. However, SLE can also help improvement of the surface quality after SLM by about 50-60% depending on the selected parameters without laser re-melting. This will be discussed in the present chapter.

In addition to erosion applied on top surfaces, this chapter presents the experimental work of applying erosion after each layer either with big or small aperture selection. The aim is to decrease the layer thickness by removing a part of it after each layer so that the resolution of the SLM process is improved and the stair-effect is suppressed. However, during the experiments with erosion after every layer, it is observed that a significant limitation exists: 'bark' formation. The bark is defined as a structure forming around the SLM parts when exposed to SLE due to partial melting of the surrounding powder and sticking to the part's walls. The thickness of the bark highly depends on the selected SLE parameters, especially the spot size. When the big aperture is selected, the bark formation is more severe and does not form homogenously all around the part. The physical phenomena for the bark generation are explained in this chapter with different examples.

This next sub-sections present experimental results obtained by combining SLM and SLE on the Concept Laser M3 Linear machine. The material used in the experiments is AISI 316L stainless steel with an average particle size of 42 µm (coarse powder) commercially available from Concept Laser (CL20ES). The range of particle size is 10-100 µm. During SLM, the parameters recommended by Concept Laser are utilized: a laser power of 105 W, a scan speed of 380 mm/s, a scan spacing between scan tracks of 125 µm (a_1= 0.70) with a selection of the big aperture and island scanning.

§3.2 presents the results of test cases when erosion is applied only on the top surface of the SLM sample parts to improve the surface quality (§3.2.1) or to improve the precision and micro machining capability of SLM (§3.2.2). Next, the experiments conducted by applying SLE after every layer deposited by SLM, are presented in two sub-sections regarding the spot size (in §3.3). The tests are made either by big (§3.3.1) or small (§3.3.2) apertures leading to different spot sizes and laser power values.

3.2 Eroding the top surfaces after completing SLM

3.2.1 Surface Roughness Improvement

In order to improve the surface roughness, SLE is applied to the parts as a finishing touch after the SLM is completed. In this manner, the top surfaces having a vertical normal vector axis can be modified easily with the existing Concept Laser software. For inclined and curved surfaces, the software should be modified to accommodate the movement of the building platform together with laser scanning to keep the laser beam in focus.

The surface quality can be gradually improved with a multiple step approach by the combined process of SLM and SLE. The first surface improvement step is called "erosion". It is performed

with a high energy intensity input which is obtained by the selection of laser and process parameters so that the total depth of erosion is high enough to remove the peaks left behind by the melting process. Thus, an amount of material which is dependent on the selection of laser and process parameters and number of eroded layers is removed by the SLE process. The second step involves re-melting of the surface applying a lower energy input and switching to continuous laser mode. This 2nd step can be proceded by further erosion steps which do not remove any significant amount of material but rather a very thin layer in order to remove any peaks from previous erosion steps. In this study, only two surface finishing steps are accomplished (1x erosion, 1 x re-melting) yet resulting in a great enhancement.

In order to allow a comparison, first the results for parts produced by SLM only are presented in Figure 3.1: i.e. no erosion or laser re-melting is applied. These graphs represent the average and total roughness values (R_a and R_t) measured on different parts that were built by SLM with the same laser and process parameters, in the same environment, with the same amount of oxygen, on the same base plate. As observed from the figures, the roughness data show a great spread. The standard deviation for R_a is 3.4 µm with a mean of 12.3.µm, while it is equal to 27.7 µm for R_t with a mean of 101.5 µm. The large spread of the data shows that although the parts are built under the same conditions on the same base plate, it may result in different roughness values due to the nature of the process.

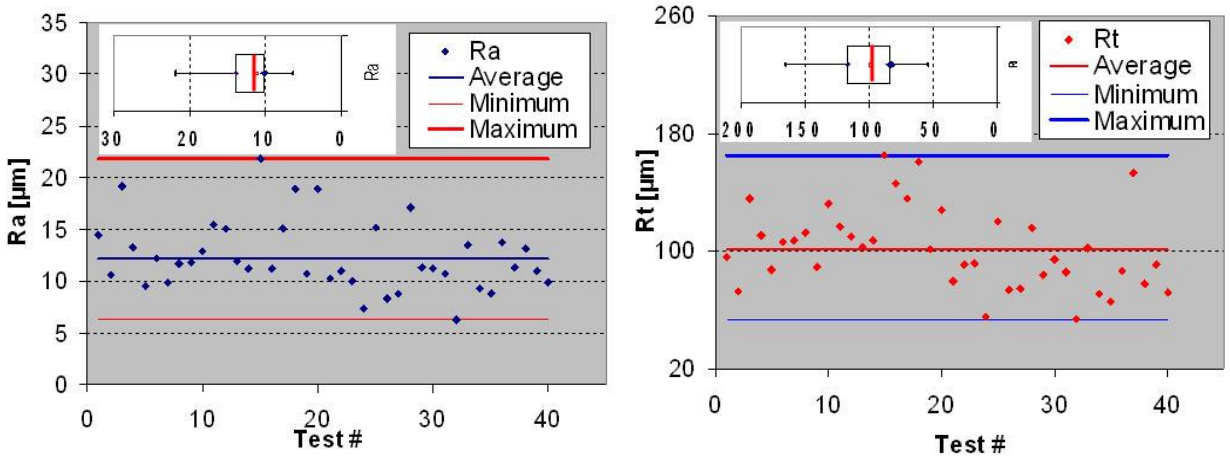

Figure 3.1: Average roughness (R_a) and total roughness (R_t) for parts produced by SLM only

The average R_a and R_t values of the parts without any improvement step (only SLM processed parts) are used as reference values in the following sections when improved results are presented. Chapter 2 presented a parameter study investigating the influence of input parameters (e.g. scan speed, laser power, scan spacing, scan strategy, spot size, etc.) on the output parameters (e.g. depth of erosion and surface roughness) for 2D erosion. Those parameter study tests were always conducted on grinded surfaces having an average roughness of about 1 µm. However, during the combined process of SLM and SLE, the erosion is performed on SLM surfaces having much higher roughness values. In order to understand the effect of starting surface quality in the SLE process, some more parameter tests were conducted on SLM surfaces.

To find the best parameters for the first step (erosion) applied on SLM parts, some rectangular parts are built by SLM and half of top surfaces is eroded with a different parameter set for each part (See Figure 3.2a). The resulting 3D roughness profile of one part is also depicted in Figure 3.2b. As evident from the figure, erosion can significantly increase the surface quality by removing the high peaks generated during SLM if right parameters are allocated. The following sub-sections will focus on the details of the process parameter optimization for a good surface roughness obtained by SLE on SLM surfaces. In this case, the erosion rate is not taken into account since only the top layer has to be eroded and since this does not have a significant influence on the total production time.

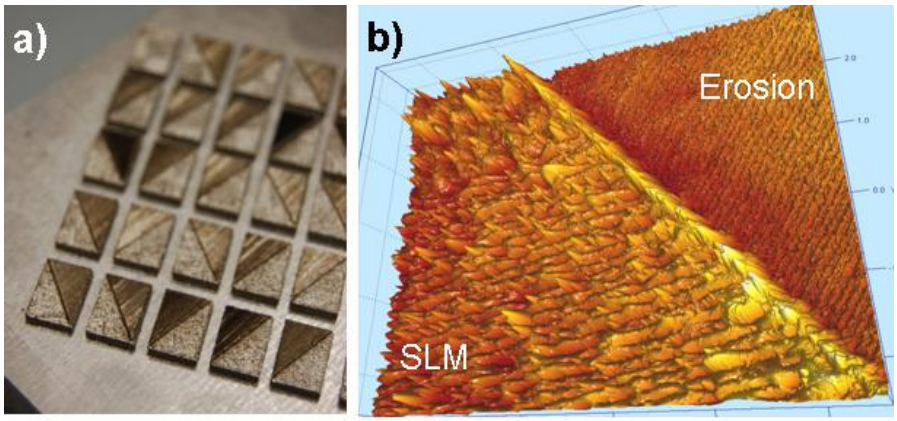

Figure 3.2 : Parts built for the roughness improvement – Step 1 a) built parts on the base plate b)surface profile of the top surfaces of the parts

Some initial tests were performed to get an idea about the ranges where the parameters would be further tested and to understand which parameters play a more significant role for the surface quality when erosion with big aperture is applied. As a result of these tests, it was observed that the selection of pulse frequency and scan spacing between successive scan lines is critical in terms of the surface quality left behind by the erosion. The effect of the pulse frequency is illustrated in Figure 3.3. The other parameters during these experiments were set as follows: a scan spacing of 120 µm, a scan speed of 600 mm/s and a laser power of 75 W. The top surface of the part was scanned with a grid strategy for 10 times. As observed from Figure 3.3, the best results are obtained with high frequency values such as 45 and 50 kHz. This was also a conclusion obtained from the experiments made on grinded surfaces (see Figure 2.61).

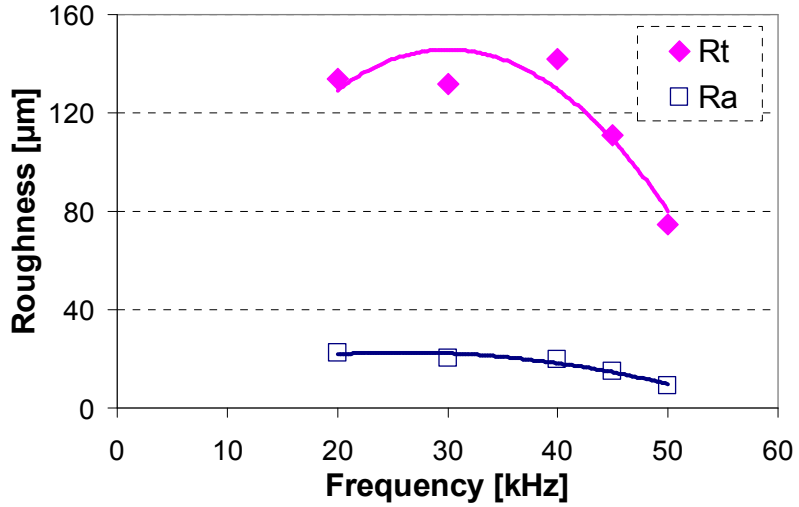

Figure 3.3 : The effect of pulse frequency on surface roughness (R_a and R_t)

The influence of scan spacing between successive scan lines on the surface quality is depicted in Figure 3.4 for three different settings for the other parameters. The scan spacing is related to the scan spacing factor (a_1) that may vary between 0 and 1. Figure 3.4 gives the results of the tests done with spacing factors varying from 0.4 to 0.9 with 10 scans of erosion on top of SLM surfaces. The rest of the parameters were fixed and presented in the plots (32 A corresponding to 70 W and 33 A corresponding to 75 W). As the figure suggests, high scan spacing factors result in bad surface quality in terms of average and total roughness values, for the three different settings. This is due to generation of separate erosion tracks. Separate erosion tracks leave a very rough surface behind because the material in between these tracks is not totally removed. Therefore, scan spacing values greater than 50% should be avoided for a good surface quality.

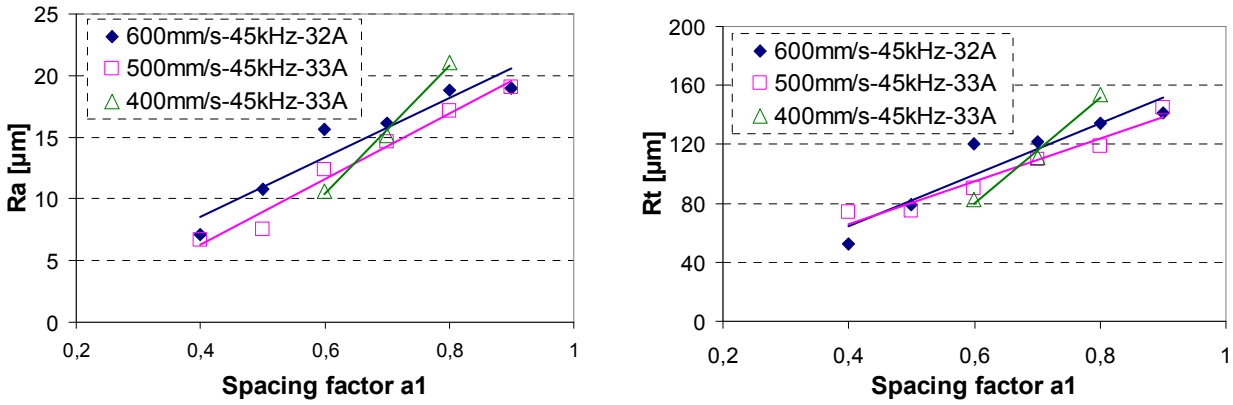

Figure 3.4 : The effect of scan spacing on the average roughness (R_a) and the total roughness (R_t)

a. Parameter Study for Step 1: Erosion on SLM surfaces

Single factor experiments are utilized to study the effect of each parameter and to find the best parameters for the 1st step of roughness enhancement (erosion). The parameters under investigation here are scan speed, pulse frequency, laser power, scan spacing and the number of eroded layers. The experimental work concludes that applying SLE significantly improves the surface quality. However, the rate of enhancement depends on the selected parameters. As a result of the experiments presented in the following sub-sections, it is concluded that a combination of low laser power, high pulse frequency, medium or low scan spacing factor and alternating scan strategy results in good surface quality. The influence of scan speed was found to be less important than the other factors. Moreover, better surface quality is obtained when the surface is exposed to erosion more than 20-30 times. However, in terms of productivity a lower number of erosion scans (less than 5) will also improve the surface quality more than 50%.

Scan Speed

The scan speed influences the overlap between subsequent laser pulses: the lower the speed, the greater the overlap and the deeper the material removal due to multi-pulse radiation. Thus scan speed is a key factor for specifying the production rate of the process. However, for the surface quality, it is of less significance especially at high frequency values and medium laser powers. This case is illustrated in Figure 3.5. The other parameters during the tests are indicated above the first plot. As evident, the average and total roughness do not significantly depend on the scan speed in the selected range with the given parameters.

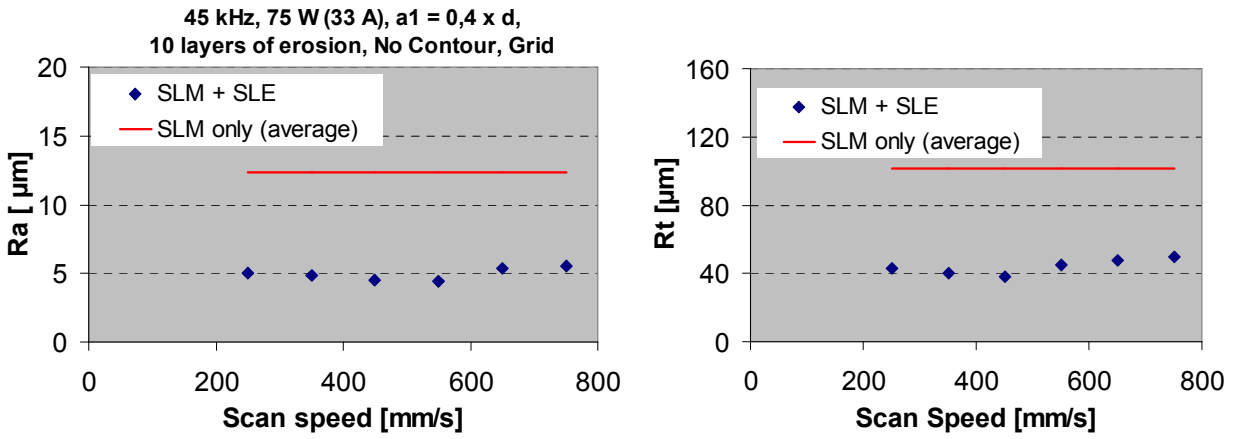

Figure 3.5 : The effect of the scan speed on average roughness (R_a) and on total roughness (R_t)

Pulse Frequency

If the aim is to achieve a good surface finish, it is best to keep the pulse frequency at higher values such as 45 and 50 kHz (See Figure 3.3). Therefore, the tests were conducted only at these two values varying the other parameters as presented in the plots. The graphical results are presented in Figure 3.6 which shows that the roughness values at 50 kHz are lower than those obtained at 45 kHz for three cases and changing the process parameters (scan speed and laser power) does not significantly alter the results obtained at 50 kHz.

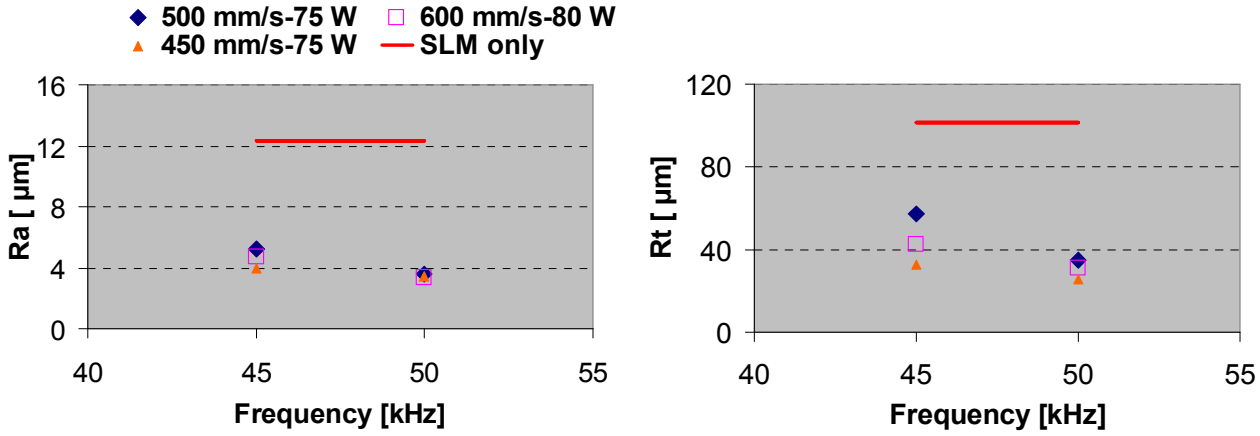

Figure 3.6 : Effect of frequency on average roughness (R_a) and on total roughness (R_t), a_1=40%, 10 times grid scanning, no contours

Laser Power (pump current)

As previously mentioned, the pump current is one of the most important process parameters for SLE due to its direct effect on laser power. The linear relationship between the laser power and pump current, as depicted in Figure 3.7, stays the same all the time. However, the laser power that is obtained with a specific value of the pump current may change depending on many factors related to the machine. During the maintenance of the machine, this line which is shown in Figure 3.7 may shift due to the limited lifetime of the diodes. Therefore, in the thesis text, different linear relations may be encountered showing the relationship between laser power and current. For the purpose of comparison, the laser power values should be taken into account; not the pump current values since they may correspond to various laser power values measured at different times.

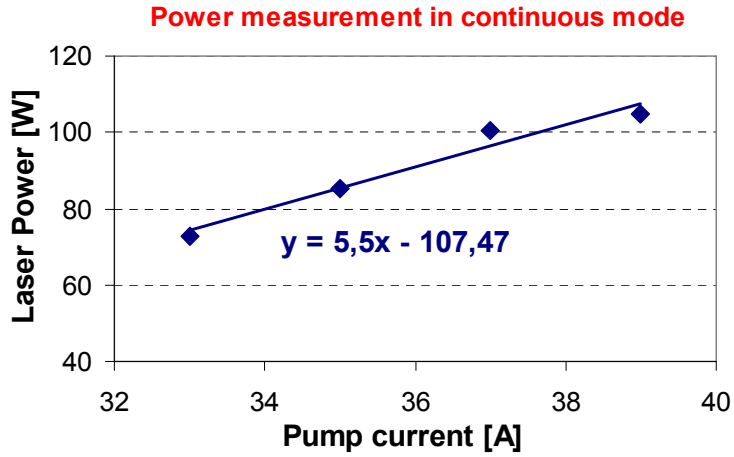

Figure 3.7 : The relationship between the pump current and laser power with the big aperture

Figure 3.8 suggests that increasing the laser power deteriorates the surface quality since the average and total roughness values increase. Therefore for a good surface quality, low or medium

laser power values should be selected. In terms of productivity, higher laser power values certainly results in deeper erosion cavities but a rough surface.

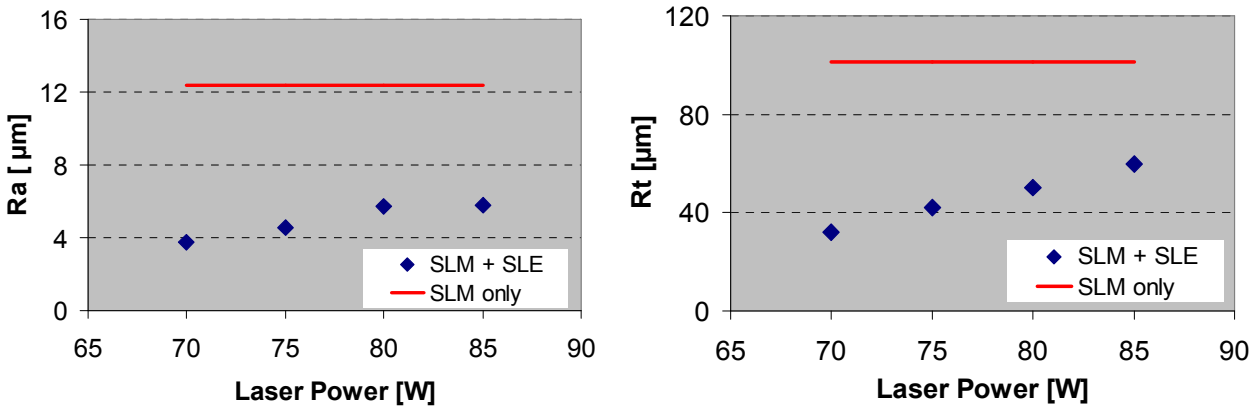

Figure 3.8 : The influence of laser power on average roughness (R_a) and on total roughness (R_t) (500 mm/s, 45 kHz, a_1 = 0.4, 10 grid scans without contours)

Scan Spacing

The laser power intensity is highly dependent on the pulse overlap and the overlap between successive scan lines. The scan spacing together with the spot size defines the overlap between the successive scan lines whereas the pulse overlap is a function of scan speed, frequency and spot size (See §2.2.3c). In order to make smooth surfaces, high scan spacing values should be avoided. Medium or low values for scan spacing offer better results as seen in Figure 3.9. A scan spacing factor (a_1) above 50% results in bad surface quality.

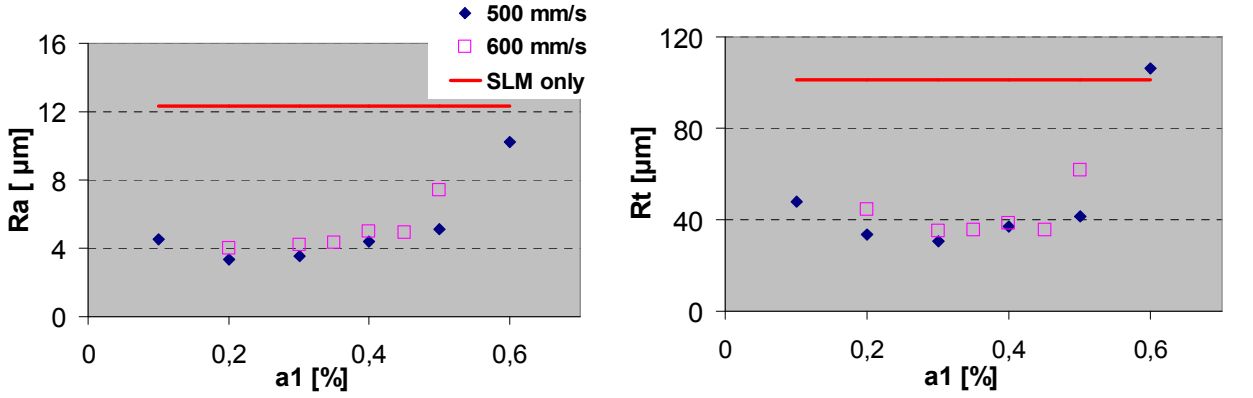

Figure 3.9: The effect of scan spacing on average roughness (R_a) and on total roughness (R_t) (45 kHz, 75 W, 10 grid scans without contours)

Number of eroded layers

The last parameter under investigation in this study is the number of applied erosion layers. When erosion is applied for 2 or 5 times, the surface quality enhancement is not as good as when it will be applied for 20 or 30 times as seen in Figure 3.10. However, even applying for 2 times provides a significant enhancement compared to SLM surfaces where no erosion was applied (more than 50% improvement depending on the SLE parameter set). In terms of productivity, applying low number of layers should be preferred whereas it is best to choose higher number of layers in cases requiring low roughness values. As Figure 3.10 shows, after a certain number, the roughness values converge to a certain value or are insignificantly improved and after this point it not anymore useful to erode more times.

As a result of single factor experiments in this section, the following values are selected as the input parameters for the first step (erosion): as scan speed of 600 mm/s, a pulse frequency of 50 kHz, a laser power of 80 W (34 A), a scan spacing factor of 40% of the spot size, big aperture and 10 grid scans. Thus, in further tests, these parameters are kept constant for all parts being exposed to the first step: erosion.

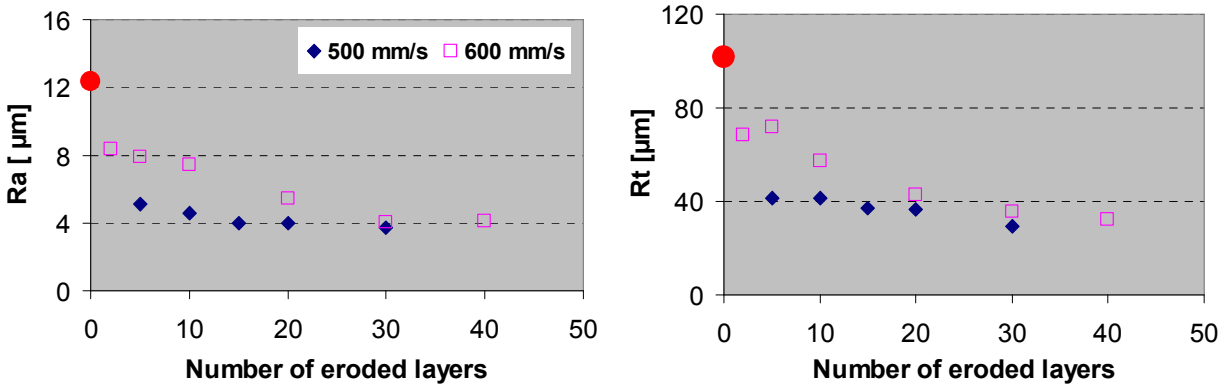

Figure 3.10: The effect of number of eroded layers on average roughness (R_a) and on total roughness (R_t) (75 W, 45 kHz, a_1= 0.4, no contour scanning)

b. Parameter Study for Step 2: Re-melting

The second step involves re-melting of the top surfaces after they are exposed to SLE in the first step. This re-melting of the surface is expected to bring an extra enhancement. In order to find the correct parameters, a series of tests are conducted studying the effect of the laser power, scan speed and the scan spacing. Since the re-melting process is performed in continuous mode, the frequency value is set to 0 kHz. A set of sample parts is shown in Figure 3.11a. All the parts were made with the same SLM parameters as given in the previous sub-section. The three parts at the top are not eroded or re-melted to keep as reference parts. Then, the three parts at the bottom are only exposed to erosion but not re-melted and used as reference parts to compare the results at the end. The rest of the parts were first eroded with the selected set of erosion parameters and then exposed to laser re-melting with different sets of parameters.

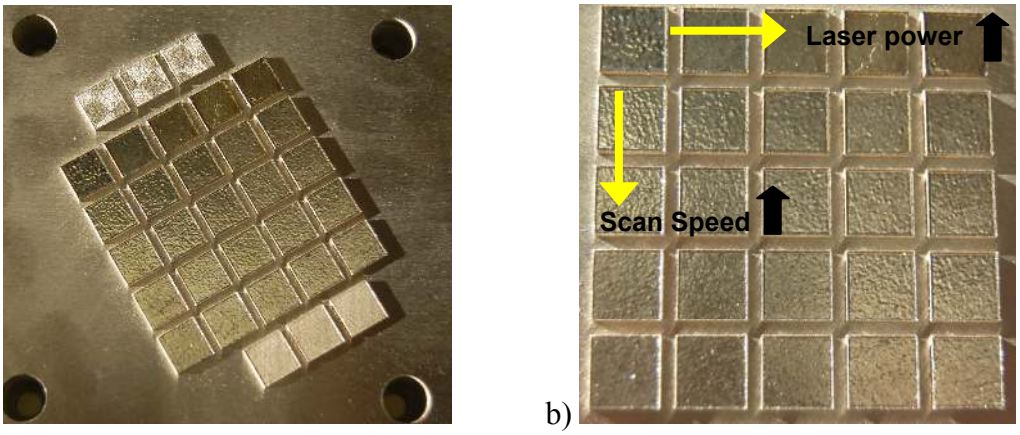

Figure 3.11: Step 2: re-melting a) parts built on the base plate; reference parts, only eroded parts and parts exposed to erosion + laser re-melting b) parts exposed to erosion + laser re-melting with different parameter sets

As depicted in Figure 3.11 b, different scan speed and laser power values are tested on one base plate keeping the scan spacing constant for the second step. For a different scan spacing value, a new set of parts on a different base plate was built. Three sets of parts were built with scan spacing

factors (a_1) of 0.7, 0.4 and 0.1 (See Figure 3.12). The scan speed varies between 50 to 800 mm/s while the laser power values are set to 60 to 105 W (corresponding pump current values are 31 and 39 A). The second step is applied on the surfaces 10 times with a diagonal grid strategy and the big aperture.

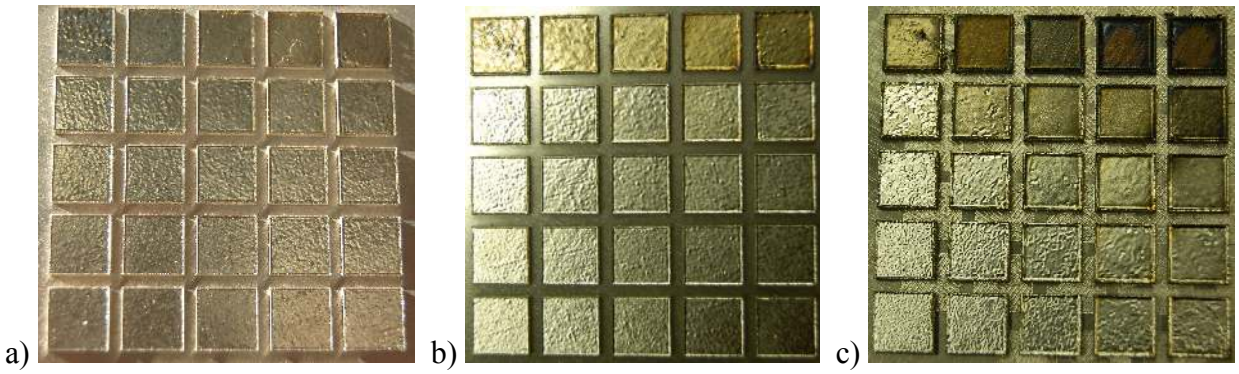

Figure 3.12: Three test cases with different scan spacing value a) 70% b) 40% and c) 10%

The first test case with a scan spacing value of 70% results in better results compared to the parts that were built with only SLM or to the parts exposed to only erosion (See Figure 3.13). The solid line in the figures show the average roughness value of the three parts that were built by SLM with no erosion or laser re-melting and the dashed line shows the average roughness value of the three parts that were exposed to erosion (only step 1) after SLM. The other points correspond to the parts that were exposed to both erosion (step 1) and laser re-melting (step 2). Some of them show an improvement as is the case with 85 W (35 A) and 200 mm/s but some of them result in higher roughness compared to the reference parts. Especially the highest laser power (39 A) results in bad surface quality regardless of the selected scan speed due to very high energy input. However, as evident from Figure 3.12, the surfaces mostly look the same.

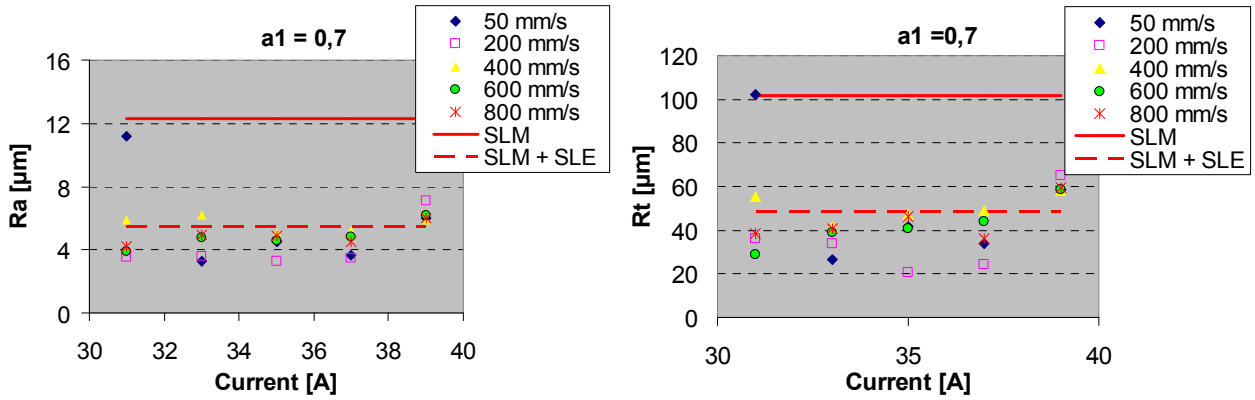

Figure 3.13: Results for 1st test case for step 2 (laser re-melting) after SLM and step 1 (erosion)

In the second test case, the scan spacing between the scan lines is set to 40% of the spot size. In this case, the results with the highest laser power are not as bad as the first case and improvement with the best parameter set is greater as depicted in Figure 3.14. As the last case, the scan spacing set at 10% of the spot size is used and the results are depicted in Figure 3.15. Due to very high overlap factor between the scan lines, the energy input to the substrate is very high, especially at low scan speeds and high laser powers. Thus, the combination of low scan speed (50 mm/s) with high overlap results in bad surface quality. However, the highest improvement is provided with this scan spacing (or overlap) value at medium scan speeds (200-400 mm/s) and medium laser powers (85-95 W). The column diagrams for the three cases are given in Figure 3.16.

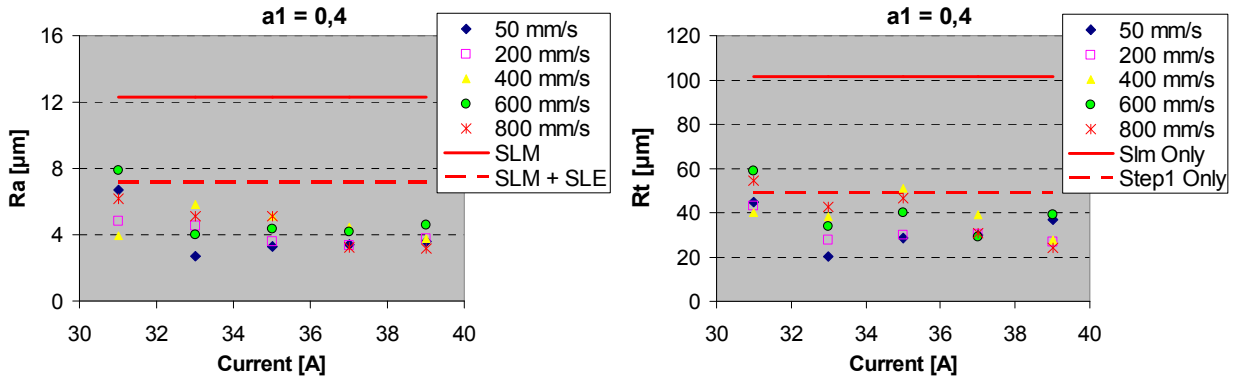

Figure 3.14: Results for 2nd test case for step 2 (laser re-melting) after SLM and step 1 (erosion)

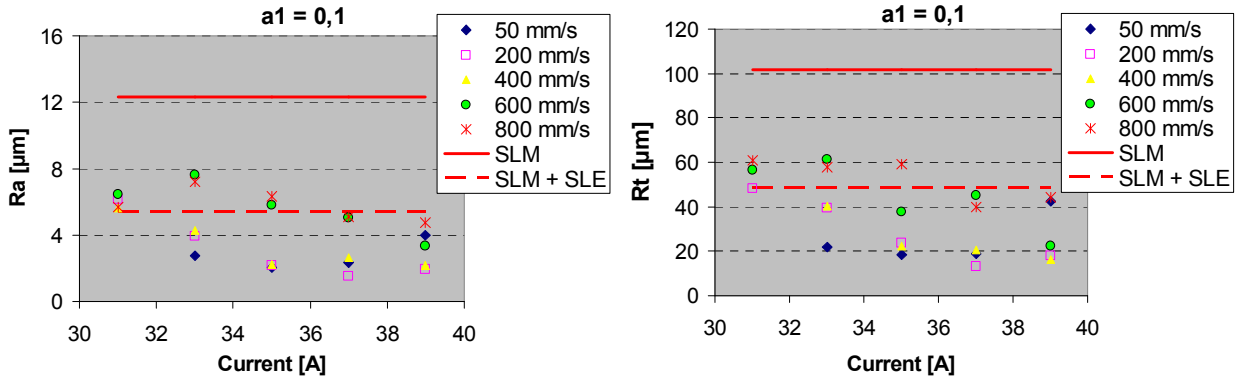

Figure 3.15 : Results for 3rd test case for step 2 (laser re-melting) after SLM and step 1 (erosion).

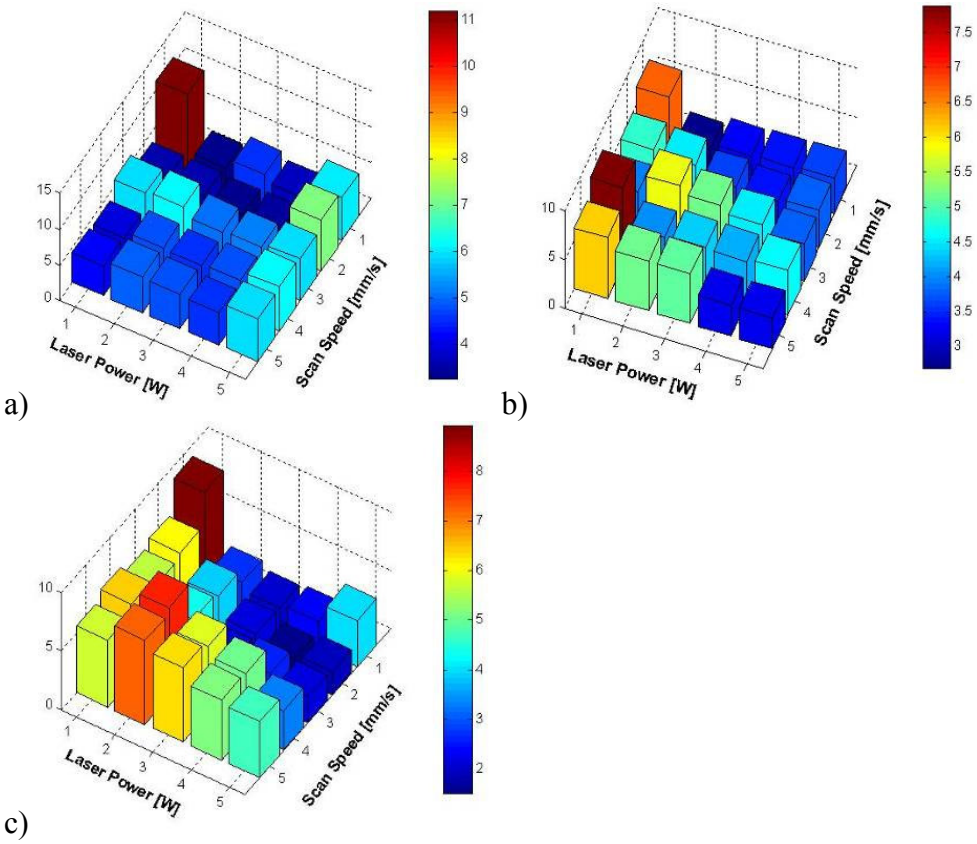

Figure 3.16: Column diagrams of average roughness (R_a) results for a) $a_1 = 0.7$ b) $a_1 = 0.4$ c) $a_1 = 0.1$

The best results of all experiments, which were achieved with $a_1 = 0.1$ (10% of the spot size), are depicted in Figure 3.17. These best results correspond to the following scan speeds and pump current values respectively: 1) 200 mm/s and 35 A (85 W) 2) 200 mm/s and 37 A (100 W) and 3) 400 mm/s and 37 A (100 W). The pictures, taken with a Mitutoyo Quick Vision system at 1000x magnification with photographs taken on the top surfaces of the parts showing the edge effect, are depicted in Figure 3.18 with the laser re-melting parameters.

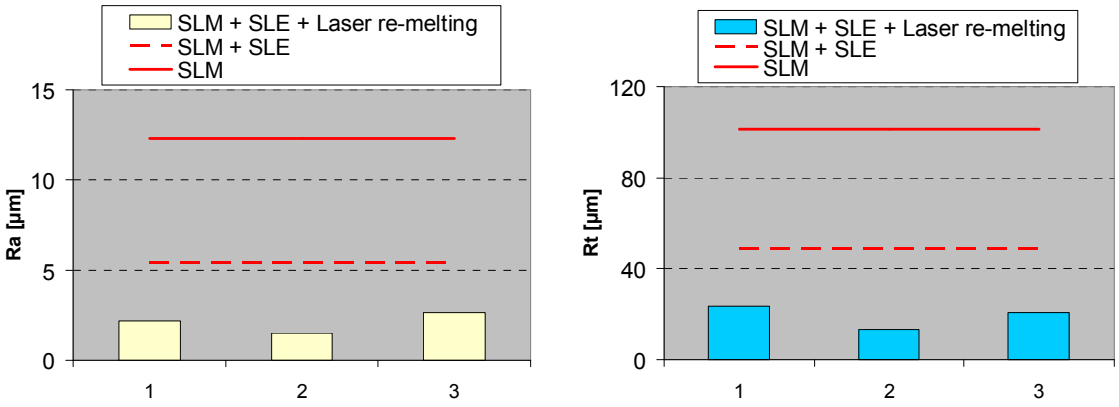

Figure 3.17: Best results in the third case in terms of average (R_a) and total roughness (R_t)

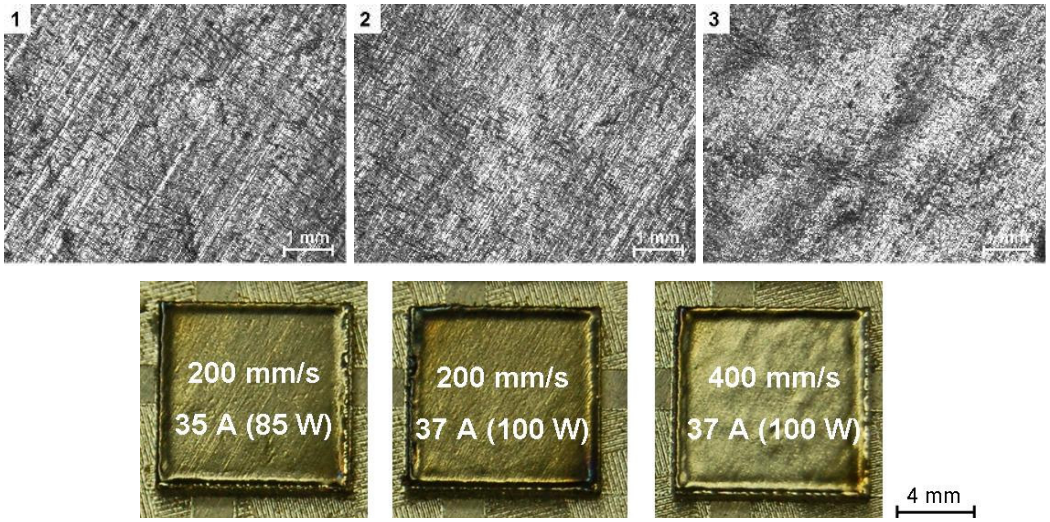

Figure 3.18: Pictures taken on the surfaces of the best samples

During laser surface re-melting, the edges do not occur due to powder particles being dragged to the melt pool since no powder material is involved in laser-re-melting. At sufficiently high energy intensities, evaporation of material may occur during laser re-melting conducted with continuous mode laser beam. However, the laser energy is not high enough at the sides due to insufficient overlapping of successive scan tracks and due to Gaussian profile of the laser beam. As the material inside the contours starts to evaporate, the melted material is expelled towards the sides creating an elevated edge. The cross-sectional view of a laser re-melted sample is presented in Figure 3.19b. If the provided energy intensity in laser re-melting is not high enough for evaporation, only the melted material being pushed to the sides and backward of scanning direction causes the edges (for more information on the formation of elevated edges, §4.3.6 can be referred to). Mainly, the formation of recoil pressures with high energy inputs, leading to severe edges, also pushes the melt pool towards the part and improves the surface roughness significantly. Different studies showed that sufficiently high recoil pressures flatten out the melt pool and produce an enforced wetting of the melt to the substrate [7, 66, 106-108, 148].

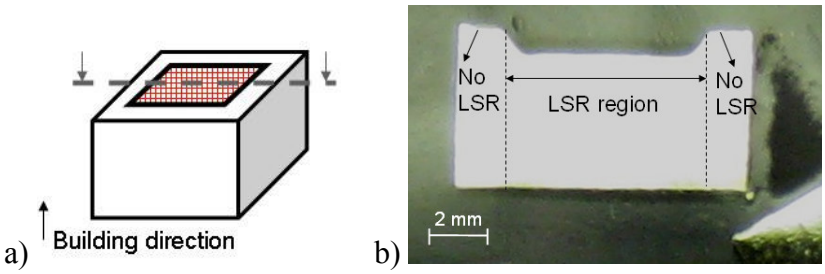

Figure 3.19: The explanation of the edge effect by material evaporation a) illustration of how parts were produced b) cross-sectional view of the part to observe the edges

The total enhancement derived by the first and second steps is illustrated in Figure 3.20 in terms of average and total roughness values. The average roughness R_a for the parts that are made by SLM without any erosion or laser re-melting is about 12 µm while the total roughness R_t is about 100 µm. When the first step, erosion, is applied with the best parameter set that gave minimum roughness values, these values are reduced to 6 µm and 55 µm for Ra and R_t, respectively (more than about 50% reduction). After laser re-melting, which is applied as the second step on the surfaces that were treated with erosion, the surface quality is even improved further and the roughness values decreased to 1.5 µm and 13 µm for R_a and R_t, respectively. The total improvement including two steps (erosion and re-melting) is about 90% for both average and total roughness.

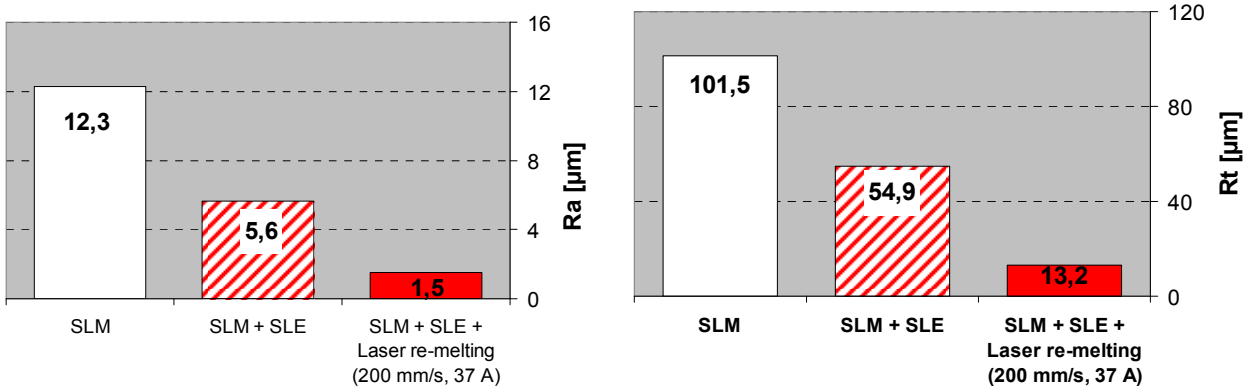

Figure 3.20: The enhancement in the average (R_a) and total roughness (R_t)

The roughness of the starting surface plays an important role for erosion in terms of surface quality enhancement. If the starting surface has a high roughness value, the surface quality enhancement is smaller than the case with a good starting surface quality. Moreover, if the surface is very rough (this is not the case with SLM parts), erosion cannot improve the surface quality at all. However, the starting surface quality is less important for laser re-melting. In order to prove this, the parts which are not exposed to SLE are directly treated with laser re-melting and the results are compared to the parts exposed to SLE and laser re-melting in Figure 3.21. As shown, when re-melting is applied, it does not matter if the starting surface has an average roughness of about 12 (after SLM) or 6 µm (after SLM + SLE). Therefore, if SLE is followed by laser re-melting for the surface quality, there is no need to apply SLE. It is better to apply directly laser re-melting regarding the productivity. That's why there is no third or fourth step in this multiple-step approach.

In this section, the surface quality improvement of SLM surfaces by SLE and laser re-melting was experimentally investigated with a multiple-step approach. The idea was to consecutively apply erosion and laser re-melting on SLM surfaces. The aim was to remove the peaks by erosion and to smoothen the surface by applying laser re-melting. The experiments concluded that erosion with properly selected parameters increases the surface quality by 50% while removing very little material (less than 5 µm). When laser re-melting is applied either directly on SLM parts or after

erosion on SLM parts, the surface quality improvement is even higher exceeding 90% for both average and total roughness values. This high improvement is due to recoil pressure pushing the melt pool towards the surface leading to some material vaporization at low scan speeds combined with high laser power and high overlap between scan tracks.

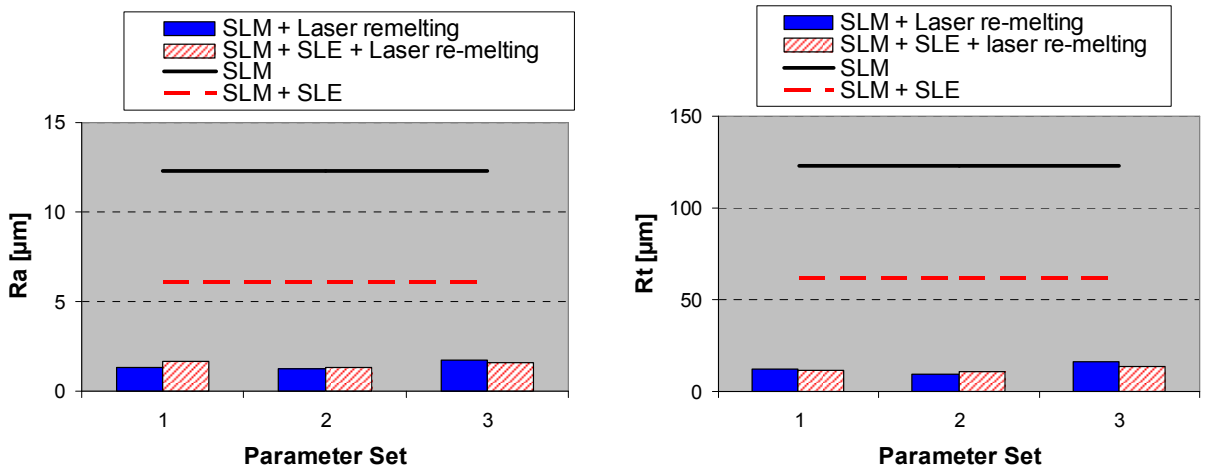

Figure 3.21: The enhancement in average (R_a) and total roughness (R_t) with re-melting (step 2) showing that erosion (step 1) is not necessary

3.2.2 Precision and Micro Machining After SLM

Using SLE after SLM may as well improve precision of lateral contours as allow producing small features (micro machining). During SLM, it is not possible to make small outer features if hard blades for the coater are used due to collisions. The smal features cannot withstand the collision forces between the recoater scraper and the rough top surface of the parts during powder deposition. The production of inner features (holes, slits, etc.) is also limited, not due to the collisions with the coater blades, but due to the partially melted and sticking powder particles in the inner feature walls. For example, the experiments made with Ti6Al4V material on a Concept Laser M3 Linear machine for scaffold production with hard coater scrapers showed that the minimum designed pore size is between 300 and 400 µm whereas the underlimit for the strut width was 750 µm [3, 110]. However, with some machine adaptations, i.e. replacement of hard steel scrapers by soft silicone scrapers and use of small aperture during SLM instead of big aperture, it was possible to make thinner struts (~200 µm) and smaller designed pores (250-300 µm). More details can be found in [3].

In order to demonstrate the micro machining capability of erosion after SLM, a circular hole having a diameter of 100 µm is made on a surface having a normal parallel to the building axis. The tests were made on the Concept Laser M3 Linear machine with standard SLM parameters optimized for maximum density and productivity. The big aperture was used together with hard coater scrapers. Figure 3.22 shows the part when the hole is attempted to be made during SLM without erosion. As evident from the micrographs, the hole is totally blocked with the melted material.

Figure 3.23 shows the holes made by erosion with different parameters. During erosion, only one scan track along the contour of the circle is made to remove the material due to the small diameter. When the holes are eroded with the small aperture, it was not possible to drill through because the energy density per unit area is not enough for evaporation. In this case, the spot size was entered as 80 µm (which is actually the spot size corresponding to the small aperture) to the machine software so that the software locates the scan track following the contour of circular hole, but the big aperture was employed during erosion. In this manner, it was possible to drill the hole through. The pictures of two different parts, taken with a Mitutoyo Quick Vision system, show that the hole is completely

drilled through with good circularity. The erosion per layer/scan was about 4 μm for both cases. The actual diameter is about 20% greater than the nominal one (100 μm) as shown in Figure 3.23. Moreover, not all parts exposed to erosion after SLM exhibited successfully built circular holes as depicted in Figure 3.24. When low laser power values (<90 W) are used, the holes are either blocked or partially drilled with a very small diameter. At low laser power, (80 W) melting takes place instead of evaporation blocking the hole with the melted material.

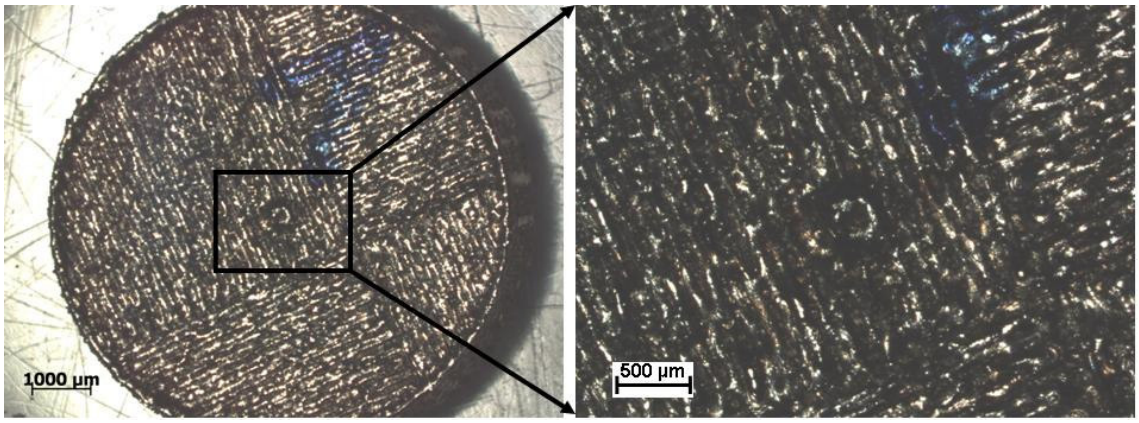

Figure 3.22: The part built made by SLM without erosion afterwards – hole totally blocked

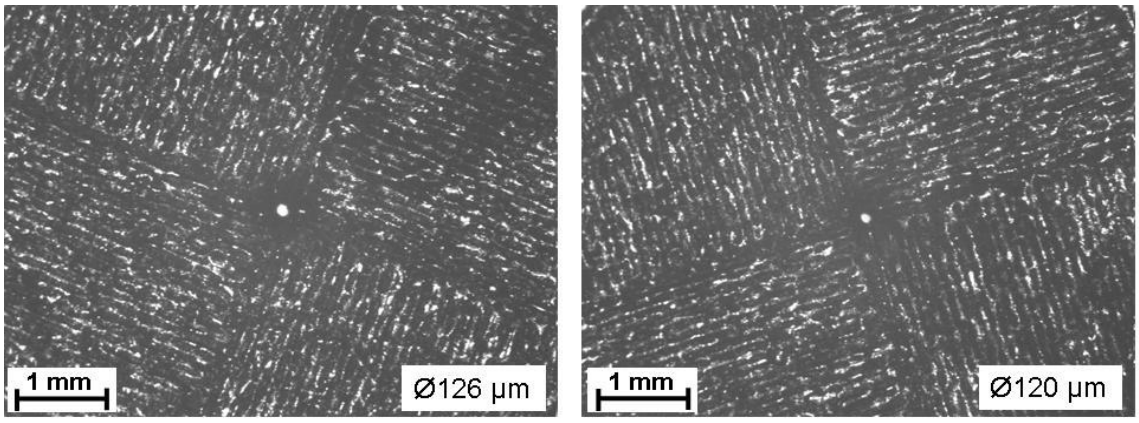

95 W, 300 mm/s, 30 kHz, big apert. 105 W, 400 mm/s, 30 kHz, big apert.

Figure 3.23: Top view of SLM parts, holes made by erosion (design diameter in Magics = 100 μm)

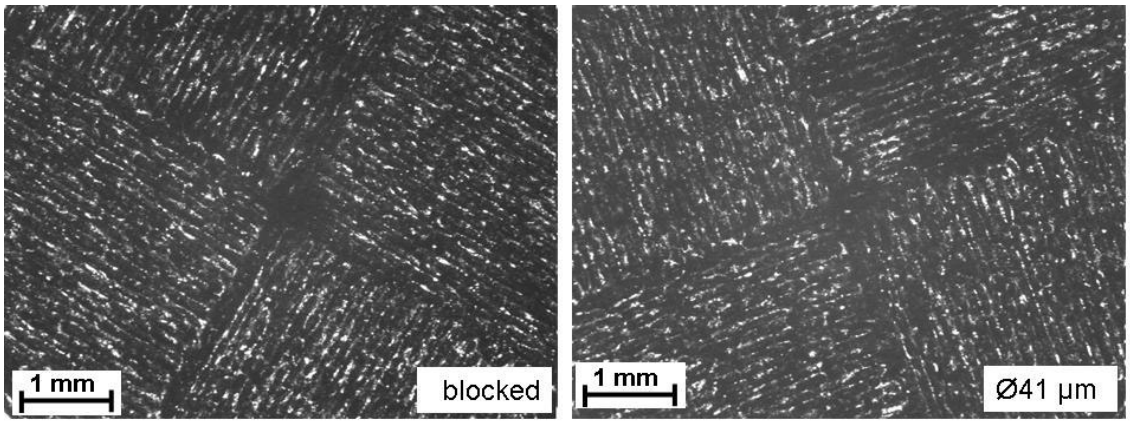

80 W, 350 mm/s, 30 kHz, big apert. 90 W, 350 mm/s, 30 kHz, big apert.

Figure 3.24: Top view of SLM parts, holes almost blocked or completely blocked (design diameter in Magics = 100 μm)

Figure 3.25 demonstrates two micrographs taken by optical microscopy from two different parts made by SLM and exposed to SLE afterwards with identical parameters. In these parts, during file

preparation, the hole diameter is set to 80 µm to compensate for overly large diameters after SLE and to provide a good accuracy for the circular hole. As given in the figure, the actual diameters become approximately 100 µm with 3-4% deviation from the nominal value. The circularity is also better than the ones obtained with SLM even at higher diameters due to sharp edges. Due to the lack of stage illumination on the optical microscope, two holes appear dark but they are actually drilled through completely.

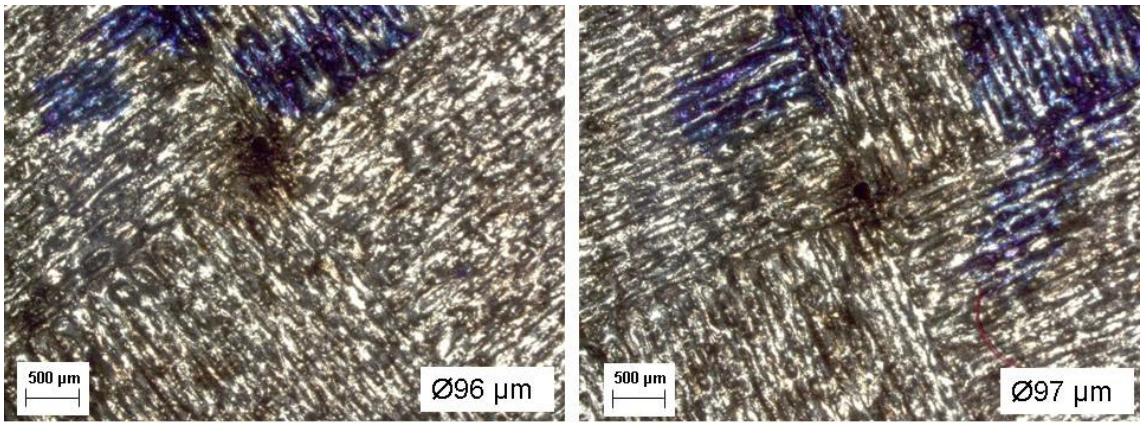

Figure 3.25: Top view of SLM parts, holes made by erosion (design diameter in Magics = 80 µm)

Another micro machining case is depicted in Figure 3.26. The part shown in the figure has four thin slits (having widths of 0.1 and 0.2 mm) and 4 holes (with diameters of 0.2 and 0.1 mm). As depicted in Figure 3.26a, the part made completely by SLM is not capable of making those slits or holes with success. The slits are mostly blocked with partially melted powder particles stuck to the inner walls unlike the case depicted in Figure 3.26b which shows the result of combining SLM and SLE (a laser power of 105 W, a pulse frequency of 30 kHz and a scan speed of 400 mm/s). In case of SLM, when the slit width or hole diameter is 100 µm, it is not possible to make the features due to the blockage of the cavities by the partially melted and sticking powder. The circular holes (and slits) having a diameter (and a width) of 200 µm are only partially blocked by the melted material deteriorating the dimensional and geometrical accuracy. Figure 3.26b depicts the case when the main part is made by SLM and the other features are made by erosion (a laser power of 105 W, 30 kHz, 400 mm/s, big aperture) after the SLM process is completed. As evident, all features are successfully made without any blockage problem. Moreover, the part produced by combining SLM and SLE exhibits sharp edges along the slits/circular holes. If the part was exposed to erosion after being made by SLM together with unsuccessful features, the results would not be the same. First of all, the powder material would be involved bringing up the 'bark' problem (See §3.3.1 for more explanation and discussion). Secondly, the melted material causes deviations in the form of the surface. For example, the lower right micrograph in Figure 3.26a shows one of the circular holes having a diameter of 0.1 mm. It is not very clear due to focusing, but the material in the middle of the hole is actually towards the reader. Therefore, it is better to apply erosion on SLM surfaces produced while discarding the tiny features during SLM.

With these two micro machining cases having dimensions less than 200 µm, it is shown that erosion makes it possible to produce very tiny features which are impossible to be made by SLM. However, there are a few conditions to be able to perform this micro machining by erosion. First of all, there should be no powder material involved during erosion. If this is the case, then the powder laying out of focus may partially melt and stick to the part being generated. This is called as 'bark formation' and exhibits a severe limitation. It will be discussed more into detail in the next section about erosion with big aperture after every layer. It can be shortly noted that the bark formation is

highly undesired and may cause blocking of small holes or slits. Therefore, no powder should be involved. Secondly, the erosion parameters depend on the geometry when micro machining is aimed at since the number of scan tracks per scan/layer is very few. To provide the necessary energy density, the number of scan tracks should be also taken into account for process optimization at this range of geometrical features.

a)

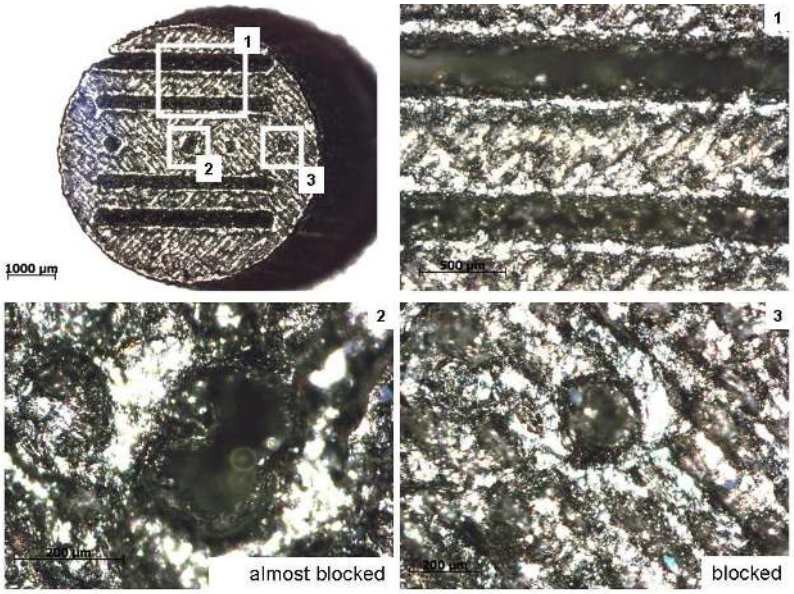

b)

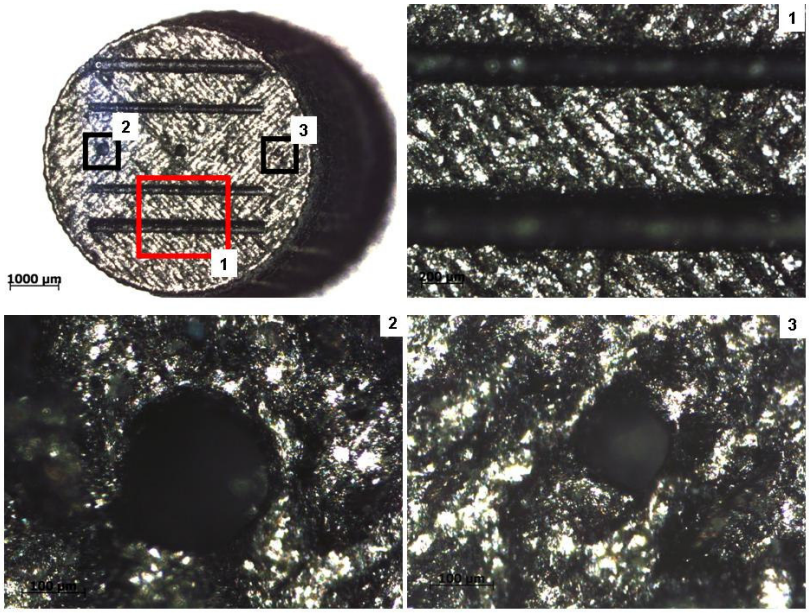

Figure 3.26: a) made by SLM without erosion b) part made by SLM, slits and holes made by erosion (laser power of 105 W, 30 kHz, 400 mm/s, big aperture)

The parts shown in Figure 3.22 to Figure 3.26 were manufactured with a small thickness of about 1.2 mm (along the building direction) to keep test times short. However, the inner features may be eroded to a higher depth. The total depth of inner features is mainly limited by the distance between the laser protection window and build platform's top surface (when the top of the build platform is close to the focus plane), which is a fixed value for the Concept Laser M3 Linear machine and equals to about 8 cm, as well as the height of the workpiece (or the part to be produced by SLM) as illustrated in Figure 3.27. As the workpiece height increases, the possible depth of inner features is smaller. Thus, the main criterion for the depth of inner features to be eroded is related to the total height of the workpiece.

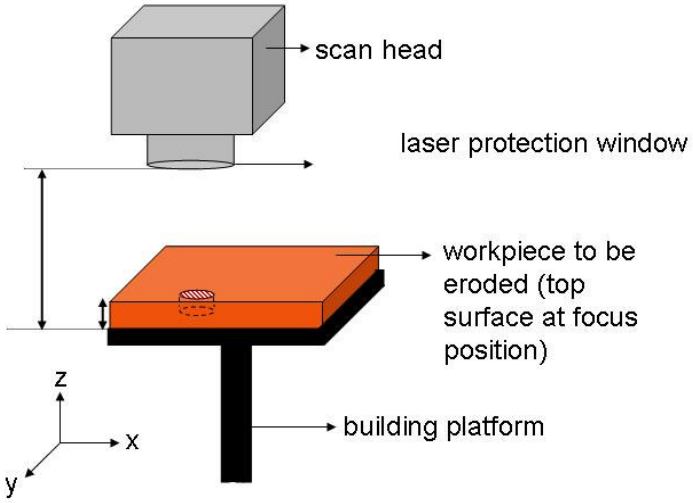

Figure 3.27: Illustration of the critical height which determines the total depth of inner features made by SLE after completion of SLM

3.3 Eroding after every SLM layer

In this approach, the erosion is applied after each layer either only on the contours or during hatching in addition to contour scanning. There are mainly two purposes: to decrease the layer thickness so that the resolution along the building axis is improved or to increase the surface quality of every layer to make a new layer deposition possible without breaking any tiny structures built by SLM. A third purpose could be to increase accuracy in the xy-plane (which has a normal parallel to the building axis). This has not been further investigated here. The experiments made with small and big aperture showed quite different features and therefore the results are presented in the following sub-sections in terms of the selected aperture.

3.3.1 Erosion with big aperture

During the SLM process, thin parts may break or be damaged when a new powder layer is deposited especially when using a hard coater blade. Because of the bad surface finish of the SLM process and the elevated edges, the edges and sometimes the peaks of the last melted surface come into collision with the coater which lays a new powder layer. As a result of these collisions, tiny parts easily break or are not manufactured successfully. Figure 3.28 illustrates the problem. Five series of 3 pins with diameters respectively of 1, 0.7 and 0.5 mm have been built (from left to right) from AISI 316L stainless steel powder with default SLM parameters optimized for maximum density. The two first pins of 0.5 mm (third and sixth pins in the row) are broken while the other 0.5 mm pins (ninth and twelfth) are highly distorted. Thus, it is not possible to manufacture pins with a diameter of 0.5 mm or less successfully by SLM on a Concept Laser M3 Linear machine equipped with a hard coater. Soft coaters are more preferable in terms of micro machining capability (the minimum diameter becomes about 0.3-0.4 mm). However, they wear out very rapidly; in some cases the soft coaters should be replaced after every build, increasing the production costs.

The contact of the last built layer with the coater should be avoided or minimized by eroding part of the last SLM built layer in order to remove the peaks by SLE (see Figure 3.29). The experiments in this paper are performed by combining SLM and SLE using AISI 316L stainless steel powder on a Concept Laser M3 Linear machine. The layer thickness selected in the experiments is 30 µm which is a commonly used value in SLM dependent on the powder particle size and required resolution. The other parameters used for SLE and SLM processes are given in the Table 3.1.

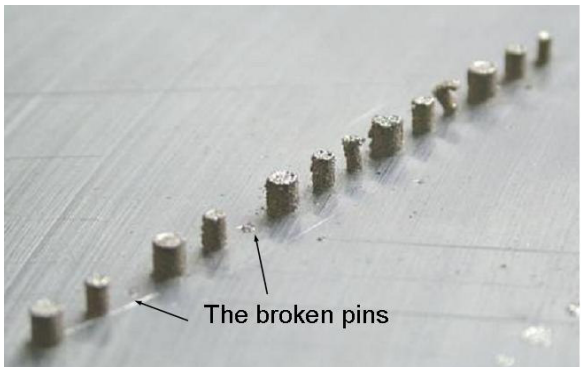

Figure 3.28: The demonstration of the problem

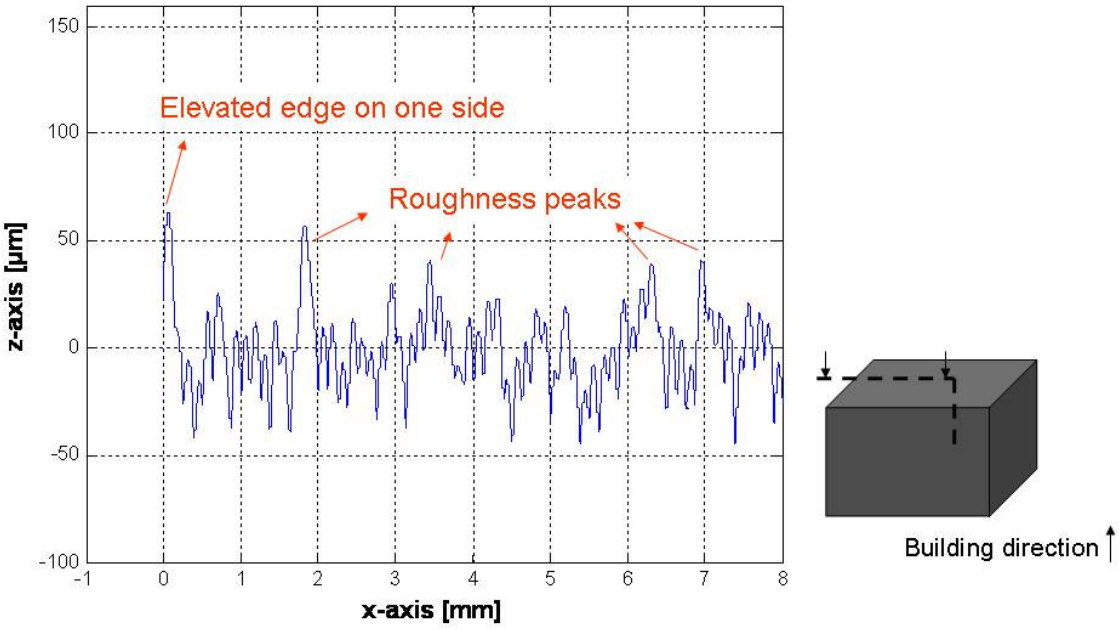

a)

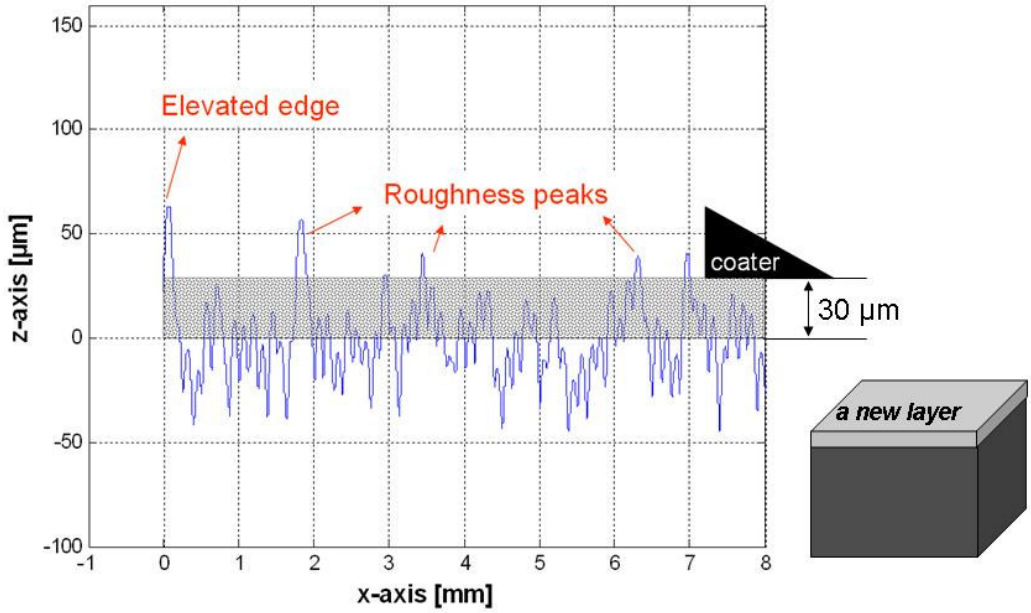

b)

Figure 3.29: Schematically illustration of the problem a) cross-sectional view of a cubic part after any layer with elevated edge formation and roughness peaks b) cross-sectional view of a cubic part while the coater is putting a new layer of powder with a thickness of 30 µm showing collisions with the roughness peaks and elevated edge

Table 3.1: The parameters used in the experiments

	SLE	SLM
Power (W)	100	100
Pump Current (A)	36	36
Frequency (kHz)	30	0 (CW)
Scan Speed (mm/s)	400	400
Scan Spacing (µm)	50	105
Spot Size $Ø_{99\%}$ (µm)	180 - big	180 - big
Layer thickness (µm)	-6 (per layer/scan)*	30 µm

** layer thickness for erosion, in other words depth of erosion, is not an adjusted parameter but is a result of other selected parameters*

The first tests confirm that the combined process improves the ability of SLM to machine small objects. Figure 3.30 shows a successfully built cylinder of 0.5 mm diameter and other objects that are built by combined machining without breakage. The surface quality and dimensional accuracy of the built objects are however not good: a 'bark-like' structure is formed surrounding the object, which has a different density from the base object (See Figure 3.31). It is observed that the height of the bark is shorter than the height of the object. The bark formed around a rectangular block is observed more into detail with a stereo microscope as shown in Figure 3.32.

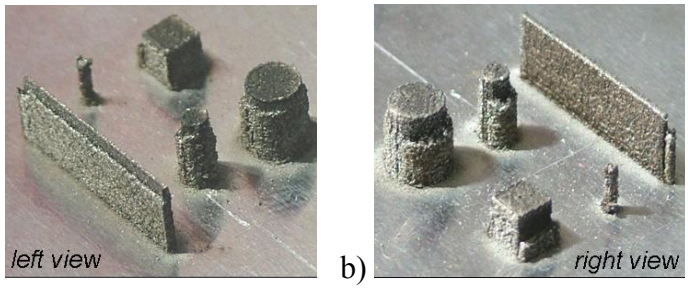

Figure 3.30: Wall with 0.5 mm thickness, with bark formation on one side (a), and no bark on the other side (b)

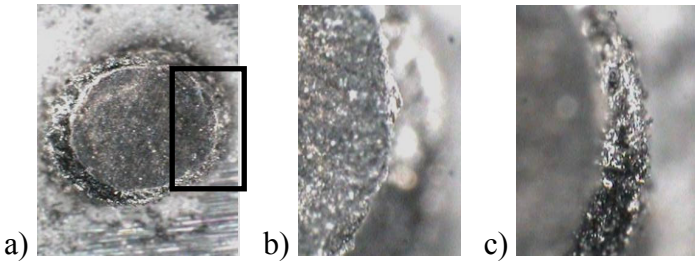

Figure 3.31: a) Top view of the cylinder with bark around it b) same view of rectangular area, but focused on part (bark is unsharp) c) same view of rectangular area, but focussed on bark (cylindrical part is unsharp)

Figure 3.32a shows the orientation of the block together with an exaggeratedly thick bark, built along the z-axis. As mentioned in the previous paragraph, the bark formation is present around the part's contours. However, it looks highly porous. In Figure 3.32c and d, the side view of the bar is depicted with views from bottom and top, respectively. The bark is partially not well connected to the part and thus easily peeled off by hand. However, it is not possible to remove the bark completely without machining. Figure 3.32c shows partially removed bark around the part whereas the shorter height of the bark is clearly visible in Figure 3.32d. It is important to note that the discrepancy between the heights of bark and the part depends on the selected parameters and is not consistent along all the bark formation around the part.

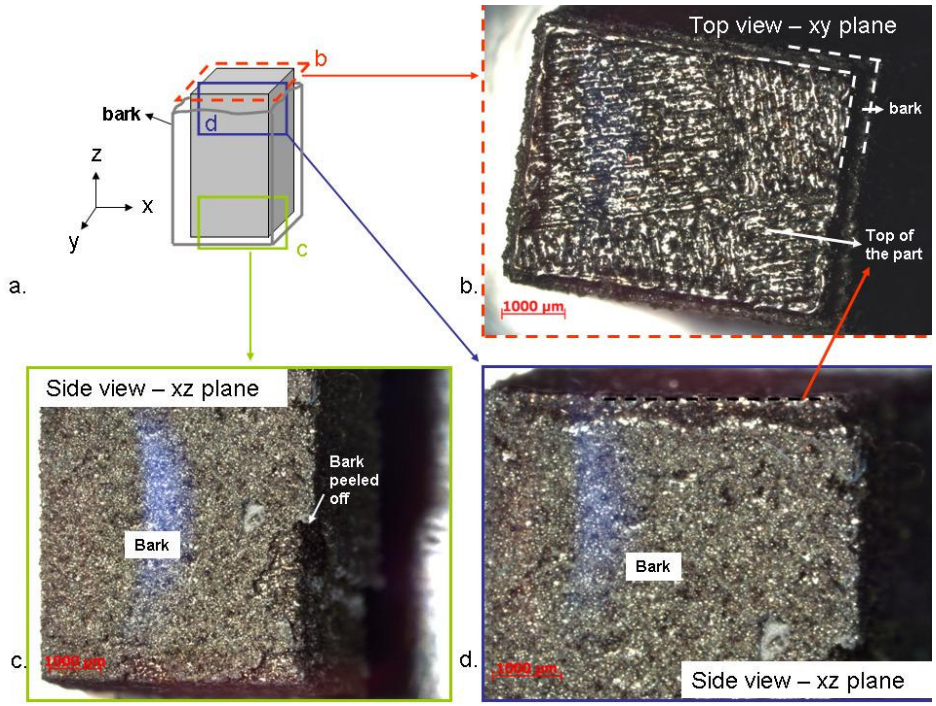

Figure 3.32: The bark formation around a rectangular bar a) z-axis is taken as the building direction during SLM b) top view of the bar with the surrounding bark c) side view of the bar showing partially peeled-off bark at the bottom of the part d) side view of the bar at the top showing the shorter height of the bark

Different tests were conducted in order to investigate the factor that influences the bark formation and the results showed that the part geometry (cylinder, wall or cube) and the position of the object on the work plane of the machine do not have any influence on the bark formation. Therefore, it is not dependent on the part geometry or position on the machine. For details: see studies given in [105, 109].

The formation of the bark is however dependent on how the scan tracks are located from the border of the object. With different dimensions of the object, the location of the scan tracks may be different. Figure 3.30 shows a wall with a thickness of 0.5 mm, which has bark on only one side, whereas Figure 3.33 illustrates a wall with a thickness of 0.7 mm, which has bark formations on both sides. The scan tracks that the laser beam follows during the SLE process are also investigated to study the bark formation more in detail.

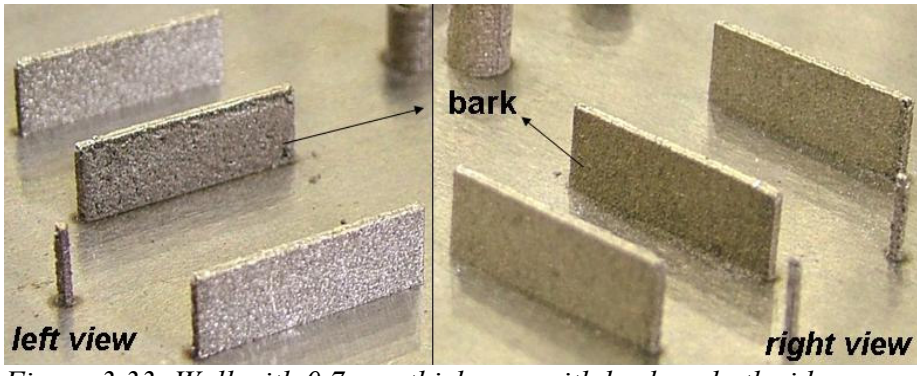

Figure 3.33: Wall with 0.7 mm thickness, with bark on both sides

Analysis of scan tracks used for erosion

An analysis of the laser scan tracks is necessary to explain the bark formation. The laser follows these tracks to melt the metal powder during the construction of the object. Figure 3.34a illustrates

the scan tracks for the case of a thin wall with a thickness of 0.5 mm. The full lines represent the scan tracks, while the dashed lines indicate the theoretical borders of the wall. The figure depicts that the scan tracks of the wall with a thickness of 0.5 mm are not symmetrical. At the bottom side, the scan track is very close to the border. This side is actually where the bark is formed. On the other side, where no bark is existent, there is a larger spacing between the last scan track and the border (shown at the top).

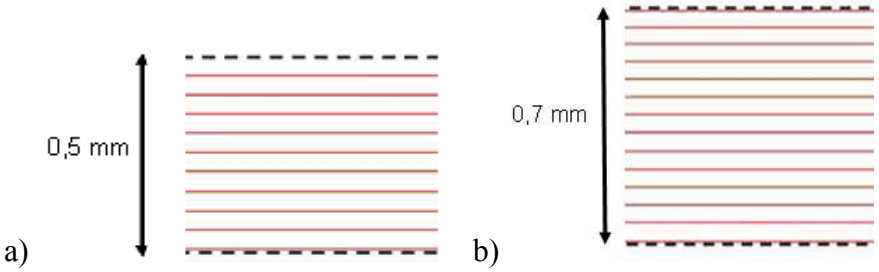

Figure 3.34: Scan tracks of a wall with thickness a) 0.5 mm b) 0.7 mm

The scan tracks of the 0.7 mm wall (Figure 3.34b) are also analysed. It is observed that they are symmetrical and very close to the border on both sides resulting in barks at both sides (see Figure 3.33). This reveals that there is a strong relation between the distance from the closest scan track to the border and the formation of the bark.

The irregular form of the bark around the cylinder is also a result of the distance between the border and the scan track. Figure 3.35 illustrates this irregular form of the bark which is close to an ellipse rather than a circular shape. At the sides of the cylinder, the thickness of the bark is larger while at the top and the bottom there is less bark formation. The scan tracks of a cylinder with a diameter 0.5 mm are shown in Figure 3.36. In the middle of the circle, at the sides, the length of the contour between the tracks is small as shown with a thick line in the figure. As a consequence, the powder surrounding the sides of the circle is more exposed to SLE and this results in a thicker bark. At the top and the bottom of the circle, the length of the contour between the tracks is larger, thus there is less erosion close to the border and less bark formation.

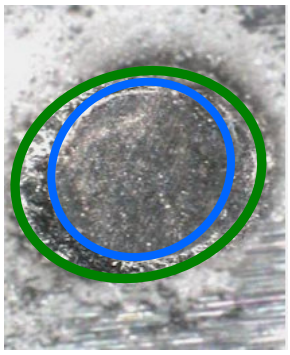

Figure 3.35: Irregular form of the bark

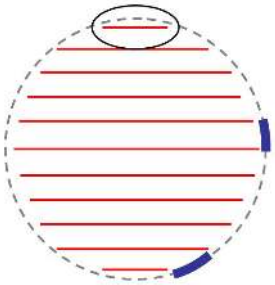

Figure 3.36: The scan tracks of a cylinder with 0.5 mm diameter

The last phenomenon that can be explained by the analysis of the scan tracks is the existence of two vertical lines along the bark of cylinders shown in Figure 3.37 whereas Figure 3.36 shows the scan tracks used to build such a cylinder with 0.5 mm diameter. The vertical lines formed along the building direction, visible on Figure 3.37, are related to the length of the scan track at the top (or bottom) of the circulated contour shown in Figure 3.36. This track is very close to the border, so at the top (or bottom) of the circle bark is formed. On the left and on the right of that track, there is no erosion, thus no bark. The lack of bark on these positions in each layer leads to the two vertical lines in the bark. The analysis of scan tracks concludes that the influence of the distance of the scan tracks to the border of the object on the bark formation is significant. In order to produce parts without bark formation, the scan tracks need to be analysed in detail and controlled.

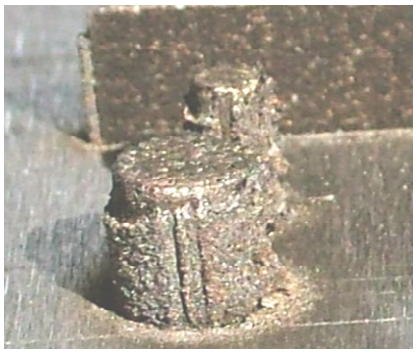

Figure 3.37: Vertical lines in the bark of cylinders

Explanation of bark formation

The formation of bark is explained by the divergence of the laser beam (Figure 3.38). When the scan track is close to the border of the object to be built, the laser partially scans the surrounding powder. During the erosion of the first layer, this layer is in focus and the intensity of the laser energy is very high due to the small focus diameter. The energy evaporates or melts some of the surrounding powder while the vapour pressure blows the rest of the powder away.

During the second layer, some powder is evaporated by the laser beam and the vapour pressure blows some surrounding material powder away (Figure 3.38b). After some layers, the difference in height between the melted object and the powder that is not blown away is so big that this powder is not anymore in focus. Therefore, the energy intensity is not high enough to evaporate the powder but only melts it. Here begins the formation of the bark (Figure 3.38c). As observed during the tests, the formed bark is less high than the object due to the blown away powder surrounding the object. A case where the powder particles around the parts are blown away due to the recoil pressure encountered in erosion is depicted in Figure 3.39. Since the recoil pressure depends on the energy density, the amount of expelled powder also depends on the selected process parameters, especially the spot size diameter and the laser power. As illustrated in the previous paragraphs with cylinders with diameters of 0.5 and 0.7 mm, the location of the scan tracks plays an important role in the formation of bark around the object. When the distance of the scan tracks to the borders is small, the laser beam scans a lot of loose powder, and a thick bark is formed, whereas the laser beam only scans the melted object if the distance is bigger, resulting in no bark.

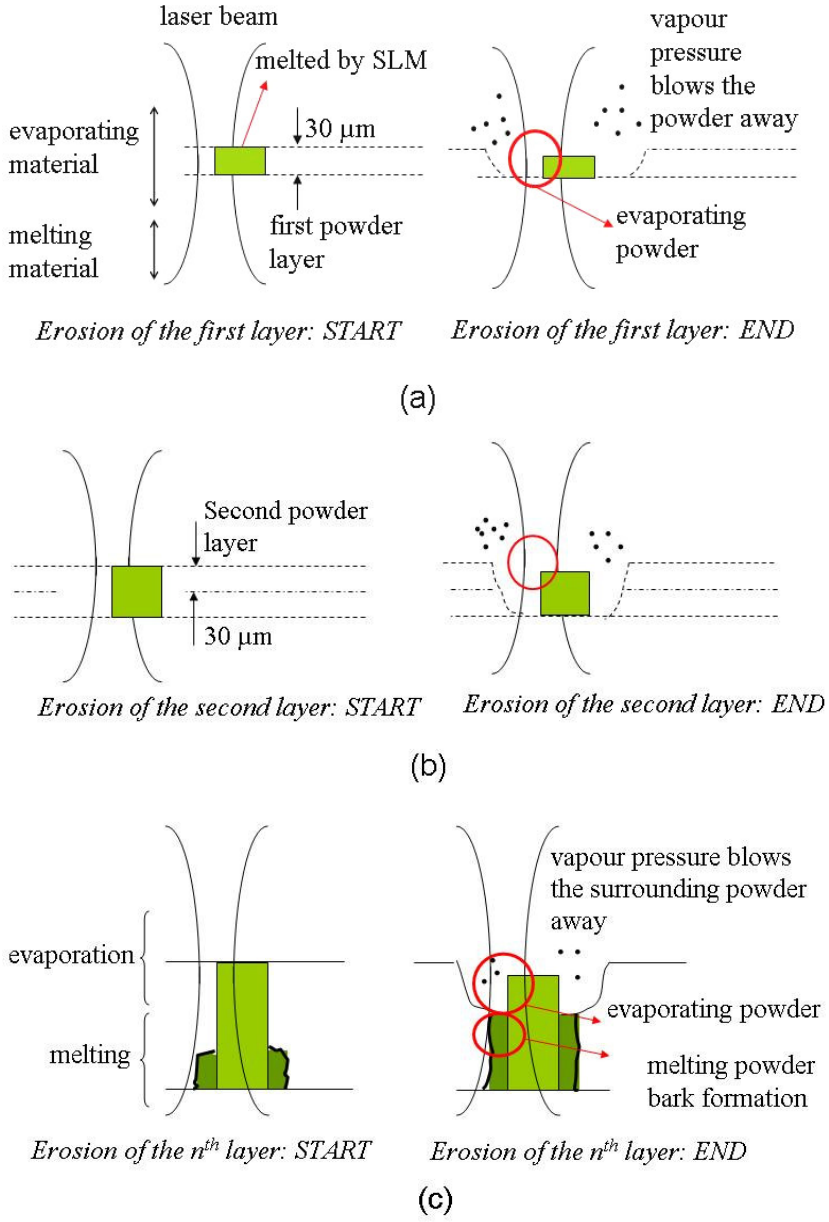

Figure 3.38: Formation of bark

Figure 3.39: Top of the powder bed showing the expelled powder

In order to prevent bark formation the scan tracks should be located far enough from the border. This prevents the melting of loose powder around and formation of bark. Figure 3.40 shows the result of a test with a spacing of 100 µm between the scan tracks and the border. As expected, no bark is formed, but the small cylinder (0.5 mm) is not successfully completed. In order to achieve tiny objects, the erosion scan tracks have to be close enough to the border of the object to scan the

surface completely and erode the full area. During the powder deposition, the hard blades of the coater collide actually with the edges of the melted layer because the edge height is generally higher than the height of the roughness peaks. If the surface of melted layer is not completely eroded including the edges, the collisions become inevitable. Thus, the coater has still the risk of colliding with the non-eroded material which results in broken or deformed small objects when the erosion tracks are located far from the part borders/contours. In order to avoid or partially eliminate the bark formation, the following tests were conducted with the small aperture. The results are presented in the next sub-section.

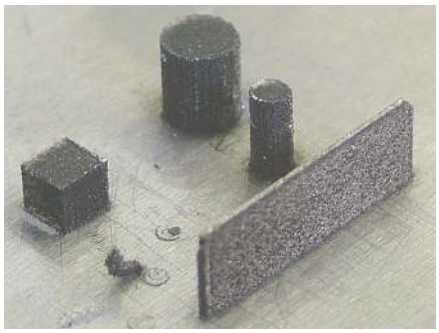

Figure 3.40: No bark formation because of the scan spacing of 100 µm between scan tracks and border

3.3.2 Erosion with small aperture

A set of benchmark parts are made by SLM without erosion, while another set is made by combining SLM with SLE, trying different erosion parameters and strategies with the small aperture to test whether the combined process of SLM and SLE would improve the stair-effect and micro machining capability when erosion is applied after each layer during SLM.

Geometrical design and produced benchmark parts are shown Figure 3.41. The benchmark part have many features including cylindrical holes having varying diameters from 3.5 down to 0.5 mm and thin walls/slits having a width between 0.9 and 0.3 mm. Moreover, those benchmark parts allow to study the effect of erosion on the side surface roughness and the stair-effect encountered inclined surfaces. The results are summarized in the following paragraphs.

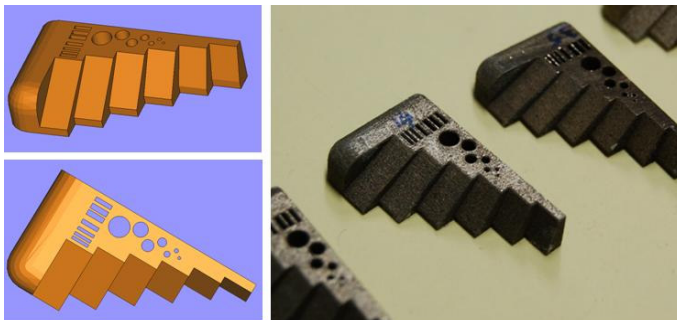

Figure 3.41 : A sample benchmark part

The built benchmark parts are compared in terms of micro machining capability for making thin walls/slits having a width down to 300 µm in Figure 3.42a. The pictures were taken by using a Mitutoyo Quick Vision System. The walls and slits on the left were made by SLM without erosion, whereas the walls and slits on the right were made by combining SLM with SLE only applied on the contours. The SLE parameters are given under the picture (400 mm/s, 22 W and 45 kHz). The figure reveals that it is not possible to make the tiny features in this benchmark part by SLM due to the collisions of the hard blades of the coater with the part. With the combined process of SLM and SLE, all the features regarding thin walls and slits were successfully completed in the benchmark part.

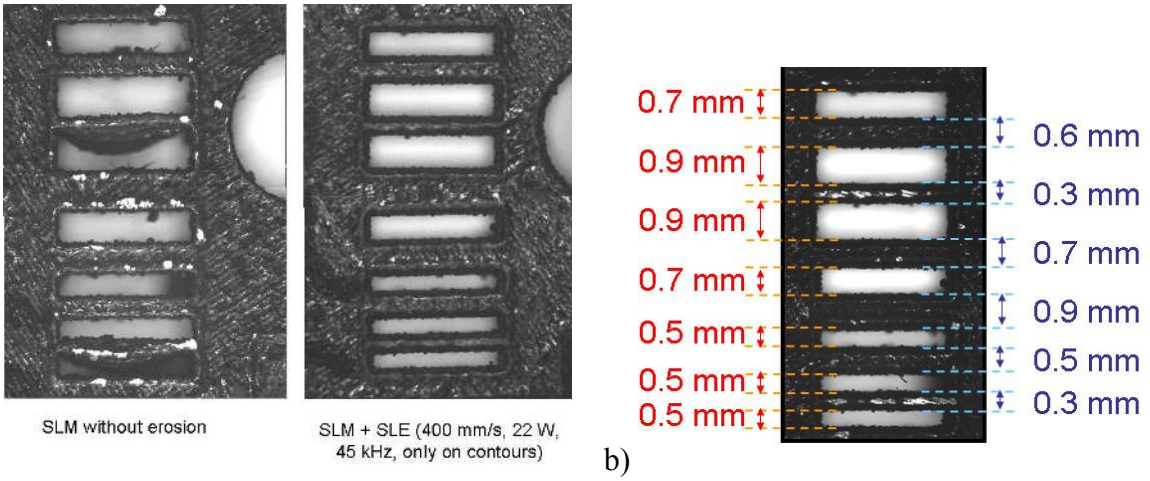

Figure 3.42 : a) Comparison of thin slits made by SLM without erosion or made by combining SLM and SLE b) Widths of the slits and walls

The benchmark parts were also observed with an optical microscope and the pictures are presented from Figure 3.43 to Figure 3.47. Figure 3.43 depicts the part built by SLM without erosion in terms of circular holes and thin slits/walls. In Figure 3.43a, the circular holes having a diameter between 3 and 1.5 mm are successfully made by SLM without erosion. Not shown in the figure but also the circular holes having a diameter of greater than 0.5 mm were made without any problems. However, the circularity and dimensional accuracy is not very good as shown in Figure 3.44. The main problem in producing small diameter holes by SLM is the loose powder that should stay unmelted inside the hole. As the diameter is reduced, this becomes more difficult. When the contours are exposed to laser radiation, the loose powder inside the hole is partially melted sticking randomly to the periphery of the hole. This causes the holes to deviate from the nominal geometry and results in non-circular forms. Moreover, the achieved diameter is generally 100 µm less than the nominal value. Figure 3.43b and c shows the top views of the slits and walls. All were made successfully except the wall with a width of 300 µm. In Figure 3.43d, the bottom view of the same walls shown in Figure 3.43c is depicted clearly showing the wall is deformed probably due to the collision with the coater.

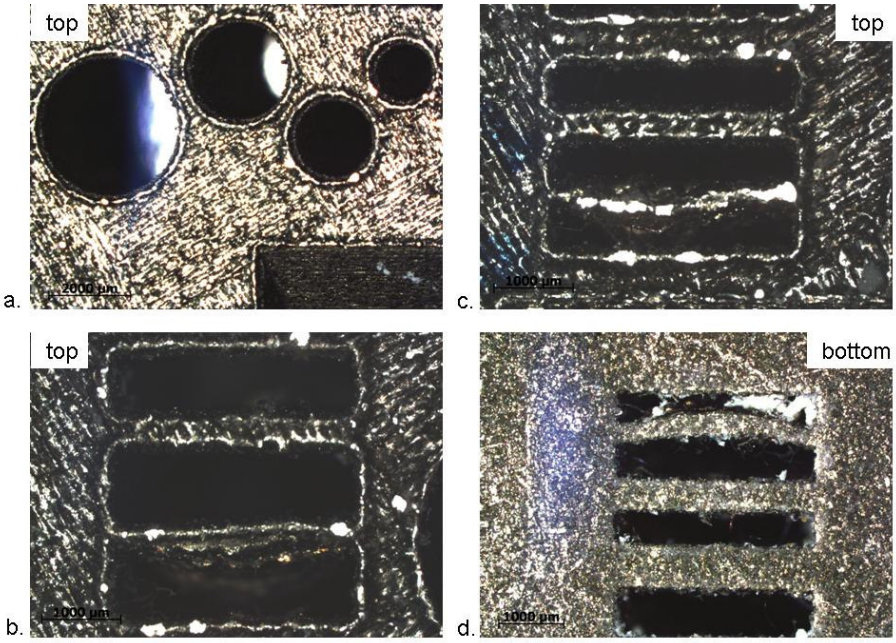

Figure 3.43 : The benchmark produced by SLM without erosion

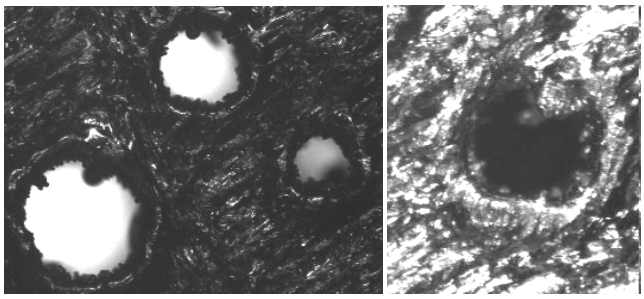

Figure 3.44 : SLM processed cylindrical holes a) holes with diameters of 1, 0.7 and 0.5 mm b) zoomed-in view of the hole with a diameter of 0.5 mm

The benchmark parts produced by combining SLM and SLE showed better micro machining capability. Benchmark parts made with different SLE parameters are shown in Figure 3.45 to Figure 3.47. Even made with different SLE parameters, the walls with a thickness of 0.3 mm were successfully made. Only the benchmark parts made with very low energy input during SLE (e.g. a laser power of 15 W and a scan speed of 600 mm/s) resulted in unsuccessful features. However, the dimensional accuracy is affected by the bark formation. The cylindrical holes showed good circularity at all dimensions but the bark formation deteriorated the diameters with an amount of about 200 µm which is more or less constant for different nominal diameters and SLE parameters (See Figure 3.48 where the average discrepancy between the nominal and actual diameters made by different SLE parameters is depicted with standard deviations). The thickness of the bark slightly depends on the utilized parameters during SLE (only the effect of spot size is significant) but once the parameters are selected and set, the thickness of the bark is quite repeatable. Hence, with a compensation strategy employed during CAD design of internal holes, the deterioration of the dimensional accuracy can be avoided. If the design diameter of the circles is kept about 200 µm larger than the nominal value, the actual diameter of the hole made by the combined process will be very close to the desired diameter. In order to verify this statement, some more parts are made by SLM and by SLM/SLE without any compensation, and by SLM/SLE with compensation. The results are illustrated in Figure 3.49 for three different hole diameters (4, 3 and 2 mm). As the figure reveals, it can be concluded that compensation strategy helps SLM/SLE to have a better dimensional accuracy comparable to the one of SLM parts without erosion.

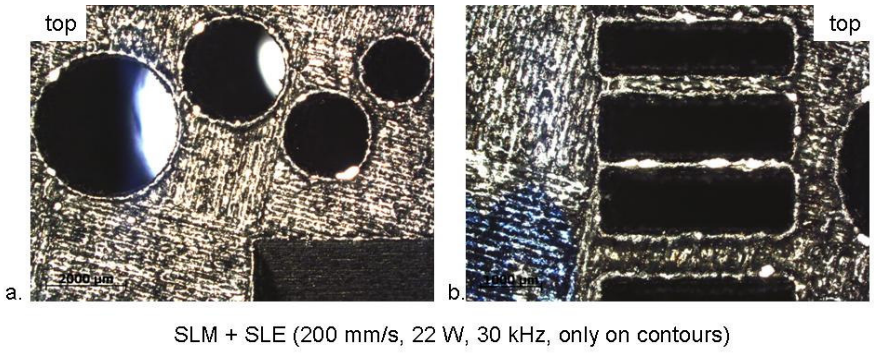

Figure 3.45 : The benchmark produced by SLM with erosion

The main conclusions from this benchmark study are that the tiny features which are difficult or impossible to be made by only SLM (e.g. thin walls having a thickness of 0.3 µm) can be successfully made when SLE is employed after each layer while the accuracy of larger features can be improved. When SLE is used, even with the selection of the small aperture, the bark formation deteriorates the dimensional accuracy. On the other hand, the bark formation can be compensated since the thickness of the bark is more or less constant for big (~300 µm) and small apertures (~200 µm) although they slightly change with the energy density of the laser beam. With the combined process of SLM and SLE, the circularity of the circular holes is better despite the bark formation than the circular holes made by only SLM.

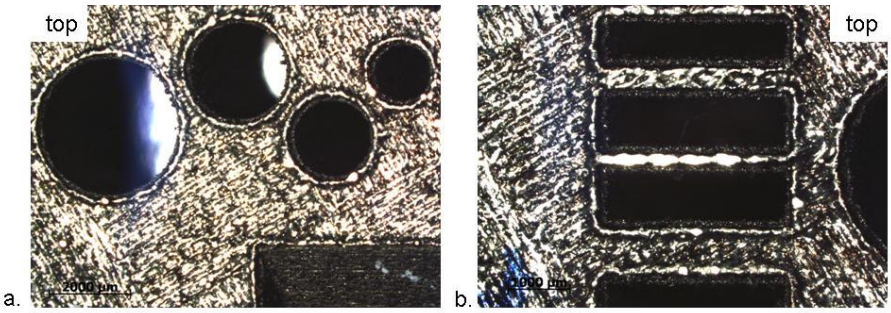

SLM + SLE (400 mm/s, 22 W, 45 kHz, only on contours)

Figure 3.46 : The benchmark produced by SLM with erosion

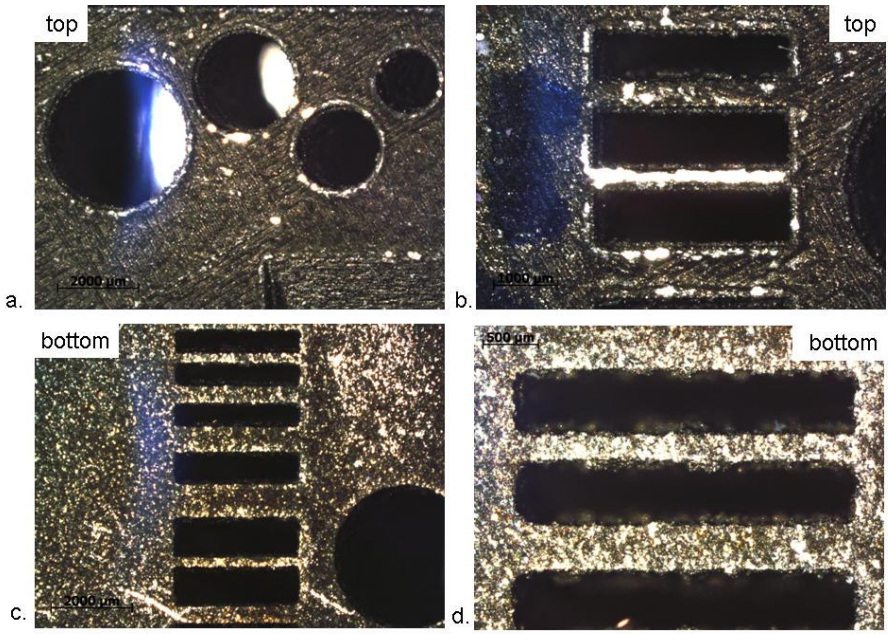

SLM + SLE (600 mm/s, 22 W, 30 kHz, hatching + contours)

Figure 3.47 : The benchmark produced by SLM with erosion

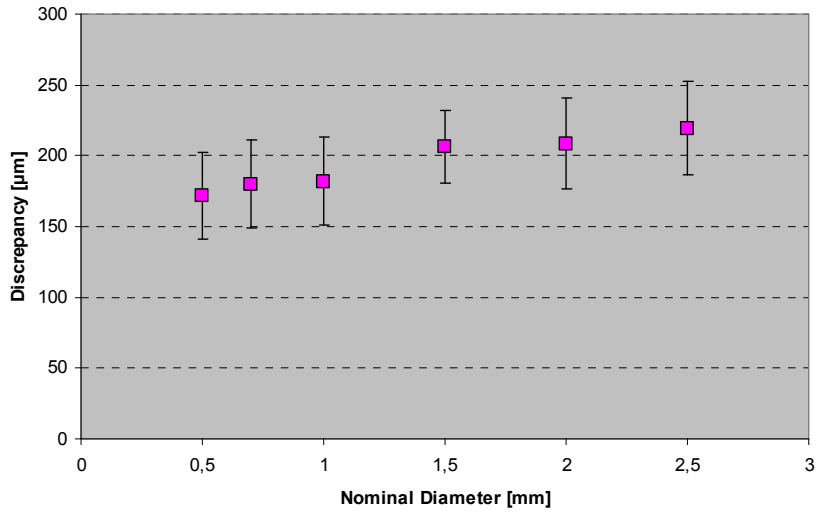

Figure 3.48 : The discrepancy between the nominal and actual diameters of the circular holes made by the combined process of SLM and SLE when the small aperture is employed for erosion, the bars show one standard deviation for benchmark parts made with different SLE parameters

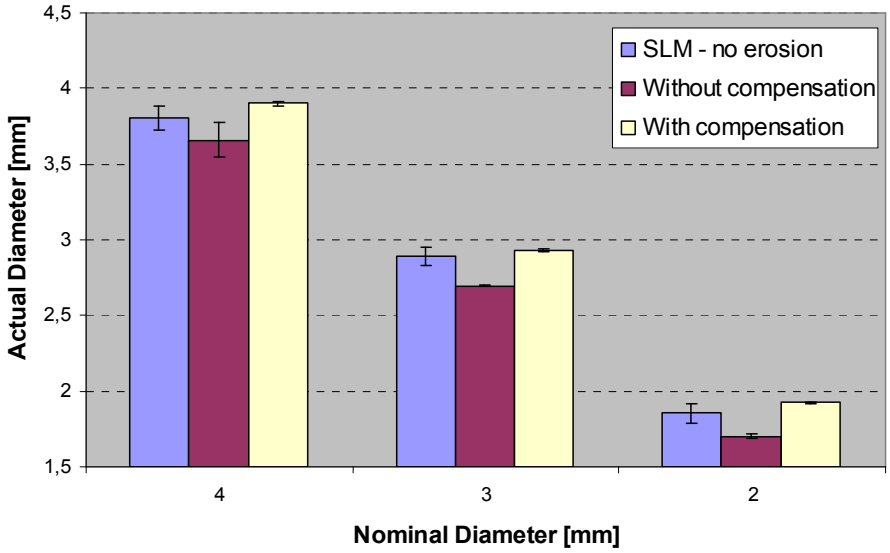

Figure 3.49 : The improvement of the dimensional accuracy with the compensation for the bark

In order to further test the capability for micro and precision manufacturing, some more benchmark parts with a slight difference in the geometry were made by SLM and SLE. The geometrical design is shown in Figure 3.50. This benchmark study also proved the same conclusions as the previous benchmark study in terms of micro machining capability. The parts made by SLM without erosion did not successfully exhibit the walls having a thickness of 0.3 mm. The pictures of SLM parts are depicted in Figure 3.51. All the holes having a diameter smaller than 0.6 mm (0.3 and 0.2 in this case) are totally blocked and all the walls having a thickness of 0.3 mm could not be made. Furthermore, the micrographs clearly show the formation of sticking powder which is partially melted around the SLM parts. The micrographs shown in Figure 3.52 shows the case for a part made by combining SLM and SLE (600 mm/s, 30 kHz, 90 W, only on contours). All walls and slits were again made successfully with the combined process of SLM and SLE. Moreover, the small holes having a diameter of 0.3 mm were made successfully unlike the ones made by SLM whereas not all the ones with a diameter of 0.2 were made successfully. (Difference not always clearly to see on pictures).

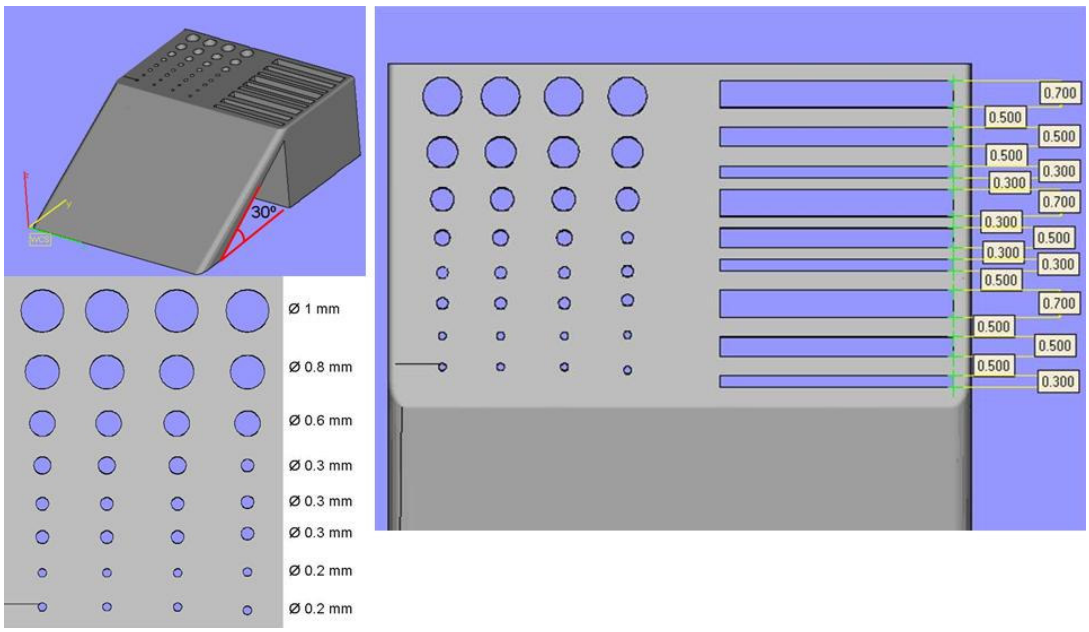

Figure 3.50 : Second benchmark design with dimensions of the circular holes and walls

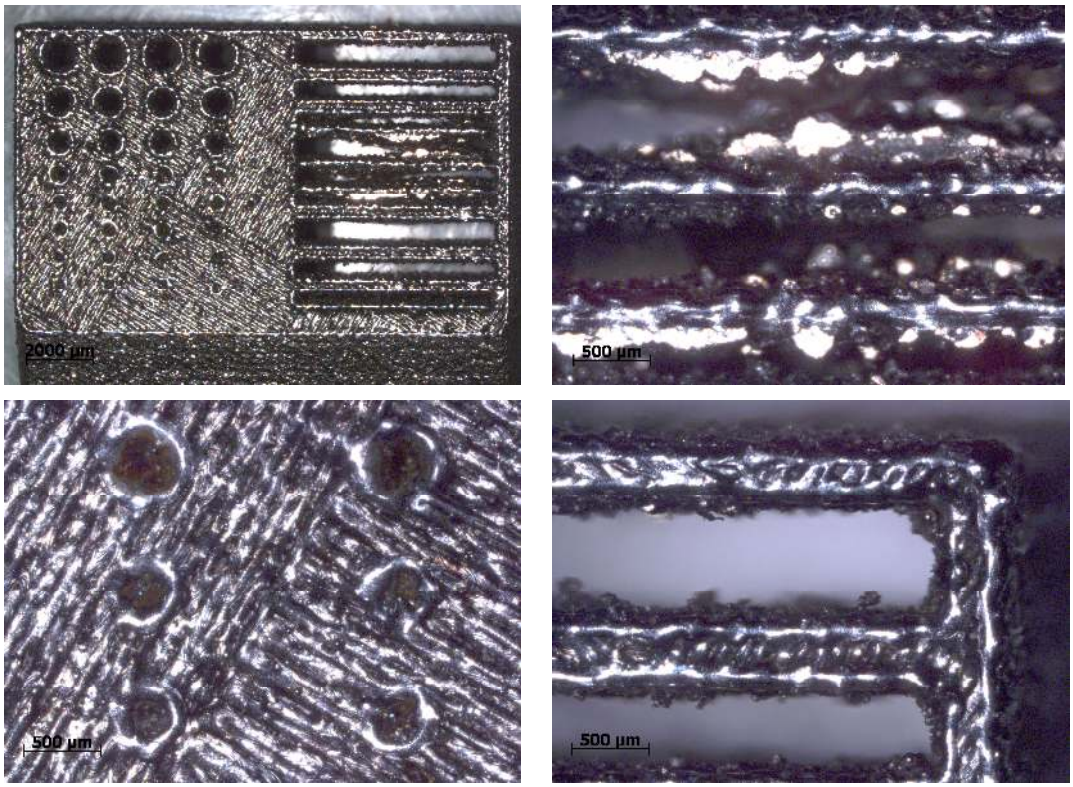

Figure 3.51 : Top view of a benchmark part made by SLM without SLE

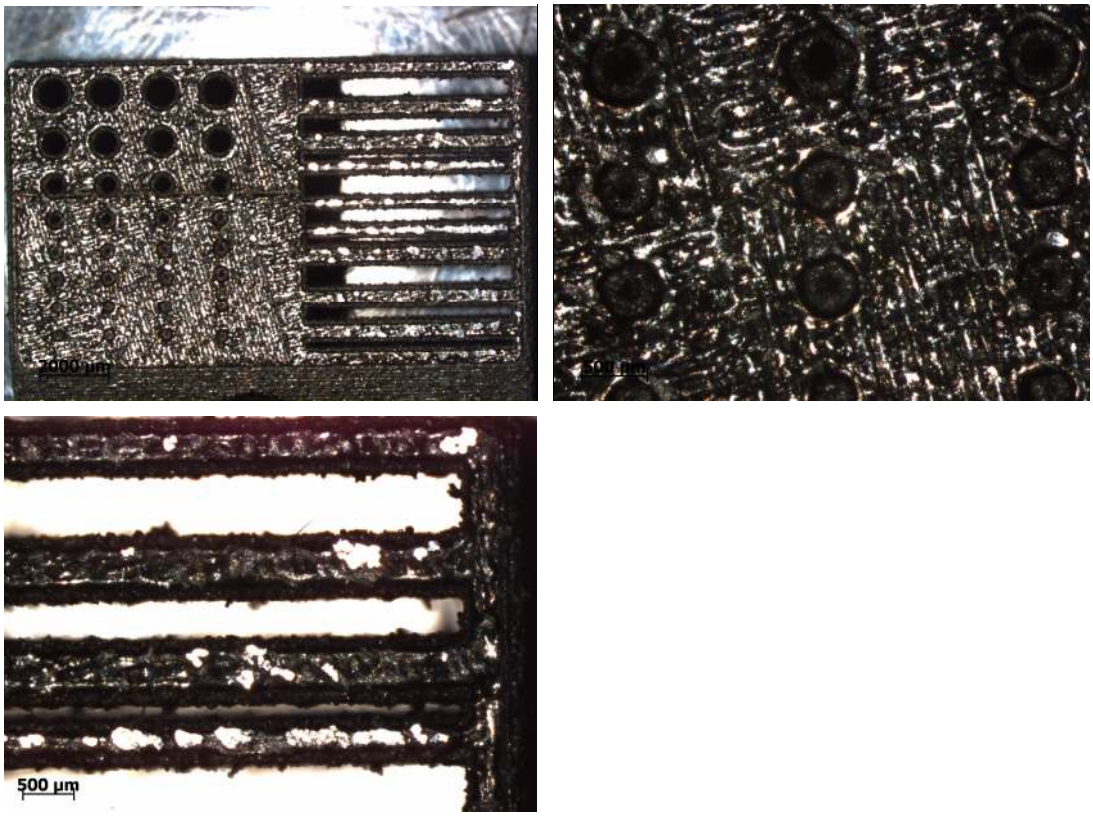

Figure 3.52 : Top view of a benchmark part made by the combined process of SLM and SLE

The side roughness values of the first set of benchmark parts were also measured using a Taylor Hobson Talysurf 120L surface profilometer. The surface of the benchmark part where these measurements were carried out is shown in Figure 3.53 together with the building direction. Generally, the roughness values encountered on the side surfaces are higher than the ones measured on the top surfaces of the SLM parts. This is due to partially melting and sticking powder around

the part to be produced by SLM. Moreover, it is difficult to improve the surface quality of the vertical walls in SLM, e.g. it is not possible to apply laser re-melting on those surfaces since the laser beam does not have any access. Different techniques are employed to address this problem, such as melting the contours after the hatching vectors during SLM to have a better surface quality. However, this solution does not significantly lower the roughness.

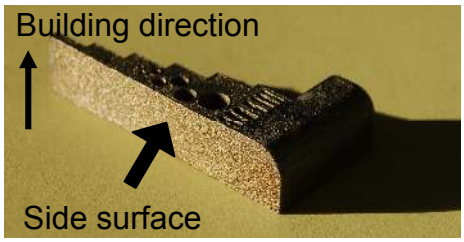

Figure 3.53 : The surface on the benchmark where the side surface is measured

The benchmark parts were produced by combining SLM and SLE employing different SLE parameters to investigate the side surface quality. The results showed that only a few sets of parameters improved the surface quality. Most of the parameter sets increased the roughness values due to the bark formation. The best improvement was achieved with the following SLE parameters: a scan speed of 400 mm/s, a laser power of 22 W and a pulse frequency 45 kHz. Employing these parameters to erode only the contours of the successive SLM layers improved the average roughness R_a on lateral surfaces from 14.8 µm to 10.5 µm and the total roughness R_t from 118 µm to 86.4 µm. Three-dimensional measurement results are illustrated in Figure 3.54 and Figure 3.55 for only SLM and for the combined process of SLM and SLE. Employing erosion with this scan speed only on contours does not significantly increase the production time and provides an improvement of about 33% in the surface quality. Therefore, combining SLM and SLE on contours only can be performed when the side surface roughness is important.

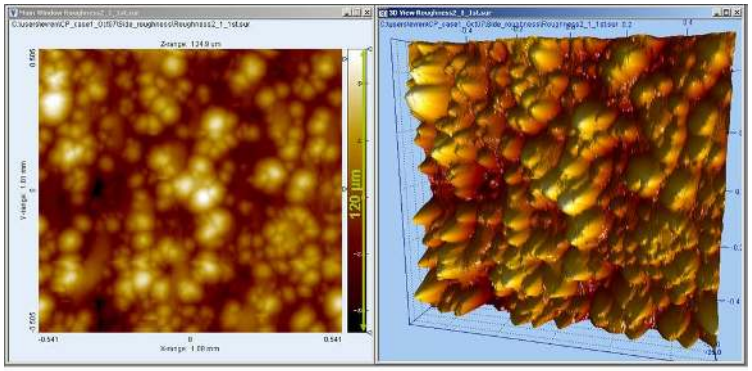

Figure 3.54 : The side surface roughness results with 3D measurements for the SLM parts

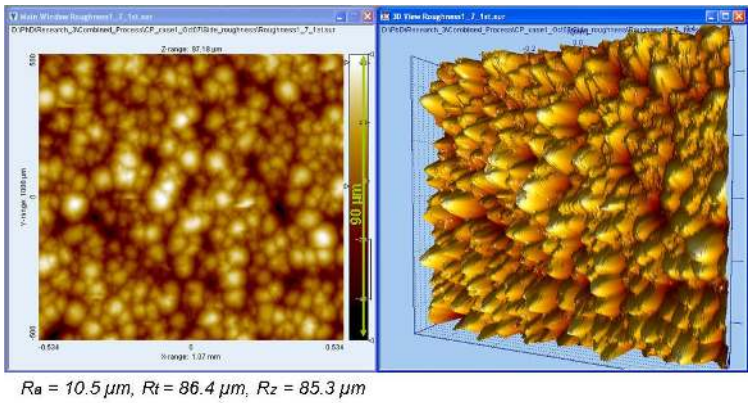

Figure 3.55 : The side surface roughness results with 3D measurements for the combined process of SLM and SLE (400 mm/s, 45 kHz and 22 W)

The last topic under investigation by this benchmark study was to test if there is any improvement on the stair-effect of inclined surfaces when the combined process of SLM and SLE is applied. In this case, SLE is applied after every SLM layer to remove part of SLM layer before adding the next layer to reduce the effective layer thickness. The stair-effect is a limitation for all layer manufacturing techniques for the production of parts with inclined or curved surfaces and depends mainly on the layer thickness and the inclination or the curvature of the surface. §4.3.4 and §4.3.5 explain the stair-effect more in detail and will show that it is possible to eliminate the stair-effect to a high extent by applying laser re-melting on the inclined surfaces after the SLM is completed and surrounding powder is blown away. As explained above, a second solution may be combining SLM and SLE and applying erosion after every SLM layer to improve the resolution along the building axis (or to reduce the effective layer thickness). This requires the evaporation of the whole layer area to a certain depth which is melted by SLM and significantly increases the production time. Another disadvantage of this method is the bark formation as the SLE scan tracks approach the borders of the layer. In case a significant depth of the SLM layer is evaporated, a bark formation cannot be avoided around the part. Figure 3.56 illustrates a comparison between two samples which were produced either by SLM or by combining SLM and SLE (eroding the whole layer area with a scan speed of 600 mm/s, a laser power of 22 W, a pulse frequency of 30 kHz, a scan spacing of 120 µm with the selection of small aperture). Figure 3.56b shows an almost uniform bark formed on the side walls of the slanted surface. There is also a significant change in color of the part as illustrated on the side surfaces of benchmarks in Figure 3.56c. Thus, with the powder involved in the process, it is quite difficult to improve the building resolution of the SLM process without a bark generation. However, the inclined surfaces made by the combined process of SLM and SLE showed a slight improvement in terms of average roughness which can be used as an indicator of the stair-effect when the settings are properly selected for SLE. The average profiles measured on an inclined surface with an inclination angle of 30° on the benchmarks either produced by only SLM or by combined SLM and SLE are separated into two components, i.e. the waviness and roughness. The profiles for the total measurement and waviness component are shown in Figure 3.57a and b respectively for SLM and combined SLM/SLE.

a) 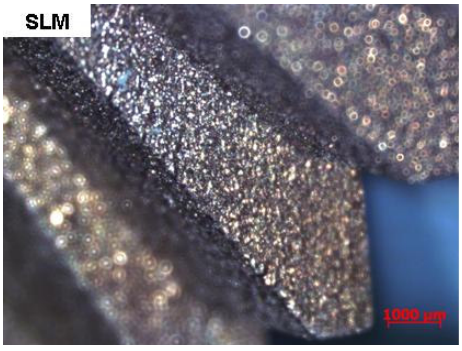

b) 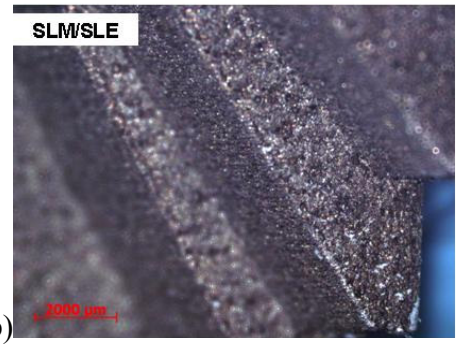

c) 

Figure 3.56 : a) Side views of slanted surfaces of benchmark samples made by SLM and b) by SLM/SLE c) Side surfaces of two benchmark parts made by only SLM (at the bottom) and by combining SLM/SLE (at the top)

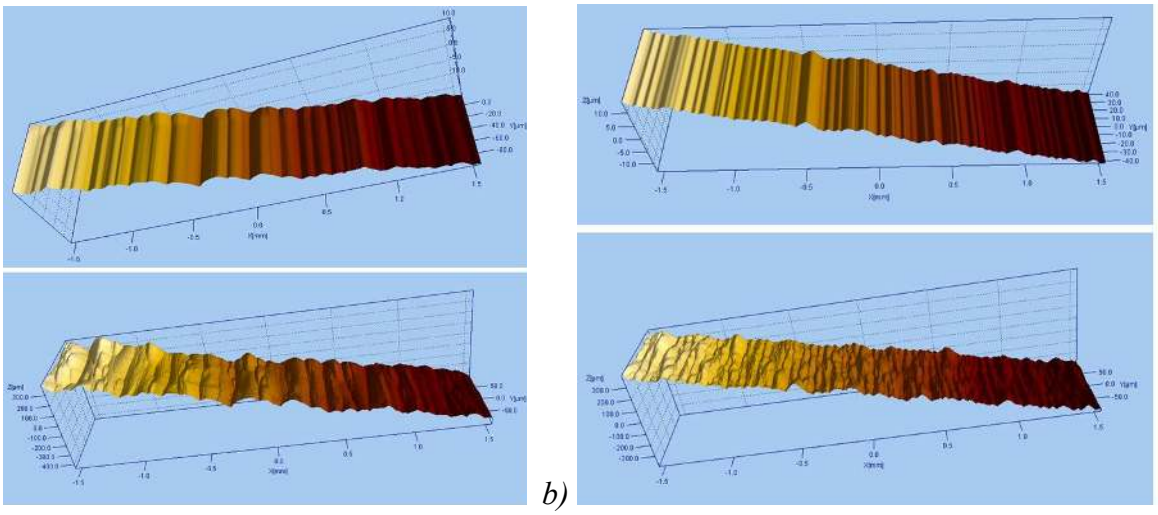

Figure 3.57 : The waviness (top) and total profiles (bottom) of two benchmark parts produced by a) SLM only b) by combining SLM and SLE

Figure 3.58 compares the two inclined surfaces shown in Figure 3.57 after the removal of the slopes while Figure 3.59 presents the plot for the two profiles obtained by SLM or combining SLM/SLE. Roughness values as given in Figure 3.58, indicate that the surface produced by combining SLM/SLE has significantly lower average roughness (S_a) as well as RMS (S_q) and total roughness (S_y) values. Density of summits (S_{ds}) is a parameter showing the number of peaks in the sampling area and is much higher with the surface made by combining SLM and SLE. The comparison of the profiles plotted together in Figure 3.59 also shows the improvement when SLE is applied. Most of the peaks are suppressed when erosion is applied. Therefore, it is concluded that the combined process of SLM and SLE can result in a lower step size or a lower surface roughness. However, the stair-step effect cannot be totally eliminated or suppressed to a high extent such as the case with laser re-melting as will be discussed in §4.3.4.

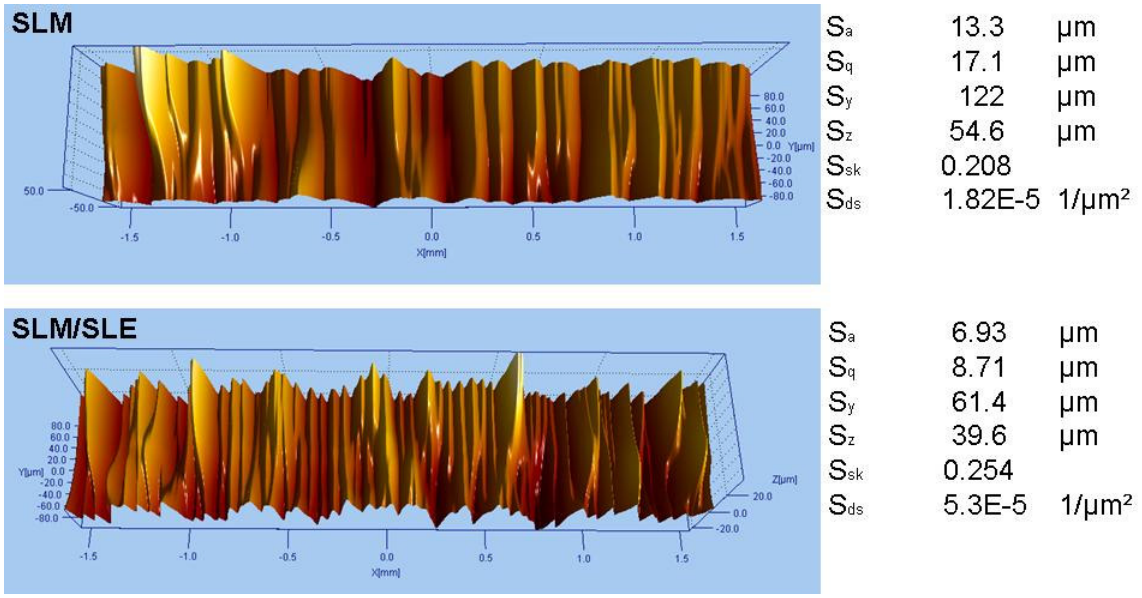

Figure 3.58 : The waviness profiles of the slanted surfaces produced by SLM or SLM/SLE after slope removal with all surface roughness parameters (S_a, S_q, S_y, S_z, S_{sk} and S_{ds})

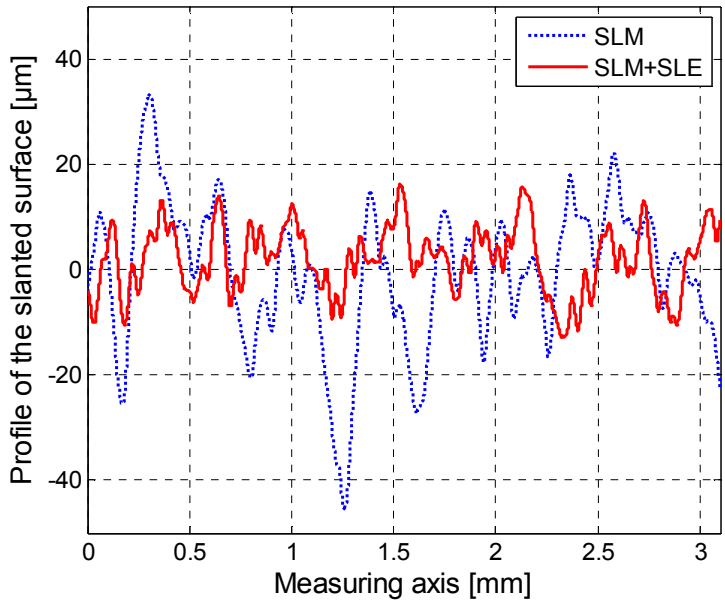

Figure 3.59 : The comparison of average waviness profiles of the slanted surfaces produced by SLM or SLM/SLE

3.4 Conclusions

This chapter summarizes the advantages and limitations of combining Selective Laser Melting (SLM) and Selective Laser Erosion (SLE) and presents the experimental results regarding the surface quality, contour accuracy, building resolution and micro machining capability. The experiments point out that by applying SLE after the SLM process is completed, the surface quality of SLM parts is improved about 50%. However, a better improvement of about 90% is obtained when laser re-melting follows the SLE process. Moreover, the surface quality improvement with laser re-melting does not depend on the surface quality of starting surface. It does not matter whether it is a rough SLM surface (R_a of about 12 µm) or a smoother surface obtained by SLE (R_a of about 6 µm). Therefore, laser re-melting is studied in more detail and the results are presented in the following chapter. The scan speed and scan spacing to obtain a good surface quality with SLE (600 mm/s and 40% of the spot size) is higher than what is needed for laser re-melting (200-400 mm/s and 10% of the spot size) meaning that the production time with SLE is much shorter (6 times). Therefore, SLE of the top surface can easily be applied as a finishing process when 50% improvement in the surface roughness is satisfactory.

The in-plane micro machining capability of SLM process is limited to the size of the melt pool which is bigger than the spot size of the laser beam due to dragging of the surrounding powder. The melt pool size also depends on the material-laser beam interaction. If the heat conductivity of the material is very high, the melt pool size is smaller compared to low conductive materials that do not transfer a lot of heat to the surrounding powder material. The experiments carried out in the scope of this research with AISI 316L stainless steel and or with Ti6Al4V at K.U.Leuven [3] showed that it is not possible to make small features having dimensions less than 500 µm on the Concept Laser M3 Linear machine when the steel coater scrapers are utilized. However, SLE can increase the micro machining capability of the process significantly if no powder is involved around the area exposed to SLE (which is needed to avoid bark formation). The minimum circular hole diamater and slit size is about 100 µm with the combined process of SLM and SLE when SLE is applied after SLM is completed. Yet, combining SLM and SLE may be accomplished during the process at an intermediate level (after a number of layers) for making small features in the part provided that the powders filling in the internal features can be emptied after the process is completed.

Another approach was taken as applying SLE during the process after every layer to remove the roughness peaks and edges formed during SLM that may hamper the deposition of further powder layers. However, this requires the erosion of the whole surface of the SLM layer which is surrounded by the powder material. This generally leads to 'bark' formation. The bark can be defined as a structure sintered of loose powder material, which should stay as unmelted, sticking to the part's inner and outer walls of the samples. The thickness and uniformity of the bark depends on the selected aperture and slightly on the selected process parameters. With the big aperture, the bark is a thick and rough structure formed around the SLM parts with a slightly lower height due to the fact that powder is blown away around the part by the recoil pressure. With the small aperture, the bark formation is less severe. It is smooth and uniformly appears around the parts. It is difficult to distinguish the bark from the part with naked eye. The bark formation deteriorates the dimensional accuracy but it could be compensated for since the thickness does not depend on the geometry. The influence of the process parameters is not that significant on the bark thickness. For the small aperture, the compensation value should be about 200 μm and this value can be taken into account in the design stage for an improved dimensional accuracy and micro machining capability.

Lastly, the side surface roughness (vertical walls and slanted surfaces) of SLM parts is addressed by combining process of SLM and SLE in different manners, e.g. eroding the whole layer area to reduce the effective layer thickness or by eroding the contours only. By applying SLE with small aperture only on the contours of every SLM layer, the side surface roughness measured on vertical walls decreased about 33%, mainly due to the formation of a smooth and uniform bark around the part. However, applying SLE on the whole surface area to improve the resolution and accuracy in the build direction does not drastically reduce the stair-effect but only shows a slight improvement (compared to laser re-melting) in the average roughness of the inclined surfaces, used as an indicator of the stair-effect. However, the stair-effect is almost completely removed when laser re-melting is applied on inclined surfaces as explained in the following chapter.

4 Manufacturing by combining Selective Laser Melting and Laser Re-melting

4.1 Introduction and Literature Review

Although the SLM process provides many advantages compared to conventional machining, low surface quality is one of the major drawbacks encountered in the process. Secondly, in spite of the fact that the process is capable of making almost full dense (~98-99%) parts, little residual porosity may still be problematic for some applications where high strength and fatigue resistance are necessary. In the scope of this study, laser re-melting is employed during or after the SLM process to overcome these problems. That is after scanning a layer (intermediate or final layer) and melting the powder, the same slice is scanned again before putting a new layer of powder. This solution might increase the production time substantially depending on the selected scan speed and scan spacing, but on the other hand, it can be the ultimate solution for applications where a density of 98-99% is not sufficient or where surface density is very critical for crack formation and propagation. Laser re-melting can also be applied to only the last layer or the outer skin of the part if it is aimed to enhance the surface quality or density. In this case, the process is named Laser Surface Re-melting (LSR).

Laser re-melting is not only used for surface modifications for lower roughness values [111-115] and densification but also to improve other surface material properties such as micro hardness [116-118], friction and wear behavior [116, 119, 120], corrosion resistance [121-123], wettability [113, 124, 125] and microstructural properties [126]. Laser re-melting is also reported to reduce the residual stress in the top layer with about 55% when sufficiently high energy per unit area in re-scanning is selected (150% of the forming energy of a layer during SLM) [125]. However, the experimental study of residual stresses at K.U.Leuven show that laser re-melting after every layer, in other words post-scanning, improves the residual stresses only about 10%. The results of this work have been published elsewhere and can be found in the Appendix 3 [13]. Although laser re-melting is a common method for surface modifications of parts produced by conventional techniques, the use of laser re-melting during an additive manufacturing technique is not studied in detail regarding many aspects.

In this chapter, the potential of laser re-melting to enhance the density and surface quality of SLM parts is investigated, as well as to eliminate some problems encountered with SLM, i.e. stair effect and elevated edges. Stair effect reduction is aimed at by applying laser re-melting after every layer only on the contours whereas the phenomenon of elevated edges of the solidified material is a problem encountered with many laser processing techniques but more pronounced with laser re-melting. The microstructures obtained by laser re-melting after each layer and after laser surface re-melting are also reported.

4.2 Experimental Procedure

All experiments are carried out on a Concept Laser M3 Linear machine which employs a Nd:YAG laser. The laser can be operated in either Q-switched or continuous modes. In this study, laser re-

melting is conducted in the continuous mode whereby the maximum laser output power is approximately 100 W. It is possible to adjust the laser spot diameter, $Ø_{1/e^2}$ to 70 and 130 µm ($Ø_{99\%}$ respectively 80 and 180 µm). AISI 316L stainless steel powder is used as material during the experiments.

The parameters used during additive melting (SLM) of a layer are the standard SLM values optimized for maximum density (scan speed 380 mm/s, laser power 105 W, scan spacing 125 µm and spot diameter 180 µm) and recommended by the machine maker. Various strategies of laser re-melting with different parameter sets are tested. It is applied after each layer, either only to the layer contour or to the whole scanned layer area. Alternatively, laser re-melting can be employed after the SLM process is completed on either top or inclined part surfaces. The utilized parameters for laser re-melting are presented in each section since different parameter selections are required for different purposes.

4.3 Results and Discussion

In this section, the experimental results with laser re-melting regarding many aspects are presented. First, the density improvement by applying laser re-melting after each layer is presented when laser re-melting is applied after every layer on the whole scanned area to fill the pores with melted material (§4.3.1). Then the potential of laser re-melting to enhance surface quality of SLM parts by applying laser re-melting only on top surfaces with a normal parallel to the building direction is explored (§4.3.2). In the following section, the microstructural changes that are accomplished by applying laser re-melting after each layer or on top surfaces are discussed (§4.3.3). To show the possibility of applying laser re-melting on inclined surfaces, a benchmark study is accomplished and the results are presented (§4.3.4). As a solution to the stair effect in SLM, laser re-melting is utilized to re-melt the contours in each layer (§4.3.5). As will be discussed in the following sub-sections, laser re-melting provides many advantages to improve the SLM process. On the other hand, some problems arise like the formation of elevated edges of re-solidified material. Although the edge effect problem is more severe with laser re-melting, it is also encountered during SLM as well as other laser processing techniques involving melt pools. In the last sub-section, the physical phenomena behind the edge effect and possible solutions to suppress this problem are presented (§4.3.6).

4.3.1 Density Improvement

For density improvement, the same slice is scanned with a different set of re-melting parameters after SLM of each layer. While changing some parameters such as scan spacing, scan speed, number of re-melting scans or laser power, some parameters were kept constant throughout the experiments: the selection of the big aperture and a scan strategy of all 0° hatch lines. With the big aperture, a pump current of 39 A corresponds to a laser power of 105 W whereas a pump current of 35 A corresponds to 85 W. The scan spacing factor (a_1) determines the scan spacing between two consecutive scan lines. As a_1 decreases, the scan lines are located closer to each other. In the laser re-melting experiments to enhance the density, the scan speed is changed in the range of 50 to 200 mm/s whereas a scan spacing factor is varied between 5% and 20% of the spot diameter (180 µm). The effect of the laser power is investigated in the ranges of 85 to 105 W for two different numbers of re-melting scans.

The cross-sectional view of a SLM part without any re-melting process observed with an optical microscope (OM) is shown in Figure 4.1. The black spots throughout the part are the pores that are created during the SLM process. They are homogeneously distributed and can be formed due to several reasons such as decrease in the solubility of the dissolved elements in the melt pool during cooling and solidification and evaporation of elements with a high vapor pressure [6]. An

insufficient surface quality can lower the density as well: High roughness peaks and valleys that are formed after each layer can prevent the coater depositing a homogenous powder layer. Moreover, the laser energy may be not enough to melt the new layer completely since the depth of the powder in some regions will be thicker. Morgan et al. states that a rough surface causes the entrapment of gas upon deposition of a new powder layer. When the new layer is being scanned, the gas is superheated and expands rapidly removing the liquid metal above it, thus creating a pore [128].

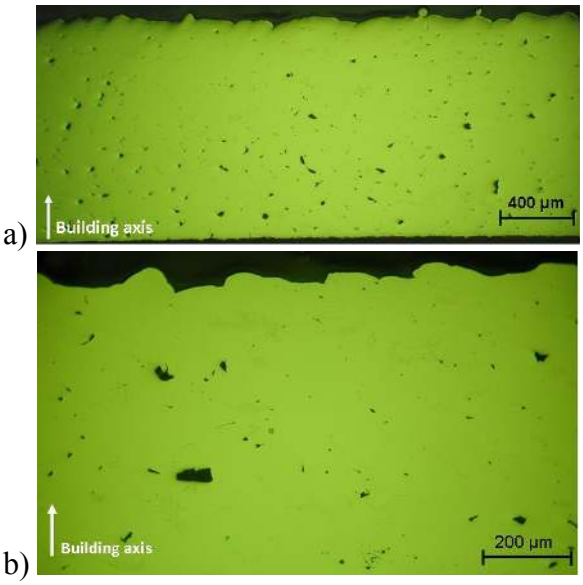

Figure 4.1: Cross-section of a SLM part a) 4x magnification b) 10 x magnification

In order to get a quantitative comparison between parts produced with applying different laser re-melting parameters and SLM parts produced with no re-melting, the densities of the parts are measured using cross-sectional images obtained with optical microscopy. In order to achieve this, the OM pictures are first converted to black and white images using a constant threshold value. Then the ratio of the number of black pixels to the white pixels is calculated for each image. For every set of parameters, at least three pictures are taken at different locations of the cross-section. The average density results measured in this way are given in Figure 4.2 with a confidence level of 95%.

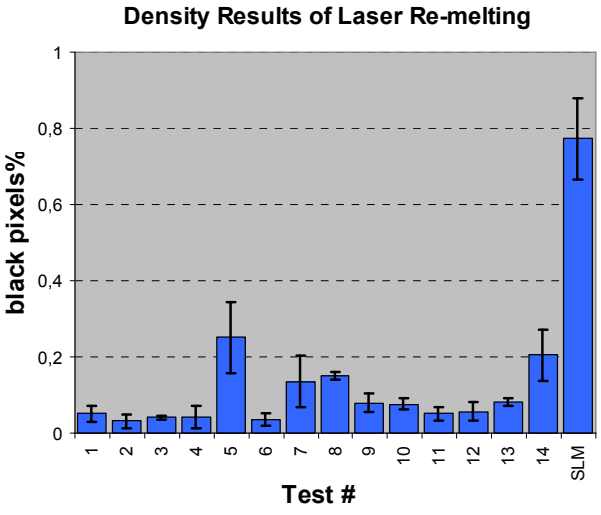

Test #	Scan Speed [mm/s]	Pump Current [A]	Scan Spacing (a1)*	# of re-melting scans
1	200	35	0,1	1
2	200	35	0,1	3
3	200	35	0,2	3
4	200	35	0,05	1
5	200	35	0,05	3
6	200	35	0,2	1
7	200	39	0,1	3
8	200	38	0,1	3
9	200	37	0,1	3
10	200	39	0,1	1
11	200	38	0,1	1
12	200	37	0,1	1
13	100	35	0,1	1
14	75	35	0,1	1
15	50	35	0,1	1
16	SLM only - no re-melting			

*Scan spacing = scan spacing factor (a1) x spot size

Figure 4.2: Density results of laser re-melting

In the ranges that are tested in this study, a higher re-melting scan speed (200 mm/s) in combination with low laser power (35 A or 85 W) resulted in better density values (see test parts 1,

2, 3 and 4 in Figure 4.2). Applying the re-melting multiple times 1 or 3 times does not significantly decrease the porosity for low laser energy inputs to the substrate.

Figure 4.2 shows that all parameter sets of laser re-melting improve the density when compared to the porosity of the SLM part without laser re-melting (shown as the last bar in the figure). The average porosity of SLM parts is about 0.77%, whereas the densest re-melted part obtained with the 2nd parameter set has a porosity of only 0.032%. The standard deviations decrease when laser re-melting is applied and low porosity levels are reached. The OM images of some parameter sets are depicted in Figure 4.3 and Figure 4.4. The laser re-melting parameters for each part are given under the image. In Figure 4.3, the parts look almost fully dense which is also validated from the porosity percentages shown on right top corners.

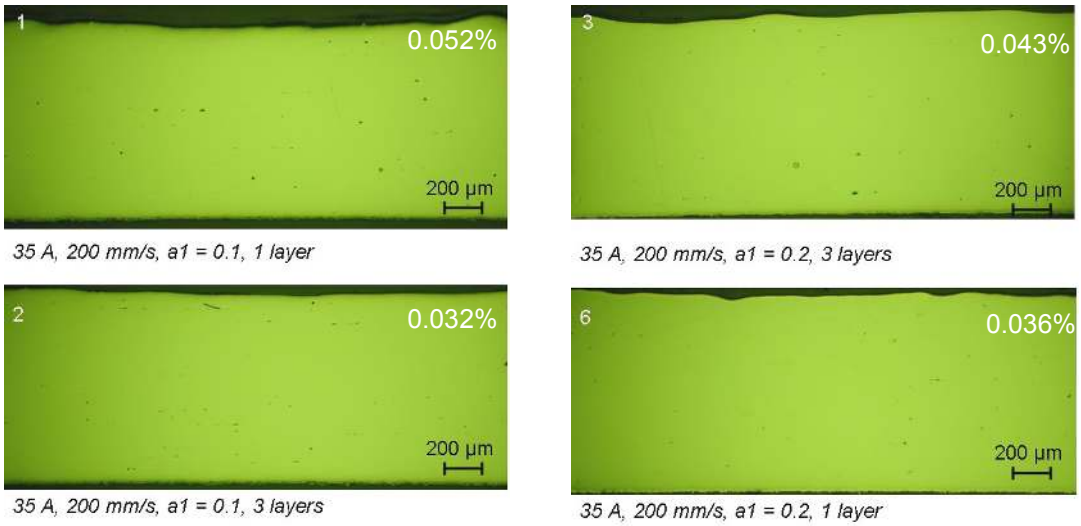

Figure 4.3: Optical microscopy images of the laser re-melted parts with different parameters (porosity<0.06)

In Figure 4.4, the optical microscopy images of lower density parts that were also exposed to laser re-melting are displayed. Almost all parts with high laser power (105-95 W) or with low scan speed exhibited a higher porosity, greater than 0.136%. Applying multiple re-melting scans at high energy inputs worsens the density. However, when compared to parts produced by SLM only without laser re-melting, laser re-melting improves the density significantly in any case.

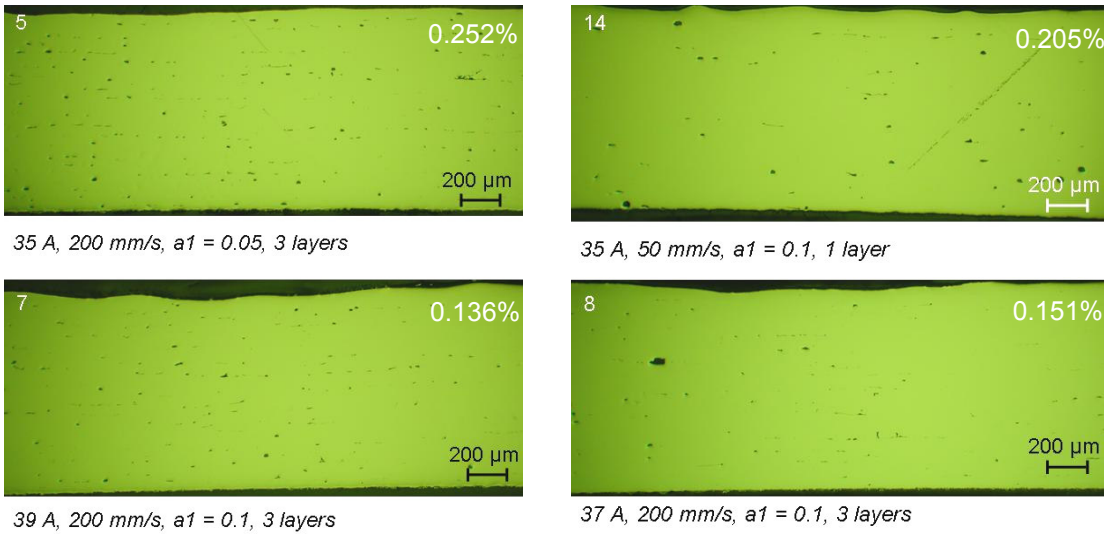

Figure 4.4: Optical microscopy images of the laser re-melted parts with different parameters (porosity>0.13)

The effects of process parameters (scan speed, scan spacing, number of re-melting scans and laser power) on the density improvement are separately illustrated in Figure 4.5. High porosity is mainly related to too high energy inputs into the substrate. When the scan speed is increased, the remaining porosity decreases in the range of 50-200 mm/s (Figure 4.5a). Very low scan spacing factor (5%) results in higher porosity whereas there is no significant change between 10% and 20% (Figure 4.5b). The number of re-melting scans is more dependent on other parameters. It becomes important when the selected laser power is high or there is high overlap (Figure 4.5c). The effect of laser power is less significant compared to other three process parameters in the range of 85-105 W (Figure 4.5d).

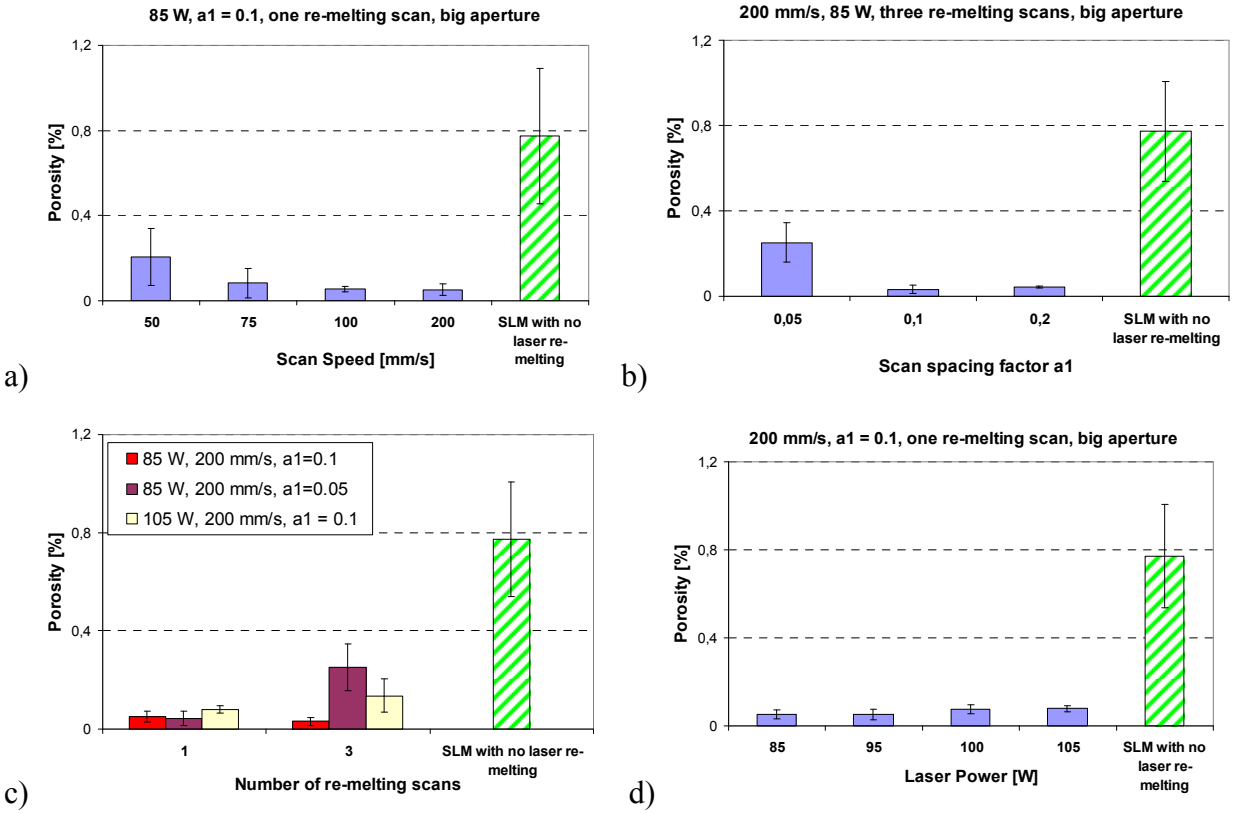

Figure 4.5: Effect of each process parameter on the remaining porosity (a) scan speed (b) scan spacing (c) number of re-melting scans (d) laser power

The improvement of the density by applying laser re-melting after each layer does not only hold true for AISI 316L stainless steel. Ti6Al4V [129] and maraging steel 300 are also tested and the results show that laser re-melting significantly helps to densify SLM parts (refer to §5.1.3e). It can be concluded that the improvement of the density by applying laser re-melting holds for a wide range of materials used in SLM.

4.3.2 Surface Quality Improvement

Being one of the most important limitations of the SLM process, the insufficient surface quality can be enhanced by employing a variety of surface modification technologies that are available in the market, including mechanical (e.g. machining and abrasive sandblasting), chemical (e.g. acid etching and oxidation) and thermal processes (e.g. plasma spray) [130]. Laser re-melting may be an easy solution for the improvement of the surface quality of the top surfaces of SLM parts without removing the part from the building platform which avoids any fixation errors. In order to investigate the potential to decrease the surface roughness values of SLM parts, the laser surface re-melting (LSR) process is applied only after the part is completely made by SLM and the last slice

info is used for laser re-melting. For the roughness measurements, a Talysurf roughness meter (120 L) is used and three-dimensional roughness measurements are taken without any filter.

All laser re-melted surfaces exhibited a better surface quality compared to SLM parts without laser re-melting. The details of surface quality improvement are reported in §3.2.1b and in [131, 132] which can be also found in the Appendix 4. Briefly, the work involved surface quality enhancement of SLM parts in a step by step approach. The top surfaces of SLM parts were first exposed to SLE and then laser re-melted with various combinations of scan speed (50-800 mm/s), laser power (60-105 W) and scan spacing factors (10-70% of the spot size). The last slice is exposed to laser re-melting after SLE for 10 scans with a grid scanning strategy. Each LSR scanning was rotated 90 degrees with respect to the previous one in order to improve the surface quality.

The results showed that a low scan spacing factor (10% or 40%) together with a medium scan speed (200-400 mm/s) and a medium to high laser power (85–95 W) results in better surface quality compared to other parameter sets. The necessity of the erosion step was also investigated and it is found that without any SLE, laser re-melting is individually sufficient to achieve the same surface quality enhancement [132]: see Figure 26 in the Appendix 4.

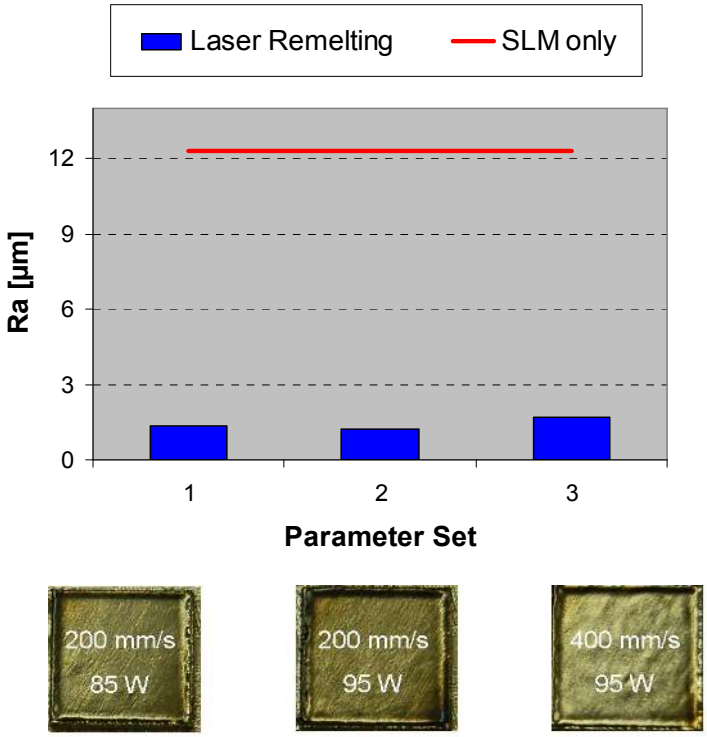

Figure 4.6: Roughness values with laser re-melting and only SLM parts

The best achieved results for three sets of laser re-melting parameters are depicted in Figure 4.6 (without any erosion step in this case). Applying laser re-melting improves the surface quality significantly for all three sets of parameters. The scan speed and laser power values used during the tests are mentioned in the figure. The average roughness of a SLM part without laser re-melting measured on the top surfaces is shown with a horizontal line which is at about 12 µm with a standard deviation of 2 µm. After LSR, R_a value decreases from 12 µm to 1.5 µm. The cross-sections of a SLM part with no laser re-melting and a part with LSR (parameter set 2) are compared in Figure 4.7: the enhancement of the top surface by LSR is evident.

a)

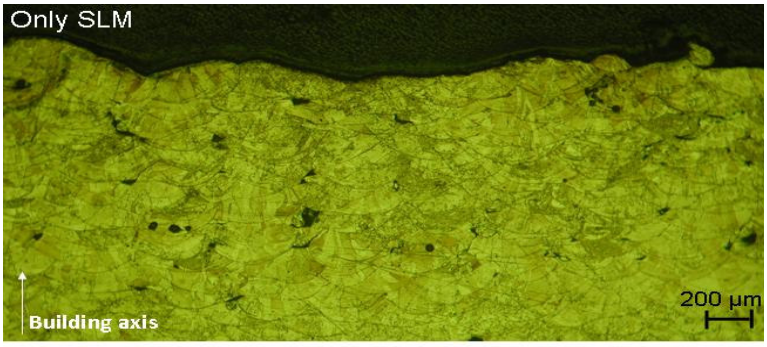

b)

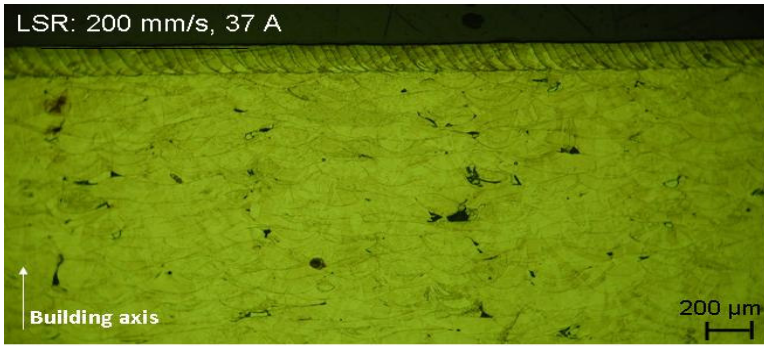

Figure 4.7: Surface quality enhancement with laser re-melting a) SLM-only part b) Laser re-melted part with 200 mm/s and 95 W exhibiting a very smooth surface

Positioning the scan lines far from each other (a_l = 0.7) or selecting very low power values (60 W) deteriorates the surface quality possibly due to the low energy input to the material which is not sufficient to melt all the peaks and fill in the valleys. On the other hand, the recoil pressure generated due to high energy densities pushes the melt towards the substrate and this smoothes the surface resulting in a better surface quality [7].

To sum up, the smoothness of SLM parts could be greatly improved by re-melting the outer surface. The best results were obtained with relatively high energy settings (high laser power, small scan spacing, medium scan speed, possibly several re-melting scans). This adds to the production time, yet to a limited extend since only the outer layer has to be re-melted in this case.

4.3.3 Microstructural Analysis

Before presenting the microstructures of laser re-melted parts, the microstructures of SLM parts with no re-melting are first presented to allow comparison.

a. SLM parts with no laser re-melting

The top view and a cross-section of a SLM part with no re-melting taken with an optical microscope (OM) are shown in Figure 4.8. The scan tracks are clearly visible and the direction of the laser scanning is shown with the arrows in Figure 4.8a. From the figure, the width of the melted track is measured to be approximately 140 µm.

In Figure 4.8b, the cross-sections of the melted scan tracks are visible showing that the stainless steel powder particles are completely fused together within melted and solidified zones having curved edges. The laser tracks overlap so that each melted track is a bonded onto the other tracks surrounding it. Figure 4.8b also indicates that during SLM a fully melt pool with a depth higher than the layer thickness (~100 µm versus layer thickness of 30 µm) is formed.

Figure 4.9 depicts the scanning electron microscope (SEM) images of the cross-section of a SLM part with no re-melting. A fine cellular/dendritic structure is visible. This microstructure is formed

as a result of rapid solidification due to very high cooling rates encountered in SLM like casting [6]. It is a common microstructure obtained by laser processing techniques.

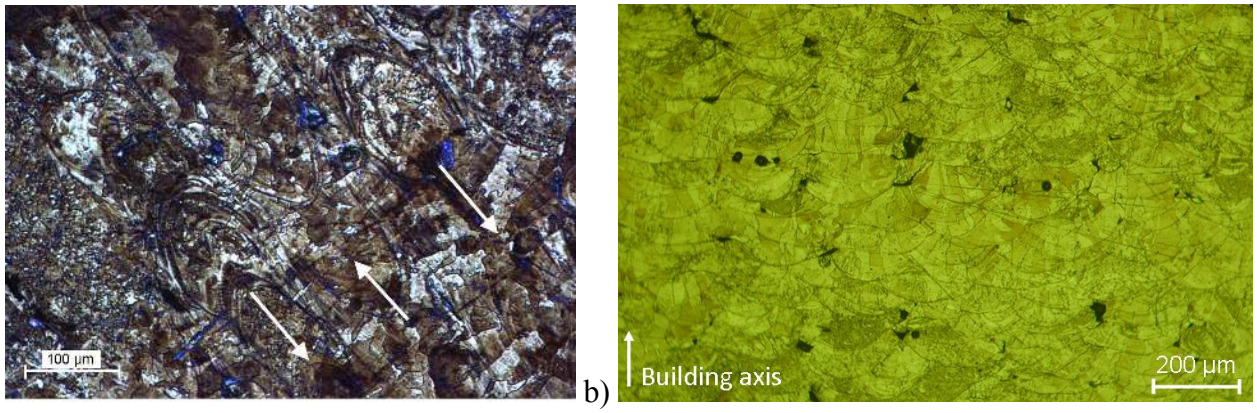

Figure 4.8: OM images of a SLM part without laser re-melting (polished and etched) a) top surface b)cross-sectional view

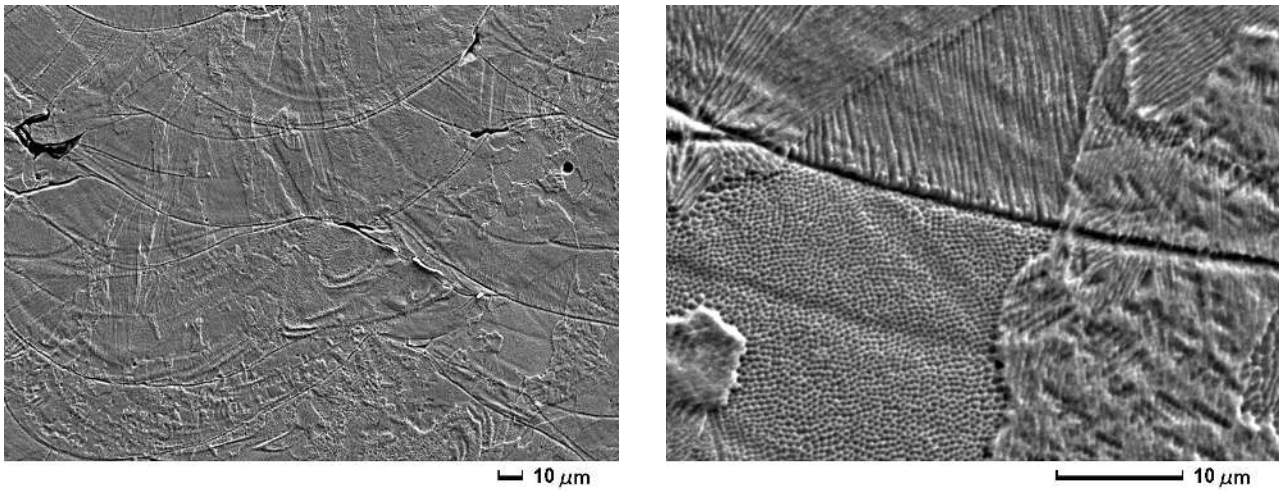

Figure 4.9: SEM images of a cross-section of a SLM part without laser re-melting

b. Laser re-melting after each layer

Figure 4.10 depicts one of the samples treated with laser re-melting after each layer with following parameters: a scan speed of 200 mm/s, a pump current of 38 A (100 W), a spot size of 180 µm, a scan spacing of 20 µm (a_1 of about 10%) and three re-melting scans for each layer. The contour and its connection with the core of the part are clearly distinguishable. In the contour zone, the cross-sections of the melted scan tracks are visible having curved edges. The layered or lamellar structure inside the part shows a smaller thickness than a SLM layer and that re-melting erases the scan tracks contours visible after SLM (see Figure 4.8b) and causes more uniform and smooth layers to appear. The thickness of visible layers in the optical microscopy picture of this part was found to be around 20 µm whereas in SLM one layer thickness was chosen to be 30 µm. This distance between horizontal lines depends on the process parameters of laser re-melting. For comparison, the optical micrographs of laser re-melted parts with various process parameters are presented in Figure 4.11 together with a SLM part with no laser re-melting. The figure reveals that a higher number of scans in laser re-melting leads to a significantly finer lamellar structure. The fact that the interlayer lines are not straight in Figure 4.10 and rise to the edge of the part is due to the "edge effect" that will be discussed in §4.3.6.

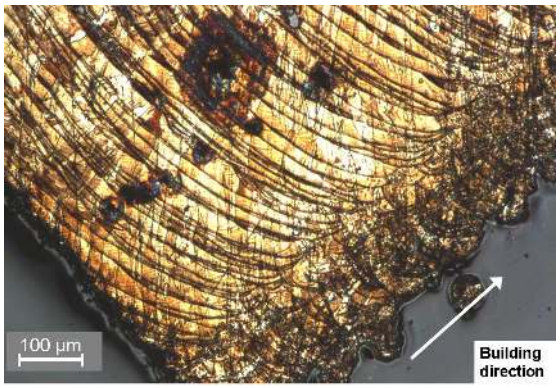

Figure 4.10: Cross-section of a part with laser re-melting after each layer showing the contour scanning

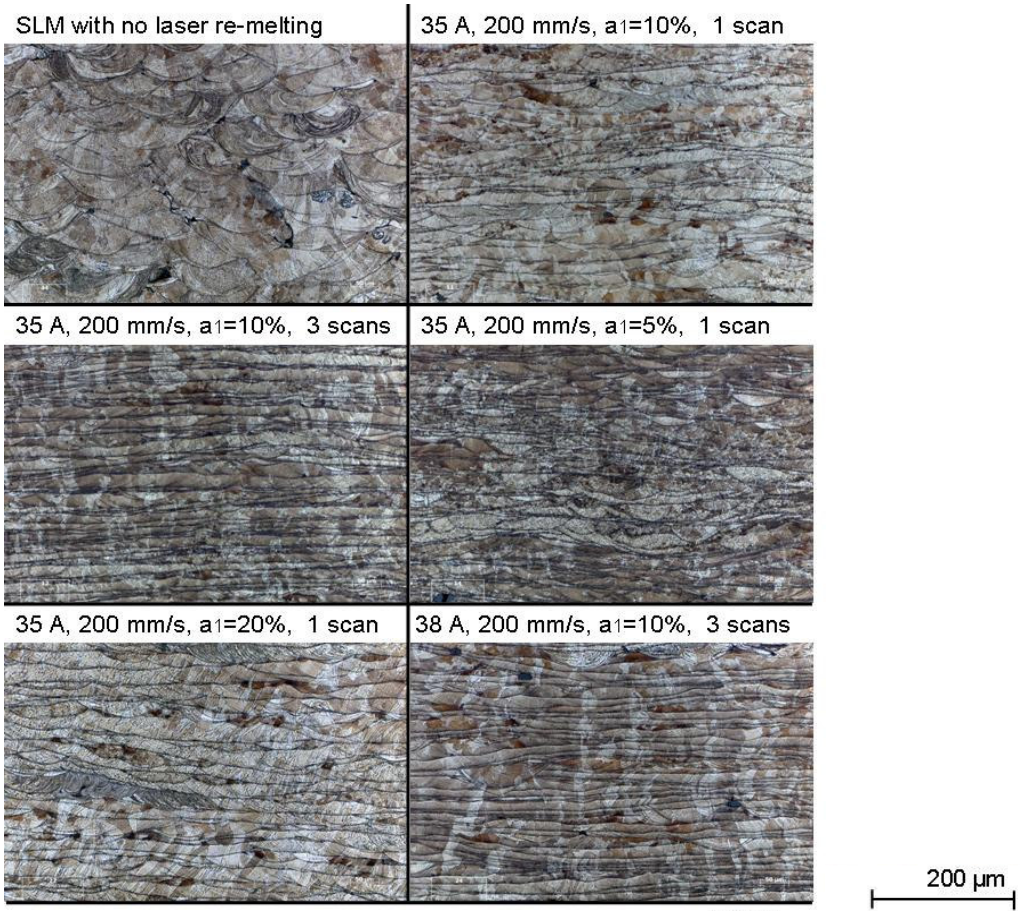

Figure 4.11: Cross-sectional views of parts with different laser re-melting parameters applied after each layer together with a SLM part with no re-melting

When laser re-melting is applied, the layers are apparently seen with borders of dark lines whereas the layers are not distinguishable in SLM parts with no laser re-melting whereby only the borders of the melted scan tracks are visible (See Figure 4.8b). The layers in laser re-melting are actually visible as horizontal dark lines due to very low scan spacing (5-10%). The cross-section of multiple scan tracks that overlap significantly appear as a line instead of curved melt lines which is also shown in Figure 4.7b. In Figure 4.11, the cross-sectional view of the part which was re-melted with a scan spacing factor of 20% depicts less visible horizontal bands compared to the parts with a scan spacing factor of 5 or 10%. Due to the reason that laser re-melting efficiently improves the density of SLM parts by removing pores formed between neighboring melt pools in the borders (see arrows in Figure 4.12), lamellar structures are desired for improved density leading to better

mechanical properties and avoiding unexpected failures of SLM parts. SEM images of two parts exposed to laser re-melting with different parameters given in Figure 4.13 clearly show the lamellar structure where no irregular pore is present. Figure 4.14 depicts the very fine microstructure encountered with laser re-melting (38 A, 200 mm/s, a_1 of 10%, big aperture and 3 scans). Both microstructures reveal a size of less than 500 nm.

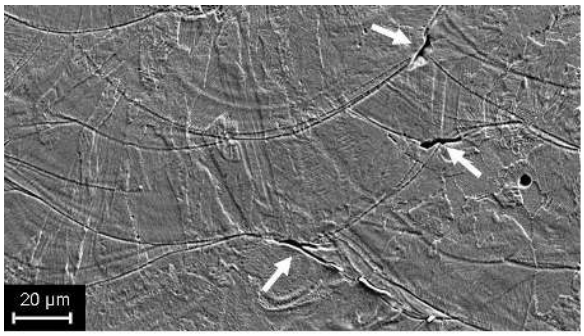

Figure 4.12: SEM image of a SLM part without laser re-melting having pores between the melt pools

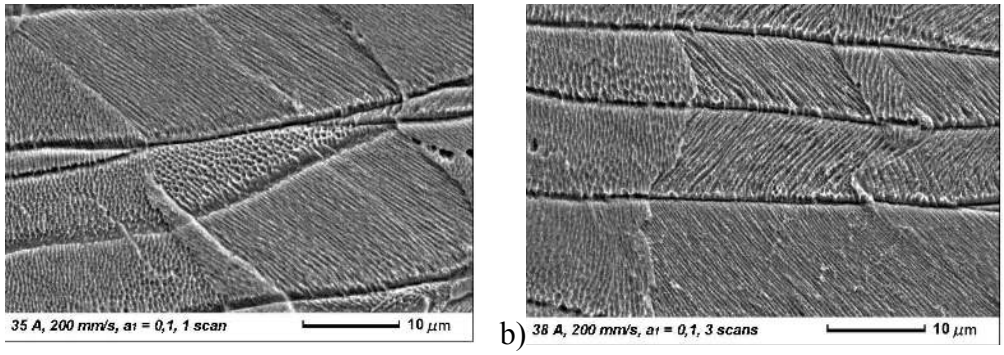

Figure 4.13: SEM images of two SLM part with laser re-melting at different parameters showing almost full density a) 35 A, 200 mm/s, a_1=0.1 and 1 scan b) 38 A, 200 mm/s, a_1=0.1 and 3 scans

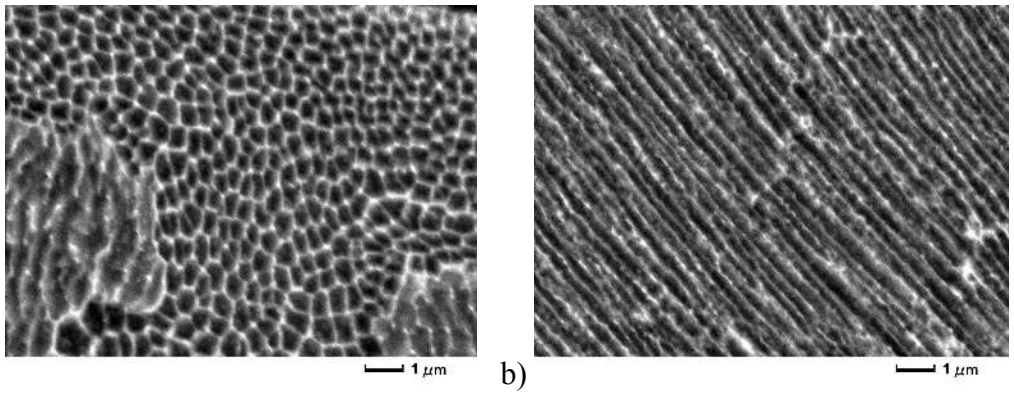

Figure 4.14: SEM pictures of a part with laser re-melting a) cellular structure b) dendritic structure

c. Laser surface re-melting on top surfaces

Some examples of LSR parts are shown in Figure 4.15 and Figure 4.16. When the last layer is subjected to laser re-melting, a re-melted zone is formed. The thickness of this zone highly depends on the selected parameters, especially the scan speed and the laser power. The scan spacing factor changes the overlap between successive tracks but the depth stays almost constant, as evident from Figure 4.16. However, as the scan speed is decreased and laser power is increased, the re-melted depth becomes significantly higher. Another important observation from the microstructures of LSR parts is the densification of the re-melted zone where a full density is achieved and no pore is encountered.

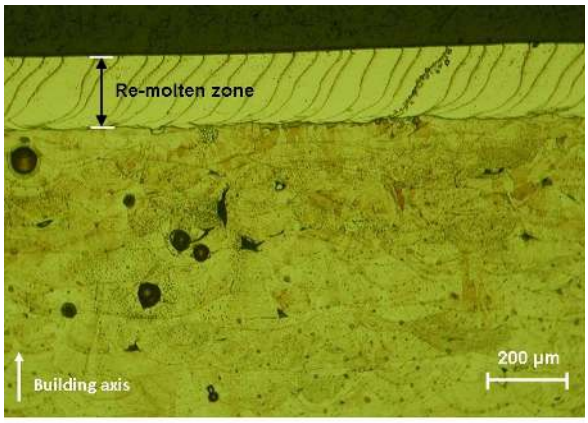

50 mm/s, 35A (85 W), a1 =0.1, 10 re-melting scans

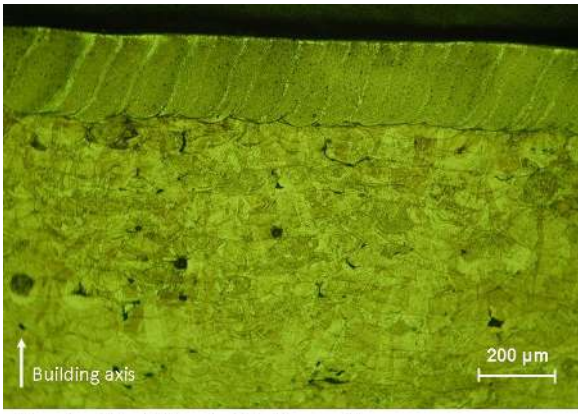

10 mm/s, 37A (95 W), a1 =0.3, 10 re-melting scans

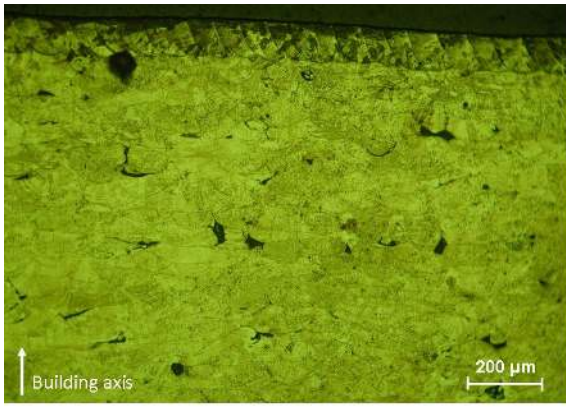

100 mm/s, 37A (95 W), a1 =0.3, 10 re-melting scans

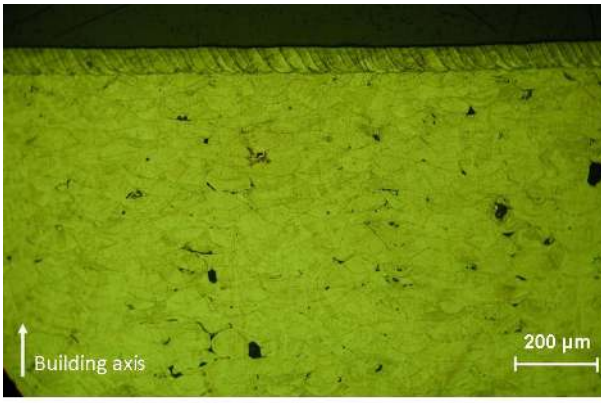

200 mm/s, 37A (95 W), a1 =0.1, 10 re-melting scans

Figure 4.15: Cross-section of LSR parts with different parameter sets

200 mm/s, 35A (85 W), a1 =0.3, 10 re-melting scans

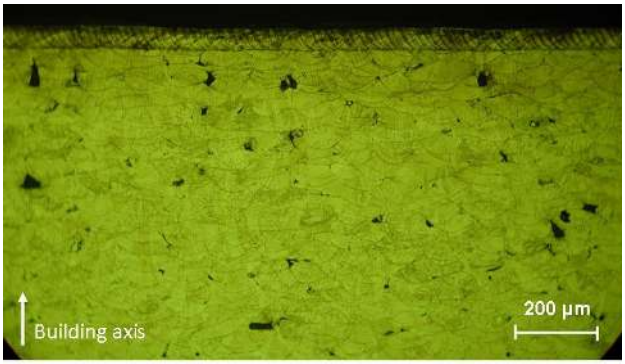

200 mm/s, 35A (85 W), a1 =0.05, 10 re-melting scans

200 mm/s, 35A (85 W), a1 =0.5, 10 re-melting scans

Figure 4.16: Effect of the scan spacing factor on the re-melted depth

The cellular/dendritic structure is more apparent in the laser re-melted zone than the SLM parts without laser re-melting. Besides, the cell size is finer in LSR microstructures. It is equiaxed and

homogenously visible throughout the re-melted zone. The SEM images of a sample part are shown in Figure 4.17. The overlapping laser tracks in the re-melted zone are clearly visualized.

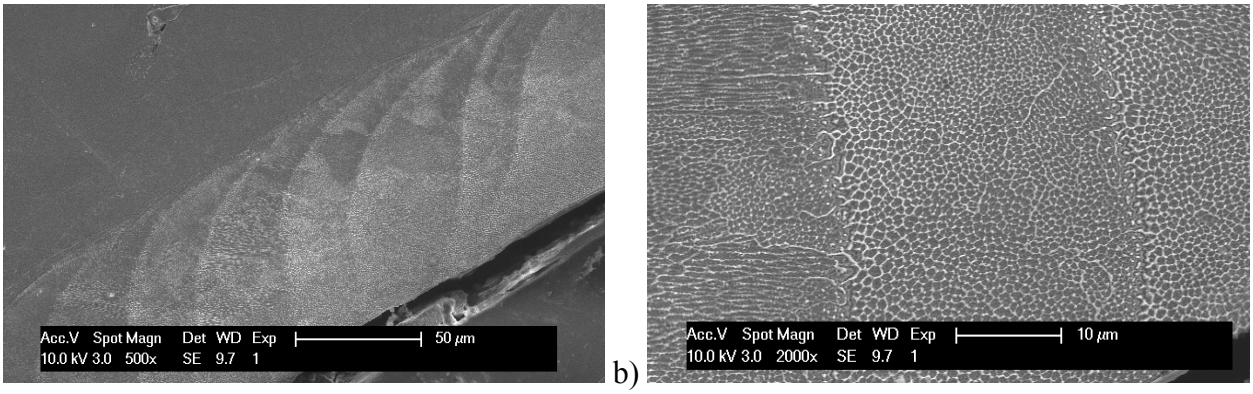

a) b)

Figure 4.17: SEM pictures of the LSR part with 200 mm/s, 39 A (105 W), a_1 = 0.1 and 10 scans a) low magnification b) high magnification

4.3.4 Laser Surface Re-Melting On Inclined Surfaces

To demonstrate the possibility of applying laser re-melting on inclined surfaces, a set of parts, as shown in Figure 4.18, are produced with standard SLM parameters (§4.2). While they are anchored to the building platform of the machine together with the base plate, the powder particles that surround the parts are completely blown away with pressurized air so that the inclined surfaces become directly reachable by the laser beam. Since there is no dedicated machine software to perform laser re-melting on inclined surfaces, all machine operations, e.g. decrease/increase the building platform, apply laser radiation for every layer, etc., are done manually in the standard CL machine software. The procedure to carry out the laser re-melting on inclined surfaces is shown in Figure 4.19 and Figure 4.20. The inclined surface is divided into small bands at different heights. After all bands located at a given height are scanned on one inclined surface with LSR parameters for multiple times, the height of the building platform is adjusted (the base plate is lifted up when starting from the top of the part) to keep the laser beam in focus. Then the next band is scanned. This continues until whole the surface is scanned. The band width and the height change (ΔH) of the building platform are depicted in Figure 4.19 from the side view. Various band widths with and without overlapping were tested and the results are shown in Figure 4.21 for slopes of 10 and 30 degrees. The roughness values were obtained via three-dimensional measurements without any filters.

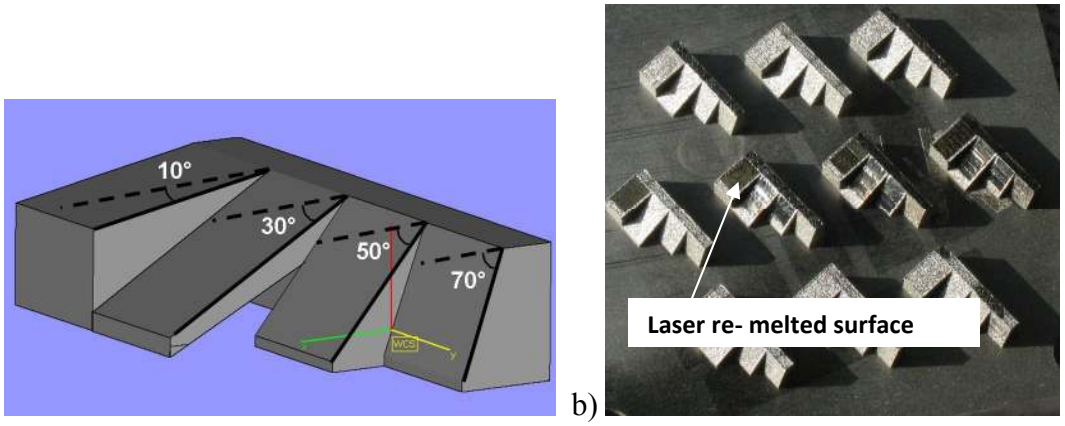

b)

Figure 4.18: a) The geometry shown in Magics software with the angles of the inclined surfaces and b) the parts with inclined surfaces produced by SLM, some of them are exposed to laser re-melting on the inclined surfaces

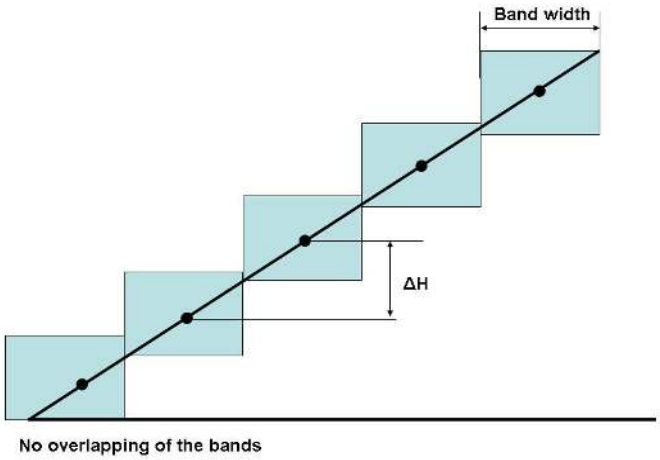

Figure 4.19: Schematic illustration of how the bands are located on an inclined surface (side view) depicting the band width and change of the building platform height

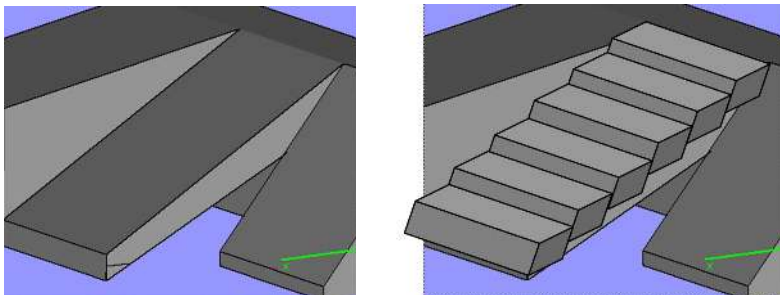

Figure 4.20: Schematic illustration of how the bands are located on an inclined surface

As depicted in Figure 4.21, the laser re-melted surfaces show better surface quality compared to SLM parts without laser re-melting. The laser re-melting process parameters were constant (200 mm/s, 95 W-37 A, a scan spacing of 60 µm, grid scan strategy, 10 re-melting scans, only hatching, no contours) for all parts. The band width was taken as 1, 2 and 2.5 mm in part 1, 2 and 3 respectively. The obtained S_a (i.e. 3D R_a) roughness values are very close to each other in these parts for 10 and 30 degrees (See Figure 4.21). Since there was no overlapping in these samples, the transition from one band to another is visible in the three-dimensional measurements as shown in Figure 4.22 and these sharp transitions deteriorate the surface quality. Within one band the surface roughness is, as expected, still much better, i.e. R_a measured perpendicular to the bands on the inclined surface of 10 degrees in part 2 is 8.19 µm, whereas it reduces to 5.18 µm when measured within one band (i.e. parallel to the bands). This also holds true for the roughness R_t values. In order to overcome this problem, overlapping (~50%) of the bands is employed in part 4 where the band width is kept as 2 mm. This resulted in even lower roughness values. The height maps of the same inclined surface (10 degrees) from four parts (three without overlap and the 4^{th} one with overlap) are depicted in Figure 4.23. As a result of these tests, it is concluded that a larger band is better for small slope surfaces to avoid many transitions. Even with larger bands, it is useful to employ overlapping to overcome severe transition regions with deep valleys in between the bands. If the inclination is significant, as was the case with the last surface in the parts that has an angle of 70 degrees, the height should be adjusted more often to keep the laser beam in focus. Therefore, smaller band widths are necessary with steeply inclined surfaces. The smallest band width tested in this experimental work was 0.5 mm but that was even not small enough for the surfaces having an angle of 70 degrees. However, all the other three inclined surfaces having angles of 10, 30 and 50 degrees were significantly improved in terms of surface quality. The enhancement was about 70%. This work proves that LSR can also be applied to inclined and curved surfaces. With this method, the problem of stair effect, which is explained in detail in the next sub-section, is also completely

eliminated. However, for the ease of operations, dedicated software development is necessary to apply laser re-melting on any curved or inclined surface.

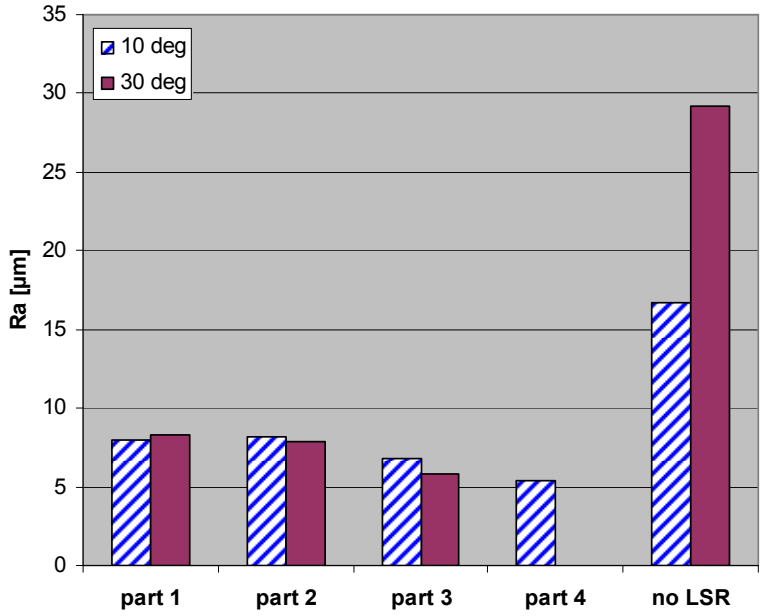

	Band Width [mm]	Overlapping	
part 1	1	none	Not suitable for 70 deg
part 2	2	none	Not suitable for 70 deg
part 3	2,5	none	Not suitable for 70 deg
part 4	2	yes	Not suitable for 70 deg

Figure 4.21: Experimental results of 3D R_a roughness measurements on inclined surfaces with slope angles of 10 and 30 degrees

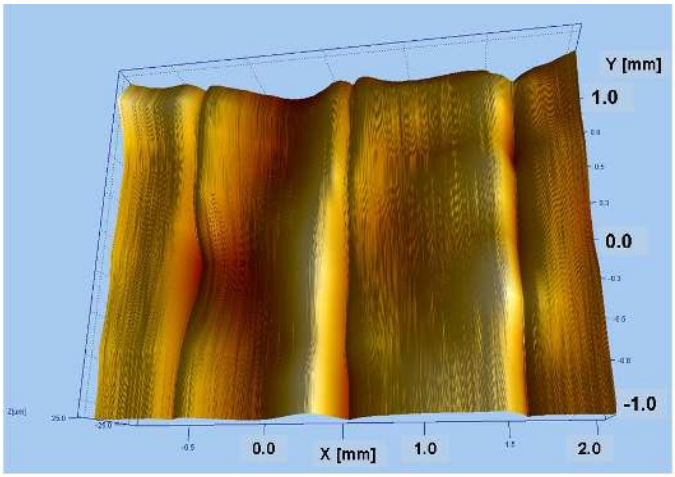

Figure 4.22: 3D view of the inclined surface from part 4 with 30 degrees inclination

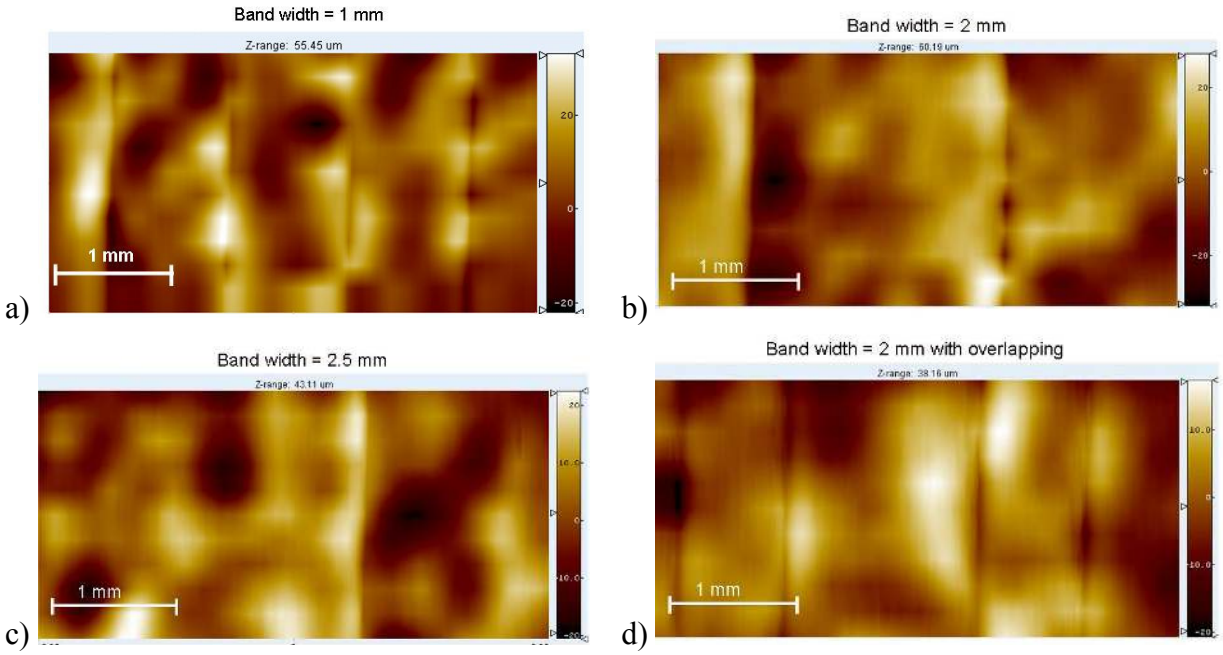

Figure 4.23: Height maps of the inclined surfaces with slope angles of 10 degrees for different parts a) part 1 b) part 2 c) part 3 and d) part 4

4.3.5 Laser Re-Melting Only on Contours to Overcome Stair Effect

As mentioned in the previous section, laser re-melting on inclined surfaces after the process is completed and all surrounding powder is blown away can be employed to reduce the stair effect. Another solution may be applying laser re-melting of the contours in each layer. Thus, each contour is scanned twice during SLM to test if this would help to minimize the stair effect.

The stair effect, which is also regarded as stair-step effect, is a limitation for all layer manufacturing techniques for the production of parts with inclined or curved surfaces: see Figure 4.24. The stair effect depends on the inclination angle as well as the layer thickness. As the inclination angle is reduced or the layer thickness is increased, the stair effect becomes more pronounced (See Figure 4.25 where s is the stair size, ℓ is the layer thickness and α is the inclination angle). The effect of the inclination angle on the stair effect is illustrated quantitatively in Figure 4.26 that shows roughness measured on various inclined surfaces built with a layer thickness of 30 µm. As depicted, low inclination angles result in a more severe stair effect. When the inclination angle reaches a certain value (~50 degrees), the roughness converges to the roughness measured on side walls.

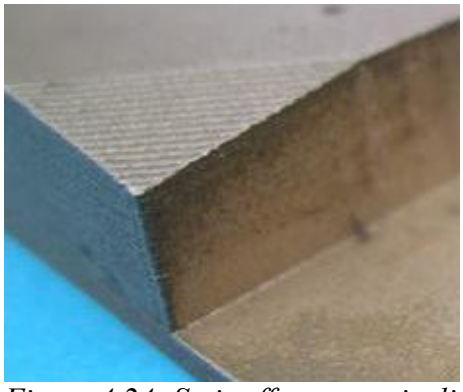

Figure 4.24: Stair effect on an inclined surface

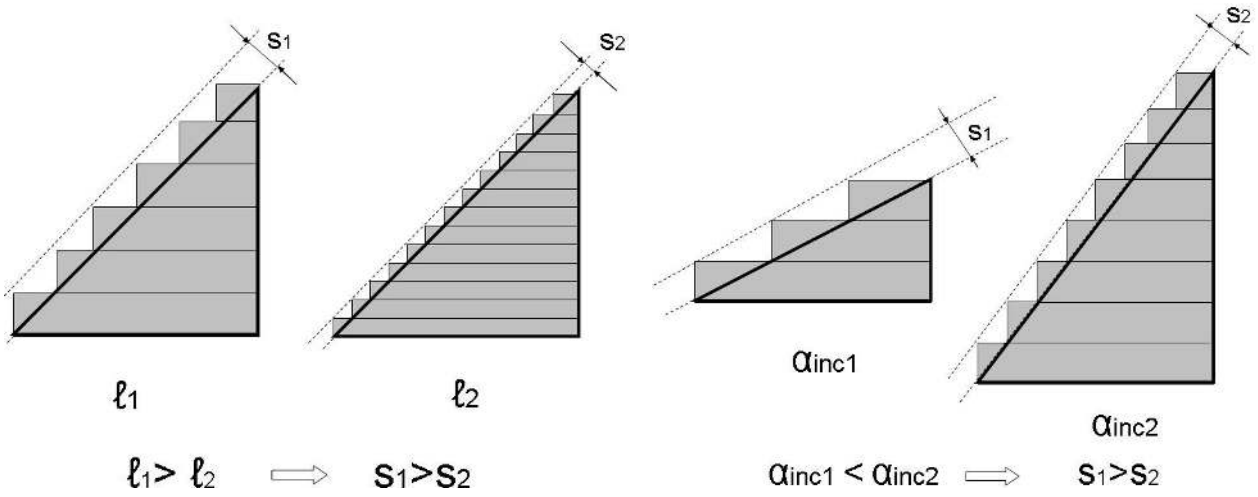

Figure 4.25: Illustration of the stair effect as a function of layer thickness and slope (inclination) angle

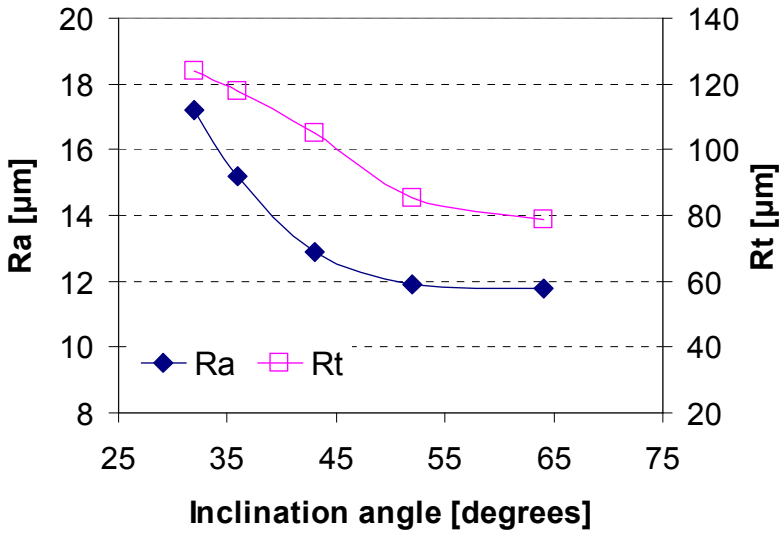

Figure 4.26: Effect of inclination angle on stair effect (layer thickness of 30 µm)

In order to overcome or to weaken the stair effect, laser re-melting is applied only on the individual layer contours of SLM parts having an inclined surface with an inclination angle of 20 degrees (See Figure 4.27a). During the production of the specimens, SLM parameters were kept the same as with island scanning whereas different laser re-melting parameters were applied on the contours before deposition of a new layer of powder. Every layer then results from Selective Laser Melting of a new powder layer with prior contour scanning followed by contour re-melting with different parameters. The scan speed was varied between 50 and 450 mm/s whereas the laser power was set to 105 W, 100 W and 85 W. The scanning of each layer is illustrated in Figure 4.27b. Every layer is first exposed to contour scanning followed by filling the inside of the contours by island scanning. Then before a new layer of powder material is deposited, the contours are scanned again.

The average roughness R_a measured on the inclined surface is taken as an indicator of the stair effect while no filter is used during the measurement analysis. The roughness values are obtained with three-dimensional measurements (i.e. S_a instead of R_a). The results are depicted in Figure 4.28 for R_a (S_a) and R_t (S_t) roughness values. The horizontal line shows the results obtained with only SLM without second scanning and re-melting of the contours. The results with low scan speeds (at any selected power) exhibit lower R_a and R_t roughness values. However, the improvement of about 10-15% is not that significant. The roughness values obtained with medium or high scan speeds

results in almost the same surface quality as parts produced by SLM. Therefore, it can be concluded that applying laser re-melting only on the contours during the SLM process does not help to solve the stair effect. The cross-sections of the parts are also observed to see if laser re-melting improves the connection between the contours and inside of the part by eliminating the pores. The cross-sectional views from two parts are illustrated in Figure 4.29; one from a SLM part with no laser re-melting (upper) and one from a laser re-melted part with 85 W and 150 mm/s showing the highest improvement in terms of average roughness. However, as evident from the cross-sections, not much improvement is obtained with laser re-melting on the contours in terms of decreasing porosity or increasing the interconnectivity of the contours with inside of the part.

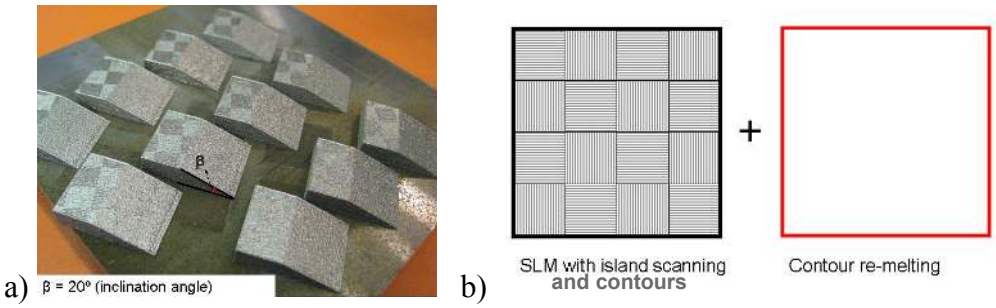

Figure 4.27: a) Specimens produced to investigate the effect of contour re-melting on stair effect b) Production procedure (SLM with contour and island scanning followed by contour re-melting)

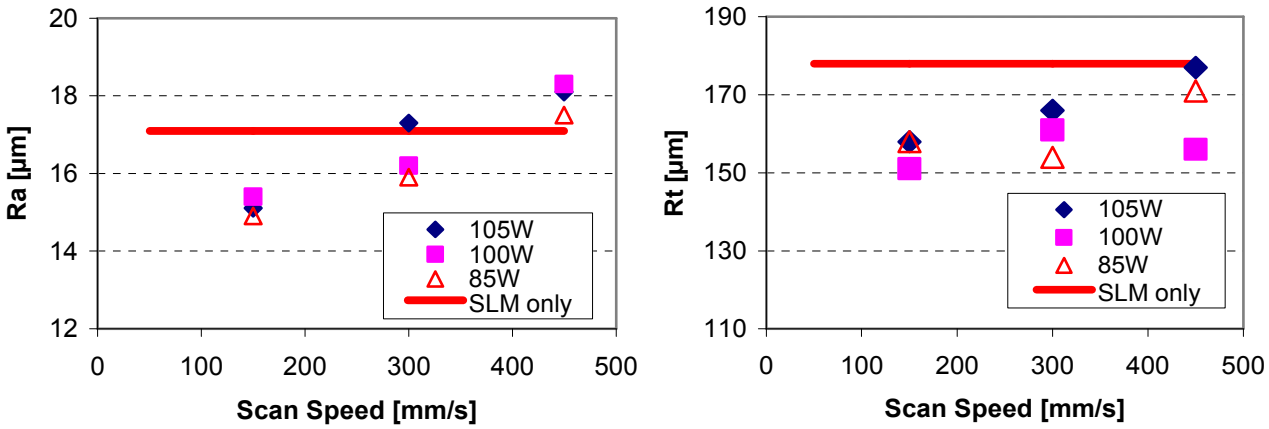

Figure 4.28: The effect of laser re-melting on the contours with different parameters on the average roughness measured on the inclined surface

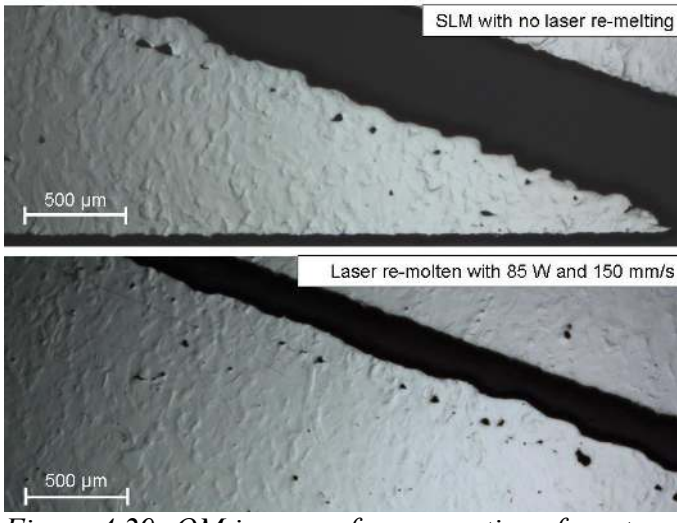

Figure 4.29: OM images of cross-sections from two parts; SLM part with no re-melting (upper) and laser re-melted part with 85W and 150 mm/s (lower)

4.3.6 Edge Effect

Laser re-melting may be a perfect remedy for some problems of SLM like surface quality and porosity. On the other hand, it intensifies a SLM problem: edge effect. The elevated edges of the solidified material formed along the sides of the SLM parts are one of the problems encountered in SLM. The severeness of the problem depends on the process parameters and employed scan strategies. It may be a serious problem since it deteriorates the surface topology and dimensional accuracy (See edges of part in Figure 4.30). The existence of the elevated edges, on the other hand, may also worsen the stair effect that is inherent to all layer manufacturing techniques. One of the important disadvantages of having elevated edges on the contours of the parts is the likely collision of these edges with the powder coater blades. Since the height of the produced edges is generally higher than one layer thickness, the coater blades may hit the edges causing vibrations during powder deposition. This results in a waviness on the surface of deposited powder layers, thereby causing aligned porosity in the produced SLM parts, which in turn, may yield anisotropy in mechanical properties.

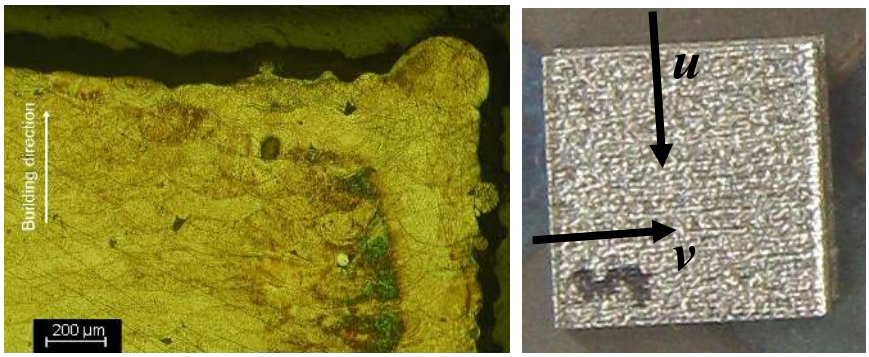

Figure 4.30: Edge effect seen on a frontal cross-section (left) of a SLM part (right)

The problem of elevated edges is not only encountered in Selective Laser Melting [133, 134], but also in laser engineered net shaping (LENS™) [135, 136] and electron beam melting [137]. In fact, the generation of circular cross-section tracks is a well known observation in metal melting technologies at some processing conditions. This phenomenon can be understood as the consequence of surface tension effect so that the melt track will assume a form such that its surface area will be a minimum and its volume a maximum i.e. cylindrical in shape with a rounded cross section. The latter incident may speed up through the absence of good wetting between the melted track and the underlying surface [138-140].

During the SLM process, the first scan line of the layer that is being scanned (part's border) is surrounded at both sides with powder particles with very low thermal conductivity. Due to the change of shape of the melt pool in most cases, more powder particles are dragged to the melt volume thereby increasing the size of melt pool as well as affecting the solidification rate of the melt. In addition, insufficient amount of powder remains for the subsequent scans. The first track then acts as a heat sink when the second one is scanned, resulting in a significantly smaller track [141, 142].

Within the melt pool, on the other hand, surface tension gradients coupled with temperature gradients in the surface, result in a rapid flow of melt known as thermo-capillary or Marangoni flow [138, 143]: see §2.1.1. This flow might be large enough to push the melt back while the laser scans the powder bed.

Test specimens were produced from two commercially available powder alloys of stainless steel and titanium. A Concept Laser M3 Linear machine was used to produce the parts from AISI 316L stainless steel. The titanium alloy Ti6Al4V was processed using the LM machine, developed at K.U.Leuven.

In order to study the influence of the effective parameters on the edge effect, series of cubic parts with various process parameters and scanning strategies were produced on both machines. The ultimate aim was to find a solution to produce parts having no significant edges, and without a density reduction either in the outer shell or in the core of the produced parts. Generally, the solution of decreasing the laser power or increasing the scan speed when approaching the edges results in a better surface flatness. However, this has a potential to weaken the connection between the contours and the part's core.

While the Concept Laser M3 Linear equipment allows applying a few dedicated scanning strategies such as island scanning, it is easier to program any desired scanning strategy with a complete freedom in the LM machine. This study only reports the most promising tested scan strategies. The studied factors can be summarized as changing the contour or overall SLM processing parameters, applying multiple or no contours, island scanning, various filling strategies with uni- and bi-directional scanning, applying different profiles for the power in one scan vector and making one part as a combination of two parts such as core and shell made with different parameters.

A contact surface profilometer, Talysurf 120L from Taylor Hobson Ltd., was used to measure the edge height of the top surface. These measurements were carried out by scanning an area of 8 mm x 1 mm along parallel lines taken each 50 µm in y direction. Based on the individual surface profiles taken at an interval of 50 µm, an average profile of the top surface was then determined. The parts' cross-sectional topography was also observed using an optical microscope. The edges formed along the sides of the parts were measured in two directions as shown in Figure 4.30 with *u* and *v* direction which are perpendicular and parallel to scanning directions, respectively.

Following the experimental method described in the previous paragraph and from the average profile of the top surface, the edge height (h_e) is determined as the distance between the first peak located on the edge of the part (h_{p1}) and the mean value of the flat surface (l_0): see Eq. 4.1. An example is shown in Figure 4.31 where h_e denotes the edge height.

$$h_e = h_{p1} - l_0 \tag{4.1}$$

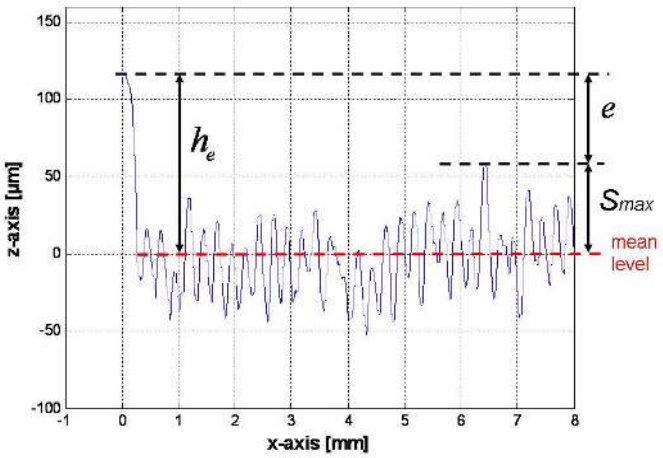

Figure 4.31: The edge height shown on an average cross-section

In Eq. 4.1, the edge height is independent of the SLM part's surface quality. However, the surface peaks of the SLM part are important to evaluate the edge height. A surface which exhibits high peaks close to the edge height may be less critical compared to a surface with a very smooth surface in terms of elevated edges. Therefore, edge elevation, e, and relative edge elevation, e_R, are defined to express the edge height as follows:

$$e = h_e - S_{\max} \tag{4.2}$$

$$e_R = \frac{e}{S_{\max}} \times 100 \tag{4.3}$$

where $S_{\max}$ is the maximum peak height on the average profile of the measured surface (see Figure 4.31). The remainder of this section presents results and discussion concerning the work on edge height in the conducted SLM experiments.

a. SLM process parameters effect

The first set of tests aims to investigate the influence of SLM process parameters such as the scan speed and laser power on the edge effect. These experiments were conducted using AISI 316L stainless steel powder for which the nominal scan speed and laser power are given as 360 mm/s and around 100 W respectively. During these tests, the scan speed was varied between 120 to 360 mm/s while the laser power was changed from 72 to 105 W. The contour of the parts was also scanned before the core, at the same processing parameters used for fill vectors. One set of the measured profiles for the scan speed of 120 mm/s, at the four laser powers of 72, 83, 93 and 105 W is illustrated in Figure 4.32. The recorded profiles in all cases are qualitatively similar so that each part reveals an elevated edge regardless of the used parameters even though the edge height is significantly affected by the laser power.

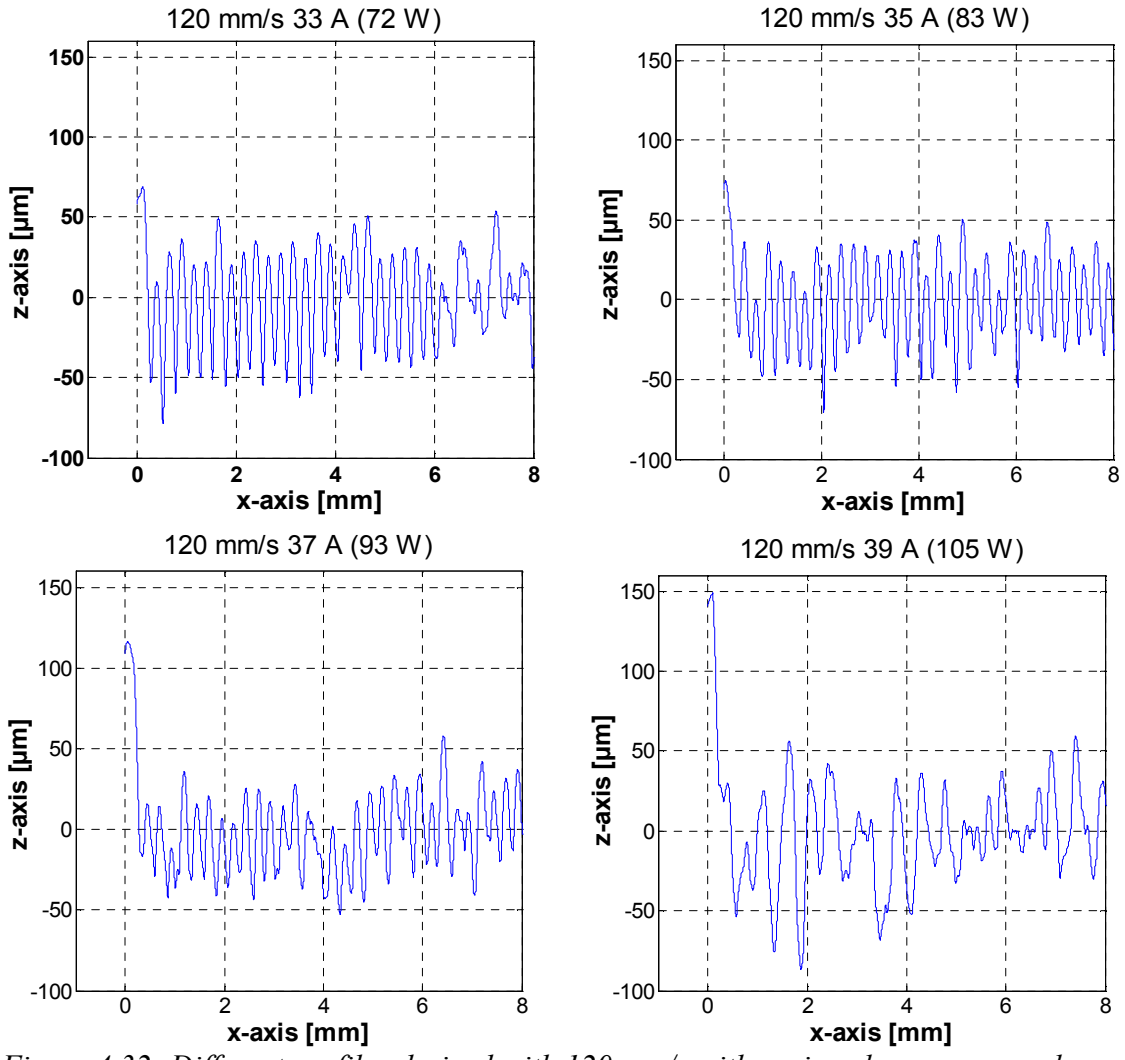

Figure 4.32: Different profiles derived with 120 mm/s with various laser power values

Figure 4.33 shows the measured edge heights of the parts as a function of laser power at four scan speeds from 120 to 360 mm/s. Figure 4.33a reveals that the edges become more pronounced especially at low scan speeds (120 mm/s) when the laser power is increased. At higher scan speeds, the effect of the laser power becomes less significant. The higher energy input entered to the powder bed, the higher the edges become. Figure 4.33b depicts the relative edge height taking the maximum peak height on the SLM surface into account and shows that the relative edge elevation (e_R) increases with the laser power for all scan speeds. With nominal SLM parameters, the relative edge elevation is about 185%. As Figure 4.33 suggests, decreasing the laser power to 72 W improves the edge effect. However, the density achievable with this laser power will not be acceptable. To keep the density at its maximum, the scan speed may be lowered (e.g. 120 mm/s) resulting in e_R about 125%. However, this solution will significantly deteriorate the productivity of the process. Other tested laser power values exhibit similar or higher relative edge elevations to the nominal edge elevation. Therefore, changing the SLM parameters does not solve the edge effect problem in an efficient way.

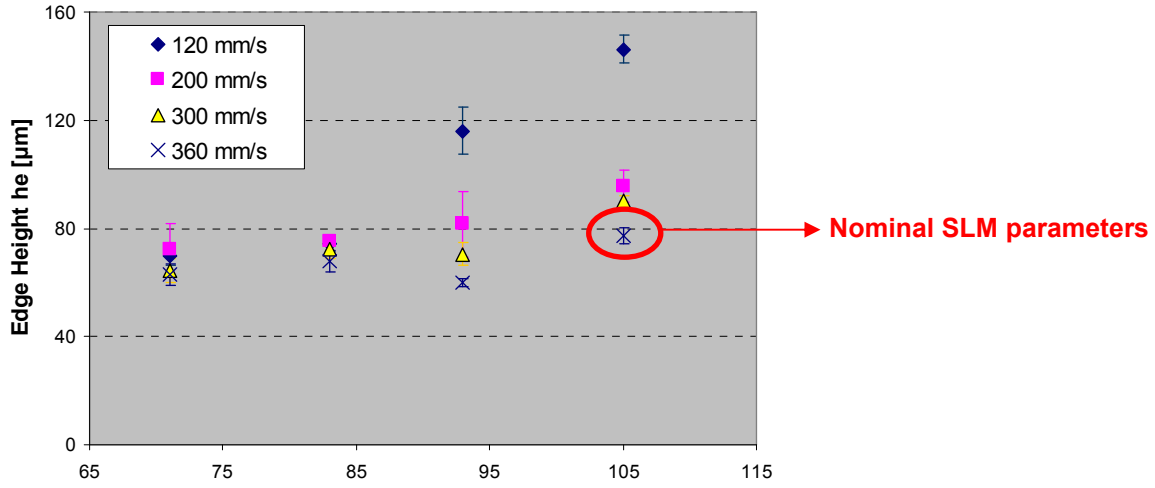

a)

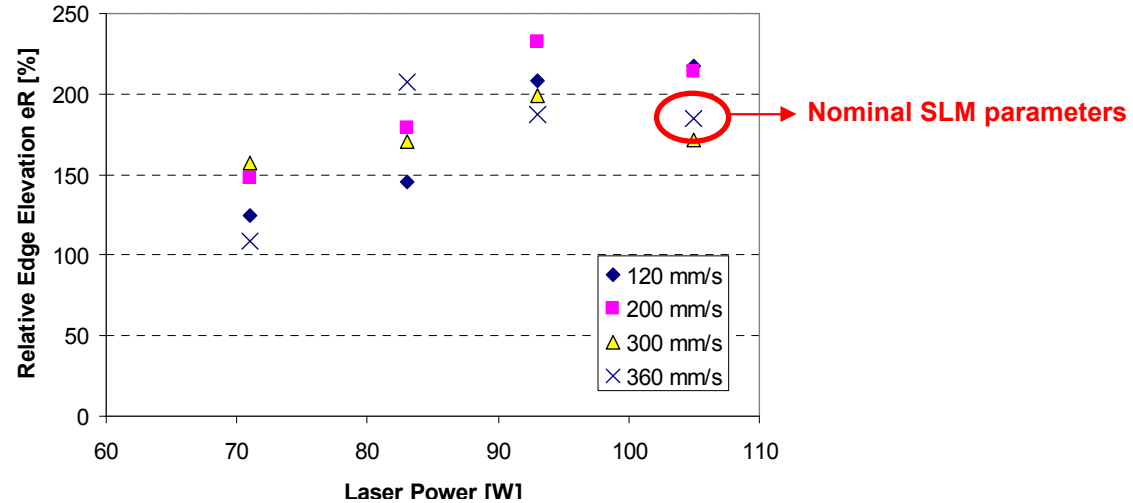

b)

Figure 4.33: Effect of SLM parameters (laser power and scan speed) on the edge effect a) on the edge height measured from the zero level (h_e) b) relative edge elevation (e_R)

b. Scanning direction effect

In order to investigate the influence of the orientation of the scanning vectors on the elevated edges of SLM parts, a number of specimens were built from Ti6Al4V material using uni-directional as

well bi-directional scanning (see Figure 4.34). These samples were produced without contour scanning to eliminate other effects on the results. Figure 4.35 compares parts' elevated edges for two scanning patterns. While uni-directional scanning causes a very high edge on one side of the part and a rounded corner on the other side (Figure 4.35a), bi-directional scanning is found to be a better scanning option lowering the edge height at both sides (Figure 4.35b). The rapid flow motion towards the sides and back of the melt pool caused by the surface tension gradient (thermal gradient) within the melt pool might be responsible for expelling the melt pool thereby forming high edges at the starting points of the scan lines.

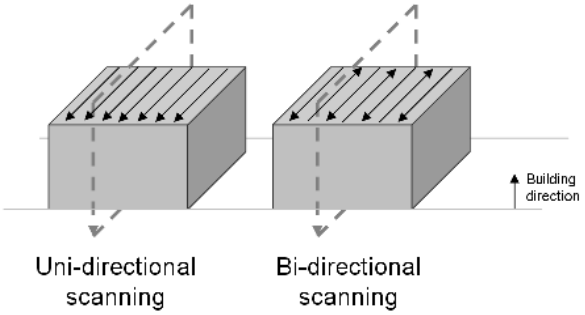

Figure 4.34: Uni-directional and bi-directional scanning together with the cross-sections

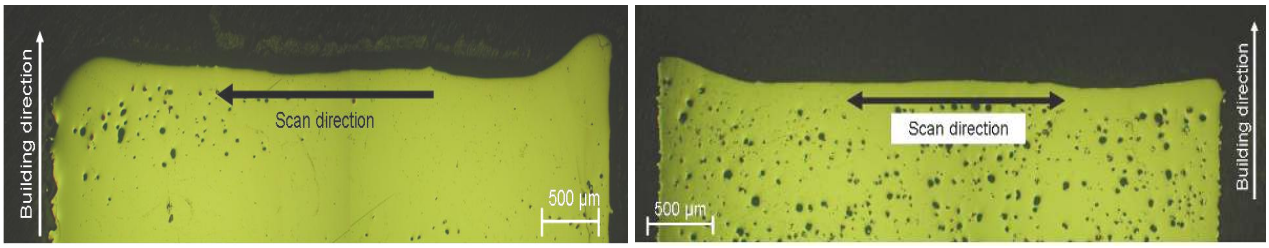

Figure 4.35: Effect of uni-directional scanning versus bi-directional scanning

c. Middle-fill and random-fill scan strategies

This section is concerned with the first scan line conditions, in order to verify the hypothesis of formation of elevated ridges as a consequence of first line scanning. A number of test specimens were produced using Ti6Al4V powder at nominal SLM parameters for this material (laser power 42 W, scan speed 225 mm/s and scan spacing 74 µm) and without contour scanning. The scanning strategy comprised of starting with a first line being scanned at the middle of the layer, followed by filling the area to the right and then to the left of the middle line as depicted in Figure 4.36a. A scan speed of 750 mm/s for the first scan line was also used to avoid any peak in the middle of the part.

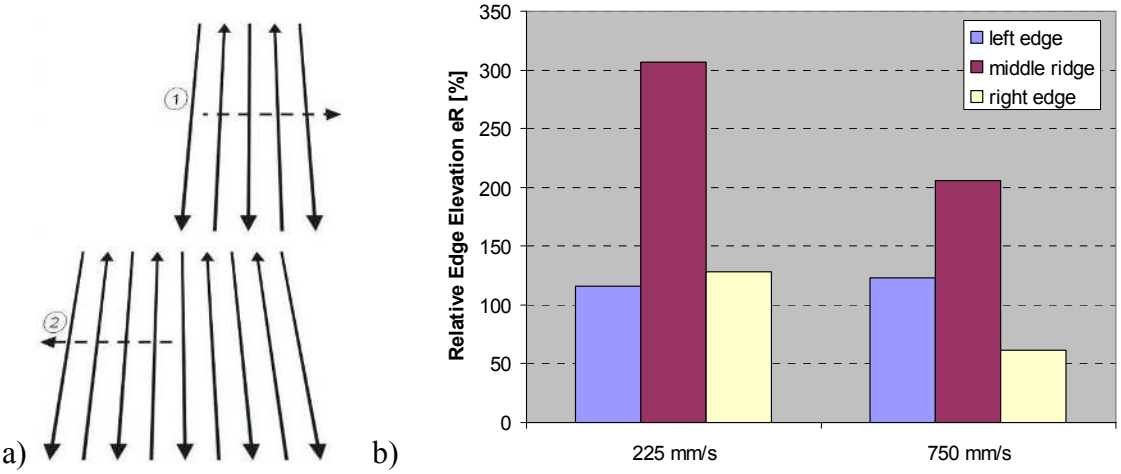

Figure 4.36: a) Fill middle scan strategy, the arrows represent the direction and order in which the surface was scanned, b) measured heights at left, middle and the right side of part

Figure 4.36b shows the obtained relative elevated ridges that were measured in the direction perpendicular to the scan direction (in *u* direction perpendicular to the scanning direction in Figure 4.30). The measured profiles show no significant edges anymore at the left and the right borders of the part. Instead a high ridge is visible at the middle of the top surface. The middle ridge height decreases with increasing scan speed. The height map of the part produced by locating the first scan track in the middle and scanned with a higher scan speed than the rest of the scan tracks is shown in Figure 4.37. The finding here is in good agreement with the above mentioned hypothesis advancing the thesis that for every scanned layer, the first scan track is the largest and causes the edge effect.

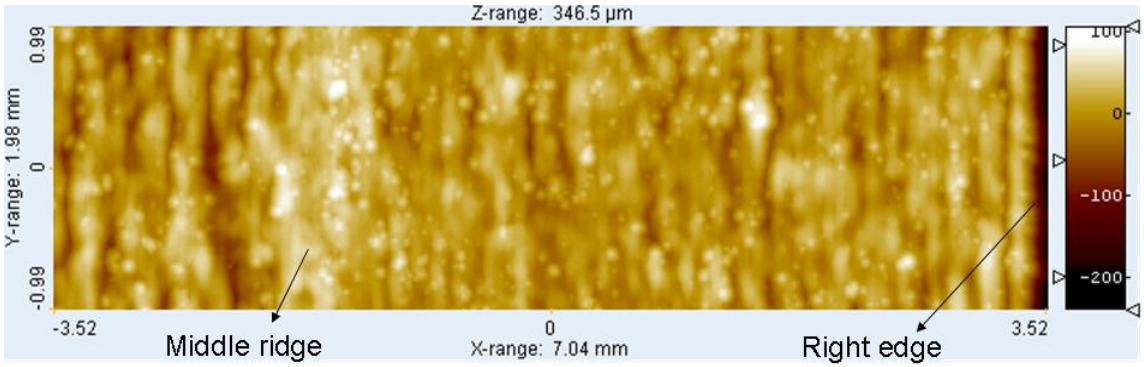

Figure 4.37: The height map of the part produced by locating the first scan track in the middle and scanned with a higher scan speed than the rest of the scan tracks (750 mm/s)

In the foregoing experiments, the first scan line position always remained at the middle of successive layers. For the next series of tests, the first line of each layer was scanned at a randomly chosen position. The recorded profile and the measured ridge height from the mean level (h_e) are depicted in Figure 4.38. Here the entire part was produced at 225 mm/s. It can be seen that not only no elevated edge was formed at the edge of the part (see Figure 4.39), but also the highest peak height in the top layer (which coincides with the first scan line at the top layer) was comparable with previous series when the first line was scanned at 750 mm/s. These findings imply that random-fill strategy may reduce the edge effect without lowering the attainable density.

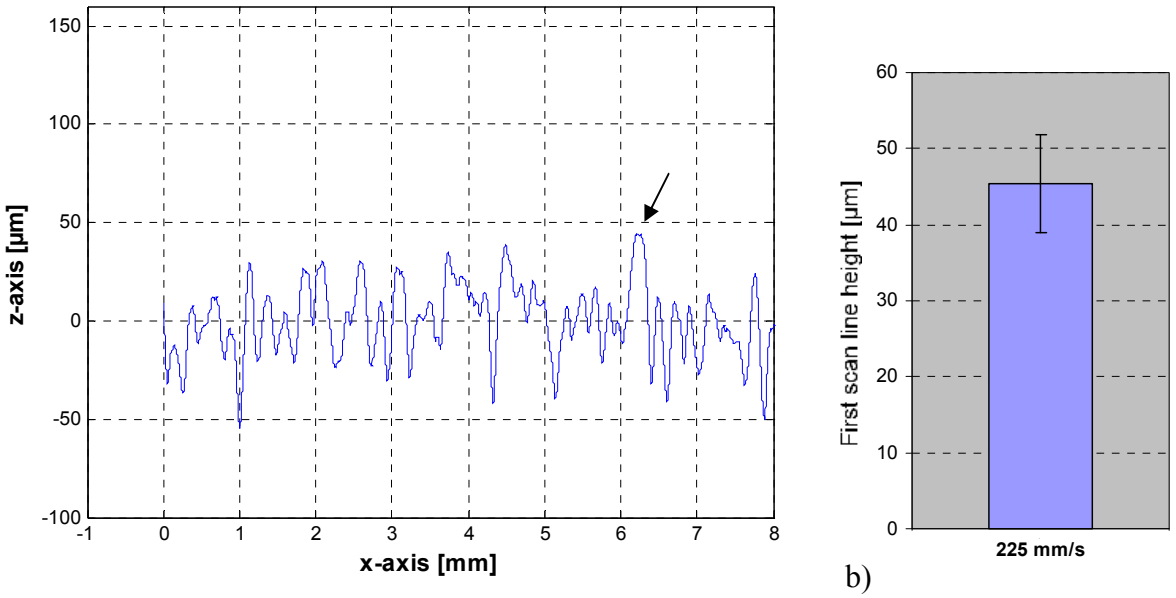

a) b)

Figure 4.38: Profile derived with a random-fill scan strategy (a) alongside with the peak ridge (b)

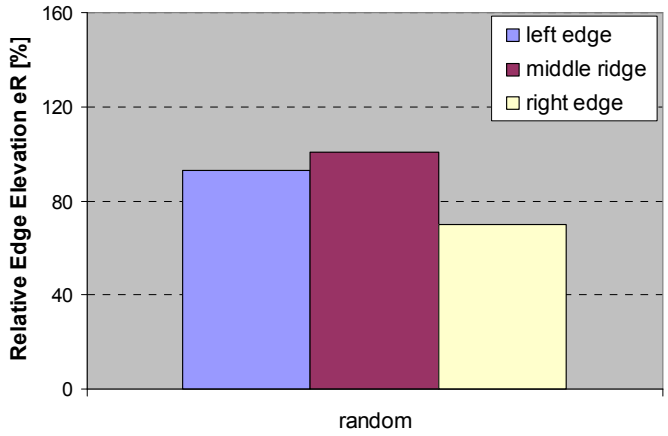

Figure 4.39: The relative edge elevation of the part produced with the first scan track located randomly

d. Island scanning strategy and contour scanning

In order to decrease the residual thermal stresses, Concept Laser divides the layer area to be scanned into smaller islands (5 mm x 5 mm), and these islands are raster scanned with shorter scan tracks in a random order. This is called island or sectoral scanning and is a patented scanning pattern from Concept Laser GmbH [12]. In island scanning, the locations of the islands are displaced by 1 mm in both x and y directions and the scan vectors are rotated by 90° in each island from layer to layer. More details on island scanning can be found in §5.3 which aims at optimization of scan spacing factors in island scanning. In the following set of AISI 316L stainless steel experiments, the influence of island scanning was investigated as well as the effect of contour scanning on the edge effect. Figure 4.40 compares the results of island scanning to long vector raster scanning. The figure shows that the island scanning does not worsen or improve the edge effect, which means the vector length does not play any role on the edge height. The figure is also concerned with the effect of contour scanning on the edge height. The parts made without contours have lower edges regardless of being scanned in islands or with long scan vectors. The production of parts without contours mostly solves the problem of edges but that cannot be used as an ultimate solution since the dimensional accuracy and side surface roughness are highly affected by contour scanning as also reported by other researchers [144]. Figure 4.41 depicts two SLM parts which were produced with or without contour scanning. The one built without contour scanning exhibits a globular side whereas the one built with contour scanning has a more linear surface due to the linear scan track located on the border of the part framing the area to be scanned. During SLM, the contours of a part are scanned on the powder bed firstly to define the borders of the melt pool, and then the inside the contours is scanned. Therefore, contours are necessary for the dimensional accuracy and cannot be left out during SLM. However, the contours can be scanned after hatching (filling inside the contours). In this way, the edge effect is less pronounced.

When too high edges are encountered, the general solution from the SLM equipment suppliers is to alter the contour parameters. In order to verify this technique, the SLM parameters for filling were kept at nominal values for AISI 316L (360 mm/s and 100 W) whereas different combinations of laser power and scan speed values were applied to the contours. Eight scan speeds starting from 250 mm/s to 700 mm/s together with three laser power values (105, 93 and 83 W) were examined. The measured edge heights (h_e) are presented in Figure 4.42a while the relative edge elevations are illustrated in Figure 4.42b. Close to the nominal scan speed (as shown with a cross in the plots), decreasing the laser power increases the edge heights. At high scan speeds, there seems to be a small reduction in the edge height with maximum laser power but the standard deviation is too high

to assure reliable results. Thus, it is concluded that increasing the scan speed or decreasing the laser power of the contour section is not a feasible solution to the edge effect problem encountered in the SLM process.

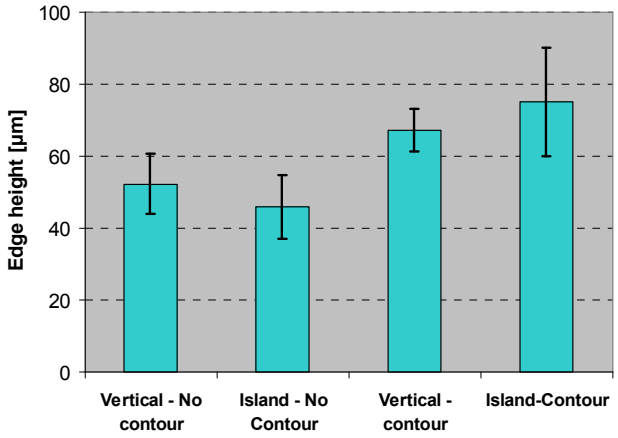

a)

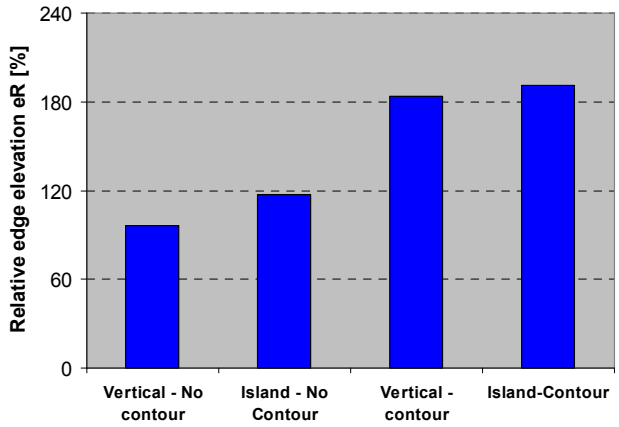

b)

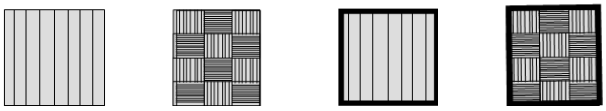

Figure 4.40: The influence of island scanning and contour scanning on the edge effect problem a) the edge height from the mean level (h_e) b) relative edge elevation (e_R)

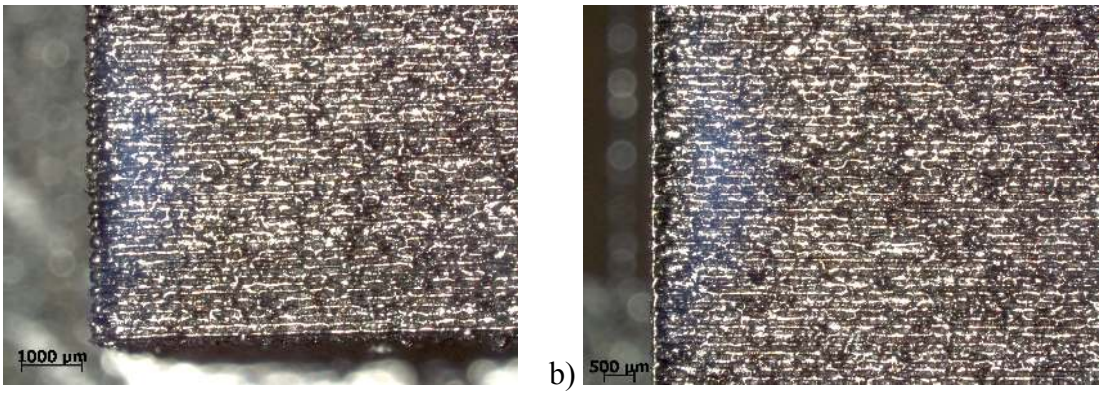

a) b)

Figure 4.41: Optical microscopy pictures of SLM parts' top views a) without contour scanning b) with contour scanning

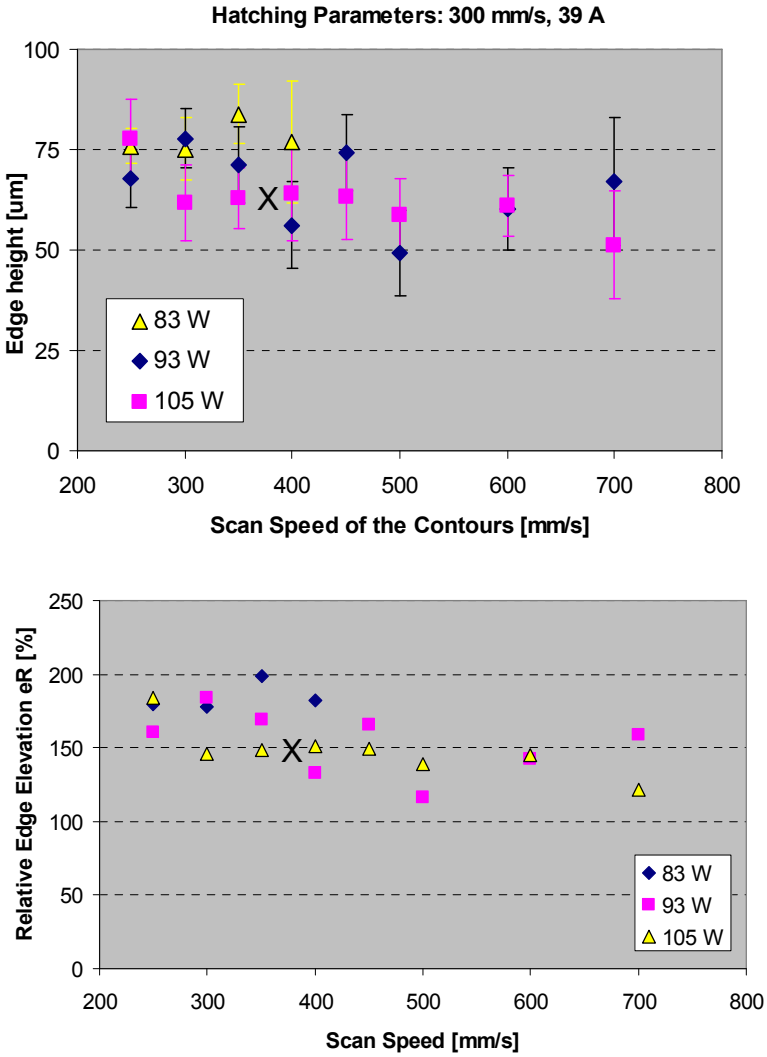

Figure 4.42: Different edge heights derived with various contour parameters at fixed filling parameters, X showing the estimation of where the nominal SLM parameters would lie

e. Fill vector scanning patterns

This section is concerned with the effect of various filling vector scan patterns. Figure 4.43a reveals the edge height of AISI 316L parts for four different cases which were produced with a scan speed of 300 mm/s and a laser power of 105 W both for filling (hatching) and contours. The arrow shows the direction of measuring the edges height for all cases. The first scan strategy consists of all horizontal scan tracks whereas the scanned area is exposed to laser radiation twice in the second strategy (i.e. re-melting). The third column represents the results for the scan strategy where all hatch lines were scanned diagonally. The last one is the same case as the first one rotated over 90°. This test is basically the same as the third one in Figure 4.40. Figure 4.44b shows the relative edge elevation for the same scanning patterns. The 3D height maps of the same parts are shown in Figure 4.44 where the surface texture is clearly seen. In terms of the edge effect, the second strategy which includes melting of the powder followed by re-melting with a rotation of 90° for the fill lines, the edge height is higher than the others. This is in good agreement with the results obtained for re-melting of stainless steel and Ti6Al4V powders [129]. The grid scanning reveals a much more severe edge effect than the others since the surface quality is improved with the re-melting ($S_{\max\_grid}$ = 14.8 µm whereas $S_{\max\_all\_vertical}$ = 36.6 µm). The other three cases give more or less the

same results. Consequently, it seems that laser re-melting during SLM, used to improve density or surface quality, results in a more pronounced edge effect. The 3D height maps given in Figure 4.44, however, clearly demonstrate the lower surface roughness results obtained with laser re-melting.

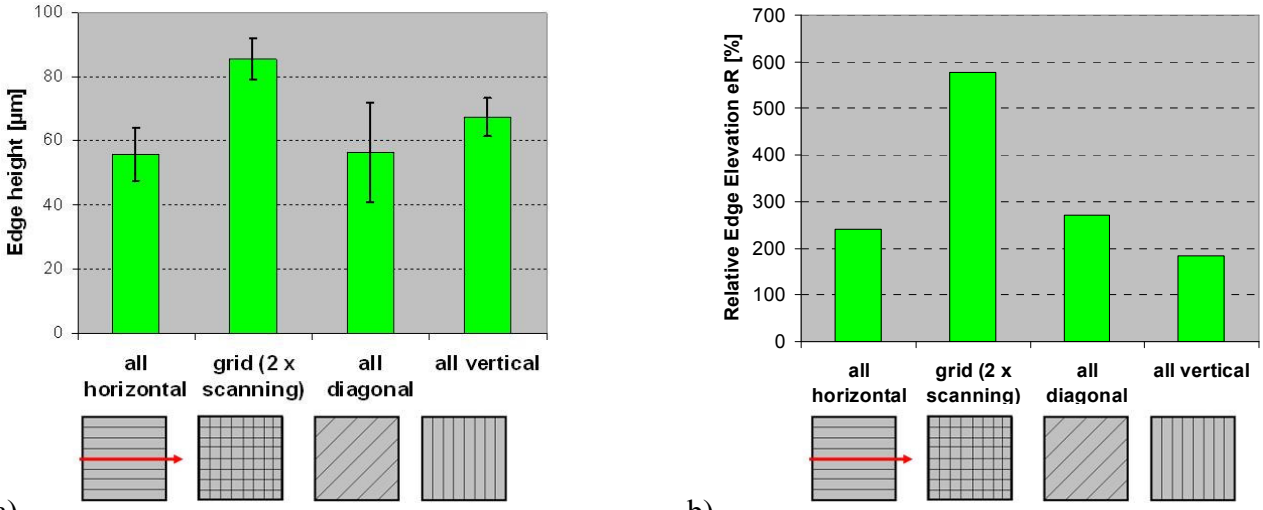

a) b)

Figure 4.43: Influence of different scan strategies on the edge effect problem

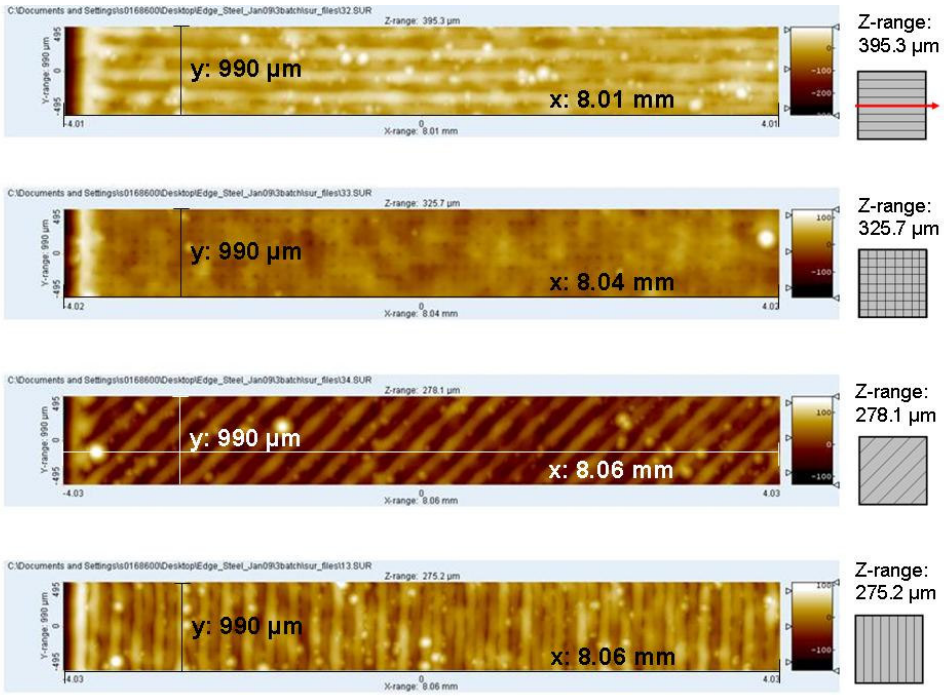

Figure 4.44: 3D height maps of the surfaces with different scan strategies

f. Shell and core

The last set of experiments conducted with stainless steel powder (AISI 316L) was the separation of a part into two sections such as core and shell and applying different set of parameters to each section. The thickness of the shell was chosen to be 0.4 mm which was wide enough to locate a few scan tracks next to each other. In each layer, the shell was first scanned and then the core was scanned starting on the already solidified shell so that the scanning of the core is not started on the loose powder (See Figure 4.45). In these tests, the core SLM parameters were kept constant (laser power 105 W corresponding a pump current of 39 A and scan speed 300 mm/s), but different parameters were applied to the shells (see the scan speed and laser power under the bars in Figure

4.46). A reference part was also built using the same settings (300 mm/s and 105 W) for contour and fill vectors.

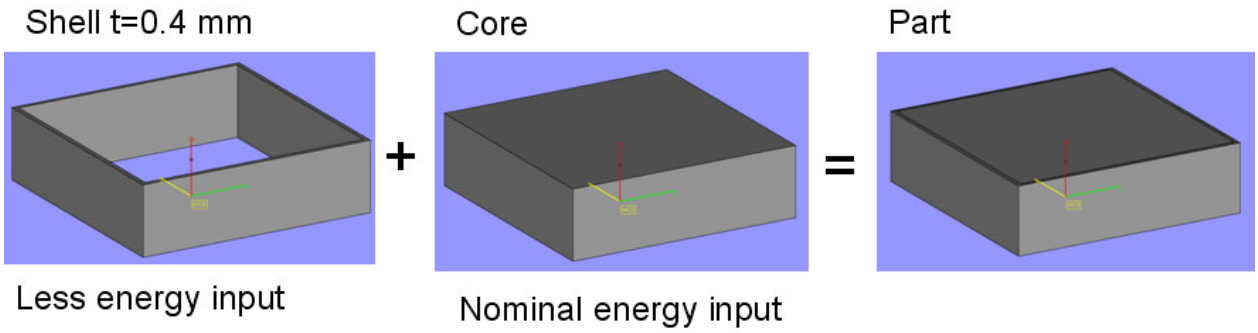

Figure 4.45: Dividing the part into shell and core

The results presented in Figure 4.46a show that the edge height decreases although the standard deviations of the edges derived in shell and core parts are higher than the reference part. The relative edge elevations also indicate a less severe edge effect with shell and core parts as expected due to lower energy input. When the three-dimensional profiles are observed in Figure 4.47, it can be concluded that there is no significant edge formation for shell and core parts whereas in the part which was scanned as one part with contour scanning, the edge is clearly distinguishable from the top of the surface. However, since low energy inputs are used in the shell, it is probable that the shell density would not be as high as the density in the core [129].

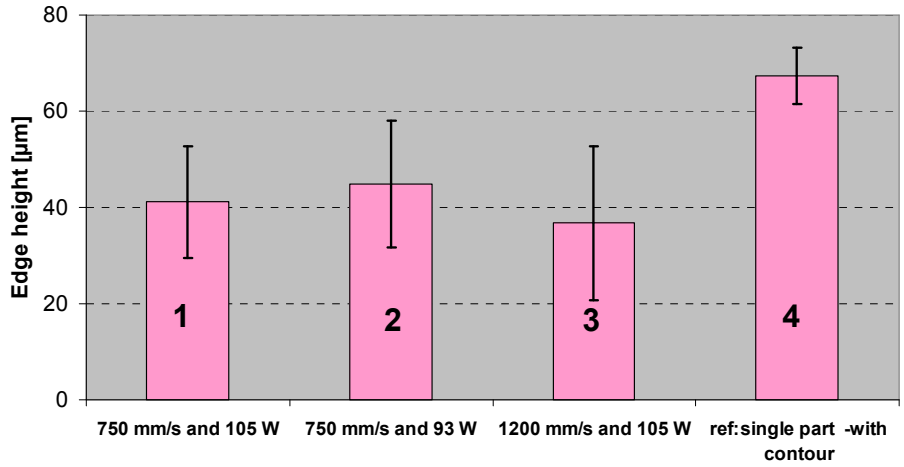

a)

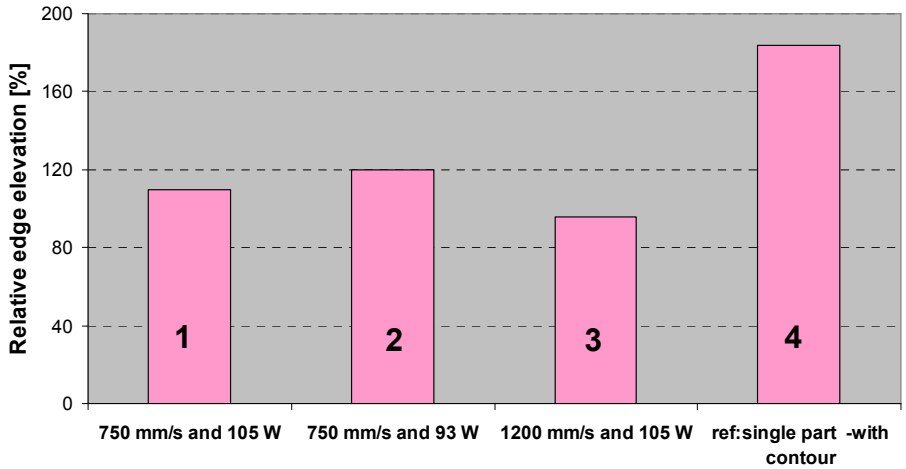

b)

Figure 4.46: Shell and core part results a) edge height b) relative edge elevation

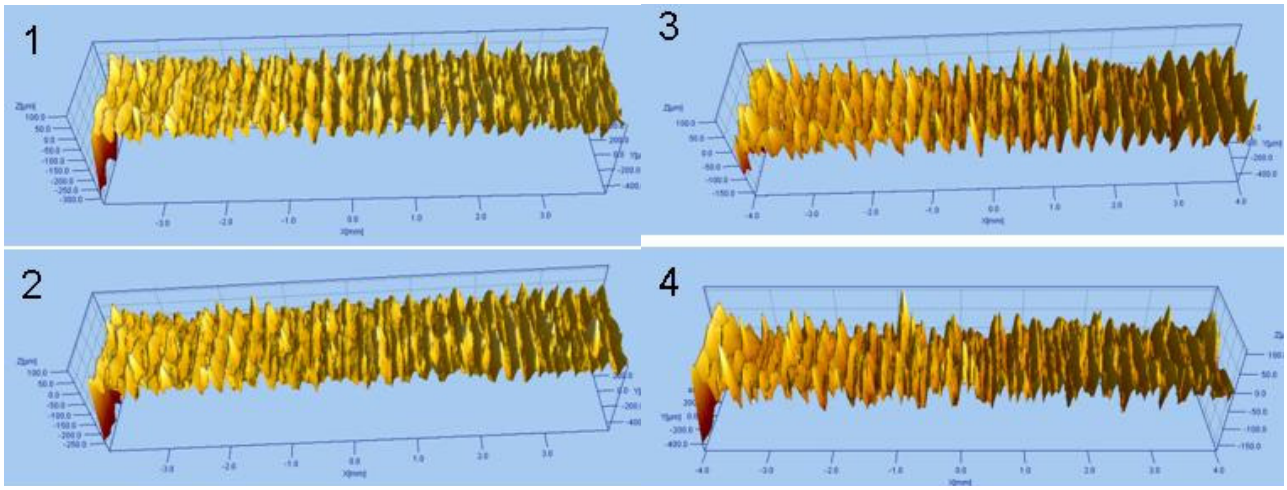

Figure 4.47: 3D profiles of the core+shell parts

g. Ramping laser power profile

One important derivation of the tests with the LM machine was how the edge effect could be improved by using a ramp profile for the laser power in one scan vector. As the laser beam approaches the free edge, the laser power is gradually decreased, and this resulted in almost no edge as shown in Figure 4.48. The starting power was selected as 40 W which is around the nominal power for Ti6Al4V alloy with a scan speed of 225 mm/s and as the laser moved to the core of the part, it was gradually increased to 80 W which was actually very high and resulted in very porous structure as seen in the figure due to evaporation or key hole-effect taking place during the process. Normally, with the default parameters, it is possible to reach up to 99.5% relative density on that equipment with this material. However, when the edges are investigated, it is clear that the ramp profile for the power solves the problem but the starting and threshold laser powers should be optimized for part density.

Figure 4.48: Result of ramp power profile

h. Post-fill scan strategy

The goal of this strategy was to compensate the edge effect by filling up the valleys that were formed by the edges during the SLM processing after the part is built. The test specimens from Ti6Al4V were produced at the material's nominal parameters (laser power 42 W, scan speed 225 mm/s and scan spacing 74 µm). The contour of the parts was scanned before the core with the same processing parameters used for fill vectors. The distance between the contour vectors and fill vectors for all the layers was chosen to be 45 µm and 75 µm (See Figure 4.49) which are 55% and 95% of the spot size (80 µm) on this machine. Upon completion of part scanning, either one or three extra powder layer(s) were deposited and scanned without lowering the building platform and without scanning the contours.

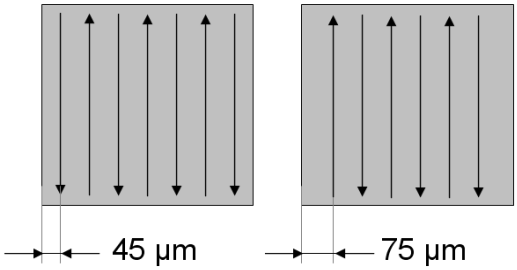

Figure 4.49: Showing the location of scan tracks for the post-fill strategy

Figure 4.50a represents the measured edge heights for 45 µm and 75 µm fill contour distances respectively. These findings suggest that the post-fill strategy gives the lowest edge height when a distance of 75 µm between the contour and fill vectors, and 3 extra powder layers are selected. The edge heights of the part made by this strategy are about 35 µm and the relative edge elevation is about 100% meaning that the edges are not more significant that the parts' roughness peaks. Since the edge height of a part made by standard scanning strategy is about 70 µm (e_R of about 160-180%), this strategy gives a significant reduction without lowering the part density in the shell or the core.

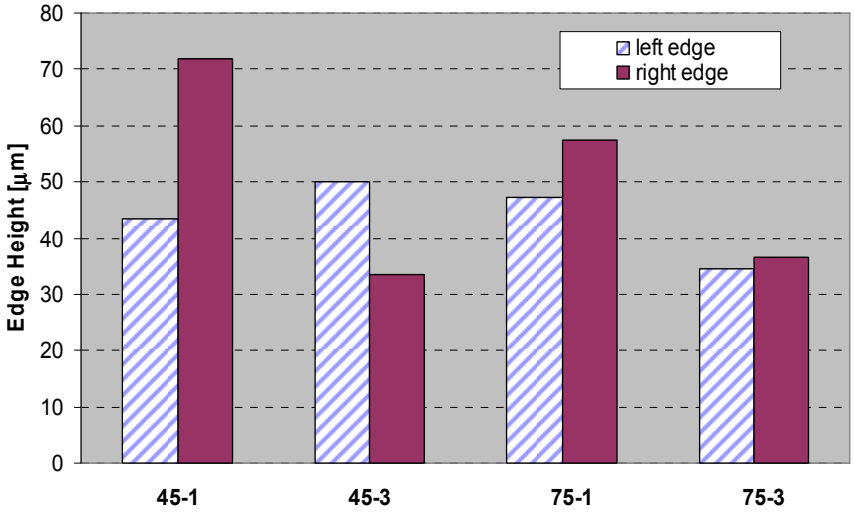

a)

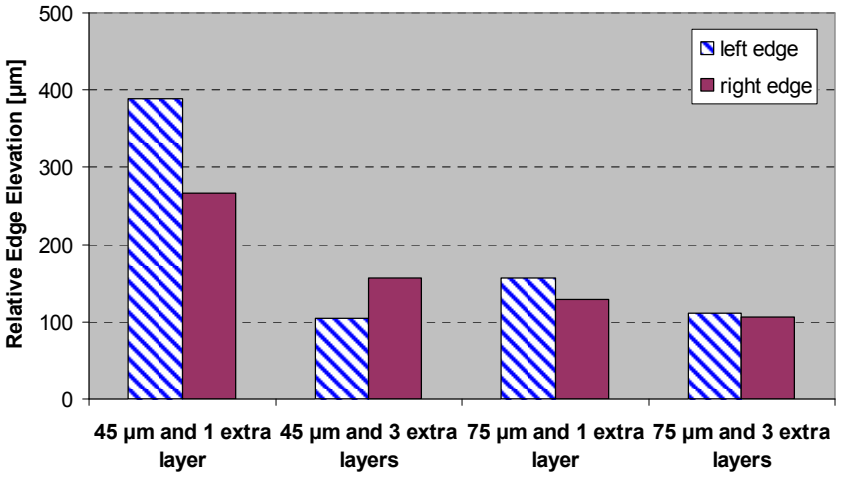

b)

Figure 4.50: Measured height of the left and right edge for parts made with post-fill scan strategies a) edge height from the mean level (h_e) b) relative edge elevation (e_R)

i. Conclusions

The edge effect problem as one of the deleterious phenomena encountered during SLM was studied in order to minimize or eliminate it. The work has demonstrated the main physical mechanisms that influence the elevated ridges within the SLM part's top surfaces. This incident is likely associated with the melt flow, and affected by material properties as well as processing parameters.

SLM experiments with stainless steel AISI 316L and Ti6Al4V have shown that, while it is not possible at this stage, to eliminate the formation of elevated edges completely, the flatness of the top surface can be greatly improved by applying appropriate process parameters as well as adapted scanning strategies. It is found that contour scanning before hatching enlarges the edge effect, but, on the other hand, the part's dimensional accuracy implies the borders of part to be scanned first. Dividing the part into a shell and a core with an overlap between them, not only may reduce the edge heights, but also improve the part quality as contour scanning does. The part's density homogeneity, however, has also to be considered.

Applying the middle-fill scan strategy, where the first line scan of each layer is positioned at the middle of the part, shows that the high ridge is also shifted to the middle of the part. The high height ridge from the top surface almost disappears when the random-fill scan strategy is used. In the latter technique, the first scan line's position is changed in a random order for each layer being scanned. This technique, however, does not imply contour scanning, which is necessary to achieve good dimensional accuracy. The post-fill scan strategy can be used together with contour scanning in order to reduce the edge effect successfully. A reduction of about 50% in the edge height is obtained when an appropriate distance between the contour vectors and fill vectors is chosen during the SLM process, and without lowering the building platform, three further extra powder layers are deposited and scanned upon completion of the part. This seems to be the best solution without any sacrifice in the density of the part either in the core or the shell. The only disadvantage of this method is the additional production time due to scanning of extra layers to fill in the valley in between the edges.

4.4 General Conclusions

Selective Laser Melting (SLM) is an advantageous additive manufacturing process to make functional three-dimensional prototypes, products and tools with very complex geometries although it suffers from 1-2% porosity and insufficient surface quality among other limitations. In this work, laser re-melting was experimentally studied in order to enhance the SLM process. It is found that laser re-melting is a promising method to increase the density of SLM parts to almost 100% and to enhance the surface quality of about 90% at a cost of longer production times. However, the process parameters in laser re-melting affect the results significantly and therefore should be selected properly.

When applied after each SLM layer to remove any pores formed during SLM, laser re-melting can be an ultimate solution for some applications where fatigue loading or excellent strength with high ductility is necessary. For an effective improvement in density, too high energy inputs to the substrate should be avoided by not selecting very low scan spacing or scan speed values. In this manner, the additional production time is kept to a minimum.

Additionally, laser re-melting is an easy method to improve the surface quality significantly (more than 90%) without removing the parts from the SLM machine and any fixation errors when applied on top surfaces after the parts are completely built by SLM. It can also be easily applied on the inclined or curved surfaces after the surrounding powder is blown away around the parts. With a few basic software changes to allow the movement of the building platform to keep the laser beam in focus, it can be applied automatically. For surface quality enhancement, the production time is not necessarily affected since the laser re-melting is applied only on the outer surfaces of the SLM

parts. Surface quality enhancement by laser re-melting also leads to a fully dense shell around the part. Since surface porosity is known to affect both the stress distribution and deformation of subsurface layers leading to subsurface crack formation and propagation, fully dense shells are especially important for applications requiring high wear resistance. Not only wear resistance but also other surface properties such as thermal and electrical conductivity are highly dependent on the surface porosity.

The potential of laser re-melting to eliminate the stair effect by applying only on contours during the SLM process is explored. However, no significant benefits could be obtained. The main disadvantage of laser re-melting is found to be the formation of elevated edges of the solidified material which deteriorates the dimensional accuracy and causes collisions with the hard blades of the coater. This phenomenon is not only seen in laser re-melted parts but also in all processes involving melt pools like SLM, EBM and LENS. The possible reasons causing this unwanted effect have been investigated and possible solutions have been searched in the scope of this work. Post-fill scanning strategy seems to be the best solution among others without lowering the shell density of SLM parts.

5 Selective Laser Melting

Selective Laser Melting (SLM), just like other additive manufacturing techniques, provides particular advantages over conventional machining techniques like almost unlimited geometrical complexity. However, there are also some problems encountered in the process, e.g. stair stepping effect, porosity, low surface quality and insufficient mechanical properties as explained in detail in the first chapter. Some of these problems were targeted to be solved by combining SLM and SLE or laser re-melting in the previous chapters. Besides, some more fundamental research was performed involving only the Selective Laser Melting process. This chapter summarizes the work aimed to improve some of the weak sides of Selective Laser Melting without using any secondary process. It consists of three main sections. The first section is about the investigation of the process parameters like the scan speed or layer thickness on the obtained density, surface quality and microstructure for maraging steel 300 material, which is a good candidate where high toughness and strength are required, e.g. plastic injection molding and metal die casting applications. This study aims to find the process parameters on two different machines with different laser types for the same material (maraging steel 300) for high density and good surface quality and investigates the possible mechanisms responsible for porosity or bad surface quality. The interaction between the productivity and process outputs (density and surface quality) is also discussed. Productivity is one of the issues related to economical aspects of SLM that plays a key role for further applications of SLM as a competitive manufacturing technology.

Moreover, macro and micro hardness measurements were conducted on the parts' cross-sections to test if the process parameters have any significant influence on the hardness. The same material is mechanically tested after age hardening which is a standard heat treatment for this material to achieve its superior properties. The most appropriate combination of aging time and maximum temperature for the aging heat treatment is found and applied for further testing of this material (§5.1). Not only maraging steel 300 was tested with impact toughness tests, but also two other materials widely used in SLM, i.e. Ti6Al4V and AISI 316L stainless steel, were experimentally studied by Charpy impact tests. The most significant factors determining the toughness of SLM parts have been explored. The influence of building axis and different heat treatments have been experimentally determined (§5.2). As a result of those toughness tests, it was concluded that the island scanning can deteriorate the mechanical properties of SLM parts significantly if the process parameters are improperly selected. A low overlapping between scan tracks or islands drop the toughness severely. Therefore the island scanning, which is a patented scanning strategy by Concept Laser developed for reducing residual stresses [12], is taken under investigation in the last section of this chapter. The scan spacing factors between the scan tracks and islands were studied to provide a good connection and to prevent any aligned porosity. The effect of island scanning on residual stresses is also demonstrated (§5.3).

5.1 SLM of Maraging steel 300

5.1.1 Introduction and Literature Review

The maraging steels are well known for combining good material properties like high strength, high toughness, good weldability and dimensional stability during aging heat treatment. For many applications including plastics injection moulding and metal die casting applications with intricate cooling channels, SLM of maraging steels may be interesting. The work presented in this section

aims to investigate Selective Laser Melting of maraging steel 300 powders to achieve a high density with good mechanical properties while keeping productivity as a key factor, which is directly connected to the process parameters, e.g. scan speed and layer thickness.

Only a few published studies deal with SLM productivity enhancement. One of the possible solutions to increase the productivity is to use higher scan speeds or higher layer thicknesses during the SLM process. At Fraunhofer ILT Aachen, an improvement from 1.2 mm^3/s to 6.5 mm^3/s building rate is reported by using a wider laser beam diameter along increasing laser power from 250 W to 600 W [21]. Despite of such significant improvement in the productivity, process resolution is likely to be sacrificed because of expanded laser beam. A more recent study from Fraunhofer ILT Aachen combines high productivity with good resolution in the SLM process. A 200 W laser with a spot size of 0.18 mm is used to scan the contours for a good resolution and surface quality for a layer thickness of 50 µm whereas 1 kW laser with a spot size of 1 mm is used to scan the fill vectors only every 8 layers (for a layer thickness of 400 µm) reducing the scan time by a factor of 10 [145]. A density close to full density is achieved but the effect of such scanning on the microstructure or mechanical properties is not explored yet. At K.U. Leuven, in order to provide an insight in the economical aspect of SLM, production times of a benchmark case produced by five different SLS/SLM machines have been compared [15].

This work aims to investigate the change of part density and surface quality when the process parameters (scan speed, layer thickness) are varied from the recommended values by the machine makers to search for solutions to increase the productivity for the specific case of maraging steel 300. Moreover, two different SLM equipments with different laser sources (a fiber laser and an Nd:YAG laser) were employed to test the influence of the laser type on the productivity.

After achieving an almost full density, micro and macro hardness measurements have been conducted on the produced specimens to test the effect of the process parameters, i.e. scan speed and layer thickness, on hardness of as-built parts. Since maraging steels obtain their superior mechanical properties, i.e. high strength and toughness, after an aging heat treatment, different aging conditions were tested to find the relationship between aging time, temperature and obtained hardness.

5.1.2 Experimental Procedure

The test specimens were built from gas atomized maraging steel powders of specification and size fraction listed in Table 5.1. Reported powder particle sizes supplied by Concept Laser (CL50WS) and EOS Company (MS1) have been determined by laser diffraction technique at MTM, K.U.Leuven. Although the average powder size of MS1 is lower than the one of CL50WS, the size ranges are almost the same. The powders are available to be processed by their dedicated SLM machines.

Table 5.1: Specification and size ranges of gas atomized maraging steel powders

Material type	*DIN No.*	*Mat. Name*	*Size ranges (µm)*	*d_{50} (µm)*	*Bulk density (g/cm^3)*
CL50WS	1.2709	X3NiCoMoTi 18-9-5	25-63	43.7	8.1
MS1	1.2709	X3NiCoMoTi 18-9-5	20-65	35.6	8.1

Figure 5.1 provides typical morphology of the tested powders before processing. SEM micrographs show that the majority of the powder particles bear spherical and near-spherical

morphology. The spherical morphology without sharp edges and corners ensures free flow of the powder during layer deposition, thereby increasing process efficiency [146]. More details about the powders can be found in the first chapter in §1.2.2.

a) 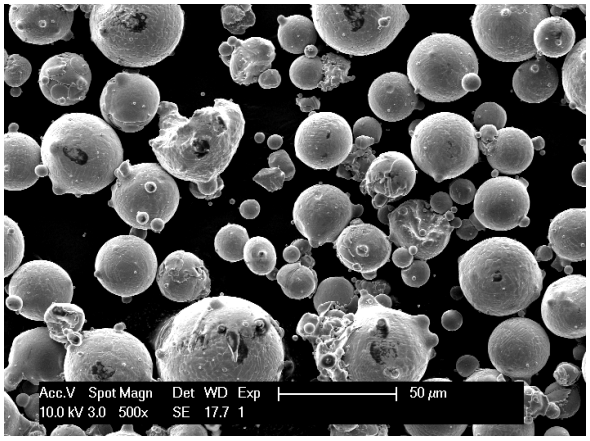

b) 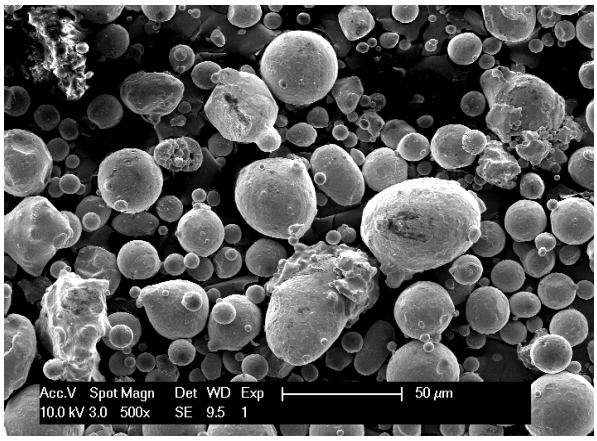

Figure 5.1 : SEM micrographs of used powders (a) CL 50WS maraging steel, (b) MS1 maraging steel

The test pieces were manufactured using two SLM machines, which differ in laser source and output power. CL50WS powder was processed on a Concept Laser M3 Linear SLM machine [61] equipped with a 100 W Nd:YAG laser. An EOSINT M270 SLM machine, employing a 200 W Yb-fiber laser was used to process MS1 [147]. The comparison of EOSINT M270 and Concept Laser M3 Linear regarding laser and machine properties is presented in Table 5.2.

Table 5.2: Comparison of two machines utilized during SLM of maraging steel 300

Machine properties		**Concept Laser M3 Linear**	**EOSINT M270**
Laser	Type	Diode-pumped Nd:YAG	Yb-fiber laser
	Wavelength (µm)	1.064	1.070
	Mode	Continuous (CW), pulsed	Continuous (CW)
	Spot size $Ø_{99\%}$ (µm)	~ 180	~ 140
	Max. laser power (W)	~100 in CW mode	~ 195
	Max. laser power intensity (W/mm^2)	~3000	~10000
	Beam quality factor M^2	<9.1	<1.05
	Scraper type	double side deposition	single side deposition
	Build volume (in mm)	250 x 250 x 250	250 x 250 x 215
	Protective gas	N_2	N_2
	Max. pre-heating temperature	180 ºC	80 ºC

Experiments were carried out using maximum available laser powers. A wide range of scan speed and scan spacing values at various layer thicknesses were examined as given in Table 5.3 with different scan strategies. In order to minimize the effect of thermal gradients on the produced parts for the powders processed on M3 Linear machine, island scanning (a patented scan pattern from Concept Laser) was used. In this scanning strategy, part area at each slice is divided into small square islands of 5 mm x 5 mm. Consequently, the islands are scanned in a random order while the scanning direction is altering 90° with respect to the neighbouring islands. Islands borders are also shifted 1 mm in x and y directions for the next layer. A part that is produced by island scanning is shown in Figure 5.2. More details on the island (or sectoral) scanning can be found in §5.3.

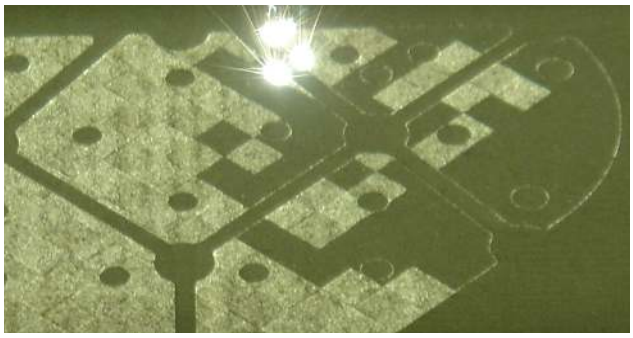

Figure 5.2 : Island scanning shown on a layer of a produced sample (Source: Concept Laser [61])

The surface roughness of the as-processed samples was measured on top surfaces using a contact surface profilometer, Talysurf 120L from Taylor Hobson Ltd. Measurements were carried in two dimensions (2D) without any cut-off filter.

Table 5.3: Experimental processing parameters

Material	*Scan speed (mm/s)*	*Scan spacing (µm)*	*Layer thickness (µm)*
CL50WS	120-600	125 (70% beam dia. $\phi_{99\%}$)	30, 40, 50, 60
MS1	450-3000	100 (70% beam dia. $\phi_{99\%}$)	40, 50, 60, 70

Density was measured according to the Archimedes method by weighing the samples in air and subsequently in ethanol. The Archimedes method is a simple and fast method to evaluate different processing conditions. However, it is not suitable to compare parts having very close results. This is discussed further in §5.3.2. A coating with lacquer was also applied to avoid ethanol absorption in open pores at lower densities (<90%). Density results are presented as the arithmetic means of three measurements on three different samples at each processing condition and are expressed as relative density by taking materials' bulk density as 8.1 g/cm^3 (See Table 5.1).

5.1.3 Experimental Results and Discussions

Part density and surface quality are the main concerns in SLM. The former parameter determines the part's mechanical properties which in turn has direct influence on the component performance. The latter is not only a primary concern to the users, but also a key issue in completion of the component during the fabrication. If the melted layer exhibits a very rough surface, the powder deposition for the next layer by the hard coaters may not be possible due to the collision of the high peaks with the coater. The results of measured density as well as surface quality for the tested powders are presented in the following two sub-sections. Following those, the macro and micro hardness of the parts built with different process parameters are measured and analyzed. The microstructural investigation of maraging steel 300 parts is also accomplished for a better understanding of the process. In order to have almost fully dense parts, the effect of re-melting is tested for this material. The improvement of the density by applying laser re-melting after each layer is illustrated with optical microscopy images. In the last sub-section, the age hardening, which is a standard procedure for this material, is taken under investigation and optimized for SLM parts testing different combinations of aging time and maximum temperature to which the parts are re-heated in the heat treatment. In the same section, the constants in an existing model to predict the achievable hardness with this material are calculated and presented. The impact toughness of the parts, of which the SLM and aging parameters are optimized, is conducted. The results are presented in §5.2 about Charpy impact testing of SLM materials where all results with different SLM materials are explained.

a. Relative Density

Figure 5.3 shows the specimens produced on the Concept Laser M3 Linear machine with different processing parameters. The specimens were produced in a step-like form in order to apply two different layer thicknesses in one batch but to be still able to measure the roughness for lower case parts. Figure 5.4 and Figure 5.5 shows the relative density results at different scan speeds and layer thickness values for the parts produced on the Concept Laser M3 Linear (Nd:YAG laser) and EOSINT M270 (fiber laser) machines, respectively.

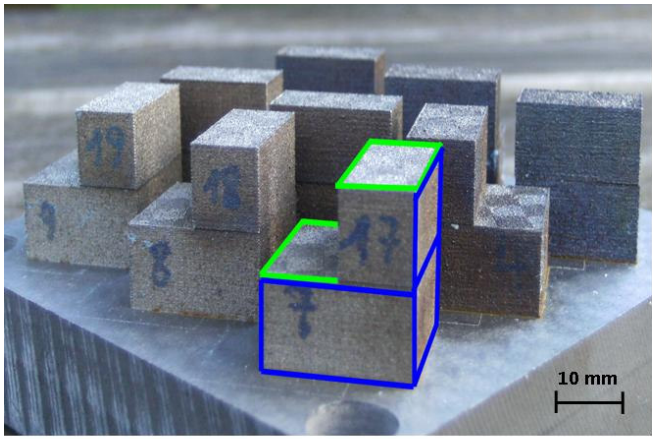

Figure 5.3 : Maraging steel samples produced on the Concept Laser M3 Linear machine

Figure 5.4 depicts that relative density reduces with increasing scan speed even though its decline is less obvious at lower speed ranges for all layer thicknesses for CL50WS. The observed trend is logical since the delivered energy density decreases with increasing scan speed. Results indicate that an increase of layer thickness from 30 to 40 µm for instance, at a constant scan speed, has little deteriorating effect on the density as long as the scan speed is equal or less than the "recommended" speed. Such an increase in layer thickness corresponds to 25% lower scanning time as well as 25% reduction on layer deposition time for this material [14]. As shown in the figure, the recommended parameters for CL50WS by Concept Laser are a scan speed of 200 mm/s, scan spacing of 125 µm and 30 µm layer thickness.

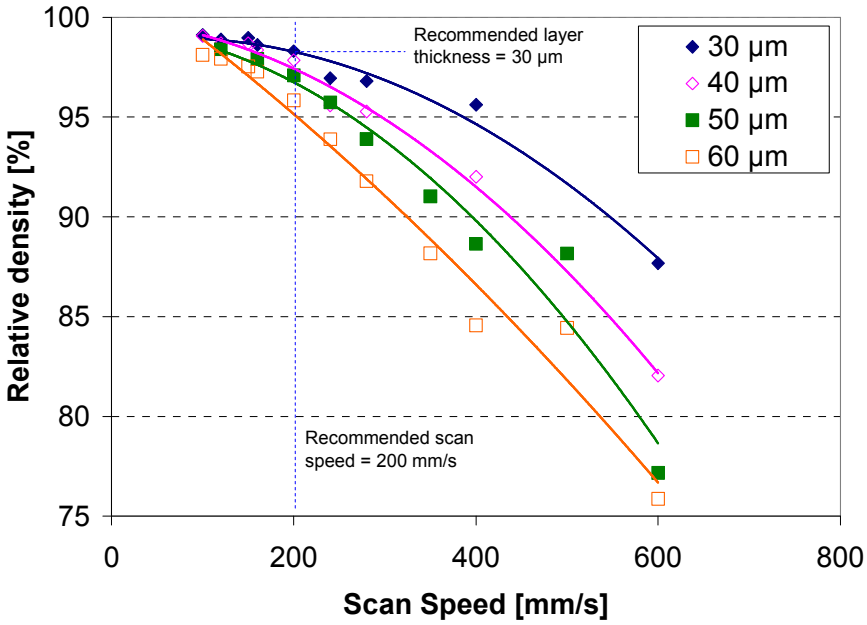

Figure 5.4 : Relative density versus scan speed for different layer thickness values (CL50WS processed on Concept Laser M3 Linear)

For MS1 powder, regardless of the layer thickness, there is a scan speed range that results in the highest relative density as illustrated in Figure 5.5. The reason for the lower density at low scan speeds may be due to the formation of a rough surface as a result of excessive energy density that in turn prevents the coater to deposit a homogenous layer of powder. The latter phenomenon may leave behind some areas without fresh powder to be processed as well as very thick powder depth in some other areas preventing the underlying layer to re-melt (inhomogeneous layer thickness). As a result of the tests, the optimum scan speed is found to be at the material's recommended scan speed, i.e. 750 mm/s (the other standard parameters set are 100 µm scan spacing and 40 µm layer thickness). An improvement of 20% on the building time is again achieved for this material by only increasing layer thickness to 50 µm. Lower densities were obtained when the layer thickness increased to 60 µm. However, with a 20% reduction in the scan speed (600 mm/s instead of 750 mm/s), a higher density, comparable to that obtained with 40 µm and 750 mm/s, is achievable.

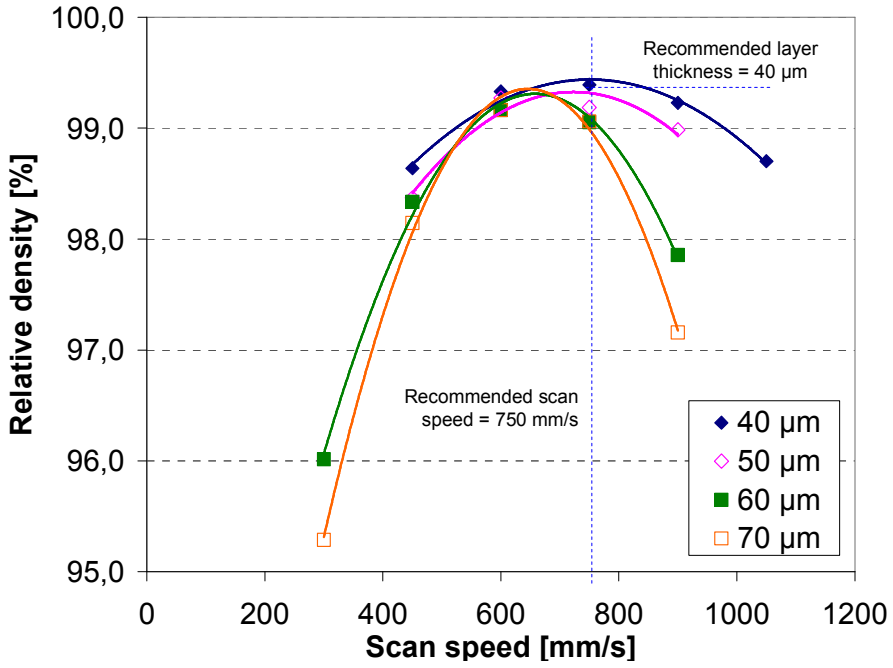

Figure 5.5 : Relative density versus scan speed for different layer thickness values (MS1 processed on EOSINT M270)

The comparison of two machines (or two laser systems) with the powders having commercially different names but same composition is done in Figure 5.6. The relative densities obtained at different theoretical energy density values are illustrated in a plot for Concept Laser M3 (Nd:YAG laser) and EOSINT M270 (fiber laser). The theoretical energy density is calculated by dividing the laser power by the product of scan speed, scan spacing and layer thickness without taking the spot size into account. As evident, the relative density converges to a maximum value after a threshold energy density is reached for each laser system. As shown, the EOSINT M270 reaches a maximum relative density at a lower energy density compared to the Concept Laser M3 Linear machine. The possible reasons of this fact are a lower beam diameter and higher quality beam with the fiber laser of the EOSINT M270 machine (see Table 5.2).

The maximum densities obtained from both powders (MS1 and CL50WS) range between 98% and 99% of the material' bulk theoretical density, showing promising capabilities for many application areas. Yet, SLM still falls short for some applications where fatigue loading or excellent strength with high ductility is necessary.

The findings of this study also point to the importance of laser power density and scan speed for the highest attainable relative density after SLM. Note that MS1 and CL50WS powders were

processed using an Yb-fiber laser power density of about 9000 W/mm^2 and an Nd:YAG laser power of 3000 W/mm^2, respectively. Comparing Figure 5.4 and Figure 5.5 indicate that although the two processed powders were the same in composition (but differ in suppliers), the overall density obtained with a fiber laser (MS1 powder) was higher than that obtained with an Nd:YAG laser (CL50WS powder), although obtained at greatly higher scan speeds than the speed ranges used for processing CL50WS with an Nd:YAG laser.

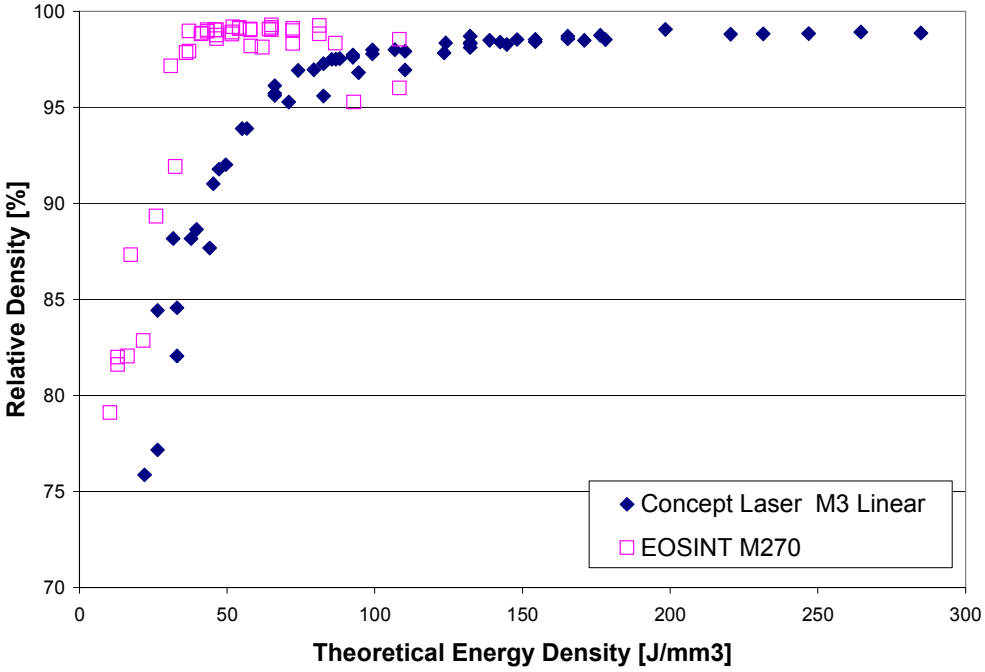

Figure 5.6 : Relative density versus theoretical energy density for two machines with different lasers

b. Surface quality

In order to investigate the influence of building rate on the parts' surface quality, the surface roughness R_a has been measured on horizontal top surfaces of parts produced with different scan speeds and layer thicknesses without using any cut-off filter. Figure 5.7 and Figure 5.8 depict the average value and 95% confidence intervals of R_a measurements (1 sample built per setting and 10 R_a measurements on each sample) for the specimens produced on EOSINT M270 and Concept Laser M3 Linear, respectively.

For the MS1 powder processed on the EOSINT M270 machine with a fiber laser, the scan speed range is much wider than the one that was under investigation in Concept Laser M3 Linear machine equipped with an Nd:YAG laser. This is due to the laser source and available laser intensity. For both powders (MS1 and CL50WS), the surface quality deteriorates as the layer thickness is increased. This is probably connected to the larger melt pool formed with thicker layer thickness. As depicted in Figure 5.7, the average roughness increases with increasing scan speed for MS1 powder processed on an EOSINT M270. However, at low scan speeds (300 and 450 mm/s) and high layer thicknesses (60 and 70 µm), the roughness values, which are not shown in the graph, exhibit the highest value probably due to the effect of severe balling as shown in Figure 5.9a. As depicted in Figure 5.9b, balling is the breakup of the melt pool into small droplets obstructing a smooth layer deposition and decreasing the density of the produced part (See Figure 5.5 for the density reduction at low scan speeds). The volume of the melt pool produced increases when low scan speeds are employed. As stated in [148], balling can increase with the generation of excessive melted material which is the case with low scan speeds and high layer thicknesses. Higher layer thicknesses promote multi-stage balling as explained in [149].

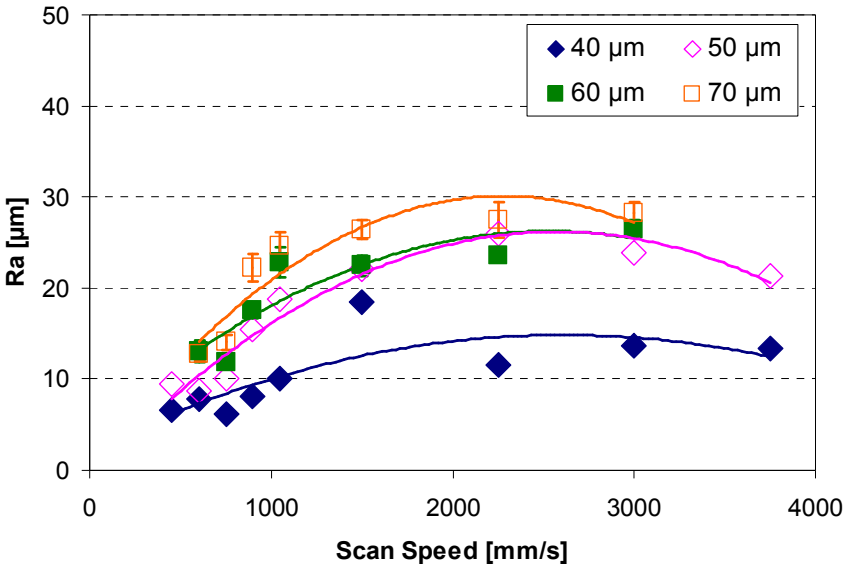

Figure 5.7 : R_a measured on top surfaces versus scan speed for different layer thicknesses with 95% confidence intervals (MS1 processed on EOSINT M270, with a fiber laser)

The results regarding the combination of high layer thicknesses and low scan speeds are not shown in Figure 5.7 due to the fact that the equipment used to measure the roughness (Talysurf 120L) was not able to handle that rough surfaces. In the scan speed range (500-1000 mm/s), where a high density is achievable, low layer thicknesses possess a good surface quality and the effect of scan speed is not that significant. The effect of the scan speed on the surface quality becomes more important as the layer thickness is increased. In the tested range covering the scan speeds greater than 1000 mm/s, the average roughness first increases but then levels out. The deterioration of the surface quality in this zone is due to insufficient melting and re-melting of underlying layers. Thus, due to high scan speeds, the fragmentation of the scanning tracks occurs and the surface is not cohesive. This also increases the porosity as depicted in Figure 5.5.

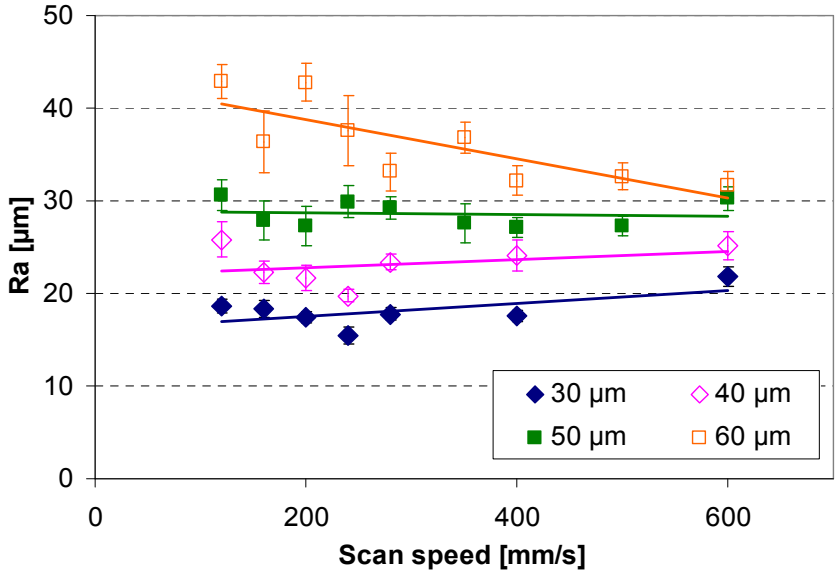

Figure 5.8 : R_a measured on top surfaces versus scan speed for different layer thicknesses with 95% confidence intervals (CL50WS processed on Concept Laser M3 Linear machine, with an Nd:YAG laser)

a) 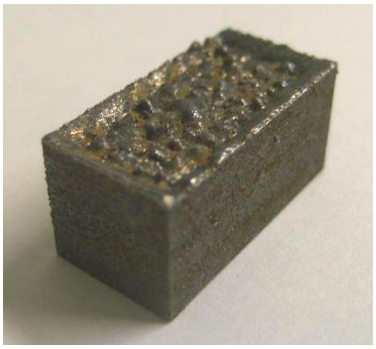 b) 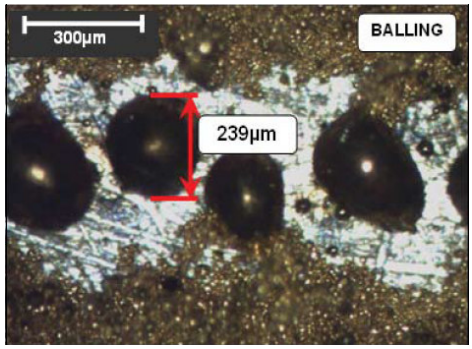

Figure 5.9 : a) Balling effect encountered at a scan speed of 300 mm/s and a layer thickness of 70 µm with MS1 processed on EOSINT M270 b) Severe balling occurred during SLM of pure gold [150]

To sum up, three zones occur for MS1 processed on EOSINT M270:

- Low scan speed range where the balling effect is dominating the surface quality (<500 mm/s)
- Optimum scan speed range where a good surface quality with high density is obtained (500-1000 mm/s)
- High scan speed range where the surface quality deteriorates due to the insufficient energy input (>1000 mm/s)

Figure 5.8 depicts the surface quality results in terms of average roughness R_a for CL50WS powder processed with an Nd:YAG laser. In the tested scan speed range, which is much more limited than the one tested for MS1, the roughness is almost independent of the selected scan speed at low layer thickness values (30-50 µm). For the highest layer thickness, i.e. 60 µm, the relation between the scan speed and the surface quality seems to be inversely proportional. However, the high variations obtained at low scan speeds with this layer thickness make the relationship difficult to draw concrete conclusions for a layer thickness of 60 µm.

c. Macro and micro hardness measurements

In order to investigate the effect of the process parameters on hardness, macro and micro scale hardness measurements were conducted on the side cross-sections (cs1) of the produced specimens with different settings of scan speed and layer thickness (see Figure 5.10 for the definition of side cross-section). The macro hardness measurements were employed in order to get an idea of overall hardness of the samples taking porosity into account whereas the micro hardness tests were used to measure the hardness only of the material to see if the microstructure and hardness changes with utilization of different process parameters. The macro hardness results were obtained with Rockwell A tests by measuring the depth of penetration of an indentation under a specified load (60 kg) compared to the penetration made by a preload (10 kg). Before Rockwell A, Rockwell C test which employs higher loads were carried out. However, the obtained results with Rockwell C were not reliable and logical for porous parts giving hardness values greater than 100 HRC. This is because at high loads and high indentation, the indentor holder was making contact with the sample, thereby biasing the measurement.. Therefore, Rockwell A is more suitable for both the low hardness values obtained and porous SLM samples. The results of performed Rockwell A tests are presented in Figure 5.11. Comparing Figure 5.11 to Figure 5.5 shows that the hardness is mostly affected by the density. At low scan speed range close to the recommended speed (200 mm/s), where the obtained densities are close to each other for different layer thickness values, there is a very slight change in the measured hardness. As the scan speed is increased, the hardness values are significantly reduced due to increased porosity.

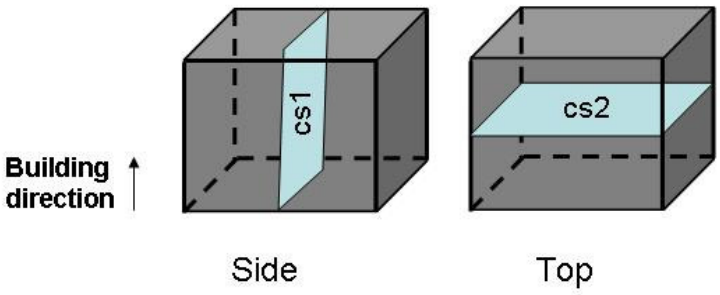

Figure 5.10 : Illustration of side and top cross-sections with respect to the building axis

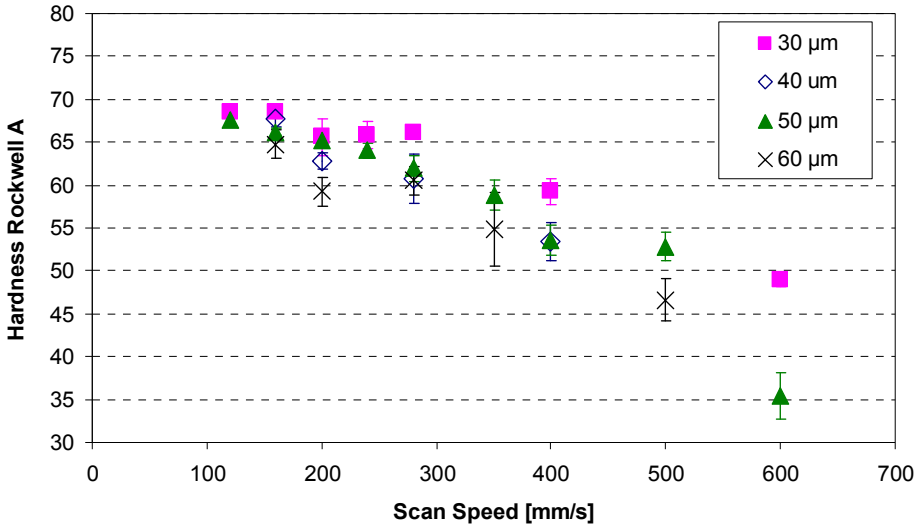

Figure 5.11 : Average macro hardness measured on cross-sections versus scan speed for CL50WS processed on the Concept Laser M3 Linear for different layer thicknesses with 95% confidence intervals

The average results for micro hardness measurements, which were conducted with Vickers hardness measurement device with a test load of 0.5 kg and a pyramidal indenter, are depicted in Figure 5.12 for two different layer thickness values. 8 measurements were taken for one sample on one side cross-section. It should be noted that the measurements were only taken on samples which were dense enough to take measurements with proper spacing between indentations and pores. It was difficult to find solid regions to take reliable measurements as suggested by the ASTM standard for the parts produced at high scan speeds and layer thickness values. At low scan speed range, the change of the scan speed or layer thickness does not significantly alter the micro hardness as depicted in Figure 5.12. Since the process parameters don't significantly influence the micro hardness, it may be concluded that their influence on the macro hardness is only due to their influence on the density.

The work presented in [151] also investigates the effect of the process parameters, scan speed and laser power, on the hardness for the same material processed on a similar SLM equipment with the same laser source. However, the hardness measurements are only conducted in macro scale for a very limited scan speed range (180-220 mm/s). The findings in that study are consistent with the results presented here and reveal that macro hardness of 18Ni(300) maraging steels processed with SLM decreases with increasing speed due to the reduction in the density.

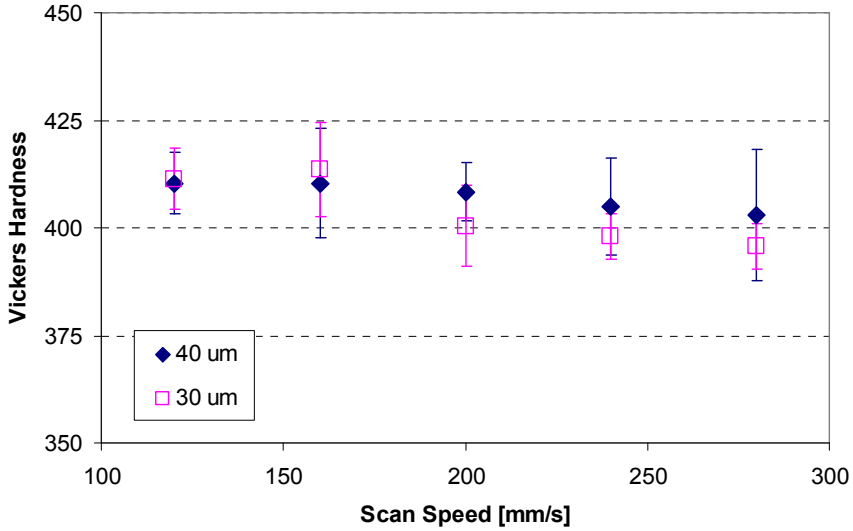

Figure 5.12 : Average micro hardness measured on cross-sections versus scan speed for CL50WS processed on the Concept Laser M3 Linear for different layer thicknesses with 95% confidence intervals (with a test load of 0.5 kg)

d. Microstructural investigation of CL50WS specimens

The microstructural investigation of the samples produced on Concept Laser M3 Linear machine is accomplished by preparing the samples' cross-sections in two directions. One cross-section is taken along the building axis (cs1–side) whereas the other has a normal parallel to the building axis (cs2-top) (see Figure 5.10). The samples are observed with optical (OM) and scanning electron microscopy (SEM). To reveal the microstructure, a mixture of 15 ml H_2O, 15 ml acetic acid, 60 ml HCl and 10 ml HNO_3 was used to etch the samples. In Figure 5.13, the micrograph taken on a top cross-section (cs2) is shown. The part was made on the Concept Laser M3 Linear machine with a layer thickness of 60 µm and a scan speed of 120 mm/s. The micrograph depicts the bi-directional scan tracks (shown with dashed arrows in the figure) which appear after the etching process and pores left after the process. As evident, spherical and irregular pore formations are possible. It is also observed that most of the irregular porosities are present on the connection of scan tracks, meaning that a scan spacing factor (a_1) of 70%, recommended by machine vendor, is too high for the tested layer thickness and scan speed. The overlap should be increased in order to have a better connection and less porosity (See §5.3 for a better explanation of scan spacing factors between consecutive scan tracks and sectors as well as the optimization of those scan spacing factors: a_1, a_2 and a_3).

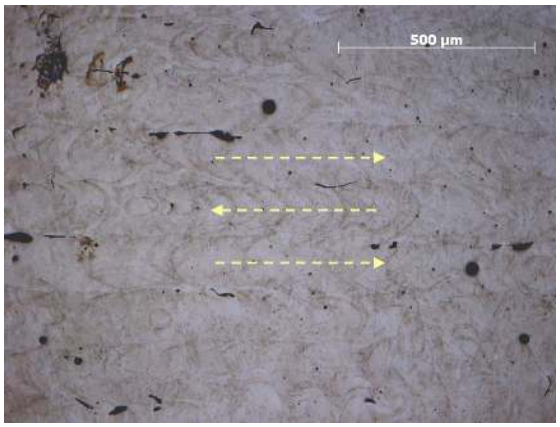

Figure 5.13 : Micrograph of cross-section (cs2) of a CL50WS sample after etching (layer thickness 60 µm and scan speed 120 mm/s)

The cross-section (cs1) taken along the building axis is depicted in Figure 5.14a. The sample was produced on the Concept Laser M3 Linear machine with island scanning. Therefore, the orientation of the tracks in one island was altered at each successive layer: in one layer the tracks are perpendicular to the cross-section; in the next layer the tracks are parallel to the section (See Figure 5.14b). As a consequence, those alternating tracks appear differently in the cross-section. If the scanning direction is taken towards the section, the cross-section of a scan track can be identified as curved lines showing the boundary of the melted track. Some EBSD scans were performed to analyze the reason for the presence of those dark melt edge lines after etching. However, the melt edge lines are so thin that the resolution of EBSD was not good enough to make an analysis on those lines. These curved melt pool lines formed during the last layer of the part can be used to calculate the depth of the melt pool which is about 80-90 µm for the case depicted in Figure 5.14a. Not only the melt pool lines of overlapping scan tracks are visible, but also the cross-sections of longitudinal scan tracks are present (see the arrows in the figure).

a) 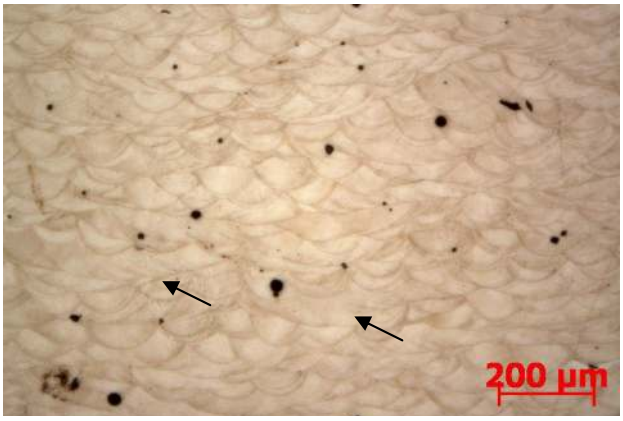

b) 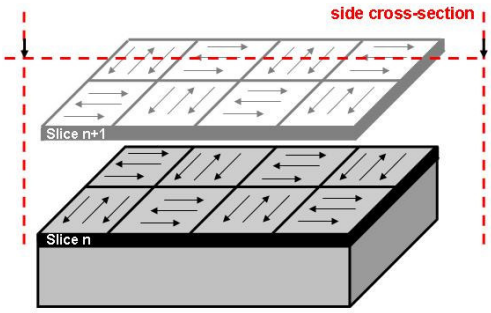

Figure 5.14 : a) Micrograph of cross-section (side) of a CL50WS sample after etching (layer thickness 30 µm and scan speed 150 mm/s) b)orientation of scan tracks in island scanning from layer to layer

The cross-sectional (cs1) views of two samples produced with different layer thickness values (60 and 40 µm) at a constant scan speed of 240 mm/s are demonstrated in Figure 5.15. As evident from the figure as well as the density results depicted in Figure 5.4, the pores are bigger and plenty when a higher layer thickness is employed during the process.

Layer Thickness: 60 µm

Layer Thickness: 40 µm

a) 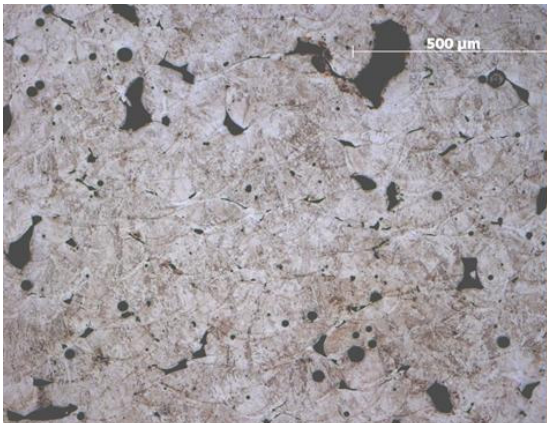

b) 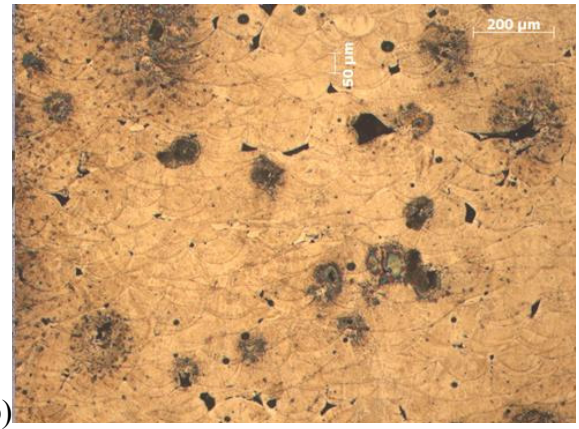

Figure 5.15 : Micrographs of the cross-sections (side) of two samples produced at a scan speed of 240 mm/s and a layer thickness of a) 60 µm b) 40 µm

The cross-sections were also observed under a SEM at high magnification. The SEM micrographs taken on two cross-sections (cs2 and cs1, respectively) are depicted in Figure 5.16. The micrograph (cs2) on the left shows again bi-directional scan tracks while the one on the right depicts cellular/dendritic morphology and epitaxial growth on a section perpendicular to the layer build sequence. In SLM, the cooling rate is very high and rapid solidification prevents formation of a lath martensite. Intercellular spacing is less than 1 µm for the cellular structure and this contributes to the excellent strength and hardness. These statements are also validated by other researchers working on direct metal laser sintering of maraging steel 300 processed on an EOS machine [152]. One could observe some large inclusions with a size of about 10-20 µm, visible in the two cross-sections in Figure 5.16 as dark spots. The EDX analysis carried out on these samples confirmed that these were titanium and aluminum combined oxides (TiO_2:Al_2O_3). Those inclusions deteriorate the mechanical properties of components, especially at aged conditions where the maraging steel is more brittle than as-built condition [152].

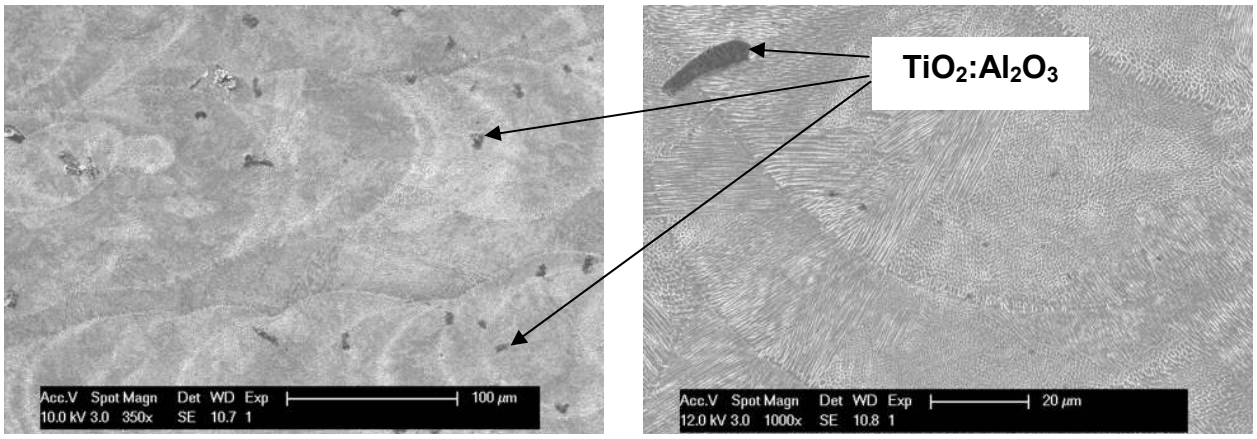

Figure 5.16 : SEM pictures of the cross-sections (cs2 top and cs1 side) of a sample produced with a scan speed 120 mm/s and layer thickness 60 µm

e. Effect of re-melting

In order to decrease the porosity present in SLM parts, laser re-melting may be an easy solution which can be applied during the process after each layer at a cost of longer production times. For some applications where 1-2% porosity plays a very critical role, this additional production time may not be very critical. Many mechanical and thermal properties, e.g. fatigue resistance, yield strength, corrosion resistance, ductility, thermal conductivity, etc. highly depend on the part density. One of the previous sections, §5.1.3c about hardness measurements is also in good agreement with this statement. Therefore, the effect of re-melting on the density and hardness is tested alongside with microstructural investigation.

The processing conditions of the tested parts are given in Table 5.4. Except for the last part, the SLM parameters were the same for all produced samples. The scan spacing factor to be utilized on the Concept Laser M3 Linear for a high density without any aligned porosity has been optimized yielding an scan spacing (a_1) of 62% of the beam diameter (180 µm) between scan tracks. The overlapping between islands (a_3) is also changed to be 50% of the beam diameter. The distance between the last scan track and the border of the islands (a_2) was taken as 35% of the beam diameter (for more details on the optimization of overlapping factors, refer to §5.3 about sectoral scanning). The laser power was taken as 105 W with the selection of big aperture. The scan speed was selected to be 150 mm/s to achieve a high density. One of the samples (part 1) was not treated with laser re-melting in order to make a comparison. The other two were exposed to laser re-melting with a different scan speed, and strategy. The last part was also exposed to laser re-melting after every layer. However, the scan speed during SLM was a bit higher than the other three parts (200 mm/s).

The SLM parameters and laser re-melting parameters for all parts are summarized in Table 5.4 with their measured densities by the Archimedes method.

Table 5.4 : Comparison of relative density, micro hardness and scan time for one layer for parts produced with different SLM and laser re-melting parameters

	SLM Parameters	**Laser Re-melting Parameters**	**Relative density (by Archimedes technique)**	**Micro hardness (HV) with a load of 0.5 kg**	**Scanning time for one layer**
Part 1	scan speed = 150 mm/s, laser power = 105 W, layer thickness = 30 µm a_1=62%, a_2=35%, a_3=50%	no re-melting	99.15%	395.8	t*
Part 2	same as given for part 1	island re-melting (every island is scanned twice in perpendicular directions with the same SLM parameters)	99.41%	412.6	2t*
Part 3	same as given for part 1	long scan vectors scan speed = 100 mm/s, laser power = 105 W, a_1=30%	99.48%	414.0	4t*
Part 4	scan speed = 200 mm/s, laser power = 105 W, layer thickness = 30 µm a_1=62%, a_2=35%, a_3=50%	island re-melting	99.25%	390.3	1.5t*

**approximately calculated based on the scan speed and scan spacing factor (a_1) for comparison*

As evident, all samples exhibit a very good density above 99% although laser re-melted samples give slightly higher results. It should be noted here that the optimization of scan spacing factors resulted in less amount of aligned porosity obtained with SLM without any laser re-melting. The differences between the samples with and without laser re-melting are clearer when the optical micrographs, given in Figure 5.17, are observed. The first row of micrographs shows the top cross-sections (cs2) of three parts where the scan tracks are clearly visible, whereas the second row illustrates the (cs1) side cross-sectional views. As evident from these micrographs, the amount of pores present in cross-section or on the top surface is much higher in the first part whereas it drops by 40% in the second and third parts compared to the first part (porosity drops from 0.85% to 0.52-0.59%). The micrograph taken on the cross-section of the third part, as shown in Figure 5.18b, depicts some porous slit-like zones throughout the part which may be due to long scan vectors with high overlap (see Figure 5.18c for scan tracks of laser re-melting). Figure 5.18a shows the cross-sectional view of the second part which is highly dense with only some spherical pores. Therefore, scanning every island twice with the same parameters is more preferable. The last part produced with a slightly higher scan speed also exhibited no aligned or irregular porosity.

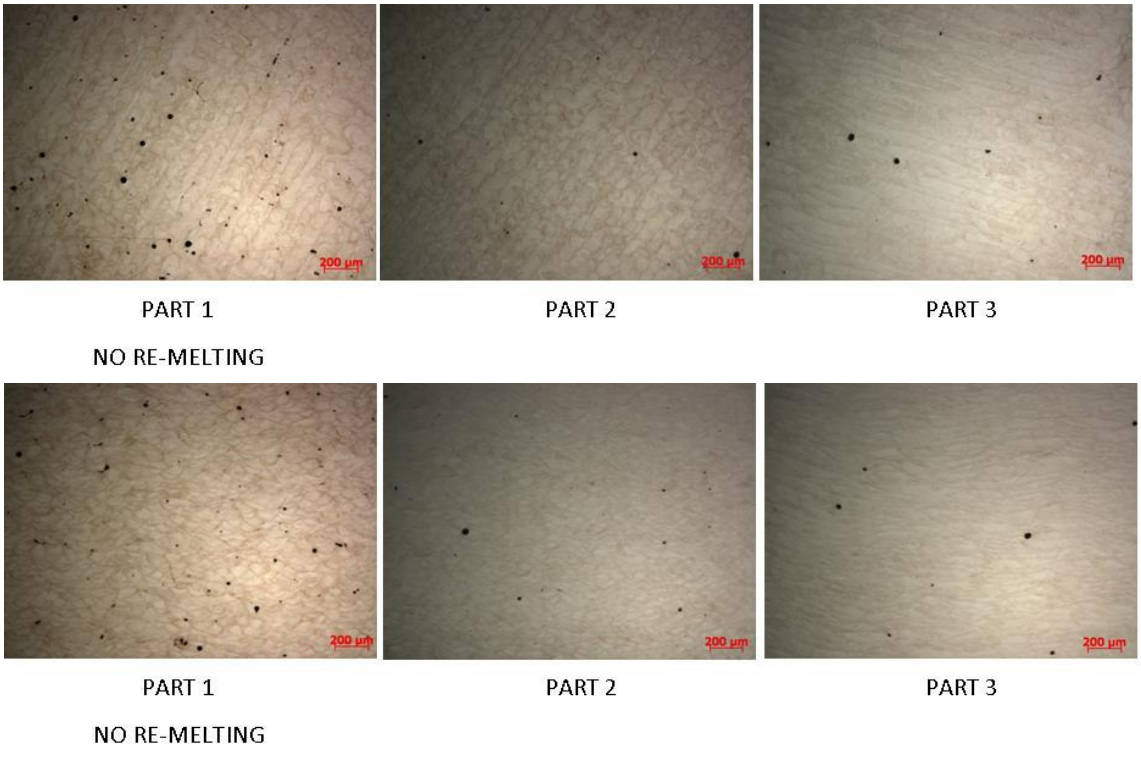

Figure 5.17 : Micrographs of (a) top surfaces (cs2) (b) cross-sections of the produced specimens (cs1)

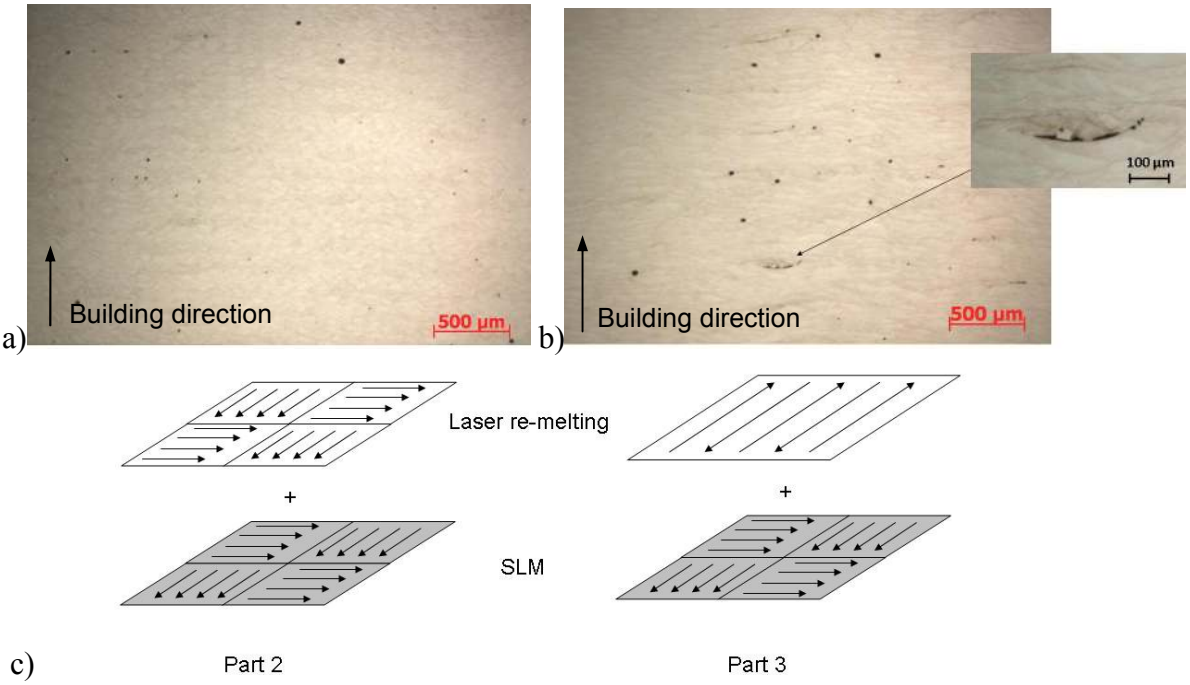

Figure 5.18 : Micrograph taken on cross-section of a) part 2 (cs1 – side) b) part 3(cs1 – side) showing slit-like porosity c)orientation of the laser re-melting and SLM scan tracks in part 2 and part 3

The micro hardness results of these parts, conducted with a test load of 0.5 kg, are also given in Table 5.4. In the solution treated condition (i.e. after solution precipitation heat treatment, but without age hardening heat treatment, see Chapter 1), the maraging steels presents a soft and deformable martensitic structure with hardness values between 280 and 320 HV [151-153]. The obtained hardness values after SLM of maraging steel 300 are 30% higher than those of normal solution treated maraging steel (See Table 5.4). In the literature, this is attributed to the natural

aging taking place during SLM which leads to formation of fine precipitates with a size of 20-100 nm [152].

For mechanical testing, it is very important to achieve almost full density without any aligned or irregular porosity. The density achieved by SLM without any laser re-melting is quite high, i.e. >99%. However, higher densities are still obtained after laser re-melting. Therefore, it was decided to perform mechanical tests on parts produced with settings of part 4 in Table 5.4, as those settings combine a high density due to laser re-melting and a relatively high production rate due to the re-melting and SLM scan speed of 200 mm/s.

f. Effect of heat treatment on hardness

The superior properties of the maraging steels, i.e. good strength and toughness, are achieved by the age hardening of a ductile, low-carbon body-centered cubic (bcc) martensitic structure with relatively good strength. Therefore, the aging treatment is standard for maraging steels. Even the name 'maraging' of these steels come from 'aging of martensite'. It is mainly aimed to form a uniform distribution of fine nickel-rich intermetallic precipitates during the aging of the martensite. These precipitates serve to strengthen the martensitic matrix. Secondly, it is aimed to minimize or eliminate the reversion of metastable martensite into austenite and ferrite by aging [154]. Fortunately, the kinetics of the precipitation reactions of iron-nickel maraging steels are such that significant age hardening of about 20 HRC points occurs before the reversion reaction producing austenite and ferrite starts.

Depending on the temperature, two things may happen when the martensite of maraging steels is re-heated for aging. If the reheating temperature exceeds the austenite start temperature, the previously formed martensite transforms back to austenite of the same composition. Otherwise, the martensite initially age hardens, followed by decomposition into equilibrium ferrite and austenite compositions. The rate of this reaction occurs depends on the re-heating temperature. This phenomenon of slow austenite reversion coupled with rapid age hardening forms the basis for the aging heat treatments of maraging steels [154].

In the literature, the hardening of maraging steels during aging has been attributed to two mechanisms, namely the short-range ordering in the cobalt-bearing solid solution and precipitation of nickel-rich intermetallic compounds in the lath martensitic structure. The short-range ordering reaction occurs first, exerting a significant influence on the later precipitation reaction. Therefore, two mechanisms are closely interrelated although they occur separately. The short range ordering phenomenon results in the formation of iron-, cobalt- and nickel-rich regions. The two mechanisms are strongly interrelated since the useful precipitates formed in maraging steels during aging, intermetallic compounds, i.e. nickel-molybdenum and nickel-titanium compounds ($Ni_3(Mo, Ti)$), occur primarily in the nickel-rich regions that were formed in the short-range ordered structure. Moreover, the formation of iron- and cobalt-rich regions helps to stabilize the same precipitates due to strong interatomic attraction between iron and cobalt inhibiting the diffusion of iron to the nickel-rich regions. This delays the replacement of the metastable nickel-rich precipitates by equilibrium iron-rich precipitates [154].

The aging heat treatment for maraging steels can be performed for different durations at various temperatures providing that the temperature is lower than the austenite start temperature. For maraging steel 300, the values recommended by the ASM Handbook are 3 to 8 hours at a temperature between 460 and 510°C [154]. Therefore, the specimens produced on the Concept Laser M3 Linear machine with laser re-melting were heat treated in a furnace at MTM under argon atmosphere with different conditions summarized in Table 5.5. The resulting hardness values are also given in the same table, whereas Figure 5.19 shows the same measured micro hardness results in a plot vs. various aging durations at different maximum temperatures. When the maximum

temperature that the part is heated up to is 460 °C, the hardness shows a linear relationship with aging time. As you keep the part longer at this temperature, the hardness continues to increase without any sign of overaging. However for other temperatures tested in the scope of this study, at prolonged durations, the hardness starts to slightly drop. This is an indication of overaging meaning that the reversion of metastable martensite upon re-heating into austenite, which is an equilibrium phase, starts. Additionally, when a maraging steel is overaged, the coarsening of the intermetallic precipitates takes place. These two phenomena together decrease the hardness as the part is kept at elevated temperatures for a prolonged time. The supplier of the maraging steel powder recommends an aging heat treatment after SLM of 3 hours at 480°C which increases the hardness above 634 HV. As a result of these tests, it is seen that keeping the parts 5 hours at 480°C results in a higher micro hardness close to 650 HV. Although the maximum hardness is achieved with the combination of 8 hours at 460°C, the former heat treatment (5h at 480°C) is preferred due to shorter aging duration. The shrinkage of the samples is also tested and found to be less than 0.7%.

Table 5.5 : Age hardening conditions and resulting hardness with a test load of 0.5 kg

#	***Time (hours)***	***Maximum Temperature (°C)***	***Hardness Results (HV)*** Mean ± 95% confidence interval
1	3	460	618.3 ± 8.6
2	3	480	634.8 ± 9.7
3	3	500	645.3 ± 8.2
4	5	460	638.0 ± 9.2
5	5	480	648.4 ± 9.8
6	5	500	642.6 ± 6.7
7	8	460	658.3 ± 9.4
8	8	480	648.0 ± 8.5
9	1	490	596.0 ± 9.1
10	2	490	628.0 ± 6.4
11	3	490	633.0 ± 4.0

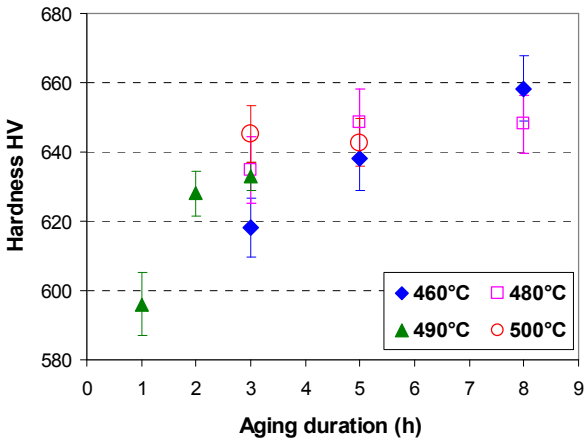

Figure 5.19 : Effect of various age hardening treatments on the micro hardness with 95% confidence intervals with a test load of 0.5 kg

In the literature, the model for kinetics of early stages of aging of precipitation hardenable alloys is given by an expression [152] derived by the equation of Avrami [155]:

$$\Delta H = (Kt)^n \qquad (5.1)$$

where K is the temperature dependent rate constant, n the time exponent (slightly temperature dependent), ΔH the increase of hardness (HV), t the aging time.

The equation is only valid for the parts that did not reach the overaging region. Therefore, two cases from our study which did not show any indication of overaging, i.e. at 460°C and 490°C, are used for the determination of the constants n and K. These constants are obtained by plotting $\ln(\Delta H)$ versus $\ln(t)$ as shown in Figure 5.20. For the calculation of $\ln(\Delta H)$, 390 HV is taken as the starting hardness after SLM (as given in Table 5.4 for part 4) and the average micro hardness values obtained after aging treatments are used. High correlation coefficients are obtained due to small number of data points. Nevertheless, the two lines give very close results for n which is slightly temperature dependent (See Table 5.6). It is normal that the temperature dependent rate constants (K) obtained with two temperatures are significantly different. Thus, using these constants and Eq. 5.1, one can predict the hardness increase by applying different aging times at these maximum temperature values.

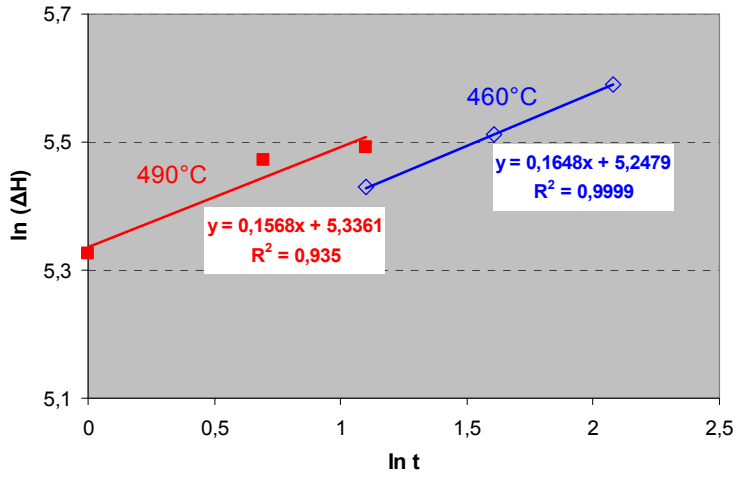

Figure 5.20 : $\ln(\Delta H)$ *vs.* $\ln(t)$ *for the samples aged at 460 and 490°C*

Table 5.6 : Constants in the model for kinetics of early stages of aging precipitation hardenable alloys

Temperature	***n: the time exponent***	***K: temperature dependent rate constant***
460°C	***0.165***	***6.75. 10^{13}***
490°C	***0.157***	***6.02. 10^{14}***

5.1.4 Conclusions

In this study, the Selective Laser Melting of maraging steel 300 was taken under investigation with many aspects. This section presented the effect of different process parameters, namely the scan speed and layer thickness, on the obtained density and surface quality on two machines employing different laser sources. It is concluded that a machine with a fiber laser can be operated at a higher scan speed and layer thickness values to obtain high density parts compared to one with a Nd:YAG laser. To achieve a maximum density, there is a certain minimum threshold for the energy density and below that the density decreases with decreasing energy density. Above the threshold, the

density is not significantly affected by increasing energy densities in the tested scan speed range. Besides, too high roughness values obtained at very high energy inputs deteriorate the obtained densities. For the Concept Laser M3 Linear machine, the effect of the scan speed and layer thickness on the relative density was found to be important, especially at high scan speed. With rising layer thickness, the density dropped significantly in this range. At low scan speed where the maximum density is obtained, the effect of layer thickness and scan speed become less significant. For the Concept Laser M3 Linear machine with an Nd:YAG laser, the maximum density is obtained at the lowest scan speed values used in the tests. For the EOSINT M270, the maximum density is achieved at a mid-range scan speed depending on the selected layer thickness, as recommended by the machine vendor. Below or above this optimum scan speed range, the density decreases due to either too low energy input resulting in partially melting or too high energy input leading to very bad surface quality. The influence of layer thickness on the relative density at the optimum range of the scan speed is also very little. The effect of the layer thickness on the surface quality is more important than the influence of the scan speed. As the layer thickness is increased, higher roughness values are obtained due to bigger melt pools. As expected, the macro hardness results showed that the porosity decreases the hardness that can be achieved. The influence of the scan speed and layer thickness is not as significant as the porosity itself. Therefore, changing the process parameters in the selected and tested ranges does not change the cooling rates significantly to alter the obtained hardness in the parts. In order to test the mechanical properties of maraging steel 300, the maximum density should be attained in the specimens. Laser re-melting employed after every layer is a good solution to increase the density at a cost of higher production times. With this technique, the mechanical specimens produced by SLM did not have any aligned porosity or irregularity.

The effect of aging has been tested on the specimens produced by combining laser re-melting and selective laser melting. Different aging times and temperatures have been tested to find out the best combination. 5 hours at 480°C is found out to give high hardness within a relatively short time. With aging tests, it is seen that keeping the specimens at a prolonged times in the heat treatment may deteriorate the material properties since it causes the precipitates to coarsen as well as austenite reversion. These two mechanisms decrease the hardness. Therefore the aging heat treatment should be selected in a range where overaging has not started yet. In the scope of this study, the constants in the expression derived from Avrami's equation are determined for this material as a result of aging treatments done at different temperatures. The SLM parameters used with laser re-melting parameters are used to build mechanical specimens which were age hardened 5h at 480°C in argon atmosphere. The results of toughness tests regarding this material along with others (stainless steel and Ti6Al4V) are given in §5.2.

5.2 Charpy Impact Tests on Metallic SLM parts

5.2.1 Introduction and Literature Review

The mechanical material properties obtained with SLM might be different than the ones of bulk material produced by conventional techniques due to several reasons. Laser processing of materials generally results in high cooling rates due to the short laser/material interaction time due to high scan speeds and high thermal gradients. This might lead to the formation of non-equilibrium phases such as glasses, quasi crystalline phases and new crystalline phases with extended composition ranges [6]. Finer structures may be observed in the microstructure at sufficiently high cooling rates compared to conventional manufacturing methods. Moreover, gas bubbles can become entrapped in the material during solidification due to various causes such as decrease in the solubility of the dissolved elements in the melt pool during cooling and solidification, chemical reaction or trapped gas [6]. Many material properties, such as strength, thermal conductivity, corrosion or wear resistance and ductility highly depend on microstructural properties. One of the most striking

examples of a structure-sensitive property is the fracture toughness which measures the ability of a structural material to inhibit crack propagation. Very small changes in the chemical composition and highly localized grain boundary segregation may cause a catastrophic loss of ductility [156]. Thus, the mechanical properties of SLM parts do not only depend on material composition, but also on the microstructures and the presence of defects in the final product that are determined by the process parameters and manufacturing strategy [157]. This dependence is illustrated in Figure 5.21.

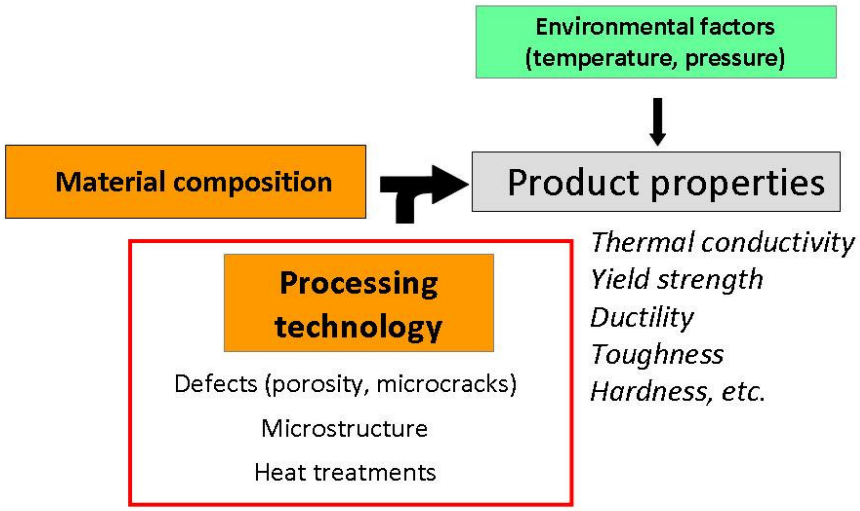

Figure 5.21 : The dependence of product properties on the material composition, processing technology and environmental factors

The mechanical properties obtained with SLM and other layer manufacturing processes are widely studied by many research groups in the world. At the University of Leuven, the mechanical properties (hardness, tensile and bending properties) of SLM samples from Ti6Al4V materials were studied concluding that the obtained mechanical properties of SLM samples are comparable to those of bulk material [158]. Paul et al. reports about an investigation of additive laser cladding of Inconel-625 components by the Taguchi method. They produced tensile and impact tests in order to study the effects of different processing parameters, such as powder feed rate, scan speed and laser power [159]. For another laser cladding process, i.e. Laser-Engineered Net Shaping (LENS™), mechanical properties of Ti6Al4V have been investigated with tension, fatigue and crack-growth tests. The tests indicate that the static tensile strength and ductility, fatigue strength and fracture toughness of hot isostatic pressurized (HIP) parts produced via LENS™ compare favourably to those of wrought products [160]. The mechanical properties of pure titanium samples processed by SLM are also investigated [161] showing that the impact and torsional fatigue strengths are low because of porosity and oxygen pick-up, although the tensile strength tests show results comparable to the wrought material. A recent study by Spierings, investigates the influence of the powder particle size distribution on the mechanical properties by tensile testing [162]. Tensile testing is also used by other research groups such as the work by Sehrt for the static strength analysis of SLM parts made of stainless steel. This study investigates the possible influences of different manufacturing orientations, exposure strategies and surface finishes on the mechanical properties [163]. There are also some investigations for other layer manufacturing processes such as for stereolithography [164] and selective laser sintering [165, 166]. Some computer tools were also developed to simulate the mechanical properties of scaffolds for tissue engineering as a function of the pore size and selected material [165, 167].

In this research, Charpy impact tests are applied to samples that were produced by SLM from three different metallic powders; a titanium alloy (Ti6Al4V) which is commonly used for medical applications, stainless steel AISI 316L (X2CrNiMo18-14-3) and 18Ni-300 (maraging steel 300: X3CoMoTi18-9-5). The influence of various heat treatments applied on the samples after SLM

process was investigated as well as the effect of the building axis. Hardness measurements were also conducted and the microstructures of the specimens were analyzed.

5.2.2 Experimental Procedure

Three different materials (from different suppliers) and three different machines were used during the production of the specimens. Table 5.7 summarizes the use of materials and machines. The stainless steel AISI 316L and maraging steel 300 were both processed with island scanning on a Concept Laser M3 Linear machine equipped with a 100 W Nd:YAG laser and on an EOSINT M270 machine which employs a 195 W Yb-fiber laser. The third powder material, titanium alloy Ti6Al4V, is processed only on a self-made SLM machine at the University of Leuven equipped with a 300 W fiber laser. All specimens were manufactured with the selection of optimized parameters for density and roughness. Figure 5.22 depicts the scanning electron microscopy images of three powder materials showing that they bear spherical or near-spherical morphology with different particle size distributions as given in Figure 5.23.

Table 5.7: Materials and machines used in this study

Powder	**Maraging Steel** *(MS1 and CL50WS)*	**AISI 316 L** *(CL20ES and from EOS)*	**Ti6Al4V**
Machine	EOSINT M270 Yb-Fiber laser 200 W and Concept Laser M3 Linear (Nd:YAG 100 W)	Concept Laser M3 Linear (Nd:YAG 100 W) and EOSINT M270 Yb-Fiber laser 195 W	Self-made LM machine Yb:YAG fibre laser 300 W

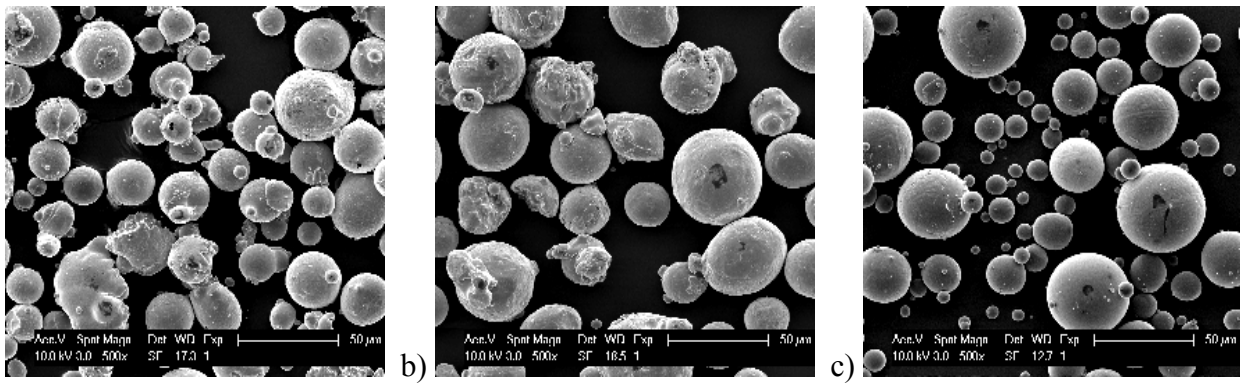

Figure 5.22 : Powder particles observed with scanning electron microscopy a) maraging steel 300 from EOS (MS1) b) AISI 316L stainless steel from Concept Laser (CL50WS) c)Ti6Al4V

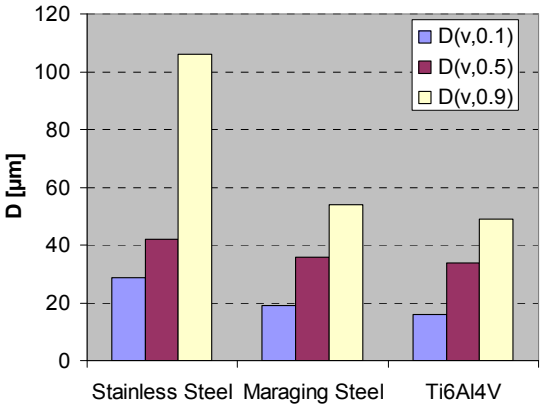

Figure 5.23: Powder particle size distribution (CL20ES, MS1 and Ti6Al4V)

The Charpy impact test is used to determine material toughness by hitting a test specimen with a hammer, mounted at the end of a pendulum (See Figure 5.24a). The specimen is broken by a single blow from the pendulum that strikes the middle of the specimen on the un-notched side. The height of rise subtracted from the height of fall gives the amount of energy absorption involved in deforming and breaking the specimen. A V-shaped notch is generally used in the impact specimen in order to control the fracture process by concentrating stress in the area of minimum cross-section. In this study, Charpy tests are done according to ASTM E23 standard [168]. The size of the standard specimen is 10x10x55 mm with a notch as defined in the same standard.

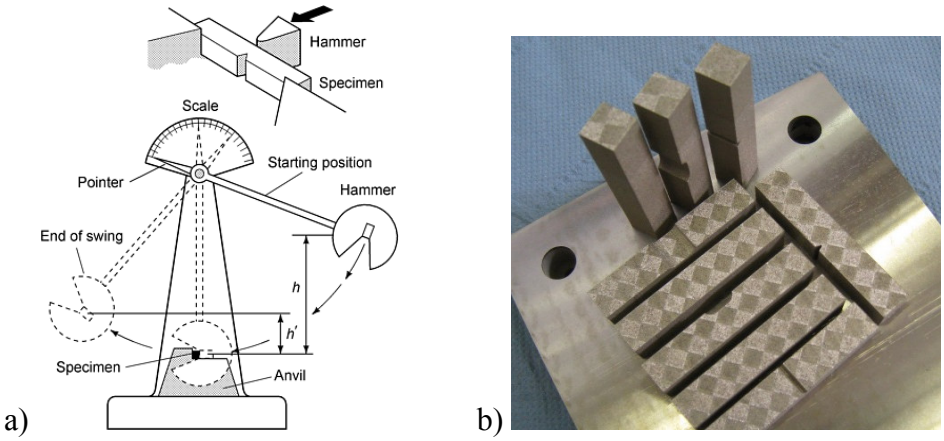

Figure 5.24: a) Charpy impact test setup [169] b) Produced specimens by SLM in three building axes on Concept Laser with AISI 316L

The experimental procedure was the same for all specimens. First, the samples were made by SLM (See Figure 5.24b for AISI 316L specimens produced on Concept Laser M3 Linear) and then they were cut off the base plate by electro-discharge machining (EDM). Due to the SLM process, the loose powder that should stay as un-melted around the scanned contours sometimes melts and sticks to the part walls. In order to remove these loosely sticking powder particles, all produced samples were treated with sand blasting. Afterwards, the densities of the parts were measured with Archimedes method (See Figure 5.25). The theoretical densities for AISI 316L, Ti6Al4V and the maraging steel 300 were taken as 8.0, 4.3 and 8.1 g/cm^3, respectively. Figure 5.25 depicts that all specimens have an average relative densities of more than 98.5%. The next step was to apply the impact test at room temperature if no heat treatment was applied. Otherwise, the parts were first treated in a furnace with an argon atmosphere according to a certain heat treatment cycle. After the impact test, the broken surfaces and the parts' insides were analyzed for their fracture surfaces and microstructures. Vickers hardness measurements were also conducted.

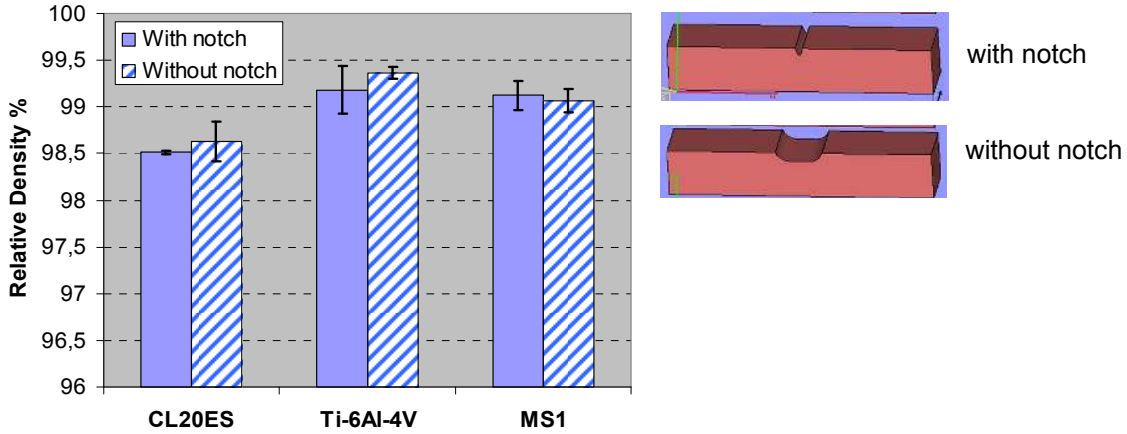

Figure 5.25: Relative density results of the specimens by Archimedes method

Other than the standard specimen specified in the ASTM E23 standard [168], two more specimens were designed to be produced by SLM to test different factors. The part designs are shown in Figure 5.26a. One of the specimen designs did not include any notch or a smaller cross-section (design: notch to be made by EDM). In this case, a bar was produced by SLM and then the standard notch was made by EDM. In the second design, there was no notch but the minimum cross-section length was identical to the minimum cross-section of the standard specimen (i.e. cross-section under the notch). This design was to test if the high roughness values of SLM causes any stress-concentrating notch behaviour during the fracture. The coordinate system attached to the part is also shown in Figure 5.26b which demonstrates a part produced while the building direction coincides with the x-axis.

a) 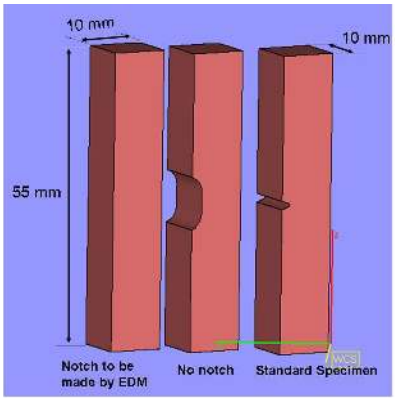

b) 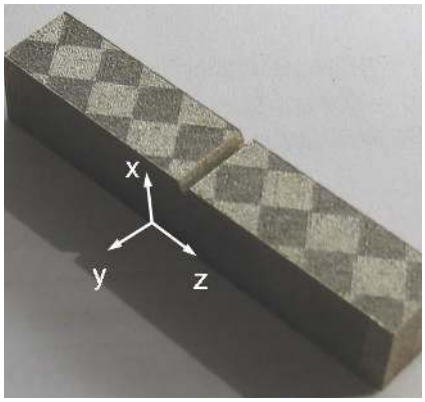

Figure 5.26: a) Three part designs to be used in Charpy tests b) orientation of a standard specimen manufactured with the building axis coinciding x-direction

5.2.3 Experimental Results And Discussions

In this section, the experimental results are presented separately for each material. The toughness results as well as other problems or microstructural features are explained.

a. Ti6Al4V

All specimens from Ti6Al4V were processed on the in-house developed LM machine to test the effect of building axis and different heat treatments. As a starting experiment, the specimens were produced with nominal parameters (a laser power of 42 W, a scan speed of 225 mm/s, a layer thickness of 30 μm and a hatch spacing of 74 μm) that were optimized for density in two designs: standard specimen with a notch and no-notch specimen where the minimum cross-section is kept the same with the standard specimen. The cross section of one of the specimens is shown in Figure 5.27. The acicular Ti6Al4V parts consist of large grains oriented along the building direction. The elongated grains are the result of epitaxial solidification and extend over multiple layers. Inside the grains a needle-like martensitic phase, α', which is formed as a result of the rapid solidification, can be distinguished instead of the two-phase hexagonal close packed (hcp) alpha, α, and body centered cubic (bcc) beta, β, structure that would be present in equilibrium conditions. The micro Vickers hardness is 369 ± 5. The hardness that is achieved in Ti6Al4V with SLM increases as the energy density is increased in the range of 370-420 HV [158]. Hardness values of bulk material from literature vary from 340 to 395 HV depending on thermal treatment. The hardness of SLM samples is higher, because during the process the melt pool cools down very rapidly when the laser beam has passed [158]. The density obtained with Ti6Al4V parts was measured to be about 99% (See Figure 5.25). In order to check the repeatability of the process, 3 replicates for each specimen design and material were produced with a building direction parallel to the x-axis of the specimen. The Charpy impact testing of this material without any heat treatment resulted in an average toughness energy of 11.5±0.64 J for the standard specimens and an average toughness energy of

55.59±16.02 J for no-notch specimens with a 95% level of confidence (See Figure 5.28). The Charpy test results show that the specimens of the same material with and without a notch absorb quite different energy values before breakage. For all materials, the specimens with a notch have less resistance to breakage which means that the high roughness of the SLM process does not behave like stress-concentrating notches. Both specimen designs follow the same trend for three materials. As shown in Figure 5.29, fracture of the Ti6Al4V parts is mainly brittle as indicated by the minor lateral deformation of the cross section at the position of fracture.

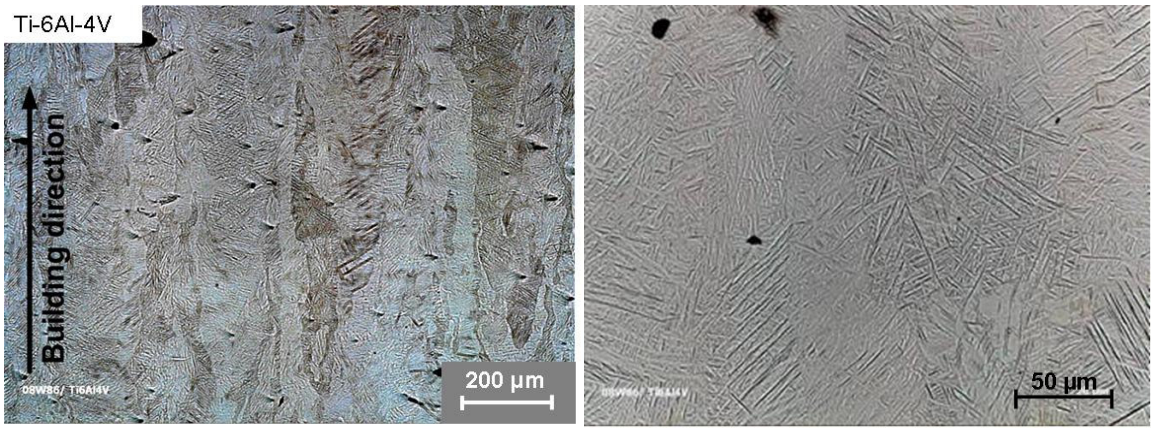

Figure 5.27: Micrographs of etched SLM parts – Ti6Al4V

For the Ti alloy, two different heat treatments were applied. The first one was the full annealing conducted at 735°C for 2 hours in a BIP argon furnace. The second heat treatment was the stress relieving at 595°C for 3 hours. As illustrated in Figure 5.30, the first heat treatment did not improve or worsen the toughness of this material as well as the hardness (362 ± 9 HV). The second heat treatment decreased the toughness of Ti alloy slightly and increases the hardness to 386 ± 5 HV. During heat treatment the martensitic structure transforms into a mixture of hexagonal closed pack (hcp) alfa and body-centered cubic (bcc) beta phases. The lower Charpy energy after heat treatment at 595°C may be attributed to the higher amount of less ductile alfa phase present than after heat treatment at 735°C. However, as evident from Figure 5.30, the common heat treatments applied after SLM for this material does not increase the ductility or the toughness due to insufficient phase transformations. A re-crystallization annealing may be a better heat treatment to be applied to form more beta phase which is more ductile.

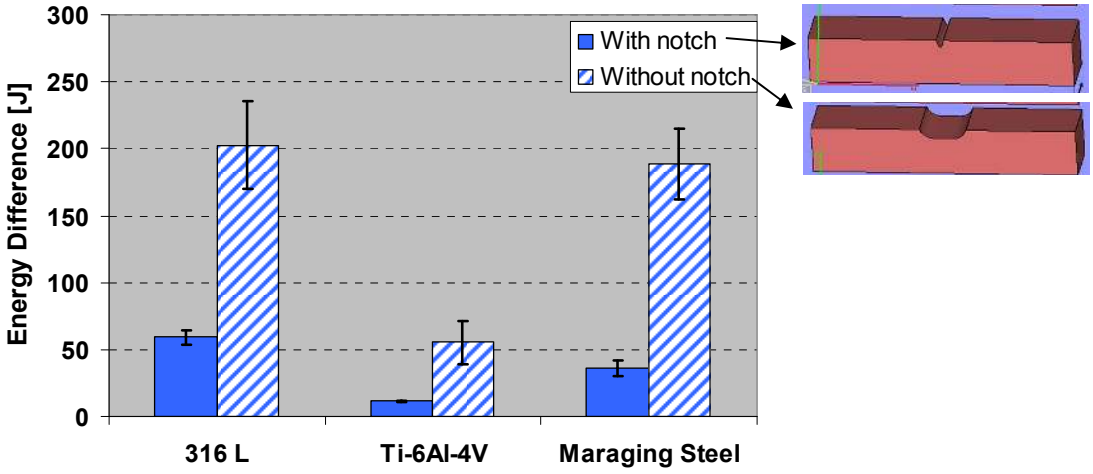

Figure 5.28: The Charpy results of three materials for two designs

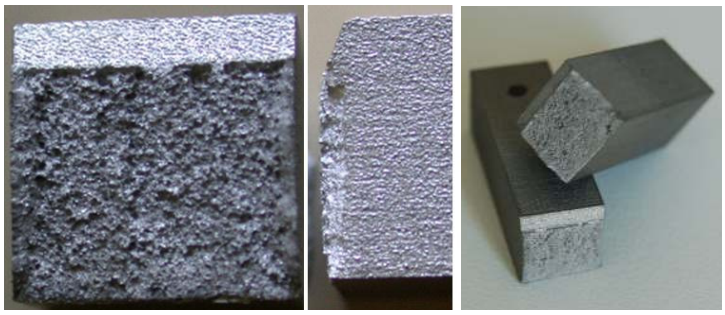

Figure 5.29: Fracture surface of Ti6Al4V standard specimens

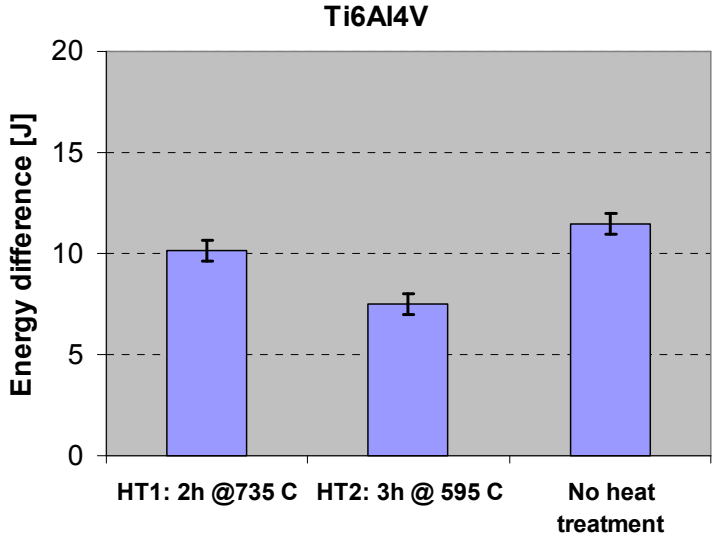

Figure 5.30: The Charpy results of Ti alloy for full annealing and stress relieving compared to not heat treated parts

b. AISI 316L Stainless Steel

The cross section of the parts produced on a Concept Laser M3 Linear from CL20ES powder and observed with SEM is shown in Figure 5.31. The stainless steel AISI 316L part consists mainly of an austenitic phase, as revealed by X-Ray Diffraction. The cellular-dendritic microstructure looks similar to the structure obtained after casting of austenitic stainless steel: delta ferrite in an austenitic matrix. Normally, delta-ferrite should be avoided since it is a high-temperature ferrite which should be totally reverted to austenite during cooling. However, due to high cooling rates encountered in the process, there is not enough time for such reversion. The micro Vickers hardness (0,5 kg) is measured to be 235 ± 5 which is higher than the one of conventionally produced stainless steel (200 HV) [170].

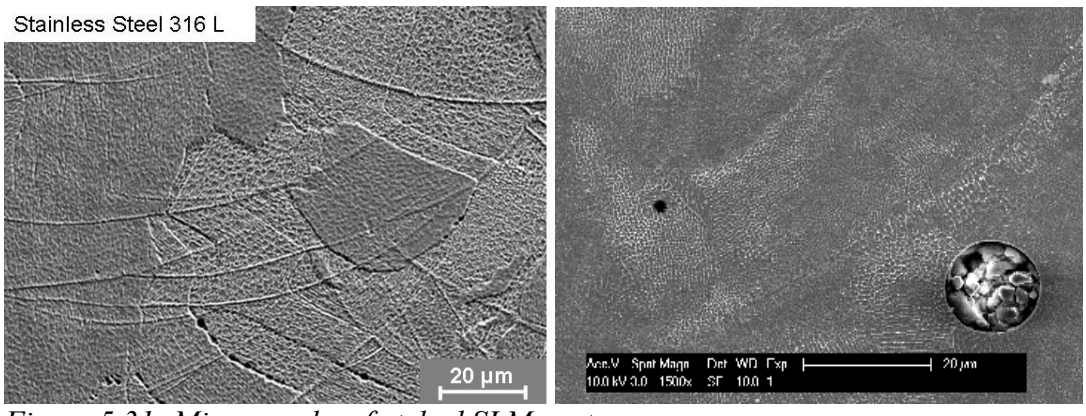

Figure 5.31: Micrographs of etched SLM parts

Compared to conventionally produced specimens, the Charpy test results for stainless steel specimens indicate a very low toughness energy of 59.19±4.83 J for standard specimen design and a toughness energy of 202.74±29.12 J for no notch samples when produced by SLM on a Concept Laser M3 Linear machine (See Figure 5.28). Moreover, all stainless steel specimens have a waved fracture surface as evident in Figure 5.32. Figure 5.33 and Figure 5.34 show that the waviness is a result of aligned porosity along which the fracture has occurred. The reason for such an aligned porosity in the samples is the wrong selection of scan spacing factors (a_1=70%, a_2=a_3=13%) resulting in too little overlapping. Island scanning is a good scanning strategy which decreases the residual stresses by about 40% in SLM parts [13]. However, if the spacing parameters are selected in an improper way, it may still result in high density (when measured by Archimedes method) but can create aligned porosity at the interface between islands or in between scan tracks leading to dramatic failures. An insufficient overlap between islands led to a fracture following the islands' edges as shown in Figure 5.35 and a very low toughness. Therefore, as explained in §5.3, the optimization of scan spacing factors between scan tracks and islands is crucial not only for high density but also for good mechanical properties without any unexpected failures.

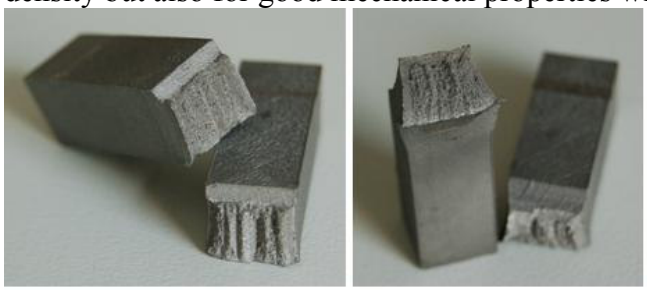

Figure 5.32: Fracture surfaces of 316L stainless steel specimens in macro scale

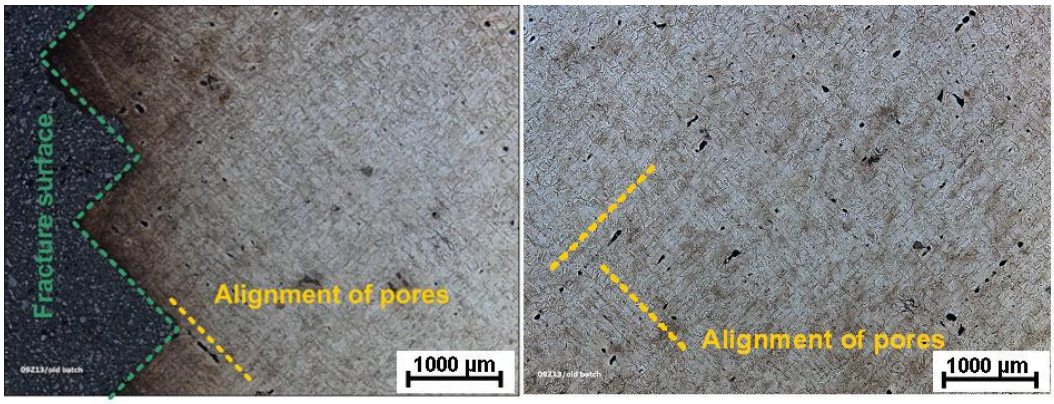

Figure 5.33: Top cross section of stainless steel 316L perpendicular to the building direction

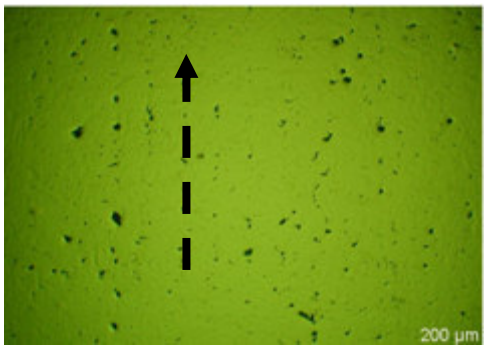

Figure 5.34: Side cross section of AISI 316L showing oriented porosity along the building direction

After the scan spacing factors are optimized for island scanning, new standard specimens were produced with a lower scan spacing between scan tracks (a_1 = 62% which was 70% in the former

case) and higher overlapping between islands (a_2 = 35% and a_3 = 50% which were 13% in the former case) (See §5.3 for details of the optimization) on a Concept Laser M3 Linear machine with CL20ES powder. Laser re-melting of every island with scan tracks perpendicular to melting scan tracks was also conducted after every layer to improve the density. Moreover, the same material (from a different supplier) is used to build parts on an EOSINT M270. The density results of three different sets of specimens are depicted in Figure 5.36 whereas the toughness results after full annealing (2 hours at 1095 °C) are shown in Figure 5.37 for three different building directions.

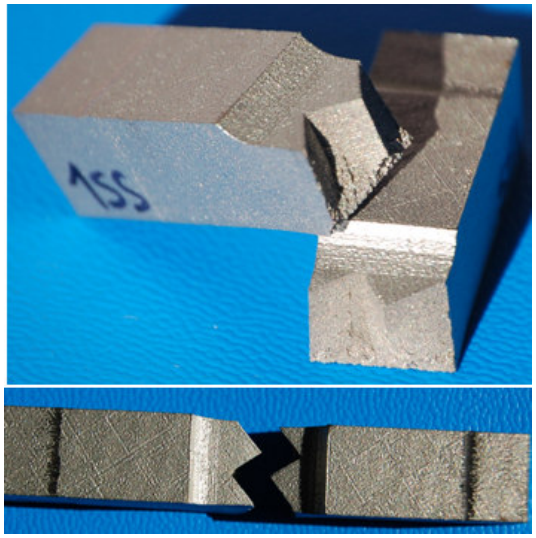

Figure 5.35: AISI 316L parts produced on a Concept Laser M3 Linear with island scanning and insufficient overlapping between islands

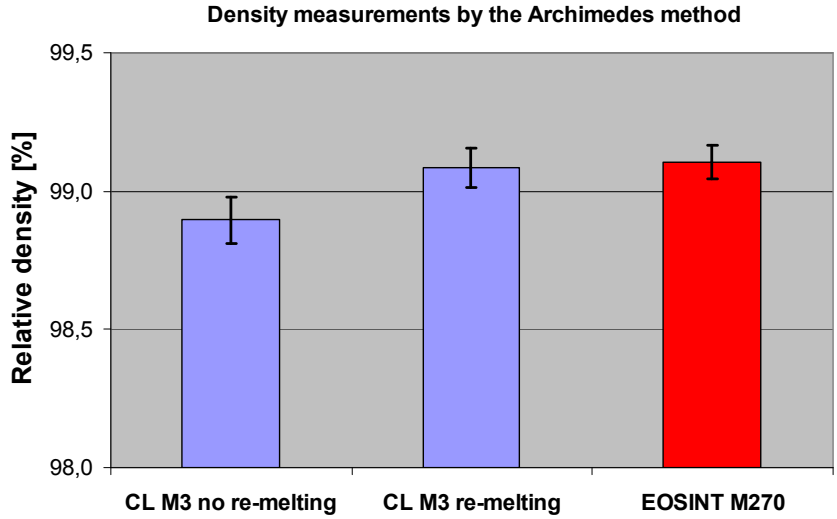

Figure 5.36: Density results of AISI 316L parts produced on a Concept Laser M3 Linear with and without laser re-melting and on a EOSINT M270 machine with the same material from a different supplier

As shown, laser re-melting improves the density and EOS parts produced without laser re-melting exhibit almost the same density with re-melted parts produced on a Concept Linear M3 Linear machine (about 99.1%). The toughness results, shown in Figure 5.37, reveal that the building axis is not necessarily the weakest direction if there is a good connection between layers, i.e. enough wetting of the previous layer. The optimization of scan spacing factors on the Concept Linear M3 Linear machine improved the toughness by about 50% and the fracture surfaces did not show any strange fracture pattern as shown in Figure 5.38. Figure 5.39 depicts the side and top views of the specimens built along two different axes and shows that the fracture was ductile.

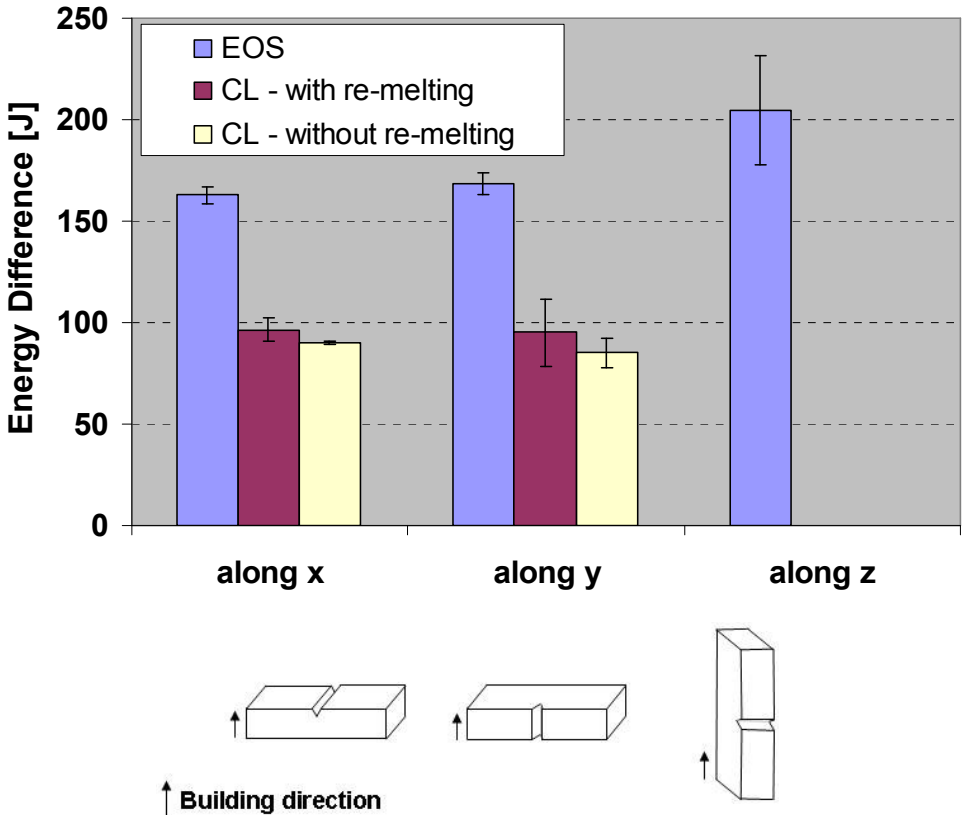

Figure 5.37: Toughness results of AISI 316L parts produced along different building axes on a Concept Laser M3 Linear with and without laser re-melting and on a EOSINT M270 machine with the same material from a different supplier

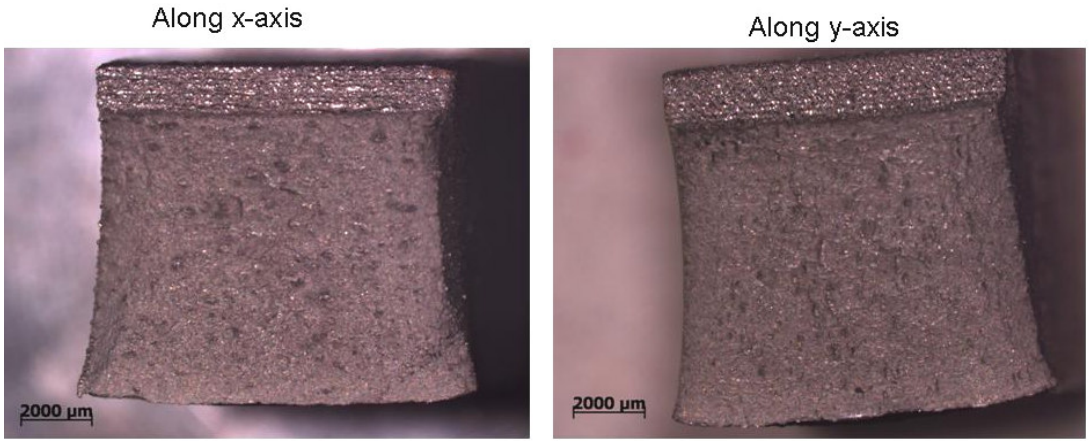

Figure 5.38: Fracture surfaces of 316L specimens built on Concept Laser M3 linear machine without re-melting

Although the toughness results were improved by 50% with the optimized scan spacing factors (90 ± 1 J), the results of EOS parts are much higher (163 ± 4 J). The results obtained with EOS specimens are similar to what is achieved with conventional production techniques [171]. The fracture surfaces for EOS specimens are displayed in Figure 5.40 and Figure 5.41 showing a more ductile fracture than Concept Laser specimens. The material characterization conducted at VITO by Marleen Rombouts showed that the specimens produced on EOS or Concept Laser machines both have oxides observed on the fracture surfaces as Figure 5.42 and Figure 5.43 reveal and that the cross-sections depict similar amounts of porosities. The reason for higher toughness exhibited by EOS specimens may be the material composition of the powders supplied by the machine vendors and is under investigation.

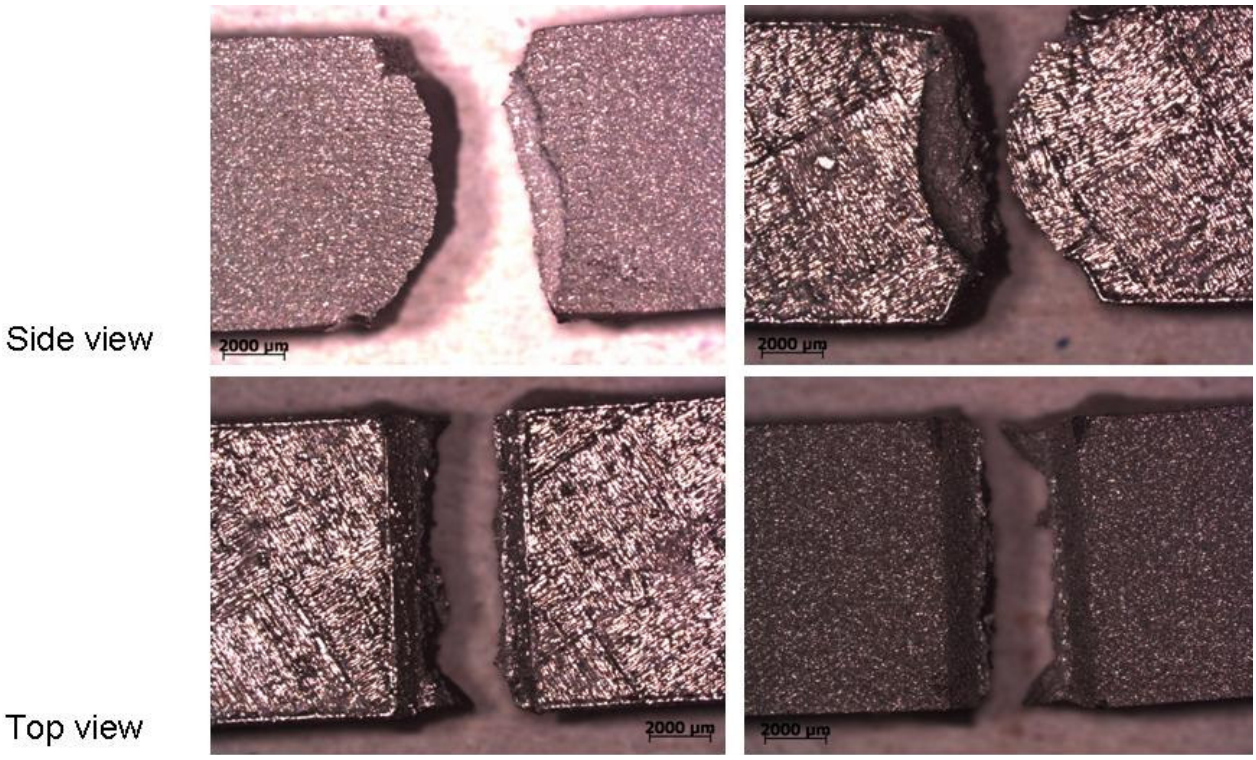

Figure 5.39: Side and top views of 316L specimens built on Concept Laser M3 linear machine without re-melting after Charpy testing

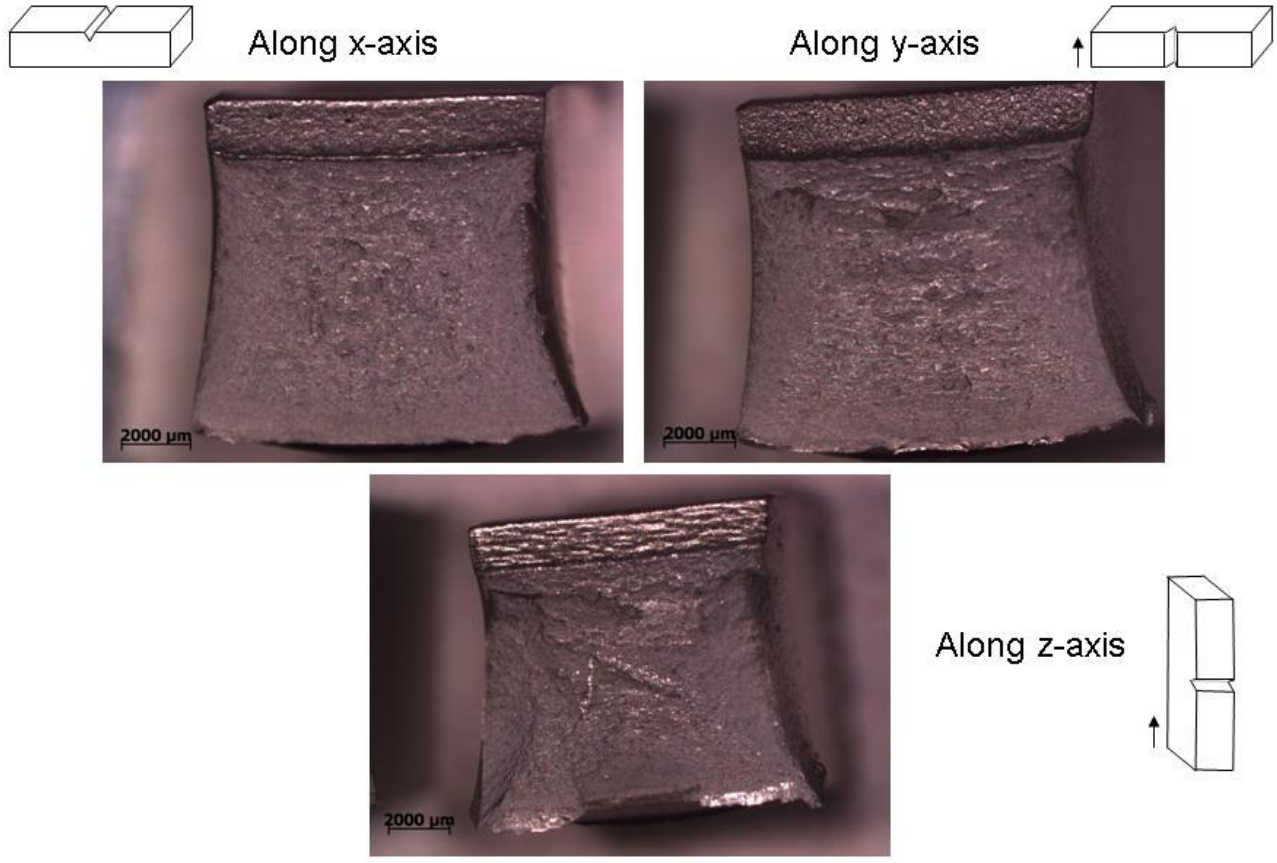

Figure 5.40: Fracture surfaces of 316L specimens built on EOSINT M270

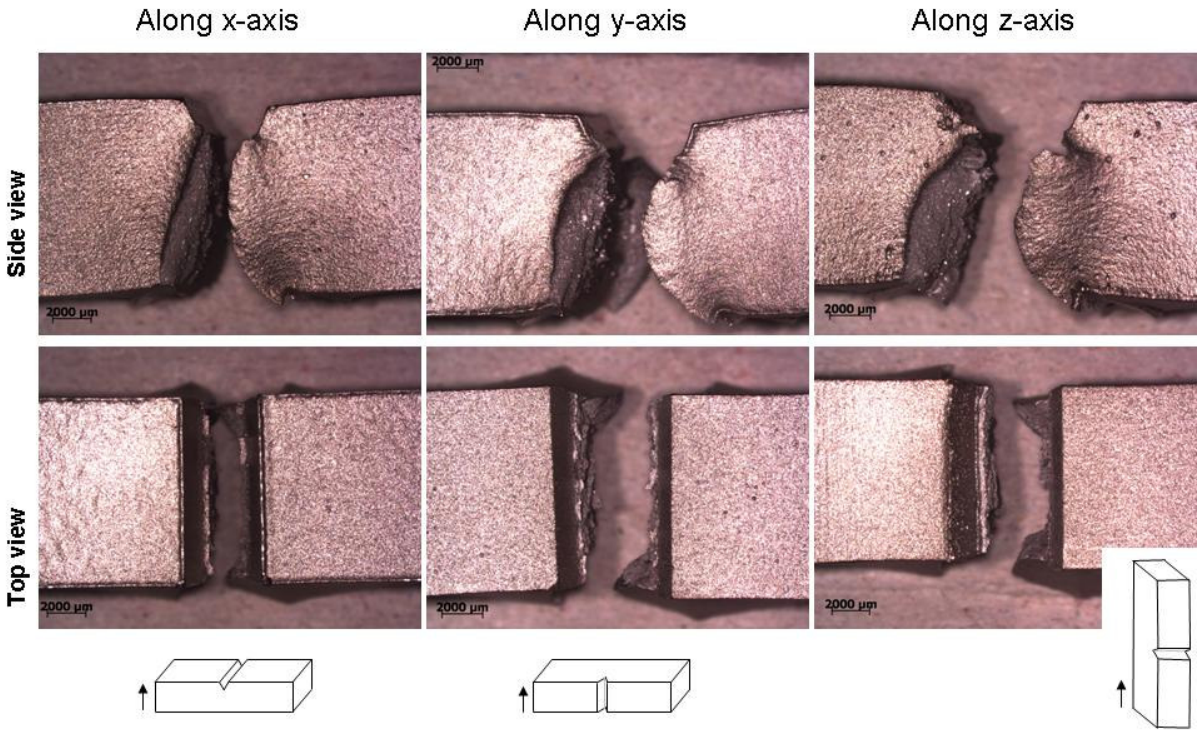

Figure 5.41: Side and top views of 316L specimens built on EOSINT M270 after Charpy testing

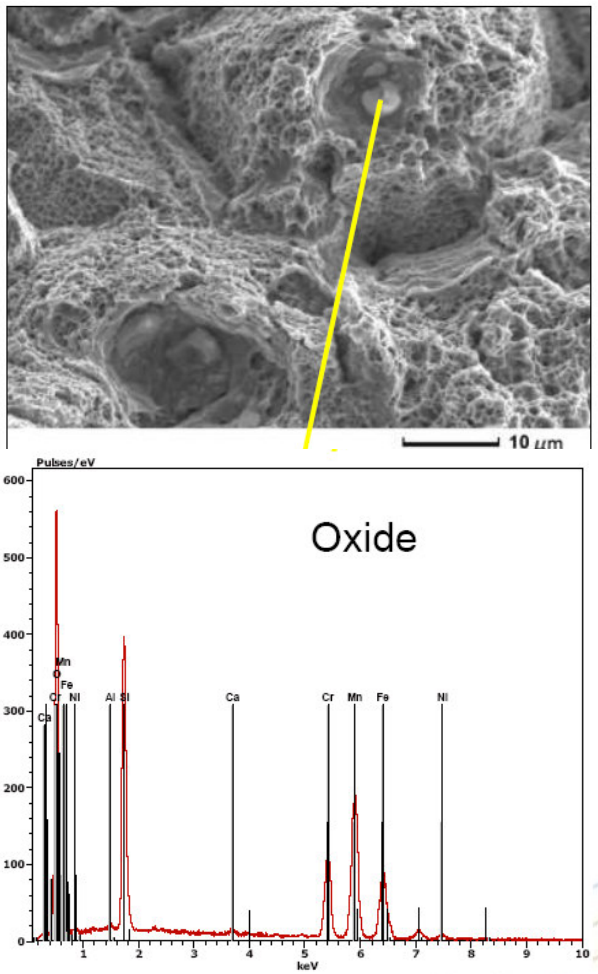

Figure 5.42: Fracture surfaces of a specimen built on EOSINT M270

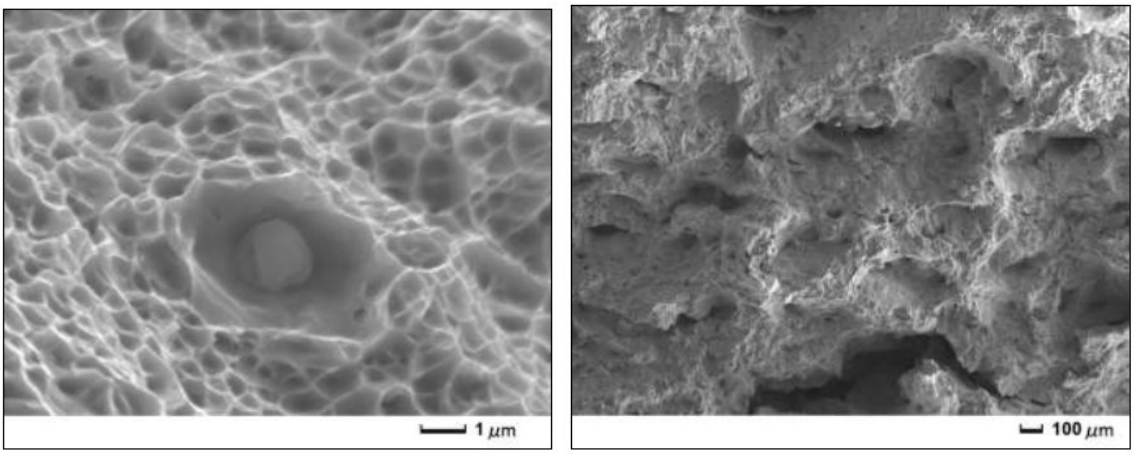

Figure 5.43: Fracture surfaces of a specimen built on a Concept Laser M3 Linear with re-melting

c. Maraging Steel 300

The density obtained with maraging steel parts was measured to be above 99% with a very small variation (See Figure 5.25). The Charpy impact testing of this material processed on an EOSINT M270 machine with a fiber laser without any further heat treatment resulted in an average toughness energy of 36.3±5.19 J for the standard specimens and an average toughness energy of 188.68±23.55 J for no-notch specimens with a 95% level of confidence (See Figure 5.28). Fracture of the maraging steel parts is more ductile compared to Ti6Al4V as indicated by the deformation of the cross section at the position of fracture and shear lips. This is illustrated by the macroscopic examination of the fracture surfaces in Figure 5.44.

Figure 5.44: Fracture surface of maraging steel standard specimens

For the maraging steel, the applied two heat treatments decrease the resistance to breakage significantly as depicted in Figure 5.45. It can also be observed that the amount of plastic deformation is significantly lower than the one without heat treatment (see Figure 5.46). The first heat treatment was the solution annealing at 815 °C for 1 hour and cooling to room temperature followed by aging conducted at 480°C for 3 hours. The second was only aging at 480 °C for 3 hours. The results also show that the solution annealing is not necessary to homogenize the microstructure after SLM since the results with and without solution annealing were almost the same. The hardness increases to 572±7 HV as a result of aging. The hardening during aging has been attributed in literature to short-range ordering in the cobalt-bearing solid solution and the precipitation of nickel-rich intermetallic compounds in the lath martensitic structure [154]. X-ray diffraction has revealed that after aging a face-centered cubic (fcc) phase appears, which was not present without heat treatment. In literature, it is reported that during aging of 18 Ni maraging steel 300, austenite can precipitate and adversely affect the toughness of the material [154].

The effect of different building axes is tested for this material and the results are depicted in Figure 5.47. The specimens were built along three axes and then heat treated with solution annealing followed by aging. The building directions are also shown in the illustrations below the graph. Although there was only one part for each tested condition, it is seen with all three part designs that the z-axis is not necessarily the weakest direction to build the parts in terms of impact toughness. As was the case with 316L, the building axis does not play an important role if the connection between layers is well established. The fracture surfaces of the specimens built along different axes are shown in Figure 5.48. As evident, the standard specimens built along different directions all show similar fracture surfaces and do not exhibit any indication of layer-wise production. Moreover, from Figure 5.47, it is evident that the notch generation either by EDM or during SLM does not change the results significantly.

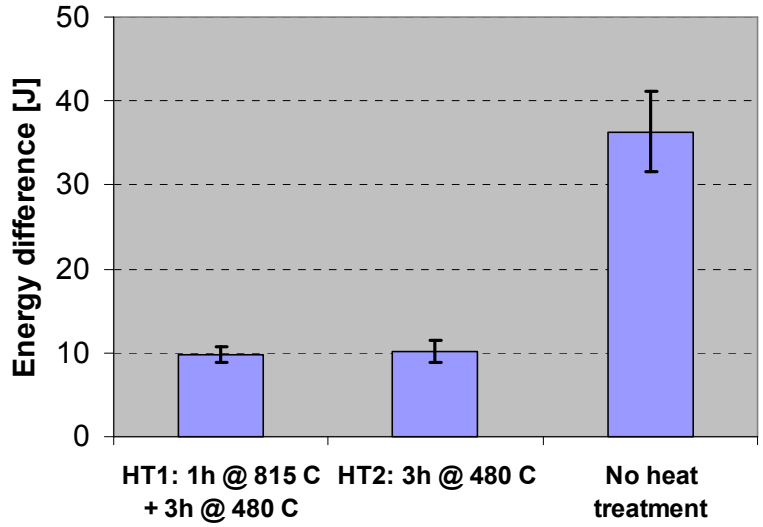

Figure 5.45: Effect of heat treatments for maraging steel 300 processed on EOSINT M270

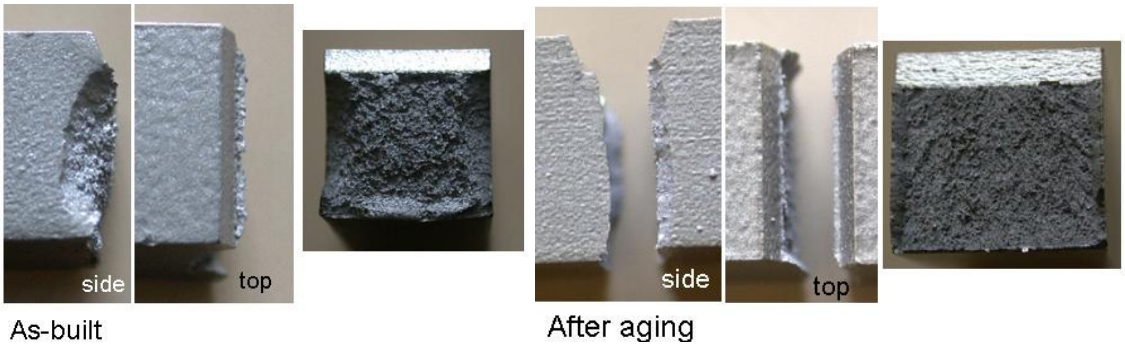

Figure 5.46: Different views of the fracture surfaces (MS1 processed on an EOSINT M270)

The maraging steel was also tested on a Concept Laser M3 Linear machine with island scanning. Laser re-melting was also applied after each layer for maximum density without any aligned porosity. The details of process optimization can be found in §5.1 for the process parameters for SLM of maraging steel 300 in terms of density, surface quality and microstructure (see Table 5.4 and part 4 for the SLM and laser re-melting parameters in §5.1.3e) The results for those specimens with and without heat treatment are presented in Figure 5.49 for standard specimens. The results obtained from the parts produced on M3 Linear without heat treatment (41.9±1.5 J) exhibits slightly higher toughness results compared to those made on an EOSINT M270 (36.3±4.3 J) when a high density is achieved without any aligned porosity. This is accomplished by selecting the parameters for island scanning properly and applying laser re-melting after every layer. However, the obtained toughness is still lower than that of conventionally produced maraging steel 300 which may be due to the formation of inclusions (titanium and aluminium oxides) as shown in Figure 5.16. Like in

casting, the formation of inclusions, which act as stress raisers, adversely influence the mechanical properties. Some of the mechanical properties, e.g. elongation or reduction in area, ductility, etc., are more sensitive to inclusions than others [172].

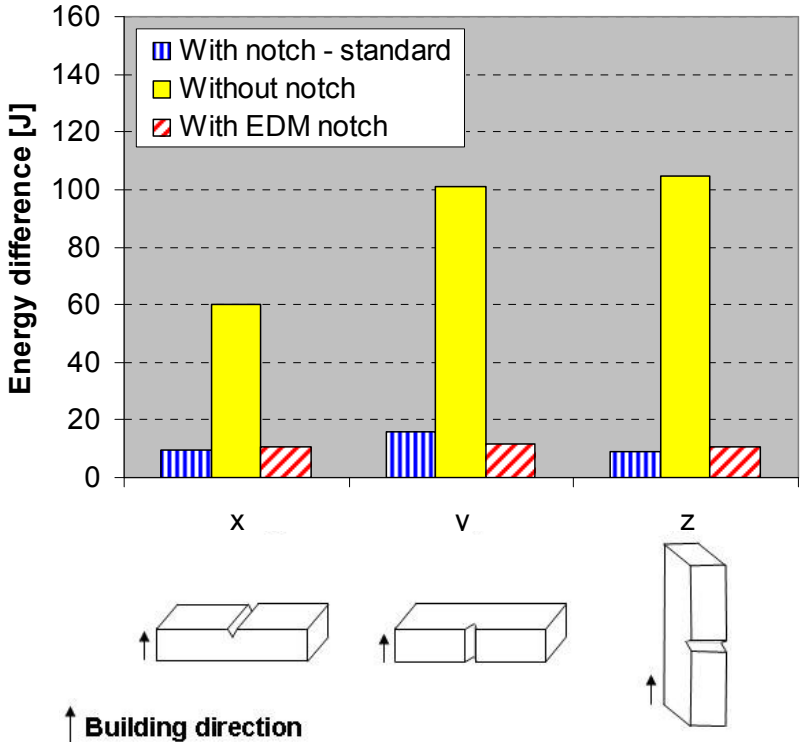

Figure 5.47: Effect of different building axis on the toughness of maraging steel 300

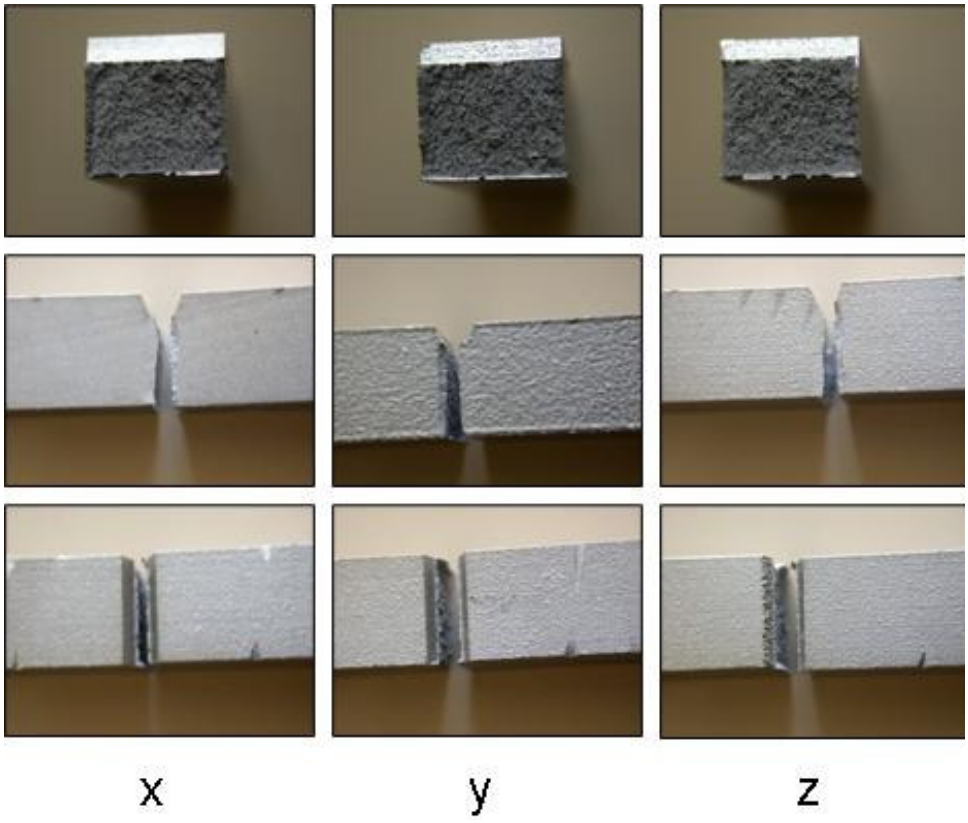

Figure 5.48: Fracture surfaces of standard specimens produced along different axes (18Ni-300)

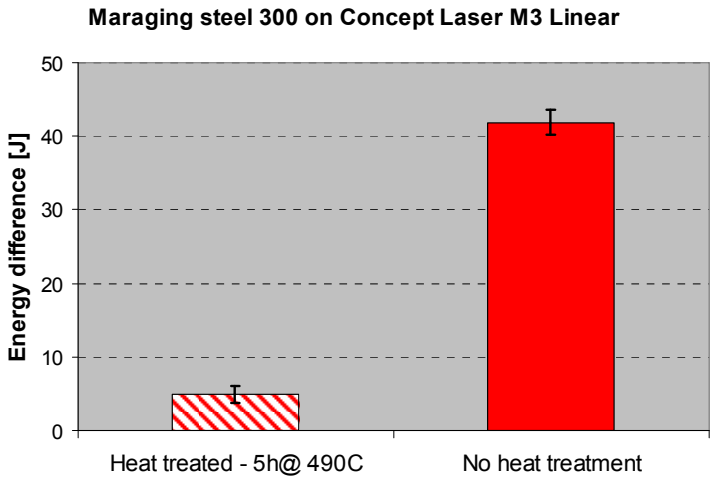

Figure 5.49: Effect of aging on the maraging steel 300 samples produced on a Concept Laser M3 Linear with island scanning

5.2.4 SLM versus Conventional Production Techniques

In this study, the toughness of materials produced by conventional methods is found to be higher than one of SLM parts. For bulk annealed stainless steels, the impact Charpy energy for V-notched parts is generally greater than 180-190 J [171, 173]. For Ti6Al4V, cast specimens exhibit an impact energy of 17 J for V-notched samples [174] whereas SLM parts reach up to only 11.5 J without any heat treatment in the present work. After full annealing or stress relieving, the toughness does not change or slightly decreases. Bulk maraging steel 300, i.e. a pre-alloyed high strength and hardness steel, absorbs an impact energy of 18 J at room temperature after aging [175]. Our experiments showed an impact energy of approximately 10 J for this material when heat treated in the same way. Without any heat treatment, the impact energy is found to be between 30 to 40 J, thus yielding a higher toughness but sacrificing the strength and hardness normally obtained through aging for this material. The comparison between test results of SLM and conventional manufacturing processes is summarized in Table 5.8. For Ti alloy and maraging steel, the obtained toughness results by SLM are lower than the ones of conventionally produced specimens. However, similar results are obtained for AISI 316L stainless steel specimens when the EOSINT M270 machine is utilized. Therefore, it is difficult to make general judgements about the toughness of SLM compared to conventional techniques. The comparison mostly depends on the material and machine selections. The influence of the machine may be due to the type of the laser, the purity of the atmosphere, the scanning strategy, etc.

Table 5.8: Comparison of SLM and conventional processes in terms of Charpy V-notch toughness

Produced by	**SLM**	**Conventional**
Ti6Al4V	11,5 ± 0,5 J (as built) 10,1 ± 0,5 J (full annealed)	17 J for investment casting
Maraging 300	36,3 ± 4,8 J (as built on EOSINT M270) 41.9 ± 1.5 J (as built on M3 Linear) 10,1 ± 1,4 J (aged 3h at 480°C - EOSINT M270) 4.98 ± 1 J (aged 5h at 490°C - M3 Linear)	18 J after aging
AISI 316L	96.5 ± 5 J (annealed - M3 Linear) 162.8± 4 J (annealed - EOSINT M270)	180-190 J (annealed)

The reason of having lower toughness with SLM can be attributed to the presence of defects like pores, pick-up of impurities like oxygen and nitrogen (especially for titanium alloys) and the presence of more brittle non-equilibrium phases. The un-melted powder particles that were left in the part after SLM were revealed through the examination of fracture surfaces as illustrated in Figure 5.50. All three materials exhibited the same problem although they were manufactured on three different machines.

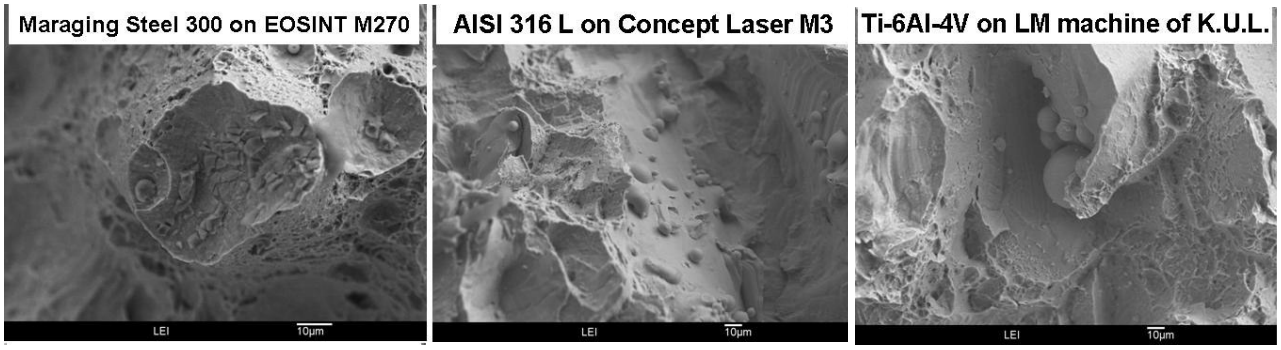

Figure 5.50: Un-melted powder particles in the pores of all samples produced on different machines

This work has also revealed that the porosity of SLM parts is of high importance since it might cause a significant reduction in toughness. Controlling the process in terms of density is hence most critical: a slight drop of density due to unexpected loss of laser energy (e.g. dirt on optics) may substantially reduce the toughness. Testing density should best be done with different methods since Archimedes may overestimate the relative density if the pores still contain un-melted powder particles (See Figure 5.50 and also Figure 5.52 in §5.3.1). Moreover, it is impossible to detect aligned porosity problem with the Archimedes method. The results were not presented here but a slight change of alloying element compositions may significantly reduce the toughness due to undesired phases such as high amount of high temperature delta ferrite in the austenite phase in the case of AISI 316L stainless steel. Thus the material composition should also be strictly determined to ensure a good repeatability for mechanical properties. Heat treating (full annealing) may be a solution to remove the undesired phases such as delta ferrite for austenitic 316L stainless steel. Although this material is almost always used without any heat treatment after SLM, it is recommended that full annealing is applied to avoid any problems related to the presence of brittle delta ferrite phase.

Therefore we can group the reasons of lower toughness results by SLM under three different categories such as

- The reasons due to the nature of the process, e.g. high cooling rates resulting in brittle phases, un-melted powder particles in the pores formed during SLM, etc.
- Process defects, e.g. insufficient overlapping between scan tracks or islands in case of island scanning, bad connection between layers, dirty laser window resulting in a lower laser power, bad protective atmosphere (e.g. O_2 leak), etc.
- Material defects, e.g. wrong composition, or being very close to the limits of alloying element amount.

In order to manufacture parts with good mechanical properties, all problems related to process defects should be solved so that high density parts without any aligned porosity or irregularities are built. Some of the problems related to the nature of the process can be solved via heat treatments. However, the proper heat treatments should be selected to address the specific problems such as beta annealing or re-crystallization annealing to form higher amount of bcc beta phase in case of Ti6Al4V instead of stress relieving or full annealing which are done at comparatively lower temperatures. Some problems, like un-melted powder particles left in the pores formed during SLM,

cannot be solved with heat treatments. More fundamental research should be conducted to address and solve that problem.

5.2.5 Conclusions

The important conclusions from this work can be summarized as,

- The roughness of SLM parts does not behave like stress-concentrating notches. The parts without a notch showed significantly higher impact energies compared to specimens with a notch, either made during the SLM process or after SLM by EDM. This also concludes that the way of production of the notch does not affect the toughness results for this case.
- The tests with maraging steel 300 and AISI 316L revealed that the building axis does not play an important role on the toughness results if the connection between successive layers is well established without any directional porosity.
- When compared to conventionally manufactured parts, SLM lowers the impact toughness due to the nature of the process, e.g. un-melted powder particles, 1-2% porosity or undesired brittle phases due to high cooling rates for some materials, e.g. Ti6Al4V. This does not imply that all materials processed by SLM exhibit a lower toughness like AISI 316L processed on EOSINT M270.
- Process defects like a dirty laser window or improper selection of process parameters, can reduce the toughness dramatically. For repeatable mechanical properties, the material composition of the powder should be well controlled and kept in a limited range; the process defects should be avoided and proper heat treatments to form desired ductile phases should be employed.

5.3 Sectoral Scanning in SLM

5.3.1 Introduction and Literature Review

The scan strategy in SLM is defined as the pattern used to scan the area corresponding to each layer and can be performed in many different ways such as refill strategy [177], double-scan mode whereby each layer is scanned twice with bi-directional scan lines [178], knit-strategy with bi-directional scan lines [128], sectoral scanning with linear x or y [7], emanative star-like and angled emanative starlike scan [179] and fractal scanning strategies [180, 181]. Some of these, such as double-scan and refill strategy, increase the production time significantly while solving some limitations of SLM.

Sectoral or island scanning is a patented scan strategy announced to decrease the residual stresses [12]. However, if the scan spacing factors are not properly selected, the bad connection between islands or scan tracks can lead to very bad mechanical properties although the obtained densities will be high (See toughness results in §5.2.3b). In this study, sectoral scanning is taken under investigation regarding many quality aspects, such as density, surface quality and residual stresses. The area of each layer to be scanned is divided into smaller square sectors, of which the size and orientation can be set to any desired value. There is no specific scanning order of the sectors; they are rather scanned randomly (see Figure 5.51). The neighbouring sectors are scanned perpendicular to each other. In the scope of this study, the influence of the scan spacing between scan tracks and the sector offset, a parameter to set the overlap between islands, are investigated with respect to density and surface quality. Additionally, the influence of the orientation of scan tracks and sector size on the residual stresses is studied.

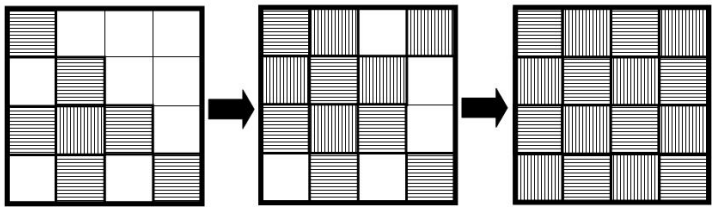

Figure 5.51: Random scanning of sectors with different hatch angles (β=90°, see Figure 5.71)

5.3.2 Experimental Procedure

The experiments are carried out on the Concept Laser M3 Linear machine with AISI 316L stainless steel powder (CL20ES). The density of the produced specimens was first measured with the Archimedes method. Although this method gives a general overview to compare the density of different samples, it may not be the best method to measure the density of SLM parts. The pores formed during the SLM process may contain some un-melted powder particles as illustrated in Figure 5.52. As a result, the measured density by Archimedes method will not be equal to the real density. Moreover, the produced samples with more than 10% porosity should be covered with lacquer before the measurements in order to avoid the measuring liquid to be absorbed by the open pores on the surfaces. In order not to misinterpret the density values, besides the Archimedes method, cross-sectional views are observed.

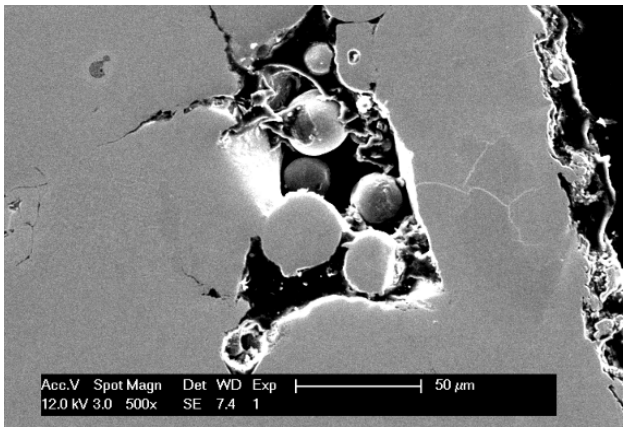

Figure 5.52: SEM micrograph of a SLM part showing pores with un-melted powder particles

To investigate the surface quality, the top surfaces of the produced samples were measured by a 3D profilometer, i.e. Talysurf 120L [62]. The average R_a and ten point mean roughness R_z are obtained by three-dimensional measurements without any cut-off filter so that a general insight about the top surface profile can be revealed. The method used to measure the residual stresses, or part deformation, is explained in detail in §5.3.3d where the experimental results are presented.

5.3.3 Experimental Results

a. Scan Spacing between Scan Tracks

The scan spacing between scan tracks is a very important parameter determining the overlap between consecutive scan tracks. If the overlap is not enough, there will be some areas in between scan tracks which are not completely melted resulting in low density due to regularly formed pores. The experiments to investigate the scan spacing between scan tracks are conducted without island scanning as shown in Figure 5.53. The scan spacing factor a_1 is entered to the machine software as well as the spot size (d). The scan spacing ($ScSp$) is then calculated as given in the following equation:

$$ScSp = a_1 \times d \tag{5.2}$$

where d is the spot size entered in the software by the user and taken as 180 µm and a_1 is the scan spacing factor between scan tracks.

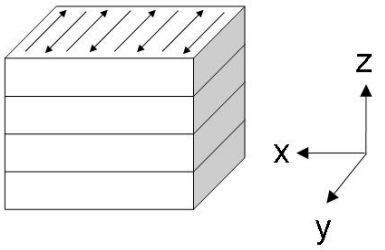

Figure 5.53: Orientation of the part, z-axis corresponding to the build direction

As the scan spacing factor is increased, the scan tracks are located further from each other. During the tests, the scan speed was taken as 300 mm/s with a laser power of 100 W and a layer thickness of 30 µm, whereas the scan spacing factor a_1 is varied from 45% to 70%. After the tests are completed, the top surfaces were first examined with optical microscopy. Micrographs are depicted in Figure 5.54. At a high scan spacing factor (a_1 = 70%), the scan tracks can be distinguished from each other easily which makes the density become lower due to insufficient melting of the powder particles between scan tracks. At lower scan spacing factors, the scan tracks overlap sufficiently.

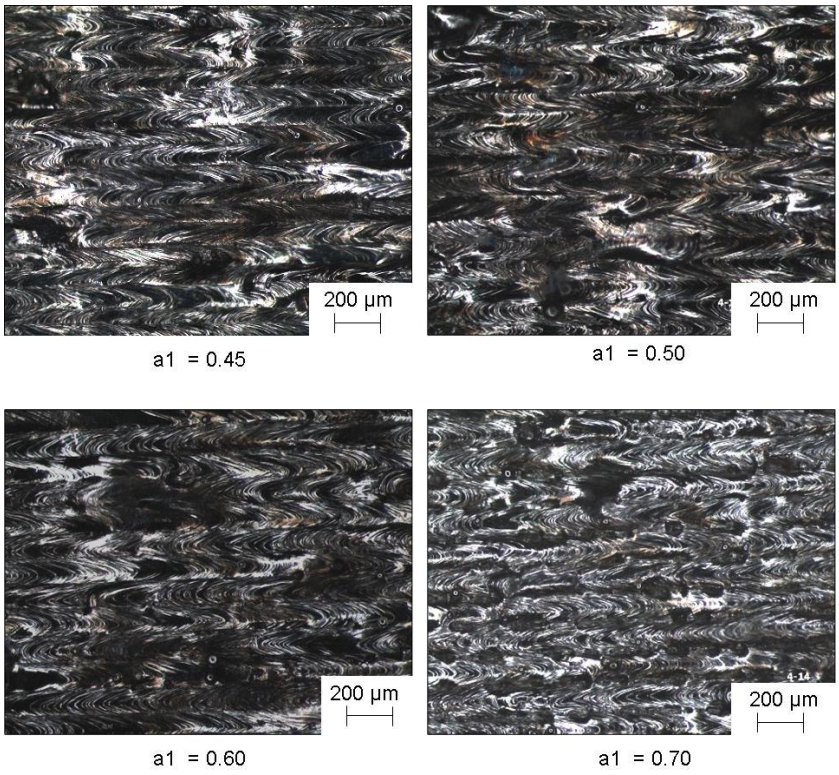

Figure 5.54: OM images of the top surfaces (xy-planes) at different scan spacing (a_1) values from 0.45 to 0.7

The relative densities of the produced specimens at different scan spacing factors (a_1) are measured with Archimedes method without applying any lacquer since the remaining porosity was much less than 10%. For each scan spacing factor, 3 specimens with dimensions of 20x20x10 mm were made. From the measured densities, the relative densities were calculated using a theoretical density of 8.0 g/cm^3 which corresponds to the bulk density of stainless steel AISI 316L. The mean densities corresponding to the 3 specimens for each scan spacing factor are shown in Figure 5.55 with a 95% confidence level along with all measurements. The maximum standard deviation at a

constant scan spacing factor is 0.036% and the results corresponding to different scan spacing factors are also very close to each other. All results lie in a range of 98.4-98.9% and thus it is difficult to make a concrete conclusion by only looking at the results obtained by the Archimedes method. However, the maximum density is achieved at a scan spacing factor a_1 of 60% with a standard deviation of 0.006% in the tested range.

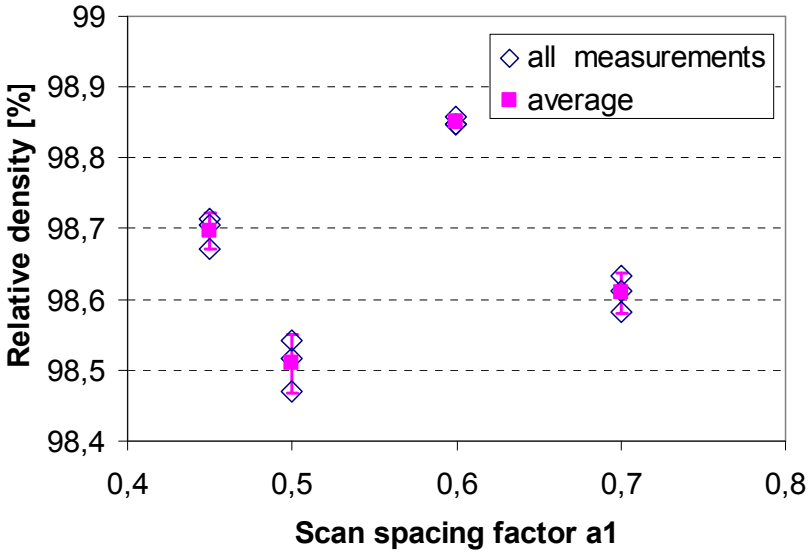

Figure 5.55: Relative densities of the SLM parts with different scan spacing (a_1) values measured by the Archimedes method

The produced samples were also investigated by cross-sectional views as depicted in Figure 5.56. A surface on xy-plane and a surface on xz-plane were investigated (See Figure 5.53). At low scan spacing factors, the scan tracks overlap sufficiently but due to the high energy density entered into the powder bed, some irregular and big pores are formed whereas the powder particles are not completely melted at higher scan spacing factors resulting in an excessive and aligned porosity as shown in Figure 5.56 for the case of a_1=0.7. The aligned porosity is evident on both planes. The presence of so many pores at a scan spacing factor of 0.7 would not be detected with Archimedes density measurements. The scan spacing factor a_1 should be optimized close to 0.6 where a maximum density is achievable as evident from cross-sectional views.

The effect of the scan spacing factor a_1 on the surface quality of the top surfaces is tested and given in Figure 5.57 in terms of the arithmetical mean (R_a) and ten point mean (R_z) values of 3D roughness measurements. As depicted, the roughness values are reduced as the scan tracks are located further from each other. The 3D map heights are also shown in Figure 5.58. The lightest colour represents the highest peaks whereas the darkest shows the deepest valley. The 3D map heights show that the scan tracks are not distinguishable from each other at low scan spacing (0.45) whereas the separate scan tracks are observed as the scan spacing is increased to 0.7. At low scan spacing factors, bigger pits and peaks are formed deteriorating the surface quality significantly.

As a result of the experiments, it was concluded that neither a very low nor a high scan spacing factor (a_1) is an optimum for density and surface quality. The scan spacing factor should be set to a medium value which is low enough to ensure sufficient overlap between scan tracks to avoid excessive and aligned porosity and which is high enough to avoid excessive energy input into the material resulting in bad surface quality and irregular big pores. The optimized value is found to be 0.62 for AISI 316L material with a scan speed of 300 mm/s and a laser power of 100 W with a spot size ($Ø_{99\%}$) of 180 µm (layer thickness = 30 µm).

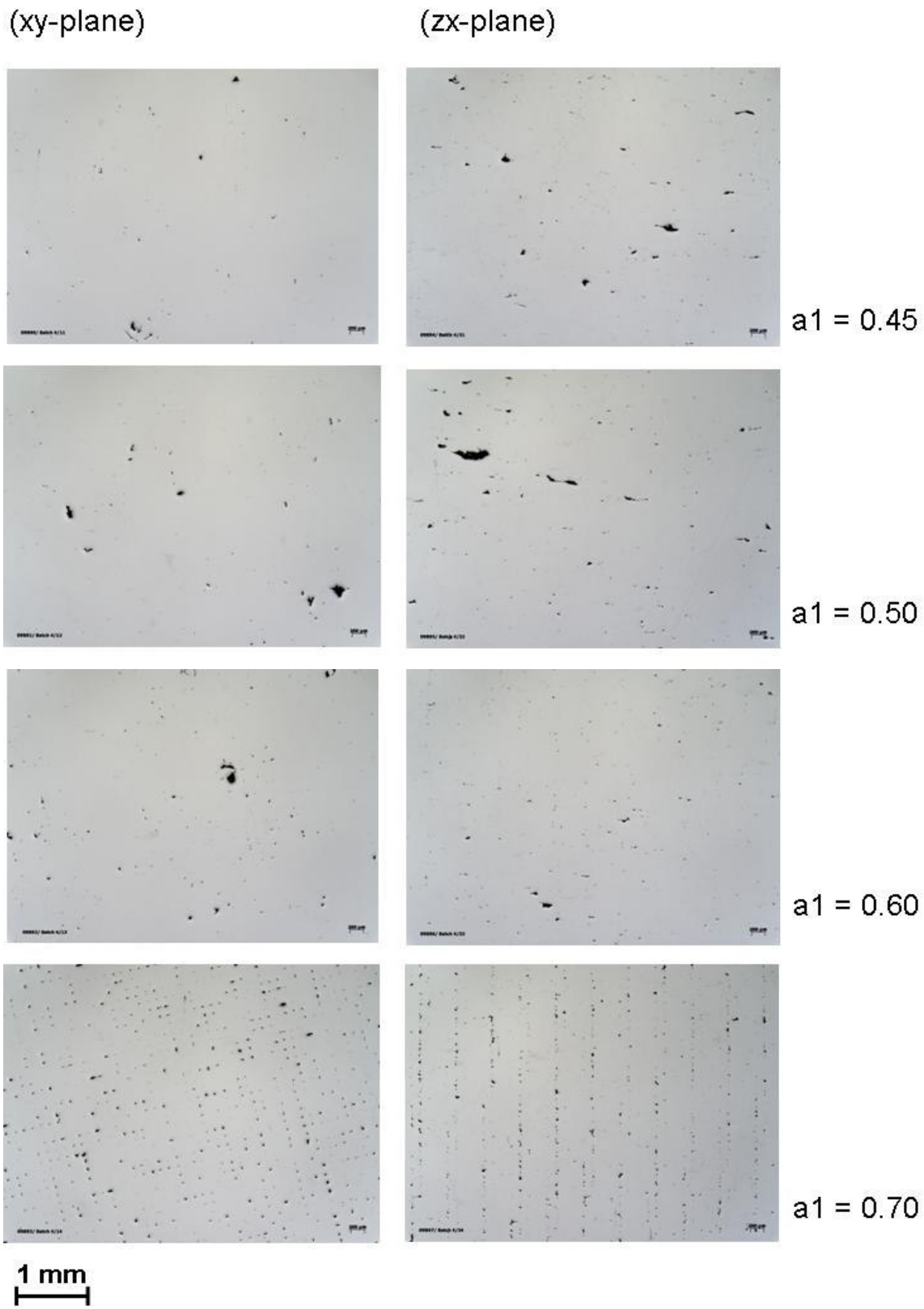

Figure 5.56: OM pictures of two planes: xy-plane and xz-plane, from parts with different a_1 values

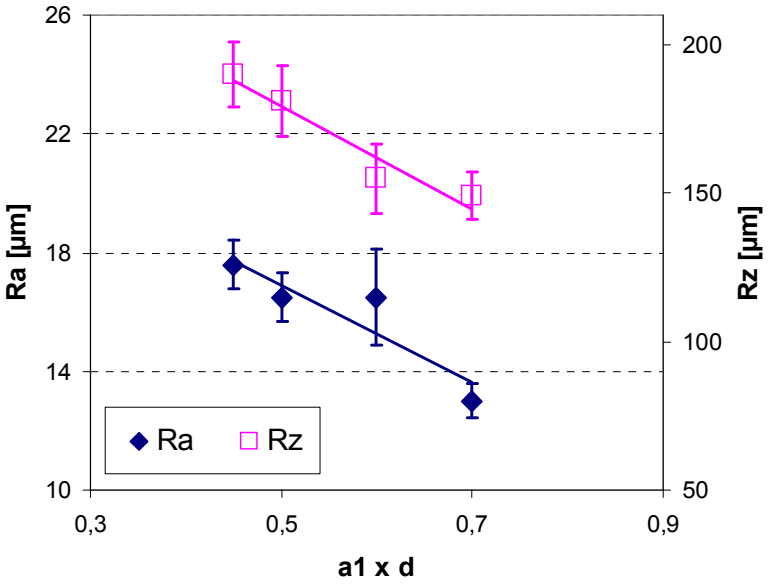

Figure 5.57: Effect of a_1 on the surface quality (in terms of R_a and R_z)

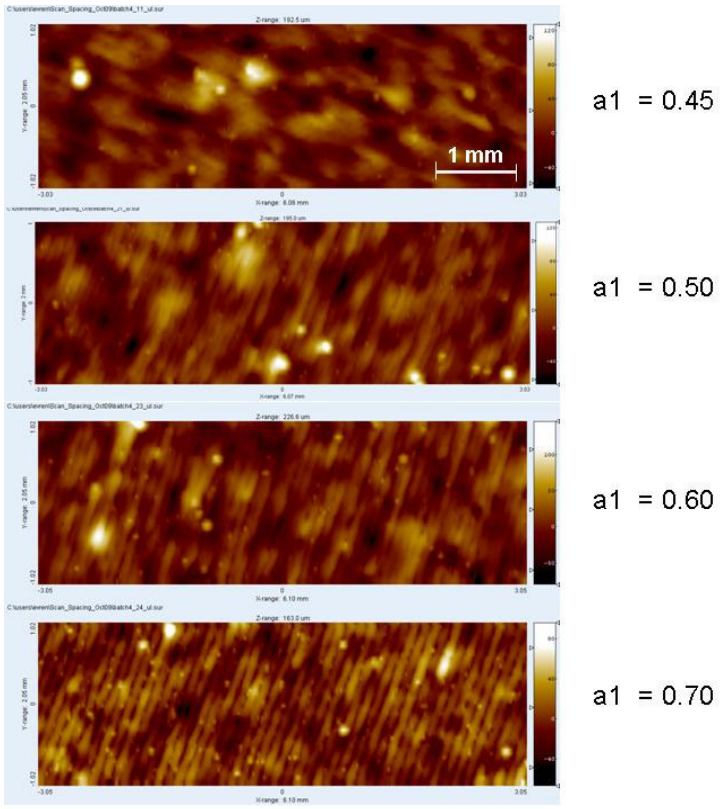

Figure 5.58: 3D height maps of parts produced with different scan spacing (a_1) - top surfaces

b. Overlap between sectors

The sector offset (a_2) specifies how the scan tracks are located in one sector together with the scan spacing between consecutive scan tracks. In Figure 5.59, the dashed lines show an island with the scan tracks located inside with an exaggeratedly high a_1 factor which is the scan spacing factor between neighbouring tracks scanned in reverse directions. In order to ensure an overlap between neighbouring sectors, the scan tracks are elongated in the scanning direction with a certain length which is determined by the sector offset a_2 which is also used to calculate the distance between the border sector and the last/first scan track as depicted in Figure 5.59.

In order to test different sector offset values, experiments are conducted where a_1 was taken as 0.7 with a scan speed of 300 mm/s and 100 W. The top surfaces of the produced samples were first observed with optical microscopy. The sector offset is varied between 5% and 100% and the micrographs taken at the cross-sections of the sectors are shown in Figure 5.60.

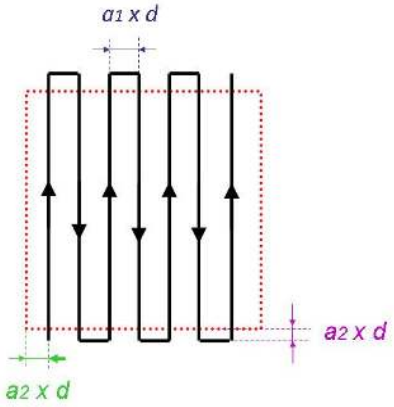

Figure 5.59: Schematic illustration of scan spacing and sector offset

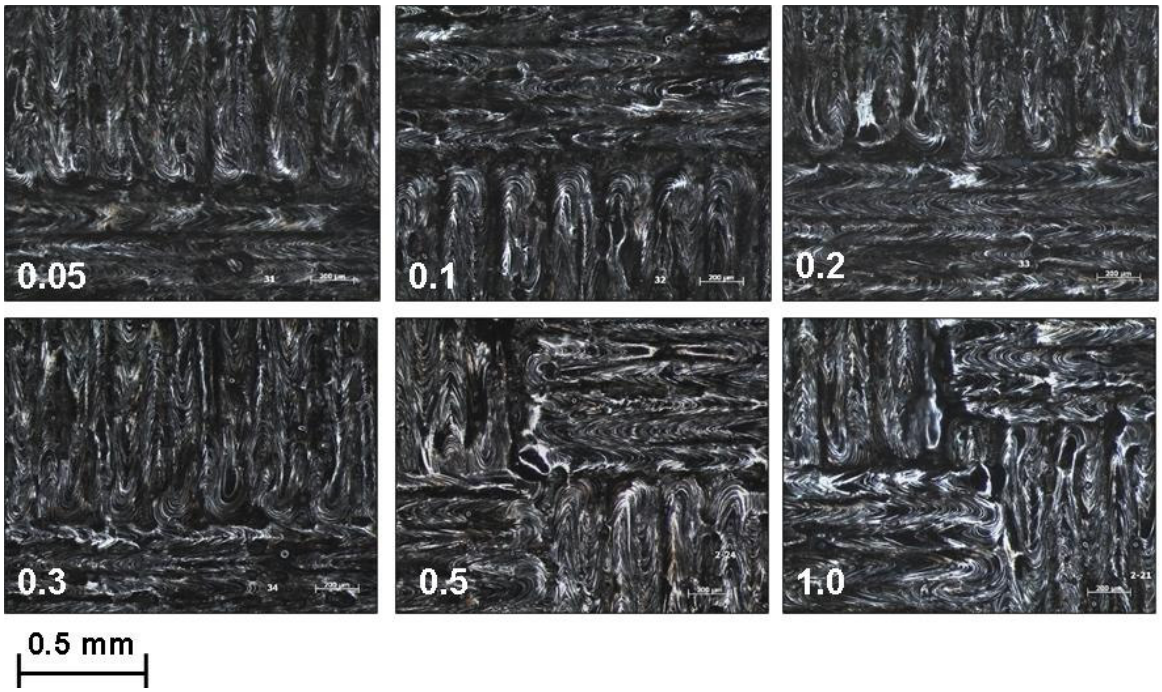

Figure 5.60: OM pictures from the top surfaces of the samples produced with different sector offset values

At low sector offset values (<30%), the scan tracks in one sector do not overlap sufficiently with the neighbouring sectors. For the sector offset of 5%, there are porous lines on the locations where the sectors meet as depicted in Figure 5.61 which is highly undesired due to significant reduction in mechanical properties of the produced parts. On the other hand, if the sector offset is selected close to 100%, there are some square regions in between the sectors that are not scanned in each layer. The un-scanned areas do not appear as three-dimensional square holes but rather in the form of porosity at different locations throughout the part. The way how these square un-scanned areas are formed is depicted in Figure 5.62. For instance, when the sector offset is set to 0, the scan tracks are not elongated along the scan direction but they are also located starting from exactly the border of the sectors. If the sector offset is set to a value greater than 50%, then the scan tracks are elongated with 0.5 x 180 μm = 90 μm. On the other hand, the scan tracks are shifted from the border of the sector with an equal amount, i.e. 90 μm. Therefore, the scanned areas become rectangular instead of square at high overlap factor resulting in un-scanned square areas between sectors (Figure 5.62).

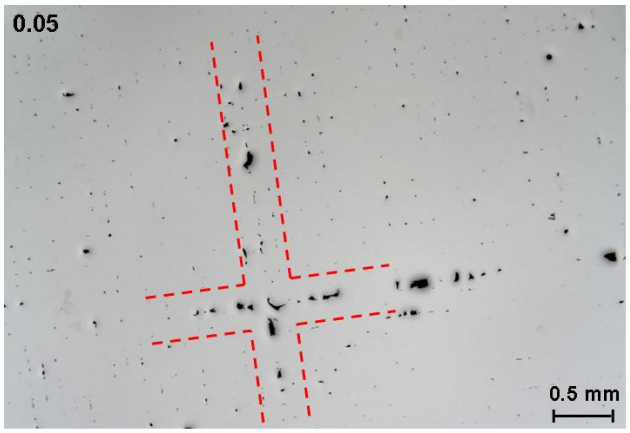

Figure 5.61: OM image of a cross-section along the building axis of a sample produced with a_2 of 0.05 and a_1 of 0.7

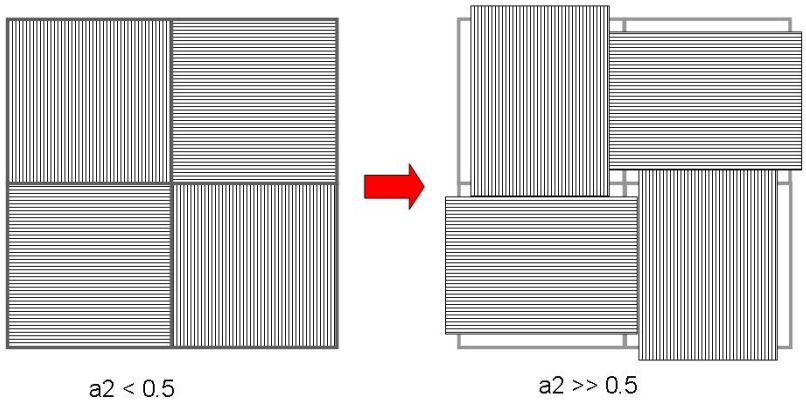

Figure 5.62: Schematic illustration of high sector offset

The relative densities of the samples produced with different sector offsets are first measured by the Archimedes method. The results are given in Figure 5.63 with a 95% confidence level. All measurements lie in a range of 98.5% to 98.8% which is rather low. The densities of these samples do not seem to be affected by different sector offset values if they are measured by Archimedes method. However, optical micrographs taken at the place where sectors meet show aligned porosity along the edges of the sector when insufficient overlap exits as depicted in Figure 5.61.

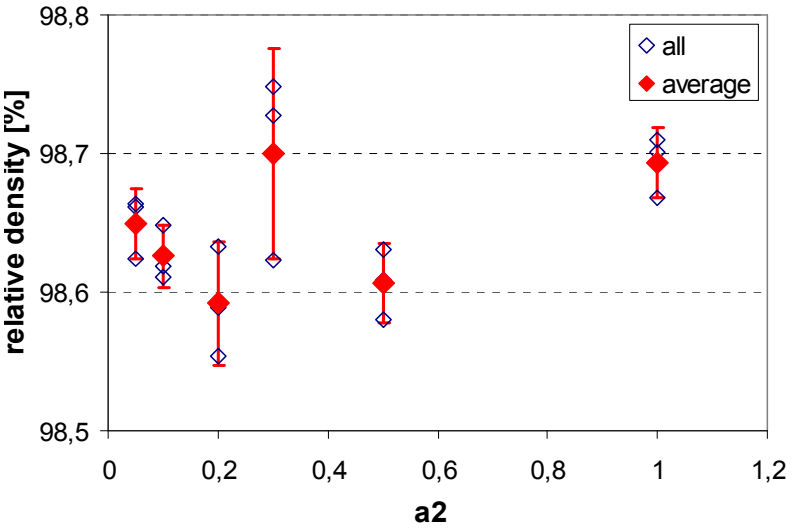

Figure 5.63: Relative densities of the parts with different sector offsets measured by the Archimedes method

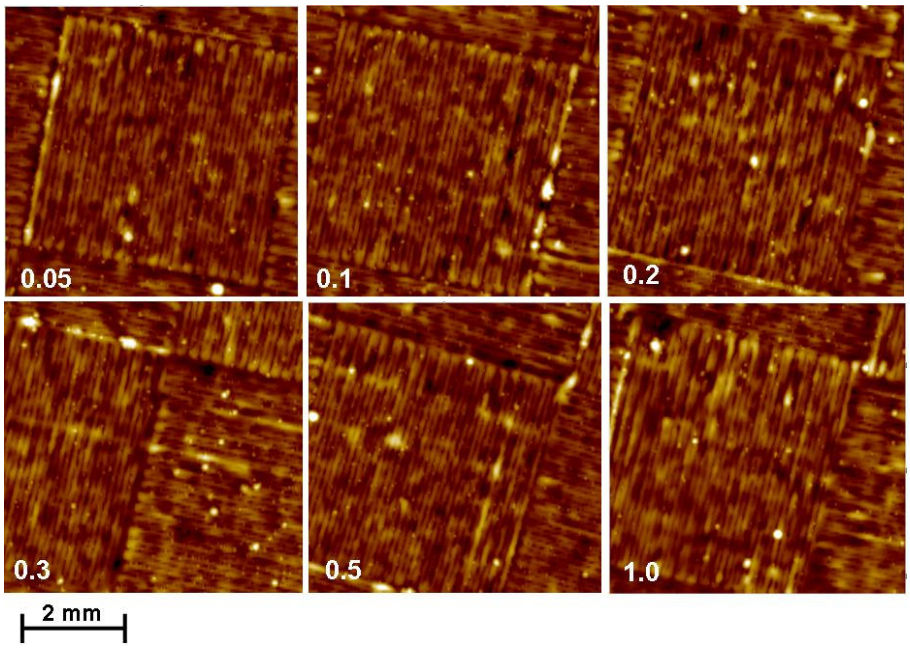

Figure 5.64: 3D height maps from the top surfaces of the samples produced with different sector offsets (a_2)

The surface quality is also investigated at different sector offsets in terms of arithmetical mean (R_a) and ten point mean roughness values (R_z). The 3D height maps of the surfaces are illustrated in Figure 5.64 for sector offsets starting from 5% to 100%. The roughness results are shown in Figure 5.65 with a 95% confidence level. The average roughness (R_a) deviates in the range of 11-16 µm when a_2 is set from 5% to 30%. The variation of average roughness is in the range of the variations resulting in the fact that sector offset does not significantly alter the results in the tested range. However, R_z which is a mean measure of peak to valley roughness, is reduced from 200 µm to 165 µm at a sector offset of 0.3. This reduction is also evident from the measurements conducted by white light interferometer and 3D profilometer at 5% and 30% (See Figure 5.66 and Figure 5.64 respectively). At a low sector offset, pronounced linear peaks and valleys are formed in between sectors. As the sector offset is increased, the variation in the height becomes less, reducing the roughness R_z.

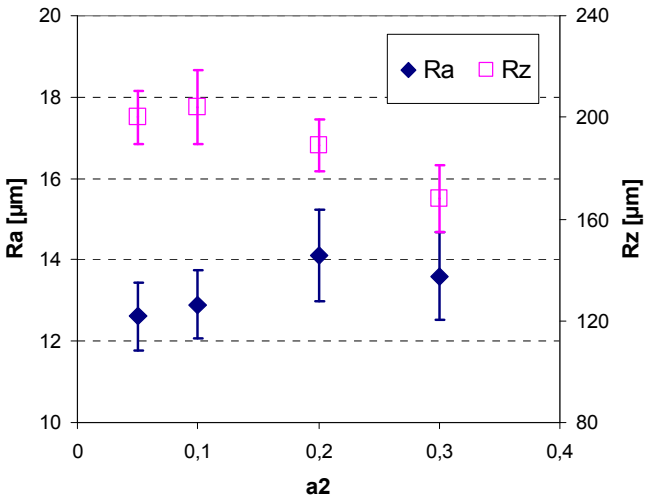

Figure 5.65: Roughness measurements of samples produced with different sector offsets

a)

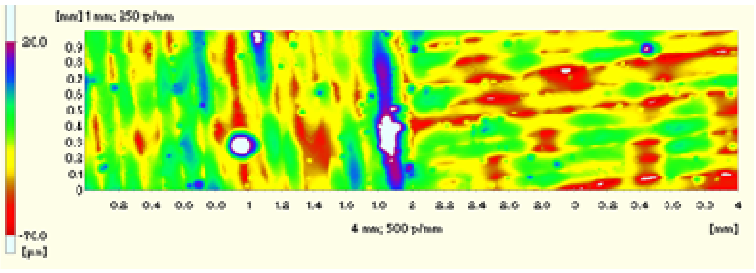

b)

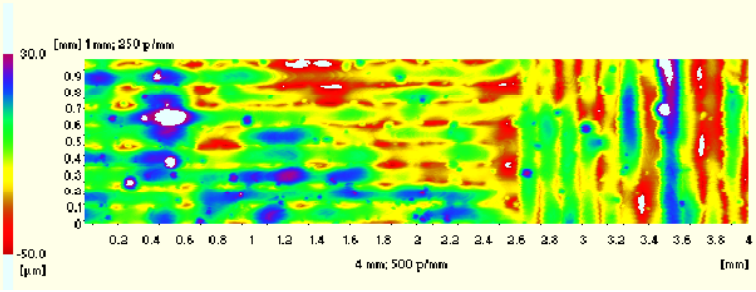

Figure 5.66: Measured profiles by white light interferometer for a) a_2= 5% b) a_2= 30%

As a result of the experiments, it is concluded that an offset of about 30% provides good connection between sectors and a relatively low ten point mean roughness value (R_z). During the tests, the offsets in four sides of the contours were taken the same. However, it is better to have a slightly greater offset in one direction than the other. For example, a test specimen made with an offset value of 35% (for the distance between the sector border and the first scan track=a_2) and an offset value of 50% (for the elongation of the scan tracks in the scanning direction=a_3) gave satisfying results in terms of density without aligned porosity as depicted in Figure 5.67.

a)

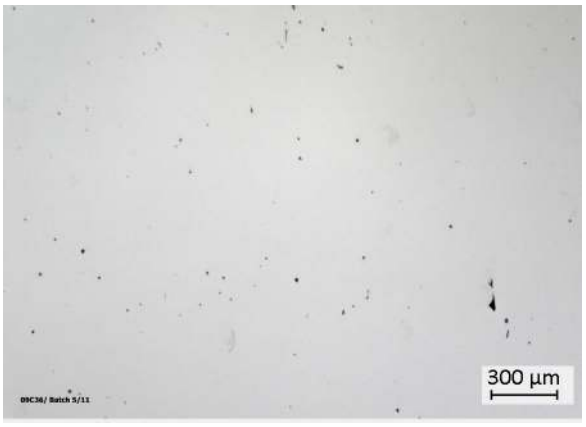

b)

Figure 5.67: A cross-sectional view of a part made with a_1=62%, a_2=35% and a_3 =50% a) xy-plane b) xz-plane

c. Effect of re-melting after each layer

To demonstrate the influence of re-melting on the surface quality and density, every sector is scanned twice with the same parameters; only the scan direction is shifted 90 degrees in the second scanning in one sector. The average relative density, measured by Archimedes method rises from 98.7% to 98.9% when re-melting is applied. The improvement in terms of densification is much better seen in the cross-sectional views as given in Figure 5.68 and Figure 5.69. Figure 5.68 shows the two cross-sectional views of the sample with re-melting, whereas Figure 5.69 shows the cross-section perpendicular to the building axis without re-melting. It is seen that re-melting significantly reduces porosity.

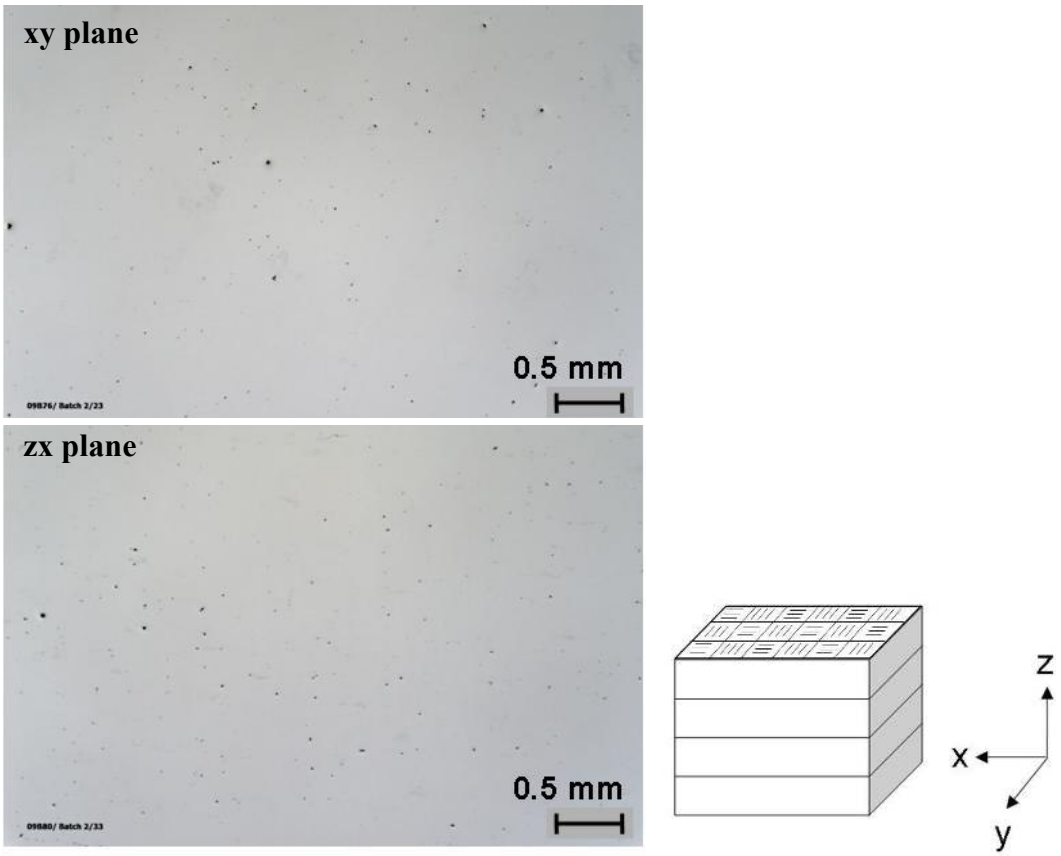

Figure 5.68: Optical micrograph along two cross-sections (xy- and xz-planes) of a sample produced with re-melting of every sector with a_2= 30% and a_1= 70%

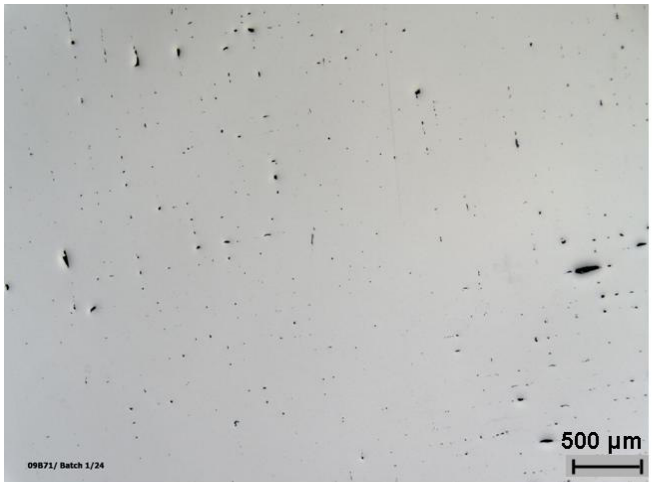

Figure 5.69: Optical micrograph taken perpendicular to the building axis (xy-plane) without re-melting (melting with a_2= 30% and a_1= 70%)

d. Effect of sectoral scanning on residual stresses

A new test method, a qualitative assessment of residual stresses in additive manufacturing, the bridge curvature method, has been developed by R. Wauthlé [13, 182, 183]. It is a simple, fast, accurate method resembling the layer removal methods and allowing a comparative assessment of the amount of level of the residual stresses, rather than quantitative assessment of the magnitude of the residual stresses. The method involves building a bridge-like test part and cutting it off the base plate by wire EDM after the build process (See Figure 5.70). The bridge curls due to the residual tensile stresses at the top of the part. The planes at the bottom of the pillars deviate from their normal position and form an angle α which is a measure for the residual stresses in this method. For

each test part, the curling angle is measured 10 times by a Mitutoyo Quick Vision Pro 202 (5 times on each side of the part). From the measured data the mean value and standard deviation with a confidence interval of 95% are calculated. A detailed uncertainty analysis of the method (e.g. the influence of a bad EDM cut on the measured angle) can be found in [13]. The angle obtained will depend on the geometry and the dimension of the bridge and on the magnitude of the residual stress which depends on the material, build parameters, scan strategy, etc. (see Table 5.9). Since the method is a comparative one, a reference component has been defined. Table 5.9 shows the standard parameters used to produce reference parts to make comparisons with sectoral scanning. The reference part is made with long scan vectors with a scanning direction parallel to x-axis. The obtained curling angle with the reference part is 1.333° with a 95% confidence level of 0.024°.

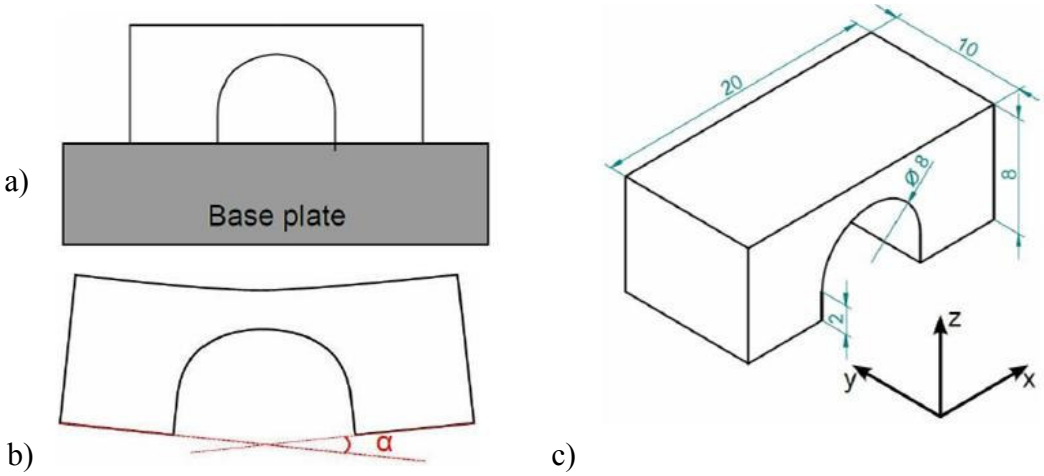

Figure 5.70: Principle of the method for measuring the residual stresses in the test parts (a) bridge structure built on a base plate (b) bridge structure cut off the base plate by wire EDM (c) geometry of the test parts

Table 5.9: Reference parameters used to build test parts

Material	316L stainless steel
Scan vectors	x-direction, bi-directional
Hatch spacing	126 µm
Scan speed	380 mm/s
Laser power	100 W
Contour scan	before fill
Layer thickness	30 µm
Reference value	$\alpha_{ref,\,LM}$ = 1,333°± 0,024°

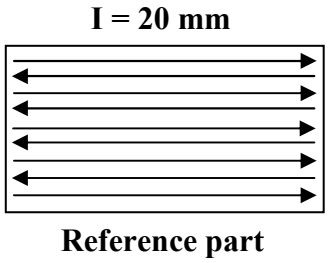

As mentioned earlier, the island strategy divides the area to be scanned into small square sectors. The sequence in which the sectors are scanned is chosen randomly. The slicing algorithm allows changing the size of the sectors, the orientation of the sectors, and it is also possible to shift the sectors in the x- and y-direction between different layers as depicted in Figure 5.71.

The effect of the sector size is shown in Figure 5.72 for sectors rotated (β) 15° from the x-direction. The use of sectoral scanning reduces the measured angle α, but the size of the sectors doesn't seem to influence the results. Figure 5.73 illustrates the effect of the rotation β for sectors of 5x5 (ℓ) mm. If the rotation β is 45°, the measured angle is decreased by 36% compared to the reference part scanned with long scan vectors. This is done in correspondence with another test which has been reported in [13] showing that thermal stresses in the direction perpendicular to the scan vectors are lower as thermal stresses parallel to the scan vectors.

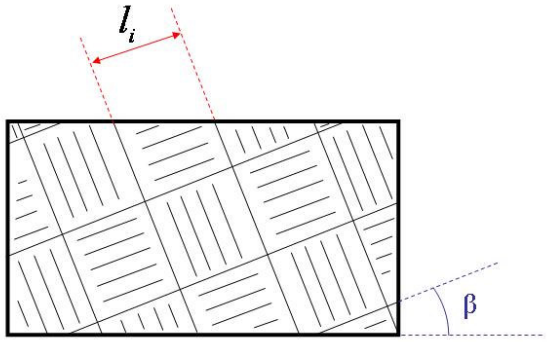

Figure 5.71: Illustration of the sector size and orientation of the sectors

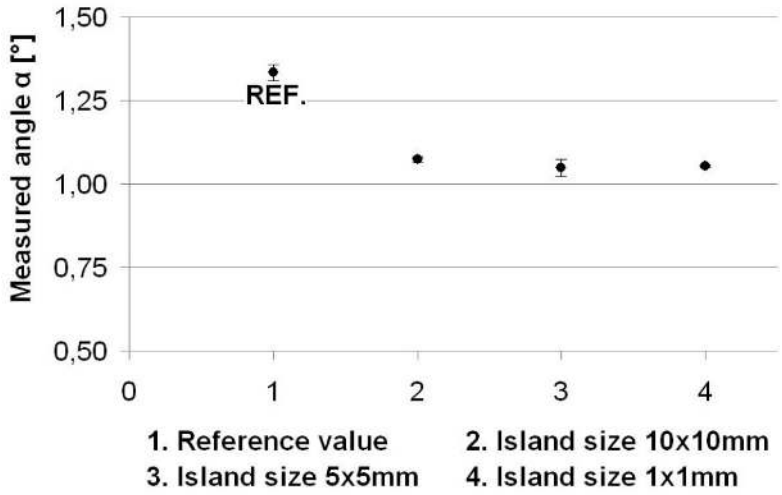

Figure 5.72: Results of sectoral scanning with different sector size

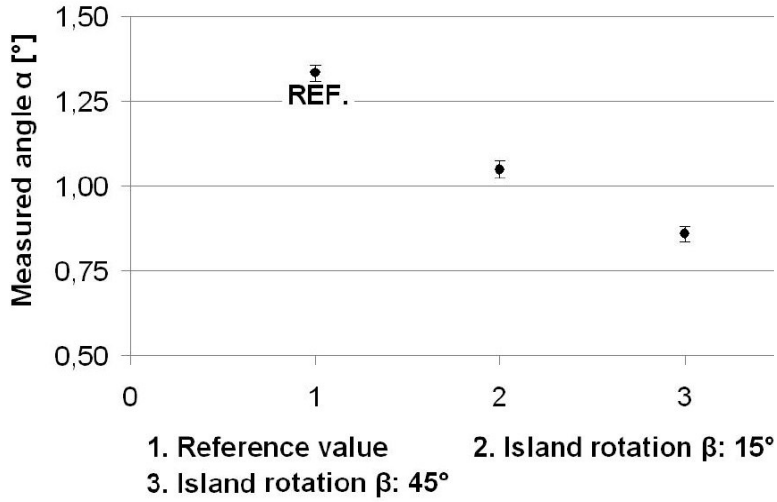

Figure 5.73: Results of sectoral scanning with different orientation

As a result of residual stress measurements, it is concluded that sectoral scanning reduces the residual stresses significantly. However, changing the sector size does not contribute to any further improvement, whereas the maximum reduction is achieved when the sectors are oriented 45 degrees with respect to the x-axis (i.e. x scan direction).

The influence of pre-scanning and post-scanning (or laser re-melting after every layer) on residual stresses was tested on the LM1 machine using Ti6Al4V powder without island scanning. When pre-scanning is applied, the laser first sinters the powder material, before melting the material completely with the reference parameters (a scan speed of 225 mm/s, a laser power of 42 W, a scan spacing of 74 µm and a layer thickness of 30 µm). The results for pre-scanning with 800 mm/s and 1600 mm/s and a constant laser power of 42 W are presented in Figure 5.74a. The value at 0 mm/s is the reference value without pre-scanning. Pre-scanning reduces the measured angle α only slightly with a maximum reduction of 6% for pre-scanning with 800 mm/s. The results for laser re-melting performed with different scan speeds on the LM1 machine are shown in Figure 5.74b where the value at 0 mm/s corresponds to the reference part without post-scanning). Only the low scan speeds reduce the measured angle. A scan speed of 100 mm/s gives the maximum reduction of 8%. For a discussion of the influence of the other SLM parameters (scan pattern, orientation of the scan vectors, layer thickness, preheating of the base plate, heat treatment, etc.), the studies reported in [13, 183] can be referred to.

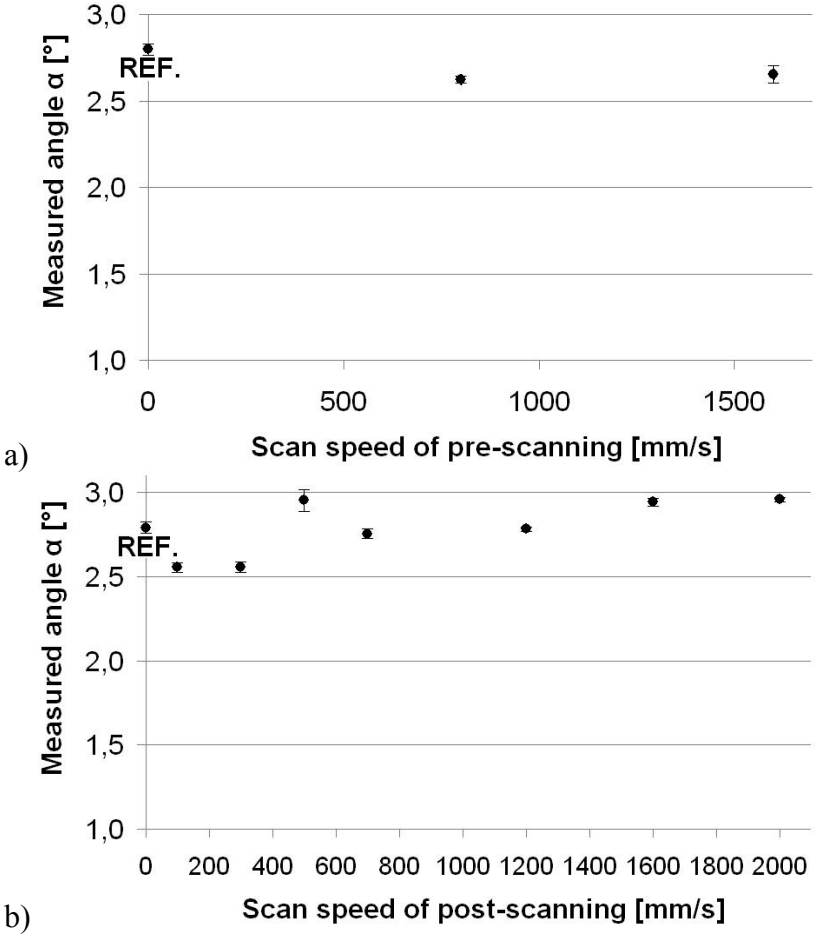

Figure 5.74: Results of pre- and post-scanning (laser re-melting)

5.3.4 Conclusions

In this study, a scanning strategy for SLM, i.e. island scanning, is taken under investigation to see if this strategy can solve some limitations of SLM. The scan spacing factors between successive scan tracks and neighbouring sectors are studied to test how they influence the surface quality and the obtained part density. The scan spacing between successive scan tracks is found to be optimal at 62% of the spot size for process parameters yielding a scan speed of 300 mm/s, a laser power of 100 W, a spot size of 180 µm and a layer thickness of 30 µm. Very low scan spacings resulted in excessive energy intensity into the powder material resulting in irregular and big pores, whereas

very high scan spacing factors resulted in un-melted regions between tracks resulting in aligned and excessive porosity. The effect of sector offset on density and surface quality is also studied revealing that the sectoral scanning may result in poor connections between sectors which will deteriorate the mechanical properties significantly unless a suitable overlap is set. Finally, the island scanning is shown to reduce the residual stresses compared to common scan strategies, especially when the orientation of the scan tracks is set to 45°. The sector size does not play any significant role on the residual stresses. Laser re-melting after every layer does not influence the residual stresses significantly.

5 Summary of Achievements and Main Conclusions

This last chapter repeats the main conclusions and achievements that were presented in the previous chapters, and proposes some recommendations for future work.

The Additive Manufacturing Group at K.U.Leuven mainly aims at improving the SLM process to a level enabling production of functional parts and tools with good part and material properties, even when very complex geometries are involved. This thesis mainly targets to improve the SLM process regarding various aspects such as surface roughness, density, mechanical properties and precision and micro machining capability by employing secondary processes such as Selective Laser Erosion (SLE) and laser re-melting. In order to accomplish manufacturing by combining SLM with SLE or laser re-melting, the secondary processes were first studied in detail to understand the different mechanisms in those processes other than SLM. Moreover, some other issues related to the process productivity, mechanical testing and process optimization are addressed in the frame of SLM without any secondary process.

- ***Selective Laser Erosion***

SLE can be considered as the reverse operation of SLM due to its subtractive nature. In SLE, the energy of a high intensity laser beam, operated in pulsed mode, is used to remove material by different mechanisms that were introduced in the second chapter. SLE is a complex process since it involves different mechanisms like melting, evaporation, melt pool expulsion, plasma formation and recoil pressure. Therefore, the SLE process was first studied step by step. Firstly, one-dimensional erosion, in other words laser marking, was studied. The laser mark profiles made with different combinations of scan speed, laser power and pulse frequency values, were measured with a 3D surface profilometer and the cross-sectional views of the marks were observed by optical microscopy. The results showed that the investigated process parameters, i.e. laser power, scan speed and pulse frequency, all play an important role on the obtained geometries of the laser marks. Depending on the dominant mechanisms, the laser mark had a different profile (a bump in the middle or a crater with shoulder formations on the sides) which changes the readability of the mark significantly. From a visual point of view, the highest contrast is obtained by the marks having a sharp peak in the middle. However, the optical microscopy pictures revealed that these marks have excessive porosity underneath the bulb going 1.5 mm deep in the marked surface. Therefore, the laser marks with deep groove and short rims are preferable as they are free of any porosity. It is also seen that most of the parameter combinations do not result in evaporation of material, but only melting and re-solidification. At very low scan speed (around 1 mm/s) and high laser powers (greater than 85-90 W), which lead to excessive laser intensity, the plasma generation limits the energy given to the substrate, resulting in no evaporation. At this scan speed, only low laser power values result in evaporation of material in one-dimensional erosion. At high scan speed (>200 mm/s), the laser mark profile is in the shape of a crater with shoulder formations without any sign of significant evaporation. Thus, only enough overlapping of scan tracks at high scan speeds may give a possibility for two or three dimensional erosion. Secondly, two-dimensional erosion, in other words laser milling, is taken under investigation. Two-dimensional erosion is actually the most important step in this research since SLE is employed in a layer-wise manner during SLM in most of the experiments combining SLM and SLE. The process window studies for two-dimensional

erosion were conducted to find out optimal combinations of laser power and scan speed at two different settings for the rest of parameters (scan spacing, pulse frequency, aperture selection). The results showed that low scan speeds combined with high laser powers resulted in high erosion depths and very rough surfaces with a significant colour change. High scan speeds combined with low laser power lead to only melting or almost no change on the irradiated surfaces. The region in between these two zones gives good results yielding a compromise in between good surface quality and high productivity.

After the process window study, the influence of process parameters in SLE was tested on the depth of erosion and surface roughness. As a result of single-factor tests, applied on different materials, it is concluded that the investigated parameters have very important influence on the depth of erosion, in other words erosion rate, and on the surface quality left behind. The optimal values of some parameters, e.g. scan spacing and pulse frequency, are the same when aiming a high depth of erosion with a good surface quality. On the other hand, depending on the application, parameters like scan speed and laser power should be either adjusted for a good surface quality or for a high erosion rate or combinations of two regimes may be employed.

As a last step in SLE, three-dimensional (3D) erosion was taken under investigation to demonstrate the ability of the SLM/SLE equipment to perform 3D engravings on metallic substrates. As a result of the tests carried out on the Concept Laser M3 Linear machine, it is concluded that the small aperture, giving a smaller spot size and lower laser power compared to the big aperture, should be preferred in order to erode tiny structures or small details. The small aperture also gives better results in terms of visual quality due to lower edges formed during erosion compared to the big aperture. For satisfying results, the depth of erosion per layer should be precisely known before the process starts in order to be able to prepare the slicing data accurately. A better solution is the online measurement of the depth of erosion during the process to provide that the laser beam stays in focus. Due to the divergence of the laser beam, the energy density varies as the targeted surface moves out of the focus with a distance more than the Rayleigh length. This reduces the laser energy density due to increase in the spot size, which may result in only melting with no evaporation of the targeted material. However, online monitoring of the erosion depth is not currently possible on the Concept Laser M3 Linear machine. To sum up, with this study on Selective Laser Erosion , the influences of many process parameters (scan speed, laser power, scan spacing, scanning strategy, material, spot size, etc.) were investigated on the output parameters (depth of erosion and surface quality) as well as dominating mechanisms in the SLE process.

- ***Selective Laser Melting + Selective Laser Erosion***

Chapter 3 reports about manufacturing by combining Selective Laser Melting and Selective Laser Erosion, exploring the advantages and limitations. Depending on the ultimate goal, combining these two processes can be done in several ways, i.e. applying SLE after every SLM layer either on contours or on the whole layer area, or applying SLE on the top surfaces after the SLM process is completed, etc. The experiments pointed out that the surface roughness is improved by about 50 % by applying SLE on the top surfaces after the SLM process is completed. However, a better improvement of about 90% is obtained when laser re-melting follows the SLE step. Moreover, the improvement of surface roughness with laser re-melting, unlike SLE, does not depend on the initial roughness of the surface: it does not make any difference whether it is a rough SLM surface (R_a of about 12 μm) or a smoother surface obtained by SLE (R_a of about 6 μm). Therefore, laser re-melting is studied in more detail and the results are presented in Chapter 4. However, the scan speed and scan spacing to obtain a good surface roughness with SLE (600 mm/s and 40% of the spot size to achieve 6 μm of R_a) are higher than the ones needed for laser re-melting (200-400 mm/s and 10% of the spot size to achieve ~1.5 μm of R_a) meaning that the production time with SLE is much

shorter (6 times). Therefore, SLE can easily be applied when a 50-60% improvement in surface roughness is satisfactory.

The in-plane micro machining capability of SLM process is limited to the size of the melt pool which is bigger than the spot size of the laser beam due to dragging of the surrounding powder. The melt pool size also depends on the material-laser beam interaction. If the heat conductivity of the material is very high, the melt pool size is smaller compared to low conductive materials that do not transfer a lot of heat to the surrounding powder material. The experiments carried out in the scope of this research with AISI 316L stainless steel and or with Ti6Al4V at K.U.Leuven [3] showed that it is not possible to make small features having dimensions less than 500 μm on the Concept Laser M3 Linear machine when the steel coater scrapers are utilized. However, SLE can increase the micro machining capability of the process significantly if no powder is involved around the area exposed to SLE (which is needed to avoid bark formation). The minimum circular hole diamater and slit size is about 100 μm with the combined process of SLM and SLE when SLE is applied after SLM is completed.

Another approach was taken being laying SLE during the process after every layer to remove the roughness peaks and edges formed during SLM that may hamper the deposition of further powder layers. However, this requires the erosion of the whole surface of the SLM layer which is surrounded by powder material. This generally leads to 'bark' formation. The thickness and uniformity of the bark depends on the selected aperture and slightly on the selected process parameters. Generally, it is difficult to distinguish the bark from the part with naked eye. The bark formation deteriorates the dimensional accuracy but it could be compensated for since the thickness mainly depends on the aperture selection but does depend on either the geometry or the selection of other process parameters.

The side surface roughness (vertical walls and slanted surfaces) of SLM parts is addressed by combining process of SLM and SLE in different manners, e.g. eroding the whole layer area to reduce the effective layer thickness or by eroding the contours only. By applying SLE with small aperture only on the contours of every SLM layer, the side surface roughness measured on vertical walls decreased about 33%, mainly due to the formation of a smooth and uniform bark around the part. However, applying SLE on the whole surface area to improve the resolution and accuracy in the build direction does not drastically reduce the stair-effect but only shows a slight improvement in the average roughness of the inclined surfaces, used as an indicator of the stair-effect. However, the stair-effect is almost completely removed when laser re-melting is applied on inclined surfaces as explained in the following chapter.

- ***Laser Re-melting***

Chapter 4 presents the results of laser re-melting experiments conducted to enhance the SLM process mainly regarding density and surface roughness. It is found that laser re-melting is a promising method to increase the density of SLM parts to almost 100% and to reduce the surface roughness by about 90% at a cost of longer production times. However, the process parameters in laser re-melting affect the results significantly and therefore should be selected properly. For an effective improvement in density, too high energy inputs to the substrate should be avoided by not selecting very low scan spacing or scan speed values. In this manner, the additional production time is kept to a minimum. Additionally, laser re-melting is an easy method to improve the surface quality significantly, without removing the parts from the SLM machine and introducing any fixation errors, when applied on top surfaces after the parts are completely built by SLM. It can also be easily applied on the slanted or curved surfaces after the surrounding powder is blown away around the parts. With a few basic software changes to allow the movement of the building platform to keep the laser beam in focus, it can be applied in a continuous manner. For surface roughness enhancement, the production time is not necessarily affected since the laser re-melting is applied

only on the outer surfaces of the SLM parts. Surface quality enhancement by laser re-melting also leads to a fully dense shell around the part. Since surface porosity is known to affect both the stress distribution and deformation of subsurface layers leading to subsurface crack formation and propagation, fully dense shell is especially important for applications requiring high wear resistance. Not only wear but also other surface properties such as thermal and electrical conductivity are highly dependent on the surface porosity.

The potential of laser re-melting to eliminate the stair effect by applying it only on layer contours during the SLM process is also explored. However, no significant benefits could be obtained. The main disadvantage of laser re-melting is found to be the formation of elevated edges of the solidified material which deteriorates the dimensional accuracy and causes collisions with the hard scrapers of the coater. This phenomenon is not only seen in laser re-melted parts but also in all processes involving melt pools like SLM, EBM and LENS or other laser cladding additive processes. The possible reasons causing this undesired effect are investigated and possible solutions are searched in the scope of this work. Post-fill scanning strategy seems to be the best solution among others without lowering the shell density of SLM parts.

- ***Selective Laser Melting as initial production step***

Chapter 5 searched to improve the basic SLM process independently of the application of a secondary process. First of all, optimization of a commonly used material in tooling applications, maraging steel 300 (18-Ni 300), is performed taking density, surface quality and productivity into account. This work showed how the optimum process parameters (in terms of productivity and density) may deviate from the ones recommended by SLM equipment vendors. For a more productive process, the scan speed, the layer thickness and the scan spacing are considered as the most important parameters if the maximum laser power is set as constant. Among these three factors, the layer thickness plays the most critical role since it determines the total time for laying powder together with the total scanning time. The effect of different process parameters, namely the scan speed and layer thickness, on the obtained density and surface roughness is studied for two machines (a Concept Laser M3 Linear and an EOSINT M270) employing different laser sources (an Nd:YAG laser and a fiber laser). To achieve maximum density, there is a certain threshold for the energy density and below that, the density decreases with decreasing energy density. Above the threshold, the density is not significantly affected by increasing energy densities. Besides, too high roughness values obtained at very high energy inputs deteriorate the obtained densities, probably due to inhomogenous powder deposition. For the Concept Laser M3 Linear machine, the effect of layer thickness on the relative density found to be important especially at high scan speed. With rising layer thickness, the density dropped in this high speed region. At low scan speed, where the maximum density is obtained, the effect of layer thickness and scan speed becomes less significant. On the Concept Laser M3 Linear machine, the maximum density is obtained at the lowest scan speed values used in the tests. For EOSINT M270, the maximum density is achieved at a mid-range scan speed depending on the selected layer thickness as recommended by EOS. Below or above this optimum scan speed range, the density decreases due to either too low energy input resulting in partially melting or too high energy input leading to very bad surface quality. The influence of layer thickness on the relative density at the optimum range of the scan speed is also very little. The effect of the layer thickness on the surface quality is more important than the influence of the scan speed. As the layer thickness increases, higher roughness values are obtained due to bigger melt pools. In addition to density and surface roughness measurements, the hardness of this material after SLM was tested. As expected, the macro hardness results showed that the porosity decreases the hardness. The influence of the scan speed and layer thickness is not as significant as the porosity itself. Therefore, it can be concluded that changing the process parameters in the selected and tested ranges does not significantly change the cooling rates to alter the obtained hardness of the parts. In order to test the mechanical properties of maraging steel 300, the maximum density should be

attained in the specimens. Therefore, laser re-melting is employed after every layer to increase the density at a cost of higher production times. With this technique, the mechanical specimens produced by SLM did not have any aligned porosity or irregularity. The effect of metallurgical aging is tested on the specimens produced by combining laser re-melting and selective laser melting. Different aging times and temperatures are tested to find out the best combination giving highest hardness improvement taking the post-processing time into account. 5 hours at 480°C is found out to give high hardness within a relatively short time. With aging tests, it is seen that keeping the specimens at a prolonged time in the heat treatment may deteriorate the material properties since it causes the precipitates to coarsen and austenite reversion. These two mechanisms decrease the hardness. Therefore, the duration for aging should be selected in a range where overaging has not yet started for the selected temperature. In the scope of this study, the constants in the expression derived from Avrami's equation are determined for maraging steel 300 as a result of aging treatments done at different temperatures.

As a second sub-section in Chapter 5, the results regarding Charpy impact toughness testing of this material together with other commonly used materials in SLM (AISI 316L stainless steel and Ti6Al4V) are presented. The experiments were carried out to test the influence of various factors on the toughness. It is found out that the roughness of SLM parts does not behave like stress-concentrating notches. The parts without a notch showed significantly higher impact energies compared to specimens with a notch, either made during the SLM process or after SLM by EDM. This also concludes that the way of production of the notch does not affect the toughness results for this case. Secondly, the tests with maraging steel 300 and AISI 316L revealed that the building axis does not play an important role on the toughness results if the connection between successive layers is well established without any directional porosity. When compared to conventionally manufactured parts, SLM may lower the impact toughness which is due to many reasons. It may be due to the nature of the process, e.g. un-melted powder particles, 1-2% porosity or undesired brittle phases due to high cooling rates for some materials like Ti6Al4V. However, this does not imply that all materials processed by SLM exhibit a lower toughness: for example, stainless steel processed on the EOSINT M270 exhibits a toughness as high as the one obtained by conventional techniques. In addition to the nature of SLM, process defects like a dirty laser window or improper selection of process parameters, can reduce the toughness dramatically. For repeatable mechanical properties, the material composition of the powder should also be well controlled and kept in a limited range; the process defects should be avoided and proper heat treatments to form desired ductile phases should be employed.

As the last section in Chapter 5, a scanning strategy for SLM, i.e. island scanning, is taken under investigation to test if this strategy can solve some limitations of SLM. The scan spacing factors between successive scan tracks and neighbouring sectors are studied to test how they influence the surface quality and the obtained part density. The scan spacing between successive scan tracks (a_1) is found to be optimal at 62% of the spot size at constant process parameters (a scan speed of 300 mm/s, a laser power of about 105 W and a spot size of 180 μm). Very low scan spacing factors, in other words very high overlaps, resulted in excessive energy intensity into the powder material resulting in irregular and big pores, whereas very high scan spacing factors resulted in unmelted regions between tracks resulting in aligned and excessive porosity. The effect of island offset (a_2) on density and surface quality is also studied revealing that the island scanning may result in poor connections between sectors which will deteriorate the mechanical properties significantly unless a suitable overlap is set. Finally, the island scanning is shown to reduce the residual stresses compared to common scan strategies, especially when the orientation of the scan tracks is set to 45°. The sector size does not play any significant role on the residual stresses.

- ***General conclusion***

To conclude, this study has contributed to a better understanding of the fundamentals of Selective Laser Erosion of steel substrates and demonstrated how that knowledge could be used to improve the Selective Laser Melting process regarding the surface quality and micro machining capability. Moreover, laser re-melting is studied in detail and employed during SLM for a higher density part or shell, a better surface quality and improved hardness. The work involving only SLM showed that it is very important to optimize the process parameters for each material to obtain a good density leading to comparable part and material properties to those of conventionally produced parts.

Reference List

1. Reeves, P. 2009, “Rapid Manufacturing’s Socio-Economic Benefits”, *Medical Manufacturing 2009 (supplement to Manufacturing Engineering)*, pp.19-21.
2. Wohlers, Terry, Wohlers Report 2009, printed in USA, 2009, ISBN: 0-9754429-5-3.
3. Vandenbroucke, B., Selective Laser Melting of biocompatible metals for rapid manufacturing of medical parts, PhD Thesis, Catholic University of Leuven, Leuven, Belgium, 2008.
4. Kruth, J.-P., Leu, M.C. and Nakagawa, T. 1998, “Progress in Additive Manufacturing and Rapid Prototyping”, *CIRP Annals*, Vol. 47, No. 2, pp.525-540.
5. Van Vaerenbergh, J., Process optimization in Selective Laser Melting, PhD thesis, University of Twente, Twente, The Netherlands, 2007.
6. Rombouts, M., Selective Laser Sintering/Melting of iron-based powders, PhD thesis, Catholic University of Leuven, Leuven, Belgium, 2006.
7. Kruth, J.-P., Froyen, L., Van Vaerenbergh, J., Mercelis, P., Rombouts, M. and Lauwers, B. 2004, “Selective Laser Melting of iron-based powder”, *Journal of Materials Processing Technology*, Vol. 149, No. 1-3, pp. 616-622.
8. Mumtaz, K. and Hopkinson, N. 2008, “Selective Laser Melting of Inconel 625® using pulse shaping”, *Proc. of Solid Freeform Fabrication Symposium*, August 4-5, Austin, TX, USA, pp. 165-179.
9. Regenfuss, P., Streek, A., Hartwig, L., Kloetzer, S., Brabant, Th., Horn, M., Ebert, R. and Exner, H. 2007, “Principles of laser micro sintering”, *Rapid Prototyping Journal*, Vol. 13, No. 4, pp. 204-212.
10. Osakada, K. and Shiomi, M. 2006, “Flexible manufacturing of metallic powders by Selective Laser Melting of powder”, *International Journal of Machine Tools and Manufacture*, Vol. 48, No. 11, pp. 1188-1193.
11. Meiners, W., Wissenbach, K. and Gasser, A. 2001, Selective laser sintering and melting temperature, U.S. Patent US0062150993B1.
12. Herzog, F., 2001, Method for the production of three-dimensional sintered workpieces, patent of CL island scanning Europaeische Patentschrift EP 1 441 897 B1, 30.10.2001.
13. Kruth, J.-P., Deckers, J., Yasa, E. and Wauthlé, R. 2010, “Assessing influencing factors of residual stresses in Selective Laser Melting using a novel analysis method”, *Proc. 16th International Symposium on Electromachining (ISEM XVI)*, Shanghai, China,19-23 April, pp.531-540.
14. Badrossamay, M., Yasa, E., Van Vaerenbergh, J. and Kruth, J.-P. 2009, “Improving productivity rate in SLM of commercial steel powders”, *RAPID 2009 Conf. and Expo.*, May 12-14, Schaumburg, IL, USA.
15. Kruth, J.-P., Vandenbroucke, B., Van Vaerenbergh, J. and Mercelis, P. 2005, “Benchmarking of different SLS/SLM processes as rapid manufacturing techniques”, *International Conference on Polymers & Moulds Innovations (PMI)*, Gent, Belgium, April 20-23, 2005.
16. Mercelis, P., Control of Selective Laser Sintering and Selective Laser Melting Processes, PhD thesis, Catholic University of Leuven, Leuven, Belgium, 2007.
17. Van Elsen, M., Complexity of Selective Laser Melting: a new optimization approach, PhD Thesis, PhD thesis, Catholic University of Leuven, Leuven, Belgium, 2007.
18. Pham, D.T. and Wang, X. 2000, “Prediction and reduction of build times for the selective laser sintering process”, *Proc. IMechE Part B: J. Engineering Manufacture*, Vol. 214, pp. 425-430.
19. Khoshnevis, B., Asiabanpour, B., Mojdeh, M. and Palmer, V.V. 2003, “SIS-a new SFF method based on powder sintering”, *Rapid Prototyping Journal,* Vol. 9, No.1, pp. 30-36.
20. Hopkinson, N. and Erasenthiran, P.E. 2004, "High speed sintering-early research into a new rapid manufacturing process", *Proc. of 15th Solid Freeform Fabrication Symposium,* Austin, TX, August 2-4, pp. 312-320.
21. Schleifenbaum, H., Wissenbach, K. 2007, “Increasing the build-up rate of Selective Laser Melting (SLM) processes”, Fraunhofer ILT Annual Report 2007, p. 77.
22. Kannatey-Asibu, E. 2009, Principles of Laser Materials Processing, John Wiley & Sons ISBN 978-0-470-17798-3, New Jersey, USA.

23. Vanderschueren, B., Basic Contributions to the Development of the Selective Metal Powder Sintering Process, PhD thesis, Catholic University of Leuven, Leuven, Belgium, 1996.
24. ASM Handbook, Volume 1 Properties and Selection: Irons, steels and high performance alloys, 1990, ASM International, The Materials Information Company, United States of America, ISBN 0-87170-377-7 (v.1), pp.1303-1408.
25. Azo Materials: www.azom.com/details.asp?articleid=2382
26. Arcam (Ti6Al4V data sheet): www.arcam.com/CommonResources/Files/www.arcam.com/Documents/EBM%20Materials/Arcam-Ti6Al4V-Titanium-Alloy.pdf
27. LPW Technology: www.lpwtechnology.com/
28. van der Ploeg, T. 1999, "Laser marking aids product identification", *Reinforced Plastics*, Vol.43, No.5, pp. 50-52.
29. Jundt, H. and Junghans, J. 1987, "Microscopic material interactions by laser engraving", *Proc. SPIE*, Vol. 744, pp. 147-155.
30. Qi, J., Wang, K.L. and Zhu, Y.M. 2003, "A study on the laser marking process of stainless steel", *Journal of Materials Processing Technology*, Vol. 139, No.1-3, pp. 273-276.
31. Ion, J.C. 2005, Laser Processing of Engineering Materials: Principles, Procedure and Industrial Application, Elsevier Butterworth-Heinemann, ISBN 0 7506 6079 1, Norfolk, Great Britain.
32. Chen, M.-F., Hsiao, W.-T. and Huang, W.-L. 2009, "Laser coding on the eggshell using pulsed-laser marking system", *Journal of Materials Processing Technology*, Vol. 209, No.2, pp. 737-744.
33. Laser Engraving Express: www.laserengravingexpress.com/
34. Trumpf: www.lasermarking.trumpf.com
35. Schubart, D., Vollertsen, F. and Kauf, M. 1997, "Process modelling of laser ablating ferrous materials", *Modelling Simul. Mater. Sci. Eng.,* Vol. 5, pp. 79-92.
36. Beyer, E., Petring, D., Zefferer, H. and Eberl, G. 1994, "Laser caving: rapid progress in an advanced technology", *Proc. of Laser Assisted Net shape Engineering LANE'94*, October 12-14, Erlangen, Germany, pp. 477-490.
37. Dumont, Th., Lippert, T., Wokaun, A. and Leyvraz, P. 2004, "Laser writing of 2D data matrices in glass", *Thin Solid Films*, Vol. 453-454, pp. 42-45.
38. Columbia Marking Tools: www.columbiamt.com/CMT-Square-Dot-Marking/Direct_Part_Marking.html
39. Tam, S.C., Noor, Y.M., Lim, L.E.N., Jana, S., Yang, L.J., Lau, M.W.S. and Yeo, C.Y. 1993, "Marking of leadless chip carriers with a pulsed Nd:YAG laser", *Proc. Inst. Mech. Eng. Part B: Journal of Engineering Manufacture*, Vol. 207, No. B3, pp. 179-192.
40. Tezuka, S. and Yoshikawa, M. 1991, "Study on the marking processing of IC packages by YAG laser", *International journal of the Japan society for precision engineering*, Vol. 25, No. 4, pp. 297-298.
41. Hoffmann, M. and Brietenfellner, F. 1987, "High contrast and intact surface – a challenge in laser marking of plastics", *Proc. SPIE*, Vol. 744, pp. 156-180.
42. Bosman, J., Processes and strategies for solid state Q-switch laser marking of polymers, Ph.D. Thesis, University of Twente, Netherlands, 2007.
43. Peligrad, A.A., Zhou, E., Morton, D. and Li, L. 2002, "Dynamic models relating processing parameters and melt track width during laser marking of clay tiles", *Optics and Laser Technology*, Vol. 34, No. 2 pp. 115-123.
44. Valette, S., Steyer, P., Richard, L., Forest, B., Donnet, C. and Audouard, E. 2006, "Influence of femtosecond laser marking on the corrosion resistance of stainless steel", *Applied Surface Science*, Vol. 252, No. 13, pp. 4696-4701.
45. Tam, A.C, Pour, K., Nguyen, T., Krajnovich, D. and Baiumgart, P. 1996, "Experimental and theoretical studies of bump formation during laser texturing of Ni-P disk substrates", *IEEE Transactions on Magnetics*, Vol. 32, No. 5, pp. 3771-3773.
46. Lei, Y.P., Murakawa, Hidekazu, Shi, Y.W. and Li, X.Y. 2001, "Numerical analysis of the competitive influence of Marangoni flow and evaporation on heat surface temperature and molten pool shape in laser surface remelting", *Computational Materials Science*, Vol. 21, No. 3, pp. 276-290.

47. Ganesh, R.K, Faghri, A. and Hahn, Y. 1997, “A generalized thermal modeling for laser drilling process – I. Mathematical modeling and numerical methodology”, *International Journal of Heat and Mass Transfer*, Vol. 40, No. 14, pp. 3351-3360.
48. Basu, S. and DebRoy, T. 1992, “Liquid metal expulsion during laser irradiation”, *Journal of Applied Physics*, Vol. 72, No. 8, pp. 3317-3322.
49. Pham, D.T., Dimov, S.S., Petkov, P.V. and Petkov, S.P. 2002, “Laser milling”, *Proc. Instn. Mech. Engrs. Part B: Journal of Engineering Manufacture*, Vol.216, No. 5, pp. 657-667.
50. Keene, B.J. 1988, “Review of data for the surface tension of iron and its binary alloys”, International *Materials Review*, Vol. 33, pp. 1-36.
51. Sahoo, P., Debroy, T. and McNallan, M.J. 1988, “Surface tension of binary metal-surface active solute systems under conditions relevant to welding metallurgy”, *Metallurgical Transactions B*, Vol. 19B, pp. 483-491.
52. Rombouts, M., Kruth, J.P., Froyen, L. and Mercelis, P. 2006, “Fundamentals of Selective Laser Melting of alloyed steel powders”, *CIRP Annals*, Vol. 55, No.1, pp. 187-192.
53. Han, L. and Liou, F.W. 2004, “Numerical investigation of the influence of laser beam mode on melt pool”, *International Journal of Heat and Mass Transfer*, Vol. 47, pp. 4385-4402.
54. Zhang, Z., Zhou, H., Ren, L., Xin, T., Shan, H. and Li, X. 2008, “Surface morphology of laser tracks used for forming the non-smooth biomimetic unit of 3Cr2W8V steel under different processing parameters”, *Applied Surface Science*, Vol. 254, pp. 2548-2555.
55. Ropel, S.I., Tsarevskii, B.V., Pavlov, V.V. and Furman, E.L. 1975, “Combined influence of oxygen and sulphur on the surface tension of iron”, *Izv. AN. SSSR Metally*, Vol. 4, pp. 54-60.
56. Du, D., He, Y.F., Sui, B., Xiong, L.J. and Zhang, H. 2005, “Laser texturing of rollers by pulsed Nd:YAG laser”, *Journals of Materials Processing Technology*, Vol. 161, pp. 456-461.
57. O’Neill, W., Sutcliffe, C.J., Morgan, R., Landsborough, A. and Hon K.K.B. 1999, “Investigation on multi-layer direct metal laser sintering of 316L stainless steel powder beds”, *CIRP Annals*, Vol. 48, No.1, pp. 151-154.
58. Chickov, B.N., Momma, C., Nolte, S., von Alvensleben, F. and Tuennermann, A. 1996, “Femtosecond, picosecond and nanosecond laser ablation of solids”, *Applied Physics A: Materials Science and Engineering*, Vol. 63, No. 2, pp. 109-115.
59. Postma, S. Weld pool control in Nd:YAG laser welding, Ph.D. Thesis, University of Twente, Netherlands, 2003.
60. Harimkar, S.P., Samant, A.N. and Dahotre, N.B. 2007, “Temporally evolved recoil pressure driven melt infiltration during laser surface modifications of porous alumina ceramic”, *Journal of Applied Physics*, Vol.101, No.5, pp. 054911 1-7.
61. Concept Laser Gmbh: www.concept-laser.de
62. Taylor Hobson Precision:www.taylor-hobson.com
63. Rozman, R., Govekar, E. and Grabec, I. 2007, “Modelling and characterisation of plasma shielding”, *Proc. of the LANE 2007 Laser Assisted Net Shape Engineering 5*, September 25-28, Erlangen, Germany.
64. Lee, D.J. and Jeong, S.H. 2004, “Analysis of recoil force during Nd:YAG laser ablation of silicon”, *Applied Physics A Material Science and Processing*, Vol. 79, No. 4-6, pp. 1341-1344.
65. ROFIN: http://www.rofin.com
66. Mumtaz, K., Selective Laser Melting of Inconel 625 using pulse shaping, PhD thesis, Loughborough University, UK, 2008.
67. Morgan, R., Sutcliffe, C.J. and O’Neill, W. 2001, “Experimental investigation of nanosecond pulsed Nd:YAG laser re-melted pre-placed powder beds”, *Rapid Prototyping Journal*, Vol. 7, No. 3, pp. 159-172.
68. Gilmore, R., Short pulse laser machining for diesel and aerospace applications, 2007, *Proc. 15th Int. Symp. On Electromachining ISEM XV*, pp. 433-437.
69. Kaldos, A., Pieper, H.J., Wolf, E. and Krause, M. 2004, “Laser machining in die making – a modern rapid tooling process”, *Journal of Materials Processing Technology*, Vol. 155-156, pp. 1815-1820.
70. Lu, S., Fuji, H. and Nogi, K. 2004, “Marangoni convection and weld shape variations in Ar-O2 and Ar-CO2 shielded GTA welding”, *Materials Science and Engineering A*, Vol. 380, pp. 290-297.

71. Kalinichenko, A.S., Devoino, O.G. and Kalinichenko, U.A. 2007, “Laser alloying of Al-Si alloys with transition metals”, *Proc. of the LANE 2007, Laser Assisted Net Shape Engineering 5*, September 25-28, Erlangen, Germany, pp. 761-765.
72. Titovay, V., Smurov, I. and Ignatiev, M. 1996, “Erosion plume dynamics during pulsed laser alloying”, *Applied Surface Science*, Vol. 96-98, pp. 387-392.
73. Tani, G., Orazi, L., Campana, G., Fortunato, A. and Ascari, A. 2007, “A numerical model for laser heat treatment of steels with microstructure evolution and the annealing”, *Proc. of the LANE 2007, Laser Assisted Net Shape Engineering 5*, September 25-28, Erlangen, Germany, pp. 779-789.
74. Mahmoudi, B., Torkamay, M.J., Sabour Rouh Aghdam, A.R. and Sabbaghzade, J. 2009, “Laser surface hardening of AISI 420 stainless steel treated by pulsed Nd:YAG laser”, *Materials and Design*, Vol. 31, No. 5, pp. 2553-2560.
75. Miokovic, T.,Schulze, V., Voeringer, O. and Loehe, D. 2007, “Influence of cyclic temperature changes on the microstructure of AISI 4140 after laser surface hardening”, *Acta Materialia*, Vol. 55, pp. 589-599.
76. Merklein, M., Vogt, U. and Geiger, M. 2007, “Enhanced formability of aluminum blanks by local laser heat treatment”, *Proc. of the LANE 2007, Laser Assisted Net Shape Engineering 5*, September 25-28, Erlangen, Germany, pp. 1279-1288.
77. Kano, S. and Inoue, T. 2006, “Surface softening and hardening of WC-Co using pulsed laser irradiation”, *Surface & Coatings Technology*, Vol. 201, pp. 223-229.
78. Meijer, J. 2004, “Laser beam machining (LBM), state of art and new opportunities”, *Journal of Materials Processing Technology*, Vol. 149, pp. 2-17.
79. Huis in ‘t Veld, B., Groenendijk, M. and Fischer, H. 2008, “On the origin, growth and application of ripples”, *Journal of Micro/Nanoengineering*, Vol. 3, No. 3, pp. 206-210.
80. Wagner, K., Voelkl, R., Engel, U., Geiger, M. and Meyer-Pittroff, F. 2007, “Locally optimized tool surfaces by laser treatment in cold forging”, *Proc. of the LANE 2007, Laser Assisted Net Shape Engineering 5*, September 25-28, Erlangen, Germany, pp. 859-870.
81. Vilhena, L.M., Sedlacek, M., Podgornik, B., Vizintin, J., Babnik, A. and Mozina, J. 2009, “Surface texturing by pulsed Nd:YAG laser”, *Tribology International*, Vol. 42, pp. 1496-1504.
82. Soveja, A., Jouvard, J.M., Grevey, D. and Cicala, E. 2007, “Studies on q-switched Nd:YAG laser texturing of metallic surfaces”, *Proc. of the LANE 2007, Laser Assisted Net Shape Engineering 5*, September 25-28, Erlangen, Germany, pp. 687-701.
83. Willis, E. 1986, “Surface finish in relation to cylinder liners”, Wear, Vol. 109, pp. 351-366.
84. Komvopoulos, K. 2003, “Adhesion and friction forces in microelectromechanical; systems: mechanisms, measurement, surface modification techniques, and adhesion theory”, *Journal of Adhesion Science and Technology*, Vol. 17, No.4, pp. 477-517.
85. Etsion, I. 2005, “State of the art in laser surface texturing”, *Journal of Tribology*, Vol. 127, pp. 248-253.
86. Truong, S.L., Levi, G., Bozon-Verduraz, F., Petrovskaya, A.V., Simakin, A.V. and Shafeev, G.A. 2007, “Generation of nanospikes via laser ablation of metals in liquid environment for the surface-enhanced Raman scattering of organic molecules”, *Applied Surface Science*, Vol. 254, pp. 1236-1239.
87. Tam, A.C. 2001, “Laser processes for precise microfabrication of magnetic disk-drive components”, *RIKEN Review, No.32: Focused on Laser Precision Microfabrication (LPM2000)*, pp. 71-76.
88. Nayak, B.K., Gupta, M.C. and Kolasinski, K.W. 2007, “Ultrafast-laser-assisted chemical restructuring of silicon and germanium surfaces”, *Applied Surface Science*, Vol. 253, pp. 6580-6583.
89. Prinsloo, F.J., van Heerden, S.P. and Ronander, E. 2007, “Efficient TEA CO2 laser based coating removal system”, *XVI International Symposium on Gas Flow, Chemical Lasers, and High-Power Lasers, Proc. of SPIE,* Vol. 6346, pp. 63462Q-2.
90. Coutouly, J.-F., Deprez, P., Breaban, F. and Longuemard, J.-P. 2009, “Optimisation of a paint coating ablation process by CO2 TEA laser: Thermal field modelling and real-time monitoring of the process”, *Journal of Materials Processing Technology*, Vol. 209, pp. 5730-5735.
91. Harald, E., Lothar-bernhard, H., Tillmann, D., 2009, Laser-assisted coating removal method, United States Patent 7525065.
92. Lentjes, M., Dickmann, K. and Meijer, J., 2004, “Controlled laser cleaning and ablation by laser induced plasma emission analysis via miniature spectrometer”, *Proc. of LANE 2002 Laser Assisted Net Shape Engineering 4*, Erlangen, Germany, pp. 803-810.

93. Zhou, X., Imasaki, K., Furukawa, H., Umino, H., Sakagishi, K., Nakai, S. and Yamanaka, C. 2001, “Simulation study and experiment on laser-ablation surface cleaning”, *Optics and Laser Technology*, Vol. 33, pp. 189-194.

94. Giedl-Wagner, R., Ut Huynh, Q., Hopfinger, R. and Pauli, A. 2007, “Ablation behaviour of metals for the mould and die industry”, *Proc. of LANE 2007 Laser Assisted Net Shape Engineering 5*, September 25-28, Erlangen, Germany, pp. 705-713.

95. Klocke, F. and Kordt, M. 2004, “Laser microablation: tribological microstructures for hydraulic components”, *Proc. of LANE 2002, Laser Assisted Net Shape Engineering 4*, pp. 803-810.

96. Yasa, E., A study on Selective Laser Erosion and its applications, Pre-doctoral thesis, K.U.Leuven, Heverlee, Belgium, 2006.

97. AISI Grade 316L stainless steel properties: www.azom.com/details.asp?ArticleID=2382

98. AISI Grade 18Ni (300) maraging steel nominal annealed properties:
www.matweb.com/search/DataSheet.aspx?MatGUID=a46fae23f0a542f790d932f628934d8c

99. Trumpf: www.trumpf-laser.com/

100. Oxford Lasers: www.oxfordlasers.com/micromachining/applications/micro_milling

101. Laser Cusing NL: www.lasercusing.nl/content.php/en/237

102. Fleischer, J. and Haupt, S. 2007, “Laser material processing of micro structures by using picosecond lasers”, *Proc. of LANE 2007 Laser Assisted Net Shape Engineering 5*, September 25-28, Erlangen, Germany, pp. 1187-1193.

103. Sam’s Laser FAQ: http://an.hitchcock.org/repairfaq/sam/laserioi.htm

104. Encyclopedia of Laser Physics and Technology: www.rp-photonics.com/m2_factor.html

105. Gysen, B. and Vanparys, M., Het toepassen van selectieve laser erosie voor het verbeteren van selectief laser gesmolten stukken, Dept. of Mech. Eng., K.U.Leuven, Master thesis, 2006 *(in Dutch)*.

106. Morgan, R., Sutcliffe, C.J. and O'Neill, W. 2004, "Density analysis of direct metal laser re-melted 316L stainless steel cubic primitives", *Journal of Materials Science*, Vol. 39 No.4, pp.1195-205.

107. O'Neill, W., Sutcliffe, C.J., Morgan, R. and Hon, K.K.B. 1998, "Investigation of short pulse Nd:YAG laser interaction with stainless steel powder beds", Proc. of Solid Freeform Fabrication Symposium, Austin, TX, USA, pp.147-60.

108. Glardon, R., Karapatis, N., Romano, V. And Levy, G.N., 2001, “Influence of Nd:YAG parameters on Selective Laser Melting of metallic powders”, CIRP Annals, Vol. 50, No.1, pp.133-136.

109. J.-P. Kruth, E. Yasa, M. Vanparys and J. Van Vaerenbergh, The enhancement of micromachining ability of Selective Laser Melting by Selective Laser Erosion, International Conference on Polymers and Moulds Innovations, PMI Gent, Belgium (2007).

110. Van Bael, S., Vandenbroucke, B., Kerckhofs, G., Schrooten, J. and Kruth, J.-P. 2009, “Design and production of bone scaffolds with selective laser melting”, *Proc. TMS 2009, 138th TMS Annual Meeting and Exhibition*, February 15-19, San Francisco, CA, USA.

111. Henari, F.Z. and Blau, W. 1995, “Excimer-laser surface treatment of metals for improved adhesion”, *Applied Optics*, Vol. 34, pp. 581-584.

112. Nicolas, G., Autric, M., Marine, W. and Shafeev, G.A. 1997, “Laser induced surface modifications on ZrO ceramics”, *Applied Surface Science*, Vol. 109-110, pp. 289-292.

113. Triantafyllidis, D., Li, L. and Stott, F.H. 2005, “The effects of laser-induced modification of surface roughness of Al_2O_3-based ceramics on fluid contact angle”, *Materials Science and Engineering A*, Vol. 390, pp. 271-277.

114. Lamikiz, A., Sanchez, J.A., Lopez de Lacalle, L.N. and Arana, J.L. 2007, “Laser polishing of parts built up by selective laser sintering”, *International Journal of Machine Tools and Manufacture*, Vol. 47, No.12-13, pp. 2040-2050.

115. Ramos-Grez, J.A. and Bourell, D.L. 2004, “Reducing surface roughness of metallic freeform-fabricated parts using non-tactile finishing methods”, *International Journal of Materials and Product Technology*, Vol. 21, pp. 297-316.

116. Kac, S. and Kusinki, J. 2004, “SEM structure and properties of ASP2060 steel after laser melting”, *Surface and Coatings Technology*, Vol. 180-181, pp. 611-615.

117. Xianqing, Y., Chengjun, Z., Xuefeng, S., Manping, H. and Jianguo, M. 2007, “Microstructure evolution of WC/steel composite by laser surface re-melting”, *Applied Surface Science*, Vol. 253, pp. 4409-4414.

118. Pinto, M.A., Cheung, N., Ierardi M.C.F. and Garcia, A. 2003, “Microstructural and hardness investigation of an aluminum-copper alloy processed by laser surface melting”, *Materials Characterization*, Vol. 50, pp. 249-253.

119. Zhang, Y., Chen, J., Lei, W. and Xv, R. 2008, “Effect of laser surface melting on friction and wear behaviour of AM50 magnesium alloy”, *Surface and Coatings Technology*, Vol. 202, pp. 3175-3179.

120. Felgueroso, D., Vijande, R., Cuetos, J.M., Tucho, R. and Hernandez, A. 2008, “Parallel laser melted tracks: Effects on the wear behaviour of plasma-sprayed Ni-based coatings”, *Wear,* Vol. 264, pp. 247-263.

121. Tang, C.H., Cheng, F.T. and Man, H.C. 2004, “Improvement in cavitation erosion resistance of a copper based propeller alloy by laser surface melting”, *Surface and Coatings Technology,* Vol. 182, pp. 300-307.

122. Xu, W.L., Yue, T.M., Man, H.C. and Chan, C.P. 2006, “Laser surface melting of aluminium alloy 6013 for improving pitting corrosion fatigue resistance”, *Surface and Coatings Technology*, Vol. 200, pp. 5077-5086.

123. Guozhi, X., Jingxian, Z., Yijun, L., Keyu, W., Xiangyin, M. and Pinghua, L. 2007, “Effect of laser remelting on corrosion behavior of plasma-sprayed Ni-coated WC coatings”, *Materials Science and Engineering A*, Vol. 460-461, pp. 351-356.

124. Hao, L. and Lawrence, J. 2006, “Effects of Nd:YAG laser treatment on the wettability characteristics of a zirconia based bioceramic”, *Optics and Lasers in Engineering*, Vol. 44, pp. 803-814.

125. Lawrence, J. and Li, L. 2001, “A laser based technique for the coating of mild steel with a vitreous enamel”, *Surface and Coatings Technology*, Vol. 140, pp. 238-243.

126. Grabowski, A., Formanek, B., Sozanska, M. and Nowak, M. 2006, “Laser remelting of Al-Fe-TiO_3 composite powder incorporated in an aluminum matrix”, *Journal of Achievements in Materials and Manufacturing Engineering*, Vol. 18, No. 1-2, pp. 95-98.

127. Shiomi, M., Osakada, K., Nakamura, K., Yamashita, T. and Abe, F. 2004, “Residual stress within metallic model made by Selective Laser Melting Process”, *CIRP Annals - Manufacturing Technology*, Vol. 53, No.1, pp. 195-198.

128. Morgan, R.H., Papworth, A.J., Sutcliffe, C., Fox, P. and O’Neill, W. 2002, “High density net shape components by direct laser re-melting of single phase powders”, *Journal of Materials Science*, Vol. 37, pp. 3093-3100.

129. Kruth, J.-P., Deckers, J. and Yasa, E. 2008, “Experimental investigation of laser surface re-melting for the improvement of Selective Laser Melting process”, *Proc. of the 19th Solid Freeform Fabrication Symposium*, Aug 4-6, Austin, TX, USA.

130. Braga, F.J.C., Marques, R.F.C., Filho, E.A. and Guastaldi, A.C. 2007, “Surface modification of Ti dental implants by Nd:YVO_4 laser irradiation”, *Applied Surface Science*, Vol. 253, pp. 9203-9208.

131. Yasa, E. and Kruth, J.-P. 2008, “Experimental study of the combined process of Selective Laser Melting and Selective Laser Erosion”, *Proc. of RAPID 2008 Conference*, May 20-22, Lake Buena Vista, FL, USA.

132. Kruth, J.-P., Yasa, E. and Deckers, J. 2008, “Roughness improvement in selective laser melting”, *Proc. of international Conference PMI 2008*, September 17-19, Ghent, Belgium, pp. 170-183.

133. Mumtaz, K.A., Erasenthiran, P. and Hopkinson, N. 2008, “High density Selective Laser Melting of Waspaloy”, *Journal of Materials Processing Technology*, Vol. 195, pp. 77-87.

134. Mumtaz, K.A. and Hopkinson, N. 2010, “Selective Laser Melting of thin wall parts using pulse shaping”, *Journal of Materials Processing Technology*, Vol. 210, pp. 279-287.

135. Aggarangsi, P. and Beuth, J.L. 2003, “Melt pool size and stress control for laser based deposition near a free edge”, *Proc. of the 15th Solid Free Fabrication Symposium*, August 4-6, Austin, TX, USA, pp.196-207.

136. Rangaswamy, P., Griffith, M.L., Prime, M.B., Holden, T.M., Rogge, R.B., Edwards, J.M. and Sebring, R.J. 2005, “Residual stresses in LENS components using neutron diffraction and contour method”, *Materials Science and Engineering A*, Vol. 399, pp. 72-83.

137. Ruffo, M., 2009, “Metal rapid manufacturing: Laser versus electron beam technology”, *Proc. of RAPID 2009 Conf. & Expo.*, May 12-14, Schaumburg, IL, USA.

138. Kruth, J.-P., Levy, G., Klocke, F. and Childs, T.H.C. 2007, “Consolidation phenomena in laser and powder-bed based layered manufacturing”, *CIRP Annals-Manufacturing Technology*, Vol. 56, No. 2, pp. 730-759.

139. Shiomi, M., Yoshidome, A., Abe, F. and Osakada, K. 1999, “Finite element analysis of melting and solidifying processes in laser rapid prototyping of metallic powders”, *International Journal of Machine Tools and Manufacture,* Vol. 39, pp. 237-252.

140. Childs, T.H.C., Hauser, C., and Badrossamay, M. 2005, “Selective laser sintering (melting) of stainless and tool steel powders: experiments and modeling”, *Proc. of the Institution of Mechanical Engineers, Part B: Journal of Engineering Manufacture,* Vol. 219, No. B4, pp. 339-358.

141. Das, S. 2003, “Physical aspects of process control in selective laser sintering of metals”, *Advanced Engineering Materials*, Vol. 5, No. 10, pp. 701-711.

142. Taylor, C.M., Direct laser sintering of stainless steel: thermal experiments and numerical modeling, Ph.D. Thesis, School of Mechanical Engineering, University of Leeds, UK, 2004.

143. DebRoy, T. and David, S.A. 1995, “Physical processing in fusion welding”, *Reviews of Modern Physics*, Vol. 67, No.1, pp. 85-112.

144. Senthilkumaran, K., Pandey, P.M. and Rao, P.V.M., 2009, “Influence of building strategies on the accuracy of parts in selective laser sintering”, *Materials and Design*, Vol. 30, pp. 2946-2954.

145. Schleifenbaum, J.H. 2010, “High power Selective Laser Melting (HP SLM) – Upscaling the productivity of additive metal manufacturing by factor 10”, *Proc. 21st Annual International Solid Freeform Fabrication Sympoium*, August 9-11, Austin, TX, USA.

146. Niu, H.J. and Chang, I.T.H. 1999, “Selective laser sintering of gas and water atomized high speed steel powders”, *Scripta Materialia*, Vol. 41, No. 1, pp. 25-30.

147. EOS, 2009, “EOS for rapid success/ products”, Web-Based Data, EOS-GmbH Electro Optical Systems, Germany, http://www.eos-gmbh.de, as 15.04.2009.

148. Mumtaz, K. and Hopkinson, N. 2009, “Top surface and side roughness of Inconel 625 parts processes using selective laser melting”, *Rapid Prototyping Journal*, Vol. 15/2, pp. 96-103.

149. Tolochko, N.K., Mozzharov, S.E., Yadroitsev, I.A., Laoui, T., Froyen. L., Titov, V.I. and Ignatiev, M.B. 2004, “Balling processes during selective laser treatment of powders”, *Rapid Prototyping Journal*, Vol. 10/2, pp. 78-87.

150. Khan, M. and Dickens, P., 2010, “Selective Laser Melting of pure gold”, *Gold Bulletin*, Vol.43, No.2, pp.114-121.

151. Campanelli, S.L., Contuzzi, N. and Ludovico, A.D., 2010, “Manufacturing of 18 Ni marage 300 steel samples by selective laser melting”, *Advanced Materials Research*, Vols. 83-86, pp.850-857.

152. Stanford, M., Kibble, K., Lindop, M., Mynors, D. and Durnall, C., 2008, “An investigation into fully melting a maraging steel using direct metal laser sintering (DMLS)”, *Steel Research Inst. 79, Special Edition Metal Forming Conference*, Vol. 2, pp. 847-852.

153. Pardal, J.M., Tavares, S.S.M., Terra, V.F., Da Silva, M.R. and Dos Santos, D.R. 2005, “Modeling of precipitation hardening during the aging and overaging of 18Ni-Co-Mo-Ti maraging 300 steel”, *Journal of Alloys and Compounds,* Vol. 393, pp.109-113.

154. ASM Handbook, Volume 4 Heat Treating, 1991, ASM International, The Materials Information Company, United States of America, ISBN 0-87170-379-3, pp.528-548.

155. Avrami, M., 1941, “Kinetics of phase change. III Granulation, Phase Change and Microstructure”, *Journal of Chemical Physics*, Vol. 9, No. 2, pp. 177-184.

156. Brandon, D. and Kaplan, W.D. 2001, Microstructural Characterization of Materials, 2nd edition, John Wiley & Sons Ltd. ISBN 0-471-98501-5, West Sussex, UK.

157. Yadroitsev, I., Thivillon, L., Bertrand, Ph. and Smurov, I. 2007, “Strategy of manufacturing components with designed internal structure by Selective Laser Melting of metallic powder”, *Applied Surface Science*, Vol. 254, pp. 980-983.

158. Vandenbroucke, B. and Kruth, J.-P. 2007, “Selective Laser Melting of biocompatible metals for rapid manufacturing of medical parts”, *Rapid Prototyping Journal*, Vol. 13 No. 4, pp. 196-203.

159. Paul, C.P., Ganesh, P., Mishra, S.K., Bhargava, P., Negi, J. and Nath, A.K. 2007, “Investigating laser rapid manufacturing for Inconel-625 components”, *Optics and Laser Technology*, Vol. 39, pp. 800-805.

160. Kobryn, P.A. and Semiatin, S.L. 2002, “Mechanical properties of laser-deposited Ti-6Al-4V”, *Proc. of 13th Annual International Solid Freeform Fabrication Symposium,* August 5-7, Austin, TX, USA.

161. Santos, E., Abe, F., Kitamura, Y., Osakada, K. and Shiomi, M. 2002, “Mechanical properties of pure titanium models processed by selective laser melting”, *Proc. of 13th Annual International Solid Freeform Fabrication Symposium*, August 5-7, Austin, TX, USA.

162. Spierings, A.B. and Herres, N. 2010, “Influence of the particle size distribution on surface quality and mechanical properties in additive manufactured stainelss steel parts, *Proc. of 21st Annual International Solid Freeform Fabrication Symposium*, August 9-11, Austin, TX, USA.

163. Sehrt, J.T. and Witt, G. 2010, “Static strength analysis of beam melted parts dependent on various influences”, *Proc. of 21st Annual International Solid Freeform Fabrication Symposium*, August 9-11, Austin, TX, USA.

164. Saleh, N., Mansour, S. and Hague, R. 2002, “Investigation into the mechanical properties of rapid manufacturing materials”, *Proc. of 13th Annual International Solid Freeform Fabrication Symposium*, August 5-7, Austin, TX, USA.

165. Miani, F., Kuljanic, E. and Sortino, M. 2001, “Modelling the mechanical properties of direct metal selectively laser sintered parts”, *Proc. Laser Assisted Net Shape Engineering 3 LANE 2001*, August 29-31, Erlangen, Germany, pp.383-390.

166. Hague, R.J., Dickens, P.M., Mansour, S., Saleh, N., and Sun, Z. 2002, “Design for Rapid Manufacture”, *Proc. of the Society of Rapid Manufacturing Engineers’ Rapid Prototyping and Manufacturing Conf.*, April 2002, Cincinnati, USA, 10 pp, [CD ROM].

167. Almeida, H.A., Bartolo, P.J. and Ferreira, J.C. 2008, “Mechanical behavior and vascularisation analysis of tissue engineering scaffolds”, *Proc. Virtual and Rapid Manufacturing*, Taylor and Francis Group, London, pp.71-80.

168. ASTM, E 23-96, Standard Test Methods for Notched Bar Impact Testing of Metallic Materials.

169. ASM Handbook, Volume 20 Material Selection and Design, 1997, ASM International, The Materials Information Company, United States of America, ISBN 0-87170-377-7.

170. Laroudie, F., Tassin, C. and Pons, M. 1994, “Laser surface alloying of 316L stainless steel: different hardening routes and related microstructures”, *Journal de Physique*, Vol.4, pp.C4-77-80.

171. Interlloy Company: http://www.interlloy.com.au/data_sheets/stainless_steel/316L.html

172. ASM Handbook, Volume 15 Casting, 1992 (second printing), ASM International, The Materials Information Company, United States of America, ISBN 0-87170-377-7.

173. ASM handbook: Casting, Vol. 15, 1992 (second printing), ISBN 0-87170-007-7.

174. Kubota Metal Corporation: http://www.kubotametal.com/alloys/corrosion_resistant/CF-3M.pdf

175. Matweb, The online Materials Databases, Titanium Ti-6Al-4V (Grade 5), Annealed AMS 4928 AMS 4911.

176. Latrobe Specialty Steel Company: www.latrobesteel.com, MARVAC™ 300 VIM-VAR Data-sheet

177. Beal V.E., Erasenthiran, P., Hopkinson, N., Dickens, P. and Ahrens, C.H. 2006, “The effect of scanning strategy on laser fusion of functionally graded H13/Cu materials”, *Int. J. Advanced Manufacturing Technology,* Vol. 30, pp. 844-852.

178. Wu, W., Yang, Y. and Huang, Y. 2007, “Direct manufacturing of Cu-based alloy parts by selective laser melting”, *Chinese Optics Letters*, Vol. 5, No.1, pp.37-40.

179. Shi, Y., Zhong, Q., Chen, X., Huang, S. and Zhou, Z., 2002, “Research and implement of a new kind of scanning mode for selective laser sintering”, *Chin. J. Mech. Eng.,* Vol. 38, No.2, pp.35-39.

180. Yang, J., Bin, H., Zhang, X. and Liu, Z., 2003, “Fractal scanning path generation and control system for selective laser sintering (SLS*)”, Int. J. of Machine Tools and Manufacture,* Vol. 43, pp.293-300.

181. Ma, L. and Bin, H., 2007, “Temperature and stress analysis and simulation in fractal scanning-based laser sintering”, *Int. J. Advanced Manufacturing Technology,* Vol. 34, pp.898-903.

182. Wauthlé, R. 2009, Verminderen van thermische spanningen bij selectief laser smelten, Master thesis, Dept. of Mechanical Engineering, Katholieke Universiteit Leuven, Heverlee, Belgium *(in Dutch)*.

183. Kruth, J.-P., Deckers, J., Yasa, E. and Wauthlé, R., 2010, “Assessing influencing factors of residual stresses in Selective Laser Melting using a novel analysis method”, *Journal of Materials Processing Technology*, (submitted).

184. Hopkinson, N., Hague, R.J.M. and Dickens, P.M. (Ed.s) 2006, Rapid Manufacturing An Industrial Revolution for the Digital Age, John Wiley and Sons, Ltd., ISBN-13 978-0-470-01613-8, West Sussex, England.
185. Diegel, O., Singamneni, S., Reay, S. and Withell, A. 2010, "Tools for sustainable product design: Additive manufacturing", *Journal of Sustainable Development*, Vol.3, No.3, pp.68-75.
186. Campbell, R.I. 2008, "Creating a design for additive fabrication feature repository", *RAPDASA 2008 Rapid Product Development Association of South Africa Conference*, November 13-15, Bloemfontein, South Africa.
187. MTT Technologies Group: http://www.mtt-group.com/selective-laser-melting.html
188. EOS E-manufacturing: http://www.eos.info/en/products/materials/materials-for-metal-systems.html
189. Becker, D., Meiners, W. and Wissenbach, K., 2009, Additive manufacturing of copper alloy by Selective Laser Melting, *Proc. of the Fifth WLT-Conference on Lasers in Manufacturing*, June 15-18, Munich, Germany.
190. Ng, C.C., Savalani, M.M., Man, H.C. and Gibson, I., 2010, "Layer manufacturing of magnesium and its alloy structures for future applications", *Virtual and Physical Prototyping*, Vol.5/1, pp.13-19.
191. ASTM F2792-09e1, 2009, "Standard Terminology for Additive Manufacturing Technologies" DOI: 10.1520/F2792-09E01.

APPENDIX 1

Badrossamay, M., Yasa, E., Van Vaerenbergh, J. and Kruth, J.-P. 2009, "Improving productivity rate in SLM of commercial steel powders", *RAPID 2009 Conf. and Expo*., May 12-14, Schaumburg, IL, USA.

Improving Productivity Rate in SLM of Commercial Steel Powders

M. Badrossamay, E. Yasa, J. Van Vaerenbergh, J.-P. Kruth
Department of Mechanical Engineering, Catholic University of Leuven, 3001 Leuven, Belgium

Abstract

Selective laser melting (SLM) is a powder-based additive manufacturing process capable to generate 3D parts from a CAD model. The competitive advantages of SLM are geometrical freedom, shortened design to product time, mass customization and material flexibility. Recent technical improvements have made a shift of the process applications from rapid prototyping to rapid manufacturing. Currently there is a growing interest in industry for applying this technology for generating high geometrical complexity and low quantity parts, among them are medical parts and tooling inserts. To turn the SLM process into a production technique for real components, some conditions have to be fulfilled. Productivity is one of those conditions that play a key role for further applications of this process and that is discussed in this paper.

However, compared to selective laser sintering (SLS), the productivity rate is lower because SLM is carried out at scanning speeds much slower than the speed range normally used in SLS. This study attempts to improve the SLM parts productivity rate for commercial steel powders, 316L stainless steel and DIN 1.2709 maraging steel. The influences of processing parameters on the parts' relative density as well as surface quality are investigated. A wide range of scanning speed, scan spacing and layer thickness as well as part shape's effect are considered. The effect of particle size on the results is also investigated.

INTRODUCTION

More than a decade of extensive research and improvements in selective laser melting (SLM) of metals have made this process to be a promising technique in the field of metal rapid manufacturing (RM). SLM is a powder-based additive manufacturing process capable to generate 3D parts from a CAD model. It refers to the direct route of selective laser sintering (SLS) when complete melting of powder occurs rather than sintering or partial melting [1]. Near full dense functional parts with complex geometry are currently produced by SLM without further post processing other than surface finishing. The competitive advantages of SLM are geometrical freedom, shortened design to product time, mass customization and material flexibility [2]. Currently there is a growing interest in industry for applying this technology for generating high geometrical complexity and low quantity parts. Among them are medical parts and tooling inserts [3-6]. Some examples of parts produced by SLM are presented in Figure 1.

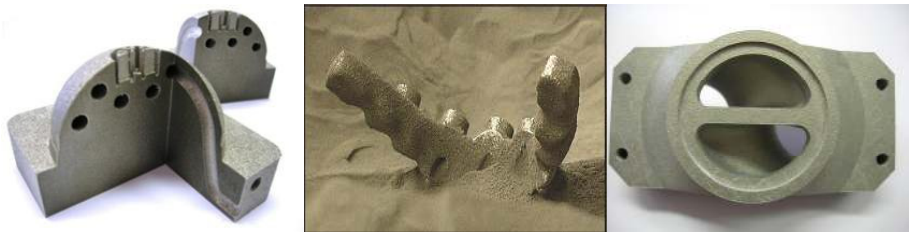

Figure 1 Sample parts produced by SLM

Despite advantages offered by SLM, there is however some shortcomings accompanying the process either because of its inherent specification, lack of full knowledge on the phenomena occurring during laser melting, or technological limitations. Remaining porosity after SLM, substantial thermal gradients that in turn may produce residual stresses or part deformation, poor dimensional accuracy and surface quality, stair stepping effect, poor qualitative down-facing surface and low building rate are the major obstacles encountered in the process. Part's mechanical properties, in turn, might also be affected deleteriously because of these problems. Addressing, eliminating or bypassing these difficulties have been the subject of many research in recent years.

A lot of research effort has been invested in SLM in order to obtain a better understanding of the phenomena involved, as well as to optimize the process in terms of geometrical features, surface quality, density and mechanical properties as well as materials development. The approaches taken include numerical modeling as well as experimental studies [7-14]. At the University of Leuven (K.U.Leuven), for instance, an in-process monitoring system has been implemented to adapt processing parameters based on melt pool observation in order to improve the quality aspects of produced parts such as geometrical features and overhanging surfaces [15]. Surface quality issue has also been addressed by combining SLM and selective laser erosion (SLE) [16]. Productivity is one of the issues related to economical aspects of SLM that also plays a key role for further applications of SLM as a competitive manufacturing technology. The work of which this paper is part, aims to address that aspect by investigating a number of commercial steel powders.

Productivity is directly connected to the scanning speed; a process parameter that in turn has been increased significantly in recent years [3]. Current feasible scanning speed for SLS could reach 10 m/s [17]. SLM is however carried out at scanning speeds much lower than the speed range normally used in SLS since SLM calls for much higher laser energy densities. It is also not enough just to melt (partially or full) the surface of a powder bed, but also to ensure a strong adherent to the previous layers [8]. On the other hand, it has been realized that it is unlikely to make SLS/SLM to be commercially viable for high volume parts with simple geometries because of high production time along with high costs of machines and materials [18]. While there are a number of works regarding productivity issue in SLS in terms of either process improvement or even developing alternative faster processes [19-21], only a few published studies deal with SLM productivity enhancement. At ILT Aachen, an improvement from 1.2 mm^3/s to 6.5 mm^3/s building rate is reported by using a wider laser beam diameter along increasing laser power from 250 W to 600 W [22]. Despite of such significant improvement in the productivity, process resolution is likely to be sacrificed because of expanded laser beam. At K.U. Leuven, in order to provide an insight in the economical aspect of SLM, production times of a benchmark case produced by five different SLS/SLM machines have been compared [2].

This paper aims to improve productivity of standard alloy steels by a parametric study of selective laser melting without sacrificing part properties. The considered properties are part density and surface quality. Two types of commercial steel powders, namely AISI 316L stainless steel and hot work maraging steel 300 are examined. The influences of processing parameters on the mentioned parameters are studied. By investigating a wide range of processing parameters, a threshold for the layer thickness is proposed. The possible influences of particle size and part's shape on the results are also investigated.

BUILDING RATE IMPACT

Costs incurred for SLM parts usually include costs of raw material, laser processing, post processing and the overhead or fixed costs as shown in Figure 2. Although raw material cost depends on the part's volume, it has a minor contribution (less than 10%-15%) in total costs since not only the overall SLM part's size is relatively small but also unprocessed powder can be reused. Post processing costs, on the other hand, depend on the application of the SLM part will be work for. In most cases, cutting off the part from base plate or its supports, accompanied by a simple surface finishing stage, such as sand blasting or shot peening fulfills application requirements. In latter case, post processing costs have slight influence on the total costs compared to the other expenses. There are, however, some application areas demanding further post processing such as high speed machining (for tool inserts for instance), or heat treatment after SLM. These activities, in turn, are more time and effort consuming thereby increasing post processing costs' portion massively. However, among the parameters listed in Figure 3, in general, laser processing costs play a major role in determining the incurred costs of SLM part and could reach as high as 90% of total costs. This segment, on the other hand, is directly related to the processing time.

Activities within laser processing, categorized into three sub-groups, are shown in Figure 3 including pre-production activities (such as part's CAD file loading); activities during production (such as powder

depositioning and laser scanning), and activities upon laser scanning completion. Pre-production activities belong to design methodology that is beyond the direct production time.

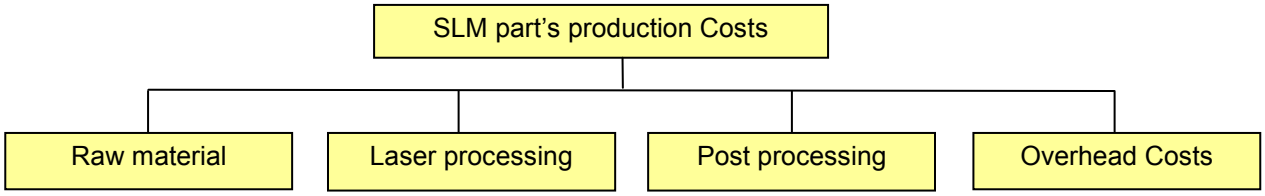

Figure 2 SLM part's production costs elements

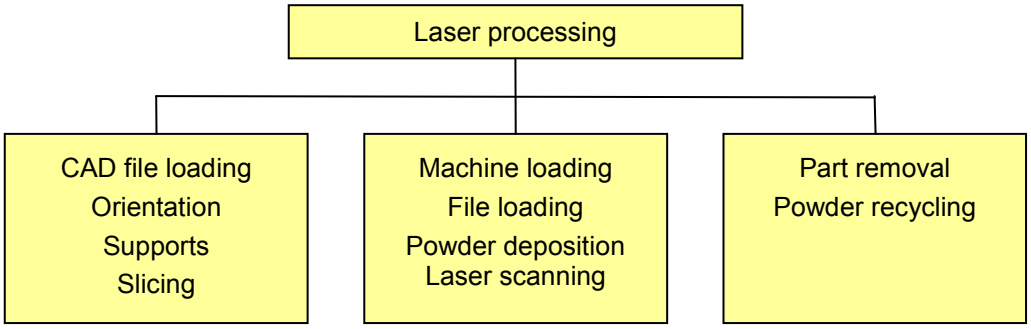

Figure 3 Laser processing activities

Production time (building rate) including powder deposition time, laser scanning time and file loading time is the dominant component of laser processing activity which in turn is a representative criteria for economical aspect of SLM process [2]. The powder deposition time is proportional to the part height (h) and layer thickness (t_{layer}), so that

$$t_{depos} = n_{layers} \cdot t^{*}_{depos} \tag{1}$$

where t^{*}_{depos} is the time to deposit one layer of powder, which is an SLM machine characteristic, and n_{layers} is the total number of layers defined by $n_{layers} = h/t_{layer}$. The total scanning time is given by

$$t_{scan} = \sum_{i=1}^{n_{layer}} \sum_{j=1}^{n_{part}} \frac{A^{scan}_{i,j}}{U \cdot s} \tag{2}$$

where $A^{scan}_{i,j}$ is the area of part j in layer i being scanned, U is the laser scanning speed, s is the scan spacing, and n_{part} is the number of parts being built. The file loading time is influenced by component geometrical complexity as well as scan vectors. It also depends on the performance of the SLM machine executive software. Equations 1 and 2 imply that building rate not only depends on the volume of the material that has to be built, but also on the processing parameters.

EXPERIMENTATION

The test specimens were built from gas atomized powder of specification and size fraction listed in Table 1. CL 20ES is a stainless steel powder whose composition corresponds to AISI 316L and is commercially available from Concept Laser GmbH. The maraging steels are standard hot-work steels suitable for production of functional parts as well as tooling applications supplied by Concept Laser (CL 50WS) and EOS Company (MS1) respectively. Reported powders particle size has been determined by laser diffraction technique. All mentioned powders are available to be processed by their dedicated SLM machines.

The test pieces were manufactured by two SLM machines, which differ in laser source and output power. CL 20ES and CL 50WS powders were processed on a Concept Laser M3 Linear SLM machine [3]. The machine is equipped with a 100 W Nd:YAG laser with a laser beam diameter of about 180μm at the powder bed surface. EOSINT M270 SLM machine was used to process maraging steel MS1 [24]. This machine employs a 200 W Yb-fiber laser with focus diameter of 140 μm.

Experiments were carried out using maximum available laser powers, i.e. around 100W and 200 W respectively. A wide range of scanning speed and scan spacing at various layer thicknesses were examined as revealed in Table 2. In order to minimize the effect of thermal gradients on the produced parts for the processed powders on M3 Linear machine, island scanning, a patented scanning pattern from Concept Laser was used. In this scanning strategy part surface at each slice was divided to small square islands of 5mm x 5mm. Consequently, the islands were scanned in a random way while scanning direction was altering a right angle respect to the neighboring islands. Islands borders were also shifted in *x* and *y* directions for the next layer. A schematic view of scan strategy is shown in Figure 4.

Table 1 Specification and size ranges of gas atomized stainless and maraging steel powders

Material type	*DIN No.*	*Mat. Name*	*Size ranges (μm)*	*d_{50} (μm)*	*bulk density (kg/m^3)*
CL 20ES stainless steel- fine	1.4401	X2CrNiMo17-12-2	-25	16.6	8.0
CL 20ES stainless steel- coarse	1.4401	X2CrNiMo17-12-2	-53/+25	42.5	8.0
CL 50WS maraging steel	1.2709	X3NiCoMoTi 18-9-5	-63/+25	43.7	8.1
MS1 maraging steel	1.2709	X3NiCoMoTi 18-9-5	-	35.6	8.1

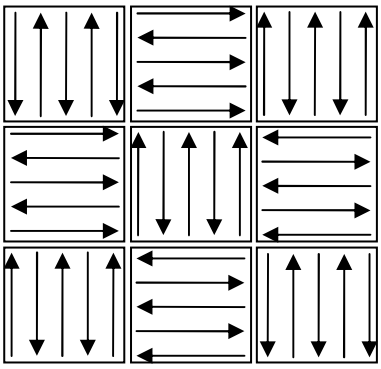

Figure 4 Traverse scanning patern

Table 2 Experimental processing parameters

Material	*Scanning speed (mm/s)*	*Scan spacing (μm)*	*Layer thickness (μm)*
CL 20ES	150 ÷ 750	60 -180 (35%-100% beam dia.)	20, 30, 40, 60
CL 50WS	120 ÷ 600	125 (70% beam dia.)	30, 40, 50, 60
MS1	450 ÷ 3000	100 (70% beam dia.)	40, 50, 60, 70

The surface roughness of the as-processed samples was measured on top and side surfaces using a Talysurf 120L from Taylor Hobson Ltd, a contact surface profilometer. Measurements were carried in 2D, i.e. along a line, as well as 3Dl. 3D measurements were carried out on an area of 10mm x 5mm considering 20 μm distance between consecutive measuring points. 2D measurements were carried out with and without filtering. A cut-off length of 2.5 mm and a total evaluation length of 15 mm were used when a filter was applied. The presented results have been averaged from five measurements on each surface.

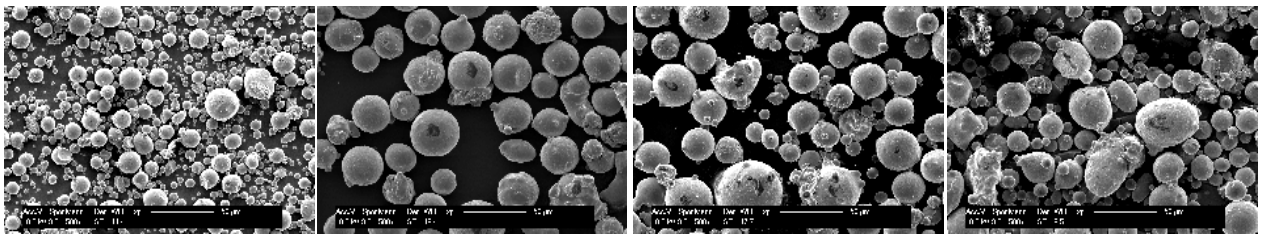

(a) (b) (c) (d)

Figure 5 SEM micrographs of used powders, (a) CL 20ES fine powder, (b) CL 20ES coarse powder, (c) CL 50WS maraging steel, (d) MS1 maraging steel

Density was measured according to the Archimedes method by weighing the samples in air and subsequently in a fluid (ethanol). A coating with lacquer was also applied to avoid ethanol absorption at lower densities. Presented density results in the next section are arithmetic means of three measurements at each processing condition and are expressed as relative density by taking materials' bulk density from Table 1.

EXPERIMENTAL RESULTS AND DISCUSSIONS

Part density and surface quality are the main concerns in SLM. The former parameter determines the part's mechanical properties which in turn has direct influence on the component performance. The latter is not only a primary concern to the users, but also a key issue in completion of the component during the fabrication. The results of measured density as well as surface quality for the tested powders are presented in this section.

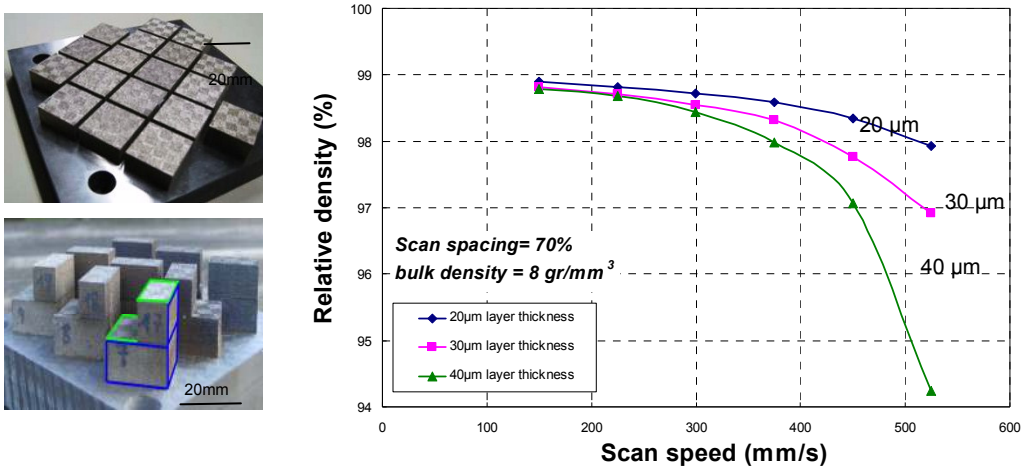

Figure 6 Relative density versus scanning speed for 316L fine powder alongside typical images of parts built on the base plate, top: 316L, bottom: maraging steel

Used powders

Figure 5 provides typical morphology of the tested powders before processing. SEM micrographs show that the majority of powder particles bear spherical and near-spherical morphology. The

spherical morphology without sharp edges and corners ensures free flow of the powder during layer deposition thereby increasing process efficiency [25].

Relative Density

Figure 6 shows the measured densities of the 20mm x 20mm x 10mm blocks made from 316L powder as a function of scan speed, for three layer thicknesses of 20 μm, 30 μm and 40 μm, at scan spacing of 126 μm (30% beam overlap). These results are for the finer powder, i.e. 16.6μm particle size. The standard deviation of the results is less than 0.01 gr/cm^3. In all cases relative density reduces with increasing speed even though its decline is less obvious at lower speed ranges. The observed trend is logical since the delivered energy density decreases with increasing scanning speed. Standard processing parameters for this material are given as scan speed 370 mm/s, scan spacing 125 μm and a layer thickness of 30 μm. Results indicate that an increase of layer thickness from 30 μm to 40 μm for instance, at constant scan speed, has little deteriorates effect on the density as long as the scanning speed is equal or less than the "standard" speed. According to equations 1 and 2, such increase in layer thickness corresponds to 25% lower scanning time as well as 25% reduction on layer depositioning time for this material.

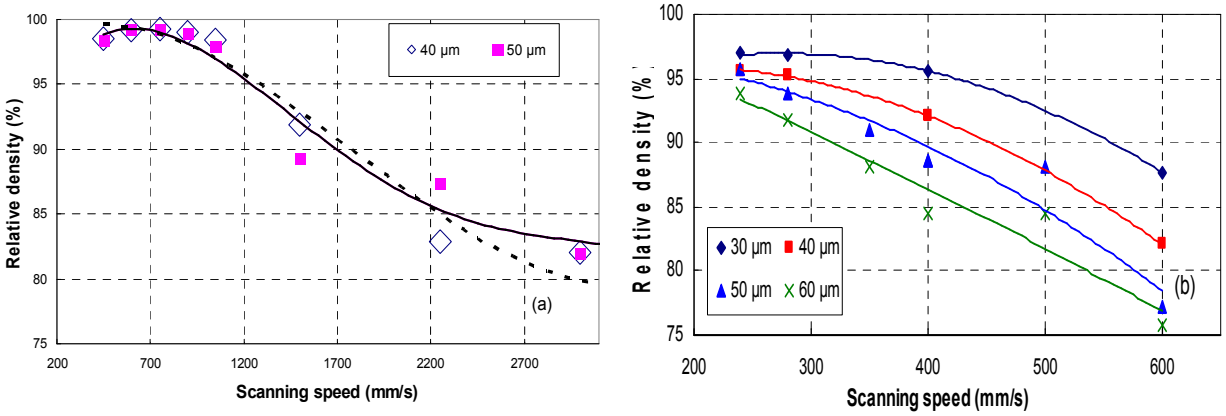

Figure 7 Relative density versus scanning speed for maraging steel powders, (a) MS1 material processed by EOS SLM machine, (b) CL 50 material processed by M3 Linear Concept Laser

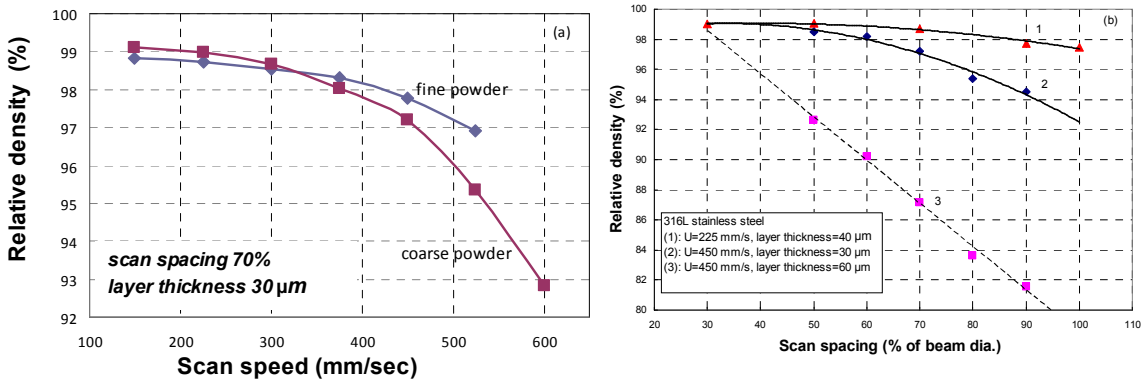

Figure 8 (a) Effect of particle size on the relative density for 316L material, (b) Dependence of attainable density on scan spacing

Investigating the variation of density with scan speed for maraging steel powders yielded results qualitatively similar to 316L powder as shown in Figure 7. For MS1 powder, regardless of layer thickness, there is a scanning speed range that results in the highest relative density. The reason for the lesser density at lower speeds may be connected to the formation of a rough surface as a result of excessive delivered energy density that in turn avoids the coater to deposit a homogenous layer of powder. The latter phenomenon may leave behind some areas without fresh powder to be processed as well as very thick powder depth in some other area preventing underneath layer to remelt. The optimum speed occurs at the material's standard scanning speed, i.e. 750 mm/s (the other standard

parameters set are 100 μm scan spacing and 40μm layer thickness). An improvement of 20% on the building time is again achieved for this material by only increasing layer thickness to 50μm. This layer thickness, however, is found to meet the likely threshold of the thickest layer thickness that can be applied for this material. Lower densities were obtained when the layer thickness increased to 60 μm as depicted in Figure 7(b). The standard parameters for CL 50WS are a speed 200 mm/s, scan spacing 125 μm and 30 μm layer thickness. SLM modeling also suggests that in order to remelt the underneath layer, using a very thin layer is required especially for the materials with narrow melting range [8].

In order to investigate the influence of particle size on the density of SLM parts, a number of specimens were built from 316L material using fine and coarse powders with the same processing parameters. Powders particle sizes are given in Table1. Figure 8(a) compares parts' measured relative densities for the both used powders. Here the layer thickness and scan spacing have been taken 30 μm and 140 μm respectively. The obtained relative density from larger particles is slightly higher than the density from finer particles at lower speed range, i.e. up to around 300mm/s. This is presumably related to the higher packing density and flowability of larger particles size with respect to the fine powders with the narrower particle size distribution. As processing speed moves to higher values, on the other hand, the laser material interaction time decreases which in turn cause a reduction in the melt pool size. For the fine powder, however, less pronounced melt volume reduction is predictable since finer particles melt faster. Consequently, processing at higher scanning speeds may result in greater melt volume for finer powder. The latter phenomenon might be a possible explanation for slightly higher attainable densities at higher scanning speed. These results suggest a higher productivity by using finer powders.

The influence of the scan spacing on relative density for 316L is depicted in Figure 8(b). Here the scan spacing is expressed as a percentage of laser beam diameter so that a spacing of 60% for instance, represents for a scan spacing of 108 μm or 40% beam overlap. This figure reports the attainable density for scan speeds 225mm/s and 450mm/s, at three layer thicknesses 30μm, 40μm and 60μm respectively. At $U = 225\text{mm/s}$ and $t_{layer} = 40\mu\text{m}$, the relative density was almost independent of scan spacing as the scan spacing was increased from 30% to 80%, even though further increase of scan spacing decreased the relative density gradually. In contrast, the relative density decreases sharply with increasing scan spacing for $t_{layer} = 60\mu\text{m}$ due to insufficient delivered energy densities at increased scan spacing. These findings suggest that scan spacing is not a determining parameter for the obtainable relative density as long as delivered energy density remains sufficient to wet and remelts underneath layer.

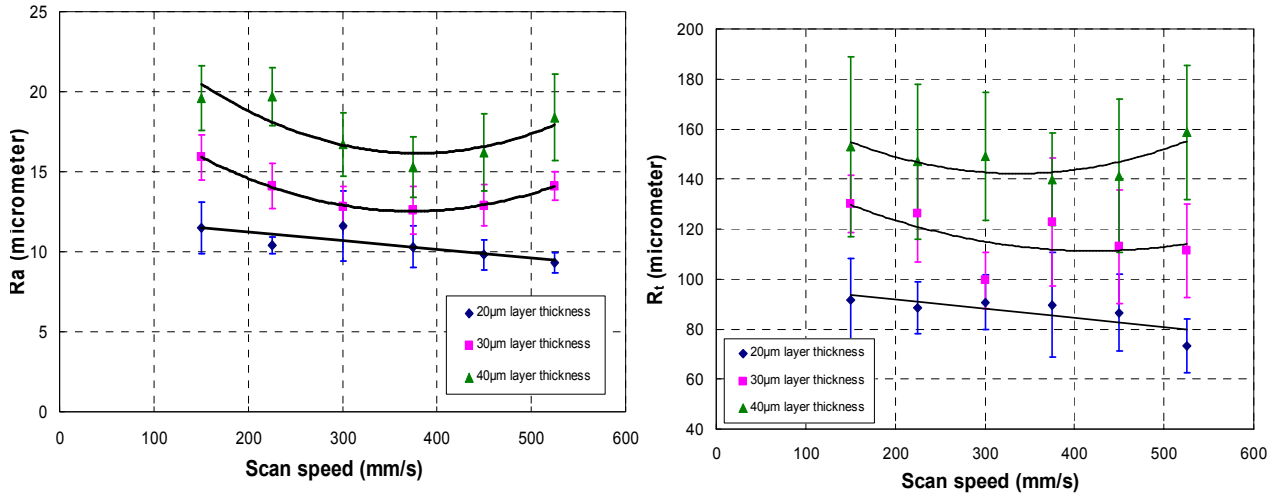

Figure 9 The effect of the scan speed and layer thickness on R_a and R_t on top surface

The majority of measured densities, for all tested materials during this study, range between 97% to 99% of the materials' bulk theoretical densities, which demonstrate promising capabilities for many

application areas. The highest achieved relative density for 316L, for instance, was 99.28% at $U = 150\text{mm/s}$ and $s = 90\mu\text{m}$. It means that the process is capable to produce almost full dense functional parts, although some little pores remain. Consequently, SLM still falls short for some applications where fatigue loading or excellent strength with high ductility is necessary. Laser remelting during SLM may address this shortcoming but could trigger other problems [16].

The findings of this study also point to the importance of laser power and scanning speed for the highest attainable relative density after SLM. Remind that MS1 and CL 50WS powders were processed using an Yb-fiber laser power of 200W and an Nd:YAG laser power of around 100W, respectively. Comparing Figures 7(a) and 7(b) indicate that although the two processed maraging powders were similar in compositions (but differ in suppliers), the overall density of MS1 was higher than that of CL 50WS, although obtained at greatly higher scanning speeds than the speed ranges used for processing CL 50WS.

Surface quality

In order to investigate the possible influence of higher building rates on the parts' surface quality, roughness of the top as well as side surfaces of the specimens were measured. Top surface means a surface with a normal vector parallel to the building axis. Figure 9 is concerned with the recorded average and total roughness, R_a and R_t respectively. Unless otherwise stated, reported roughness parameters have been taken from 2D measurements. The presented results are for the 316L fine powder.

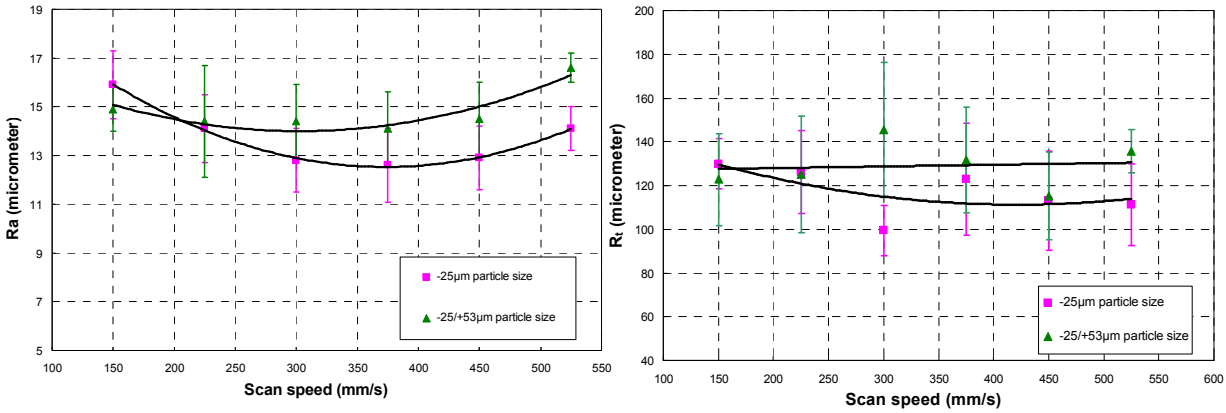

Figure 10 The effect of particle size on R_a and R_t

The measured data for the other two studied materials were also qualitatively similar to those that are reported here. It can be seen that the trend in average and total roughness are qualitatively similar although the reported data reveal a great spread. As the figures suggest, except for 20 µm layer thickness, there is no obvious trend between roughness parameters and scan speed in the studied speed range. However, R_a and R_t start to increase with further increase of scan speed where scan speed becomes too high to fully melt the powder bed surface. As evidence, the measured R_a for CL 50WS, for instance, tripled when speed increased from 250 mm/s to 1000 mm/s. For 20 µm layer thickness, roughness parameters slightly decrease with increasing scan speed. Regarding the layer thickness, it can be seen that roughness parameters are slightly higher at greater layer thickness. This is perhaps connected to the larger melt pool formed with thicker layer thickness. Based on the measured average roughness, a rule for R_a prediction might be interpreted as 0.4-0.6 of layer thickness.

Figure 10 demonstrates the influence of particle size on the measured roughness parameters. The data are for the 316L processed at a layer thickness of 30 µm and scan spacing of 126 µm. Although there is no difference on the revealed trend for both particle sizes, surfaces made from finer powder are slightly smoother when processed at higher scanning speed. Regarding the roughness on side

surface, no obvious trend was also observed between roughness parameters and processing parameters. The measured R_a on the side surface was usually lower than R_a measured on top surface. Because of latter issue, R_a and consequently R_t were independent of layer thickness.

In order to investigate the effect of scan spacing on the surface quality, a number of specimens from 316L were produced so that by varying scan speed and scan spacing, the build time remained constant. The result of roughness measurements in 3D is presented in Figure 11. Here S_a and S_y represent average and total roughness respectively. These results point to the importance of scan spacing for determining surface quality of SLM parts. As the figure suggests, there is an optimum for scan spacing that results in the lowest roughness.

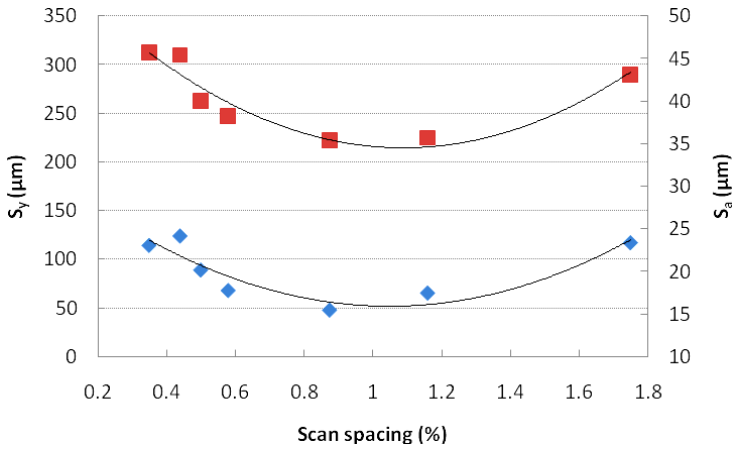

Figure 11 The effect of scan spacing on the average and total roughness for 316L powder

Component geometry

In order to investigate the part shape on the density of SLM parts, some thin walls and cylinders from 316L material were designed and built on a substrate. The walls had 20mm length, 10mm height and thickness varying between 0.1 and 10 mm. Although all the designed walls were produced successfully, a number of them encountered some difficulties. For very thin walls, particles out of the part contour remained stuck to the walls, thereby reducing parts integrity. Designed cylinders ranged from 0.1 to 10 mm. The cylinders that have a diameter less than 0.5 mm were not successfully built, but the others were produced without failure. The standard parameters were used for these experiments. Figure 12 presents typical images from produced samples. The variation of relative density with wall thickness is also illustrated in the figure. The data have been taken from the walls equal or greater than 0.3 mm thickness. The results indicate that a higher relative density was obtained for very thin walls which are similar to previous reports by other researchers [26]. This is perhaps because of less remaining devoid regions in the part cross section after powder deposition. The attainable density then decreases with increasing wall thickness until it reaches a saturation level. These results suggest that a homogenous dense part is produced in SLM for sections greater than one millimeter thickness.

CONCLUSIONS

Experimental studies on the SLM of stainless and maraging steel powders have shown that, whilst it is not possible to achieve one hundred percent dense parts, the building rate can be improved greatly by increasing layer thickness as well as scanning speed without sacrificing components' properties. By applying a thicker layer thickness only within a certain threshold limit, an improvement of 20 to 25% in productivity rate is obtained. Further enhancement can also be achieved by processing at scanning speeds higher than the default values with slightly lower attainable densities. Experimental results suggest that using fine powders could also enhance the productivity since at high scan speeds, the attainable density increases as the size of particles decreases.

This study also point to the importance of laser power and scanning speed for the highest attainable relative density after SLM. Scan spacing, on the other hand, influences the part's surface quality (roughness).

Finally, one should be aware that the most important point for SLM in practice is perhaps not the absolute amount of time to build the part but the component performance in terms of dimensional accuracy, durability and surface quality along with the production time.

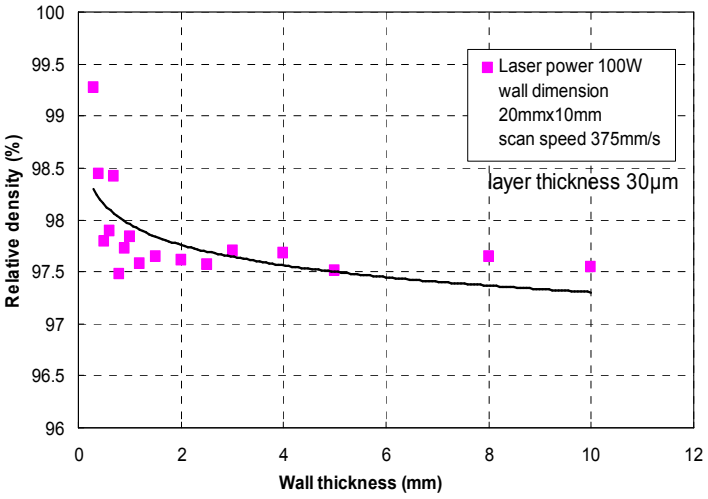

Figure 12 Effect of wall thickness on the relative density for 316L powders along built parts

ACKNOWLEDGEMENTS

This work has been supported by Belgian national funding through the IWT SBO DiRaMap project. The authors also acknowledge TUB ITAK (The Science and Technological Research Council of Turkey) for financial support to E. Yasa.

REFERENCES

[1] Kruth, J.-P., Levy, G., Klocke, F., Childs, T.H.C. (2007), “Consolidation phenomena in laser and powder-bed based layered manufacturing”, CIRP Annals-Manufacturing Technology, Vol. 56, Issue 2, pp. 730-759.

[2] Kruth, J.-P., Vandenbroucke, B., Van Vaerenbergh, J., Mercelis, P. (2005), “Benchmarking of different SLS/SLM processes as rapid manufacturing techniques”, International Conference on Polymers & Moulds Innovations (PMI), Gent, Belgium, April 20-23, 2005.

[3] Levy, G.N., Schindel, R., Kruth, J.-P. (2003), “Rapid manufacturing and rapid tooling with layer manufacturing (LM) technologies, state of the art and future perspectives”, CIRP Annals-Manufacturing Technology, Vol. 52, Issue 2, pp. 583-609.

[4] Wehmöllera, M., Warnkeb, P.H., Zilianc, C., Eufingerd, H., (2005), “Implant design and production-a new approach by selective laser melting”, International Congress Series, Vol. 1281, pp. 690-695.

[5] Vandenbroucke, B., Kruth, J.-P. (2007), “Selective laser melting of biocompatible metals for rapid manufacturing of medical parts”, Rapid Prototyping Journal, Vol. 13, No. 4, pp. 196-203.

[6] Santos, E.C., Shiomi, M., Osakada, K., Laoui, T. (2006), “Rapid manufacturing of metal components by laser forming”, International Journal of Machine Tools and Manufacture, Vol. 46, No. 12-13, pp. 1459-1468.

[7] Gusarov, A.V., Yadroitsev, I., Bertrand, P.H., Smurov, I. (2007), “Heat transfer modeling and stability analysis of selective laser melting”, Applied Surface Science, 254, 975-979.

[8] Childs, T.H.C., Hauser, C., Badrossamay, M. (2005), “Selective laser sintering (melting) of stainless and tool steel powders: experiments and modelling”, Proc. IMechE Part B: J. Engineering Manufacture, Vol. 219, pp. 339-357.

[9] Chung, H., Das, S. (2004), “Numerical modeling of scanning laser-induced melting, vaporization and resolidification in metals subjected to step heat flux input”, International Journal of Heat and Mass Transfer, Vol. 47, No. 19-20, pp. 4153-4164.

[10] Simchi, A. (2006), “Direct laser sintering of metal powders: Mechanism, kinetics and microstructural features”, Materials Science and Engineering A, 428, pp. 148-158.

[11] Osakada, K., Shiomi, M. (2006), “Flexible manufacturing of metallic products by selective laser melting of powder”, Int. J. of Machine Tools and Manufacture, 46, 1188-1193.

[12] Agarwala, M., Bourell, D.L., Beaman, J.J., Marcus, H.L., Barlow, J.W. (1995), “Direct selective laser sintering of metals”, Rapid Prototyping Journal, MCB University Press, Bradford, UK, Vol. 1, No. 1, pp. 26-36.

[13] Chen, X.C., Xie, J.W., Fox, P. (2004), “Direct laser remelting of iron with addition of boron”, Materials Science and Technology, Vol. 20, pp. 715-719.

[14] Kruth, J.P., Froyen, L., Van Vaerenbergh, J., Mercelis, P., Rombotus, M., Lauwers, B. (2004), ”Selective laser melting of iron based powder”, Journal of Materials Processing Technology, Vol. 149, No. 1-3, pp. 616–622.

[15] Mercelis, P., Kruth, J.-P. “Procedure for in-situ monitoring and feedback control of selective laser powder technologies”, patent GB 0612204.8.

[16] Yasa, E., Kruth, J.-P. (2008), ”Experimental study of the combined process of Selective Laser Melting and Selective Laser Erosion”, Proceedings of the RAPID 2008 Conference & Exposition, Florida, USA, May 20-22, 2008.

[17] 3D Systems (2009), “Selective laser sintering”, Web-Based Data, 3D Systems Inc., USA, http://www.3dsystems.com/products/sls/sinterstation_hiq/datasheet.asp, as 15.15.2009.

[18] Hopkinson, N., Dickens, P. (2003), “Analysis of rapid manufacturing-using layer manufacturing processes for production”, Proceedings of the Institution of Mechanical Engineers, Vol. 217, Part C, pp. 31-39.

[19] Pham, D.T., Wang, X. (2000), “Prediction and reduction of build times for the selective laser sintering process”, Proc. IMechE Part B: J. Engineering Manufacture, Vol. 214, pp. 425-430.

[20] Khoshnevis, B., Asiabanpour, B., Mojdeh, M., Koraishy, B., Palmer, V.V., Deng, Z. (2002), “SIS – a new SFF method based on powder sintering”, *Proceedings of the Solid Freeform Fabrication Symposium 2002*, University of Texas, Austin, Texas, USA, pp. 440-447.

[21] Hopkinson, N., Erasenthiran, P.E. (2004), "High speed sintering – early research into a new rapid manufacturing process", Proceedings from the 15th SFF Symposium, Austin, TX, August, pp.312-20.

[22] Schleifenbaum, H., Wissenbach, K. (2007), “Increasing the build-up rate of selective laser melting (SLM) processes”, Fraunhofer ILT Annual Report 2007, Page. 77.

[23] Concept Laser (2009), “Concept Laser GmbH/ M3 Linear”, Web-Based Data, Concept Laser GmbH Co., Germany, http://www.concept-laser.de/, as 15.04.2009.

[24] EOS (2009), “EOS for rapid success/ products”, Web-Based Data, EOS-GmbH Electro Optical Systems, Germany, http://www.eos-gmbh.de, as 15.04.2009.

[25] Niu, H.J., Chang, I.T.H. (1999), “Selective laser sintering of gas and water atomized high speed steel powders”, Scripta Materialia, Vol. 41, No. 1, pp. 25-30.

[26] Morgan, R.H., Papworth, A.J., Sutcliffe, C., Fox, P., O’Neill, W. (2002) “High density net shape components by direct laser re-melting of single-phase powders”, Journal of Materials Science, Vol. 37, pp. 3093-3100.

APPENDIX 2

Yasa, E. and Kruth, J.-P. 2008, "Experimental analysis of process and laser parameters in laser marking", *Proc. of the 9th Biennial ASME Conference on Engineering Systems Design and Analysis (ESDA2008)*, July 7-9, Haifa, Israel.

Proceedings of the 9th Biennial ASME Conference on Engineering Systems Design and Analysis
ESDA08
July 7-9, 2008, Haifa, Israel

ESDA2008-59375

EXPERIMENTAL ANALYSIS OF PROCESS AND LASER PARAMETERS IN LASER MARKING

Jean-Pierre Kruth **Evren Yasa**

Department of Mechanical Engineering
Catholic University of Leuven
3001 Heverlee, Belgium

ABSTRACT

Laser marking is a relatively new process to produce a mark on a product by the energy of a laser beam, mostly for the purpose of product identification and traceability. Compared to other techniques such as ink-marking, mechanical engraving and electro-chemical methods, laser marking has many advantages. In this study, laser marking is done with the laser of a standard RP/RM machine, i.e. a selective laser melting machine. This makes laser marking especially suited for marking parts produced by laser RP/RM techniques. On the other hand, the major difficulty in the process is the number of parameters and their complex relations which have not yet been investigated thoroughly. In the current study, the influences of scan speed, laser pump current (laser power) and pulse frequency of a Q-switched Nd:YAG laser on the mark qualities were investigated by single-factor experiments on stainless steel parts. It was found that these parameters substantially affect mark width, depth and rim formation which is caused by the expelled molten material due to the recoil pressure during the marking process. In order to investigate the influence of cross interactions, a design of experiment methodology was used to evaluate the effects of the same parameters on the success of the laser marking process in terms of removed material and clarity of the mark (visibility, sharpness, etc.).

Keywords: Laser Marking, Experimental Design, Selective Laser Erosion

1. INTRODUCTION

Laser marking is a relatively new method as compared to other marking technologies such as ink-marking, mechanical engraving and electro-chemical methods [1]. Yet, laser marking has many advantages compared to the conventional marking techniques: fast processing and free choice of geometry to be marked [2]. Moreover, it is possible to mark even very hard materials, including most metals and ceramics.

The process of laser marking is defined as the removal of material due to the energy provided by the incident laser beam to perform a permanent trace on the surface of the produced parts. The application areas cover a wide range of manufacturing fields including medical, automotive, aerospace and electronic component industries. Some examples of laser marking on metallic parts are shown in Fig. 1 [3].

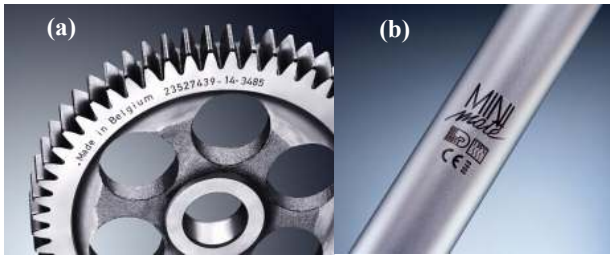

Figure 1: Laser marking (a) gear wheel (b) dentist tool [3]

The laser marking process is mostly applied to satisfy the needs of traceability and product identification. It is promising for marking parts produced by laser Rapid Manufacturing (RM), since the same laser may be used for the main manufacturing process as well as the subsequent marking of the product. For example; once dental implants become widely accepted to be produced in serial production by Selective Laser Melting (SLM), the identification of each individual part will be very important to distinguish the implant of one customer from others. It may be necessary to put the name of the patient,

the doctor or the clinic's name, operation date, etc. on the product. In a reverse way, marking might soon become a major requirement in RM to ensure high reliability: in case of a break down of a part, it is necessary to know on which machine and under which conditions and when the part was produced. A quick and easy method to satisfy this need in RM is the laser marking of information on the part as a final step even before it is removed from the machine.

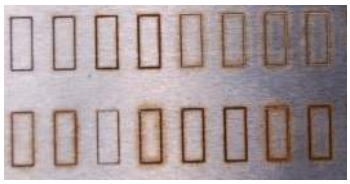

Figure 2 : Marked samples in M3 Linear machine

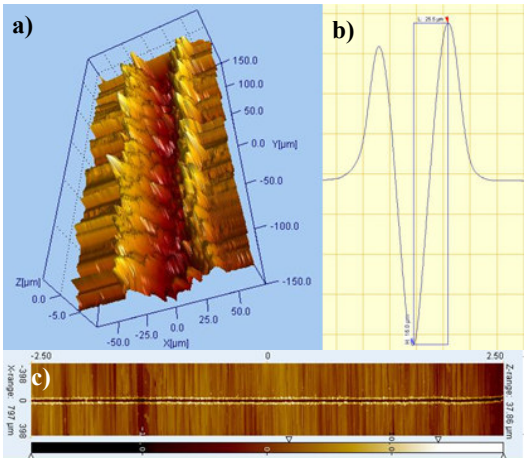

Figure 3: a) 3D view of the measurements b) average cross section in x-direction c) the view of the scanned line in 2D

In recent years, laser marking studies conducted with different lasers have been reported. The effect of pulse frequency on mark quality was investigated by Qi, et al. It has been found that the mark depth, width and mark contrast depend on the interaction process of the laser beam and the material, which was highly affected by the pulse frequency [2]. Tam, et al. [4], and Tezuka and Yoshikawa [5] studied the laser marking of integrated circuit packages with pulsed Nd:YAG laser and Q-switched YAG laser, respectively. Extensive research was conducted for the laser marking of polymers by Hoffmann et al. [6] and by Bosman [7]. Valette et al., investigated the enhancement of corrosion resistance of laser marked surfaces in surgical applications using a femto-second laser source which causes a small heat-affected area [8]. In addition to studies directly focused on laser marking, there are some others about laser milling which has also the same basic principles. Campanelli, et al., used the design of experiment methodology to evaluate the influence of the parameters (laser power, frequency, overlapping, etc.) involved in laser milling on the success of the ablation process in terms of removed depth and surface roughness [9]. Pham et al., studied the laser milling process of ceramic components reviewing the main parameters (lamp current, pulse duration, pulse frequency and scan speed) affecting the material removal characteristics of the process [10]. In the field of laser micro-millling, Vasco et al., tested different scanning strategies and operating conditions regarding the surface quality and material removal rate on a laser milling machine [11]. Moreover, short pulse laser machining for diesel and aerospace applications was investigated for hole drilling by Gilmore [12].

There are mainly three operating parameters used in laser marking, namely the pulse frequency, pump current and scan speed. In the present study, the effects of the three parameters are explored using an Nd:YAG laser source with a nano-second pulse duration. Single factor experimental strategy is utilized to derive the initial understanding of their influences on the mark properties such as mark depth, width and rim formation. Later the methodology of design of experiments is employed to study the cross interactions if there exits any.

2. EXPERIMENTAL PROCEDURE

All performed laser marking experiments are carried out on a Concept Laser M3 Linear machine [13], which is the sole machine in the market combining Selective Laser Erosion with an additive process, namely SLM. The machine employs an Nd:YAG laser with a wavelength of 1064 nm and a maximum laser output power in continuous mode of approximately 100 W. Workpieces of stainless steel (AISI 1085) were marked on this machine according to a rectangular geometry (Fig. 2) under different marking parameters and the surface profiles were measured by means of a roughness tester (Form Talysurf 120L) without any filter. The profiles are measured in 3D in order to derive average values of several cross-sections (Fig. 3). The view of a mark as displayed by the SPIP program is depicted in Fig. 3. At the left, a 3D view is shown, whereas the average X-profile is illustrated at the right. The marked line is also shown in Fig. 3c. The marking depth, width and other geometrical dimensions regarding the rim formation are derived using SPIP software.

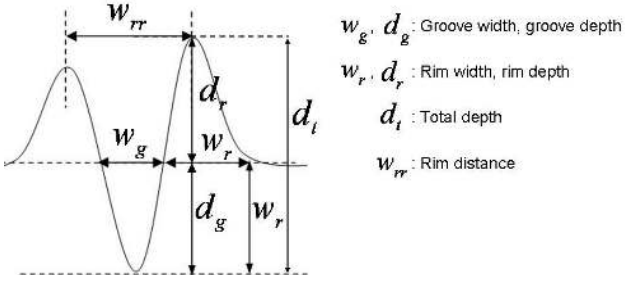

Figure 4: General cross-section of a laser marked line

In order to obtain a clear mark, the rim formation should be suppressed by applying suitable operating parameters. The groove depth (d_g) and width (w_g)also play an important role for the readability of the mark. The output parameters such as rim distance (w_{rr}), rim width (w_r) and rim depth (d_r) are measured regarding the rim formation whereas groove width (w_g) and groove depth (d_g) are the dimensions to define the groove (see Fig. 4). In order to have a mark free of rim, the rim depth (d_r) should be as small as possible just like the rim width (w_r).

The sketch of a general cross-section of a marked line by a laser beam with nano-second pulse duration is shown in Fig. 4. The rim that is formed during laser marking is due to long pulse duration and the recoil pressure. When a laser beam interacts with the workpiece, the primary effect is the heating of the solid structure. After the melting temperature is reached, the surface material starts to melt and if the laser intensity is sufficiently high (generally about 1010 W/m2), rapid evaporation at melt surface generates strong recoil pressures [14]. For lasers with nanosecond pulse duration, there is enough time for a thermal wave to propagate into the material and to create a relatively large layer of molten material. In this case, liquid metal starts evaporating, which makes precise material processing of metal targets in vacuum with nanosecond pulses very complicated. Thus, a rim formation is caused due to the recoil pressure and large amount of molten material. In hole drilling, this phenomena results in a crown-like rim around the hole [12, 15] as illustrated in Fig. 5 . However, when the material is irradiated with shorter pulses (pico- or femto-second durations), the penetration depth and, therefore, the interaction volume is generally smaller, slowing the material removal process. Since there are less secondary thermal effects, the pico- and femto-second machining process results in better quality and cleaner surfaces at the expense of high processing times [12, 15].

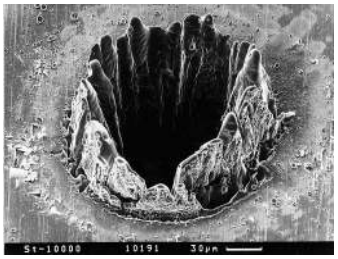

Figure 5: Crown generation in hole drilling in a 100 µm thick steel foil with 3.3 ns [15]

3. SINGLE FACTOR EXPERIMENTS

In order to derive the general relationships between the input and output parameters of the process, single factor experiments are utilized. One of the parameters, which is under investigation, is changed gradually while keeping all others constant at pre-specified values. Thus, only the relation between the changed parameter and the output can be derived.

In this study, scan speed, pulse frequency and pump current are investigated by single factor experiments. The results are given in the following sub-sections.

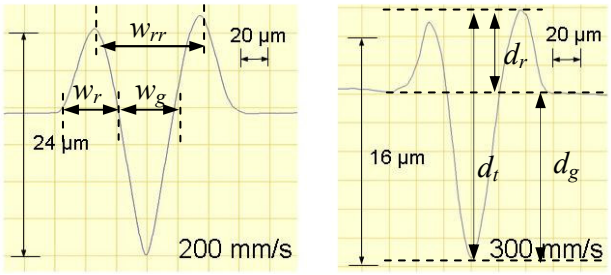

Figure 6 : The average profiles of marks under different scan speeds

3.1. Scan Speed

The scan speed is a very important parameter for the marking process. As the scan speed increases, the energy per unit area decreases, so does the depth per laser scan. On the contrary, the process time increases substantially when low scan speeds are selected. The scan speed influences the overlapping between subsequent laser pulses; the lower the speed, the greater the overlap and the deeper the marking due to multi-pulse radiation. A higher scan speed thus results in a lower depth as shown in Fig. 6 in which the average profiles of marked lines under different scan speeds (200 and 300 mm/s) are presented.

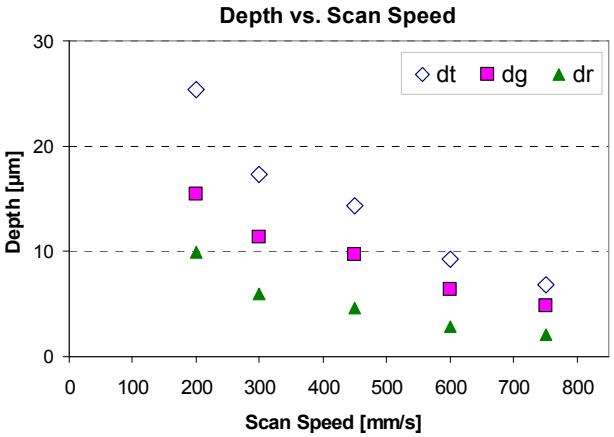

Figure 7 : The influence of scan speed on marking depths

The results for varying scan speed values are depicted in Fig. 7 and 8. The other parameters during these tests were fixed at the following values; laser power P = 20 W (with a pump current of 35 A), pulse frequency f = 30 kHz, spot size d = 70 µm (small aperture). As observed from the figures, the effect of scan speed is more crucial for the depth values rather than for the width. As the scan

speed increases, the groove depth (d_g) decreases due to the decrease in energy. The same trend is followed by the total depth (d_t). As explained, this is due to decreasing energy intensity on the marked surface due to decrease in overlapping of consecutive pulses. The equation (Eq. 1) for the overlap factor between laser pulses clearly indicates this relationship [20].

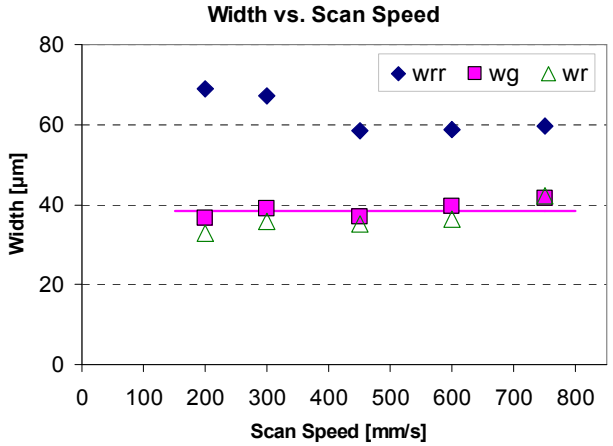

Figure 8 : The influence of scan speed on marking widths

$$U_p = \left[1 - \frac{v}{f \cdot d}\right] \times 100 \qquad (1)$$

where v is the scan speed, f is the frequency, d is the spot diameter and U_p is the overlapping percentage of the laser pulses.

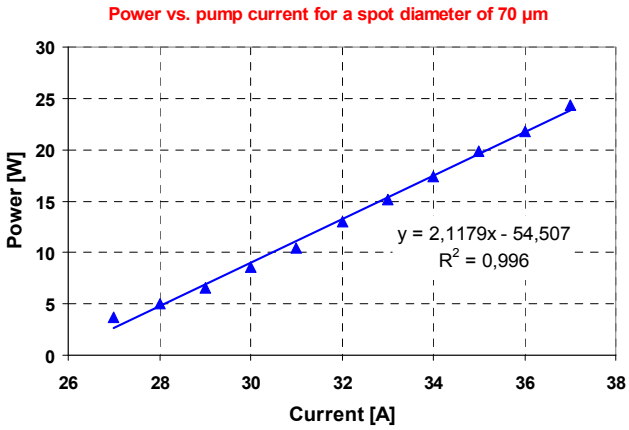

Figure 9 : The change of average power with increasing pump current for the small aperture (d = 70 µm)

On the other hand, the groove width (w_g) does not depend on the scan speed as shown in Fig. 8. A line having zero slope is a good fit to w_g-data with an intercept value of 38.78 µm (y = 38.78). However, this zero slope does not hold for rim distance (w_{rr}). The sudden reduction in the distance between the rims (w_{rr}) after 300 mm/s from 67 µm to 58.4 µm may be due to be the high energy input from the laser source for low scan speeds which is consistent with the results in laser erosion for surface roughness [16] and also due to the experimental uncertainty. In terms of material removal rate, lower scan speeds are preferred; however the surface quality is significantly deteriorated. As the scan speed increases, rim width (w_r) does not show a clearly changing trend.

3.2. Laser Pump Current (Laser Output Power)

The laser pump current has a potent influence on the removal rate due to its direct effect on the laser power. The change of laser average power in continuous mode with respect to the pump current is shown in Fig. 9. A lower limit for the laser power ensures the evaporation of material necessary for laser marking. Otherwise, only melting of the surface occurs, rather than material removal. Thus, it is crucial not to go beyond this lower limit in laser erosion applications.

While investigating the effect of the pump current (or laser power), the other parameters during the tests were kept constant at the following values; scan speed v = 450 mm/s; pulse frequency f = 30 kHz; spot diameter d = 70 µm (small aperture). The average profiles of marked lines under different pump current values (29 and 37 A, corresponding to the power values of approximately 7 and 14 W, respectively) are shown in Fig. 10 whereas the graphical representations of all results are depicted in Fig. 11 and 12.

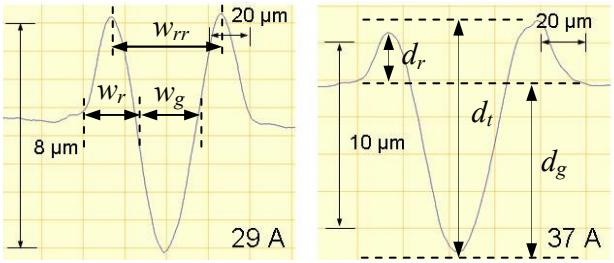

Figure 10 : The average profiles of marked lines under different pump current values

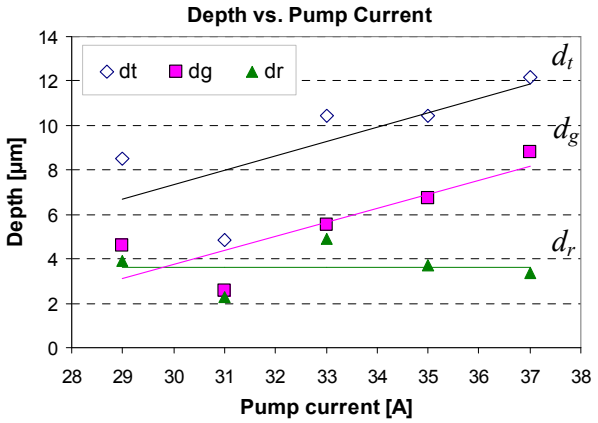

Figure 11 : The effect of pump current on marking depths

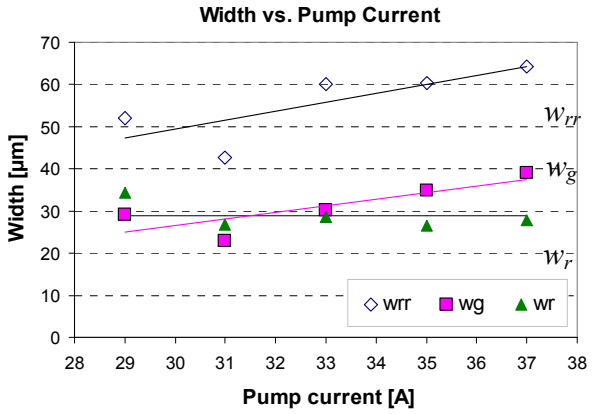

Figure 12 : The effect of pump current on marking widths

As the laser power is increased by raising the pump current, the groove and total depths (d_g and d_t) linearly increase following almost the same trend with similar slopes. Thus, the difference between these two depths or in other words, the rim depth, (d_r) stays almost the same at all pump current values as shown in Fig. 11 with a zero-slope line.

The groove width (w_g) also increases with an increasing laser power as well as the rim distance (w_{rr}) (Fig. 12). However, the width of the rims (w_r), which are present along the laser mark on two sides, stays almost constant for different laser power values. Hence, high current values give better results in terms of visibility.

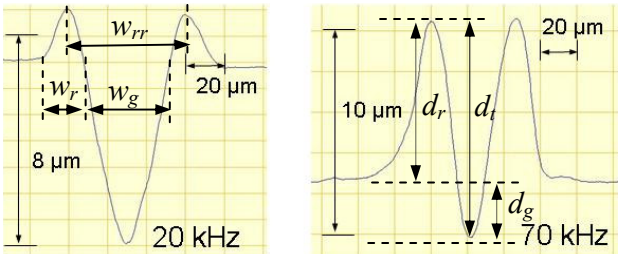

Figure 13 : The average profiles of marked lines under different frequency values

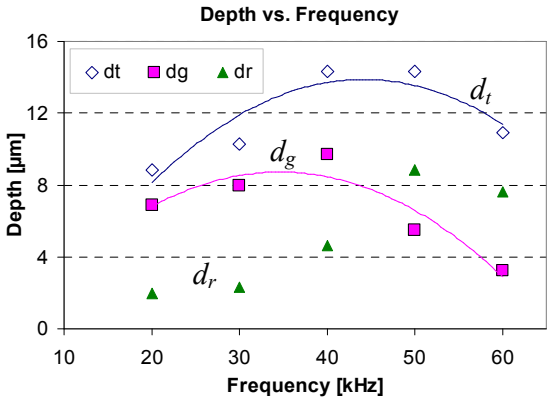

Figure 14 : The effect of pulse frequency on marking depths

3.3. Pulse Frequency

In single-factor experiments, the last processing parameter under investigation is the pulse frequency. Nd:YAG lasers are able to operate in both pulsed and continuous mode. In the pulsed-mode, the peak power of the laser beam is high enough to allow the material removal by evaporation whereas in continuous mode, the energy for evaporation cannot be provided. The average profiles of the marked lines under different frequency values (20 and 70 kHz) are shown in Fig. 13 while the values for the other parameters during the tests were set as follows; scan speed v = 450 mm/s; laser power P = 20 W (corresponding to a pump current of 35 A) and spot diameter d = 70 µm (small aperture).

The influence of the pulse frequency on the groove depth (d_g), width (w_g) and rim formation is presented in Fig. 14 and Fig. 15. As seen in Fig. 14, the groove depth (d_g), reaches to its maximum value when the pulse frequency is approximately 40 kHz (medium frequency). This also holds for the total depth (d_t). The relationship between the frequency and the depths can absolutely not be expressed linearly. A second-order fit is a better option as illustrated in the figures. This phenomenon (second-order relationship) is explained by the change of peak and average output powers of the laser beam with the changing of the pulse frequency [2]. The peak power decreases and the average output power increases with increase in the pulse frequency. At low frequency, the peak power is high enough to make materials evaporate during laser marking. Then the volume of evaporated material is determined by the average output power. So at low frequencies, the driving power is the average power. In high frequencies, the peak power is not enough to evaporate material thoroughly and a part stays in molten state. Thus, the driving power becomes the peak power. This makes the relationship between frequency and depth values (d_t and d_g) rather complicated.

Regarding the widths, the rim distance (w_{rr}) shows a decreasing trend as the pulse frequency is increased. The groove width (w_g) also reduces as the frequency increases whereas the rim width (w_r) hardly depends on the pulse frequency. The relationships between the pulse frequency and the widths (w_{rr} and w_g) can be expressed either linearly or by a second-order fit. Looking at these results, one can consider that a more visible mark will be obtained at low frequency values. However, at low frequency values, it is evident that heat affected zone around the mark groove is bigger causing the mark to be less sharp. The heat affected zone exhibits a noticeable colour change around the mark groove (Fig. 16) which is not

observable in measurement results. This statement is valid for all rectangles marked with frequency values lower than 25 kHz in the experiments. Therefore, higher frequency values should be preferred for better visual aspects.

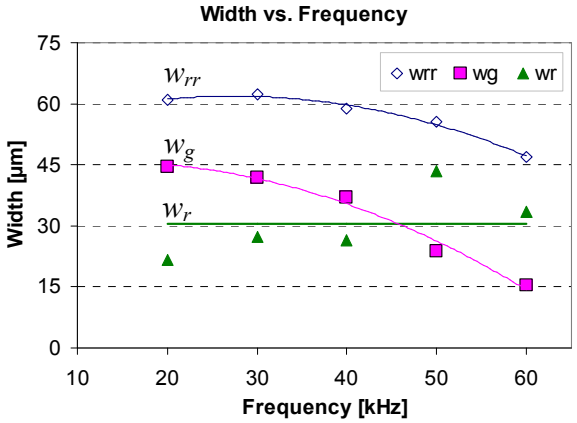

Figure 15 : The effect of pulse frequency on marking widths

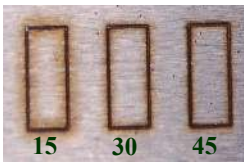

Figure 16: Frequency effect at 15, 30 and 45 kHz

Table 1: Marking parameters and their levels

Marking Parameter	Unit	Level 1	Level 2	Level 3
Scanning speed	mm/s	300	400	500
Pump current	A	33	35	37
Frequency	kHz	15	30	45

4. DESIGN OF EXPERIMENTS

Following the single-factor experiments, a full factorial experimental method was utilized to study the entire parameter space with all interactions between the selected factors. For the analysis of the data, Taguchi's method based on S/N ratio analysis which is a powerful tool for the optimization of high quality and robust systems was employed in addition to analysis of variance (ANOVA).

The effects of three control factors and their interactions were explored the full factorial experiments. The three variables are the scan speed, pump current and pulse frequency as chosen in single-factor experiments. All factors were explored at three different equally spaced levels. The selected levels for the parameters are given in Table 1 while Table 2 shows the experimental layout with the number of experiments and all values of the factors assigned to each marked rectangle. During the laser marking process, complete randomization of the treatment conditions was practiced.

Each set of parameters was performed on three different rectangles in order to ensure the repeatability of the experiments. After the tests are completed, all depth and width values are measured in the same procedure as explained in previous sections. The results are then transformed into a signal-to-noise (S/N) ratio because Taguchi recommends the use of the signal-to-noise ratio to measure the quality characteristics deviating from the desired values. S/N ratio is used as a measurable value instead of standard deviation due to the fact that as the mean decreases, the standard deviation also decreases and vice versa. In other words, the standard deviation cannot be minimized first and the mean brought to the target. Taguchi has empirically found that the two stage optimization procedure involving S/N ratios indeed gives the parameter level combination, where standard deviation is minimum while keeping the mean on the target [17]. Like the quality loss function, the signal-to-noise ratio is an objective measure of quality that takes both the mean and the variance into account.

In addition to S/N ratio analysis, a statistical analysis of variance (ANOVA) was performed to see which process parameters are statistically more significant for the output values than others. Combining S/N ratio and ANOVA analyses, the optimal combination of the operating parameters can be predicted.

Table 2: Experimental layout for full factorial experiments

	Scan Speed [mm/s]	Pump Current [A]	Frequency [kHz]
1	300	33	15
2	300	33	30
3	300	33	45
4	300	35	15
5	300	35	30
6	300	35	45
7	300	37	15
8	300	37	30
9	300	37	45
10	400	33	15
11	400	33	30
12	400	33	45
13	400	35	15
14	400	35	30
15	400	35	45
16	400	37	15
17	400	37	30
18	400	37	45
19	500	33	15
20	500	33	30
21	500	33	45
22	500	35	15
23	500	35	30
24	500	35	45
25	500	37	15
26	500	37	30
27	500	37	45

Table 3: S/N response table for the total depth (d_t)

Marking Parameter	Mean S/N Ratio (dB)			
	Level 1	Level 2	Level 3	Max-Min
Scanning Speed	28,86	25,4	24,24	4,62
Pump Current	23,31	27,37	27,83	4,52
Frequency	22,53	27,6	28,39	5,86

4.1. Analysis of S/N Ratio

In the Taguchi method, the desirable value for the output characteristic is represented by the term 'signal' whereas the term 'noise' represents the undesirable value for the output characteristic. Thus, signal to noise ratio (S/N) is defined as the ratio of the mean to the undesirable value [19]. The S/N ratio is formulated as follows;

$$S/N = -10\log(M.S.D.) \qquad (2)$$

where *M.S.D.* is the mean square deviation for the output characteristic.

In the following subsections, the S/N ratio analyses for marking depths and widths are presented.

Marking depths

To obtain optimal laser marking characteristics, the-higher-the-better quality characteristic for marking depths must be taken. For a visible and clear mark, the groove depth should be large enough.

$$M.S.D. = \frac{1}{n}\sum_{i=1}^{n}\frac{1}{d_i^{\,2}} \qquad \text{The-higher-the-better} \qquad (3)$$

where n is the number of observations and d_i is the observed value for the depth for the i^{th} test.

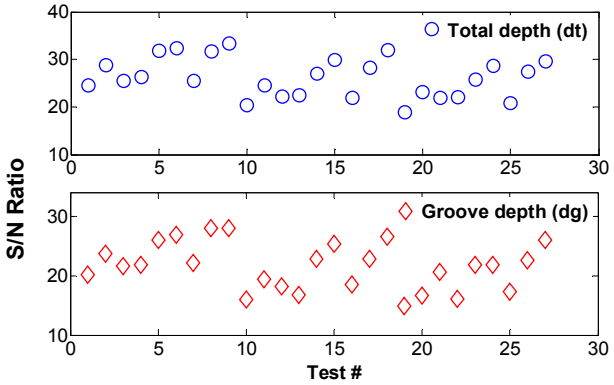

Figure 17: S/N ratios for marking depths, d_t and d_g

The derived results for d_g and d_t are shown in Fig. 17. Since the experimental design is orthogonal, it is possible to separate out the effect of each parameter at different levels. For example, the mean S/N ratio for the scanning speed at levels 1, 2 and 3 (300, 400 and 500 mm/s) can be calculated by averaging the S/N ratios for the experiments numbered as 1-9, 10-18 and 19-27 respectively. The mean S/N ratio for each level of the other laser marking parameters can be derived in a similar fashion. An example of a S/N ratio response is presented in

Table **3** for the total depth (d_t) showing the mean S/N ratio values for each level of the marking parameters. Figure 19 (a) shows the S/N response graph for the marking depths (d_t and d_g). As shown in Eq.2, the greater the S/N ratio, the smaller the variance of marking depth around the desired (the-higher-the-better) value. However, the relative importance amongst the marking parameters still needs to be investigated (see §4.2: Analysis of Variance) so that optimal combinations of the marking parameter levels can be accurately identified.

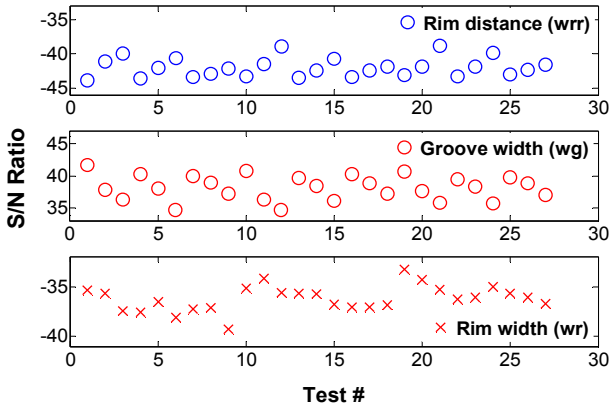

Figure 18: S/N ratios for marking widths (w_{rr}, w_g and w_r)

Marking Widths

For the marking widths, the same procedure is followed. However, for w_{rr} and w_r, which are related to the rim formation, the-lower-the-better quality characteristic is employed whereas the-higher-the-better quality characteristic is selected for the groove width, w_g. For the-lower-the-better characteristic, the following equation is used:

$$M.S.D. = \frac{1}{n}\sum_{i=1}^{n} w_i^{\,2} \qquad \text{The-lower-the-better} \qquad (4)$$

where n is the number of tests and w_i is the value of width for the i^{th} test.

The calculated S/N values of w_{rr}, w_g and w_r are illustrated in Fig. 18. The effect of each parameter at different levels for marking widths is also derived and Fig. 19 (b) and (c) depict the S/N response graphs for w_{rr}, w_g and w_r. Regardless of the quality characteristic (the-lower-the-better or the-higher-the-better), a greater S/N ratio means the variance of the output characteristic around the desired value is smaller and thus preferred.

Once the significant main effects and interactions are derived by ANOVA, then their levels corresponding to the required quality characteristics are identified by S/N ratio analysis (see §5: Results and Conclusions).

4.2. Analysis of Variance (ANOVA)

As defined in the e-Handbook of Statistical Methods [18], ANOVA is a general technique to test the hypothesis that the means among two or more groups are equal assuming that the sampled populations are normally distributed. It is extensively used to identify the performance of a group of parameters under investigation and to understand which design parameters have a significant effect on the quality characteristics of the outputs. This aim is achieved by separating the total variability of the S/N ratios into contributions by each of the design parameters and the error. The total sum of squared deviations (SS_T) from the total mean S/N ratio can be calculated as introduced in the following equation:

$$SS_T = \sum_{i=1}^{n} [(S/N)_i - (S/N)_m]^2 \qquad (5)$$

where n is the number of experiments, $(S/N)_i$ the mean S/N ratio for the i^{th} test and $(S/N)_m$ overall mean S/N ratio.

The total sum of squared deviations (SS_T) is partitioned into two components: 1) the sum of squared deviations due to each design parameter and, 2) the sum of squared errors.

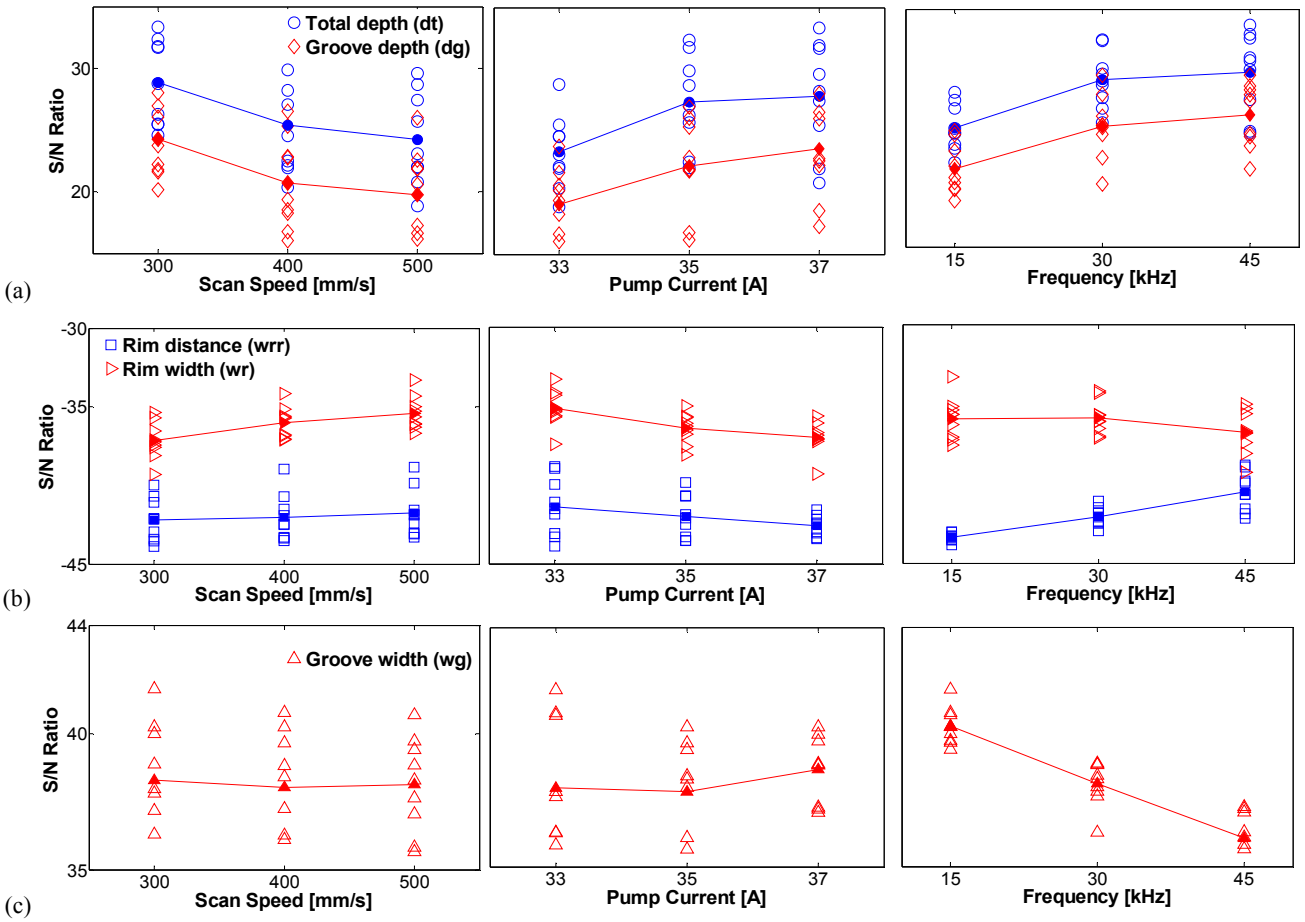

Figure 19: S/N ratio graphs for (a)d_t and d_g, (b)w_{rr} and w_r and (c)w_g

$$SS_T = \sum_{j=1}^{n_p} SS_j + SS_e \qquad (6)$$

where SS_j is the sum of squared deviations for each design parameter and n_p is the number of significant parameters and SS_e is the sum of squared error without or with pooled factor, which is the sum of squares corresponding to the insignificant factors. The percentage contribution by each of the design parameters in the total sum of squared deviations (SS_T) is a ratio of the sum of the squared deviations (SS_j) due to each design parameter to the total sum of squared deviations SS_T.

A statistical tool, an F-test, named after Fisher [19] is used to understand which design parameters have a significant

influence on the quality characteristic. The F value for each design parameter is simply the ratio of mean of squared deviations to the mean of squared error. Thus, the mean of squared deviations due to each design parameter needs to be calculated while performing an F-test. The mean squared deviations (SS_m) is equal to the division of the sum of squared deviations (SS_j) by the number of degrees of freedom associated to the design parameter (DOF_j). An example is given for the scan speed with the required equations:

The sum of squared deviations for scan speed:

$$SS_{scanspeed} = \left[\sum_{i=1}^{k_V}\left(\frac{V_i^2}{n_{v_i}}\right)\right] - \frac{T^2}{m} \quad (6)$$

The mean squared deviations for scan speed:

$$SS_m = \frac{SS_{scanspeed}}{DOF_{scanspeed}} \quad (7)$$

The sum of squares due to errors:

$$SS_e = \sum_{j=1}^{k_v}\sum_{i=1}^{n_{v_j}}(V_i - \bar{A}_j)^2 \quad (8)$$

where k_v is the number of levels for scan speed, T sum of all observations, m total number of observations, n_{v_i} the number of observations at v_i level, V_i is the sum of observations at v_i level, SS_m the mean squared deviations for scan speed, $DOF_{scanspeed}$ degrees of freedom associated to scan speed, and $\bar{A}_j$ average of observations under *Aj* level.

The F-ratio is calculated by dividing the mean sum of squares (SS_m) by the sum of squared error (SS_e).

$$F_{scanspeed} = \frac{SS_m}{SS_e} \quad (9)$$

Usually, it is assumed that a change of the corresponding design parameter has a significant effect on the quality characteristic and the control factor is strong compared to experimental error when F value is greater than 4. If F-ratio is less than 1, the experimental error outweighs the control factor effect and the control factor is insignificant and indistinguishable from the experimental error.

All calculations are done for each design parameter and for each interaction of two parameters. The calculations are done by a statistical software called JMP.

Results for the laser marking depths (d_t and d_g)

Table 4 and Table 5 show the results of ANOVA for the total depth (d_t) and groove depth (d_g). The tables consist of degrees of freedom (*DOF*), sum of squares, mean square values and F-ratios for each parameter and the most significant interaction. The F-ratios for all main factors show that they are highly significant for the total and groove depths. Additionally, the interaction effect of the current and the frequency is the most significant interaction (more than frequency x scan speed and also current x scan speed) having an F-ratio greater than 4.

Table 4: The ANOVA results for the total depth (d_t)

Analysis of variance for the total depth (dt)					
Source	DOF		Sum of squares	Mean Square	F ratio
Model	10	$\sum SS_j$	3081,98	308,20	27,4952
Error	16	SS_e	179,35	11,21	
Total	26	SS_T	3261,33		
Source	**DOF**		**Sum of squares**	**F ratio**	**Prob > F**
Scan Speed	2	SS_{j1}	732,48	32,67	<,0001
Current	2	SS_{j2}	767,38	34,23	<,0001
Frequency	2	SS_{j3}	1129,17	50,37	<,0001
Current x Frequency	4	SS_{j4}	452,94	10,10	0,0003

Table 5: The ANOVA results for the groove depth (d_g)

Analysis of variance for the groove depth (dg)					
Source	DOF		Sum of squares	Mean Square	F ratio
Model	10	$\sum SS_j$	924,74	92,47	34,24
Error	16	SS_e	43,22	2,70	
Total	26	SS_T	967,96		
Source	**DOF**		**Sum of squares**	**F ratio**	**Prob > F**
Scan Speed	2	SS_{j1}	244	45,16	<,0001
Current	2	SS_{j2}	244,69	45,29	<,0001
Frequency	2	SS_{j3}	359,26	66,45	<,0001
Current x Frequency	4	SS_{j4}	106,80	9,88	0,0003

Figure 20 (a) and (b) show the pie charts of the effects of significant marking parameters on the mark quality characteristics of total and marking depths. For both, the pulse frequency was the major contributor to the variations observed in the experiment and accounted for 33% and 36% of the total variations observed for the total and groove depths, respectively. The contributions of the other two marking parameters, scan speed and the pump current are observed to be almost the same for both of the depth values.

The interaction between the pump current and frequency is observed to be the sole significant interaction on the depth values which may be due to their (frequency and current's) complicated relation regarding the laser power. The pulse frequency of Nd:YAG laser is reported to be influencing the laser peak and average powers [2]. As mentioned earlier, the pump current directly affects the laser average and peak powers (Fig. 9). These two parameters are thus connected and their relation directly affects the output characteristics of the laser marking process.

Table 6: The ANOVA results for rim distance (w_{rr})

Analysis of variance for the rim distance (wrr)					
Source	DOF	$\sum SS_j$	Sum of squares	Mean Square	F ratio
Model	10		945,07	945,31	89,5855
Error	16	SS_e	158,87	17,63	
Total	26	SS_T	1103,94		
Source	**DOF**	SS_{j1}	**Sum of squares**	**F ratio**	**Prob > F**
Scan Speed	2	SS_{j2}	137,10	7,78	0,0041
Current	2	SS_{j3}	650,66	36,87	<,0001
Frequency	2	SS_{j4}	1057,63	59,95	<,0001
Current x Frequency	4		230,89	13,09	<,0001

Results for the laser marking widths (w_{rr}, w_g and w_t)

Tables from 6 to 8 show the results of ANOVA for the marking widths. The tables give degrees of freedom (*DOF*), sum of

squares, mean square values and F-ratios for each parameter and the most significant interaction. For rim distance (w_{rr}) and groove width (w_g), the frequency is the only major contributor to the variations observed in the experiment. It accounts for about 78% and 86% of the total variations in rim distance and groove width, respectively. The effect of the scan speed is almost negligible for the two widths, which is also evident from the F-ratios. For the rim width (w_r), the case is quite different. There is no significant interaction. The scan speed and the pump current are the major contributors to the variations.

Table 7: The ANOVA results for groove width (w_g)

Analysis of variance for the groove width (wg)					
Source	DOF		Sum of squares	Mean Square	F ratio
Model	10	$\sum SS_j$	8673,22	867,322	60,628
Error	18	SS_e	228,89	14,306	
Total	28	SS_T	8902,11		
Source	**DOF**		**Sum of squares**	**F ratio**	**Prob > F**
Scan Speed	2	SS_{j1}	1,28	0,04	0,9564
Current	2	SS_{j2}	197,18	6,89	0,0069
Frequency	2	SS_{j3}	7679,04	268,4	<,0001
Current x Frequency	4	SS_{j4}	795,73	13,9	<,0001

Table 8: The ANOVA results for rim width (w_r)

Analysis of variance for the rim width (wr)					
Source	DOF		Sum of squares	Mean Square	F ratio
Model	6	$\sum SS_j$	1776,37	296,06	14,13
Error	20	SS_e	419,15	20,96	
Total	26	SS_T	2195,52		
Source	**DOF**		**Sum of squares**	**F ratio**	**Prob > F**
Scan Speed	2	SS_{j1}	758,32	18,09	<,0001
Current	2	SS_{j2}	713,93	17,03	<,0001
Frequency	2	SS_{j3}	304,11	7,26	0,0043

The pie charts showing the percentage contributions of significant effects for w_{rr}, w_g and w_r are given in Fig. 21. For the rim distance (w_{rr}) and the groove width (w_g), the major contributor is the main effect of the frequency. The other main effects the most significant interaction only account for a total of about 19% and 10% of the total variations of w_{rr} and w_g respectively. Thus, the level for the frequency is very important to have required laser marking widths of w_{rr} and w_g. For the rim width (w_r), the frequency is the least important main parameter whereas the scan speed and the current play an important role accounting for almost 63% of the total variations.

5. RESULTS AND CONCLUSIONS

Laser marking, which is a new and advantageous marking method, is experimentally investigated in this study to achieve better quality marks with a higher visibility and less rim formation. The investigation is done in two parts with different experimental strategies. The first part involves single factor experiments in order to investigate the influence of three parameters individually on the process. The studied parameters namely scan speed, pulse frequency and laser pump current generally have significant effect on the process outputs. Single factor experiments are adequate to get a general understanding about the change of output factors (widths and depths) with respect to input parameters. However, they do not give any information about the interactions that may significantly affect the relationship between inputs and outputs. Thus, the second part of the study is conducted to derive the important interactions with an experimental design. The experimental data from the full factorial design are analysed by S/N ratio analysis and ANOVA. As a result of theses analyses, it is observed that all main factors play an important role on almost all outputs in their selected ranges. The pulse frequency is the major contributor to all the widths and the depths whereas the interaction between the frequency and the pump current is the most significant interaction excluding the rim width (w_r). For the depth values (d_t and d_g) and rim width (w_r), scan speed and pump current account for almost the same percentage values. On the other hand, all significant main factors and interactions other than the pulse frequency account for a very small percentage for rim distance (w_{rr}) and groove width (w_g).

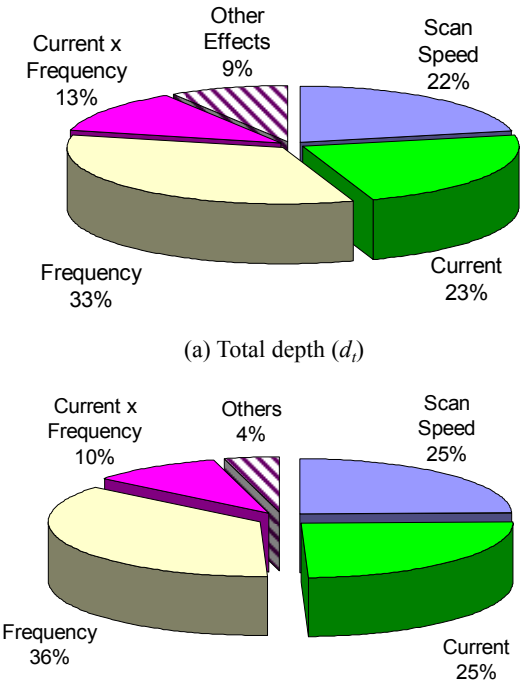

(a) Total depth (d_t)

(b) Groove depth (d_g)

Figure 20: Pie chart illustrating the relative percentage contributions of the various highly significant process parameters on the marking depths: (a)d_t and (b)d_g

For a clear mark, the depth (d_t and d_g) and groove width (w_g) are preferred to be high whereas the widths (w_{rr} and w_r) regarding the rim effect are chosen to be minimum. Regarding the depth, the selection of a low scan speed, a high current (laser power) and a medium or high frequency give better results in the studied ranges for this type of material (AISI 1085). From the single-factor tests, it is apparent that the depth value decrease as you rise the frequency up to its limit around 60 kHz. Therefore, staying in the range of (30-45 kHz) is recommended for the conditions mentioned above.

Although the minimum for the rim distance (w_{rr}) is achieved at the highest frequency value (in the selected range in design of experiments), it is better to keep this parameter at a medium value. This is due to the fact that the groove depth (w_g) is also dependent on the frequency and its value at the highest value is very low for a readable and high-contrast mark. For the rim width (w_r), the frequency is not significantly of importance. According to the S/N ratio analysis, a low current and a high scan speed is necessary for low total width (w_{rr}); however, the effect of these two parameters is much more important for depth values. Therefore, a selection of a high pump current (37 A), a low scan speed (300 mm/s) with a selection of medium frequency (30-45 kHz) is the best set for optimum values of all marking dimensions.

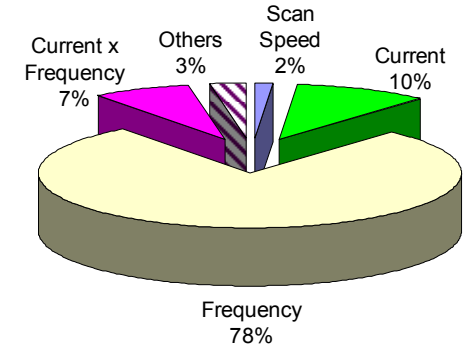

(a) Rim distance (w_{rr})

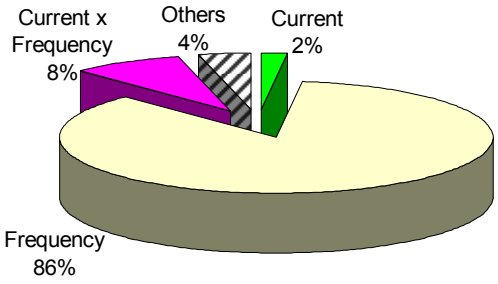

(b) Groove width (w_g)

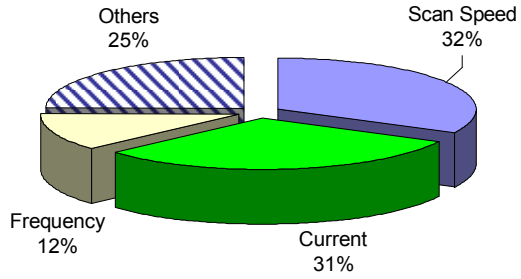

(c) Rim width (w_r)

Figure 21: Pie chart illustrating the relative percentage contributions of the various highly significant process parameters on the mark depths, (a)w_{rr}, (b)w_g and (c)w_r

6. ACKNOWLEDGEMENTS

The authors thank TUBITAK (Scientific and Technological Research Council of Turkey) for its financial support given to Evren Yasa under "Ph.D. support program for students in foreign countries" and Catholic University of Leuven for the support through the project GOA/2002-06.

7. REFERENCES

[1] Jundt, H., Junghans, J., 1987, Microscopic material interactions by laser engraving, Proc. SPIE 744, 147-155.

[2] Qi, J., Wang, K.L., Zhu, Y.M., 2003, A study on the laser marking process of stainless steel, Journal of Materials Processing Technology, 139, 273-276.

[3] http://www.lasermarking.trumpf.com

[4] Tam, S.C., Noor, Y.M., Lim, L.E.N., Jana, S., Yang, L.J., Lau, M.W.S., Yeo, C.Y., 1993, Marking of leadless chip carriers with a pulsed Nd:YAG laser, Proc. Inst. Mech. Eng., 207, 179-192.

[5] Tezuka, S., Yoshikawa, M., 1991, Study on the marking processing of IC packages by YAG laser, Int. J. Jpn. Soc. Prec. Eng. 25 (4) 297-298.

[6] Hoffmann, M., Brietenfellner, F., 1987, High contrast and intact surface – a challenge in laser marking of plastics, Proc. SPIE 744, 156-180.

[7] Bosman, J., 2007, Processes and strategies for solid state Q-switch laser marking of polymers, University of Twente, Netherlands, Ph.D. Thesis.

[8] Valette, S., Steyer, P., Richard, L., Forest, B., Donnet, C., Audouard, E., 2006, Influence of femtosecond laser marking on the corrosion resistance of stainless steel, Applied Surface Science 252, 4696-4701.

[9] Campanelli, S.L., Ludovico, A.D., Bonserio, C., Cavalluzzi, P., 2006, Artificial neural network modelling of the laser milling process, Int. Sem. on CIRP ICME, Ischia, Italy.

[10] Pham, D.T., Dimov, S.S., Petkov, P.V., 2007, Laser milling of ceramic components, International Journal of Machine Tools and Manufacture, 47, 618–626.

[11] Vasco, J.C., Bartolo, P. J., 2007, Processing conditions of laser micro-drilling, Proc. 15th Int. Symp. On Electromachining ISEM XV, 427-432.

[12] Gilmore, R., Short pulse laser machining for diesel and aerospace applications, 2007, Proc. 15th Int. Symp. On Electromachining ISEM XV, 433-437.

[13] www.concept-laser.de

[14] Harimkar, S.P., Samant, A.N., Dahotre, N.B., 2007, Temporally evolved recoil pressure driven melt infiltration during laser surface modifications of porous alumina ceramic, Journal of Applied Physics, 101, (DOI: 10.1063/1.2710288).

[15] Chickov, B.N., Momma, C., Nolte, S., von Alvensleben, F., Tuennermann, A., 1996, Femtosecond, picosecond and nanosecond laser ablation of solids, Appl. Physics, A 63, 109-115.

[16] Kruth, J.-P., Yasa, E., Van Vaerenbergh, J., 2007, Parameter study for Selective Laser Erosion, 4th Int. Conf. and Exhib. on Design and Production of Machines and Dies/Molds, Turkey, CD-ROM.

[17] Taguchi, G., Introduction to Quality Engineering, Mc-Graw-Hill, New York, 1988.

[18] NIST/SEMATECH e-Handbook of Statistical Methods, http://www.itl.nist.gov/div898/handbook/, last updated on 7/18/2006.

[19] Yang, W.H., Tarng, Y.S., 1998, Design optimization of cutting parameters for turning operations based on the Taguchi method, Journal of Materials Processing Technology 84, 122-129.

[20] Kaldos, A., Pieper, H.J., Wolf, E., Krause, M., 2004, Laser machining in die making – a modern rapid tooling process, Journal of Materials Processing Technology, 155-156, 1815-1820.

Appendix 3

Kruth, J.-P., Deckers, J., Yasa, E. and Wauthlé, R. 2010, "Assessing influencing factors of residual stresses in Selective Laser Melting using a novel analysis method", *Proc. 16th International Symposium on Electromachining (ISEM XVI)*, Shanghai, China,19-23 April, pp.531-540.

Assessing Influencing Factors of Residual Stresses in SLM using a Novel Analysis Method

J.-P. Kruth, J. Deckers* , E. Yasa, R. Wauthlé

Department of Mechanical Engineering , Catholic University of Leuven, Celestijnenlaan 300B BE-3001 Heverlee, Leuven, Belgium

*Email: jan.deckers@mech.kuleuven.be

Abstract

Selective Laser Melting (SLM) is a layered manufacturing process that allows to build complex, lightweight and customized parts by consolidating successive layers of powder. Since during the SLM process the powder material is completely molten, a low degree of porosity and good mechanical properties can be achieved.

However, during the melting and solidification, the material experiences large temperature fluctuations in a short time. This causes high thermal stresses which can introduce part warpage, cracks or an unwanted decrease in strength of the parts. The goal of the reported investigation is to reduce the thermal stresses by changing standard parameters like the scan pattern or process parameters like the preheating temperature of the base plate, the layer thickness, pre-scanning a deposited powder layer or post-scanning an already scanned layer. To achieve this goal, a new method is defined which enables assessing thermal stresses in a fast way by measuring the curvature of test parts when releasing them from the base plate on which they are built.

A review of the existing literature on this topic and the results of own experiments show that changes which lower high temperature gradients reduce the thermal stresses. Also changing the orientation of the scan vectors can reduce the thermal stresses, or can reduce the fatal consequences of the thermal stresses.

Keywords:

Rapid manufacturing, Selective Laser Melting (SLM), residual stresses

1 INTRODUCTION

A material in its liquid phase doesn't contain thermal stresses. In the SLM process, thermal stresses arise in solidified material, subjected to temperature gradients, or subjected to shrinkage caused by the solidification of laser molten material.

Residual stresses arise by nonuniform plastic deformations in solid material. As long as thermal stresses are elastic, no residual stresses will remain when the temperature comes back to its original value. If the thermal stresses inside a material become higher as the yield stress, residual stresses will remain after cooling. The sign of the remaining residual stress will always be the opposite of the sign of the thermal stress. As a decrease of thermal stress will reduce the residual stresses, the terms 'thermal stress' and 'residual stress' are somewhat coupled. In the remaining of the paper, these terms will be used interchangeable.

1.1 Mechanisms of thermal stresses in SLM

During the SLM process, the laser beam melts the material and causes a temperature gradient in the solid material being radiated wherever it passes, resulting in residual stresses. If the residual stresses are too high, the produced part will crack (Figure 1).

Mercelis uses two descriptive models to explain the mechanism of the thermal stresses in SLM [1],[2]: The Temperature Gradient Mechanism (TGM) model and the cool-down phase model.

The TGM model states that during the SLM process the laser beam heats up the solidified material being radiated, which as a result tends to expand (Figure 2a). The thermal expansion (ε_{th}) is partially inhibited by the surrounding solid material, which bends away from the laser beam, yielding a compressive stress/strain condition in the radiated zone. If the compressive stress exceeds the compressive yield stress (σ_{yield}) of the material, the compressive strain will be partially elastic (ε_{el}) and partially plastic (ε_{pl}) (Figure 2b).

After the laser beam leaves that area, the radiated zone will cool and tend to shrink. The shrinkage is partially inhibited as a consequence of the plastic deformation developed during heating yielding a residual tensile stress (σ_{tens}) condition at the radiated zone and a counter-bending of the part being produced towards the radiated zone. According to the equilibria of force and momentum of the part, the radiated zone is surrounded by a zone of compressive stress (σ_{comp}) (Figure 3).

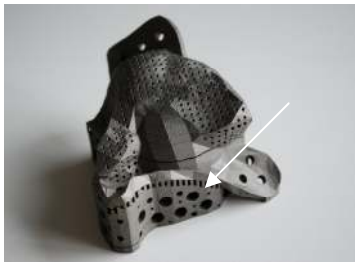

Figure 1: SLM part with cracks induced by thermal streses.

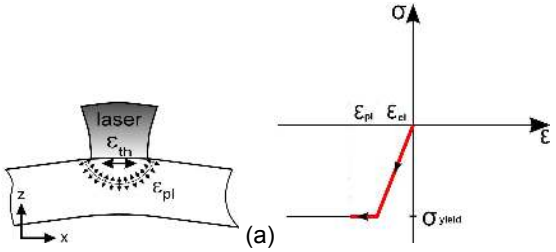

Figure 2: (a) Bending of an SLM part during laser beam heating [2]. (b) Simplified representation of the formation of thermal strains in the radiated zone.

The cool-down phase model describes the formation of residual stresses during the SLM process from a more macroscopic point of view. It states that when the laser beam has passed, the molten and resolidified top layer of the part will tend to shrink. This shrinkage is partially inhibited by the underlying material, thus introducing tensile stresses in the added top layer.

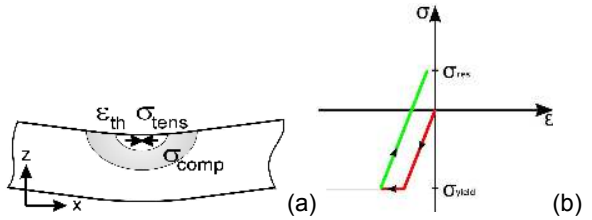

Figure 3: (a) Counter-bending of an SLM part after a laser beam has passed [2]. (b) Simplified representation of the formation of residual stresses in the radiated zone.

1.2 Modelling of thermal stresses in SLM

Mercelis and Shiomi have defined a similar simplified mechanical model which quantifies the descriptive cool-down phase model by using the equilibria of force and momentum [2],[3]. They assume the residual stresses in the latest added layer equals the yield strength of the material. This causes high tensile stresses in the SLM part, compressive stresses in the upper part of the base plate and again lower tensile stresses in the lower part of the base plate as illustrated in Figure 4. The high tensile stresses inside the SLM part partially relax when removing the part from the base plate. The occuring relaxation consists of a constant term, which effects a uniform shrinkage of the part produced, and a linear term, which effects the bending of the part produced. The stresses in the part which remain after relaxation are considered as the residual stresses (Figure 5).

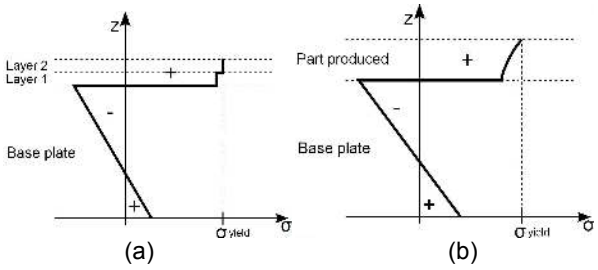

Figure 4: (a) Residual stresses after laser melting two layers on a base plate. (b) Residual stresses of a SLM part on a base plate after production. (simplified model)

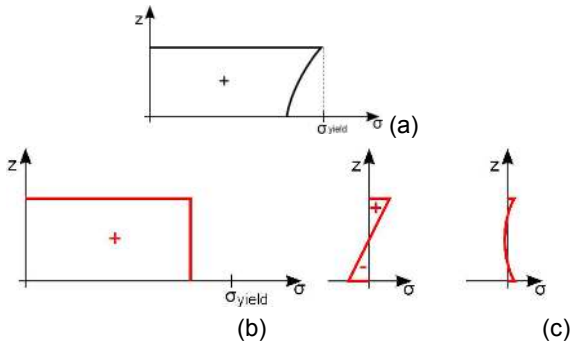

Figure 5: (a) Residual stresses of a SLM part on a base plate.(b) Constant and linear relaxation terms.(c) Residual stresses of a SLM part removed from the base plate.

Mechanical models simplify the heat input of the laser. In order to have more accurate models, it is necessary to calculate the exact temperature distribution in the part during processing. Many authors have discussed thermal modeling of other laser material processing techniques like laser welding and laser bending [4],[5],[6],[7]. Thermal modeling of the SLM process is similar, but the powder characteristics and the scanning pattern of the laser beam also have to be taken into account.

Since residual stresses do not only depend on the temperature, thermal models cannot predict the resulting residual stresses without mechanical considerations. Thermomechanical models are able to calculate a resulting stress profile from a thermal model. Many authors use ABAQUS finite element package for creating thermomechanical models [8],[9],[10],[11]. Others use an own method [12],[13] or another package [14].

Many material properties, like the heat capacity, the thermal expansion, the latent heat and the yield strength are temperature dependent and are well understood. However, all this knowledge is not been found exstensively implemented yet for the calculation of thermal stresses [15].

1.3 Observations from experiments

Besides modeling the SLM process, many researchers have performed experimental tests [2],[3],[11],[14],[16],[17],[18] to measure the residual stresses. The purpose of these tests is to verify the results of the theoretical models, or to examine the influence of non simulated phenomena.

Many measuring techniques for measuring the residual stress in a part are available [19],[20]. Usually a classification is made in two groups, whether the measurement is destructive or not. Destructive methods include the layer removal method [19],[20], the crack compliance method [2], the contour method [21] the hole drilling method [19],[20]. Non destructive methods include X-ray diffraction, neutron diffraction, ultrasonic and magnetic measuring methods [19],[20]. Since these measuring techniques are time consuming, and only qualitative information of thermal stresses is needed in this study (for comparing stress magnitude and analysing trends), a new and faster method for analysing the residual stresses is defined in the next section.

2 DESCRIPTION OF EQUIPMENT AND THE NOVEL ANALYSIS METHOD

2.1 Equipment

In this study Ti-6Al-4V test parts are produced on an in-house developed SLM machine and 316L stainless steel test parts are produced on a Concept Laser Linear M3 machine. Table 1 and Table 2 give an overview of the properties of these machines. For the measurements a non-contact vision measuring system (Mitutoyo Quick Vision Pro 202) was used.

2.2 Bridge curvature method

The novel analysis method, the bridge curvature method, is simple, fast, accurate and resembles the layer removal methods (§ 1.3, [20]). When the test part is cut off the base plate by wire EDM, the bridge curls because of the relaxation stresses [2]. Residual tensile stresses at the top of the part cause this bending. Figure 6a and Figure 6b illustrate the method whereas Figure 6c shows the geometry of the test parts. The planes at the bottom of the pillars deviate from their normal position and form an angle α which is a measure for the thermal stresses in this method. For each test part, the curling angle is measured 10 times by a Mitutoyo Quick Vision Pro 202 system (5 times on each side of the part). From the measured data the mean value and standard deviation with a confidence interval of 95% are calculated.

A detailed uncertainty analysis of the method (e.g. the influence of a bad EDM cut on the measured angle) can be found in [22]. Table 3 and Table 4 show the standard

parameters used to produce the reference parts and show the obtained values for the curling angle α.

Laser type	Yb:YAG
Laser wavelength	1085 nm
Maximum power	300 W
Build envelope	Ø 100mm x 100mm

Table 1: Properties of the KUL-SLM machine.

Laser type	Nd:YAG
Laser wavelength	1064 nm
Maximum power	100 W
Build envelope	250mm x 250mm x 250mm

Table 2: Properties of the Concept Laser M3 Linear Machine.

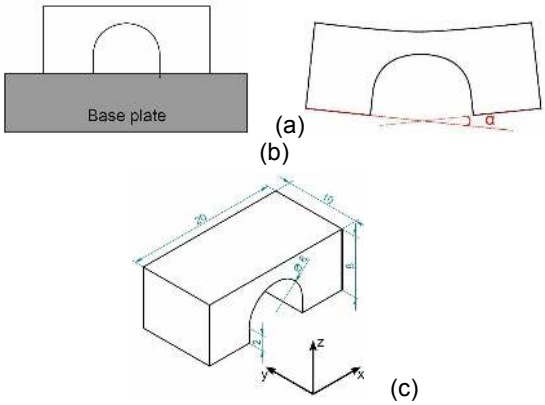

Figure 6: Principle of the method for measuring the residual stresses in the test parts. (a) Before and (b) after removal from base plate. (c) Geometry of the test parts.

Material	Ti-6Al-4V
Scan vectors	x-direction, bi-directional
Hatch spacing	74 µm
Scan speed	225 mm/s
Laser power	42 W
Contour scan	before fill
Layer thickness	30 µm
Reference value	$\alpha_{ref,\,LM}$ = 2,797°± 0,033°

Table 3: Reference parameters used to build Ti-6Al-4V test parts on the KUL-SLM machine.

Material	316L stainless steel
Scan vectors	x-direction, bi-directional
Hatch spacing	126 µm
Scan speed	380 mm/s
Laser power	100 W
Contour scan	before fill
Layer thickness	30 µm
Reference value	$\alpha_{ref,\,LM}$ = 1,333°± 0,024°

Table 4: Reference parameters used to build 316L stainless steel test parts on the Concept Laser machine.

3 EXPERIMENTS AND RESULTS

The first section of this paragraph describes the influence of the scan pattern on the measured curling angle of the test parts. Scan strategies can be adapted in a relatively easy way by changing the scanning software. The second section describes the influence of more fundamental process changes which are not yet commonly used for SLM.

3.1 Change in scan pattern

Length of the scan vectors

The parallel bi-directional scan vectors, often used in SLM, do not always have the same length. The first test checks the influence of the vector length (l) in the x-direction on the bending of the part and is performed on the KUL-SLM machine. Figure 7 shows the scan pattern used to investigate the influence of shorter scan vectors on the thermal stresses. The sequence of the vectors scanned by the laser is determined by the path of the dotted line.

The results for shorter vector lengths are shown in Figure 8. Three test parts with shorter vector lengths are compared to the reference part. There is almost no difference in measured angle between vectors of 20 mm and 10 mm. At lower vector lengths, the measured angle decreases. This effect is more pronounced if the vector length is reduced further. Vector lengths of 2 mm record the largest improvement of 13%.

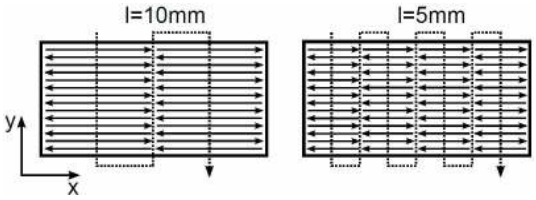

Figure 7: Scan pattern to investigate short scan vectors.

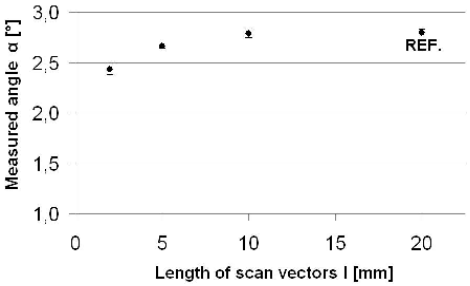

Figure 8: Influence of vector length (l) in the x-direction on curling of the test part (REF. = reference part).

Orientation of the scan vectors

To see the influence of the orientation of the parallel scan vectors on the measured angle α, different test parts are made on the KUL-SLM machine, in which the angle β between the parallel scan vectors and the direction of measurement (x-direction) changes from 0°(reference) to 90°. Figure 9 illustrates this rotation for 45° and 90°.

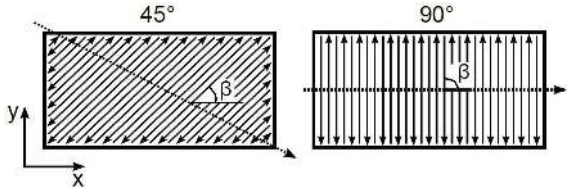

Figure 9: Scan pattern to investigate the orientation β of the scan vectors.

The measured angle α decreases for rotations going from 0° to 90° (Figure 10). The bending of the test part reduces by 59% if the scan vectors are oriented 90° from the direction of measuring. If the parallel scan vectors are layerwise alternated (β =0°-90°) after each layer, the reduction of the measured angle is found to be 45%.

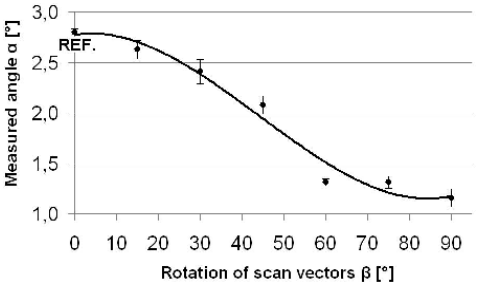

Figure 10: Influence of the orientation β of the scan vectors on the curling of the test part.

Notice that during this rotation of the scan vectors also the length of the vectors changes. Due to the small difference in curling angle for test parts with vector lengths of 20 mm and 10 mm (Figure 8), this change in vector length (l) has a negligible influence on the obtained results.

Island scanning

Island scanning is a scan strategy patented by Concept Laser GmbH. This scan strategy divides the area to be scanned into small square islands. The sequence in which the islands are scanned is chosen randomly. The special slicing algorithm embedded in Magics® software allows to change the size of the islands, the orientation of the islands, and it is also possible to shift the islands in the x- and y-direction between different layers. Figure 11 shows a possible scan pattern for islands of 5x5 mm and a 15° rotation β from the x-direction.

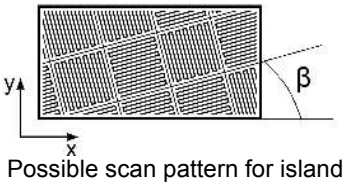

Figure 11: Possible scan pattern for island scanning with islands of 5x5 mm and a 15° rotation β.

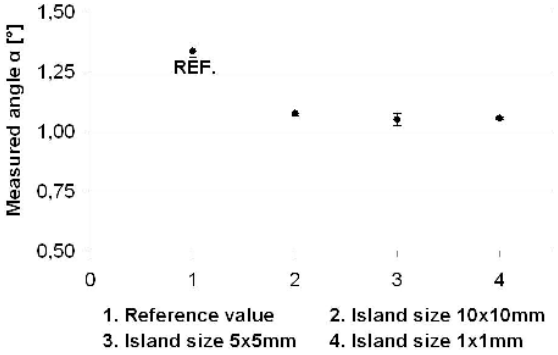

Figure 12: Results of island scanning with different island size on the Concept Laser machine.

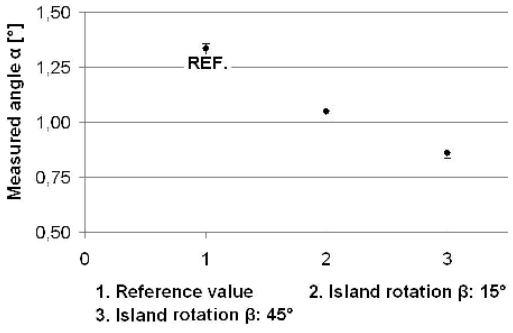

Figure 13: Results of island scanning with different island orientations β on the Concept Laser machine.

The effect of the island size is shown in Figure 12 for islands rotated 15° from the x-direction. The use of island scanning reduces the measured angle α, but the size of the islands doesn't seem to influence the results. Figure 13 illustrates the effect of the rotation β for islands of 5x5 mm. If the rotation β is 45° instead of 15°, the measured angle further decreases. Island scanning with islands of 5x5 mm, rotated 45° from the x-direction reduces the measured angle by 36%.

3.2 Process changes

Post-scanning

Post-scanning means re-scanning a laser molten and consolidated layer: the cross-section of each layer is first molten by the reference parameters given in Table 3 or Table 4. Then the cross-section is re-scanned with the same scan pattern and spot size. The results for post-scanning with different scan speeds on the KUL-SLM machine are shown in Figure 14. In this figure, the value at 0 mm/s is the reference value without post-scanning.

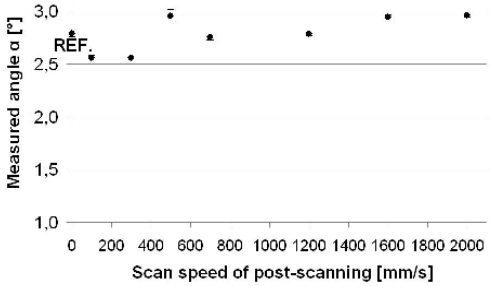

Figure 14: Results of post-scanning with different scan speeds on the KUL-SLM machine.

Only the low scan speeds reduce the measured angle. A scan speed of 100 mm/s gives the maximum reduction of 8% (the values at 0 mm/s are the reference values without post-scanning). Also some test part were produced on the Concept Laser machine, but none of this parts showed any noticeable reduction in curling angle [22].

Pre-scanning

When pre-scanning is applied, the laser first sinters the powder material, before melting the material completely with the reference parameters of Table 3. The results for pre-scanning with 800 mm/s and 1600 mm/s and a constant laser power of 42 W on the KUL-SLM machine are presented in Figure 15. The value at 0 mm/s is the reference value without pre-scanning. Pre-scanning reduces the measured angle α only slightly with a maximum reduction of 6% for pre-scanning with 800 mm/s.

Different layer thickness

The KUL-SLM machine and the Concept Laser machine both employ a standard layer thickness of 30 µm. Larger layer thicknesses can be used to increase the production speed of the process, but also can induce unwanted porosities which decrease the strength of the produced parts drastically. Since the stress normal to a pore is zero, porosities tend to decrease the residual stresses.

The scan speed needed to produce optimal density parts was not known. Therefore multiple test parts with a layer thickness of 60 µm but with different scan speeds (v) are produced on the Concept Laser machine and investigated. For each part produced, the curling angle is measured (Figure 16). Also the part densities are measured with the Archimedes method (Table 5) and the cross-sections are investigated by an optical microscope (Figure 17).

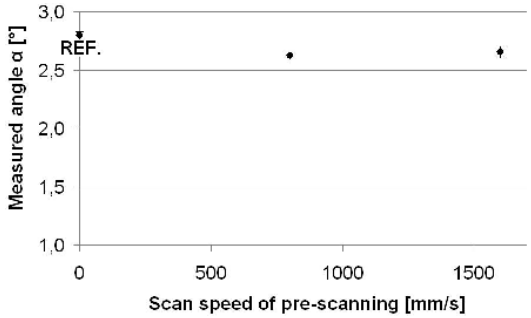

Figure 15: Results of pre-scanning with different scan speeds on the KUL-SLM machine.

A low scan speed is expected to heat up more material around the laser spot and to reduce in this way the temperature gradient and related thermal stresses. Contrary to this expectation, Figure 16 shows only a decrease in curling angle for scan speeds varying from 200 mm/s to 175 mm/s. Since part n° 3 has a rather high density value, the lower curling angle for its scan speed cannot be due to stress relaxation caused by a large amount of pores in the part. It seems to be difficult to compare the influence of layer thickness on thermal stresses without taking into account the combined influence of part density and scan parameters (in this case the scan speed) to achieve this density. On the other hand, it can be stated that the measured angle of the test part with a density closest to the density of the reference part (part n°3) and a layer thickness of 60µm gives a reduction of 6%.

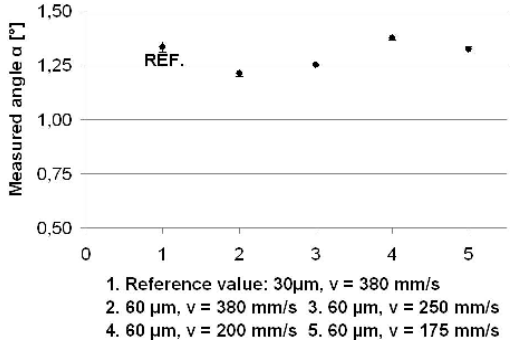

Figure 16: Influence of layer thickness and scan speed on the curling of the test part.

n°	scan speed [mm/s]	density [%]	angle $\bar{\alpha}$ [°]
1 (ref.)	380	97,57	1,333
2	380	95,83	1,212
3	250	98,23	1,251
4	200	98,82	1,374
5	175	98,88	1,323

Table 5: Density of the test parts produced with a layer thickness of 60 µm and different scan speeds.

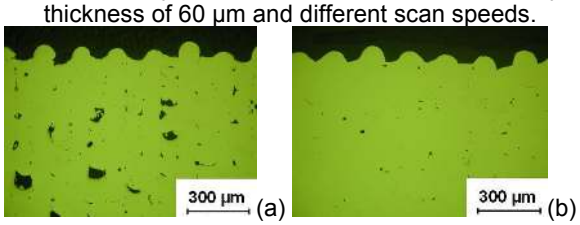

Figure 17: Investigation of the cross-sections of 60µm layer thickness parts by an optical microscope. (a) v=380mm/s, (b) v=175mm/s.

Preheating of the base plate

It is possible to preheat the base plate on the Concept Laser machine. The maximum preheating temperature is 180°C. Preheating of the base plate on the Concept Laser machine resulted in a reduction of 10% of the measured angle.

Heat treatment

Heat treatments reduce the residual stresses developed during fabrication (stress relieving) [23]. Figure 16 shows the temperature cycle that is applied to a reference part produced on the KUL-SLM machine (Table 3). This heat treatment reduces the measured angle by 80%.

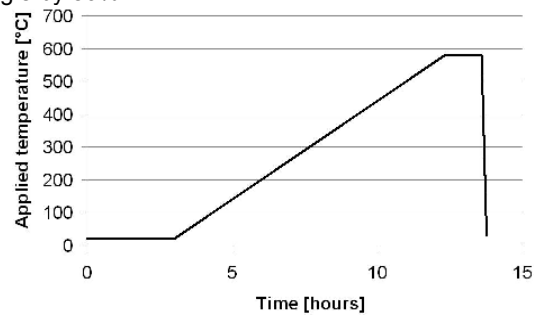

Figure 18: Temperature cycle for heat treatment.

4 DISCUSSION

Scanning with short scan vectors reduces the thermal stresses. If the length of the scan vectors is 2 mm instead of 20 mm, the measured angle is reduced by 13%. Increasing the process temperature by preheating the base plate up to 180°C reduces the curling angle by 10%. Both results indicate that changes lowering the thermal gradients reduce the thermal stresses: Shorter scan vectors experience a smaller temperature gradient due to the heat of the previous scan line. Preheating the base plate also reduces the temperature gradient during scanning.

The tests in § 3.1 'Orientation of the scan vectors' and 'Island scanning' show that the magnitude of the thermal stresses differs as the orientation of the scan vectors to the direction of measurement (x-direction) changes. Thermal stresses in the direction perpendicular to the scan vectors are lower as thermal stresses parallel to the scan vectors.

Post-scanning and pre-scanning with the same spot size and the same scan pattern only reduce the measured angle by respectively 8% and 6%. These reductions are considered to be relatively low because the same Temperature Gradient Mechanism causes the high thermal stresses.

5 SUMMARY AND CONCLUSION

The paper presents a new method for assessing thermal stresses in a simple, fast and accurate way. The method uses the angle of curvature α of SLM-made bridge structures cut off from the base plate as a measure for the thermal stresses. Table 6 and Table 7 give a summary of the most important results obtained.

The results from the experiments as well as the findings from literature lead to two general conclusions: Changes which reduce the high temperature gradient, like using short scan vectors and preheating of the base plate, reduce the thermal stresses. Also an optimal use of the orientation of the thermal stresses can reduce these stresses or make the orientation more beneficial.

Changes	Maximum procentual reduction of curling angle
Parallel scanvectors, bi-directional scanning	
* Short length of vectors: 2mm	13%
* Orientation of vectors: 90° rotated with respect to the measurement direction	59%
* Layerwise alternated: 0-90° rotated with respect to the measurement direction	45%
Postscanning or prescanning while using same spotsize and scan pattern	
* Postscanning: v=100mm/s, P=42W	8%
* Prescanning: v=800mm/s, P=42W	6%
Postprocessing in furnace	
* 75 minutes at 580°C	80%

Table 6: Summary of most important results for reduction of thermal stresses with Ti-6Al-4V on the KUL-SLM machine.

Changes	Maximum procentual reduction of curling angle
Island scanning	
* Size of islands 5mm x 5mm, rotation of 45° with respect to measurement direction	36%
Layer thickness	
* Layer thickness 60µm, v=250mm/s, P=100W	6%
Preheating of baseplate	
* 180°C	10%

Table 7: Summary of most important results for reduction of thermal stresses with 316L stainless steel on the Concept Laser machine.

6 ACKNOWLEDGMENTS

The authors thank I.W.T. for the support through the SBO project DiRaMaP and the TUBITAK Research Council of Turkey for its financial support given.

7 REFERENCES

[1] Kruth J.-P., Froyen L., Van Vaerenbergh J., Mercelis P., Rombouts M., Lauwers B., 2004, Selective laser melting of iron based powders, Journal of materials processing technology, 14th international symposium on electromachining (ISEM XIV) – 10 June, Volume 149, Issues 1-3, 616-622.

[2] Mercelis P., 2007, Control of Selective Laser Sintering and Selective Laser Melting Processes, PhD thesis K.U.Leuven – April.

[3] Shiomi. M., Osakada K., Nakamura K., Yamashita T., Abe F., 2004, Residual stress within metallic model made by selective laser melting process, Annals of the CIRP, 53/1, 195.

[4] Cheng P. J., Lin S. C., 2000, An analytical model for the temperature field in the laser forming of sheet metal, Journal of Materials Processing Technology, 101, 260-267.

[5] Kruth J.-F., 2001, Modelleren van laserbuigen: een verkennende studie, Master's thesis K.U.Leuven.

[6] Duflou J.R., Callebaut B., Kruth J.-P., 2005, Laserforming of 3D features, Advanced Materials Research, Vols 6-8, 425-432.

[7] Mackwood A., Crafer R., 2005, Thermal modelling of laser welding and related processes: a literature review, Optics and Laser Technology, 37, 99-115.

[8] Chin R. K., Beuth J. L., Amon C. H, 1996, Thermomechanical modeling of successive material deposition in layered manufacturing, Mech. Mater., 24,257-271.

[9] Li L., Achara C., 2004, Chemical assisted laser machining for the minimisation of recast and heat affected zone, CIRP annals 2004, 53/1, 175-178.

[10] Nickel A. H., 1999, Analysis of thermal stresses in Shape Deposition Manufacturing of metal parts, Ph.D. thesis Stanford University.

[11] Nickel A.H., Barnett D.M., P. F. B., 2001, Thermal stresses and deposition patterns in layered manufacturing, Materials Science and Engineering, A317/1,59-64.

[12] Matsumoto M., Shiomi M., Osakada K., Abe F., 2002, Finite element analysis of single layer forming on metallic powder bed in rapid prototyping by selective laser processing, Int. Journal of Machine Tools & Manufacture, 42, 61-67.

[13] Osakada K., Shiomi M., 2006, Flexible manufactuting of metallic products by selective laser melting of powder, International Jounal of Machine Tools & Manufacture, 46, 1188-1193.

[14] Over C., Meiners W., Wissenbach K., Hutfless J., Lindeman M., 2003, Rapid manufacturing of metal parts and tools using laser melting, Proc. WLT-Conference on Lasers in Manufacturing, 265-269.

[15] Bhadeshia H. K. D. J., 2002, Material factors, Handbook of Residual Stress and Deformation of Steel (Totten G. E., Howes M. A. H., Inoue T., eds.), chapter 'Effect of Materials and Processing', 3-10.

[16] Kruth J.-P., Mercelis P., V. Vaerenbergh J., Froyen L., Rombouts M., 2005, Binding mechanisms in selective laser sintering and melting, Rapid Prototyping Jounal, 11/1, 26-36.

[17] Rombouts M., 2006, Selective Laser Sintering/Melting of Iron-Based Powders, PhD thesis K.U.Leuven – April.

[18] Vandenbroucke B., 2008, Selective laser melting of biocompatible metals for rapid manufacturing of medical parts, PhD thesis K.U.Leuven (Dept. Mech. Eng.).

[19] Kandil F. A., Lord J. D., Fry A. T., Grant P. V., 2001, A review of residual stress measurement methods – a guide to technical selection, tech. rep. NPL Materials Centre.

[20] Withers P. J., Bhadesia H. K. D. H., 2001, Residual stress part 1: Measurement techniques, Materials Science and Technology, 17.

[21] Prime M. B., 2001, Cross-sectional mapping of residual stresses by measuring the surface contour after cut, Journal of Engineering Materials and Technology, 123, 162-168.

[22] Wauthlé R., 2009, Verminderen van thermische spanningen bij selectief laser smelten, Master thesis K.U.Leuven (Dept. Mech. Eng.).

[23] Gilbert R., Shannon R., 1991, Heat treating of titanium alloys, ASM Handbook, 4.

Appendix 4

Kruth, J.-P., Yasa, E. and Deckers, J. 2008, “Roughness improvement in selective laser melting”, *Proc. of international Conference PMI 2008,* September 17-19, Ghent, Belgium, pp. 170-183.

Roughness Improvement in Selective Laser Melting

J.P. Kruth, E. Yasa, J. Deckers
K.U. Leuven, Dept. of Mechanical Engineering, Heverlee, Belgium

ABSTRACT: Selective laser melting (SLM) is a layer manufacturing process to fabricate 3D complex and functional parts directly from powder material. During the process, successive layers of powders are completely melted and consolidated by the energy of a high intensity laser beam. The process is capable of producing high-density parts having mechanical properties comparable to those of bulk materials. On the other hand, one of the major problems encountered in SLM is the poor surface quality. The high roughness of SLM (R_a typically 10-30 µm for iron-based powders) is a limitation of the process, among others for micromachining applications. In this study, the roughness enhancement in SLM is achieved by means of Selective Laser Erosion (SLE) and re-melting. SLE is a process to remove material mostly by evaporation due to the heat provided by the incident laser beam working in pulsed mode. In addition to SLE, laser re-melting of the top layer(s) is applied for titanium and stainless steel powders. Different scanning strategies and parameter sets are investigated for an optimized surface quality in terms of average and total roughness values.

1 INTRODUCTION

The first Rapid Prototyping (RP) techniques became available in the late 1980s and were used to manufacture parts and prototype parts within a very short time [17]. Today, they are used more commonly and for a much wider range of applications. A shift of RP to Rapid Manufacturing (RM) has come up due to the technical improvements of layer manufacturing processes including Selective Laser Melting (SLM). The processes are no longer used only for prototyping and visual concept models but also for real manufacturing applications in many fields including biomedical, aerospace and automotive industries (Figure 1). SLM is a layer-wise material addition technique that allows complex 3D solid model production by selectively consolidating successive layers of pre-deposited powder, each corresponding to a particular slice from the CAD model. The consolidation is accomplished by the thermal energy supplied by a focused and computer controlled laser beam. For the production of functional metallic prototypes, parts or tools, a high part density is desired and this can be obtained from SLM without any post-processing steps [18]. The other competitive advantages of SLM include geometrical freedom, mass customization and material flexibility [19]. Figure 2 illustrates the SLM process [25]. Many research groups investigate several aspects of the SLM process. Regarding material aspect of the process, various ferrous powders have been investigated by processing them by SLM [6][23][26] [28][33][50]. Non-ferrous powder materials are also used in SLM for medical and aerospace applications [1][2][34][43][47]. Parametric study of the process has been conducted experimentally to find the optimum process and laser parameters for improved mechanical properties [7][35][45][52][53] whereas some researchers focus on physical modelling of the process together with experimentation [8][55].

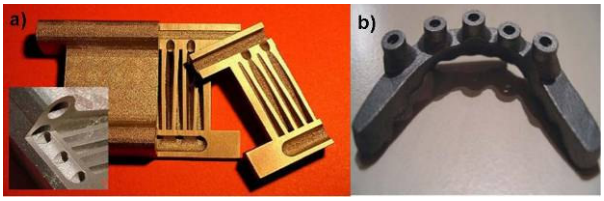

Figure 1. Sample parts produced by SLM a) internal cooling channels b) oral implant.

Although SLM provides many advantages, it still has some major drawbacks such as insufficient surface quality (R_a values of 10-30 µm for iron based powders [18]). In order to overcome this problem, a variety of surface modification technologies are available in the market including mechanical processes (machining and abrasive sandblasting), chemical processes (acid etching and oxidation) and thermal processes (plasma spray) [4]. Laser remelting is a valuable alternative to these techniques being a clean and reproducible process with a good controllability of the variables

involved in the process. Generally, laser remelting is performed to improve the material surface properties such as microhardness [16][49], friction and wear behaviour [10][16][56], corrosion resistance [37][51], bio-integration [42], wettability [13][21][40], surface quality [14][24][40] for different materials including metals, polymers and ceramics [13] with different laser sources (Nd:YVO_4, Nd:YAG, CO_2). Laser remelting is also used to repair/prevent surface cracks [12][41], to modify the microstructure [4][49] or for surface alloying [9][39]. Mathematical modelling of the laser heating process with a pulsed laser source applied on solid parts has also been conducted examining the heat transfer mechanism, including conduction, phase change and convection processes [54]. Some other work has focused on experimental mathematical modeling of laser interaction with material, combining experimental techniques with theoretical approach of dimensional analysis [22]. None of the studies mentioned here concentrates on laser surface remelting after Selective Laser Melting or any RP/RM technique. In this study, surface laser remelting (SLR) is applied on the last layers of the parts produced by Selective Laser Melting as a finishing process and by the same laser on the same machine without any fixation problem.

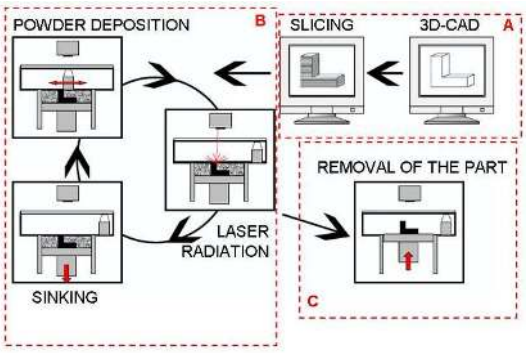

Figure 2. The working principle of the SLM process A)Pre-process data file preparation B)SLM process C)Post-process removal of the part (modified from [25]).

This study also applies Selective Laser Erosion (SLE) to SLM stainless steel parts in order to investigate if it can provide an enhancement in the surface quality when it is used before a laser remelting step. Selective Laser Erosion is a layer manufacturing technique applying material subtraction rather than material addition. Due to the pulsed mode of the laser beam, high peak laser powers are obtained, facilitating material evaporation. Laser erosion has found great interest in industry especially in the field of laser marking but will be used here only for the purpose of improving surface finish in SLM.

Figure 3. Equipment used in the experiments.

In recent years, laser marking studies conducted with different lasers have been reported by many researchers. They found that mark quality (mark depth, width and mark contrast) was highly affected by the pulse frequency [30]. Tam, et al. [36], and Tezuka and Yoshikawa [38] studied the laser marking of integrated circuit packages with pulsed Nd:YAG laser and Q-switched YAG laser, respectively. Extensive research was conducted for the laser marking of polymers by Hoffmann et al. [15] and by Bosman [3]. Valette et al. investigated the enhancement of corrosion resistance of laser marked surfaces in surgical applications using a femto-second laser source which causes a small heat-affected area [44]. In addition to studies directly focused on laser marking, there are some others about laser milling. Campanelli, et al., used the design of experiment methodology to evaluate the influence of the parameters (laser power, frequency, overlap, etc.) involved in laser milling on the removed depth and surface roughness [5]. Pham et al., studied the laser milling process of ceramic components reviewing the main parameters (lamp current, pulse duration, pulse frequency and scan speed) affecting the material removal characteristics of the process [29]. In the field of laser micro-millling, Vasco et al., tested different scanning strategies and operating conditions regarding the surface quality and material removal rate on a laser milling machine [48].

2 EXPERIMENTAL PROCEDURE

All performed experiments are carried out on two Selective Laser Melting machines: a Concept Laser

M3 Linear machine (Figure 3) and the LM machine which was developed at K.U.Leuven. The Concept Laser M3 machine employs an Nd:YAG laser with a wavelength of 1064 nm. This laser can be used in pulsed mode (Q-switched) or in continuous mode. Until now Selective Laser Erosion (SLE) is only possible using a pulsed mode. In this paper Surface Laser Remelting (SLR) is only done using a continuous mode. In continuous mode the maximum laser output power is approximately 100 W. The laser also has two possible beam diameters Φ_{1/e^2}: 53 and 133 µm ($\Phi_{99\%}$ respectively 80 and 200 µm). The LM machine employs an Yb:YAG fibre laser with a wavelength of 1085 nm. This laser can be used in a modulated mode (which is not used) and in continuous mode. The maximum laser output power in continuous mode is 300W and the standard beam diameter Φ_{1/e^2} is 50µm.

Two different powder materials were used in order to make a comparison about the effect of laser remelting on surface quality taking the material issue into account: i.e. ASTM 316L stainless steel (CL20ES) and Ti-6Al-4V (CL40TI) which is the most commonly used titanium alloy [27]. Both powders are commercially available from Concept Laser. The parts having a rectangular cross-section (mostly 10 x10 mm2) as shown in Figure 4 are first produced by SLM.

The surface quality of the top surfaces was measured by a roughness tester (Taylor Hobson Form Talysurf 120L). In this paper the roughness of the parts is mostly expressed by the arithmetic mean surface roughness (R_a). The total height of the roughness profile (R_t) and the surface roughness depth (R_z) were measured too and follow the same trend.

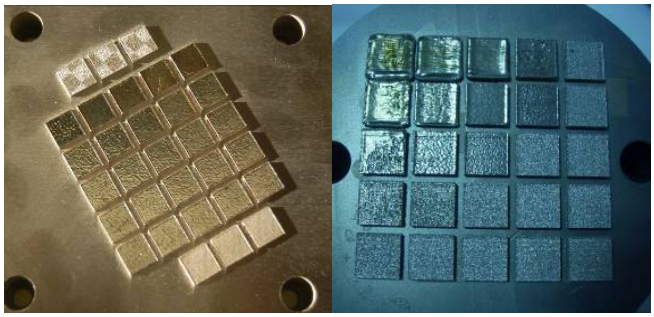

Figure 4. Parts made for parameter study for laser surface remelting; stainless steel on the left and Ti-6Al-4V on the right.

3 EXPERIMENTAL RESULTS AND DISCUSSION

The best surface roughness achievable by SLM is limited due to the powder particle size distribution that is used for the process. This particle size may not be chosen too small due to the need for flowability and dense powder particle packing [31]. Therefore, it is generally a compromise between density and surface quality.

In the following sub-section, the experimental results in terms of roughness are presented separately for the two different materials (1.4404 /ASTM 316 L and Ti-6Al-4V) since the experiments for two materials were conducted on different machines employing different laser sources. The tests with stainless steel are carried out using the Concept Laser M3 Linear machine. For the tests with Ti-6Al-4V, the LM machine of the K.U.Leuven is used.

3.1 *Stainless Steel*

The metallurgical composition of the stainless steel used in the experiments is: 17% Cr, 11% Ni and 2% Mo.

After the parts are built by SLM, the top layers are in a first step exposed to Selective Laser Erosion (SLE step) with an expectation of removing any peaks resulting from the SLM process and improving the surface quality. The erosion process is performed with a high energy intensity input which is supplied by selection of suitable laser and process parameters so that the total depth of erosion is high enough to remove the peaks left behind by the melting process. Thus, an amount of material is removed which is dependent on the selection of laser and process parameters and number of eroded layers. In a second step, the resulting eroded surfaces are remolten to smoothen it (SLR step). This remelting step applies a lower energy input in continuous laser mode. In order to apply this two-step scheme the parameters for SLE and SLR are optimized. To know how much the SLE and SLR step improves the surface roughness, first the surface quality of SLM processed parts is investigated.

3.1.1 *Surface Quality of SLM Processed Parts*

In order to make a comparison, first the results for SLM parts without erosion or remelting are

presented in Figure 5 which represents R_a values measured on different parts. These parts were built by SLM with the same laser and process parameters, in the same environment, with the same amount of oxygen on the same base plate. As observed from the figure, the roughness data shows a great spread. The standard deviation for R_a is 2.7 µm with a mean of 13.4 µm. The total roughness also follows the same trend and the standard deviation is equal to 23.1 µm for R_t with a mean of 113.5 µm.

The average R_a and R_t values of the parts without any improvement step (only SLM processed parts) are used as reference values in the following sections when the results for other parts are presented. Notice that all roughness measurements on stainless steel parts are done without using a cut-off filter.

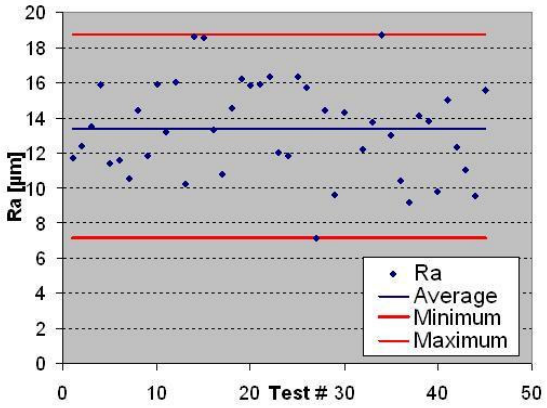

Figure 5. SLM only results for R_a.

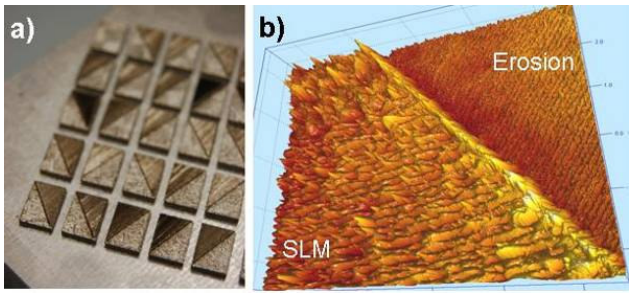

Figure 6. Surfaces left behind the first (SLE) step.

3.1.2 *Parameter Study for Rough Erosion (SLE step)*

To find the best parameters for the first SLE step (rough erosion), some parts are built by SLM and half of top surfaces is eroded with different parameters for each part. The parts are shown in Figure 6a. The resulting 3D roughness profile (derived by SPIP software) of a sample surface is depicted in Figure 6b.

Single factor experiments are utilized to study the effect of each parameter and to find the best parameters for the first SLE step of the roughness enhancement. The major parameters that are under investigation are the scan speed, the pulse frequency, laser power, scan spacing and the number of eroded layers.

a) Scan Speed

The scan speed is an important process parameter for laser erosion since it influences the amount of energy input per unit length delivered to the substrate. As the scan speed increases, the energy per unit area decreases, so does the erosion depth per laser scan. On the contrary, the process time increases substantially when low scan speeds are selected. The scan speed influences the overlap between subsequent laser pulses; the lower the speed, the greater the overlap and the deeper the material removal due to multi-pulse radiation. Thus scan speed is a key factor for specifying the depth of erosion. However, for the surface quality, it is of less significance especially at high frequency values and medium laser powers. This case is illustrated in Figure 7. A slightly lower roughness value is obtained at medium scan speeds (400-500 mm/s).

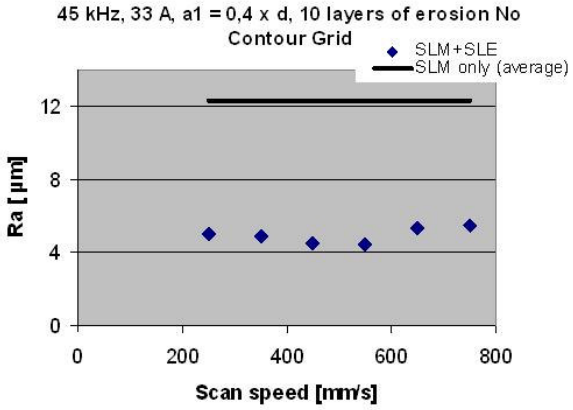

Figure 7. The effect of the scan speed on R_a.

b) Pulse Frequency

The pulse frequency of a Q-switched Nd:YAG laser has a significant effect on the process. If the aim of applying erosion is to remove the maximum amount of material, the frequency should be kept at medium values at about 30 kHz since the amount of removed material depicts a maximum at this frequency [20]. This is due to the change in peak

power and the average output power of the laser with change of the pulse frequency. At frequencies below 30 kHz, the peak power during a pulse can reach its pre-set value guaranteeing proper evaporation of material. Therefore, at low pulse frequencies, the amount of material removed depends on the power of the laser times the pulse frequency and hence increases with frequency. At pulse frequencies above 30 kHz, the peak power does not reach values high enough to evaporate material. Based on the fact that the peak power decreases by increasing pulse frequency, the depth of erosion declines as the frequency increases [30].

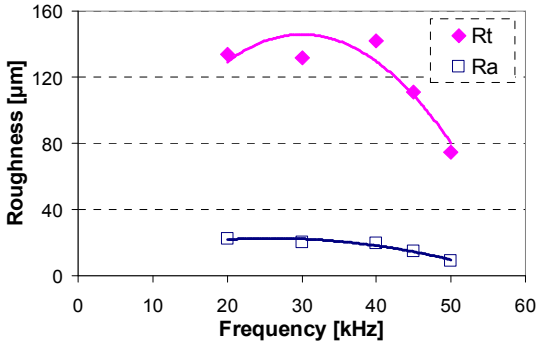

Figure 8. The effect of pulse frequency on surface quality.

The roughness R_a and R_t depicted a similar trend with a maximum at about 30 kHz: see Figure 8. In these test, the frequency is varied from 20 to 50 kHz while other parameters are set as follows: a scan spacing of 0.7 x spot size (= $\Phi_{99\%}$ = 200 µm), a scan speed of 600 mm/s and a laser pump current of 33 A. The top surface of the part was scanned 10 times. As observed, the best results are obtained with high frequency values such as 45 and 50 kHz. Therefore additional tests are done at those frequencies for scan speeeds of 450, 500 and 600 mm/s (Figure 9). These tests confirm that 50 kHz, i.e. the highest frequency, yields the lowest roughness.

c) Pump Current (Laser power)

The pump current is one of the most important process parameters for SLE due to its direct effect on laser power. The relationship between the laser power measured in continuous mode and pump current is shown in Figure 10. A lower limit for the laser power ensures the evaporation of material necessary for SLE. Otherwise, the material is only melting at the surface, rather than removed.

Figure 11 suggests that increasing the pump current, in other words the laser power, deteriorates the surface quality since the average and total roughness values increase. Depending on the other parameters selected, the laser power should be high enough to evaporate material but not too high which leaves a bad surface quality behind.

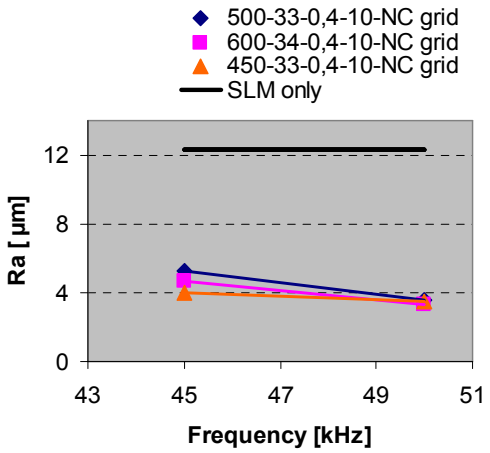

Figure 9. The effect of frequency on R_a.

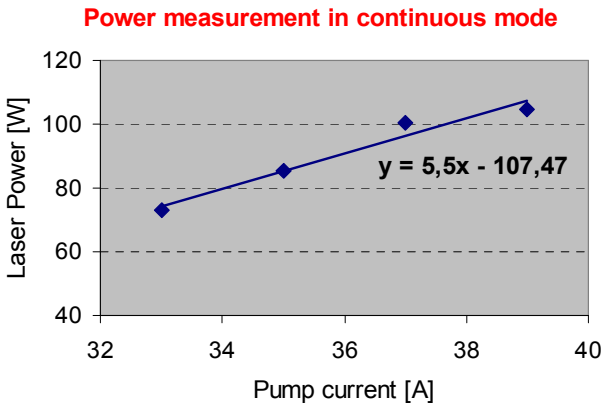

Figure 10. The relationship between the pump current and laser power.

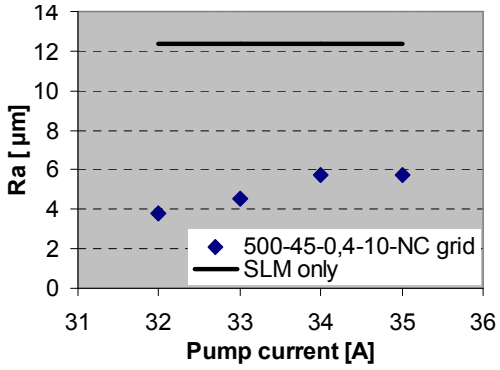

Figure 11. The influence of pump current on R_a.

d) Scan Spacing

The influence of the scan spacing between successive scan lines on the surface quality is depicted in Figure 12. The scan spacing is related to the spacing factor a1 that may vary between 0 and 1 and is defined according to following equation:

Scan spacing=a_1 x spot diameter ($=\Phi_{99\%}$ = d =200 µm) (1)

Figure 12 gives the results of the tests done with spacing factors varying from 0.4 to 0.9 and done with different sets of laser and scanning parameters. For all tests, the number of eroded layers with the parameters given in the figure was set to 10. As the figure suggests, high spacing factors result in bad surface quality due to generation of separate erosion tracks. Separate erosion tracks leave a very rough surface behind because the material in between these tracks is not totally removed. Therefore, high scan spacing value should be avoided.

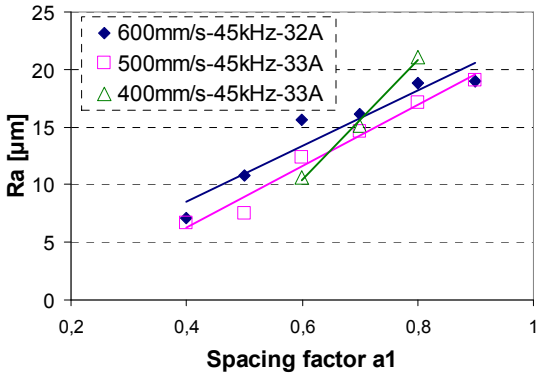

Figure 12. The effect of scan spacing on the average roughness (R_a).

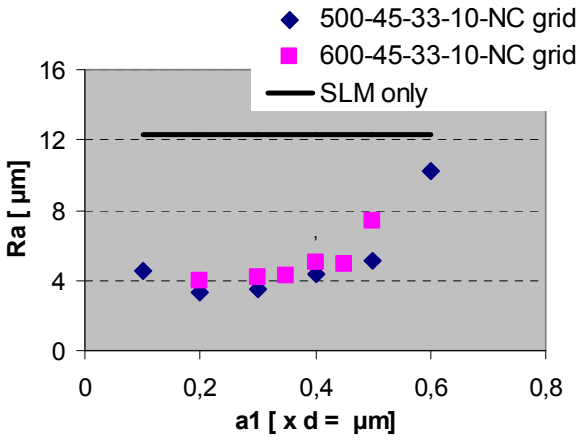

Figure 13. The influence of scan spacing on R_a.

Medium or low values for scan spacing result in better results as seen in Figure 13. A scan spacing above 0.5 x d (spot size) generally results in bad surface quality.

e) Number of eroded layers

The last parameter under investigation is the number of erosion layers applied. The more layers are eroded, the better the surface quality (Figure 14). However, eroding the surface 2 times provides already a significant enhancement. After a certain number of layers, the average roughness converges to a certain value. After this point it is not useful anymore to erode more times. In terms of productivity, applying a low number of layers should be preferred. In cases where surface quality is of great significance, it is best to choose a higher number of layers.

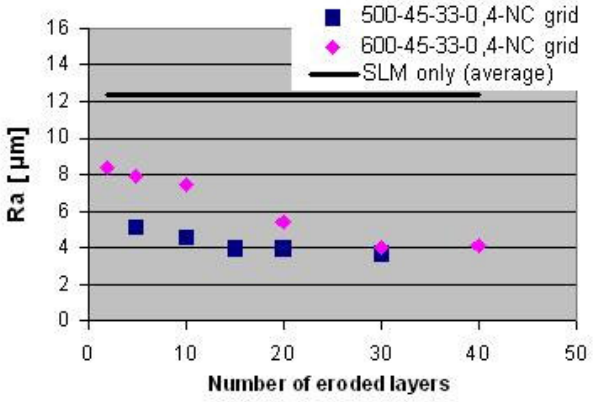

Figure 14. The effect of number of eroded layers on R_a.

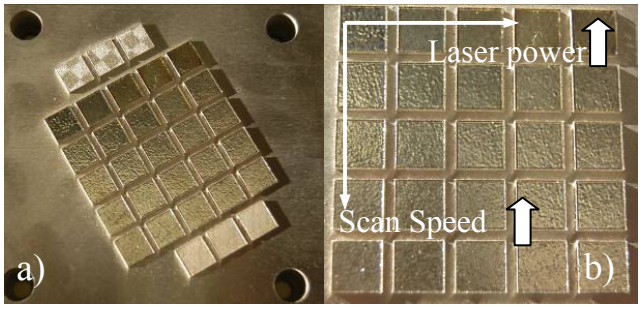

Figure 15. Paremeter study for Remelting: a set of sample parts (SLR step).

3.1.3 *Parameter Study for Remelting (SLR step)*

The second step involves remelting of the top surfaces after they are exposed to SLE in the first step. The parameters of the SLE step were always kept the same (scan speed: 600mm/s, pulse freq.: 50 kHz, pump current 34 A, scan spacing: a1 = 0.4, number of layers: 20, beam diameter $\Phi_{99\%}$: 200

µm). The remelting of the surface is expected to bring an extra enhancement. In order to find the correct parameters for this remelting step, a series of tests are conducted studying the effect of laser power, scan speed and scan spacing. Since the remelting process is performed in continuous mode, the frequency value is set at 0 kHz in all tests. Figure 15 shows a set of sample parts. The three parts at the top are not eroded or remelted (only SLM). The three parts at the bottom are only exposed to erosion but not remelted and used as reference parts to compare the results at the end.

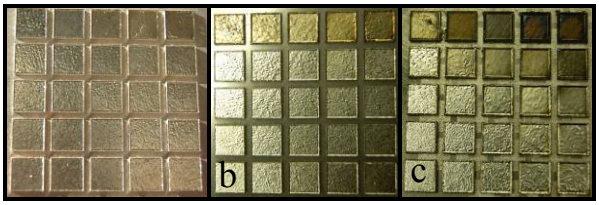

Figure 16. Three test cases with different scan spacing values a) 0.7 x d b) 0.4 x d and c) 0.1 x d.

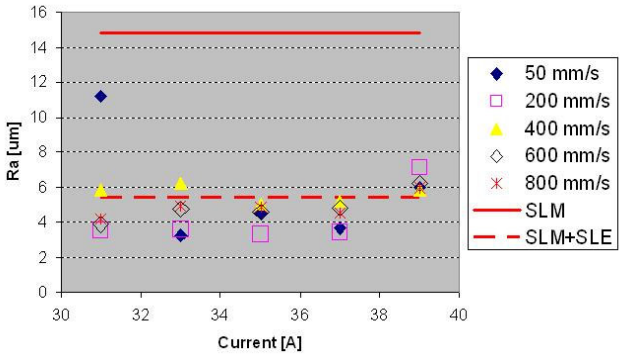

Figure 17. Results of SLR for $a_1 = 0.7$

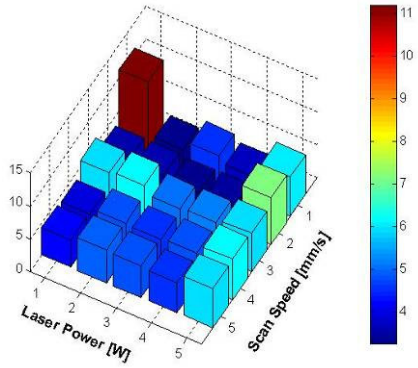

Figure 18. Column diagram of R_a results for $a_1 = 0.7$

As depicted in Figure 15, different scan speeds and laser power values are tested on one base plate keeping the scan spacing constant for the SLR step. For a different scan spacing, a new set of parts is built on a different base plate. Three sets of parts were built with scan spacing values of 0.7 x d, 0.4 x d and 0.1 x d (Figure 16). The scan speed values vary between 50 and 800 mm/s while the pump current values vary between 31 and 39 A. The SLR step is applied on the surfaces 5 times with a diagonal grid strategy and the big aperture having a spot size $\Phi_{99\%}$ (d) of approximately 200 µm.

The first test case with a scan spacing of 0.7 x d gives better results compared to parts that were built without any improvement step (SLM only) or even SLE only. The solid line in the following figures show the average roughness value of the three parts that were built by SLM only and the dashed line shows the average roughness value of the three parts that were exposed to only erosion. The other points correspond to the parts that were exposed to both erosion and remelting. Some of them show a good improvement as is the case with 35 A and 200 mm/s but some of them result in even worse results compared to reference parts. Especially the highest laser power (39 A) results in bad surface quality regardless of the selected scan speed due to excessive laser power (Figure 17 and Figure 18).

In the second test case, the scan spacing between the scan lines is set to 0.4 x (spot size). In this case, the results with the highest laser power are not as bad as for the first case and improvement with the best parameter set is greater (Figure 19 and Figure 20).

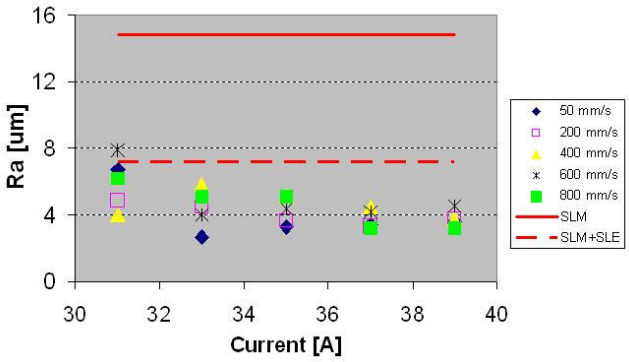

Figure 19. Results of SLR for $a_1 = 0.4$

As the last case, a scan spacing set at 0.1 x (spot size) is used and the results are depicted in Figure 21 and Figure 22. Due to a very high overlap factor between the scan lines, the energy input to the substrate is a lot especially at low scan speeds and high laser powers.

The best results are depicted in Figure 23. These best results, all from the tests with an overlap factor of 0.1, correspond to the following scan speeds and pump current values respectively: 1) 200 mm/s and 35 A 2) 200 mm/s and 37 A and 3) 400 mm/s and 37 A. Figure 24 provides photographs taken at 1000x magnification of each of those 3 best surfaces.

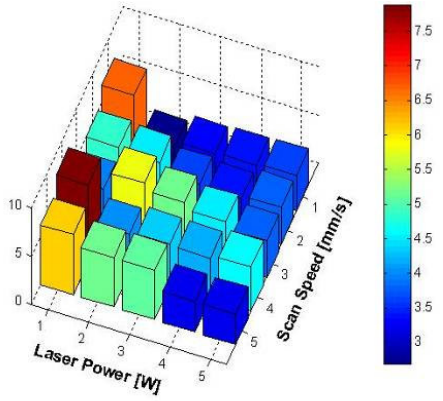

Figure 20. Column diagram of R_a results for $a_1 = 0.4$

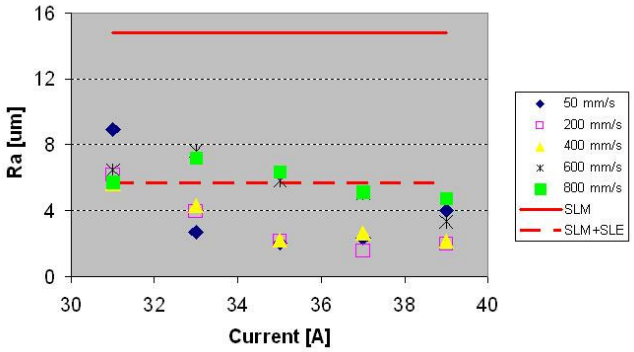

Figure 21. Results of SLR for $a_1 = 0.1$

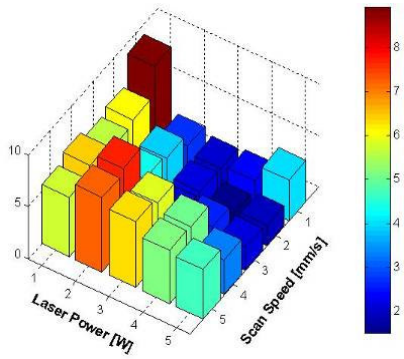

Figure 22. Column diagram of R_a results for $a_1 = 0.1$

The total enhancement obtained by SLE and SLR is illustrated in Figure 25 in terms of R_a. The trend for the total roughness R_t is also the same. The average R_a value for the parts that are made by SLM only is about 15 µm while the average R_t value is about 145 µm. When selective laser erosion is applied with the best parameter set that gave minimum roughness values, the roughness values of SLM only parts are reduced to 6 µm and 55 µm for respectively R_a and R_t. After SLR the surface quality is even improved further and the roughness values can be decreased to 1.5 µm and 13 µm (test 2 in Figure 23). The total improvement including erosion and remelting is about 90% for both average and total roughness values.

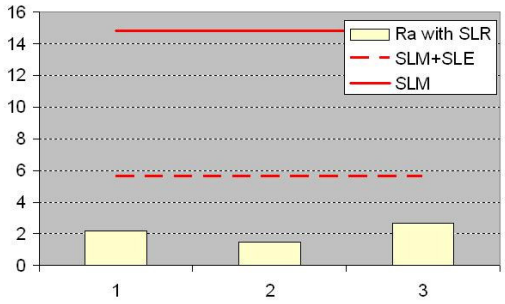

Figure 23. Best results in the third case.

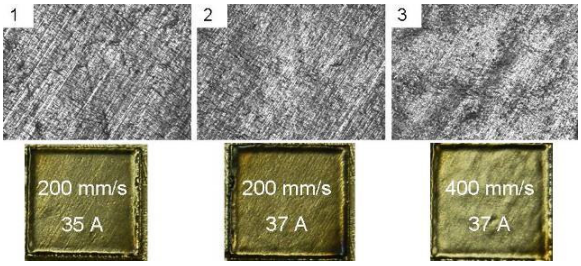

Figure 24. Pictures taken on the surfaces of the best samples.

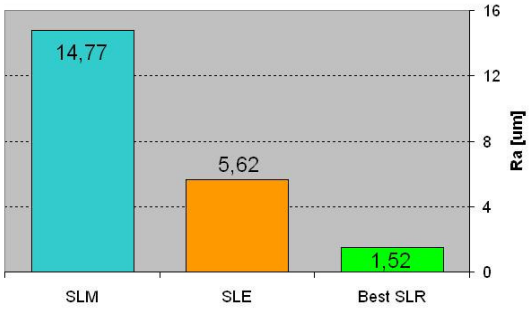

Figure 25. The enhancement of R_a.

3.1.4 *Investigation of the Necessity of Rough Erosion*

In order to show if the erosion step is necessary for an improvement in the surface quality, some more

test parts are built. Half of them are applied to erosion followed by laser remelting whereas the other half were only exposed to laser remelting with the same parameters. Erosion parameters for all parts were the same whereas for laser remelting three different sets were chosen. The parameters used are shown in Figure 26 with the results.

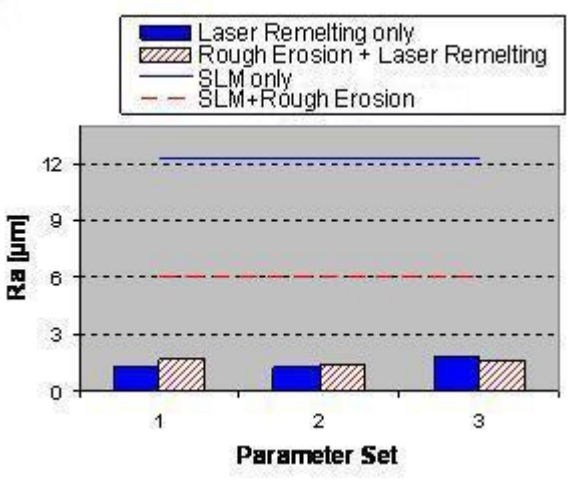

	v [mm/s]	I [A]	a1	Number of layers
1	200	35	0,1	10
2	200	35	0,1	10
3	400	37	0,1	10

Figure 26. Comparison of two cases one with rough erosion and the other without.

As the figure suggests, the results with or without erosion step do not necessarily differ. Therefore, it is not crucial to apply erosion as a first step for an improvement on the top surfaces of the parts built by SLM. Applying only laser surface remelting provides almost the same enhancement. Therefore, the results presented in the part for the titanium alloy involves only remelting after SLM.

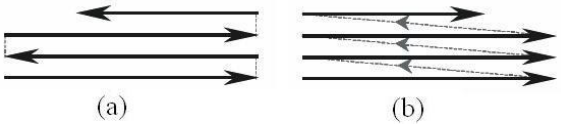

Figure 27. Scan strategies: (a) zig-zag scan strategy and (b) single direction scan strategy.

3.2 *Titanium Alloy*

The tests for laser surface remelting for the titanium alloy are done slightly differently than the ones for stainless steel. Instead of only remelting the last layer of a part, a number of layers are exposed to remelting. After a new layer of powder is deposited, the laser beam first melts the powder selectively. Then without laying a new layer of powder, the surface is remelted and this process (layer deposition, SLM, SLR) continues until the part is completely manufactured.

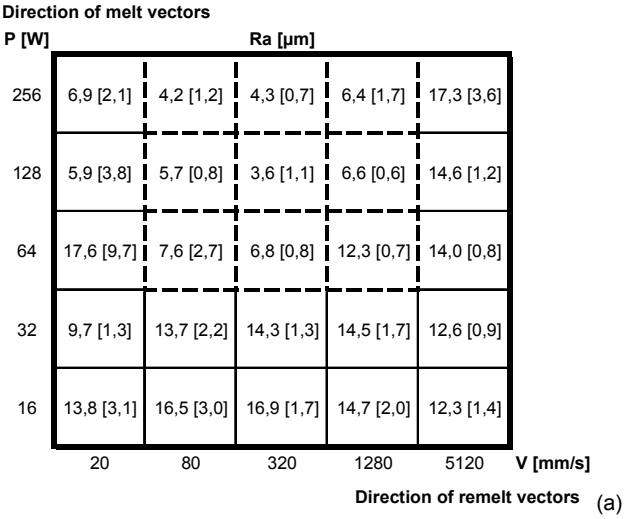

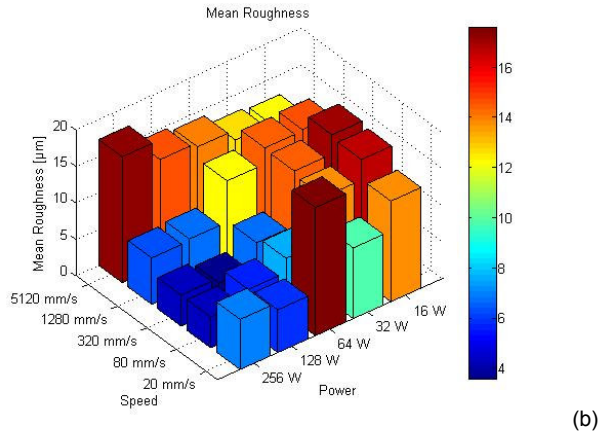

Figure 28. Roughness values of the first Ti-6Al-4V experiment [µm]: (a) mean roughness [standard deviation] (b) column diagram.

3.2.1 *First set of tests*

As a first test, 25 parts ($10x10\,mm^2$) were built with a zig-zag scan strategy (Figure 27) to search which set of scan speed and laser power lowers the surface roughness the most. The parts consist of 70 consolidated layers with a thickness of 30 µm. The last 20 layers are first melted with parameters that are optimised for density: scan spacing 74 µm, laser power 40 W, scan speed 225 mm/s. Each of these layers is then exposed to laser remelting with scan

vectors perpendicular to the scan vectors of the melting. Each part is remelted with a different combination of scan speed and laser power. The following scan speeds are used: 20 mm/s, 80 mm/s, 320 mm/s, 1280 mm/s, 5120 mm/s. Each of these scan speeds is used in combination with the following laser powers: 16 W, 32 W, 64 W, 128 W and 256 W.

On each part, three 2D roughness measurements were done in the direction of the remelt-vectors. The following R_a values (and standard deviations) were measured with a Gaussian filter and a cut-off of 2.5 mm.

The parts that were made with scan speeds between 80 and 1280 mm/s and scan powers between 64 and 256 W have lower roughness values compared to others (see dotted area in Figure 28a).

P [W] \ Ra [µm]	80	160	320	640	1280
256	Ref. 15,7 [3,8]	6,8 [1,1]	7,3 [2,7]	2,9 [0,3]	5,1 [1,1]
181	Ref. 12,7 [1,7]	6,7 [1,4]	5,6 [1,7]	3,7 [0,6]	4,7 [1,0]
128	Ref. 15,4 [0,8]	4,2 [0,4]	4,7 [1,5]	4,8 [1,6]	6,1 [1,6]
91	4,1 [0,5]	5,1 [0,6]	5,8 [0,7]	5,7 [0,3]	7,8 [0,6]
64	4,9 [0,5]	5,1 [0,7]	6,1 [0,4]	7,0 [1,7]	11,5 [2,8]

V [mm/s] (a)

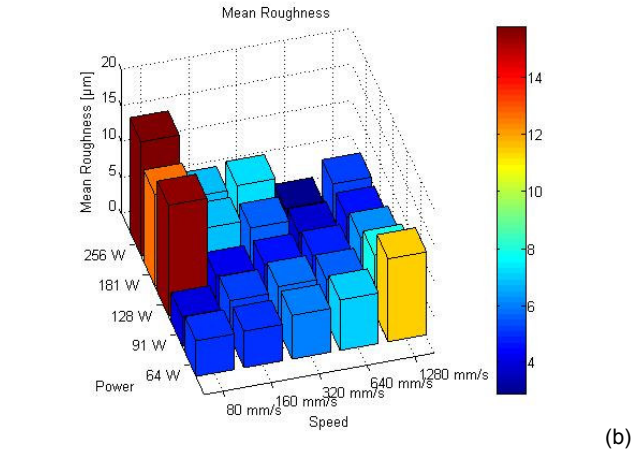

(b)

Figure 29. Roughness values of the second Ti-6Al-4V-experiment [µm] (Ref.=reference part): (a) mean roughness [standard deviation]; The darker the shading the more preferable the remelting parameters. (b) column diagram.

3.2.2 *Second set of tests*

The window giving low roughness (80 - 1280 mm/s and 64 - 256 W) is further investigated in a second analogous test: see settings in Figure 29. Three reference parts without remelting were also made at 80 mm/s and 128 to 256 W (see Figure 29).

For each part three roughness measurements were taken. The results are given in Figure 29.

The flatness of the top surface is however also affected by the occurrence of edges that arise when the remolten material is partially pushed to the contours of the part by the laser beam (Figure 24 and Figure 30). In general, edges are larger if the parts are remolten with a relatively low scan speed and high laser power. To find the power and scan speed that optimizes the given remelting process, an assessment between surface roughness and the size of the edges is necessary. Figure 31 gives the height of one of the four edges (the right edge) of the parts.

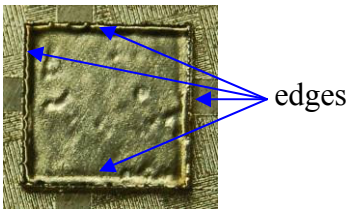

Figure 30. Four edges of a square part.

P [W] \ Height [µm]	80	160	320	640	1280
256	Ref. 62	660	364	133	85
181	Ref. X	349	200	102	45
128	Ref. 36	201	155	101	63
91	132	114	76	54	69
64	82	59	45	16	20

V [mm/s]

Figure 31. Height of the right edges of the second Ti-6Al-4V-experiment [µm]. The darker the shading the more preferable the remelting parameters. (Ref.=reference part; x=no apparent edge).

After observing Figure 29 and Figure 31, the combinations of scan power and scan speed that give the lowest roughness values with acceptable edges is considered to lie in a diagonal band as marked on Figure 29a. The most preferable zone of

this diagonal band is the one with low roughness values, low edges and high scan speeds (high productivity). The darker the shading in Figure 29a and Figure 31, the more preferable the remelting parameters.

On every diagonal the laser power (P) and the scan speed (v) have the following relation.

$$\frac{P}{\sqrt{v}} = \text{constant} \qquad (2)$$

In the area enclosed by the diagonal band this constant is varying between 1 and 10 $W/\sqrt{mm/s}$ for respectively the darker and brighter diagonals on Figure 29a.

3.2.3 *Third set of tests*

In the third test with Ti-6Al-4V, different scan strategies are investigated. Square parts (2 cm²) are built to search which scan strategy lowers the surface roughness most. A part of each layer (mostly 1 cm²) is remelted, using a particular scan strategy (power 91 W, scan speed 640 mm/s). The investigated scan strategies are:

1. Zig-zag scan strategy versus single direction scan strategy (Figure 27).
2. Remelting the top layers two or three times in different directions and with a zig-zag scan strategy.
3. Reducing the scan spacing to its half
4. Other scan strategies: Spiral scan strategy, staggered scan strategy, remelting in a direction perependicular versus parallel to the melt direction, some combinations of the scan strategies mentioned above (Figure 32).

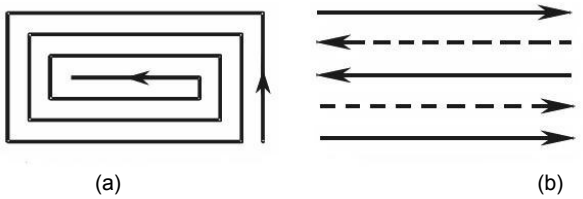

Figure 32. Scan strategies: (a) spiral scan strategy and (b) staggered scan strategy. (The dotted lines indicate the remelting pattern of the underlying layer.)

The results of this test show that multiple time remelting in different directions or with a zig-zag scan strategy, improves the surface roughness. A part that was remelted 3 times in different directions (angle between remelt and melt direction respectively 0°, 60° and 120°) has an R_a value (L_c=2.5 mm, three measurements) that is approximately 30% lower than a part that is remelted only once (R_a = 3.4 ± 0.5 µm versus R_a = 5.1 ± 1.1 µm). When using a zig-zag scan strategy, reducing the scan spacing also seems to improve the surface roughness. In this latter test, the R_a value (L_c=2.5mm, three measurements) of a part seems 10% lower when the scan spacing is reduced to its half (R_a = 4.5 ± 1.1 µm versus R_a = 5.1 ± 1.1 µm).

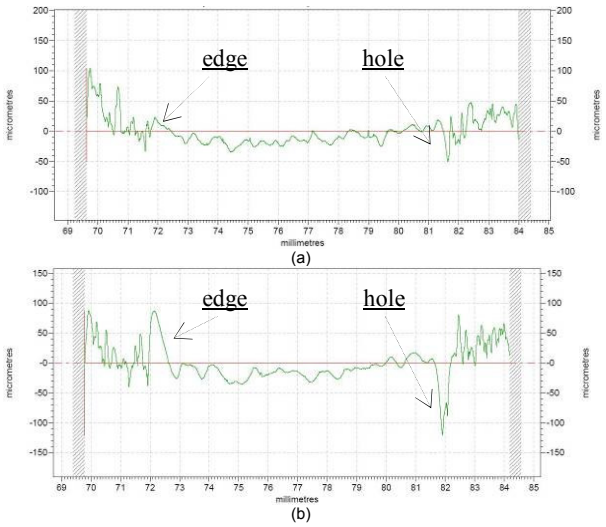

Figure 33. Remelting with a single direction scan strategy: edges and holes. Scan spacing respectively 74 µm (a) and 34 µm (b).

A single direction remelting scan strategy (Figure 27) does not seem to improve the quality of the surface compared to a zig-zag remelting scan strategy. First of all, the Ra values are not lower. The part that was made using a zig-zag scan strategy had an Ra value of 5.1 ± 1.1 µm whereas the part that was made with a single direction scan strategy had an Ra value of 5.3 ± 1.1 µm. Secondly, the parts that are made with a single direction scan strategy have a large edge at every starting point of the scan line and a hole at every end of the scanline (Figure 33a). If the scan spacing is smaller, these edges are larger (Figure 33b). An explanation for this physical phenomenon might be that the laser plume recoil pressure pushes the molten material backwards [32]. When using a zig-zag scan strategy, the holes at every end of a scan vector are filled with the edges of the starts of the scan vectors, resulting in smaller edges.

3.2.4 *Fourth set of tests*

In the last test with Ti-6Al-4V, 22 parts with top surfaces of 10x10 mm² were created with a zig-zag scan strategy to search which combination of spot sizes of the laser and laser power, together with a low scan speed (20 mm/s) offers the best surface roughness by remelting. The scan vectors of the remelting are perpendicular to the scan vectors of the melting. Each part is remelted with another combination of laser spot size and laser power. The laser powers used for the remelting are: 32 W, 64 W, 128 W, 256 W, 300 W. High remelting powers caused large deformations of the parts (Figure 34). When a remelting power of 256 W or 300 W was used only one layer is remelted as the large deformation of the surface may hamper deposition of a next powder layer or damage the recoating blade.

Figure 34. Large deformations of a part remolten with a power of 300 W, a beam diameter Φ_{1/e^2} of 100 µm and a scan speed of 20 mm/s.

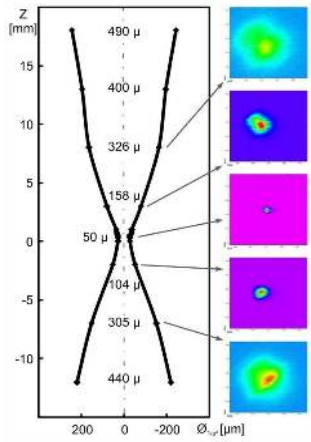

Figure 35. Beam profile measurements at different positions along the Z axis, beam diameter values Φ_{1/e^2} are indictated.

Figure 35 shows the spot size of the used Yb:YAG fibre laser beam near the focal point [46]. By lowering the build platform (0µm, 677µm, 1771µm, 2917µm, 4313µm), different spot sizes of the laser beam are generated (Φ_{1/e^2} approximately 50µm, 70.7µm, 100µm, 141.2µm, 200µm). Scan spacings are changed according to the spot sizes of the laser beam (75µm, 106µm, 150µm, 211µm, 300µm).

The following R_a values [and standard deviations] were measured (L_c=2.5mm).

If one rejects high power settings of 256 W and 300W (too large deformations), Figure 36 shows that a spot size of 200 µm and a laser power of 128 W gives the lowest roughness in this test.

Ø[µm] Depth[µm] ss[µm]	Ra values [µm]				
200	17,3 [2,0]	9,0 [1,9]	3,1 [0,3]	2,1 [0,9]	3,3 [1,1]
4313	17,4 [2,2]	5,7 [1,5]	3,4 [1,1]	6,2 [5,4]	7,3 [7,1]
300	12,8 [1,3]	5,6 [0,9]	4,7 [0,7]	4,7 [0,2]	9,3 [2,2]
141,2	9,6 [1,4]	5,6 [0,6]	12,6 [1,3]	4,3 [1,2]	5,4 [1,1]
2917	11,2 [0,3]	13,9 [4,3]	x	x	Ref. 14,3 [0,5]
211					
100					
1771					
150					
70,7					
677					
106					
50					
0					
75					
	32	64	128	256	300 P [W]

(a)

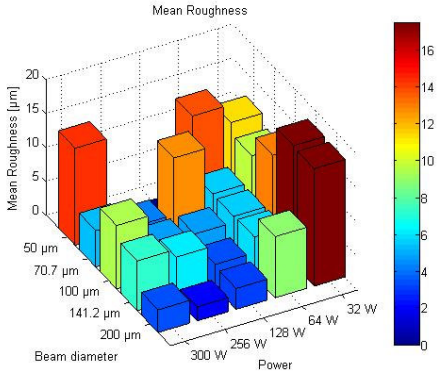

(b)

Figure 36. Roughness values of the fourth Ti-6Al-4V experiment [µm] (Ref.=reference part): (a) mean roughness [standard deviation] (b) column diagram.

3.2.5 *Discussion*

Until now two methods with Ti-6Al-4V were successful in reducing the surface roughness, without inducing large deformations. The first method (method A) is remelting the molten layers three times as shown in the third Ti-6Al-4V-experiment. The other method (method B) is remelting the molten layer with a large spot size, as shown in the fourth Ti-6Al-4V-experiment. To compare these two methods, the roughness profiles are compared instead of the R_a values (Figure 37).

These roughness profiles show that using method A leads to a serrated remelted surface,

while using method B leads to a smoother remelted surface. However, the two methods must not be seen independently. Future research will investigate whether a combination of method A and B can further improve the surface roughness.

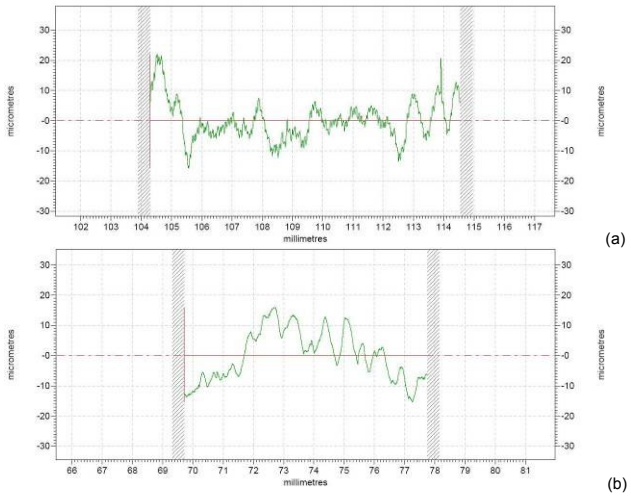

Figure 37. Roughness profile of a part made by remelting the molten layers respectively three times (method A, figure a) and with a large spot size (method B, figure b).

4 CONCLUSIONS

This paper first described how surface roughness of parts made by SLM of CL20ES stainless steel (ASTM 316L) can be improved by i) Selective Laser Erosion, ii) Selective Laser Erosion followed by Selective Laser Remelting and iii) Selective Laser Remelting on a Concept Laser M3 Linear SLM machine. The optimized parameters for Selective Laser Erosion lead to a roughness improvement of 60% (R_a from 15 µm to 6 µm). Selective Laser Remelting with optimized parameters for laser power, scan speed and scan spacing after Selective Laser Erosion leads to a roughness improvement of 90% (R_a from 15 µm to 1.5 µm). Selective Laser Remelting with the same optimized parameters, but without the erosion step leads to the same roughness improvement. Therefore, it is not crucial to apply erosion before remelting to improve the top surface roughness of the parts built by SLM.

The paper further describes how to improve the surface roughness of CL40TI titanium alloy (Ti-6Al-4V) SLM parts by Selective Laser Remelting on the LM machine developed at K.U.Leuven. An attempt is made to describe and reduce the edge effect occurring in SLM and SLR. The surface roughness is improved in two different ways by more than 75%. By remelting the surface layers three times in a different direction with optimized parameters for scan speed and laser power, R_a values are reduced from 14.1 µm (mean roughness of all reference parts) to 3.4 µm. By remelting the surface layers one time with a large spot size, a low scan velocity and sufficient laser power, R_a values are reduced from 14.1 µm to 3.1 µm.

5 ACKNOWLEDGEMENTS

The authors thank TUBITAK (The Scientific and Technological Research Council of Turkey) for its financial support given under the name of “Ph.D. support program for students in foreign countries”.The authors thank also K.U.Leuven for the support through the project GOA/2002-06 and IWT for the support through the SBO-project DiRaMaP.

6 KEYWORDS

Selective Laser Melting (SLM), laser re-melting, surface modification, roughness improvement

7 REFERENCES

[1] Abe, F., Osakada, K., Kitamura, Y., Matsumoto, M., Shiomi, M. 2000. Manufacturing of titanium parts for medical purposes by selective laser melting. *Proceedings 8th International Conference on Rapid Prototyping.* 288-293.

[2] Abe, F., Osakada, K., Shiomi, M., Uematsu, K., Matsumoto, M. 2001. The manufacturing of hard tools from metallic powders by selective laser melting. *Journal of Materials Processing Technology* 111: 210-213.

[3] Bosman, J., 2007. *Processes and strategies for solid state Q-switch laser marking of polymers.* Twente: University of Twente.

[4] Braga, F.J.C., Marques, R.F.C., Filho, E.A., Guastaldi, A.C. 2007. Surface modification of Ti dental implants by Nd:YVO_4 laser irradiation. *Applied Surface Science* 253: 9203-9208.

[5] Campanelli, S.L., Ludovico, A.D., Bonserio, C., Cavalluzzi, P. 2006. Artificial neural network modelling of the laser milling process. *Int. Sem. on CIRP ICME*.

[6] Chatterjee, A.N., Kumar, S., Saha, P., Mishra P.K., Choudhury, A.R. 2003. An experimental design approach to selective laser sintering of low carbon steel. *Journal of Materials Processing Technology* 136: 151-157.

[7] Childs, T.H.C., Hauser, C., Badrossamay, M. 2004 Mapping and modelling single scan track formation in direct metal selective laser melting. *CIRP Annals* 53: 191-194.
[8] Childs, T.H.C., Hauser, C., Badrossamay, M. 2005 Seletive laser sintering (melting) of stainless and tool steel powders: experiments and modelling. *Proc. IMechE* 219 (Part B: Engineering Manufacture): 339-347.
[9] Damborenea, J. 1998. Surface modification of metals by high power lasers. *Surface and Coatings Technology* 100-101: 377-382.
[10] Felgueroso, D., Vijande, R., Cuetos, J.M., Tucho, R., Hernandez, A. 2008. Parallel laser melted tracks: Effects on the wear behaviour of plasma-sprayed Ni-based coatings. *Wear* 264: 247-263.
[11] Gilmore, R. 2007. Short pulse laser machining for diesel and aerospace applications. *Proc. 15th Int. Symp. On Electromachining* ISEM XV: 433-437.
[12] Grum, J., Slabe, J.M. 2006. Effect of laser re-melting of surface cracks on microstructure and residual stresses in 12Ni maraging steel. *Applied Surface Science* 252: 4486-4492.
[13] Hao, L., Lawrence, J. 2006. Effects of Nd:YAG laser treatment on the wettability characteristics of a zirconia based bioceramic. *Optics and Lasers in Engineering* 44: 803-814.
[14] Henari, F.Z., Blau, W. 1995. Excimer-Laser Surface Treatment of Metals for Improved Adhesion. *Applied Optics* 34: 581–584.
[15] Hoffmann, M., Brietenfellner, F. 1987. High contrast and intact surface – a challenge in laser marking of plastics. *Proc. SPIE* 744: 156-180.
[16] Kac, S., Kusinki, J. 2004. SEM structure and properties of ASP2060 steel after laser melting. *Surface and Coatings Technology*. 180-181: 611-615.
[17] Kruth, J.P. 1991. Material incress manufacturing by Rapid Prototyping Techniques, Keynote paper. *Annals of the CIRP* 40(2): 603-614.
[18] Kruth, J.P., Froyen, L., Van Vaerenberg, J., Mercelis, P., Rombouts, M., Lauwers, B. 2004. Selective laser melting of iron-based powder. *Journal of Materials Processing Technology* 149: 616-622.
[19] Kruth, J.P., Vandenbroucke, B., Van Vaerenbergh, J., Mercelis, P. 2005. Benchmarking of different SLS/SLM processes as rapid manufacturing techniques. *Int. Conf. Polymers and Moulds Innovations (PMI)*.
[20] Kruth J.P., Yasa E., Van Vaerenbergh J. 2007. Parameter Study for Selective Laser Erosion, 4th International Conference and Exhibition on Design and Production of Machines and Dies/Molds. CD-Rom.
[21] Lawrence, J., Li, L. 2001. A laser based technique for the coating of mild steel with a vitreous enamel. *Surface and Coatings Technology* 140: 238-243.
[22] Martan J., Kunes J., Semmar N. 2007. Experimental mathematical model of nanosecond laser interaction with material. *Applied Surface Science* 253: 3525-3532.
[23] Morgan, R., Papworth, A., Sutcliffe, C., Fox, P., O'Neill, B. 2002. High density net shape components by direct laser remelting of single phase powders. *Journal of Materials Science* 37: 3093-3100.
[24] Nicolas, G., Autric, M., Marine, W., Shafeev, G.A. 1997. Laser induced surface modifications on ZrO ceramics. *Applied Surface Science* 109-110: 289–292.
[25] Over, C. 2003. *Generative Fertigung von Bauteilen aus Werkzeugstahl X38CrMoV5-1 und Titan TiAl6V4 mit Selective Laser Melting (Ph.D. Dissertation)*. Aachen: RWTH Aachen.
[26] Over, C., Meiners, W., Wissenbach, K., Lindermann, M, Hammann, G. 2001. Selective laser melting: a new approach for the direct manufacturing of metal parts and tools. *Proceedings of the LANE 2001 conference* 391-398.
[27] Pederson, R. 2002. *Microstructure and Phase Transformation of Ti-6Al-4V (Licentiate Thesis)*. Lulea: Lulea University of Technology.
[28] Petzoldt, F., Pohl, H., Simchi, A. 2001. Advances in material issues for direct metal laser sintering. *Proceedings Euro PM2001* 3: 297-302.
[29] Pham, D.T., Dimov, S.S., Petkov, P.V. 2007. Laser milling of ceramic components. *International Journal of Machine Tools and Manufacture* 47: 618–626.
[30] Qi J., Wang K.L., Zhu Y.M. 2003. A study on the laser marking process of stainless steel. *J. of Materials Processing Technology* 139: 273-276.
[31] Rehme O., Emmelmann C. 2005. Reproducibility for properties of Selective Laser Melting products. *Proc. Third International WLT Conference on Lasers in Manufacturing*.
[32] Rombouts M., Froyen L., Van Vaerenbergh J., Mercelis, P. 2004. Production and properties of dense iron based parts produced by laser melting with plasma formation. *Proceedings of World Powder Metallurgy Conference* PM2004 5: 115-121.
[33] Rombouts, M., Kruth, J.P., Froyen, L., Mercelis, P. 2006. Fundamentals of selective laser melting of alloyed steel powders. *CIRP Annals-Manufacturing Technology* 55(1): 187-192.
[34] Santos, E., Abe, F., Kitamura, Y., Osakada, K., Shiomi, M. 2002. Mechanical properties of pure titanium models processed by selective laser melting. *Proceedings Solid Freeform Fabrication Symposium 2002* 180-186.
[35] Song, Y.A. 1997. Experimental study of the basic process mechanism for direct selective sintering of low melting metallic powder. *CIRP Annals* 46(1): 127-130.
[36] Tam, S.C., Noor, Y.M., Lim, L.E.N., Jana, S., Yang, L.J., Lau, M.W.S., Yeo, C.Y. 1993. Marking of leadless chip carriers with a pulsed Nd:YAG laser. *Proc. Inst. Mech. Eng.* 207: 179-192.
[37] Tang, C.H., Cheng, F.T., Man, H.C. 2004. Improvement in cavitation erosion resistance of a copper based propeller alloy by laser surface melting. *Surface and Coatings Technology* 182: 300-307.
[38] Tezuka, S., Yoshikawa, M. 1991. Study on the marking processing of IC packages by YAG laser. *Int. J. Jpn. Soc. Prec. Eng.* 25(4): 297-298.
[39] Tian, Y.S., Chen, C.Z. 2007. Microstructures and wear properties of in situ formed composite. *Materials Letters* 61: 635-638.
[40] Triantafyllidis, D., Li, L., Stott, F.H. 2005. The effects of laser-induced modification of surface roughness of Al2O3-based ceramics on fluid contact angle. *Materials Science and Engineering* A 390: 271-277.

[41] Triantafyllidis, D., Li, L., Stott, F.H. 2006. Crack-free densificaion of ceramics by laser surface treatment. *Surface and Coatings Technololgy* 201: 3163-3173.
[42] Tritica, M., Gakovic, B., Batani, D., Desai, T., Panjan, P., Radak, B. 2006. Surface modifications of a titanium implant by a picosecond Nd :YAG laser operating at 1064 and 532 nm. *Applied Surface Science* 253: 2551-2556.
[43] Uckelmann 2002. Grenzen und Moglichkeiten bei der Herstellung individueller Bauteile mittels Lasertechnik. *Proceedings Aachener Kolloquium Fur Lasertechnik* 279-289.
[44] Valette, S., Steyer, P., Richard, L., Forest, B., Donnet, C., Audouard, E. 2006. Influence of femtosecond laser marking on the corrosion resistance of stainless steel. *Applied Surface Science* 252: 4696-4701.
[45] Van Elsen, M., Al-Bender, F., Kruth, J.P. 2008. Application of dimensional analysis to selective laser melting. *Rapid Prototyping Journal* 14: 15-22.
[46] Van Vaerenbergh J. 2008. *Process optimisation in Selective Laser Melting (PhD)*. Leuven: KULeuven.
[47] Vandenbroucke, B., Kruth, J.P. 2007. Selective Laser Melting of Biocompatible Metals for Rapid Manufacturing of Medical Parts. *Rapid Prototyping Journal* 13(4) 196-203.
[48] Vasco, J.C., Bartolo, P. J., 2007. Processing conditions of laser micro-drilling. *Proc. 15th Int. Symp. On Electromachining* ISEM XV: 427-432.
[49] Xianqing, Y., Chengjun, Z., Xuefeng, S., Manping, H., Jianguo, M. 2007. Microstructure evolution of WC/steel composite by laser surface re-melting. *Applied Surface Science* 253: 4409-4414.
[50] Xie, J.W., Fox, P., Chen, X.C., O'Neill, W., Wright, C.S., Yousseffi, M., Hauser, C., Dalgrano, K., Childs T.H.C. 2003. Direct laser re-melting of tool steels. *Proceedings of Euro PM2003* 3: 473-478.
[51] Xu, W.L., Yue, T.M., Man, H.C., Chan, C.P. 2006. Laser surface melting of aluminium alloy 6013 for improving pitting corrosion fatigue resistance. *Surface & Coatings Technology* 200: 5077-5086.
[52] Yadroitsev, I., Bertrand, Ph., Smurov, I. 2007. Parametric analysis of the SLM process. *Applied Surface Science* 253: 8064-8069.
[53] Yadroitsev, I., Thivillon, L. , Bertrand, Ph., Smurov, I. 2007. Strategy of manufacturing components with designed internal structure by selective laser melting of metallic powder. *Applied Surface Science* 254: 980–983.
[54] Yilbas, B.S. 1996. Laser heating process and experimental validation. *Int. Journal of Heat Mass Transfer* 40(5) 1131-1143.
[55] Yilbas, B.S. 1997. Theoretical and Experimental investigation into laser melting of steel samples. *Optics and Lasers in Engineering* 27: 297-307.
[56] Zhang, Y., Chen, J., Lei, W., Xv, R. 2008. Effect of laser surface melting on friction and wear behavior of AM50 magnesium alloy. *Surface and Coatings Technololgy* 202: 3175-3179.

Short Curriculum Vitae

EDUCATION

2006-Oct. 2010 — **Catholic University of Leuven (K.U.Leuven), Leuven, Belgium**
Ph.D. study focusing on non-conventional manufacturing processes: mainly processing of metallic powders by combining Selective Laser Melting (SLM) and Selective Laser Erosion (additive/subtractive layer manufacturing)

2005-2006 — **Catholic University of Leuven (K.U.Leuven), Leuven, Belgium**
Pre-doctoral study
Thesis in layer manufacturing entitled as '*A study in Selective Laser Erosion and its applications'*

2002-2004 — **University of British Columbia (UBC), Vancouver, BC, Canada**
Master of Applied Science (M.A.Sc.)
Thesis in machine tool metrology entitled as '*Mathematical modeling, measurement and correction of volumetric errors in three-axis machine tools*'

1998-2002 — **Istanbul Technical University, Gumussuyu, Istanbul, Turkey**
B.Sc. in Mechanical Eng.

RESEARCH EXPERIENCE

Sept 2005-present — **Catholic University of Leuven, Leuven, Belgium**
Research engineer in the group of Additive Manufacturing (AM) under the supervision of Prof. Dr. Jean-Pierre Kruth.

Working in various projects funded by national and university funds related to AM processes for metals, post-processing techniques, mechanical testing (tensile and compression testing, hardness measurements, impact toughness), design of experiments and material characterization.

Dec 2004-June 2005 — **Sabanci University (SU), Istanbul, Turkey**
Coordinator of a General Electric Project about machine dynamics and finite element method in thin-walled parts manufacturing with Dr. Erhan Budak focusing on machine tool dynamics, CNC machining and control.

Sept, 2002-Oct 2004 — **UBC, Department of Mechanical Engineering, Vancouver, BC, Canada**
Research assistant at the Manufacturing Automation Laboratory
Mainly focusing on machine tool metrology for three-axis machine tools; mechanics of turning and milling processes, chatter vibrations in cutting, experimental modal analysis, laser interferometer and coordinate measuring machine measurements.

Dec, 1999-June 2002 — **ITU, Department of Mechanical Engineering, Istanbul, Turkey**
Student assistant, working on constitutive equations in soil mechanics, finite element modeling and analysis of mechanical structures

TECHNICAL TRAININGS

- *Competitive FP7 Proposal Writing* course given by Hyperion describing the relevance of Framework 7 to EU policies, the common problems in proposal writing, and success criteria for proposals, K.U.Leuven, Leuven, Belgium, September 2009.
- *Radiation Protection Certificate* covering ionizing radiation and occupational risks, health effects and monitoring and codes of practice given by Health, Safety and Environment Department of K.U.Leuven, Leuven, Belgium, 2008.
- *Academic Writing for Doctoral Students,* ILT, K.U.Leuven, 2008.
- Training on geometrical error measurement techniques for machine tool metrology at National Institute of Standards and Technology (NIST, Gaithersburg, MD, USA), September 2003.
- *Renishaw Laser Interferometer* Training Program, September 2003, Renishaw, Elgin, Illinois, USA.
- *Professional Development for International Teaching Assistant Program,* University of British Columbia, December 2002.

List of Publications

In journals

- E. Yasa, J.-P. Kruth, 2010, Investigation of laser and process parameters for Selective Laser Erosion, Journal of Precision Engineering, Vol.34/1, pp.101-112. (JRC 2008 impact factor 0.895)
- E.Yasa, J.Deckers, J.-P.Kruth, M. Rombouts, J. Luyten, 2010, Charpy impact testing of metallic Selective Laser Melting parts, Virtual and Physical Prototyping, Vol. 5/2, pp. 89-98.
- E.Yasa, J. Deckers, J.-P. Kruth, The investigation of the influence of Laser Re-melting on density, surface quality and microstructure of Selective Laser Melting parts, submitted to Rapid Prototyping Journal in 2009 (JRC 2008 impact factor 1.086) (reviewed and accepted to be published).
- M. Badrossamay, E. Yasa, J. Van Vaerenbergh, J.-P. Kruth, Improving productivity rate in Selective Laser Melting process, submitted to Materials and Design (JRC 2008 impact factor 1.107) in 2009 and (reviewed and accepted to be published).
- J.-P. Kruth, J. Deckers, E. Yasa, R. Wauthlé, Assessing influencing factors of residual stresses in Selective Laser Melting using a novel analysis method, submitted to Journal of Materials Processing Technology (JRC 2008 impact factor 1.143) in 2010. (submitted)

In international conferences

1) J.-P. Kruth, E. Yasa, M. Vanparys, J. van Vaerenbergh, 2007, The enhancement of micromachining ability of Selective Laser Melting by Selective Laser Erosion, International Conference Polymers and Moulds Innovations PMI 2007, Gent, Belgium, April 19-20.

2) J.-P. Kruth, E. Yasa, J. van Vaerenbergh, 2007, Parameter study for Selective Laser Erosion, 4th International Conference and Exhibition on design and production of machines and dies/molds, Cesme, Turkey, June 21-23.

3) E. Yasa, J.-P. Kruth, 2008, Experimental study of the combined process of Selective Laser Melting and Selective Laser Erosion, Proc. of RAPID2008, Florida, USA.

4) J.-P. Kruth, E. Yasa, 2008, Experimental analysis of process and laser parameters in laser marking, Proc. of ASME ESDA 2008, Haifa, Israel.

5) J.-P. Kruth, E. Yasa, J. Deckers, 2008, Experimental investigation of laser surface re-melting for the improvement of Selective Laser Melting process, Proc. of Solid Freeform Fabrication (SFF) Symposium, Austin, TX, USA.

6) J.-P. Kruth, E. Yasa, J. Deckers, 2008, Roughness improvement in Selective Laser Melting, Proc. of PMI 2008, Gent, Belgium.

7) J.-P. Kruth, G. Levy, R. Schindel, T. Craeghs, E. Yasa, 2008, Consolidation of polymer powders by selective laser sintering, Proc. of PMI 2008, Gent, Belgium (***Keynote paper***).

8) M. Badrossamay, E. Yasa, J. Van Vaerenbergh, J.-P. Kruth, 2009, Improving productivity rate in SLM of commercial steel powders, RAPID 2009 Conference & Exposition, Schaumburg, IL, USA.

9) E. Yasa, J.-P. Kruth, 2009, Microstructure evolution of selective laser molten 316L stainless steel parts with laser re-melting, Proceedings of the Fifth International WLT-Conference on Lasers in Manufacturing (LIM), Munich, Germany.

10) J.-P. Kruth, E. Yasa, J. Deckers, 2009, Experimental investigation of laser surface re-melting for the improvement of selective laser melting process, Proc. of 14èmes Assises Européennes du prototypage Rapide, Paris, France (***Keynote paper***).

11) E. Yasa, J.-P. Kruth, 2009, An Experimental study of process parameters in laser marking, Proc. of 5th Int. Conf. and Exhibition on Design and Production of Machines and Dies/Molds, Kusadasi, Turkey, pp.213-221.

12) E. Yasa, J. Deckers, T. Craeghs, M. Badrossamay, J.-P. Kruth, 2009, Investigation on occurrence of elevated edges in SLM, Proc. of Solid Freeform Fabrication (SFF) Symposium, Austin, Texas, USA.

13) E. Yasa, J.-P. Kruth, 2009, Rapid Manufacturing research at the Catholic University of Leuven, US Turkey Workshop on Rapid Technologies, Istanbul, Turkey.

14) E. Yasa, J. Deckers, J.-P. Kruth, M. Rombouts, J. Luyten, 2009, Experimental investigation of Charpy impact tests on metallic SLM parts, 4th International Conference on Advanced Research in Virtual and Rapid Prototyping (VRAP) Conference, Leiria, Portugal ***(VRAP Best Paper Award).***

15) J.-P. Kruth, M. Badrossamay, E. Yasa, 2010, Part and material properties in Selective Laser Melting of metals, May, The International Symposium in Electromachining (ISEM XVI), May 2010, Shanghai, China (***Keynote paper***).

16) K. Kellens, W. Dewulf, W. Deprez, E. Yasa, J.R. Duflou, 2010, Environmental analysis of Selective Laser Melting and Selective Laser Sintering manufacturing processes, to be presented at CIRP Life Cycle Engineering, Anhui, China, May 2010.

17) E. Yasa, J. Deckers, J.-P. Kruth, M. Rombouts, J. Luyten, 2010, Investigation of sectoral scanning in Selective Laser Melting, accepted to be included in Proc. of 10th Biennial ASME Conference on Engineering Systems, Design and Analysis (ESDA 2010), 12-14 July, Istanbul, Turkey *(to be presented).*

18) E. Yasa, K. Kempen, J.-P. Kruth, L. Thijs, J. Van Humbeeck, 2010, Microstructure and mechanical properties of maraging steel 300 after selective laser melting, 21st Annual International Solid Freeform Fabrication (SFF) Symposium, August 9-11, Austin, Texas USA.

19) E. Yasa, J.-P.Kruth, 2010, Application of laser re-melting on SLM parts, accepted to be presented at the International Conference Polymers and Moulds Innovations PMI 2010, Gent, Belgium, 15-17 September.

20) K. Kellens, E. Yasa, W. Dewulf, J.R. Duflou, 2010, Environmental assessment of Selective Laser Melting and Selective Laser Sintering, Going Green Care Innovation 2010, November 8-11, Vienna, Austria.